



## **Terms and Conditions of Use of Digitised Theses from Trinity College Library Dublin**

### **Copyright statement**

All material supplied by Trinity College Library is protected by copyright (under the Copyright and Related Rights Act, 2000 as amended) and other relevant Intellectual Property Rights. By accessing and using a Digitised Thesis from Trinity College Library you acknowledge that all Intellectual Property Rights in any Works supplied are the sole and exclusive property of the copyright and/or other IPR holder. Specific copyright holders may not be explicitly identified. Use of materials from other sources within a thesis should not be construed as a claim over them.

A non-exclusive, non-transferable licence is hereby granted to those using or reproducing, in whole or in part, the material for valid purposes, providing the copyright owners are acknowledged using the normal conventions. Where specific permission to use material is required, this is identified and such permission must be sought from the copyright holder or agency cited.

### **Liability statement**

By using a Digitised Thesis, I accept that Trinity College Dublin bears no legal responsibility for the accuracy, legality or comprehensiveness of materials contained within the thesis, and that Trinity College Dublin accepts no liability for indirect, consequential, or incidental, damages or losses arising from use of the thesis for whatever reason. Information located in a thesis may be subject to specific use constraints, details of which may not be explicitly described. It is the responsibility of potential and actual users to be aware of such constraints and to abide by them. By making use of material from a digitised thesis, you accept these copyright and disclaimer provisions. Where it is brought to the attention of Trinity College Library that there may be a breach of copyright or other restraint, it is the policy to withdraw or take down access to a thesis while the issue is being resolved.

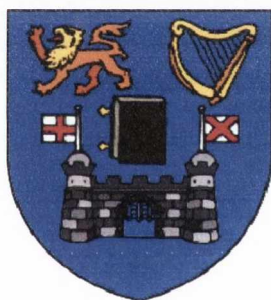
### **Access Agreement**

By using a Digitised Thesis from Trinity College Library you are bound by the following Terms & Conditions. Please read them carefully.

I have read and I understand the following statement: All material supplied via a Digitised Thesis from Trinity College Library is protected by copyright and other intellectual property rights, and duplication or sale of all or part of any of a thesis is not permitted, except that material may be duplicated by you for your research use or for educational purposes in electronic or print form providing the copyright owners are acknowledged using the normal conventions. You must obtain permission for any other use. Electronic or print copies may not be offered, whether for sale or otherwise to anyone. This copy has been supplied on the understanding that it is copyright material and that no quotation from the thesis may be published without proper acknowledgement.

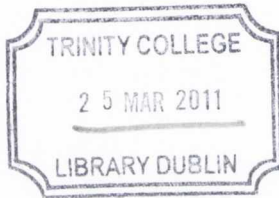
**Bipyridyl and Alkynyl-based Polyphenylenes:  
Tuning Photoluminescence  
in Metal-Organic Chromophores**

**Deanne Nolan**



**A Thesis submitted to the University of Dublin for the Degree of  
Doctor of Philosophy**

**School of Chemistry  
Trinity College Dublin  
January 2011**



THESIS  
9010

## **Declaration**

This thesis has not been submitted as an exercise for a degree at this or any other University. Except where acknowledgement is given, all work is original and was carried out by the author alone. I agree that the Library may lend or copy this thesis upon request.

## Summary

**Chapter 1** introduces two series of novel polyphenylene molecules with inherent ligand functionality. These are prepared *via* a sequence of Sonogashira cross-coupling reactions and [2+4] Diels-Alder cycloadditions and are fully characterised by NMR spectroscopy and analytical methods. The first series are asymmetric oligophenylene-substituted bipyridines, in which the polyaryl pendant is systematically increased in size, from a single phenyl-acetylene to a dendritic penta-phenyl benzene. The second ligand series represents a family of acetylene-functionalised hexaphenylbenzene molecules, from a single acetylene substituent to *ortho* and *para* configured di-ethynyl units. The alkynyl substituent allows an extension of  $\pi$ -electron delocalisation.

**Chapter 2** describes the preparation and characterisation of four asymmetric heteroleptic Ru(II) complexes, of general formula  $[\text{Ru}(\text{bpy})_2(\text{L})]^{2+}$ , where L is an asymmetric bipyridine ligand prepared in Chapter 1. Structural characterisation of two of these complexes by single crystal X-ray diffraction reveals a distorted octahedral geometry of the ligands about the Ru(II) centre, induced by the steric bulk of the polyaryl functionality. A full spectroscopic and electrochemical analysis of the complexes is undertaken. An acetylene moiety in L is shown to induce a red-shifted lower energy absorption band in the UV-Visible spectrum, compared to  $[\text{Ru}(\text{bpy})_3]^{2+}$ , due to extended  $\pi$ -conjugation. The effect of increasing the steric congestion and varying the electronic demand of the asymmetric ligand, L, on the lowest energy metal-to-ligand charge transfer emission energy is also investigated.

**Chapter 3** describes the preparation of four novel platinum(II) bis-acetylide complexes, two in *cis* square-planar geometry and two in *trans*. These incorporate either an uncyclised ethynyl-hexaphenylbenzene or a fused ligand ethynyl-HBC and monodentate or bidentate phosphines as auxiliary ligands. All the complexes are fully characterised by spectroscopic and analytical methods, including a complete photophysical study of the complexes. Both uncyclised and cyclised sets of Pt(II) compounds are dual-luminescent, possessing a high energy ligand-centred fluorescence and a lower energy phosphorescence, where the triplet excited state on the acetylide ( $^3\pi\pi^*$ ) is stabilised by the strong spin-orbit

coupling induced by the heavy metal. The *trans* arrangement of acetylide ligands on the Pt(II) centre is shown to be optimal for  $\pi$ -conjugation along the molecular axis.

**Chapter 4** details the synthesis and optical properties of complexes bearing both a polyphenylene bipyridine ligand and a Pt(II) acetylide. A series of complexes of general formula,  $[\text{Pt}(\text{N}^{\wedge}\text{N})(\text{C}\equiv\text{CAr})_2]$  are prepared, in which the diimine is held constant while the electronic and steric demands of the aryl acetylide co-ligands are altered, from electron-donating to electron-withdrawing to highly  $\pi$ -conjugated acetylides. Variable temperature  $^1\text{H}$  NMR spectroscopy indicates that the complexes are sterically constrained, an effect which is confirmed by intramolecular interactions in the X-ray crystal structures of two of the complexes. The photophysical properties of the complexes are investigated by UV-visible absorption spectroscopy, cyclic voltammetry and photoluminescence studies. With increasing electronic donicity, a red-shift in the lowest energy absorption band and the emission maximum is observed. The emissive excited states are assigned as  $^3(\text{ML})\text{LCT}$  for complexes containing unfused acetylide co-ligands and as  $^3\pi\pi^*$  for complexes with  $\pi$ -conjugated platforms.

**Chapter 5** provides a full account of the experimental details of this work.

## Acknowledgements

I would firstly like to sincerely thank my supervisor Professor Sylvia Draper for her support, encouragement and advice over my time in Trinity College, both as a postgraduate student and as an undergraduate. I would also like to express my gratitude to Dr. John O'Brien and Dr. Manuel R  ther for NMR analysis, Dr. Martin Feeney for mass spectrometry, to Dr. Tom McCabe, Dr. Sunil Varughese and Dr. Longsheng Wang for X-ray crystallography and to all the technical and administrative staff in the School of Chemistry – particularly Patsy, Brendan, Dorothy, Peggy, Kieron and Fred.

I would like to say a massive thank you also to everyone who has passed through the Draper research group over the last few years, many of whom I have been lucky enough to know as good friends. First of all to those who were there from the very beginning and helped me to settle into lab life very quickly, for all the help, good humour and boundless enthusiasm – Fran, Gar, Dilwyn, Pablo, Angelika, Dan, C  cile. To the current (and most recent) group members, B  len, Buddhie, Colin, Amy, Gear  id, Niamh, Vanesa, Colm, Lankani, Longsheng. Thank you for the chats and craic in the office and for being great co-workers. To the post-docs who have been and gone, thank you for your support – Lorraine, Ania, Tash, Sarath, Deborah, Carlos, Sunil, Philip, Oscar, Valerie. Most especially, thank you to B  len, Fran and Gar for endless help! And of course to those who got roped into proof-reading at the end, I really do appreciate your time and effort and I hope I can repay the favour some day.

To my brilliant and ever reliable past and present housemates and friends – Mary, Eimear, Sarah and Niamh – you have kept me sane with tea and chocolate!

Finally to my family- my parents, Michael and Deirdre, and my sister and brother, Emma and James, you are the most supportive, encouraging and the best family I could ever ask for – thank you for putting up with me and for always being on hand with kind words, an open ear and sensible advice.

Go raibh m  ile maith agaibh go l  ir.

## Table of Contents

<b>Declaration .....</b>	<b>i</b>
<b>Summary .....</b>	<b>ii</b>
<b>Acknowledgements .....</b>	<b>iv</b>
<b>Table of Contents.....</b>	<b>v</b>
<b>Abbreviations .....</b>	<b>xiii</b>
<b>List of Tables.....</b>	<b>xvii</b>
<b>List of Schemes.....</b>	<b>xviii</b>
<b>List of Figures .....</b>	<b>xviii</b>
<b>Chapter 1: Bipyridine and Alkynyl-based Polyaryl Ligands.....</b>	<b>1</b>
<b>1.1 Introduction.....</b>	<b>3</b>
1.1.1 Polycyclic Aromatic Hydrocarbons.....	3
1.1.2 Hexa- <i>peri</i> -hexabenzocoronene .....	3
1.1.2.1 <i>Materials applications of HBCs as processible PAH derivatives</i> .....	4
1.1.2.2 <i>Synthesis</i> .....	5
1.1.2.3 <i>Cyclodehydrogenation</i> .....	6
1.1.3 Nitrogen Hetero-SuperBenzene (N-HSB) .....	8
1.1.4 Hexaphenylbenzenes: Features and Applications.....	9
1.1.4.1 <i>Structurally rigid polyphenylene dendrimers</i> .....	10
1.1.4.2 <i>Hexaphenylbenzenes as molecular scaffolds</i> .....	11
1.1.4.3 <i>Hexaphenylbenzenes in host-guest frameworks</i> .....	13
1.1.4.4 <i>Polyphenylenes as ligands in encapsulated metal complexes</i> .....	13
1.1.4.5 <i>Hexaphenylbenzenes as ligands in organometallic complexes</i> .....	14
1.1.5 Functionalisation of polyphenylenes: Applications of the acetylene motif... 16	
1.1.5.1 <i>Molecular dyads</i> .....	16



1.1.5.2	<i>Polyphenylenes in transition metal complexes</i> .....	18
1.1.6	Ligand design: Bipyridine and hexaphenylbenzene functionalisation .....	19
<b>1.2</b>	<b>Ligand series A: Synthesis of polyaromatic-bipyridine ligands</b> .....	<b>21</b>
1.2.1	Synthesis of aryl-acetylene bipyridines 1 and 2.....	21
1.2.1.1	<sup>1</sup> H NMR spectra of 1 and 2.....	22
1.2.1.2	<sup>13</sup> C { <sup>1</sup> H} NMR Spectra of 1 and 2.....	23
1.2.1.3	<sup>19</sup> F NMR Spectrum of 2.....	25
1.2.2	Synthesis of polyphenylene-bipyridines 3, 4 and 5 .....	25
1.2.2.1	<i>Synthesis of 3</i> .....	26
1.2.2.2	<i>Syntheses of 4 and 5</i> .....	26
1.2.2.3	<i>Characterisation of polyphenylene ligands 3, 4 and 5</i> .....	29
1.2.2.3.1	<sup>1</sup> H NMR spectra of polyphenylene bipyridyl ligands 3, 4 and 5 .....	29
1.2.2.3.2	<sup>13</sup> C { <sup>1</sup> H} NMR Spectrum of 4 .....	31
1.2.3	Cyclodehydrogenation of bipyridyl-oligophenylene ligands.....	32
<b>1.3</b>	<b>Ligand Series B: Synthesis of polyaromatic ligands with one acetylene functional group</b> .....	<b>34</b>
1.3.1	Preparation of the synthetic precursor iodo-hexaphenylbenzene (18).....	34
1.3.2	Synthesis of ethynyl-hexaphenylbenzene (6) and ethynyl-HBC (7) .....	35
1.3.3	Characterisation of 19, 6 and 7 .....	37
1.3.3.1	<sup>1</sup> H NMR Spectra of hexaphenylbenzenes 19 and 6.....	37
1.3.3.2	<sup>13</sup> C { <sup>1</sup> H} NMR spectrum of ethynyl-hexaphenylbenzene (6).....	39
1.3.3.3	<sup>1</sup> H NMR Spectrum of ethynyl-HBC (7).....	40
<b>1.4</b>	<b>Ligand Series B: Synthesis of polyaromatic ligands with two acetylene functional groups</b> .....	<b>41</b>
1.4.1	Synthesis of hexaphenylbenzenes containing unsubstituted phenyl rings.....	41
1.4.2	Synthesis of <i>para</i> - and <i>ortho</i> - bis-ethynyl-hexaphenylbenzenes .....	43
1.4.2.1	<i>Characterisation of ortho- (31), (9) and para- (29), (8) compounds</i> .....	44

1.4.2.2	<i><sup>1</sup>H NMR spectra of target compounds: ortho-(9) and para-(8)</i>	45
<b>1.5</b>	<b>Summary and Conclusions</b>	<b>46</b>
<b>Chapter 2: Heteroleptic Ruthenium(II) Bipyridyl Complexes</b>		<b>49</b>
<b>2.1</b>	<b>Introduction</b>	<b>51</b>
2.1.1	Polypyridyl Ligands & Isomerism	51
2.1.2	Electronic transitions and photophysical properties of [Ru(bpy) <sub>3</sub> ] <sup>2+</sup>	52
2.1.3	Electrochemical behaviour of [Ru(bpy) <sub>3</sub> ] <sup>2+</sup>	54
2.1.4	Tuning of optical and redox properties of [Ru(bpy) <sub>3</sub> ] <sup>2+</sup> analogues	55
2.1.4.1	<i>Simultaneous <sup>3</sup>MLCT emission from two excited states</i>	56
2.1.4.2	<i>Re-ordering of excited states: <sup>3</sup>IL emission from Ru(II) complexes</i>	57
2.1.5	Selected applications of Ru(II) polypyridine complexes	57
2.1.6	Project Goals: Heteroleptic Ru(II) complexes with asymmetric ligands	59
<b>2.2</b>	<b>Synthesis of heteroleptic [Ru(bpy)<sub>2</sub>(L)](PF<sub>6</sub>)<sub>2</sub> complexes</b>	<b>61</b>
2.2.1	Synthesis of 33, 34, 35 and 36	61
2.2.2	X-Ray Crystallography: 33.2CHCl <sub>3</sub> .CH <sub>2</sub> Cl <sub>2</sub> and 35.2CHCl <sub>3</sub> .CH <sub>2</sub> Cl <sub>2</sub>	64
2.2.2.1	<i>Packing of 33.2CHCl<sub>3</sub>.CH<sub>2</sub>Cl<sub>2</sub> and 35.2CHCl<sub>3</sub>.CH<sub>2</sub>Cl<sub>2</sub> in the crystal</i>	68
2.2.3	NMR Spectroscopic Characterisation of 33, 34 35 and 36	70
2.2.3.1	<i><sup>1</sup>H and <sup>13</sup>C {<sup>1</sup>H} NMR spectra of 33 and 34</i>	71
2.2.3.1.1	<i><sup>1</sup>H NMR spectrum of [Ru(bpy)<sub>2</sub>(1)](PF<sub>6</sub>)<sub>2</sub> (33)</i>	71
2.2.3.1.2	<i><sup>13</sup>C {<sup>1</sup>H} NMR Spectrum of [Ru(bpy)<sub>2</sub>(1)](PF<sub>6</sub>)<sub>2</sub> (33)</i>	74
2.2.3.1.3	<i><sup>1</sup>H NMR Spectrum of [Ru(bpy)<sub>2</sub>(2)](PF<sub>6</sub>)<sub>2</sub> (34)</i>	77
2.2.3.1.4	<i><sup>13</sup>C {<sup>1</sup>H} NMR Spectrum of [Ru(bpy)<sub>2</sub>(2)](PF<sub>6</sub>)<sub>2</sub> (34)</i>	78
2.2.3.1.5	<i><sup>19</sup>F NMR Spectrum of [Ru(bpy)<sub>2</sub>(2)](PF<sub>6</sub>)<sub>2</sub> (34)</i>	80
2.2.3.2	<i>NMR Spectroscopic Characterisation of 35 and 36</i>	80
2.2.3.2.1	<i><sup>1</sup>H NMR Spectrum of 35</i>	81
2.2.3.2.2	<i><sup>1</sup>H NMR Spectrum of 36</i>	84
<b>2.3</b>	<b>UV-Visible Absorption Spectra</b>	<b>86</b>

2.3.1	Acetylene and polyphenylene-substituted bipyridine ligands 1, 2, 3 and 4...	86
2.3.2	Heteroleptic Ru(II) bipyridyl complexes 33, 34, 35 and 36 .....	88
<b>2.4</b>	<b>Electrochemical Properties of Ligands 1-4 and Ru(II) complexes 33-36.....</b>	<b>91</b>
<b>2.5</b>	<b>Emission Properties of Bipyridine Ligands and their Ru(II) complexes.....</b>	<b>96</b>
2.5.1	Emission properties of bipyridyl ligands 1, 2, 3 and 4 .....	96
2.5.1.1	<i>Room temperature and 77 K in solid state .....</i>	<i>98</i>
2.5.1.2	<i>Room temperature (CH<sub>3</sub>CN) and 77 K in frozen CH<sub>3</sub>CN (10<sup>-5</sup> M).....</i>	<i>99</i>
2.5.1.3	<i>Quantum Yields.....</i>	<i>101</i>
2.5.2	Emission Properties of Ru(II) heteroleptic complexes .....	103
2.5.2.1	<i>Solid State at 298 K and 77 K.....</i>	<i>104</i>
2.5.2.2	<i>Room temperature (CH<sub>3</sub>CN) and 77 K in frozen CH<sub>3</sub>CN (10<sup>-5</sup> M).....</i>	<i>106</i>
2.5.3	Nature of the emissive excited states in Ru(II) complexes 33-36.....	108
<b>2.6</b>	<b>Summary and Conclusions.....</b>	<b>110</b>
<b>Chapter 3:</b>	<b>Phosphorescent Pt(II) <math>\sigma</math>-acetylide Complexes</b>	
	<b>from Polyaromatic Ligands .....</b>	<b>113</b>
<b>3.1</b>	<b>Introduction.....</b>	<b>115</b>
3.1.1	Metal-alkynyl bonding.....	115
3.1.2	Organic and organometallic $\pi$ -conjugated materials .....	116
3.1.3	Pt-acetylide complexes: Monomers, oligomers, dendrimers and polymers	116
3.1.4	Pt-acetylide hexa- <i>peri</i> -hexabenzocoronenes & HBC complexes .....	118
3.1.5	Target Molecules: <i>Cis</i> and <i>Trans</i> Pt-acetylide complexes.....	120
<b>3.2</b>	<b>Synthesis of <i>cis</i> and <i>trans</i> Pt(II) complexes of acetylene-hexaphenylbenzene</b>	
	<b>(6) and acetylene-HBC (7).....</b>	<b>122</b>
3.2.1	Syntheses of 38 and 39: Ethynyl-hexaphenylbenzene (6) as $\sigma$ -acetylide...	123
3.2.1.1	<i><sup>1</sup>H NMR spectroscopic characterisation of 38.....</i>	<i>124</i>
3.2.1.2	<i><sup>13</sup>C NMR spectroscopic characterization of 38.....</i>	<i>127</i>
3.2.1.3	<i><sup>1</sup>H NMR characterisation of 39.....</i>	<i>128</i>

3.2.1.4	<i>The trans influence: effects on <sup>1</sup>H NMR chemical shifts of 39 vs. 38 ..</i>	130
3.2.1.5	<sup>13</sup> C { <sup>1</sup> H} NMR Characterisation of 39 .....	131
3.2.2	Syntheses of 40 and 41: Ethynyl-HBC as σ-acetylide.....	132
3.2.2.1	<sup>1</sup> H NMR spectroscopic characterization of 40 and 41 .....	134
3.2.2.2	Conc. and temp. dependence of <sup>1</sup> H NMR chemical shifts of 41 .....	136
3.2.2.3	<sup>13</sup> C { <sup>1</sup> H} NMR spectroscopic characterization of 40 and 41 .....	139
3.2.3	<sup>31</sup> P NMR and infrared spectroscopic analysis .....	140
3.2.4	An alternative route to <i>trans</i> -[Pt(6) <sub>2</sub> (PPh <sub>3</sub> ) <sub>2</sub> ] (38) .....	142
3.2.4.1	Characterisation of (42).....	143
<b>3.3</b>	<b>UV-Visible Absorption Spectra .....</b>	<b>145</b>
3.3.1	Ethynyl-hexaphenylbenzene (6), 39 ( <i>cis</i> -HPB) and 38 ( <i>trans</i> -HPB) .....	145
3.3.2	Ethynyl-HBC (7), 41 ( <i>cis</i> -HBC) and 40 ( <i>trans</i> -HBC) .....	147
<b>3.4</b>	<b>Electrochemical properties of ligands and <i>cis</i> and <i>trans</i> complexes .....</b>	<b>149</b>
<b>3.5</b>	<b>Photophysical properties of ligands and <i>cis</i> and <i>trans</i> complexes .....</b>	<b>152</b>
3.5.1	Emission properties of uncyclised ligand 6 and complexes 38 and 39 .....	152
3.5.1.1	Room temperature (CH <sub>2</sub> Cl <sub>2</sub> ) and 77 K in frozen CH <sub>2</sub> Cl <sub>2</sub> (10 <sup>-5</sup> M).....	153
3.5.1.2	Solid state at 298 K and 77 K.....	155
3.5.1.3	Nature of the emissive excited states in 6, 38 and 39.....	157
3.5.2	Emission properties of HBC ligand 7 and complexes 40 and 41 .....	158
3.5.2.1	Solid State at 298 K and 77 K .....	160
3.5.2.2	Room temperature (CH <sub>2</sub> Cl <sub>2</sub> ) and 77 K in frozen CH <sub>2</sub> Cl <sub>2</sub> (10 <sup>-5</sup> M).....	161
3.5.2.3	Emission profile of 40 and 41 in toluene (10 <sup>-5</sup> M).....	163
3.5.2.4	Nature of the emissive excited states in 7, 40 and 41.....	164
<b>3.6</b>	<b>Summary and Conclusions .....</b>	<b>166</b>

## **Chapter4:[Pt(N^N)(σ-acetylides)<sub>2</sub>]:**

### **Synthesis, Structure & Photophysics.....169**

<b>4.1</b>	<b>Introduction.....</b>	<b>171</b>
------------	--------------------------	------------

4.1.1	Room Temperature emission from [Pt(N <sup>^</sup> N)Cl <sub>2</sub> ] vs. [Pt(N <sup>^</sup> N <sup>^</sup> C)Cl]	172
4.1.2	Highly emissive [Pt(N <sup>^</sup> N)(C≡CR) <sub>2</sub> ] complexes	173
4.1.3	Applications of [Pt(diimine)(C≡CAr) <sub>2</sub> ]	175
<b>4.2</b>	<b>Synthesis: [Pt(N<sup>^</sup>N<sup>^</sup>C)Cl] (43) and [Pt(N<sup>^</sup>N)Cl<sub>2</sub>] (44) as precursors</b>	<b>176</b>
4.2.1	Synthetic procedure: 1 Step Method	177
4.2.2	Synthetic procedure: 2 Step Method	177
4.2.3	The serendipitous synthesis of [Pt(N <sup>^</sup> N <sup>^</sup> C)Cl] (43)	178
4.2.4	<sup>1</sup> H NMR Characterisation of [Pt(N <sup>^</sup> N)Cl <sub>2</sub> ] (44) and [Pt(N <sup>^</sup> N <sup>^</sup> C)Cl] (43)	179
4.2.5	X-Ray Crystal Structure of 43.H <sub>2</sub> O	182
<b>4.3</b>	<b>Synthesis and Characterisation of [Pt(N<sup>^</sup>N)(C≡C-R)<sub>2</sub>]</b>	<b>184</b>
4.3.1	Synthesis of 45 and 46	186
4.3.1.1	<sup>1</sup> H NMR Spectroscopic Characterisation of 45 and 46	186
4.3.1.2	<sup>13</sup> C { <sup>1</sup> H} NMR Spectroscopic Characterisation of 45	189
4.3.1.3	<sup>13</sup> C { <sup>1</sup> H} NMR Spectrum of 46	190
4.3.1.4	<sup>19</sup> F NMR Spectrum of 46	192
4.3.1.5	X-Ray Crystal Structure of 45.CH <sub>3</sub> OH.3H <sub>2</sub> O	192
4.3.1.6	Variable Temperature <sup>1</sup> H NMR Spectra of 46	195
4.3.2	Synthesis of the larger [Pt(N <sup>^</sup> N)(C≡CR) <sub>2</sub> ] complexes: 47, 48 and 49	198
4.3.2.1	<sup>1</sup> H NMR spectra of 47, 48 and 49	199
4.3.2.2	Variable Temperature <sup>1</sup> H NMR spectra of 47	204
4.3.2.3	<sup>13</sup> C NMR Spectra of 47 and 48	205
4.3.3	IR Spectroscopy of [Pt(N <sup>^</sup> N)(C≡CR) <sub>2</sub> ]	206
<b>4.4</b>	<b>The UV-Visible Absorption spectra of ligand &amp; complexes</b>	<b>208</b>
4.4.1	UV-Visible Absorption Spectra of ligand 4 and [Pt(N <sup>^</sup> N)Cl <sub>2</sub> ] (44)	208
4.4.2	UV-Visible Absorption Spectra of complexes 45-49	209
4.4.3	Solvent polarity: Solvatochromism	211
4.4.3.1	Solvatochromism in ligand 4 and [Pt(N <sup>^</sup> N)Cl <sub>2</sub> ]	211

4.4.3.2	<i>Solvatochromism in [Pt(N<sup>^</sup>N)(C≡CR)<sub>2</sub>] complexes (45-49)</i> .....	212
4.4.3.3	<i>Solvatochromism: lowest energy absorption band, complexes 45-49</i> ..	213
4.4.4	Nature of lowest energy excited state .....	213
<b>4.5</b>	<b>Electrochemical properties of [Pt(N<sup>^</sup>N)(C≡C<i>Ar</i>)<sub>2</sub>] .....</b>	<b>216</b>
<b>4.6</b>	<b>Photoluminescence Properties of 4 and 44-49 .....</b>	<b>220</b>
4.6.1	Emission properties of bipyridyl ligand 4.....	220
4.6.2	Emission spectra of [Pt(N <sup>^</sup> N)Cl <sub>2</sub> ] (44).....	222
4.6.3	Photoluminescence of [Pt(N <sup>^</sup> N)(C≡CR) <sub>2</sub> ] complexes (45-49) .....	223
4.6.3.1	<i>Group 1: Photoluminescence of 45, 46 and 48 .....</i>	<i>223</i>
4.6.3.1.1	<i>Solid state emission spectra of 45, 46 and 48 .....</i>	<i>224</i>
4.6.3.1.2	<i>Photoluminescence of 45, 46 and 48 in CH<sub>2</sub>Cl<sub>2</sub> solution (298 K) ...</i>	<i>226</i>
4.6.3.1.3	<i>Photoluminescence of 45, 46 and 48 in CH<sub>2</sub>Cl<sub>2</sub> solution (77 K) .....</i>	<i>229</i>
4.6.3.2	<i>Group 2: Photoluminescence of 47 and 49 .....</i>	<i>230</i>
4.6.3.2.1	<i>Solid state emission spectra of 47 and 49 .....</i>	<i>230</i>
4.6.3.2.2	<i>Photoluminescence of 47 and 49 in CH<sub>2</sub>Cl<sub>2</sub> solution (298 K) .....</i>	<i>231</i>
4.6.3.2.3	<i>Photoluminescence of 47 and 49 in CH<sub>2</sub>Cl<sub>2</sub> solution (77 K) .....</i>	<i>234</i>
4.6.4	Emission Quantum Yields .....	234
4.6.5	A comparison: The photoluminescence of (45, 46, 48) vs. (47, 49).....	235
<b>4.7</b>	<b>Summary and Conclusions .....</b>	<b>236</b>
<b>4.8</b>	<b>Future work.....</b>	<b>238</b>
4.8.1	[Pt(N <sup>^</sup> N)(σ-acetylide) <sub>2</sub> ] complexes: Diimine variation.....	238
4.8.2	Extension of the bipyridyl polyaromatic substituent .....	239
4.8.3	<i>Cis and Trans Pt(II)-acetylide HBC complexes .....</i>	<i>240</i>
<b>Chapter 5:</b>	<b>Experimental.....</b>	<b>243</b>
<b>5.1</b>	<b>General Methods.....</b>	<b>245</b>
<b>5.2</b>	<b>Synthesis of Bipyridyl and Acetylene-based polyphenylene Ligands .....</b>	<b>247</b>
<b>5.3</b>	<b>Ruthenium(II) Heteroleptic complexes.....</b>	<b>267</b>

5.4	<i>Cis &amp; Trans Pt(II) Complexes</i> .....	274
5.5	[Pt(N <sup>^</sup> N)(C≡C-R) <sub>2</sub> ]: Precursors and Complexes .....	279
	References.....	291
	Annex .....	299

## Abbreviations

<b>μL</b>	microlitre
<b>μs</b>	microsecond
<b>1D</b>	One-dimensional
<b>2D</b>	Two-dimensional
<b>A</b>	Area
<b>Å</b>	Ångström
<b>a.u.</b>	Atomic/absorbance/arbitrary units
<b>Abs.</b>	Absorption
<b>AcOH</b>	Acetic acid
<b>Anal.</b>	Elemental analysis
<b>Ar</b>	Aryl
<b>br</b>	Broad
<b>Calcd.</b>	calculated
<b>cat.</b>	Catalytic
<b>cm<sup>-1</sup></b>	wavenumber
<b>COSY</b>	Correlation Spectroscopy
<b>CT</b>	Charge transfer
<b>CV</b>	Cyclic voltammogram
<b>d</b>	Doublet
<b>DAPI</b>	4',6-diamidino-2-phenylindole dihydrochloride
<b>dd</b>	Doublet of doublets
<b>DEPT</b>	Distortionless Enhancement by Polarisation Transfer
<b>DMPD</b>	1,4-dimethylpiperazine-2,3-dione
<b>DMSO</b>	Dimethyl sulfoxide
<b>E</b>	Redox Potential
<b>e.s.</b>	excited state
<b>em.</b>	Emission
<b>eq.</b>	equivalents
<b>ES-MS</b>	Electrospray mass spectrometry
<b>EtOH</b>	Ethanol
<b>Exc.</b>	Excitation
<b>Fc/Fc<sup>+</sup></b>	Ferrocene/ferrocenium



<b>fl.</b>	Fluorescence
<b>g.s.</b>	ground state
<b>HBC</b>	Hexa- <i>peri</i> -hexabenzocoronene
<b>HMBC</b>	Heteronuclear Multi-Bond Connectivity
<b>HOMO</b>	Highest Occupied Molecular Orbital
<b>HPB</b>	Hexaphenylbenzene
<b>hr.</b>	Hour
<b>HSQC</b>	Heteronuclear Single Quantum Coherence
<b>Hz</b>	Hertz
<b>IC</b>	Internal conversion
<b>IL</b>	Intra-ligand
<b>IR</b>	Infrared
<b>ISC</b>	Inter-system crossing
<b><i>J</i></b>	Coupling constant
<b>L'LCT</b>	Ligand-to-ligand charge transfer
<b>LC</b>	Ligand-centred
<b>LF</b>	Ligand field
<b>LMCT</b>	Ligand-to-metal charge transfer
<b>LUMO</b>	Lowest Unoccupied Molecular Orbital
<b>M</b>	metal
<b>M</b>	Moles/litre (mol L <sup>-1</sup> )
<b>m</b>	Multiplet
<b>m</b>	Medium
<b>m.u.</b>	Mass units
<b><i>m/z</i></b>	Mass to charge ratio
<b>MALDI-TOF MS</b>	Matrix-assisted laser desorption/ionisation-time of flight mass spectrometry
<b>max.</b>	maximum
<b>MC</b>	Metal-centred
<b>Me</b>	Methyl
<b>MeOH</b>	Methanol
<b>mg</b>	milligram
<b>MHz</b>	Megahertz
<b>MLCT</b>	Metal-to-ligand charge transfer
<b>mmol</b>	millimole
<b>MS</b>	Mass spectrometry

<b>N-½HSB</b>	Half-cyclised nitrogen heterosuperbenzene
<b>N-HSB</b>	Nitrogen Heterosuperbenzene
<b>nm</b>	nanometre
<b>NMR</b>	Nuclear Magnetic Resonance
<b>NOE</b>	Nuclear Overhauser effect
<b>ns</b>	nanosecond
<b>OLED</b>	Organic Light Emitting Device
<b>PAH</b>	Polycyclic Aromatic Hydrocarbon
<b>PAO</b>	Platinum Acetylide Oligomer
<b>pd</b>	<i>Pseudo</i> -doublet
<b>Ph</b>	Phenyl
<b>phen</b>	1,10-phenanthroline
<b>PIFA</b>	(Bis(trifluoroacetoxy)iodo)benzene
<b>PLED</b>	Polymer Light Emitting Device
<b>ppm</b>	Parts per million
<b>Pr</b>	propyl
<b>pt</b>	<i>Pseudo</i> -triplet
<b>q</b>	Quartet
<b>Q / quat.</b>	Quaternary carbon
<b>R.T.</b>	Room temperature
<b>ROESY</b>	Rotating Frame Overhauser Effect Spectroscopy
<b>s</b>	Singlet
<b>s</b>	Strong
<b>sat.</b>	Saturated
<b>SCE</b>	Saturated calomel electrode
<b>sh</b>	shoulder
<b>SOC</b>	Spin orbit coupling
<b>T</b>	triplet (excited state)
<b>t</b>	triplet (NMR)
<b><sup>t</sup>Bu</b>	<i>tertiary</i> -butyl
<b>Terpy</b>	2,2':6',2''-terpyridine
<b>THF</b>	Tetrahydrofuran
<b>TLC</b>	Thin-layer chromatography
<b>TMS</b>	Trimethylsilyl
<b>TOCSY</b>	Total Correlation Spectroscopy
<b>UV-Vis</b>	Ultraviolet-visible

<b>V</b>	Volts
<b>vs.</b>	versus
<b>Wk or w</b>	Weak
<b>WOLED</b>	White-light emitting devices
<b>xs.</b>	Excess
<b><math>\delta</math></b>	Chemical shift
<b><math>\Delta E_p</math></b>	Peak potential separation
<b><math>\Delta E_s</math></b>	Stokes shift
<b><math>\varepsilon</math></b>	Molar extinction coefficient
<b><math>\eta</math></b>	Refractive index
<b><math>\lambda</math></b>	Wavelength
<b><math>\tau</math></b>	Excited state Lifetime
<b><math>\nu</math></b>	Stretching frequency
<b><math>\Phi</math></b>	Quantum yield

## List of Tables

Table 1.1: Electrospray mass spectral data for <b>11</b> , <b>13</b> , <b>3</b> , <b>4</b> and <b>5</b> (THF).....	29
Table 1.2: Comparative <sup>1</sup> H NMR chemical shifts, signal multiplicity and coupling constants for ligands <b>1</b> , <b>2</b> , <b>11</b> , <b>3</b> , <b>4</b> and <b>5</b> in CDCl <sub>3</sub> .....	31
Table 1.3: Comparative <sup>13</sup> C { <sup>1</sup> H} NMR chemical shifts for ligands <b>1</b> , <b>2</b> , <b>11</b> , <b>3</b> , <b>4</b> and <b>5</b> in CDCl <sub>3</sub> .....	32
Table 1.4: Mass spectral data for <b>19</b> , <b>6</b> , and <b>7</b> .....	37
Table 1.5: Electrospray mass spectral data for <b>31</b> , <b>9</b> , <b>29</b> and <b>8</b> .....	45
Table 2.1: Electrospray mass spectral data for complexes <b>33</b> , <b>34</b> , <b>35</b> and <b>36</b> .....	63
Table 2.2: Selected bond lengths (Å) bond angles (°) and tilt angles (°) for <b>33</b> and <b>35</b> .....	66
Table 2.3: <sup>1</sup> H and <sup>13</sup> C NMR chemical shifts and signal multiplicity for <b>33</b> and <b>34</b> in CD <sub>3</sub> CN.....	78
Table 2.4: UV-Visible Spectral Data for Ligands <b>1</b> , <b>2</b> , <b>3</b> and <b>4</b> and their heteroleptic Ru(II) complexes <b>33</b> , <b>34</b> , <b>35</b> and <b>36</b> in CH <sub>3</sub> CN (~10 <sup>-5</sup> M).....	87
Table 2.5: UV-Visible Absorption maxima (λ, nm) of lowest energy absorption band ( <b>1-4</b> ).....	88
Table 2.6: UV-Visible Absorption maxima (λ, nm) of the lowest energy absorption bands for complexes <b>33-36</b> .....	90
Table 2.7: Electrochemical Data for ligands <b>1-4</b> and Ru(II) complexes <b>33-36</b> .....	92
Table 2.8: Emission data for <b>1</b> , <b>2</b> , <b>3</b> and <b>4</b> in solid state and solution (CH <sub>3</sub> CN) 298 K, 77K.....	97
Table 2.9: Emission data for Ru(II) complexes <b>33</b> , <b>34</b> , <b>35</b> and <b>36</b> in solid state and in solution (CH <sub>3</sub> CN) at 298 K and 77 K.....	103
Table 3.1: <sup>1</sup> H NMR spectroscopic data and assignments of aromatic protons in <b>38</b> and <b>39</b> .....	131
Table 3.2: <sup>1</sup> H NMR chemical shifts of <b>41</b> (δ, ppm) of aromatic protons as determined from temperature and concentration dependent NMR spectra, d <sub>2</sub> -C <sub>2</sub> D <sub>2</sub> Cl <sub>4</sub> .....	138
Table 3.3: Comparative <sup>13</sup> C NMR chemical shifts of complexes <b>38-41</b> .....	139
Table 3.4: <sup>31</sup> P { <sup>1</sup> H} NMR and IR spectroscopic data for <b>38</b> , <b>39</b> , <b>40</b> and <b>41</b> .....	141
Table 3.5: UV-Visible Spectral Data for <b>6</b> , <b>7</b> , <b>39</b> , <b>41</b> , <b>38</b> and <b>40</b> in CH <sub>2</sub> Cl <sub>2</sub> (~10 <sup>-5</sup> M).....	146
Table 3.6: UV-Visible Absorption maxima (λ, nm) of lowest energy absorption band for ligand <b>6</b> and complexes <b>38</b> and <b>39</b> in THF, CH <sub>2</sub> Cl <sub>2</sub> and toluene solutions (~10 <sup>-5</sup> M).....	147
Table 3.7: UV-Visible Absorption maxima (λ, nm) of β, p and lowest energy absorption band for HBC ligand <b>7</b> and complexes <b>40</b> and <b>41</b> .....	149
Table 3.8: Electrochemical data for <b>6</b> , <b>7</b> , <b>39</b> , <b>41</b> , <b>38</b> and related Pt-HBC complex.....	150
Table 3.9: Emission data for ligand <b>6</b> , <b>38</b> and <b>39</b> in solid state and solution (CH <sub>2</sub> Cl <sub>2</sub> ).....	153
Table 3.10: Emission data for <b>7</b> , <b>40</b> and <b>41</b> in solid state and in solution (CH <sub>2</sub> Cl <sub>2</sub> ).....	159
Table 4.1: <sup>1</sup> H NMR spectroscopic data and assignments of bipyridine protons in ligand <b>4</b> and complexes <b>43</b> and <b>44</b> reported in CDCl <sub>3</sub> . Chemical shifts in ppm.....	180
Table 4.2: Selected bond lengths (Å) and bond angles (°) for <b>43</b> .....	183
Table 4.3: <sup>1</sup> H NMR spectroscopic data and assignments complexes <b>45</b> and <b>46</b> .....	187
Table 4.4: Comparative <sup>13</sup> C NMR chemical shifts and coupling constants for carbon-fluorine through bond interactions in <b>46</b> .....	191
Table 4.5: Selected bond lengths (Å) and bond angles (°) for <b>45</b> ( <sup>t</sup> Bu).....	194
Table 4.6: HR MALDI-TOF mass spectral data for complexes <b>47</b> , <b>48</b> and <b>49</b> ( <i>m/z</i> in m.u.).....	199
Table 4.7: <sup>1</sup> H NMR spectroscopic data and assignments for <b>47</b> , <b>48</b> and <b>49</b> .....	200
Table 4.8: <sup>13</sup> C { <sup>1</sup> H} NMR spectroscopic data and assignments for <b>47</b> , <b>48</b> and <b>49</b> .....	206
Table 4.9: Selected IR bands of [Pt(N <sup>^</sup> N)(C≡CR) <sub>2</sub> ] complexes.....	207
Table 4.10: UV-Visible Spectral Data for <b>4</b> , <b>44</b> and complexes, Pt(N <sup>^</sup> N)(C≡CR) <sub>2</sub> in CH <sub>2</sub> Cl <sub>2</sub> .....	208
Table 4.11: UV-Visible Absorption wavelengths (λ, nm) of lowest energy absorption bands of complexes <b>45</b> to <b>49</b> .....	211

Table 4.12: Lower energy Absorption bands ( $\lambda$ , nm) of <b>44</b> in CH <sub>3</sub> CN, CH <sub>2</sub> Cl <sub>2</sub> and Toluene .....	212
Table 4.13: Lowest energy absorption bands ( $\lambda$ , nm) for <b>45-49</b> in CH <sub>3</sub> CN, THF and Toluene .....	212
Table 4.14: Electrochemical Data for ligand <b>4</b> , [Pt(N <sup>^</sup> N)Cl <sub>2</sub> ] ( <b>44</b> ) and complexes 45-49 .....	217
Table 4.15: Emission data for ligand <b>4</b> (298 K, 77K) in solid state and solution (CH <sub>2</sub> Cl <sub>2</sub> ).....	221
Table 4.16: Emission data for complex <b>44</b> in solid state and in solution (CH <sub>2</sub> Cl <sub>2</sub> ).....	223
Table 4.17: Emission data for <b>45</b> , <b>46</b> and <b>48</b> in solid state and solution (CH <sub>2</sub> Cl <sub>2</sub> ) at 298 K, 77K..	224
Table 4.18: Emission data for <b>47</b> and <b>49</b> in solid state and solution (CH <sub>2</sub> Cl <sub>2</sub> ) at 298 K, 77K.....	230

## List of Schemes

Scheme 1.1: Synthesis of symmetrical HBC derivatives via cyclotrimerisation.....	5
Scheme 1.2: Synthetic strategy for hexaphenylbenzene derivatives with lower symmetry. ....	6
Scheme 1.3: Arenium cation (a) and Radical cation (b) mechanisms for the conversion of o-terphenyl (i) to triphenylene (ii).....	7
Scheme 1.4: Synthesis of a rigid polyphenylene dendrimer. ....	11
Scheme 1.5: Ru(II) dendritic polypyridine complexes, G1 and G2. ....	14
Scheme 1.6: Syntheses of precursor <b>10</b> and aryl-acetylene ligands <b>1</b> and <b>2</b> . ....	21
Scheme 1.7: Synthesis of <b>3</b> .....	26
Scheme 1.8: The syntheses of precursors to <b>4</b> and <b>5</b> . ....	27
Scheme 1.9: Syntheses of polyaryl bipyridine ligands <b>4</b> and <b>5</b> . ....	28
Scheme 1.10: Cyclodehydrogenation of <b>3</b> (Me <sub>2</sub> ) and <b>4</b> (Ar <sub>5</sub> ).....	33
Scheme 1.11: Cyclodehydrogenation of a terpyridyl-polyphenylene compound. ....	34
Scheme 1.12: Synthesis of iodo-hexaphenylbenzene ( <b>18</b> ).....	35
Scheme 1.13 : Synthesis of ethynyl-hexaphenylbenzene ( <b>6</b> ) and ethynyl-HBC ( <b>7</b> ).....	36
Scheme 1.14: Synthesis of hexaphenylbenzene ( <b>25</b> ).....	42
Scheme 1.15: Synthesis of hexaphenylbenzene ( <b>27</b> ).....	42
Scheme 1.16: Synthesis of <i>ortho</i> - ( <b>9</b> ) and <i>para</i> - ( <b>8</b> ) bis-ethynyl-hexaphenylbenzenes.....	44
Scheme 2.1: Synthesis of Ru(II) complexes: <b>33</b> , <b>34</b> , <b>35</b> and <b>36</b> . ....	62
Scheme 3.1: Synthesis of <i>trans</i> -[Pt( <b>6</b> ) <sub>2</sub> (PPh <sub>3</sub> ) <sub>2</sub> ] ( <b>38</b> ) and <i>cis</i> -[Pt( <b>6</b> ) <sub>2</sub> (dppe)] ( <b>39</b> ). ....	123
Scheme 3.2: Synthesis of <i>trans</i> -[Pt( <b>7</b> ) <sub>2</sub> (PPh <sub>3</sub> ) <sub>2</sub> ] ( <b>40</b> ) and <i>cis</i> -[Pt( <b>7</b> ) <sub>2</sub> (dppe)] ( <b>41</b> ). ....	133
Scheme 3.3: Attempted preparation of <b>38</b> – actual synthesis of <i>cis</i> -[Pt( <b>6</b> ) <sub>2</sub> (PPh <sub>3</sub> ) <sub>2</sub> ] ( <b>42</b> ). ....	143
Scheme 4.1: General synthetic route to [Pt(N <sup>^</sup> N <sup>^</sup> C)Cl] ( <b>43</b> ). ....	177
Scheme 4.2: Proposed 2-step synthesis of <b>50</b> , subsequent reaction to form cyclometallated <b>43</b> ...	178
Scheme 4.3: Synthesis of [Pt(N <sup>^</sup> N)Cl <sub>2</sub> ] ( <b>44</b> ). ....	179
Scheme 4.4: General reaction scheme: synthesis of diimine Pt(II) bis $\sigma$ -acetylides .....	185

## List of Figures

Figure 1.1: Examples of PAHs. ....	3
Figure 1.2: Structures of N-HSB and N- $\frac{1}{2}$ HSB .....	8
Figure 1.3: Functionalised hexaphenylbenzene displaying photoinduced molecular switching. ....	12
Figure 1.4: Hexaphenylbenzenes organic derivatives and organometallic complexes.....	15
Figure 1.5: Ru(II)-Os(II) Molecular scale dyads with aromatic and Pt(II) alkynyl spacer units.....	17
Figure 1.6: Dinuclear Ru(II) rod-like systems bridged by phenylene spacers.....	18
Figure 1.7: Target bipyridine, hexaphenylbenzene and HBC ligands. ....	20

Figure 1.8: $^1\text{H}$ NMR spectra of ligands <b>1</b> and <b>2</b> in $\text{CDCl}_3$ (400.1 MHz, R.T.).	22
Figure 1.9: $^{13}\text{C}$ $\{^1\text{H}\}$ NMR spectra of <b>1</b> and <b>2</b> showing the aromatic regions in $\text{CDCl}_3$	24
Figure 1.10: $^{19}\text{F}$ NMR spectrum of <b>2</b> in $\text{CDCl}_3$ (376.5 MHz, R.T.).	25
Figure 1.11: $^1\text{H}$ NMR spectra of <b>3</b> , <b>4</b> and <b>5</b> in $\text{CDCl}_3$	30
Figure 1.12: $^{13}\text{C}$ $\{^1\text{H}\}$ DEPT 90 experiment of <b>4</b> showing the aromatic region ( $\text{CDCl}_3$ )	32
Figure 1.13: $^1\text{H}$ NMR spectra of <b>19</b> and <b>6</b> in $\text{CDCl}_3$ at room temperature ( $\text{CDCl}_3$ )	38
Figure 1.14: $^{13}\text{C}$ $\{^1\text{H}\}$ NMR spectrum of <b>6</b> ( $\text{CDCl}_3$ )	39
Figure 1.15: $^1\text{H}$ NMR spectrum of <b>7</b> ( $\text{CDCl}_3$ , 400 MHz, R.T.) with inset <i>tert</i> -butyl region.	40
Figure 1.16: $^1\text{H}$ NMR spectra of <b>9</b> (400 MHz) and <b>8</b> (600 MHz) in $\text{CDCl}_3$ at room temperature.	46
Figure 2.1: Optical and geometric isomers of tris-diimine Ru(II) complexes.	51
Figure 2.2: Schematic molecular orbital diagram for an octahedral Ru(II) polypyridyl complex.	52
Figure 2.3: Jablonski energy level diagram for $[\text{Ru}(\text{bpy})_3]^{2+}$ complexes.	53
Figure 2.4: Substituent effects on $^1\text{MLCT}$ absorption band and $^3\text{MLCT}$ emission energy	55
Figure 2.5: Spectroscopic data of dual emissive heteroleptic Ru(II) complexes.	56
Figure 2.6: Ethynylpyrene-substituted Ru(II) heteroleptic tris-diimine complex	57
Figure 2.7: Heteroleptic Ru(II) complexes incorporating asymmetric bipyridine ligands.	60
Figure 2.8: Perspective view of the crystal structure of <b>33</b>	64
Figure 2.9: Perspective view of the crystal structure of <b>35</b> .	65
Figure 2.10: Crystal packing of molecules of <b>33</b> .	68
Figure 2.11: Expanded crystal packing in <b>33</b> viewed along the b-axis.	69
Figure 2.12: Packing of molecules of <b>35</b> in the crystal lattice as viewed along the a axis.	70
Figure 2.13: NMR numbering scheme for $[\text{Ru}(\text{bpy})_2(\mathbf{1})](\text{PF}_6)_2$ ( <b>33</b> ), $[\text{Ru}(\text{bpy})_2(\mathbf{2})](\text{PF}_6)_2$ ( <b>34</b> ).	71
Figure 2.14: $^1\text{H}$ NMR spectrum of <b>33</b> in $\text{CD}_3\text{CN}$ (600.1 MHz, R.T.).	72
Figure 2.15: $^1\text{H}$ - $^1\text{H}$ COSY experiment of <b>33</b> .	73
Figure 2.16: $^1\text{H}$ - $^{13}\text{C}$ HMBC experiment of <b>33</b> .	74
Figure 2.17: Aromatic region of the $^{13}\text{C}$ $\{^1\text{H}\}$ NMR DEPT 90 spectrum of <b>33</b> ( $\text{CD}_3\text{CN}$ )	75
Figure 2.18: HMBC experiment of <b>33</b>	76
Figure 2.19: $^1\text{H}$ NMR spectrum of <b>34</b> in $\text{CD}_3\text{CN}$ (600.1 MHz, R.T.).	77
Figure 2.20: $^{13}\text{C}$ $\{^1\text{H}\}$ NMR spectrum of <b>34</b> ( $\text{CD}_3\text{CN}$ , 150.9 MHz, R.T.)	79
Figure 2.21: $^{19}\text{F}$ NMR of <b>34</b> in $\text{CD}_3\text{CN}$ (376.6 MHz, R.T.).	80
Figure 2.22: NMR numbering scheme for $[\text{Ru}(\mathbf{3})(\text{bpy})_2](\text{PF}_6)_2$ ( <b>35</b> ), $[\text{Ru}(\mathbf{4})(\text{bpy})_2](\text{PF}_6)_2$ ( <b>36</b> )	81
Figure 2.23: $^1\text{H}$ NMR spectrum of <b>35</b> in $\text{CD}_3\text{CN}$ (600.1 MHz, R.T.).	82
Figure 2.24: ROESY experiment for <b>35</b> .	83
Figure 2.25: Comparative $^1\text{H}$ NMR spectra and NOE experiments (ii, iii) for <b>35</b> .	84
Figure 2.26: $^1\text{H}$ NMR spectrum of <b>36</b> recorded in $\text{CD}_3\text{CN}$ (150.9 MHz, R.T.).	85
Figure 2.27: UV-Visible absorption spectra of ligands <b>1</b> , <b>2</b> , <b>3</b> and <b>4</b> ( $\text{CH}_3\text{CN}$ )	86
Figure 2.28: UV-Visible absorption spectra of Ru(II) complexes <b>33</b> , <b>34</b> , <b>35</b> and <b>36</b> in $\text{CH}_3\text{CN}$	89
Figure 2.29: CVs of ligands <b>1</b> and <b>4</b> showing ligand-based oxidation process.	91
Figure 2.30: CVs of <b>33</b> , <b>34</b> , <b>35</b> and <b>36</b> showing Ru(II)-Ru(III) reversible oxidation processes.	93
Figure 2.31: CVs of Ru(II) complexes <b>33</b> , <b>34</b> and <b>35</b> showing ligand-centred reductions	94
Figure 2.32: Emission spectra of <b>1-4</b> & excitation spectrum of <b>1</b> , solid state 298 K.	98
Figure 2.33: Emission spectra of ligands <b>1-4</b> in solid state at 77 K	99
Figure 2.34: Emission spectra of <b>1-4</b> , excitation spectra of <b>2</b> , <b>4</b> , degassed $\text{CH}_3\text{CN}$ at 298 K.	100
Figure 2.35: Emission spectra of complexes <b>33-36</b> , solid state 298 K	104
Figure 2.36: Emission spectra of complexes <b>33-36</b> in solid state at 77 K	105
Figure 2.37: Excitation spectra for complexes <b>34</b> and <b>36</b> and emission spectra for complexes <b>33-36</b> in degassed $\text{CH}_3\text{CN}$	107

Figure 2.38: Emission spectra of complexes <b>33-36</b> in CH <sub>3</sub> CN (~10 <sup>-5</sup> M) at 77 K .....	108
Figure 2.39: Jablonski energy level diagram for complexes <b>33-36</b> .....	108
Figure 3.1: Structures of Pt-acetylide oligomers. ....	117
Figure 3.2: Structure and luminescence properties: branched-alkynyl Pt(II)-acetylides.....	118
Figure 3.3: Structures of Pt(II)-acetylide HBC complexes prepared to date.....	119
Figure 3.4: Ru(II) coordination complexes of N-doped and pyridine-appended HBC derivatives.....	120
Figure 3.5: <i>Cis</i> and <i>trans</i> Pt(II)-acetylide complexes .....	121
Figure 3.6: <sup>1</sup> H NMR spectrum of <b>38</b> in CDCl <sub>3</sub> (600.1 MHz, R.T.) showing the aromatic region..	125
Figure 3.7: Compiled <sup>1</sup> H NMR experiments for <b>38</b> (in CDCl <sub>3</sub> ) .....	126
Figure 3.8: <sup>13</sup> C { <sup>1</sup> H} DEPT 45 experiment for <b>38</b> (CDCl <sub>3</sub> , 150.9 MHz, R.T.).....	127
Figure 3.9: <sup>1</sup> H NMR spectrum of <b>39</b> (CDCl <sub>3</sub> , 600.1 MHz, R.T.) showing the aromatic region.....	129
Figure 3.10: <sup>13</sup> C NMR spectrum of <i>cis</i> -[Pt( <b>6</b> ) <sub>2</sub> (dpe)]( <b>39</b> ) (CDCl <sub>3</sub> ).....	132
Figure 3.11: <sup>1</sup> H NMR spectra of <b>40</b> (600.1 MHz, R.T.) and <b>41</b> (400.1 MHz, R.T.) in CDCl <sub>3</sub> .....	134
Figure 3.12: Long-range <sup>1</sup> H- <sup>1</sup> H COSY experiment for <b>40</b> ( <i>trans</i> -HBC) in CDCl <sub>3</sub> .....	135
Figure 3.13: Temperature-dependent <sup>1</sup> H NMR spectra of <b>41</b> .....	137
Figure 3.14: <sup>13</sup> C { <sup>1</sup> H} DEPT 90 experiment for <b>40</b> (CDCl <sub>3</sub> , 150.9 MHz, R.T.).....	139
Figure 3.15: <sup>31</sup> P { <sup>1</sup> H} NMR spectra of <b>38</b> and <b>39</b> (CDCl <sub>3</sub> , 162 MHz, R.T.) .....	141
Figure 3.16: <sup>1</sup> H NMR spectra of <b>38</b> and <b>42</b> (CDCl <sub>3</sub> ) .....	144
Figure 3.17: Normalised UV-Visible absorption spectra of <b>6</b> , <b>38</b> and <b>39</b> in CH <sub>2</sub> Cl <sub>2</sub> (10 <sup>-5</sup> M). .....	145
Figure 3.18: Normalised UV-Visible absorption spectra of <b>7</b> , <b>40</b> and <b>41</b> in CH <sub>2</sub> Cl <sub>2</sub> (~10 <sup>-5</sup> M). .....	148
Figure 3.19: CVs of <b>7</b> and <b>41</b> showing the Pt(II) and ligand-based oxidation processes. ....	151
Figure 3.20: Cyclic voltammograms of <b>38</b> and <b>39</b> showing the Pt(II) oxidation process.....	152
Figure 3.21: Emission spectra of <b>6</b> , <b>39</b> and <b>38</b> in argon-degassed CH <sub>2</sub> Cl <sub>2</sub> at 298K .....	154
Figure 3.22: Emission spectra of <b>6</b> , <b>39</b> and <b>38</b> in frozen CH <sub>2</sub> Cl <sub>2</sub> at 77 K .....	155
Figure 3.23: Solid state emission spectra of ligand <b>6</b> and complexes <b>38</b> and <b>39</b> , R.T.....	156
Figure 3.24: Solid state emission spectra of ligand <b>6</b> and complexes <b>38</b> and <b>39</b> at 77 K .....	156
Figure 3.25: Jablonski energy level diagram for ligand <b>6</b> and <b>38</b> ( <i>trans</i> -HPB) and <b>39</b> ( <i>cis</i> -HPB). ..	157
Figure 3.26: Solid state emission spectra of ligand <b>7</b> and complexes <b>40</b> and <b>41</b> , R.T. ....	160
Figure 3.27: Solid state emission spectra of ligand <b>7</b> and complexes <b>40</b> and <b>41</b> at 77 K .....	161
Figure 3.28: Emission spectra of <b>7</b> , <b>41</b> and <b>40</b> , and excitation spectrum of <b>7</b> , in argon-degassed CH <sub>2</sub> Cl <sub>2</sub> (~10 <sup>-5</sup> M) at 298 K .....	162
Figure 3.29: (a) Emission spectra of <b>40</b> and <b>41</b> in CH <sub>2</sub> Cl <sub>2</sub> at 77 K and in oxygenated solution at 298 K. (b) Images deoxygenated and oxygenated CH <sub>2</sub> Cl <sub>2</sub> solutions (298 K) of <b>40</b> .....	163
Figure 3.30: Normalised emission spectra of <b>40</b> and <b>41</b> in toluene solution (~10 <sup>-5</sup> M).....	164
Figure 3.31: Jablonski energy level diagram: ligand ( <b>7</b> ) and <b>40</b> ( <i>trans</i> -HBC) and <b>41</b> ( <i>cis</i> -HBC)..	165
Figure 4.1: Bidentate (N <sup>^</sup> N) and tridentate (N <sup>^</sup> N <sup>^</sup> C) coordination modes of ligand <b>4</b> .....	171
Figure 4.2: Relative energy level diagrams showing room temperature excited states of [Pt(bpy)Cl <sub>2</sub> ] and [Pt(N <sup>^</sup> N <sup>^</sup> C)Cl]. Structure of WOLED-incorporated complex. ....	173
Figure 4.3: Effect of varying the diimine and acetylide on the photophysical properties of [Pt(N <sup>^</sup> N)(C≡C <sup>Ar</sup> ) <sub>2</sub> ] systems .....	174
Figure 4.4: Vapoluminescent behaviour of a Pt(II) diimine bis-acetylide complex .....	175
Figure 4.5: Photochromic bis-alkynyl Pt(II) diimine complex and photophysical properties .....	176
Figure 4.6: <sup>1</sup> H NMR spectra of <b>44</b> (600.1 MHz, R.T.) and <b>43</b> (400.1 MHz, R.T.) in CDCl <sub>3</sub> . ....	180
Figure 4.7: Perspective view of <b>43</b> , with selected atomic numbering shown.....	182
Figure 4.8: A packing diagram of <b>43</b> along the b-axis, showing π-interactions. ....	183
Figure 4.9: Packing arrangement of <b>43</b> viewed down the c-axis. ....	184
Figure 4.10: Acetylide substituents used to generate complexes [Pt(N <sup>^</sup> N)(C≡C-R) <sub>2</sub> ].....	185

Figure 4.11: $^1\text{H}$ NMR spectra of the aromatic regions of <b>45</b> ( $^i\text{Bu}$ ) and <b>46</b> ( $\text{CF}_3$ ) in $\text{CDCl}_3$ .....	187
Figure 4.12: Aromatic region of the $^{13}\text{C}$ DEPT-90 experiment for <b>45</b> ( $\text{CDCl}_3$ ).....	189
Figure 4.13: HMBC spectrum of <b>45</b> between $\delta$ 7.0-7.5 ppm ( $^1\text{H}$ ), and $\delta$ 80-106 ppm ( $^{13}\text{C}$ ).....	190
Figure 4.14: $^{13}\text{C}$ NMR spectrum ( $\text{CDCl}_3$ , 150.9 MHz, R.T.).....	191
Figure 4.15: $^{19}\text{F}$ NMR spectrum of <b>46</b> in $\text{CDCl}_3$ (376 MHz, R.T.).....	192
Figure 4.16: Perspective view of a molecule of <b>45</b> .....	193
Figure 4.17: Perspective view of <b>45</b> showing intramolecular interactions.....	195
Figure 4.18: Variable temperature $^1\text{H}$ NMR spectra of <b>46</b> in $d_6$ -DMSO from 20-100 $^\circ\text{C}$ .....	197
Figure 4.19: $^1\text{H}$ NMR spectrum showing the aromatic regions of <b>47</b> and <b>48</b> ( $\text{CDCl}_3$ ) .....	201
Figure 4.20: $^1\text{H}$ NMR spectrum of <b>49</b> ( $d_2$ - $\text{C}_2\text{D}_2\text{Cl}_4$ , 400.1 MHz, 40 $^\circ\text{C}$ ).....	202
Figure 4.21: $^1\text{H}$ NMR spectrum of $[\text{Pt}(\text{N}^{\wedge}\text{N})(\text{HPB})_2]$ ( <b>48</b> ) ( $\text{CDCl}_3$ , 600.1 MHz, R.T.) .....	204
Figure 4.22: Variable temperature $^1\text{H}$ NMR spectra of <b>47</b> in $d_6$ -DMSO from 20-90 $^\circ\text{C}$ .....	205
Figure 4.23: UV-Visible absorption spectra of <b>4</b> , <b>44</b> and <b>45</b> in $\text{CH}_2\text{Cl}_2$ ( $10^{-5}$ M).....	209
Figure 4.24: UV-Visible absorption spectra of Pt(II) complexes ( <b>45-49</b> ) in $\text{CH}_2\text{Cl}_2$ .....	210
Figure 4.25: UV-Visible absorption spectra of <b>47</b> in $\text{CH}_3\text{CN}$ , THF and toluene .....	213
Figure 4.26: Qualitative molecular orbital diagram for <b>44</b> and $[\text{Pt}(\text{N}^{\wedge}\text{N})(\text{C}\equiv\text{C}\text{Ar})_2]$ ( <b>45-49</b> ). .....	215
Figure 4.27: Cyclic voltammograms of <b>4</b> , <b>45</b> and <b>46</b> .....	218
Figure 4.28: CVs of ethynyl-HBC ( <b>7</b> ), $[\text{cis-Pt}(\text{dppe})(\text{C}\equiv\text{C-HBC})_2]$ ( <b>41</b> ) and $[\text{Pt}(\text{N}^{\wedge}\text{N})(\text{C}\equiv\text{C-HBC})_2]$ ( <b>49</b> ) .....	219
Figure 4.29: Emission and excitation spectra of <b>4</b> in $\text{CH}_2\text{Cl}_2$ solution at 298 K and 77 K . .....	221
Figure 4.30: Emission spectra of $[\text{Pt}(\text{N}^{\wedge}\text{N})\text{Cl}_2]$ ( <b>44</b> ) in $\text{CH}_2\text{Cl}_2$ solution at 298 K and 77 K .....	222
Figure 4.31: Solid state emission spectra of <b>45</b> , <b>46</b> and <b>48</b> at 298 K .....	225
Figure 4.32: Solid state emission spectra of <b>45</b> , <b>46</b> and <b>48</b> at 77 K .....	226
Figure 4.33: Emission spectra of <b>45</b> , <b>46</b> and <b>48</b> in $\text{CH}_2\text{Cl}_2$ solution at 298 K, $\lambda_{\text{exc}} < 350$ nm .....	227
Figure 4.34: Emission spectra of <b>45</b> , <b>46</b> and <b>48</b> in $\text{CH}_2\text{Cl}_2$ solution at 298 K, $\lambda_{\text{exc}} > 420$ nm .....	228
Figure 4.35: Emission spectra of <b>45</b> , <b>46</b> and <b>48</b> in $\text{CH}_2\text{Cl}_2$ solution at 77 K .....	229
Figure 4.36: Emission spectra of <b>47</b> and <b>49</b> , 298 K in $\text{CH}_2\text{Cl}_2$ solution ( $10^{-5}$ M) .....	231
Figure 4.37: Emission spectra of <b>47</b> & <b>49</b> in $\text{CH}_2\text{Cl}_2$ ( $10^{-5}$ M) at 77 K.....	234
Figure 4.38: Structural variation of the bipyridyl ligand in $[\text{Pt}(\text{N}^{\wedge}\text{N})(\text{C}\equiv\text{CPh})_2]$ complexes. Qualitative MO diagram illustrating the effect of changes on emission profile.....	238
Figure 4.39: Ethynyl-bipyridine functionalised hexaphenylbenzenes and HBC.....	240
Figure 4.40: <i>Cis</i> - $[\text{Pt}(\equiv\text{HBC})_2(\text{dppe})]$ , <i>Trans</i> - $[\text{Pt}(\equiv\text{HBC})_2(\text{PPh}_3)_2]$ and homoleptic tetra-alkynyl $[\text{Pt}(\equiv\text{HBC})_4]^{2-}$ complexes of long-chain ethynyl-HBC derivative.....	241



**Chapter 1**  
**Bipyridine and Alkynyl-based Polyaryl Ligands**



## 1.1 Introduction

### 1.1.1 Polycyclic Aromatic Hydrocarbons

Polycyclic aromatic hydrocarbons (PAHs) are a family of compounds composed of two dimensional graphitic segments of  $sp^2$ -hybridised carbons. PAHs are of considerable research interest primarily as synthetically accessible derivatives of graphite.<sup>1</sup> This material possesses a vast  $\pi$ -electron delocalised honeycomb network of carbon atoms, with an interlayer spacing of 3.4 Å.<sup>2</sup> Consequently, graphite is known to be a highly efficient organic  $\pi$ -electronic conductor, exhibiting very high chemical and thermal stability and many desirable mechanical and electrical properties.<sup>2</sup>

Two of the most familiar classes of PAHs are the “acenes”, where benzene rings are fused in a linear arrangement, and the “phenes”, in which benzene rings are connected in an angular arrangement.<sup>1</sup> Anthracene and phenanthrene (Figure 1.1) are the smallest units of these families. “Circulenes” represent a further interesting class of PAHs, of which coronene, containing seven fused benzene rings, is an important derivative (Figure 1.1). As more versatile subunits of graphene, PAH properties can be controlled by substitution with a variety of functional groups. However, investigations into the chemistry of PAH molecules are severely hampered by the insolubility observed on increasing the platform size.<sup>3</sup>

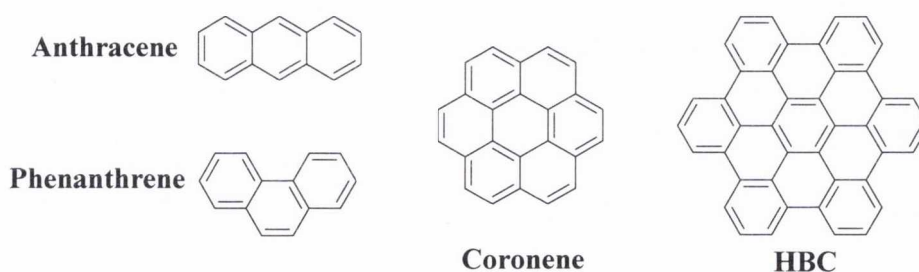


Figure 1.1: Examples of PAHs.

### 1.1.2 Hexa-*peri*-hexabenzocoronene

With this in mind, interest has focused on the disc-like PAH platform, hexa-*peri*-hexabenzocoronene (HBC), which is both synthetically accessible and easily derivatised (Figure 1.1). HBC consists of 13 fused aromatic rings. It exhibits high symmetry, stability and a highly electron delocalised  $\pi$ -conjugated network and consequently can be called

“superbenzene”.<sup>4</sup> Derivatives have been shown to undergo self-assembly in both the solid state and in solution by stacking of the disc-like molecules in a columnar fashion held together by  $\pi$ - $\pi$  stacking. In synthetic terms, such extensive aggregation is undesirable but it may be controlled by careful choice of substituent along the periphery of the HBC unit.<sup>5</sup> For example, substitution around the aromatic core by flexible aliphatic chains gives rise to discotic liquid crystal behaviour and has led to the study of HBCs functionalized with saturated alkyl chains as thermotropic liquid crystalline materials.<sup>6-8</sup> The intermolecular stacking of these HBC derivatives results in high directional charge carrier mobility along the columnar stacking axis.<sup>9</sup>

In contrast, the incorporation of *tert*-butyl substituents along the periphery of the HBC core has been shown to improve solubility of the compounds as the steric hindrance of the bulky substituents hinders, but does not entirely preclude, inter-disc association.<sup>10</sup> This is evidenced in the crystal structure of hexa-*tert*-butyl substituted HBC which reveals the formation of  $\pi$ - $\pi$  stacked dimers in the solid state.<sup>10</sup> Interestingly, the crystal structure of permethoxylated HBCs (in which every free CH position on the edges of the HBC core is substituted with an OCH<sub>3</sub> group), reveals that the molecule is non-planar.<sup>11</sup> Severe steric congestion induced by the multiple substituents forces a double concave conformation.

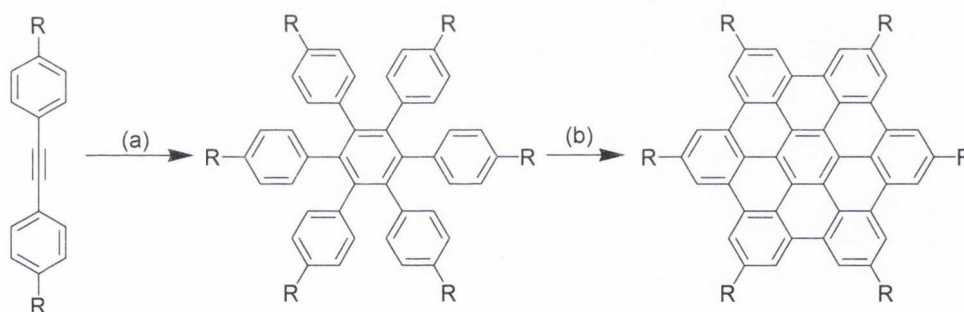
### 1.1.2.1 Materials applications of HBCs as processible PAH derivatives

HBC derivatives have been investigated as liquid crystalline materials and have also been applied as active components in organic field-effect transistors and photovoltaic devices.<sup>12</sup> In order to record field effect mobilities, which describe the flow of electrons from source to drain, aligned semi-conducting thin films of HBC were cast from solution as layers onto an oriented PTFE (poly(tetrafluoroethylene)) substrate.<sup>12-13</sup> Although the measured mobilities were lower than those of commercial organic semiconductors, the device stability (insensitivity to oxygen and visible light), solution processibility and uniaxial parallel orientation offer significant potential for further device application and tuning.<sup>13</sup> The suitability of hexa-*peri*-hexabenzocoronene derivatives as materials for solar cells has been evaluated by Müllen and co-workers.<sup>14</sup> In the preparation of organic solar cells, an efficient transport of charge from electron donor (HBC) to the electrodes generated after visible light excitation is key in the determination of device efficiency.<sup>15</sup> The compound should also absorb strongly throughout the visible to infrared regions of the spectrum in

order to maximise the harvesting of sunlight photons.<sup>16</sup> Despite the ease of processibility and high charge carrier mobilities, the photovoltaic performance of the derivatives studied was limited by weak absorption of the HBCs in the visible and near-infrared region of the spectrum.

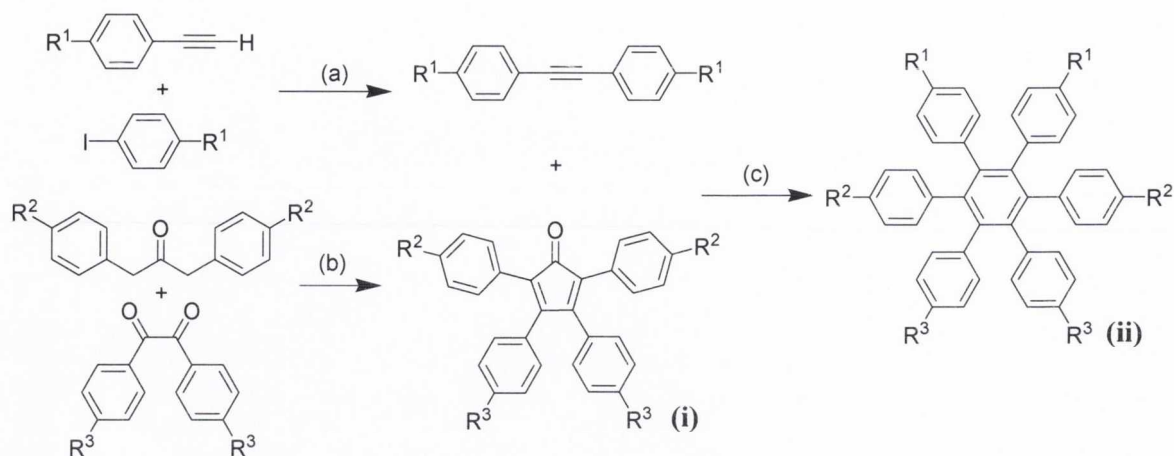
### 1.1.2.2 Synthesis

A successful high-yielding synthetic route towards hexa-*peri*-hexabenzocoronene has proven to be particularly difficult to devise. Clar's original synthesis and subsequent attempts by several other groups have produced HBC, but through poorly-yielding routes.<sup>17</sup> Much more recent work by Klaus Müllen and his research group has led to an efficient synthesis of the molecule and its derivatives.<sup>18-19</sup> For each devised route, the synthesis of hexaphenylbenzene compounds as polyphenylene precursors to HBC are required. These derivatives may be subsequently employed in oxidative cyclodehydrogenation reactions to achieve planarization of the polyphenylene (Section 1.1.2.3).



*Scheme 1.1: Synthesis of symmetrical HBC derivatives via cyclotrimerisation. (a)  $\text{Co}_2(\text{CO})_8$ , dioxane, reflux. (b) Oxidative cyclodehydrogenation.*

The synthesis of a symmetric hexaphenylbenzene derivative with six identical substituents can be achieved by transition-metal catalysed cyclotrimerisation (typically employing  $\text{Co}_2(\text{CO})_8$  as catalyst) of the corresponding substituted acetylene (Scheme 1.1, (a))<sup>10,20</sup> This is a particularly convenient route as reaction conditions will tolerate a variety of substituents on the acetylene.



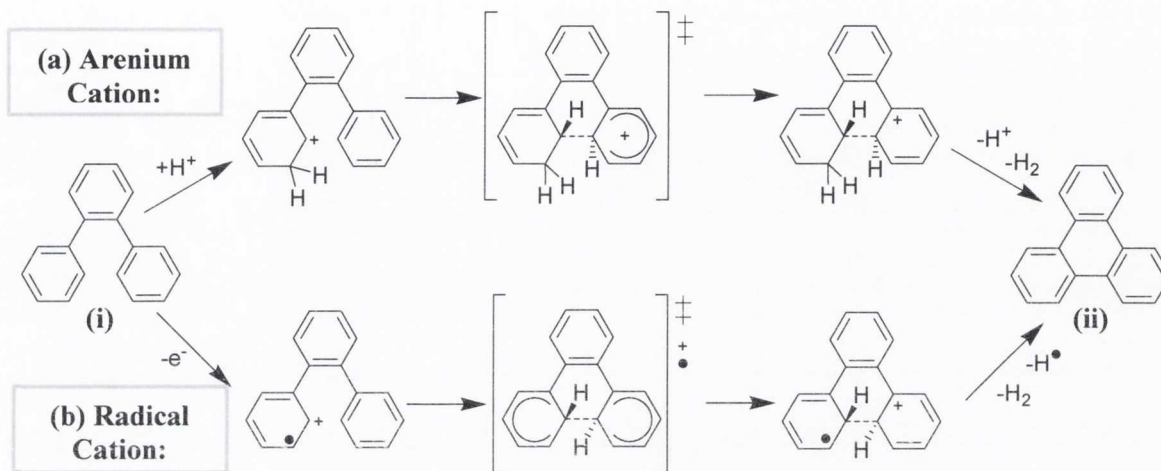
Scheme 1.2: Synthetic strategy for hexaphenylbenzene derivatives with lower symmetry. (a) Pd (cat.), CuI (cat.), amine. (b) KOH, EtOH, Reflux. (c) Benzophenone, 300 °C.

To allow for selective functionalisation of the molecule incorporating a variety of substituents onto the hexaphenylbenzene precursor, an alternative step-wise synthetic route must be applied. Work by Klaus Müllen has led to the synthesis of a broad spectrum of hexaphenylbenzene and in turn, hexa-*peri*-hexabenzocoronene, derivatives which exhibit lower symmetry substitution patterns (Scheme 1.2).<sup>4</sup> A substituted tetraarylcyclopentadienone (i) may be synthesised from a two-fold Knoevenagel condensation reaction between a functionalised 1,2-diketone and a 1,3-diarylaceton (Scheme 1.2, (b)). Reaction of the tetraarylcyclopentadienone with a suitably functionalised diarylacetylene occurs via a [2+4]-Diels-Alder cycloaddition to produce the desired hexaphenylbenzene derivatives (Scheme 1.2, (c)).

### 1.1.2.3 Cyclodehydrogenation

Carbon-carbon bond formation to achieve planarization of hexaphenylbenzene compounds is typically undertaken *via* an intramolecular Scholl reaction, known as oxidative cyclodehydrogenation (Scheme 1.1, (b)).<sup>19</sup> This is achieved using Kovacic conditions under the influence of Friedel-Crafts catalysts, for HBC synthesis most commonly using copper(II) salts and AlCl<sub>3</sub> as Lewis acid in carbon disulfide.<sup>21</sup> Alternatively, the weaker Lewis acid iron(III) chloride may be employed in a mixture of nitromethane and dichloromethane. Use of FeCl<sub>3</sub> renders the addition of an oxidant unnecessary as the reagent serves the dual role of Lewis acid catalyst and oxidising agent.<sup>1</sup> By dissolving FeCl<sub>3</sub> in nitromethane, the oxidant may be added homogenously to the reaction mixture.<sup>22</sup> In general, the marginally milder FeCl<sub>3</sub> route is the chosen method in this work. The

catalyst promotes the formation of carbon-carbon bonds, resulting in the planarization of hexaphenylbenzene to yield the flat, highly aromatic HBC (Scheme 1.1, (b)). The formation of each new carbon-carbon bond proceeds with the loss of  $\text{H}_2$ .



Scheme 1.3: Arenium cation (a) and Radical cation (b) mechanisms for the conversion of *o*-terphenyl (i) to triphenylene (ii).<sup>23-24</sup>

The mechanism of oxidative cyclodehydrogenation has been the subject of considerable debate in the literature with the result that the exact mechanism is still uncertain. Two routes are proposed, namely the arenium cation mechanism (proton transfer) and the radical cation mechanism (electron transfer), of which the first steps of each are shown for the terphenyl structural subunit (Scheme 1.3).<sup>23</sup> In both cases, it has been established that carbon-carbon bonds are most likely formed stepwise and contiguously, with the first bond formed the most slowly. The reaction is increasingly exergonic and complete cyclisation of the molecule is achieved *via* a slippery slope mechanism.<sup>23</sup> A series of computational and experimental mechanistic analyses of the reaction by King and co-workers suggests that the arenium cation route is more energetically favourable as it has lower key transition state barriers than the radical cation mechanism.<sup>23-25</sup> In this case, the reaction most likely proceeds by protonation of an aryl ring to form an arenium cation, electrophilic attack by an adjacent arene, deprotonation and subsequent oxidative dehydrogenation to restore aromaticity. However, very recently Rathore and co-workers presented significant experimental evidence for the radical cation mechanism.<sup>26</sup>

### 1.1.3 Nitrogen Hetero-SuperBenzene (N-HSB)

The incorporation of heteroatoms into the graphene structure would be anticipated to significantly alter the electronic properties of the HBC unit and enhance the solubility of the aromatic core. To this end, a series of nitrogen-containing heterosuperbenzene (N-HSB) molecules have been synthesised within the Draper group by careful modification of synthetic precursors (Figure 1.2).<sup>27</sup> The incorporation of electroactive imines on the edges of the carbon framework renders it electron-accepting in nature, hence enhancing  $\pi$ -electron mobility within the molecule. Protonation of the peripheral nitrogen atoms results in the quenching of emission, demonstrating a significant alteration in the  $\pi$ -electron density within the molecule.<sup>27</sup> The nitrogen atoms at the periphery are ideally positioned for bidentate coordination to a metal centre. As a result, the electronic and supramolecular properties of N-HSB as a ligand have been studied.<sup>28-29</sup>

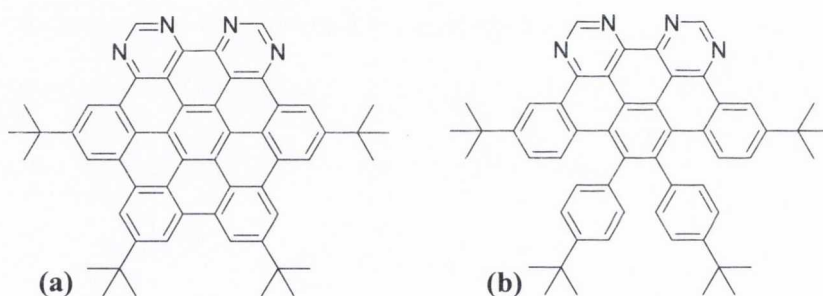


Figure 1.2: Structures of N-HSB (a) and N- $\frac{1}{2}$ HSB (b).

The product mixture obtained from oxidative cyclodehydrogenation of the polyphenylene precursor to N-HSB has been shown to be dependent on the synthetic method employed.<sup>29</sup> Use of  $\text{AlCl}_3$  and  $\text{CuCl}_2$  in carbon disulfide yields only the fully cyclised N-HSB molecule in 49 % yield (Figure 1.2, (a)).<sup>27</sup> Alternatively, using  $\text{FeCl}_3$  as the catalyst results in the formation of both the “half-cyclised” derivative N- $\frac{1}{2}$ HSB (Figure 1.2, (b)) in addition to the fully cyclised N-HSB (a).<sup>29</sup> The N- $\frac{1}{2}$ HSB molecule contains 8 fused aromatic rings with two phenyl rings free to rotate out of the plane of the aromatic platform. More recently, work within the group has isolated two thirds and five sixths cyclised derivatives from the  $\text{FeCl}_3$  reaction mixture.<sup>30</sup> Attempts to complete the cyclisation process of these partially planarised molecules employing the  $\text{AlCl}_3$  route have been unsuccessful indicating that these are also thermodynamically stable products.<sup>29</sup>



Clearly, the presence of nitrogen atoms in the periphery of the hexaphenylbenzene precursor has a significant effect on the efficacy of the Scholl reaction. King *et al.* have proposed an arenium cation mechanism to explain the formation of partially cyclised intermediates.<sup>24</sup> Protonation or double protonation of a pyrimidine ring is facile and this ring must be electrophilic enough to attack the adjacent pyrimidine ring (which is most likely also protonated). The authors suggest that the bond between the pyrimidine rings forms first. For the next ring closure, protonation of an adjacent phenyl ring will be most likely difficult as the basic ring nitrogens will already be protonated so the molecule already holds a positive charge. These difficulties provide an explanation for the partially cyclised N-HSB compounds isolated as part of the cyclodehydrogenation reaction but which are not observed generally in all-carbon polyphenylene systems.<sup>24</sup>

#### 1.1.4 Hexaphenylbenzenes: Features and Applications

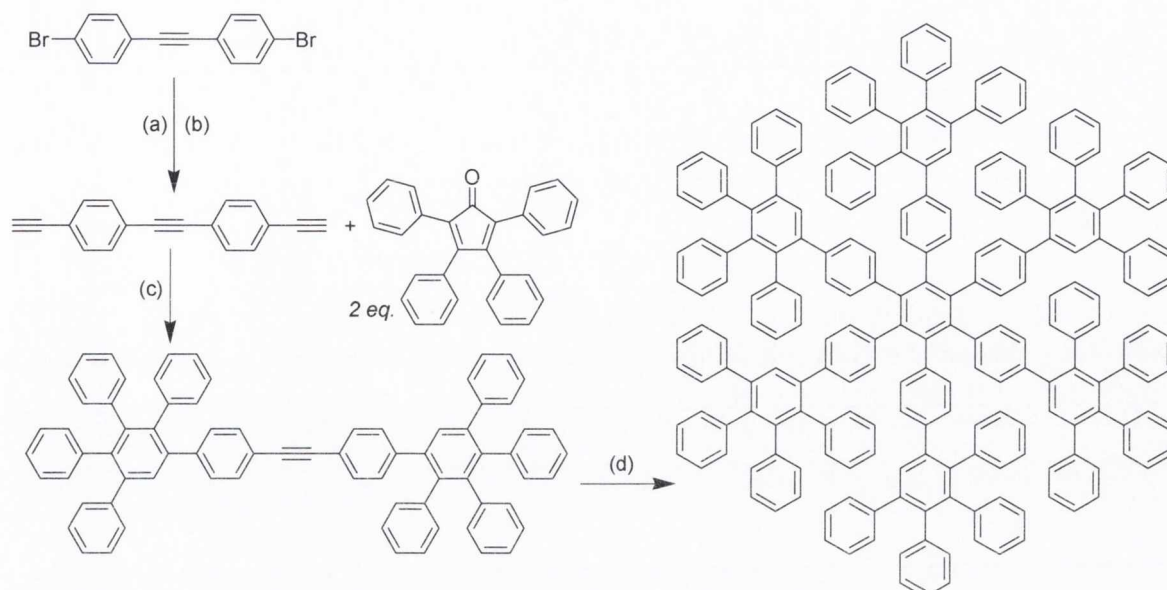
Hexaphenylbenzene (HPB) derivatives are key synthetic precursors for graphite-like HBC platforms, in which planarisation is achieved by oxidative cyclodehydrogenation (Section 1.1.2.2). However, these molecules are very important compounds in their own right and hexaphenylbenzene derivatives and expanded polyphenylene-based architectures have found a wide variety of applications.

Hexaphenylbenzene molecules may be considered as molecular propellers, in which the six outer phenyl rings twist with respect to the central benzene core. The degree of this ring tilt is influenced by both steric and electronic factors, where steric interactions are minimised by a perpendicular arrangement of the peripheral phenyl rings about the central support platform but co-planarity maximises  $\pi$ -orbital overlap.<sup>31</sup> The crystal structure of unsubstituted hexaphenylbenzene reveals a helical conformation with tilt angles between outer phenyls and the central ring falling between 65-75°. <sup>32-33</sup> Similarly, in the solid state a hexakis-alkynyl substituted hexaphenylbenzene derivative (at the *para* position on each of the peripheral rings) adopts a “paddle-wheel” configuration with an average out of plane twist angle of 67°. <sup>34</sup> Within the Draper group, several structures of polyphenylene compounds in which two peripheral phenyls are replaced by heteroaromatic rings (Figure 1.4, (a) pyrimidine, thiophene) show a unidirectional twisting of aryl and heteroaryl rings (tilt angles relative to central benzene ring within the range 59-72°).<sup>31</sup>

#### 1.1.4.1 Structurally rigid polyphenylene dendrimers

Hexaphenylbenzene molecules may be considered as monodisperse, polyaromatic dendrimers. These compounds are rigid and shape persistent, with stiff radial arms which do not allow backfolding.<sup>35</sup> This property compares favourably to other dendrimeric compounds in which flexible aliphatic dendrons within a structure can lead to uncertainty in pore size and dispersion of components. The hexaphenylbenzene structural motif may be expanded to construct higher generation dendrimeric architectures with well-defined highly branched, structurally rigid backbones in which the location of internal and external functional groups may be synthetically controlled.

Employing hexaphenylbenzene essentially as a template, rigid polyphenylene-based dendritic structures may be prepared by a series of iterative [2+4] Diels-Alder cycloaddition reactions between suitably substituted tetraarylcyclopentadienones and diarylacetylene reagents.<sup>36</sup> Peripheral bromo or iodo substituents on hexaphenylbenzene dendrons serve as “handles” for further functionalisation, for example by Sonogashira palladium-catalysed cross coupling to yield acetylene-derivatised molecules, which may be employed as the dienophile in subsequent cycloaddition reactions (Scheme 1.4).<sup>36</sup> This is a divergent synthetic method, in which a suitably functionalised core molecule is extended outwards *via* a series of iterative reactions. The application of the cycloaddition reaction for this purpose has several advantages including that it is essentially free of side reactions and the irreversible loss of CO and formation of a highly stable benzene ring shifts the reaction equilibrium towards the products.<sup>35</sup> The cyclotrimerisation of a highly substituted acetylene has also been applied as the final step in the preparation of polyphenylene molecular architectures with very high thermal stability and extremely dense packing of benzene rings (Scheme 1.4).<sup>3-4</sup>



Scheme 1.4: Synthesis of a rigid polyphenylene dendrimer. (a) Trimethylsilylacetylene (2 eq.), Pd(0), CuI cat., amine; (b) KF deprotection; (c) Cyclopentadienone (2 eq.), Ph<sub>2</sub>O, 190 °C, 66 %; (d) [Co<sub>2</sub>(CO)<sub>8</sub>], dioxane, 71 %.

#### 1.1.4.2 Hexaphenylbenzenes as molecular scaffolds

The rigidity and shape persistence of hexaphenylbenzene molecules has been exploited in the generation of large surface polyphenylene support frameworks for multi-chromophoric arrays. Müllen *et al.* have prepared a series of these light-harvesting arrays, in which three different types of chromophore are incorporated into a rigid polyphenylene scaffold.<sup>37</sup> By attaching a donor moiety on the periphery and an acceptor in the centre, efficient transfer of excitation energy is achieved by production of an energy gradient between the periphery and the core.<sup>37-38</sup> Importantly, application of a rigid polyphenylene framework ensures that self quenching of the chromophores is not observed as backfolding of dendrimeric branches is not possible.

As a further example, Moore and co-workers prepared artificial functional analogues of natural photosynthetic antenna-reaction centre complexes, in which the hexaphenylbenzene serves as a scaffold to organise five bis(phenylethynyl)anthracene antenna moieties and one porphyrin fullerene dyad as an electron donor-acceptor unit.<sup>39</sup> The molecular architecture facilitates rapid and efficient singlet energy transfer from all antenna moieties to the porphyrin, with a quantum yield near unity, upon which photoinduced electron transfer occurs. The efficient coupling of light harvesting antennae

with an electron donor-acceptor system is facilitated by the hexaphenylbenzene core, in which photoactive subunits are tethered *via* acetylene linkages.

More recently, the same group have applied hexaphenylbenzene as a scaffold for the preparation of a molecular switch which also functions as a molecular analogue of a transistor (Figure 1.3).<sup>40</sup> Five light-harvesting chromophores, bis(phenylethynyl)anthracene (BPEA), and a dithienylethene (DTE) photochrome are organised by a central hexa-ethynyl-polyphenylene scaffold. When the DTE is in its open form, fluorescence derived from the BPEA moieties is observed ( $\lambda_{em}$  520 nm) with a quantum yield near unity. When the DTE is closed, induced by steady state illumination of the hexad with an excitation wavelength  $\lambda$  365 nm, BPEA fluorescence is strongly quenched by energy transfer to the closed DTE. This emission may be modulated by illumination with red light of wavelength  $> \lambda$  610 nm, which induces photoisomerism to the open form of DTE and consequently increasing BPEA emission. Essentially the molecule acts as a nano-scale transistor, in which the  $\lambda$  520 nm fluorescence is the device output and the modulating  $\lambda$  610 nm illumination acts as the gate voltage of the transistor. This ability to control intense shorter wave fluorescence with longer wave light is relatively unusual and may have applications in biomedical imaging, facilitating the detection of emission from a probe molecule without interference from other materials.<sup>40</sup>

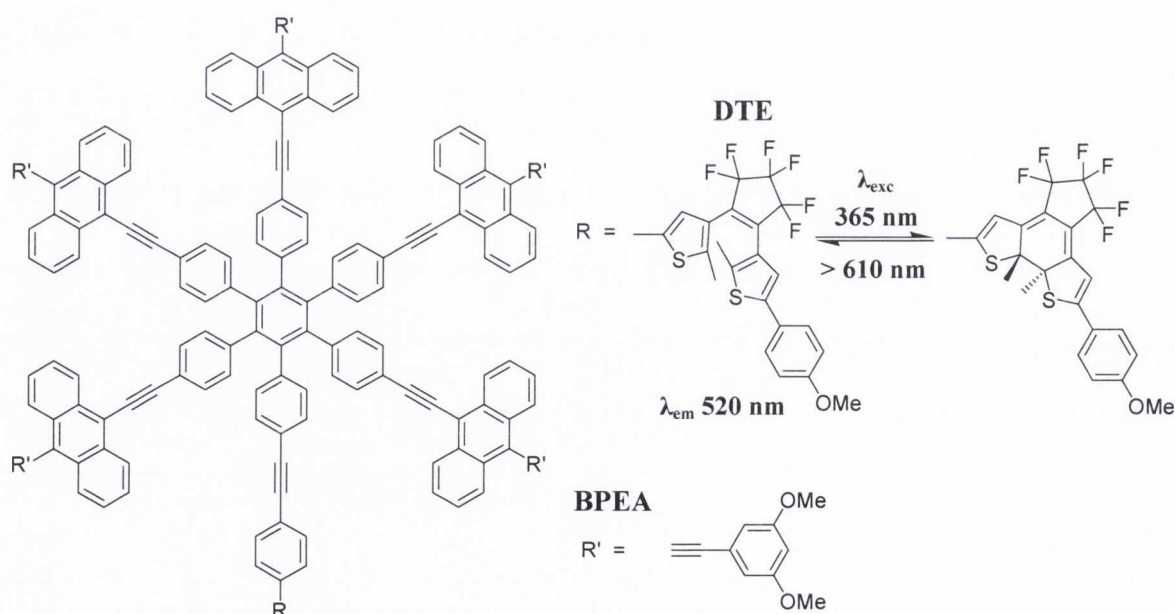


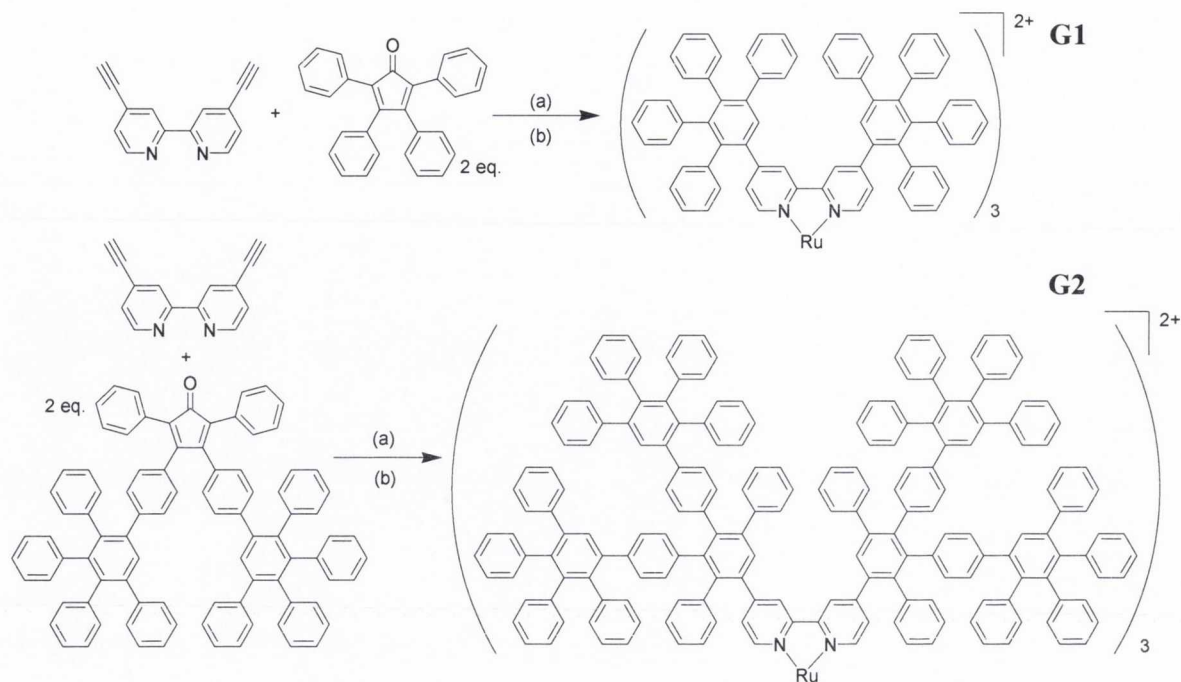
Figure 1.3: Hexa-functionalised hexaphenylbenzene displaying photoinduced molecular switching. (DTE = dithienylethene, BPEA = bis(phenylethynyl)anthracene).

### 1.1.4.3 Hexaphenylbenzenes in host-guest frameworks

Monodisperse polyphenylene dendrimers contain internal voids and channels between dendron branches as a consequence of the rigid framework. This is clearly demonstrated in the solid state, where X-ray crystal structures of hexaphenylbenzene derivatives are frequently shown to possess channels filled with solvent molecules.<sup>41-42</sup> This tendency of polyphenylene structures to fill voids with small guest molecules has been exploited by incorporating polyphenylene dendrimers as selective and sensitive host molecules for the detection of volatile organic compounds (VOCs).<sup>43</sup> The concentration of VOCs in the gas phase is monitored using a quartz microbalance (QMB) in which an electrode is coated with a polyphenylene dendrimeric compound as the sensor active layer. Exposure of the layer to different VOCs results in the reversible incorporation of the gaseous molecules into the stable cavities of the interior bulk of the host compound, detected by a decrease in resonance frequency of the QMB and from which the number of encapsulated guest molecules may be calculated. Polyphenylene molecules have been shown to be highly selective host molecules, with all-carbon derivatives selective for polar VOCs with very high sensitivity (~5 ppm), as a result of the formation of  $\pi$ - $\pi$  electron donor-acceptor complexes between host and guest. Substitution of the polyaromatic dendrons with polar functionalities can tune the selectivity such that non-polar VOCs may also be detected.<sup>43</sup>

### 1.1.4.4 Polyphenylenes as ligands in encapsulated metal complexes

Several examples of polyphenylene derivatives as dendrimeric polypyridyl ligands have been published recently.<sup>44-45</sup> In both cases, the polyphenylene scaffolds are used as a rigid matrix in which the radial arms of the dendrons do not allow backfolding so that the coordination complexes are highly shape persistent. The first shape persistent dendrimers based on octahedral geometry employ  $[\text{Ru}(\text{bpy})_3]^{2+}$  as the photoactive transition metal centred core are shown in Scheme 1.5, where G1 is the first generation dendrimer and G2 the second.<sup>44</sup> These polyaryl bipyridine ligands are prepared by divergent methods *via* a series of Diels-Alder cycloadditions between a bis-ethynyl-bipyridine and a suitably substituted tetraarylcyclopentadienone.



*Scheme 1.5: Ru(II) dendritic polypyridine complexes, G1 and G2. (a) o-xylene (solvent), 140 °C, G1: 97 %, G2: 90 %; (b) RuCl<sub>2</sub>(DMSO)<sub>4</sub>, DMF, 140 °C, G1: 55 %, G2: 23 %.*

More recently, a series of dendritic complexes with a phosphorescent Ir(III) core, based on the cyclometallating ligand phenyl pyridine (N<sup>^</sup>C coordination mode), has been described and their relative performances in phosphorescent organic light emitting devices (PhOLEDs) evaluated.<sup>45</sup> In these complexes, the rigid polyphenylene dendrons essentially encapsulate the metal centre to prevent Ir(III) cores from triplet-triplet annihilation. As a consequence, photoluminescence quantum yields of the complexes are significantly improved relative to the parent [Ir(phenylpyridine)<sub>3</sub>] complex. With increasing generation, an increase in quantum yield of emission is observed due to greater shielding of the phosphorescent core by the structurally rigid dendrons. The effect of the polyphenylene framework about the phosphorescent metal centre also provides an effective charge carrier mobility from the periphery of the dendrimer to the Ir(III) core, a property which can be carefully modulated on the basis of molecular architecture and dendrimer generation.

#### 1.1.4.5 Hexaphenylbenzenes as ligands in organometallic complexes

Hexaphenylbenzenes have been employed as ligands in the preparation of sterically encumbered organometallic-functionalised compounds.<sup>46</sup> Polyarylated organometallic compounds may exhibit correlated rotation, depending on the degree of steric encumbrance

imposed by the aryl substituents.<sup>46</sup> For example, a 17 electron Mo mixed sandwich metallocene  $[(\eta^5\text{-C}_5\text{H}_5)\text{Mo}(\eta^6\text{-C}_6\text{Ph}_6)]$  and a sterically hindered Ru(II) arene cation  $[(\eta^5\text{-C}_5\text{H}_5)\text{Ru}(\eta^6\text{-C}_6\text{Ph}_6)]^+$ , both bound  $\eta^6$  to the central benzene ring of hexaphenylbenzene, have been reported.<sup>47-48</sup> McGlinchey and co-workers report the crystal structure of a ferrocenyl-substituted polyphenylene molecule, which reveals severe twisting of the peripheral phenyls out of the plane of the central ring with an incremental progression of twist angles, as a consequence of the sterically demanding organometallic fragment (Figure 1.4, (b)).<sup>49</sup> This molecule was originally prepared *via* an analogous procedure to that described in this work, a [2+4]-Diels Alder cycloaddition between ferrocenyl-phenylacetylene and tetraphenylcyclopentadienone.<sup>50</sup> The same group has also reported a  $\text{Cr}(\text{CO})_3$  complex,  $(\text{C}_6\text{Ph}_6)\text{Cr}(\text{CO})_3$ , in which the metal centre is coordinated to one of the peripheral aryl rings.<sup>51</sup> The molecule exhibits fluxional behaviour on the NMR timescale as a consequence of the steric hindrance imposed by the metal-coordinated fragment, such that the coordinated phenyl ring is almost orthogonal to the central benzene ring at low temperature ( $-80\text{ }^\circ\text{C}$ ).

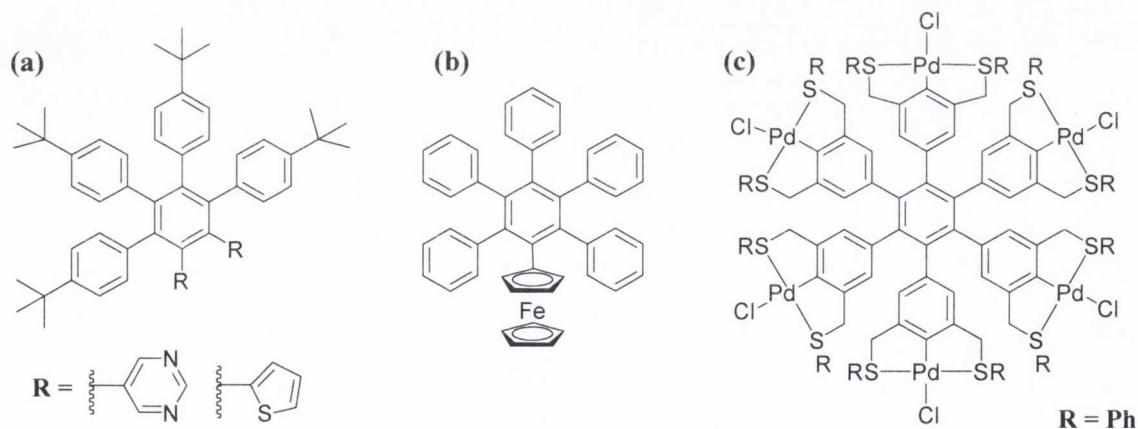


Figure 1.4: Selected hexaphenylbenzene organic derivatives and organometallic complexes whose structures have been resolved by X-ray crystallography.

Several rigid six-spoked cartwheel hexametallic complexes in which each peripheral ring bears a cyclopalladated functionality have been prepared by van Koten *et al.*<sup>52-54</sup> The crystal structure of one, in which the phenyl rings are substituted with six diorganosulfide moieties, reveals a chiral propeller-like structure in which each peripheral ring provides one anionic coordination site to a square planar Pd(II) metal complex (Figure 1.4, (c)).<sup>54</sup> These hexametallic pincer complexes have been employed as homogeneous Lewis acid catalysts with comparable catalytic activity to simple mono-pincer analogues (for the

pincer moiety  $\text{Me}_2\text{N-C}^-\text{-NMe}_2$ ).<sup>53</sup> The corresponding macromolecular homogenous catalytic systems exhibit high thermal and air stability and are large enough to be easily separated from product-containing solution by nanofiltration techniques.<sup>52</sup>

### 1.1.5 Functionalisation of polyphenylenes: Applications of the acetylene motif

It is clear that careful derivatisation of hexaphenylbenzenes and hexa-*peri*-hexabenzocoronenes by judicious choice of substituent along the periphery of the molecule has a significant effect on the electronic properties, and therefore applications, of the systems (Section 1.1.4). In terms of electronic communication, the acetylene functional group is frequently employed to tether photoactive subunits to a polyphenylene core.<sup>39-40,55</sup>

Its valuable structural and electronic properties have resulted in its frequent exploitation as an important synthetic and photophysical tool in a variety of applications. The triple bond is synthetically accessible and exhibits considerable chemical and thermal stability. Most importantly, its geometry is strictly linear and it exhibits very high electronic conductivity, with the result that alkynyl moieties provide effective pathways for electron and energy transfer. With this in mind, a considerable body of research, led by Ziessel and Harriman *et al.*, has focused on the production of molecular scale wires, where an acetylene or polyacetylenes are employed in the conduction of electronic charge between redox-active terminals.<sup>56-57</sup> In many cases, photoactive transition metal chelate complexes, such as Ru(II), Os(II) or Re(I) metal centres coordinated to bipyridyl or terpyridyl bridging ligands, serve as the terminal units in polynuclear supramolecular systems in which the rigid alkynyl bridge determines the directionality in the energy transfer.<sup>57-58</sup>

#### 1.1.5.1 Molecular dyads: Acetylene and polyaromatic spacer units for efficient energy transfer

A series of molecular scale Ru(II)-Os(II) dyads prepared by Ziessel, Harriman and co-workers are presented in Figure 1.5. In series (a), the aromatic spacer unit is varied between the  $\text{Ru}(\text{bpy})_3^{2+}$  and  $\text{Os}(\text{bpy})_3^{2+}$  termini *via* a stepwise increase in the size of the polycyclic aromatic hydrocarbon.<sup>57,59</sup> In the second series (Figure 1.5, (b)), a Pt(II) metal centre is incorporated into the molecular axis, in place of the aromatic unit, *via* the formation of metal-alkynyl  $\sigma$ -bonds.<sup>60-61</sup> When no aromatic ring is located between the two transition metal chromophores ((a),  $n = 0$ ), the polyalkynylene bridge produces very



rapid intramolecular triplet energy transfer from the Ru(II) to the Os(II) metal centres upon excitation of the complex with visible light into the Ru(II) chromophore. This is ideal for rapid transfer of information, but is inappropriate for the transfer of information at controlled rate.

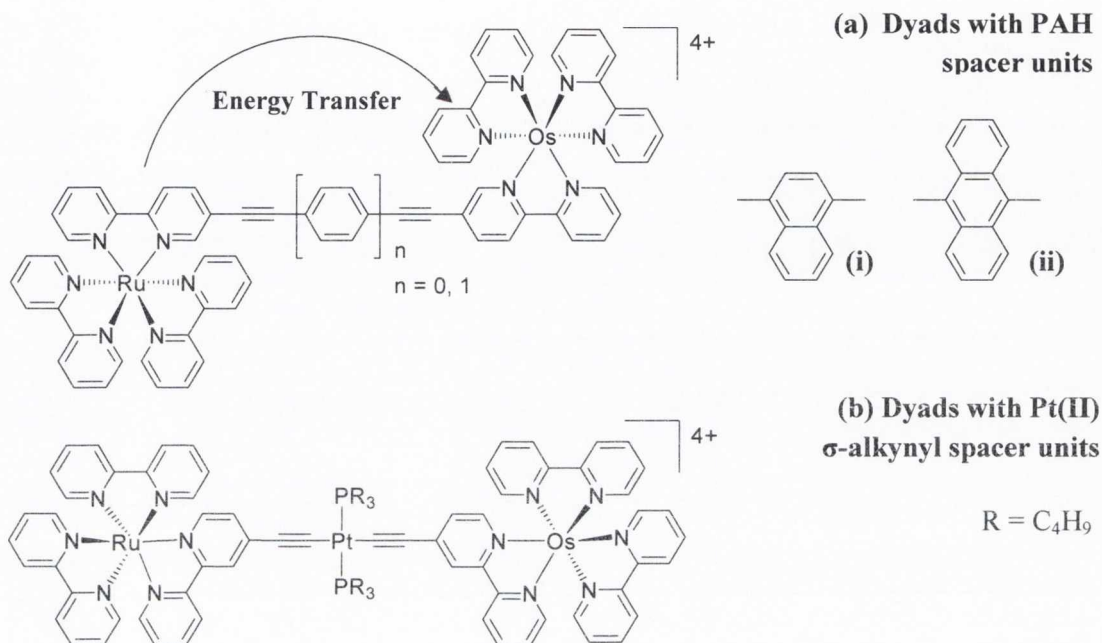


Figure 1.5: Ru(II)-Os(II) Molecular scale dyads incorporating aromatic and Pt(II) alkyne spacer units.

It has been shown that the electronic conductivity along the molecular axis can be modulated by insertion of aromatic subunits into the molecular backbone.<sup>59</sup> With this in mind, incorporation of a phenyl ring as spacer unit ( $n = 1$ ) has several consequences on the optical properties of the system. A reduction in triplet excited state lifetime and an increase in energy is observed as a result of unfavourable orientation of the phenyl ring which gives rise to poorer alignment of phenyl ring-alkynyl orbitals.<sup>57,59</sup> Accordingly, this curtails the electron flow between the Ru(II) and the Os(II) centres such that a more controlled leaking of information is possible. Incorporation of larger spacer units such as naphthalene (Figure 1.5, (i)) or anthracene (Figure 1.5, (ii)) decreases the energy of the bridging unit and consequently introduces an additional destination for the triplet energy. In the case of anthracene, triplet energy transfer occurs from both the Ru(II) and Os(II) chromophores to the bridging anthracene residue, providing a low-energy sink which quenches the triplet excited state of both termini.<sup>57,59</sup> These processes all occur rapidly and quantitatively along the molecular axis. The polyphenylene derivatives phenyl, naphthyl and anthryl operate essentially as electronic relays, which, when incorporated into the

molecular axis, provide a moderate and tuneable barrier to electron flow. In all cases, polyphenylene systems linked by acetylene moieties to photo- and redox-active chromophores exhibit fast and typically unidirectional rates of electron propagation.

These supramolecular arrangements also employ acetylene in an alternative role, as a  $\sigma$ -bonded anionic ligand in the formation of metal-alkynyl bonds (Figure 1.5, (b)). In this case, the Pt(II) bis-acetylide in the molecular axis acts as an insulator to the flow of electronic charge, inhibiting through bond energy exchange such that the rate of triplet energy transfer is significantly lowered.<sup>60-61</sup>

### 1.1.5.2 Polyphenylenes in transition metal complexes: Dinuclear complexes bridged by oligophenylene spacers

Oligophenylene-functionalised bipyridines have been effectively employed as bidentate ligands in luminescent transition metal complexes. Despite the absence of planarity between *para*-oligophenylene moieties, these have been successfully incorporated as spacer units by De Cola and co-workers into rod-like dinuclear Ru(II) and Os(II) luminescent metal complexes.<sup>62-63</sup> The structures of the Ru(II) homometallic derivatives of these complexes are given in Figure 1.6.

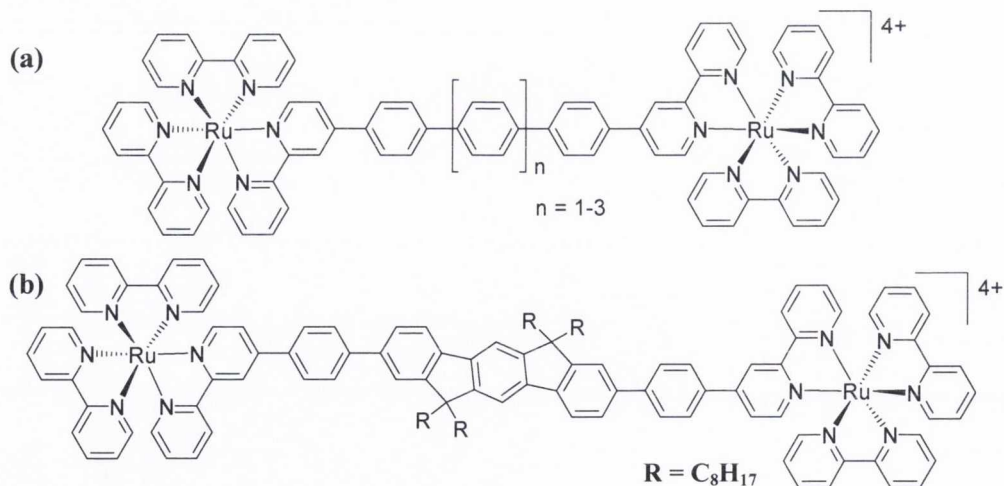


Figure 1.6: Dinuclear Ru(II) rod-like systems bridged by phenylene spacers.

With an increasing number of phenylene units a red-shift in the UV-Visible spectrum of the intra-ligand band attributable to the oligophenylene spacer unit is observed. In terms of photoluminescence, the energy of the emissive excited state changes very little relative to

$\text{Ru}(\text{bpy})_3^{2+}$  but significant increases in triplet excited state lifetime and the quantum yield of emission ( $\Phi_{\text{em}}$ ) are observed.<sup>63</sup> These features indicate an increase in delocalisation of the excited state as a result of an increase in conjugation length within the backbone of the system. An additional complex, in which the central phenyl ring has been swapped for an indenofluorene derivative (Figure 1.6) forcing the phenyl rings coplanar, displays essentially analogous photoluminescence properties to the polyphenylene derivatives. Unsubstituted *para*-connected oligophenylenes have relatively small twist angles relative to the bipyridine moieties on either end of the dyad. As a result, orbital overlap between phenylene and bipyridyl aromatic rings is relatively facile, inducing an increase in conjugation relative to the parent  $\text{Ru}(\text{bpy})_3^{2+}$  complex.<sup>63</sup> In contrast, substitution on the phenyl rings with solubilising alkyl chains leads to a more significant tilt angle and therefore less efficient orbital overlap and  $\pi$ -electron conjugation. In these complexes, a significant reduction in electronic communication along the phenylene spacers between the two photoactive components is observed.<sup>64</sup> These systems imply that the tilt angles and therefore the electronic interactions between adjacent phenyl rings may be controlled by synthetic means.<sup>62-63</sup>

### 1.1.6 Ligand design: Bipyridine and hexaphenylbenzene functionalisation

This chapter details the preparation of a series of rationally designed ligands based on the hexaphenylbenzene structural motif. The versatile polyphenylene core is employed as a molecular scaffold for the attachment of bipyridyl and acetylenic organic fragments. Hence, these systems possess inherent ligand functionality and high electronic conductivity by combining acetylene and polyaromatic spacer units. The rigidity and shape persistence of hexaphenylbenzenes ensures the generation of well-defined supramolecular architectures with some geometric control. These molecules are designed to exploit the desirable structural and electronic properties of polyphenylenes, acetylenes and bipyridine chromophores.

Two series of carefully-derivatised polyphenylene ligands have been synthesised. The [2+4]-Diels-Alder cycloaddition reaction, central to the preparation of hexaphenylbenzene (Section 1.1.2.2) and Müllen's dendritic polyphenylene superstructures (Section 1.1.4.1), is the key step in the syntheses of these novel ligands. Ligand series A describes a sequence of asymmetric oligophenylene-substituted bipyridine ligands (Figure 1.7, A). These

employ 2,2'-bipyridine as the fundamental metal-chelating moiety and a systematically increased polyphenylene scaffold, from a single pendent phenyl-acetylene to a dendritic penta-phenyl benzene core. Attaching this substituent adjacent to a pyridine ring nitrogen, which will be involved in chelation of a transition metal centre, should see a significant and increasing effect across the ligand series on the electronic properties of the corresponding complexes (Chapter 2). It is hoped that metal complexes of these functionalised polyphenylene scaffolds will exhibit enhanced photophysical properties with efficient  $\pi$ -electron delocalisation (employing **1** and **2**) and increasing encapsulation of the photoactive chromophore (from **3** to **4** to **5**).

Ligand series B represents a family of acetylene-functionalised hexaphenylbenzene molecules (Figure 1.7, B), from a single acetylene substituent (**6**), to *para*-(**8**) and *ortho*-(**9**) di-ethynyl architectures. This series also includes a fully cyclised ethynyl-HBC platform. Varying the substitution pattern of the hexaphenylbenzene provides scope for the development of structurally rigid, highly stable supramolecular architectures. These molecules have been prepared as ligands for the formation of Pt(II)  $\sigma$ -acetylide complexes (Chapters 3 and 4), in which it is anticipated that the acetylene moiety will ensure efficient electronic communication between the metal centre and oligophenylene ligand functionality.

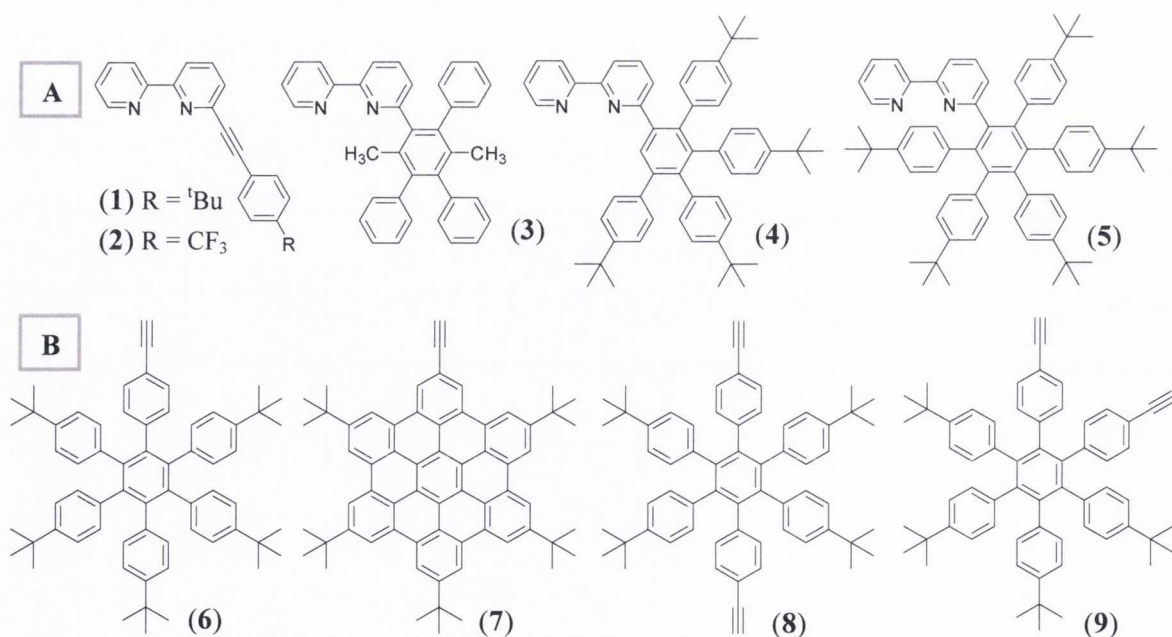


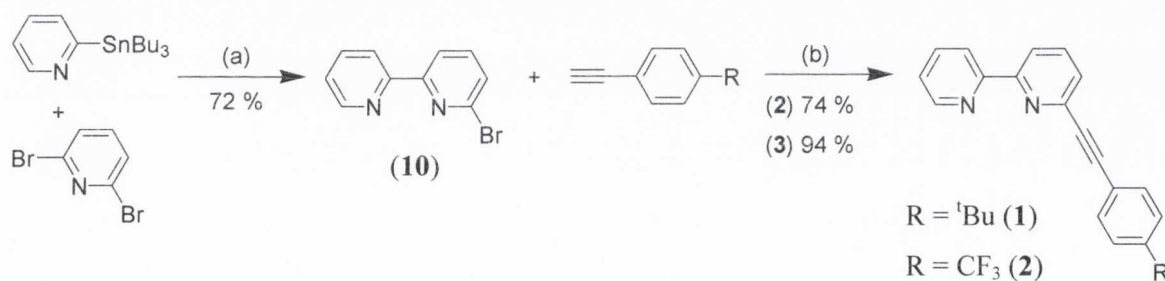
Figure 1.7: Target bipyridine, hexaphenylbenzene and HBC ligands.

## 1.2 Ligand series A: Synthesis of polyaromatic-bipyridine ligands

The syntheses of the two simple aryl-acetylene substituted bipyridine ligands **1** and **2** required a palladium-catalysed Sonogashira cross-coupling reaction. Polyphenylene-functionalised bipyridines **3**, **4** and **5** were completed by a [2+4] Diels-Alder cycloaddition reaction.

### 1.2.1 Synthesis of aryl-acetylene bipyridines **1** and **2**

The synthesis of 6-(4-*tert*-butyl-phenylethynyl)-2,2'-bipyridine (**1**) and 6-(4-trifluoromethyl-phenylethynyl)-2,2'-bipyridine (**2**) requires 6-bromo-2,2'-bipyridine (**10**) (Scheme 1.6). This synthon is prepared using a literature procedure which employs a Stille-type cross-coupling reaction between two commercially available reagents, 2-tributylstannyl-pyridine and 2,6-dibromo-pyridine.<sup>65</sup>



*Scheme 1.6: Syntheses of precursor **10** and aryl-acetylene ligands **1** and **2**. (a) Pd(PPh<sub>3</sub>)<sub>4</sub> (5 mol%), still-dried toluene, 110 °C, 24 hours. (b) *cis*-PdCl<sub>2</sub>(PPh<sub>3</sub>)<sub>2</sub> (6 mol%), CuI (6 mol%), THF:*i*Pr<sub>2</sub>NH (3:1 v/v), R.T., 18 hours.*

Palladium-catalysed Sonogashira reactions between the resulting 6-bromo-2,2'-bipyridine (**10**) and a suitable terminal aryl-acetylene (Scheme 1.6) produce **1** and **2** as novel species. Ligand **1** was prepared by addition of 4-*tert*-butylphenylacetylene (1.1 eq.) to a solution of **10** (1 eq.), *cis*-PdCl<sub>2</sub>(PPh<sub>3</sub>)<sub>2</sub> (6 mol%) as catalyst and CuI (6 mol %) as co-catalyst in a mixture of still-dried, argon-degassed THF:diisopropylamine (3:1 v/v). The reaction mixture was stirred for 18 hours under an inert atmosphere at room temperature. Purification of the ligand was achieved by column chromatography on silica using hexane:ethyl acetate (3:1 v/v) as eluent. The product was obtained as an off-white solid in 74 % yield. Ligand **2** was prepared using the same method but employing 4-ethynyl- $\alpha,\alpha,\alpha$ -trifluorotoluene (1.1 eq.). After 18 hours at room temperature, column chromatography on

silica eluting with the slightly more polar solvent mixture hexane:ethyl acetate (2:1 v/v) afforded ligand **2** as a yellow solid in excellent yield (94 %).

Ligands **1** and **2** were fully characterised using  $^1\text{H}$  and  $^{13}\text{C}$   $\{^1\text{H}\}$  NMR spectroscopy. The  $^{19}\text{F}$  NMR spectrum of **2** was also recorded. Both ligands were further characterised using elemental analysis and infrared spectroscopy. The electrospray mass spectrum of **1** displays a peak centred at  $m/z = 313.1717$  m.u. for  $[\text{M}+\text{H}]^+$  which is in excellent agreement with the calculated value of  $m/z = 313.1705$  m.u. for  $[\text{C}_{22}\text{H}_{21}\text{N}_2]^+$ . Similarly, the electrospray mass spectrum **2** has a peak at  $m/z = 325.0952$  m.u. for  $[\text{M}+\text{H}]^+$ , which corresponds well to the calculated value of 325.0953 m.u. for  $[\text{C}_{19}\text{H}_{12}\text{N}_2\text{F}_3]^+$ .

### 1.2.1.1 $^1\text{H}$ NMR Spectra of **1** and **2**

As expected the  $^1\text{H}$  NMR spectra of aryl-acetylene ligands **1** and **2** are very similar (Figure 1.8).

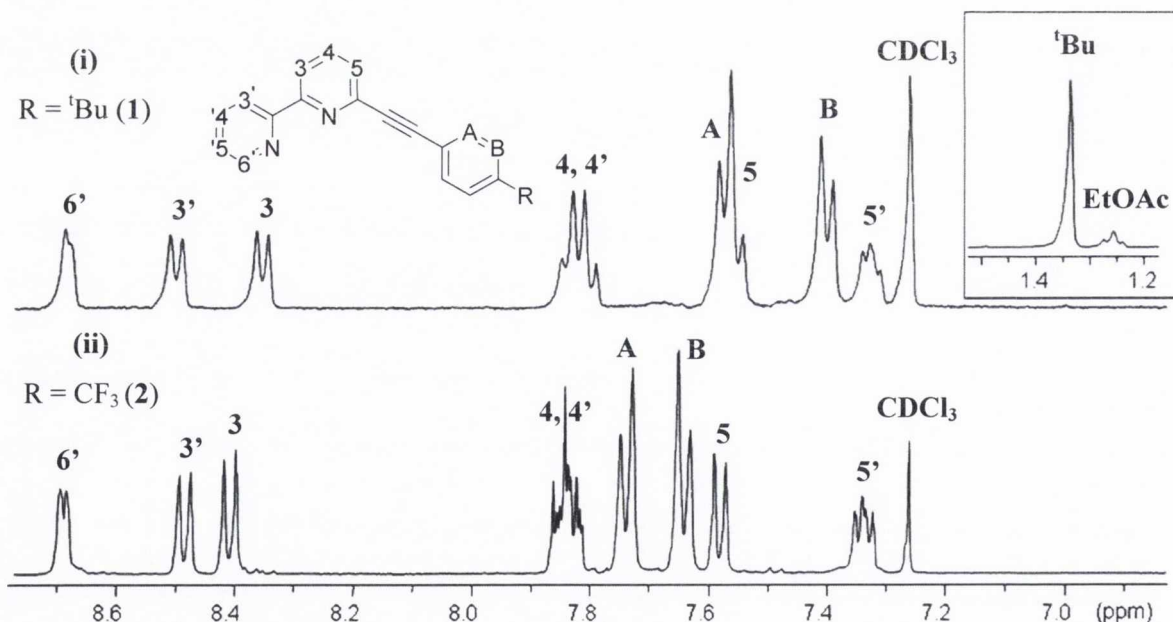


Figure 1.8:  $^1\text{H}$  NMR spectra of ligands **1** and **2** in  $\text{CDCl}_3$  (400.1 MHz, R.T.). Atom labelling as per inset figure.

The protons located on the same spin system, i.e. on the same pyridine ring, may be identified using a 2D correlation experiment, ( $^1\text{H}$ - $^1\text{H}$  COSY). The pattern observed in  $^1\text{H}$  NMR chemical shifts is common to each of the bipyridyl ligands prepared in this chapter and indeed to bipyridine-based ligands in general.<sup>66</sup> The aromatic signals for compounds **1**

and **2** integrate for 11 protons in total as expected. H6' provides the most deshielded signal, appearing at  $\delta$  8.69 ppm in both **1** and **2** and integrates for 1H in each. Its close proximity to the pyridine ring nitrogen results in its appearance as a doublet (split by a three bond interaction with the adjacent H5') with a small coupling constant (**2** for the signal at  $\delta$  8.69 ppm,  $^3J_{\text{HH}} = 4.0$  Hz). The next most downfield signal is attributable to the proton in the 3' position on the same pyridine ring (H3': **1**  $\delta$  8.50 ppm, **2**  $\delta$  8.48 ppm). H3 on the three-spin pyridine ring occurs in a very similar magnetic environment, marginally more upfield of H3' (H3: **1**  $\delta$  8.35 ppm, **2**  $\delta$  8.40 ppm). H3 and H3' on both ligands occur as doublets with  $^3J_{\text{HH}} = 8.0$  Hz. This significantly larger coupling constant is typical of all-carbon aromatic rings and is indicative of a greater distance from the pyridine ring nitrogen. In both ligands, H4 and H4' appear together as a multiplet at  $\sim\delta$  7.8 ppm in both cases (the multiplet in each spectrum integrates for 2H). H5' is the most upfield of the aromatic signals, appearing as a multiplet in both ligands at  $\delta$  7.33 ppm in **1** and in **2** at  $\delta$  7.33 ppm. In the aliphatic region of the spectrum of **1** (Figure 1.8, (i) inset), a signal at  $\delta$  1.34 ppm which integrates for 9 protons is attributable to the *tert*-butyl substituent.

The signals that undergo the most significant changes in chemical shift from **1** (<sup>t</sup>Bu) to **2** (CF<sub>3</sub>) are those attributable to HA and HB on the pendant aryl-acetylene functionality. HA and HB integrate for 2H each and occur as a pair of doublets ( $^3J_{\text{HH}} = 8.0$ -8.5 Hz) that exhibit a "roofing" effect and can be further assigned *via* the <sup>1</sup>H-<sup>1</sup>H COSY spectrum. In **2**, the attached electron-withdrawing CF<sub>3</sub> substituent results in a downfield shift of both signals (HA  $\delta$  7.73 ppm, HB  $\delta$  7.64 ppm) relative to those in **1**, which contains an electron-releasing *tert*-butyl substituent (HA  $\delta$  7.56 ppm,  $\delta$  HB 7.40 ppm). In general terms, the resonance for HA may be differentiated from that of HB on the basis of an examination of the <sup>13</sup>C {<sup>1</sup>H} NMR chemical shifts of ligand **2** (Section 1.2.1.2). HA and HB on ligand **1** were assigned by comparison with **2**.

### 1.2.1.2 <sup>13</sup>C {<sup>1</sup>H} NMR Spectra of **1** and **2**

The <sup>13</sup>C {<sup>1</sup>H} NMR spectra showing the aromatic regions of **1** (<sup>t</sup>Bu) and **2** (CF<sub>3</sub>) are presented in Figure 1.9. The spectra were assigned using a HSQC (Heteronuclear Single Quantum Coherence), a <sup>1</sup>H-<sup>13</sup>C COSY experiment, which facilitates the direct assignment of the <sup>13</sup>C signal to which each proton is attached. Two upfield quaternary carbons are evident in the spectra of both **1** and **2** (**1**  $\delta$  89.34, 88.42 ppm; **2**  $\delta$  90.97, 87.15 ppm, Figure

1.9). These signals are attributable to the two acetylenic quaternary carbons ( $C\equiv C$ ) which occur at more shielded chemical shifts as a result of the magnetic anisotropy induced by the acetylene fragment.<sup>67</sup>

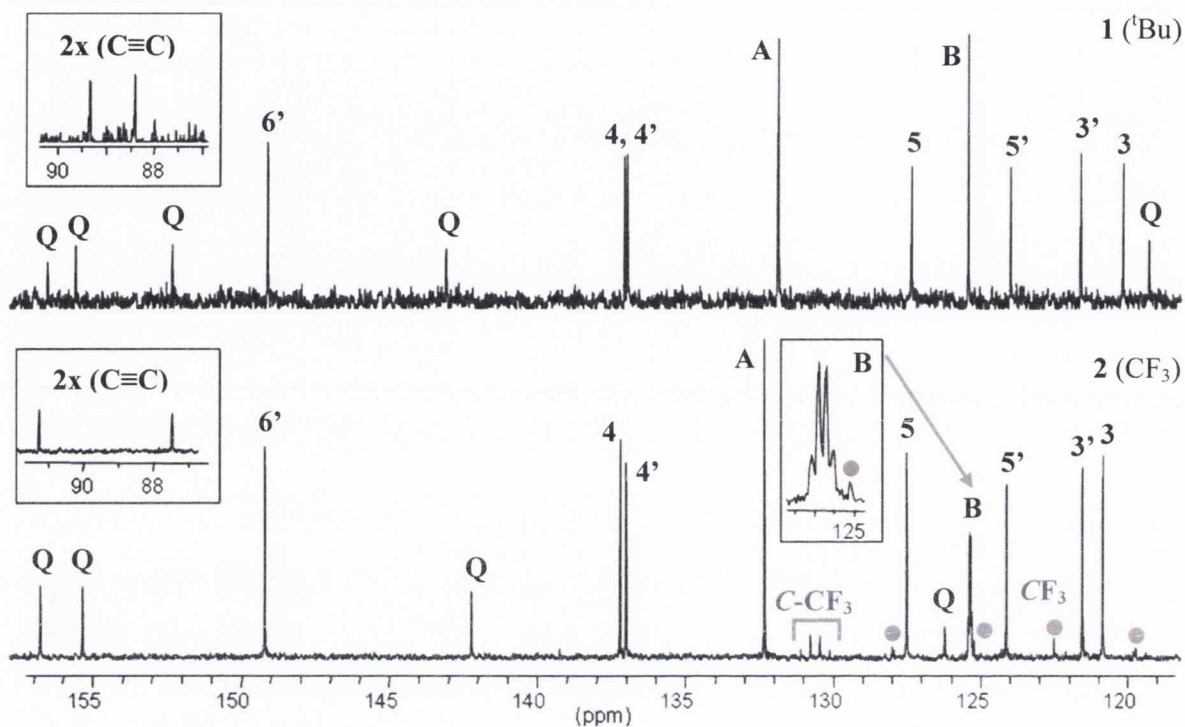


Figure 1.9:  $^{13}C \{^1H\}$  NMR spectra of **1** and **2** showing the aromatic regions in  $CDCl_3$  (100.6 MHz, R.T.). Atom labelling as per inset Figure 1.8 (Q denotes quaternary carbon).

The trend observed in ligands **1** and **2** for the  $^{13}C$  chemical shifts of the bipyridyl CH (methine) signals is common to each of the bipyridine ligands prepared in this chapter and is characteristic of bipyridines in general. Of the methine signals, in the free ligand C6' located adjacent to the electronegative pyridine ring nitrogen is always the most downfield (**1**  $\delta$  149.14 ppm, **2**  $\delta$  149.18 ppm). C4 and C4' occur in very similar chemical and magnetic environments (**1**  $\delta$  137.06, 136.97 ppm; **2**  $\delta$  137.17, 136.96 ppm), and typical of these rings systems, the most upfield CH signals are those of C3 and C3' (**1**  $\delta$  121.62, 120.18 ppm; **2**  $\delta$  121.50, 120.81 ppm). The aliphatic region of the  $^{13}C$  NMR spectrum of **1** ( $tBu$ ) exhibits two additional signals – a quaternary carbon signal at  $\delta$  34.91 ppm and a signal at  $\delta$  31.18 ppm for the  $(-C(CH_3)_3)$  unit.

The  $^{19}F$  NMR active nucleus in **2** exerts a considerable influence on the magnetic environments of the quaternary and methine carbons located in close proximity to it, such



that heteronuclear  $^{13}\text{C}$ - $^{19}\text{F}$  coupling is observed. Each carbon adjacent to the  $\text{CF}_3$  group should appear as a quartet ( $n=3$ ,  $I=1/2$ ). In Figure 1.9, the grey circles illustrate the quartet resulting from  $^{13}\text{C}$ - $^{19}\text{F}$  couplings,  $^1J_{\text{CF}}$ , between the carbon on the  $\text{CF}_3$  group itself and its directly attached fluorine atoms. This occurs as a quartet centred at  $\delta$  123.87 ppm with the largest through bond coupling constant  $^1J_{\text{CF}} = 271$  Hz. One bond further away, the carbon to which the  $\text{CF}_3$  group is attached (denoted  $\text{C-CF}_3$ ) also appears as a quartet centred at  $\delta$  130.61 ppm with a much smaller coupling constant,  $^2J_{\text{CF}} = 33$  Hz. Finally, the methine signal located closest to the  $\text{CF}_3$  substituent, CB, is also influenced by the magnetic field of the fluorine nuclei. This signal is split by three fluorine nuclei to appear as a quartet ( $\delta$  125.31 ppm) with a  $^3J_{\text{CF}} = 4$  Hz. In contrast, CA is four bonds away from a  $^{19}\text{F}$  nucleus and has only singlet multiplicity ( $\delta$  132.28 ppm). All measured carbon-fluorine coupling constants are in good agreement with literature values for other trifluoromethyl-substituted systems.<sup>68-69</sup>

### 1.2.1.3 $^{19}\text{F}$ NMR Spectrum of 2

The corresponding  $^{19}\text{F}$  NMR spectrum of **2** contains just one signal at  $\delta$  -63.3 ppm (Figure 1.10). The signal is a singlet as each fluorine atom in the trifluoromethyl-group is chemically equivalent to the others. No heteronuclear coupling constant with the attached carbon atom is observed as a result of the low natural abundance of the  $^{13}\text{C}$  isotope (1.1 %, spin  $1/2$ ).

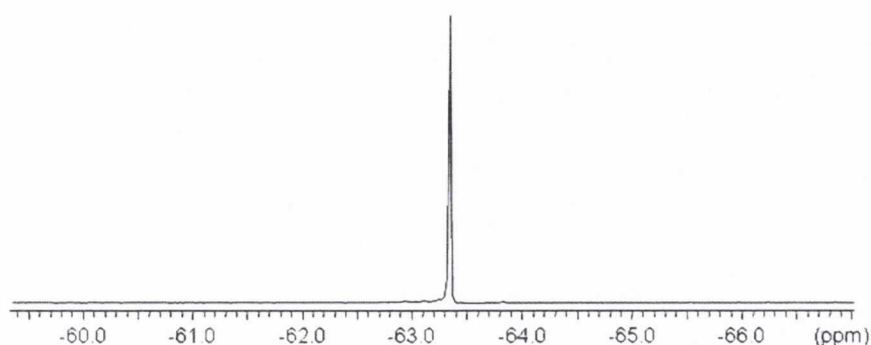


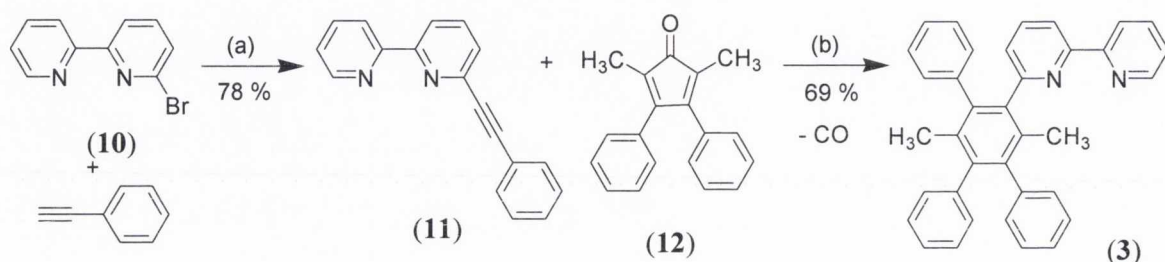
Figure 1.10:  $^{19}\text{F}$  NMR spectrum of **2** in  $\text{CDCl}_3$  (376.5 MHz, R.T.).

## 1.2.2 Synthesis of polyphenylene-bipyridines **3**, **4** and **5**

The preparation of the other three asymmetric bipyridine ligands **3**, **4** and **5** with multiple phenylene substituents required several more synthetic steps than involved in the synthesis of aryl-acetylene ligands **1** and **2**.

1.2.2.1 Synthesis of **3**

The synthesis of the first of these ligands, 6-(3,6-dimethyl-2,4,5-triphenylbenz-1-ene)-2,2'-bipyridine (**3**) is presented in Scheme 1.7. The first step was the formation of the novel compound 6-phenylethynyl-2,2'-bipyridine (**11**). This was achieved *via* a palladium-catalysed Sonogashira reaction between 6-bromo-2,2'-bipyridine (**10**) and phenylacetylene in the presence of *cis*-PdCl<sub>2</sub>(PPh<sub>3</sub>)<sub>2</sub> (6 mol%) and CuI (6 mol%). **11** was obtained following workup as a yellow/brown oil (78 % yield).

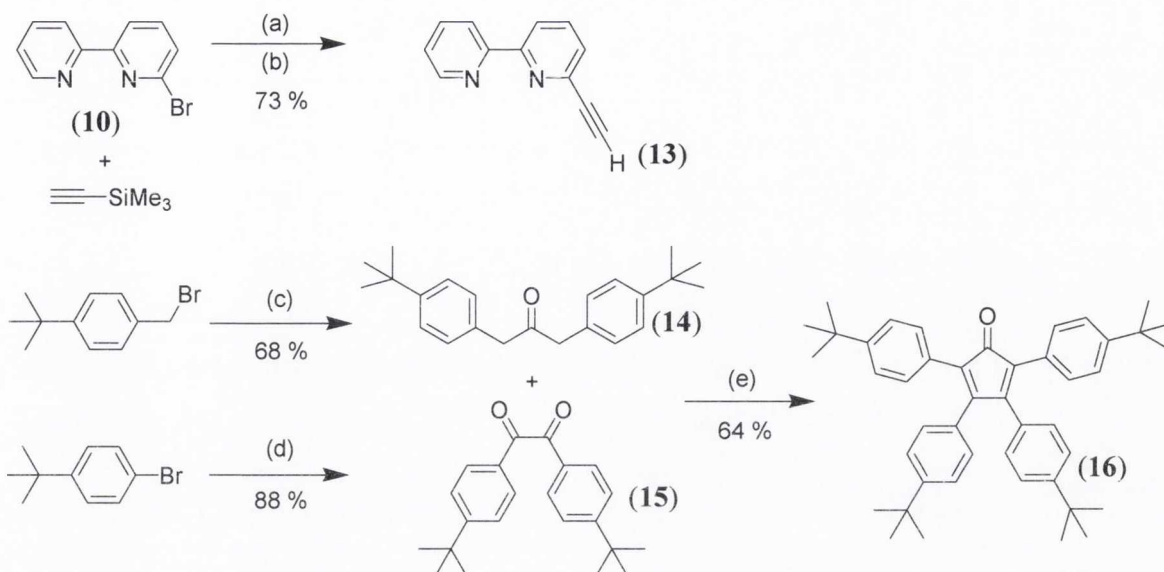


Scheme 1.7: Synthesis of **3** (Me<sub>2</sub>). (a) *cis*-PdCl<sub>2</sub>(PPh<sub>3</sub>)<sub>2</sub> (6 mol%), CuI (6 mol%), THF:<sup>i</sup>Pr<sub>2</sub>NH (2:1 v/v), R.T. (b) Benzophenone, 150-180 °C 3 hrs., 280-300 °C 6 hrs.

In order to generate **3**, compound **11** was further reacted with the commercially available compound 2,5-dimethyl-3,4-diphenylcyclopentadienone (**12**). The two reagents were heated in a benzophenone melt at elevated temperatures under an inert atmosphere for several hours. In this reaction, **12** undergoes a [2+4]-Diels-Alder cycloaddition reaction with **11** to form **3**, which proceeds with the extrusion of carbon monoxide. After column chromatography on silica gel, the target compound was produced in 69 % yield.

1.2.2.2 Syntheses of **4** and **5**

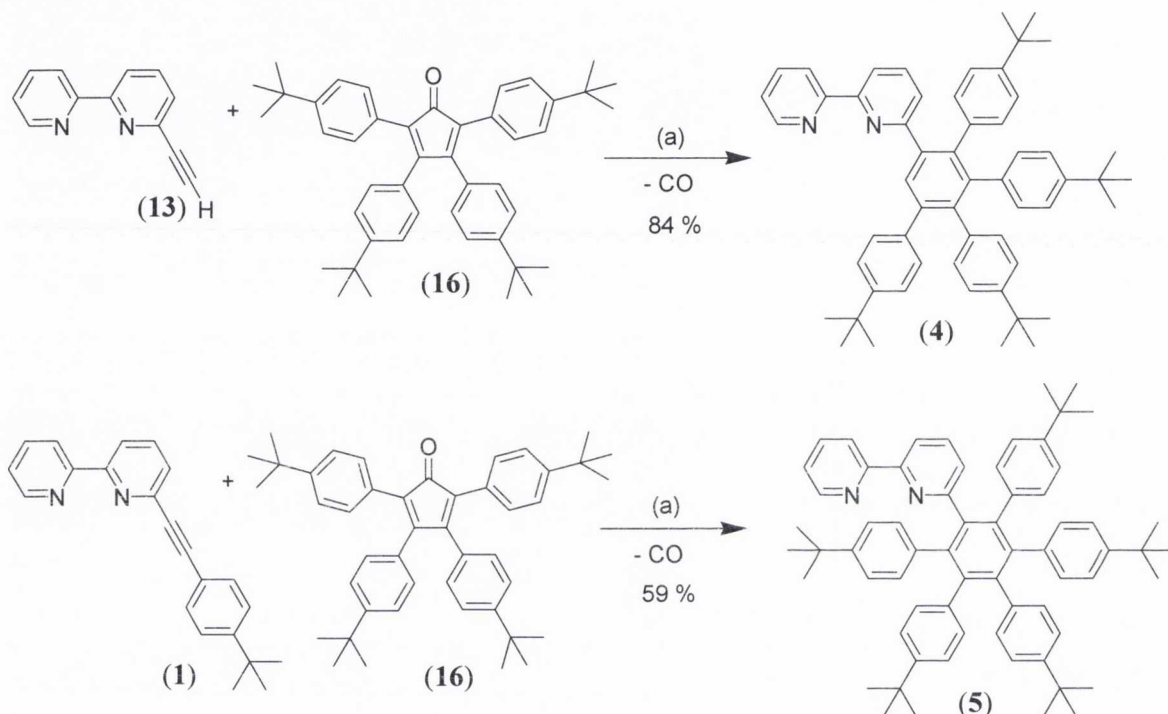
The syntheses of the two larger polyphenylene-ligands, 1-(2,2'-bipyrid-6-yl)-2,3,4,5-tetra(4-*tert*-butylphenyl) benzene (**4**) and 1-(2,2'-bipyrid-6-yl)-2,3,4,5,6-penta(4-*tert*-butylphenyl) benzene (**5**), require the assembly of several key components (Scheme 1.8).



*Scheme 1.8: The syntheses of precursors to 4 and 5. (a) cis-PdCl<sub>2</sub>(PPh<sub>3</sub>)<sub>2</sub> (6 mol%), CuI (6 mol%), THF:<sup>i</sup>Pr<sub>2</sub>NH (3:1 v/v), R.T. (b) KF (5 eq.), CH<sub>3</sub>OH:THF (1:1 v/v), R.T. (c) Ca(OH)<sub>2</sub>, <sup>t</sup>Bu<sub>4</sub>N<sup>+</sup>(HSO<sub>4</sub>)<sup>-</sup>, Fe(CO)<sub>5</sub>, CH<sub>2</sub>Cl<sub>2</sub>:H<sub>2</sub>O (1:1 v/v), R.T. (d) (i) <sup>n</sup>BuLi, -78 °C, THF, (ii) DMPD, (iii) HCl soln. (10 %). (e) KOH, CH<sub>3</sub>CH<sub>2</sub>OH, 78 °C.*

6-ethynyl-2,2'-bipyridine (**13**) is a known compound in the literature and was synthesised here *via* a modification of the literature procedure.<sup>70</sup> A palladium-catalysed Sonogashira cross-coupling reaction between **10** and trimethylsilylacetylene followed by deprotection of the silane group using KF in methanol/THF afforded **13** in a cumulative yield of 73 % (Scheme 1.8). The other three key synthetic precursors, a *tert*-butylphenyl substituted monoketone (**14**), a *tert*-butylphenyl substituted diketone (**15**) and a tetra-aryl cyclopentadienone (**16**), had been previously prepared within the research group in the synthesis of N-HSB.<sup>27</sup> The monoketone, 1,3-bis-(4-*tert*-butylphenyl)propan-2-one (**14**), was prepared *via* a liquid-liquid phase-transfer carbonylation reaction, with Fe(CO)<sub>5</sub> as the source of CO and <sup>t</sup>Bu<sub>4</sub>N<sup>+</sup>(HSO<sub>4</sub>)<sup>-</sup> as phase transfer catalyst.<sup>71</sup> The diketone, 2,5-bis-(4-*tert*-butylphenyl)ethane-1,2-dione (**15**), was prepared by lithiation of 4-*tert*-butylbromobenzene with <sup>n</sup>BuLi at -78 °C in THF, followed by reaction with DMPD (1,4-dimethylpiperazine-2,3-dione) and subsequent quenching with aq. HCl (10 %).<sup>72</sup> Finally, the cyclopentadienone, 2,3,4,5-tetra-(4-*tert*-butylphenyl)cyclopenta-2,4-dienone (**16**), was synthesised by a two-fold Knoevenagel condensation reaction between monoketone (**14**) and diketone (**15**) in the presence of KOH (0.5 eq.) in ethanol with the loss of two molecules of water.<sup>27</sup>

The novel ligand **4** (Me<sub>2</sub>) was synthesised using a [2+4] Diels-Alder cycloaddition from 6-ethynyl-2,2'-bipyridine (**13**) and tetraarylcyclopentadienone (**16**) which were heated in benzophenone in a sand-bath at elevated temperatures for 24 hours. The product was obtained as a pale brown crystalline solid after purification by column chromatography on silica eluting first with CH<sub>2</sub>Cl<sub>2</sub>:hexane (4:1 v/v) to remove unreacted cyclopentadienone and benzophenone and then changing to CH<sub>2</sub>Cl<sub>2</sub>:ethyl acetate to elute the product (84 % yield).



*Scheme 1.9: Syntheses of polyaryl bipyridine ligands **4** and **5**. (a) (i) Benzophenone, 150-200 °C, 6 hours, under Ar. (ii) 280-300 °C, 18 hours, under Ar.*

Finally **5** (Ar<sub>6</sub>), the most sterically hindered of the bipyridine ligands presented in this chapter, was prepared using a [2+4] cycloaddition reaction between **1** (t<sup>Bu</sup>) and cyclopentadienone (**16**) in a benzophenone melt at high temperature for 24 hours. Purification was achieved using silica gel column chromatography eluting first with petroleum ether:toluene (2:1 v/v) and then petroleum ether:toluene:CH<sub>2</sub>Cl<sub>2</sub> (1:1:0.1 v/v) to remove benzophenone, unreacted cyclopentadienone and side-products. The solvent system was gradually changed to toluene:CH<sub>2</sub>Cl<sub>2</sub> (3:1 v/v) and then to pure CH<sub>2</sub>Cl<sub>2</sub> in order to elute the target product, which was obtained as a pale yellow solid in 59 % yield.

### 1.2.2.3 Characterisation of polyphenylene ligands **3**, **4** and **5**

Polyphenylene-bipyridine ligands **3** (Me<sub>2</sub>), **4** (Ar<sub>5</sub>) and **5** (Ar<sub>6</sub>) were fully characterised using <sup>1</sup>H and <sup>13</sup>C {<sup>1</sup>H} NMR spectroscopy, infrared spectroscopy and elemental analysis. The NMR data of the known reactants, ethynyl-bipyridine (**13**), monoketone (**14**), diketone (**15**) and cyclopentadienone (**16**) were in good agreement with the literature.<sup>27,70</sup> The <sup>1</sup>H and <sup>13</sup>C {<sup>1</sup>H} NMR spectroscopic characterisation of phenyl-ethynyl bipyridine (**11**) was analogous to that of **1** and **2**. Chemical shifts and multiplicities of its <sup>1</sup>H NMR spectrum are detailed in Table 1.2 and full details are provided in Chapter 5-Experimental.

The electrospray mass spectra of the two bipyridyl precursors (**11** and **13**) and the three ligands (**3**, **4** and **5**) recorded in THF reveal the major peak in each corresponds to the [M+H]<sup>+</sup> molecular ion, where the compound has become charged by picking up a proton upon ionisation in the mass spectrometer. These values are in excellent agreement with the values calculated for the molecular ion. The mass spectral data is summarised in Table 1.1.

Table 1.1: Electrospray mass spectral data for precursor compounds **11** and **13** and novel polyphenylene bipyridine ligands **3**, **4** and **5** (all recorded in THF, *m/z* in *m.u.*).

Compound	Molecular Ion	Formula	Found <i>m/z</i> (%)	Calculated <i>m/z</i>
Ph-ac-Bpy ( <b>11</b> )	[M+H] <sup>+</sup>	[C <sub>18</sub> H <sub>13</sub> N <sub>2</sub> ] <sup>+</sup>	257.1077 (100)	257.1079
Ac-Bpy ( <b>13</b> )	[M+H] <sup>+</sup>	[C <sub>12</sub> H <sub>9</sub> N <sub>2</sub> ] <sup>+</sup>	181.0771 (100)	181.0766
<b>3</b> (Me <sub>2</sub> )	[M+H] <sup>+</sup>	[C <sub>36</sub> H <sub>29</sub> N <sub>2</sub> ] <sup>+</sup>	489.2321 (100)	489.2331
<b>4</b> (Ar <sub>5</sub> )	[M+H] <sup>+</sup>	[C <sub>56</sub> H <sub>61</sub> N <sub>2</sub> ] <sup>+</sup>	761.4841 (100)	761.4835
<b>5</b> (Ar <sub>6</sub> )	[M+H] <sup>+</sup>	[C <sub>66</sub> H <sub>73</sub> N <sub>2</sub> ] <sup>+</sup>	893.5803 (100)	893.5774

#### 1.2.2.3.1 <sup>1</sup>H NMR spectra of polyphenylene bipyridyl ligands **3**, **4** and **5**

The <sup>1</sup>H NMR spectra of ligands **3** (Me<sub>2</sub>), **4** (Ar<sub>5</sub>) and **5** (Ar<sub>6</sub>) in CDCl<sub>3</sub> are relatively similar and are shown together in Figure 1.11. The signals attributable to each pyridine ring system were identified by means of 2D <sup>1</sup>H-<sup>1</sup>H COSY experiments. It was not possible to distinguish pendant phenyl and *tert*-butyl phenyl ring signals from each other in either the <sup>1</sup>H or the <sup>13</sup>C {<sup>1</sup>H} NMR spectra of **3**, **4** and **5** and so these signals are marked as Ph (phenyl). The proton NMR chemical shifts, signal multiplicities and corresponding

coupling constants ( $J$ , Hz) for all novel bipyridine derivatives prepared in this chapter are detailed in Table 1.2.

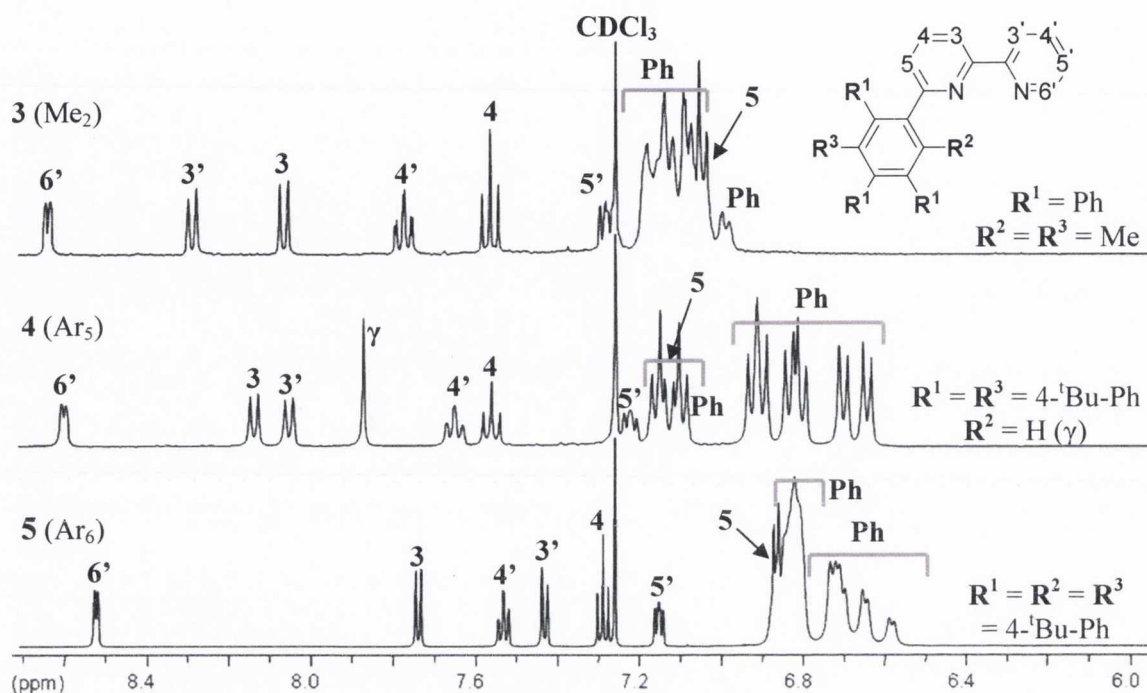


Figure 1.11:  $^1\text{H}$  NMR spectra of **3**, **4** and **5** in  $\text{CDCl}_3$  (**3**, **4** 400.1 MHz; **5** 600.1 MHz; R.T.) showing the aromatic regions. Atom labelling as per inset figure (4- $t$ Bu-Ph = 4-*tert*-butylphenyl).

As is typical of bipyridine derivatives, the proton in the 6' position is the most downfield of all the aromatic proton signals in ligands **3** ( $\delta$  8.63 ppm), **4** ( $\delta$  8.60 ppm) and **5** ( $\delta$  8.52 ppm).<sup>66</sup> Following the trend observed for aryl-acetylene ligands **1** and **2**, the most upfield bipyridyl signals may be attributed to protons in the 5 and 5' positions (Figure 1.11). As anticipated, H3 and H3' signals appear as doublets (d), split by the adjacent H4/H4' protons (Table 1.2). The signals due to H4 and H4' frequently appear as a doublet of doublets (dd), due to vicinal interactions ( $^3J$ ) with their neighbouring protons H3 and H5 (which are in different chemical environments). In some cases, H4/H4' appears as a doublet of doublets of doublets (ddd) due to an additional long-range ( $^4J$ ) coupling with H6 on the same pyridine ring system (Table 1.2). In Figure 1.11 it is clear that on moving from **3** ( $\text{Me}_2$ ) to **4** ( $\text{Ar}_5$ ) to **5** ( $\text{Ar}_6$ ), the resonances assigned to both bipyridine and phenyl ring protons become more shielded. This is as a result of greater steric hindrance within each molecule such that the individual proton signals are in closer proximity to electron rich pendant aryl substituents. The resonances of phenyl and *tert*-butyl aromatic ring protons appear as a series of overlapping signals ( $\delta$  6.5–7.2 ppm).

The aliphatic regions of each ligand (**3**, **4** and **5**) possess additional structural details. In **3** (Me<sub>2</sub>), two singlets occur at  $\delta$  1.85 and 1.90 ppm, integrating for three protons each due to the methyl groups attached to the hexa-substituted central phenyl ring. In **4** (Ar<sub>5</sub>), singlets at  $\delta$  1.26, 1.15, 1.11 and 1.10 ppm, each integrating for nine protons, are due to the *tert*-butyl groups on the pendant aryl rings. Just two signals are evident in the aliphatic region of **5** (Ar<sub>6</sub>), attributable to the five attached *tert*-butyl phenyl functional groups which overlap considerably ( $\delta$  1.11 ppm, 27H;  $\delta$  1.04 ppm, 18H).

Table 1.2: Comparative <sup>1</sup>H NMR chemical shifts, signal multiplicity and coupling constants for ligands **1**, **2**, **11**, **3**, **4** and **5** in CDCl<sub>3</sub>. Atom labelling as per inset Figure 1.11.

Ligand	<sup>1</sup> H NMR / $\delta$ , ppm (multiplicity, J/Hz)						
	6'	5'	4'	3'	5	4	3
<b>1</b> ( <sup>t</sup> Bu)	8.69 (d, 4.5)	7.33 (m)	7.81 (m)	8.50 (d, 8.0)	7.56 (m)	7.81 (m)	8.35 (d, 8.0)
<b>2</b> (CF <sub>3</sub> )	8.69 (d, 4.0)	7.33 (m)	7.84 (m)	8.48 (d, 8.0)	7.57 (d, 7.5)	7.84 (m)	8.40 (d, 8.0)
Ph-ac- Bpy( <b>11</b> )	8.68 (d, 4.1)	7.32 (m)	7.81 (m)	8.50 (d, 7.9)	7.56 (d, 7.5)	7.81 (m)	8.37 (d, 7.9)
<b>3</b> (Me <sub>2</sub> )	8.63 (d, 4.9)	7.28 (m)	7.77(ddd, 7.8, 2.0)	8.29 (d, 8.8)	7.18 (m)	7.57 (dd, 7.8)	8.07 (d, 7.8)
<b>4</b> (Ar <sub>5</sub> )	8.60 (d, 4.9)	7.22 (m)	7.65 (dd, 7.8)	8.05 (d, 7.8)	7.10 (m)	7.56 (dd, 7.8)	8.14 (d, 6.9)
<b>5</b> (Ar <sub>6</sub> )	8.52 (d, 4.2)	7.15 (m)	7.53(ddd, 7.5, 1.5)	7.43 (d, 7.9)	6.87 (m)	7.29 (d, 7.5)	7.74 (d, 7.9)

#### 1.2.2.3.2 <sup>13</sup>C {<sup>1</sup>H} NMR Spectrum of **4** (Ar<sub>5</sub>)

The <sup>13</sup>C {<sup>1</sup>H} DEPT 90 NMR spectrum of **4** (Ar<sub>5</sub>) is presented in Figure 1.12. In a DEPT-90 experiment, only methine (CH) carbons appear as positive signals and quaternary carbons are not observed. As for **1** (<sup>t</sup>Bu) and **2** (CF<sub>3</sub>), the spectrum was assigned using a 2D HSQC. The <sup>13</sup>C {<sup>1</sup>H} chemical shifts of the bipyridyl methine signals of all the novel bipyridine compounds prepared in this chapter are summarised in Table 1.3.

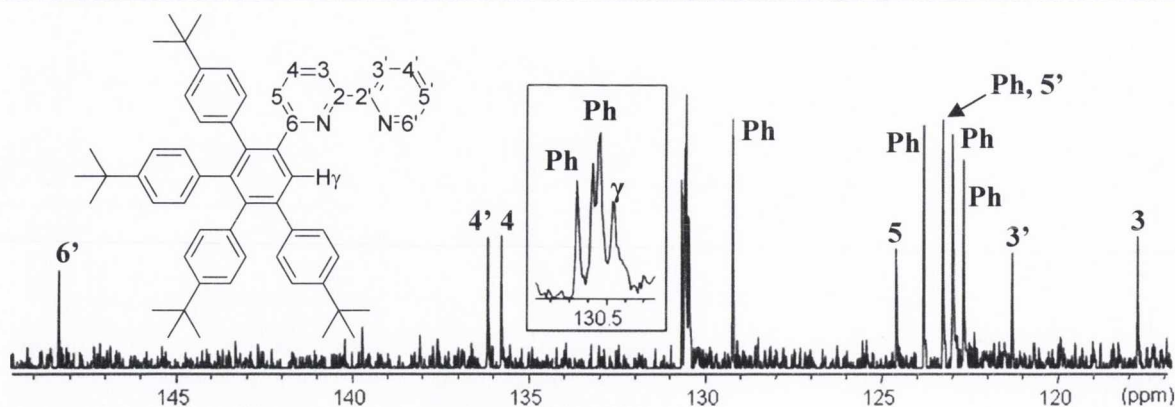


Figure 1.12:  $^{13}\text{C} \{^1\text{H}\}$  DEPT 90 experiment of **4** showing the aromatic region (100.6 MHz, R.T.). Atom labelling as per inset figure. (Ph = CH on  $^t\text{Bu}$ -phenyl ring).

For each bipyridine derivative prepared (**1**, **2**, **11**, **3**, **4** and **5**), the CH signal located in the 6' position is always the most downfield of the methine carbon signals and the C3 and C3' methine resonances are the most upfield (Table 1.3). The  $^{13}\text{C} \{^1\text{H}\}$  chemical shifts of the CH resonances on the four-spin pyridine ring system (CH positions 3'-6') vary little (<1 ppm) from one derivative to another. More significant changes in chemical shift (>2 ppm) are observed for the three-spin pyridine ring to which different polyphenylene derivatives of varying electronic-demand are directly attached.

Table 1.3: Comparative  $^{13}\text{C} \{^1\text{H}\}$  NMR chemical shifts for ligands **1**, **2**, **11**, **3**, **4** and **5** in  $\text{CDCl}_3$ . Atom labelling as per inset Figure 1.11.

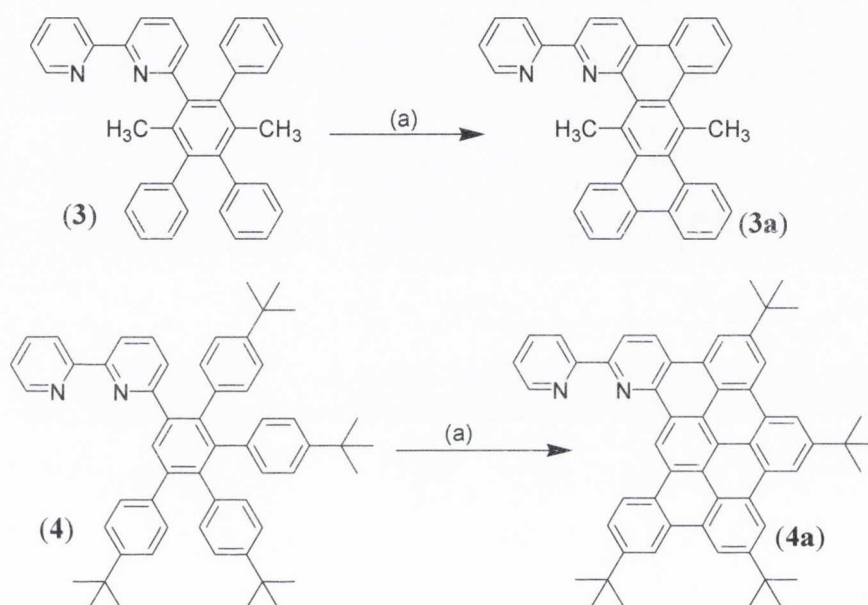
Ligand	$^{13}\text{C} \{^1\text{H}\}$ NMR / $\delta$ , ppm						
	6'	5'	4'	3'	5	4	3
<b>1</b> ( $^t\text{Bu}$ )	149.14	123.99	136.97	121.62	127.35	137.06	120.18
<b>2</b> ( $\text{CF}_3$ )	149.18	124.08	136.96	121.50	127.45	137.17	120.81
Ph-ac-Bpy ( <b>11</b> )	149.11	123.97	136.92	121.56	127.30	137.05	120.32
<b>3</b> ( $\text{Me}_2$ )	148.95	123.47	136.73	121.66	125.72	136.20	118.31
<b>4</b> ( $\text{Ar}_5$ )	148.30	122.99	136.15	121.29	124.58	135.76	117.74
<b>5</b> ( $\text{Ar}_6$ )	148.34	~123(m)	136.13	122.03	127.08	134.88	117.39

### 1.2.3 Cyclodehydrogenation of bipyridyl-oligophenylene ligands

Attempts to achieve planarisation of oligophenylene ligands **3** ( $\text{Me}_2$ ) and **4** ( $\text{Ar}_5$ ) were undertaken, prompted by the combination of enhanced  $\pi$ -electronic delocalisation and inherent ligand functionality induced by insertion of nitrogen atoms into the periphery of



the discotic HBC segment (N-HSB). In order to limit partially cyclised intermediates and consequent potential purification difficulties, interests initially focused on **3**, in which just two carbon-carbon bonds may form between adjacent aryl rings to form **3a** (Scheme 1.10). Cyclodehydrogenation of **4** to form **4a**, with the formation of four new carbon-carbon bonds, was expected to be more difficult. For each system, the two standard methods for the oxidative cyclodehydrogenation of hexaphenylbenzenes were employed (Section 1.1.2.3), namely  $\text{AlCl}_3/\text{CuCl}_2/\text{CS}_2$  and  $\text{FeCl}_3$  in nitromethane/ $\text{CH}_2\text{Cl}_2$  (Scheme 1.10).

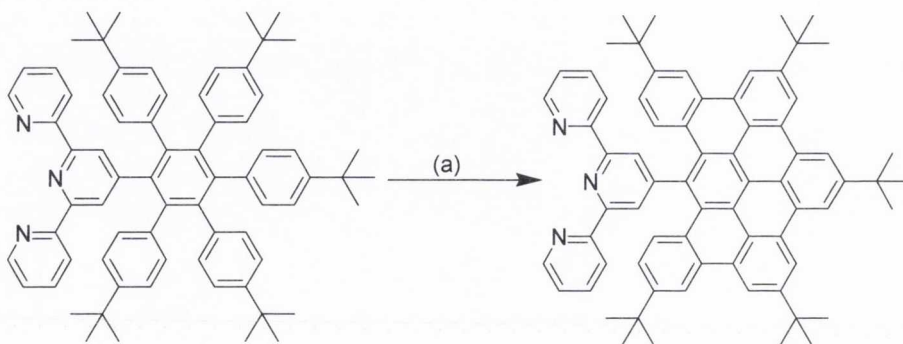


Scheme 1.10: Cyclodehydrogenation of **3** ( $\text{Me}_2$ ) and **4** ( $\text{Ar}_5$ ). (a) i)  $\text{AlCl}_3$  (16 eq.),  $\text{CuCl}_2$  (16 eq.),  $\text{CS}_2$ , 298 K, 72 hrs. ii)  $\text{FeCl}_3$  (25 eq.),  $\text{NO}_2\text{Me}$ ,  $\text{CH}_2\text{Cl}_2$ , 298 K, Ar bubbling.

Despite multiple attempts *via* both synthetic routes, neither **3a** nor **4a** were successfully isolated from their reaction mixtures. From the  $\text{AlCl}_3$  synthetic route, only unreacted polyphenylene **3** or **4** were recovered. The  $\text{FeCl}_3$  method yielded only unreacted ligand and multiple  $\text{Fe(III)}$  paramagnetic complexes, which could not be isolated.

In contrast to all carbon-hydrogen systems in which oxidative cyclodehydrogenation is relatively facile, it is clear that pyridine ring nitrogens significantly disrupt the reaction mechanism. This has been observed previously within the research group for a terpyridyl-polyphenylene molecule, in which only the *tert*-butyl phenyl ring moieties undergo ring closure (Scheme 1.11).<sup>73</sup> Assuming the arenium cation mechanism is valid (Section 1.1.2.3), the initial protonation step will most likely involve protonation of a pyridine

ring.<sup>24</sup> The protonated pyridine ring may be insufficiently electrophilic to attack an adjacent phenyl ring. Protonation of the phenyl rings will also be difficult because the molecule already bears a positive charge as the basic nitrogen atoms are already protonated.<sup>24</sup> As a result, C-C bond formation and oxidative cyclodehydrogenation of **3** and **4** are strongly deactivated.



Scheme 1.11: Cyclodehydrogenation of a terpyridyl-polyphenylene compound. (a)  $\text{FeCl}_3$  (25 eq.),  $\text{NO}_2\text{Me}$ ,  $\text{CH}_2\text{Cl}_2$ .<sup>73</sup>

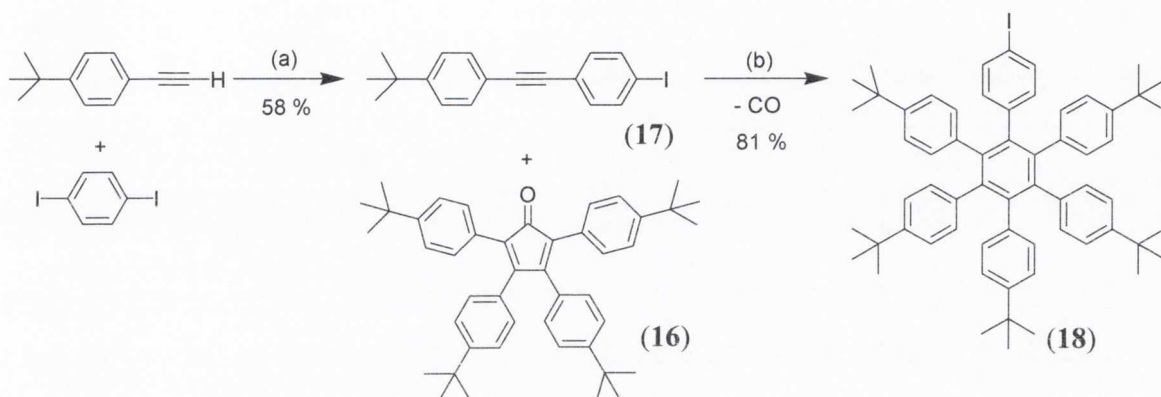
### 1.3 Ligand Series B: Synthesis of polyaromatic ligands with one acetylene functional group

The preparation of polyaromatic propeller ligand, ethynyl-hexaphenylbenzene (**6**), and its related cyclised graphene, ethynyl-HBC (**7**), require the initial assembly of the key synthetic precursor iodo-hexaphenylbenzene (Scheme 1.12, **18**). This halogenated compound provides a suitable functionalisation site to which the desired alkynyl functionality may be cross-coupled.

#### 1.3.1 Preparation of the synthetic precursor iodo-hexaphenylbenzene (**18**)

Towards the preparation of ethynyl-hexaphenylbenzene (**6**) and ethynyl-hexa-*peri*-hexabenzocoronene (**7**), two iodinated synthons were first prepared (Scheme 1.12). The first of these, 4-iodo-4'-*tert*-butylphenylacetylene (**17**), was synthesised *via* a Sonogashira palladium-catalysed cross-coupling reaction between 1,4-diiodobenzene and 4-*tert*-butylphenylacetylene using an analogous procedure to that described for aryl-acetylene bipyridine ligands **1**, **2** and **11**.<sup>74</sup> Iodo-hexaphenylbenzene (**18**) was prepared *via* a Diels-Alder cycloaddition reaction between iodo-acetylene (**17**) and the tetraarylcyclopentadienone (**16**) (whose synthesis was described in Scheme 1.8) in a

benzophenone melt at elevated temperatures.<sup>74</sup> The target compound was obtained as a precipitate from excess methanol as an off-white powder in 81 % yield. The syntheses of iodo-acetylene (**17**), iodo-hexaphenylbenzene (**18**) and ethynyl-HBC (**7**) have been previously reported within the research group in the preparation of a terpyridyl-substituted HBC platform.<sup>74</sup>



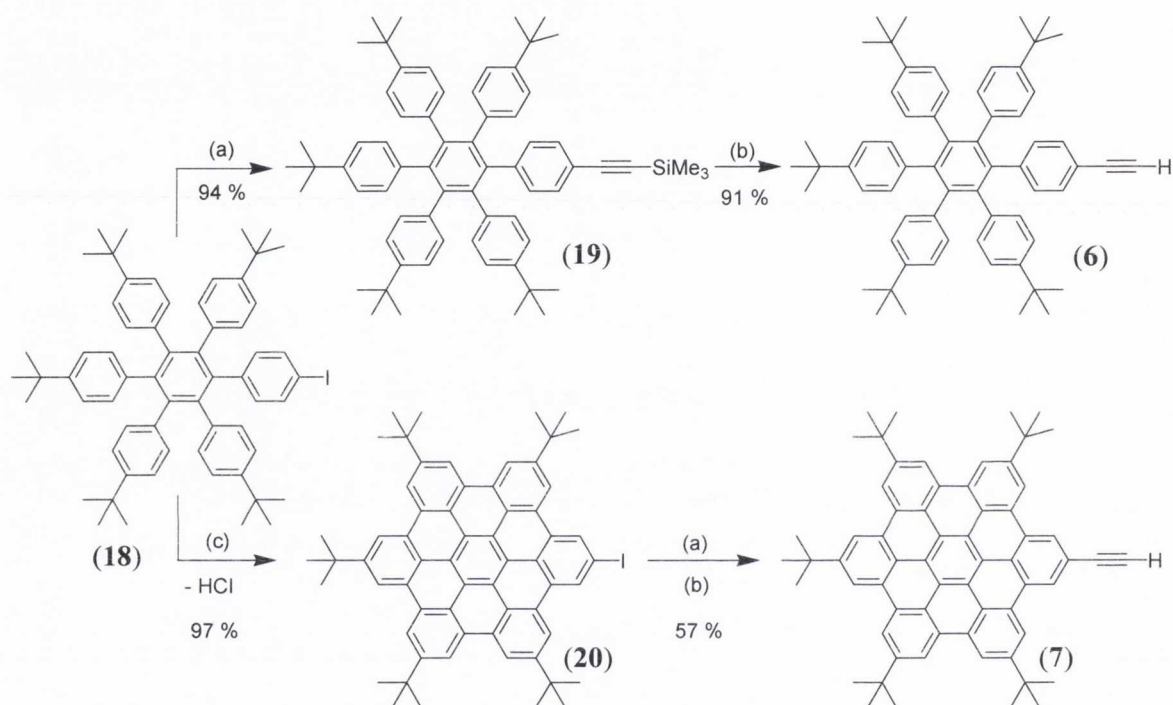
*Scheme 1.12: Synthesis of iodo-hexaphenylbenzene (18). (a) cis-PdCl<sub>2</sub>(PPh<sub>3</sub>)<sub>2</sub> (6 mol%), CuI (6 mol%), THF:<sup>i</sup>Pr<sub>2</sub>NH (3:1 v/v), R.T. (b) Benzophenone, 200 °C 2hrs., 300 °C 16 hrs., under Ar.*

### 1.3.2 Synthesis of ethynyl-hexaphenylbenzene (**6**) and ethynyl-HBC (**7**)

Iodo-hexaphenylbenzene (**18**), as shown in Scheme 1.13, is employed in the preparation of the novel compound ethynyl-hexaphenylbenzene (**6**) and the previously prepared ligand ethynyl-HBC (**7**).<sup>74</sup> Sonogashira cross-coupling between trimethylsilylacetylene and iodo-hexaphenylbenzene (**18**) using *cis*-PdCl<sub>2</sub>(PPh<sub>3</sub>)<sub>2</sub> as catalyst and CuI as co-catalyst in a solvent mixture of THF:<sup>i</sup>Pr<sub>2</sub>NH (3:1 v/v) affords the protected precursor to **6**, namely 1-(4-trimethylsilylethynylphenyl)-2,3,4,5,6-penta-(4-*tert*-butylphenyl)benzene (**19**), in 94 % yield. Subsequent deprotection using excess KF in a mixture of solvents produced the target compound **6** in 91 % yield. For each step of this procedure, purification of the products was achieved in the same way - by washing of the reaction mixture with water to remove unreacted starting materials (e.g. TMS-acetylene, KF) and by-products (e.g. SiMe<sub>3</sub>F), followed by precipitation from excess methanol and washing with cold methanol.

Towards the synthesis of the cyclised ligand ethynyl-HBC (**7**), it was first necessary to undertake the oxidative cyclodehydrogenation of iodo-hexaphenylbenzene (**18**). This was achieved by one of the standard cyclisation routes: FeCl<sub>3</sub> as the oxidant, dissolved in minimal nitromethane, added dropwise to a solution of **18** in still-dried, argon-degassed

$\text{CH}_2\text{Cl}_2$ . The reaction was stirred at room temperature for 20 hours during which time nitrogen was continuously bubbled through the solution. The evolution of HCl was monitored using pH paper and when this had ceased, the reaction was quenched with methanol to obtain a dark yellow precipitate. Purification was achieved by column chromatography using a short silica column eluting with  $\text{CH}_2\text{Cl}_2$  in order to removed iron impurities. Reduction of the solution *in vacuo* followed by precipitation from excess methanol afforded iodo-HBC (**20**) in 97 % yield.



*Scheme 1.13 : Synthesis of ethynyl-hexaphenylbenzene (6) and ethynyl-HBC (7). (a) *cis*- $\text{PdCl}_2(\text{PPh}_3)_2$  (6 mol%),  $\text{CuI}$  (6 mol%),  $\text{THF}:\text{}^i\text{Pr}_2\text{NH}$  (3:1 v/v), R.T. (b)  $\text{KF}$  (5 eq.),  $\text{CH}_3\text{OH}:\text{THF}$  (1:1 v/v), R.T. (c)  $\text{FeCl}_3$  (25 eq.),  $\text{NO}_2\text{Me}$ ,  $\text{CH}_2\text{Cl}_2$ , Ar bubbling.*

Iodo-HBC (**20**) was then reacted with trimethylsilylacetylene (Scheme 1.13) *via* a Sonogashira cross-coupling reaction in the presence of *cis*- $\text{PdCl}_2(\text{PPh}_3)_2$  (6 mol%) and  $\text{CuI}$  (6 mol%) as catalysts to afford the corresponding silyl-protected HBC platform (**21**). This compound required arduous column chromatography on silica, eluting with petroleum ether: $\text{CH}_2\text{Cl}_2$  (5:1 v/v), in order to remove a highly fluorescent iron-containing impurity picked up in the previous cyclodehydrogenation step. This could not be removed in the previous step as the impurity has very similar polarity to iodo-HBC (**20**) such that attempted column chromatography on silica or alumina using multiple solvent systems was not possible. Subsequent deprotection of **21** was achieved using excess  $\text{KF}$  in a mixture of

THF:MeOH. Ethynyl-HBC (**7**) was obtained as a yellow solid with a cumulative yield of 57 % from iodo-HBC.

### 1.3.3 Characterisation of **19**, **6** and **7**

The new compounds TMS-ethynyl-hexaphenylbenzene (**19**) and ethynyl-hexaphenylbenzene (**6**) were fully characterised using  $^1\text{H}$  and  $^{13}\text{C}$   $\{^1\text{H}\}$  NMR spectroscopy, infrared spectroscopy and mass spectrometry. Similarly, a thorough analysis of the NMR spectroscopic data and mass spectral results for ethynyl-HBC (**7**) confirmed the presence and purity of the target compound. The mass spectral data of compounds **19**, **6** and **7** are summarised in Table 1.4.

Table 1.4: Mass spectral data for novel hexaphenylbenzene compounds **19** and **6** and ethynyl-HBC ligand **7** (**19** and **6** recorded in THF, **7** in  $\text{CH}_2\text{Cl}_2$ ,  $m/z$  in m.u.).

Compound	Molecular Ion	Formula	Found $m/z$ (%)	Calculated $m/z$
TMS-HPB ( <b>19</b> )	$[\text{M}+\text{Na}]^+$	$[\text{C}_{67}\text{H}_{78}\text{NaSi}]^+$	933.5785 (100)	933.5771
Ethynyl-HPB ( <b>6</b> )	$[\text{M}+\text{Na}]^+$	$[\text{C}_{64}\text{H}_{70}\text{Na}]^+$	861.5387 (100)	861.5375
Ethynyl-HBC ( <b>7</b> )	$[\text{M}]^+$	$[\text{C}_{64}\text{H}_{58}]^+$	826.4568 (100)	826.4539

The electrospray mass spectra of the two hexaphenylbenzene derivatives, **19** (TMS-HPB) and **6** (Ethynyl-HPB) recorded in THF reveal the major peak in each spectrum corresponds to the  $[\text{M}+\text{Na}]^+$  molecular ion, where the compound has become charged upon ionisation in the mass spectrometer by picking up a sodium cation. These values are in good agreement with the calculated values. The mass spectrum of ethynyl-HBC (**7**) was recorded on a MALDI-TOF mass spectrometer. The major peak centred at  $m/z$  826.4568 m.u. corresponds with the molecular ion  $[\text{M}]^+$ , with a calculated value of  $m/z$  826.4539 m.u. for  $[\text{C}_{64}\text{H}_{58}]^+$ .

#### 1.3.3.1 $^1\text{H}$ NMR Spectra of hexaphenylbenzenes **19** and **6**

The  $^1\text{H}$  NMR spectra of ethynyl-hexaphenylbenzene (**6**) and its trimethylsilyl-protected precursor (**19**) are shown together in Figure 1.13. Both derivatives possess a  $\text{C}_2$  axis of symmetry through the acetylene (Figure 1.13, inset). The aromatic regions of the two spectra are almost identical. The signals for the aromatic protons on both compounds occur as a series of overlapping AB splitting patterns for each of the phenyl rings located

between  $\delta$  6.6-7.0 ppm. For both **19** and **6**, the phenyl ring adjacent to the acetylene moiety can be easily distinguished, with the proton closest to the acetylene (H1) appearing most deshielded (**19**  $\delta$  6.98 ppm, **6**  $\delta$  6.99 ppm) with its adjacent H2 on the same ring system located within the multiplet at  $\delta$  6.77-6.83 ppm (**19**) and  $\delta$  6.78-6.84 ppm (**6**).

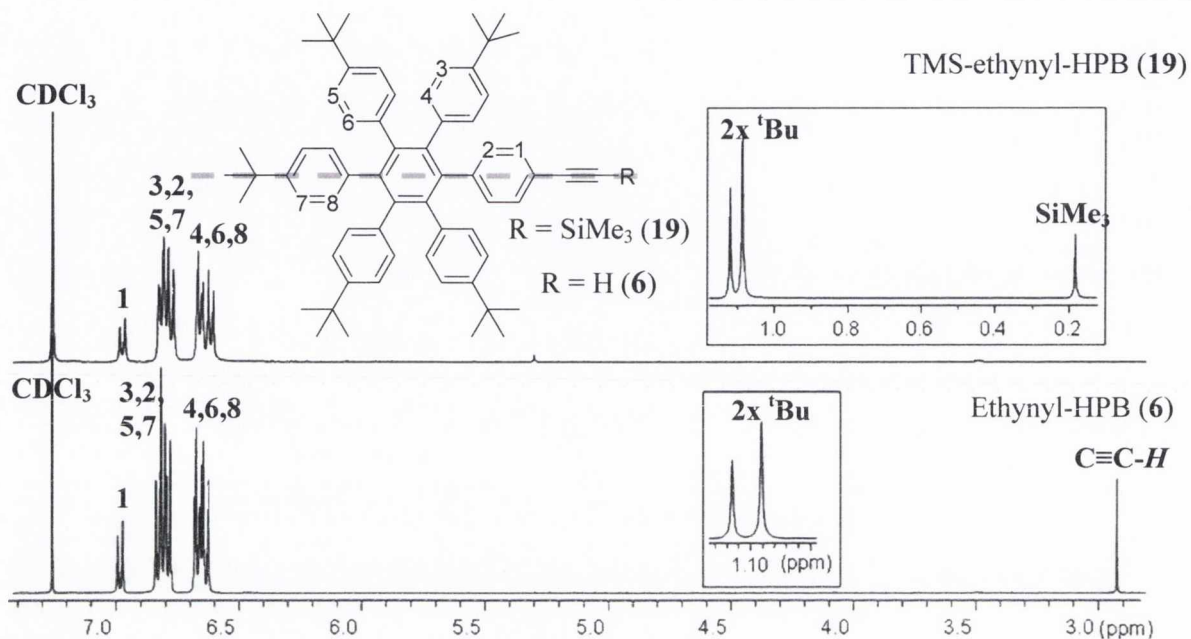


Figure 1.13:  $^1\text{H}$  NMR spectra of **19** and **6** in  $\text{CDCl}_3$  at room temperature (**19** 600 MHz, **6** 400 MHz) with inset aliphatic region. Atom labelling as per inset figure.

In general, it is possible to identify the aromatic phenyl ring signals that are closest to the *tert*-butyl functional group using selective NOE (Nuclear Overhauser Effect) experiments. By this method, selective irradiation of an individual *tert*-butyl resonance will see a NOE enhancement on adjacent spins through space. For example, irradiation of either *tert*-butyl group ( $\delta$  1.09 or 1.12 ppm) in **6** results in a positive signal for the more downfield multiplet ( $\delta$  6.78-6.84 ppm). This indicates that H3, H5 and H7 spins occur within this multiplet which integrates for 12 protons. A  $^1\text{H}$ - $^1\text{H}$  COSY experiment is then used to find the adjacent proton on each phenyl ring, such that H4, H6 and H8 (integral value 10H) are found to occur in the multiplet  $\delta$  6.62-6.68 ppm. The assignment of **19** was achieved similarly.

The distinguishing features of the two NMR spectra arise from the substituent attached to the alkynyl moiety (**19**  $\text{R} = \text{SiMe}_3$ , **6**  $\text{R} = \text{H}$ ). A singlet in the spectrum of ethynyl-hexaphenylbenzene (**6**) at  $\delta$  2.92 ppm with an integration value of one proton may be

assigned to the terminal acetylene proton. A significantly more upfield proton resonance at  $\delta$  0.18 ppm which integrates for 9 protons in the aliphatic region of the TMS-ethynyl-hexaphenylbenzene (**19**) spectrum is due to the SiMe<sub>3</sub> protecting group.

### 1.3.3.2 <sup>13</sup>C {<sup>1</sup>H} NMR spectrum of ethynyl-hexaphenylbenzene (**6**)

The <sup>13</sup>C {<sup>1</sup>H} NMR spectrum of ethynyl-hexaphenylbenzene (**6**), between  $\delta$  30-135 ppm, is shown in Figure 1.14. Carbon signals which are more downfield of this range may be attributed to aromatic quaternary carbons. C1 and C2 may be easily identified by <sup>1</sup>H-<sup>13</sup>C COSY (HSQC) and occur at  $\delta$  130.31 ppm and  $\delta$  131.61 ppm respectively. In general, CH signals in similar chemical environments but on different <sup>t</sup>Bu-phenyl rings have similar chemical shifts. For example, the three more upfield CH signals ( $\delta$  123.32, 123.06, 123.02 ppm) are assigned to C3, C5 and C7 methine carbons located closest to the *tert*-butyl substituent (Figure 1.14). A quaternary carbon at  $\delta$  84.33 ppm can be assigned as the internal alkynyl carbon signal, -C $\equiv$ CH. The acetylene CH group (denoted C $\equiv$ C-H), at  $\delta$  76.05 ppm, was used to distinguish H1 from H2 (and correspondingly C1 from C2) using a long-range <sup>1</sup>H-<sup>13</sup>C correlation experiment (HMBC).

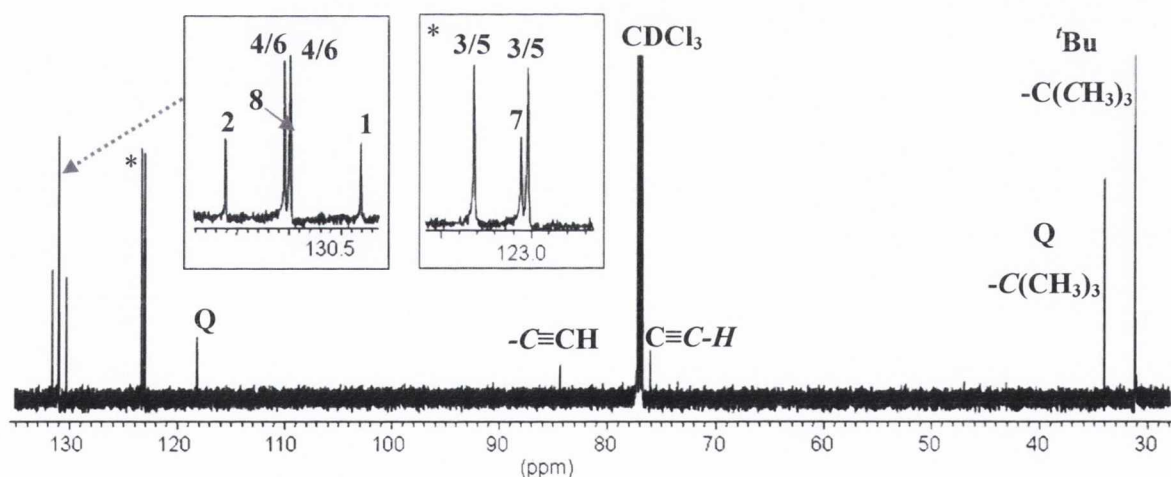


Figure 1.14: <sup>13</sup>C {<sup>1</sup>H} NMR spectrum of **6** showing the spectrum between  $\delta$  30-135 ppm (CDCl<sub>3</sub>, 150.9 MHz, R.T.). Atom labelling as per inset Figure 1.13 (R=H).

Finally, the aliphatic region of the spectrum reveals three quaternary carbon signals at  $\delta$  34.02, 34.04 and 34.10 ppm due to the central carbon of the *tert*-butyl substituent (-C(CH<sub>3</sub>)<sub>3</sub>). The methyl carbon signals for the *tert*-butyl substituents appear slightly more upfield as three overlapping singlets at  $\delta$  31.18 ppm.

### 1.3.3.3 $^1\text{H}$ NMR Spectrum of ethynyl-HBC (7)

The  $^1\text{H}$  NMR spectrum of ethynyl-HBC (7) is shown in Figure 1.15, in order to show the effect of polyphenylene cyclisation. In general, the aromatic region of the spectrum is shifted downfield compared to the polyphenylene, in this case ethynyl-hexaphenylbenzene (6) (Figure 1.13). In effect, the planar HBC platform can be considered as a “superbenzene” molecule with a significant ring current. The HBC hydrogens are deshielded by the diamagnetic anisotropy of the ring.<sup>67</sup> This phenomenon is observed in aromatic rings in general but is enhanced dramatically by the highly electron-delocalised polyaromatic HBC platform, resulting in large downfield proton resonance shifts.

The aromatic region in the  $^1\text{H}$  NMR spectrum of ethynyl-HBC (7) consists of 6 singlets ( $\delta$  8.6–9.2 ppm), each integrating for two protons as a result of the  $C_2$  axis of symmetry through the molecule. The singlet closest to the acetylene  $\text{H}^1$  is the most shielded appearing at  $\delta$  8.65 ppm. Moving around the periphery of the HBC core further from the acetylene substituent, the  $^1\text{H}$  chemical shifts become gradually more deshielded. These assignments were achieved using long-range  $^1\text{H}$ - $^{13}\text{C}$  HMBC experiments. The single *tert*-butyl resonance at  $\delta$  1.94 ppm, which integrates for 9H and correspondingly must be the substituent attached immediately opposite the alkynyl fragment, has a long range correlation to C6 (whose H6 is located at  $\delta$  9.17 ppm). H6 is linked to H5 *via* the same long-range correlation. Using this method, the aromatic resonances may be easily assigned.<sup>74</sup> Finally, the alkyne proton signal ( $\text{C}\equiv\text{C}-\text{H}$ ) appears at  $\delta$  3.59 ppm, slightly downfield from that of ethynyl-hexaphenylbenzene (6), which occurs at  $\delta$  2.92 ppm.

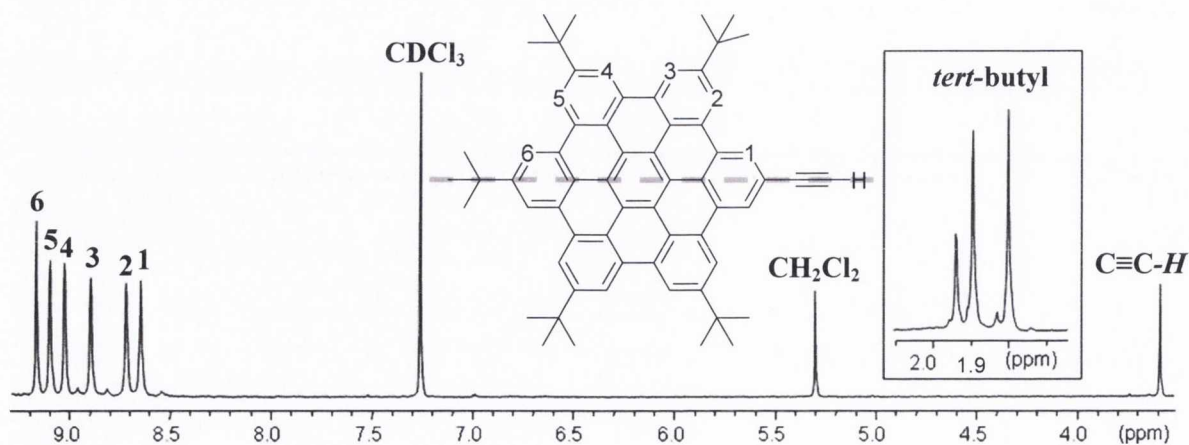


Figure 1.15:  $^1\text{H}$  NMR spectrum of 7 ( $\text{CDCl}_3$ , 400 MHz, R.T.) with inset *tert*-butyl region. Atom labelling as per inset figure.

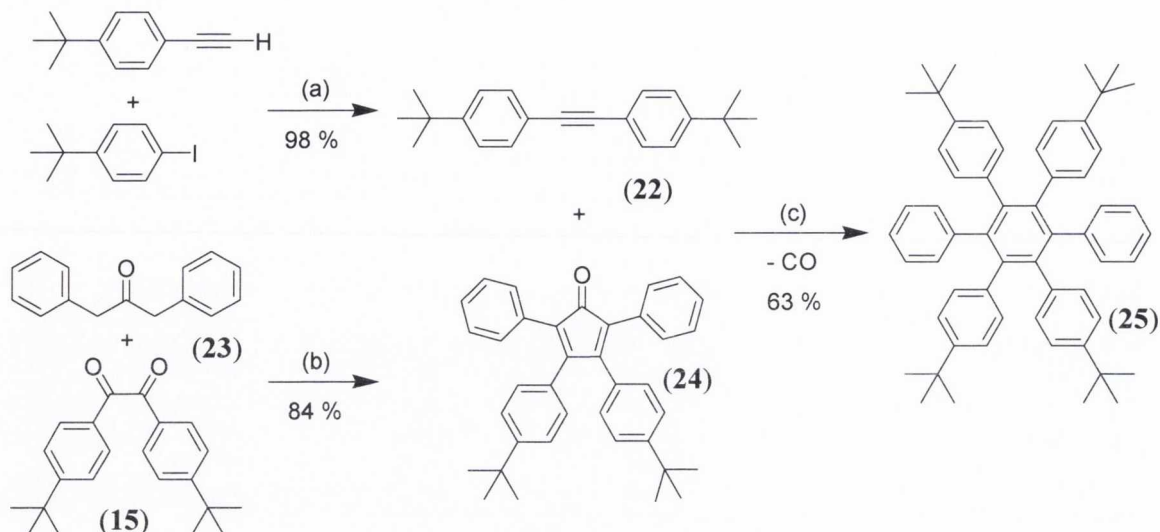


## 1.4 Ligand Series B: Synthesis of polyaromatic ligands with two acetylene functional groups

The attachment of two acetylene functionalities to the polyaromatic core may be achieved by initially incorporating two iodine substituents. In this work, two novel di-acetylene hexaphenylbenzene derivatives are prepared. In the first ligand, referred to as *ortho*-bis-ethynyl-hexaphenylbenzene (**9**), the two ethynyl-substituted phenyl rings are positioned *ortho* to each other with respect to the central phenyl ring. In the second, the ethynylphenyl rings are *para* to each other, *para*-bis-ethynyl-hexaphenylbenzene (**8**). Similar to the method employed towards the synthesis of ethynyl-hexaphenylbenzene (**6**), diiodo-hexaphenylbenzene precursors to **9** and **8** are the key synthons required. Employing a method developed within the research group, these iodo-compounds may be prepared from hexaphenylbenzene compounds with two unsubstituted phenyl rings at *ortho* and *para* positions.<sup>75</sup> Iodination at the *para*-position on each of these unsubstituted phenyl rings is then achieved *via* a mild electrophilic aromatic iodination reaction using bis[trifluoroacetoxy]phenyliodine and I<sub>2</sub>.<sup>76</sup>

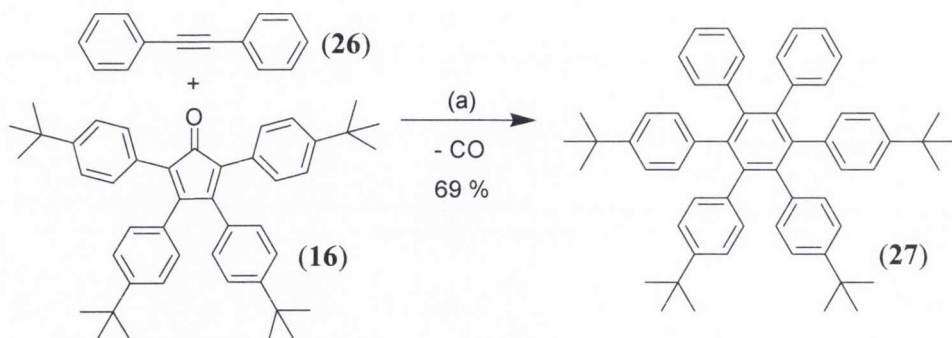
### 1.4.1 Synthesis of hexaphenylbenzenes containing unsubstituted phenyl rings

Towards the synthesis of *para*-bis-ethynyl-hexaphenylbenzene (**8**), compound (**25**) containing unsubstituted phenyl rings *para* to each other about the central benzene ring was first prepared (Scheme 1.14). This was achieved *via* a Diels-Alder cycloaddition reaction by heating bis(4-*tert*-butylphenyl)acetylene (**22**) and 2,5-bis-phenyl-3,4-bis-(4-*tert*-butylphenyl)cyclopenta-2,4-dienone (**24**) together with benzophenone under argon, heating initially for two hours (150-200 °C) and then raising the temperature to 300 °C for a further four hours.<sup>75</sup> Precipitation from excess methanol afforded hexaphenylbenzene (**25**) in 63 % yield. Bis(4-*tert*-butylphenyl)acetylene (**22**) was prepared *via* the Sonogashira coupling of 4-iodo-*tert*-butylbenzene with 4-ethynyl-*tert*-butylbenzene in piperidine.<sup>10</sup> Cyclopentadienone **24** was prepared from the Knoevenagel condensation of the commercially available diphenylacetone (**23**) and *tert*-butyl substituted diketone (**15**).<sup>4</sup>



Scheme 1.14: Synthesis of hexaphenylbenzene (**25**). (a)  $[Pd(PPh_3)_4]$  (2.5 mol%), CuI (2.5 mol%), piperidine, 18 hours, R.T. (b) KOH (1.5 eq.), EtOH, 78 °C, 5 hours. (c) Benzophenone, 150-200 °C 2 hours, 300 °C 4 hours, under Ar.

The preparation of hexaphenylbenzene (**27**) containing unsubstituted phenyl rings *ortho* to each other is detailed in Scheme 1.15. The [2+4]-Diels Alder cycloaddition reaction between commercially available diphenylacetylene (**26**) and the tetra *tert*-butylphenyl substituted cyclopentadienone (**16**) in a benzophenone melt, heating at 250 °C for 2 hours and raising the temperature to 350 °C for 3.5 hours, affords hexaphenylbenzene (**27**) in 69 % yield.<sup>75</sup> As for the other hexaphenylbenzene derivatives prepared in this work, purification was achieved by dissolving the reaction mixture in minimum  $CH_2Cl_2$  and precipitating the product from excess cold methanol.



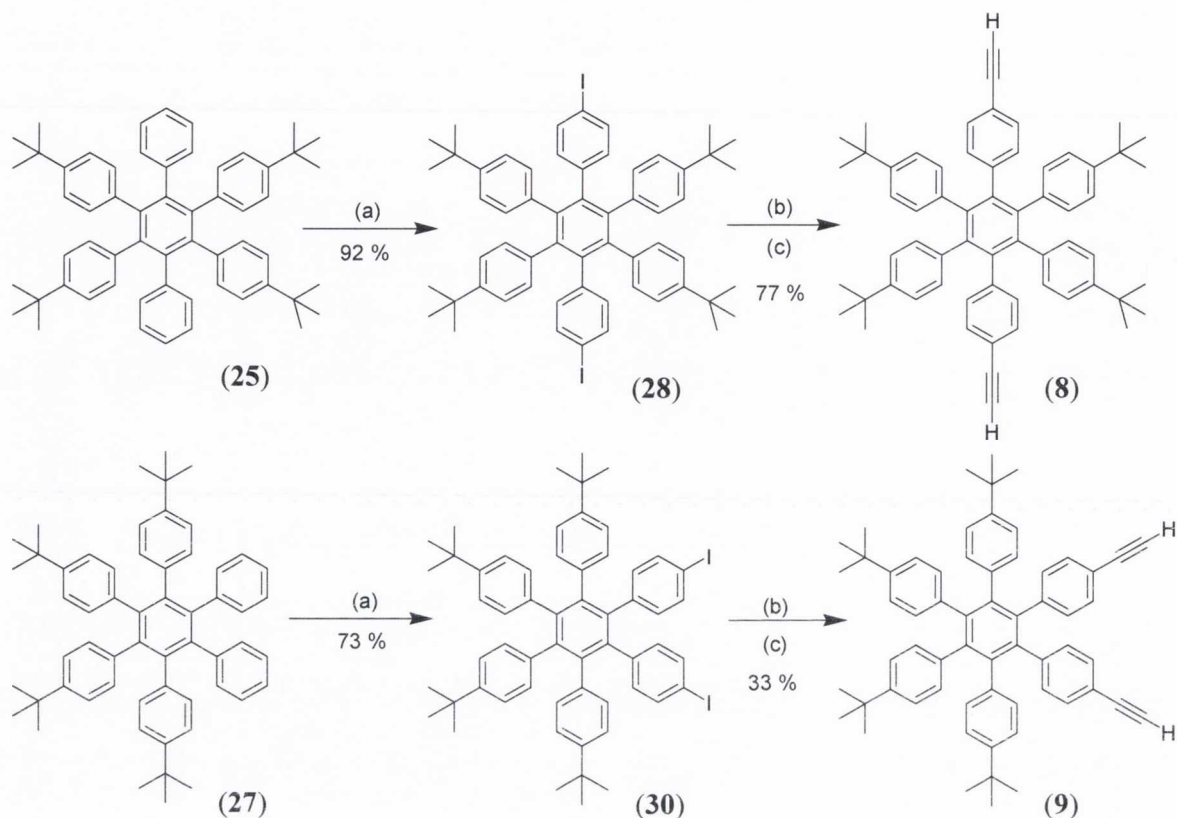
Scheme 1.15: Synthesis of hexaphenylbenzene (**27**). (a) Benzophenone, 250 °C 2 hours, 350 °C 3.5 hours, under Ar.

#### 1.4.2 Synthesis of *para*- and *ortho*- bis-ethynyl-hexaphenylbenzenes

Iodination of hexaphenylbenzenes **25** and **27** was carried out using a modification of a mild and highly efficient method originally developed by Merkushev and co-workers to iodinate an aromatic compound (Scheme 1.16).<sup>76</sup> The method employs the hypervalent iodine reagent (bis(trifluoroacetoxy)iodo)benzene (PIFA, 3.8 eq.) with I<sub>2</sub> (0.8 eq.) in a CH<sub>2</sub>Cl<sub>2</sub>:CHCl<sub>3</sub> (1:1 v/v) solvent mixture.<sup>75-76</sup> These are stirred with the required hexaphenylbenzene precursor (1 eq.) in darkness, under argon for 18 hours. After this time, two further additions of PIFA (1.3 eq. extra in total) and I<sub>2</sub> (0.3 eq. extra in total) are made over the course of an additional 24 hours reaction time in order to force the complete conversion of the starting material to the diiodo-product. The reaction mixture was washed with Na<sub>2</sub>S<sub>2</sub>O<sub>4</sub> solution in order to remove unreacted iodine, washed with water and the solvent was removed from the organic layer *in vacuo*. The residue was redissolved in the minimum of diethyl ether and the product precipitated by adding it to excess methanol. In both *para*-diiodo-hexaphenylbenzene (**28**) and *ortho*-diiodo-hexaphenylbenzene (**30**) cases, selective iodination occurs only at the *para* positions of the unsubstituted phenyl rings. This method has been previously employed in the 6-fold iodination of a hexaphenylbenzene containing 6 unsubstituted phenyl rings.<sup>42</sup>

The iodine-substituents on the periphery of hexaphenylbenzene derivatives **28** and **30** provide a site for further functionalisation of the chromophore with acetylene groups (Scheme 1.16). Towards target compound *para*-bis-ethynylhexaphenylbenzene (**8**), trimethylsilylacetylene (5 eq., excess) was coupled *via* a palladium-catalysed Sonogashira cross-coupling reaction with *para*-diiodo-hexaphenylbenzene (**28**), using *cis*-PdCl<sub>2</sub>(PPh<sub>3</sub>)<sub>2</sub> (12 mol%) as catalyst and CuI (12 mol%) as co-catalyst in THF: <sup>i</sup>Pr<sub>2</sub>NH (2:1 v/v). After 48 hours, *para*-bis-trimethylsilylethynyl-hexaphenylbenzene (**29**) was isolated in 95 % yield. The product was deprotected using KF (5 eq.) in a mixture of methanol and THF to afford *para*-bis-ethynylhexaphenylbenzene (**8**) as an off-white powder with a cumulative yield of 77 % for cross-coupling and deprotection steps. The synthesis of *ortho*-bis-ethynylhexaphenylbenzene (**9**) was achieved *via* the same method, preparing firstly *ortho*-bis-trimethylsilylethynyl-hexaphenylbenzene (**31**) which was deprotected to yield **9** in a total yield of 33 %. This reduced yield for the *ortho* derivative is as a result of a slightly poorer yielding iodination process and increased solubility of *ortho*-substituted

hexaphenylbenzenes in methanol relative to *para*, such that precipitation, despite concentration of washings, results in lower percentage yields.



**Scheme 1.16:** Synthesis of *ortho*- (**9**) and *para*- (**8**) bis-ethynyl-hexaphenylbenzenes. (a) (i) PIFA (3.8 eq.), I<sub>2</sub> (0.8 eq.), CH<sub>2</sub>Cl<sub>2</sub>:CHCl<sub>3</sub> (1:1 v/v), darkness, 18 hrs. (ii) PIFA (1.3 eq.), I<sub>2</sub> (0.8 eq.), 24 hrs. (iii) Na<sub>2</sub>S<sub>2</sub>O<sub>4</sub> wash. (b) *cis*-PdCl<sub>2</sub>(PPh<sub>3</sub>)<sub>2</sub> (12 mol%), CuI (12 mol%), THF:<sup>1</sup>Pr<sub>2</sub>NH (2:1 v/v), 48 hrs., R.T. (c) KF (5 eq.), CH<sub>3</sub>OH:THF (1:1 v/v), 24 hrs., R.T.

#### 1.4.2.1 Characterisation of novel *ortho*- (**31**), (**9**) and *para*- (**29**), (**8**) compounds

The new compounds *ortho*-bis-TMS-ethynyl-hexaphenylbenzene (**31**), *ortho*-bis-ethynyl-hexaphenylbenzene (**9**), *para*-bis-TMS-ethynyl-hexaphenylbenzene (**29**) and *para*-bis-ethynyl-hexaphenylbenzene (**8**) were fully characterised using <sup>1</sup>H and <sup>13</sup>C {<sup>1</sup>H} NMR spectroscopy, infrared spectroscopy and mass spectrometry. By comparison with literature assignments, NMR spectroscopy and mass spectrometry confirmed the presence and purity of precursor compounds **22**, **24**, **25**, **27**, **28** and **30** (full details provided in Chapter 5-Experimental).<sup>4,10,75</sup>

The electrospray mass spectral data of the four new compounds in THF are summarised in Table 1.5. The spectra of the two *ortho*-substituted compounds **31** and **9** consist of a peak

centred at  $m/z = 989.5290$  m.u. (**31**) (at  $m/z = 845.4481$  m.u. for compound **9**), for  $[M+K]^+$ , which is in good agreement with the calculated value of  $m/z$  989.5279 m.u. for  $[C_{68}H_{78}Si_2K]^+$  (**9**: calculated value  $m/z$  845.4489 m.u.  $[C_{62}H_{62}K]^+$ ). Similarly, the mass spectra of the *para* substituted compounds reveal major peaks which correspond to the  $[M+H]^+$  (**29**) and the  $[M+Na]^+$  (**8**) molecular ions respectively and match well to their corresponding calculated values.

Table 1.5: Electrospray mass spectral data for *ortho* compounds **31** and **9** and *para* compounds **29** and **8** (all recorded in THF,  $m/z$  in m.u.).

Compound	Molecular Ion	Formula	Found $m/z$ (%)	Calculated $m/z$
<i>o</i> -TMS-HPB ( <b>31</b> )	$[M+K]^+$	$[C_{68}H_{78}Si_2K]^+$	989.5290 (100)	989.5279
<i>o</i> -Ethynyl-HPB ( <b>9</b> )	$[M+K]^+$	$[C_{62}H_{62}K]^+$	845.4481 (100)	845.4489
<i>p</i> -TMS-HPB ( <b>29</b> )	$[M+H]^+$	$[C_{68}H_{79}Si_2]^+$	951.5709 (100)	951.5720
<i>p</i> -Ethynyl-HPB ( <b>8</b> )	$[M+Na]^+$	$[C_{62}H_{62}Na]^+$	829.4737 (100)	829.4749

#### 1.4.2.2 $^1H$ NMR spectra of target compounds: *ortho*-(**9**) and *para*-(**8**)

The  $^1H$  NMR spectra of *ortho*-bis-ethynyl-hexaphenylbenzene (**9**) and *para*-bis-ethynyl-hexaphenylbenzene (**8**) are given in Figure 1.16.

As would be anticipated, the  $^1H$  NMR spectra of **9** and **8** are very similar to that of monoalkynylated ethynyl-hexaphenylbenzene (**6**) (Figure 1.13). **8** (*para*) possesses two lines of symmetry through the molecule resulting in a very simple NMR spectrum with just four signals in the aromatic region. There are two sets of AB spin system, one due to H1 and H2 on the ethynyl-phenyl ring, where each signal represents four equivalent protons. The other AB spin system is assigned as H3/H4 on a *tert*-butyl phenyl ring, with H3 and H4 each integrating for 8 equivalent protons. For **9** (*ortho*), just one line of symmetry is evident through the molecule resulting in the appearance of more signals in the spectrum. In this case, three sets of AB spin systems are evident. The increased symmetry of the *para* ligand compared to the *ortho* is also evident in the aliphatic region. Just one *tert*-butyl group occurs in the spectrum of **8** ( $\delta$  1.11 ppm) whereas two signals attributable to *tert*-butyl groups appear for **9** ( $\delta$  1.09, 1.11 ppm).

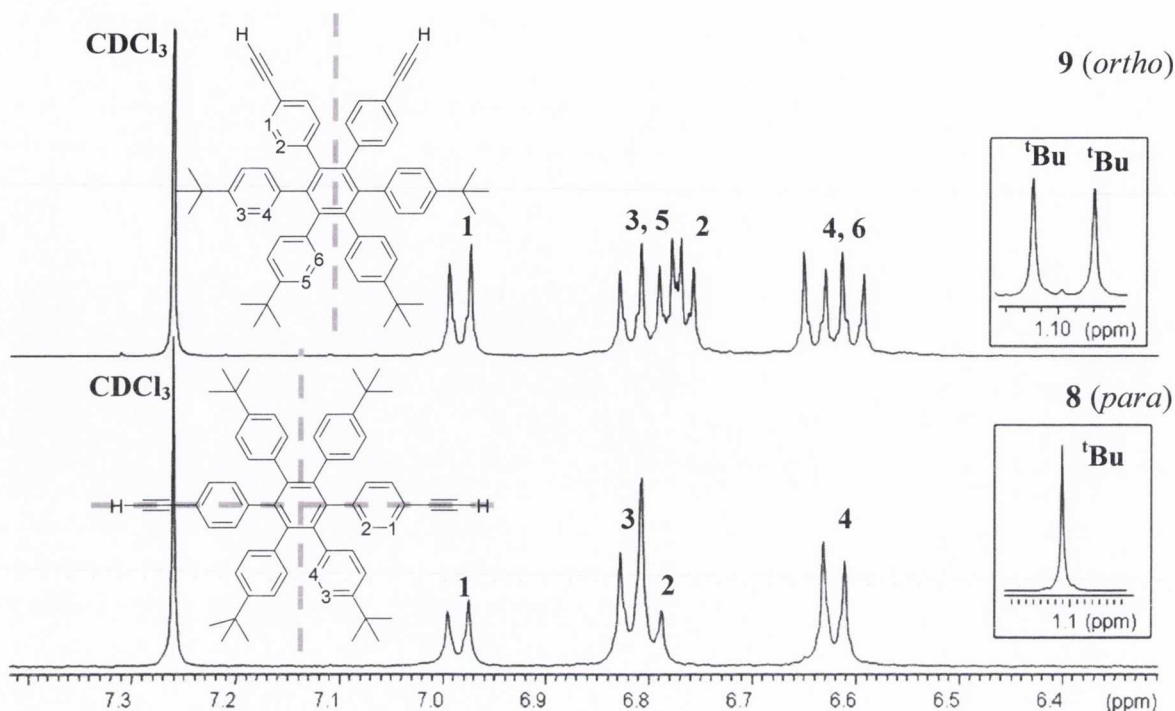


Figure 1.16:  $^1\text{H}$  NMR spectra of **9** (400 MHz) and **8** (600 MHz) in  $\text{CDCl}_3$  at room temperature. Atom labelling as per inset figures.

H1 closest to the acetylene is the most downfield signal in both compounds, appearing as a doublet with  $^3J_{\text{HH}} = 8.0$  Hz (**9**:  $\delta$  7.00 ppm, **8**:  $\delta$  6.98 ppm). As identified for ethynyl-hexaphenylbenzene (**6**), the next most downfield set of signals may be assigned as the protons closest to the *tert*-butyl substituent. For example, H3 and H5 signals are in the multiplet  $\delta$  6.78–6.86 ppm in **9 (ortho)**, in addition to H2 on the ethynyl-phenyl ring. Similarly, H3 appears in the multiplet  $\delta$  6.81 ppm in **8 (para)** with H2. The high degree of symmetry in both ligands means that the two acetylenic protons within each compound are equivalent. The signal appears at similar chemical shifts in both *ortho* and *para* compounds (**9**:  $\delta$  2.94 ppm, **8**:  $\delta$  2.92 ppm).

## 1.5 Summary and Conclusions

This chapter details the synthesis and characterisation of two series of novel compounds with ligand functionality. The first, a series of asymmetric aryl-acetylene and polyphenylene substituted bipyridine ligands, consists of five new molecules prepared by means of a sequence of Sonogashira cross-coupling reactions and [2+4] Diels-Alder cycloadditions. These ligands have been fully characterised by NMR spectroscopy,

infrared spectroscopy, mass spectrometry and elemental analysis. The primary purpose in the preparation of these compounds was to achieve systematic variation of the steric bulk and electronic demand of the attached functionality (from the electron-withdrawing trifluoromethyl substituent to the electron-releasing *tert*-butyl group). Accordingly, coordination of these ligands to transition metal centres may be achieved *via* bidentate N<sup>^</sup>N coordination through the bipyridine moiety. It is anticipated that transition metal complexes of these ligands will possess interesting optical properties, where structural variation in the ligand moiety is employed to effectively tune the absorption and photoluminescence profile, excited state lifetimes and quantum efficiencies.

The second series of compounds described in this chapter comprises a family of four polyphenylene molecules, substituted with either one or two acetylene functional groups. Three novel propeller-like molecules possessing a hexaphenylbenzene core have been prepared, whilst the fourth derivative is a planar, cyclised HBC platform. These compounds were also prepared *via* palladium-catalysed cross-coupling and cycloaddition reactions and have been fully characterised by spectroscopic and analytical methods. The attached alkynyl substituent facilitates an extension of  $\pi$ -electron delocalisation and concurrently confers on these molecules ligand potential. In its anionic form (R-C $\equiv$ C<sup>-</sup>), these compounds may form metal-carbon bonds *via*  $p\pi(L)$ - $d\pi(M)$  orbital overlap, in which the structural rigidity and linear geometry of the acetylene group is maintained. This should ensure effective communication between the metal centre and a photoactive chromophore (e.g. hexaphenylbenzene or HBC) along the acetylene molecular axis. Consequently, transition metal complexes incorporating these strong-field acetylide ligands, in the form of acetylene-substituted polyphenylenes, are expected to exhibit rich photophysical properties and a strong emission profile in both the solid state and in solution.





**Chapter 2**  
**Heteroleptic Ruthenium(II) Bipyridyl Complexes**



## 2.1 Introduction

Ruthenium(II) polypyridine complexes represent one of the most widely studied classes of luminescent metal compounds. They possess an extensive synthetic chemistry and their photophysical and electrochemical properties are very well defined. Consequently, geometric, electronic and structural diversity may be achieved relatively easily. Thus research into Ru(II) polypyridines has been driven by their development as materials for energy conversion, photocatalysis, supramolecular building blocks and as luminescent probes for biological systems.<sup>77-78</sup>

### 2.1.1 Polypyridyl Ligands & Isomerism

2,2'-Bipyridine (bpy), “the most explored chelate system in coordination chemistry”, is used extensively in the complexation of metal ions to form chemically robust and redox-stable coordination complexes.<sup>79-80</sup> It acts as a bidentate chelating ligand, where its coordination to a metal is driven by the favourable formation of five membered chelate rings. Bipyridines possess  $\sigma$ -donor orbitals located on pyridine ring nitrogen atoms and  $\pi$ -donor and  $\pi^*$ -acceptor orbitals which are delocalised on the aromatic rings.<sup>80</sup> Derivatisation of 2,2'-bipyridines is synthetically attainable and a wealth of symmetric and asymmetrically functionalised ligands have been prepared.<sup>79,81</sup> Ruthenium(II) is a  $d^6$  transition metal ion and forms low-spin octahedral complexes with 2,2'-bipyridine. The corresponding complex  $[\text{Ru}(\text{bpy})_3]^{2+}$  is inherently chiral and exists in two distinct optical isomers (Figure 2.1, (a)).<sup>82</sup> These enantiomers, denoted  $\Delta$  (right-handed) and  $\Lambda$  (left-handed), possess identical chemical properties and differ only in the direction in which they rotate plane-polarised light and in their interactions with other chiral moieties (e.g. DNA).<sup>83</sup>

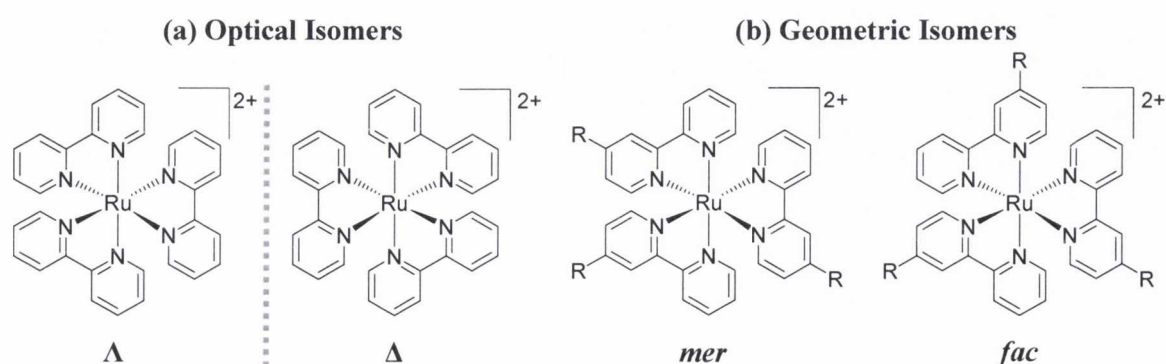


Figure 2.1: Optical and geometric isomers of homoleptic tris-diimine Ru(II) complexes.

The use of a monosubstituted bipyridine as a ligand in the formation of *tris*-diimine Ru(II) complexes results in the formation of both facial (*fac*) and meridional (*mer*) isomers (Figure 2.1, (b)). These geometrical isomers are distinguishable by NMR spectroscopy and have been known to possess different photophysical properties. Application of  $[\text{Ru}(\text{bpy})_3]^{2+}$  subunits as building blocks in polynuclear systems requires the resolution of geometric isomers and a significant body of research has been devoted to this, which may be achieved through column chromatography, fractional crystallisation or through the use of enantiomerically pure chiral salts.<sup>82,84</sup>

### 2.1.2 Electronic transitions and photophysical properties of $[\text{Ru}(\text{bpy})_3]^{2+}$

In addition to chemical stability and synthetic accessibility, a wealth of investigations into  $[\text{Ru}(\text{bpy})_3]^{2+}$  have focused on the exploitation of the desirable photophysical and redox properties of this class of compounds. The stability of Ru(II) polypyridyl complexes is derived from the symmetrical, low spin octahedral  $t_{2g}^6$  configuration.

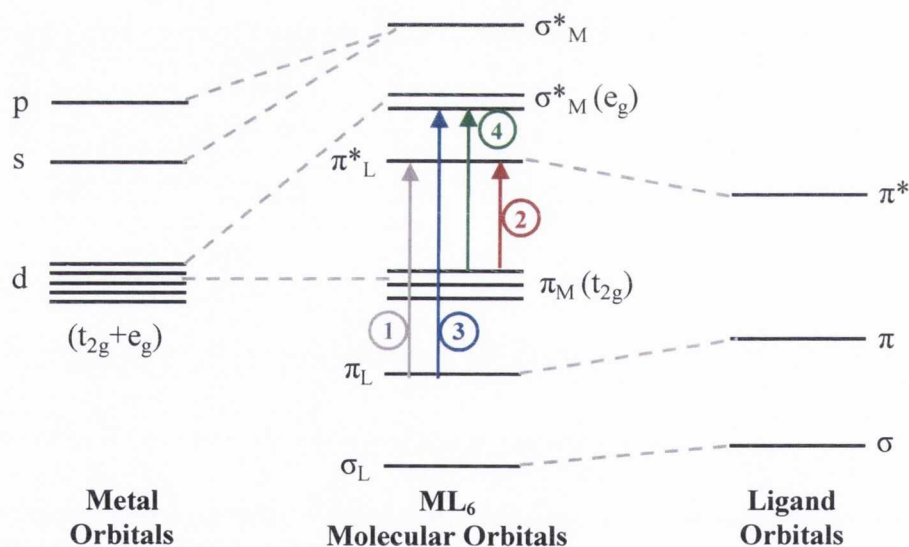


Figure 2.2: Schematic molecular orbital diagram for an octahedral Ru(II) polypyridyl complex. (1)  $\pi$ - $\pi^*$  (LC), (2)  $d$ - $\pi^*$  (MLCT), (3)  $\pi$ - $d^*$  (LMCT), (4)  $d$ - $d^*$  (MC).

When a molecule absorbs a photon of light it is converted from the ground state to an excited state and involves the promotion of an electron from a filled molecular orbital to an empty one. A simplified molecular orbital diagram summarising the major electronic transitions, which may occur at the same time, in  $d^6$  octahedral Ru(II) polypyridine is given in Figure 2.2.<sup>78,80</sup> A transition may occur between molecular orbitals localised on the

ligand, i.e. ligand centred (LC), by promotion of an electron from  $\pi_L$  to  $\pi^*_L$  [ $\pi_L \rightarrow \pi^*_L$ ] (Figure 2.2, (1)). An electron can be promoted from a metal-centred orbital ( $\pi_M$ ) to a  $\pi^*_L$  acceptor orbital, known as a metal-to-ligand charge transfer (MLCT) transition [ $\pi_M \rightarrow \pi^*_L$ ] (Figure 2.2, (2)). MLCT transitions are expected when the metal is easy to oxidise (e.g. in a low oxidation state) and if at least one of the ligands is easy to reduce. Conversely, a ligand-to-metal charge transfer transition (LMCT) involves the promotion of an electron from ligand  $\pi_L$  to a metal-based  $\sigma^*_M$  orbital [ $\pi_L \rightarrow \sigma^*_M$ ] (Figure 2.2, (3)). A low energy LMCT typically requires an easily oxidised ligand and a metal centre that is easily reduced (i.e. in a higher oxidation state). Finally, metal-centred (MC) transitions involve the Laporte forbidden promotion of an electron from a  $\pi_M$  to a  $\sigma^*_M$  orbital [ $\pi_M \rightarrow \sigma^*_M$ ] (Figure 2.2, (4)).

For  $[\text{Ru}(\text{bpy})_3]^{2+}$  and Ru(II) polypyridyl complexes in general, MLCT transitions are the most common charge transfer transitions. Ru(II), the more stable oxidation state of ruthenium, is relatively easily oxidised to Ru(III) and polypyridyl ligands are good  $\pi$ -acceptor ligands possessing a low energy  $\pi^*$  molecular orbital. Correspondingly, the lowest energy transition between the highest occupied molecular orbital (HOMO) and the lowest unoccupied molecular orbital (LUMO) occurs between metal  $\pi_M$  and ligand  $\pi^*_L$  orbitals. The energy and photophysical properties of these two molecular orbitals are of key importance and may be fine-tuned by careful choice of diimine ligand.

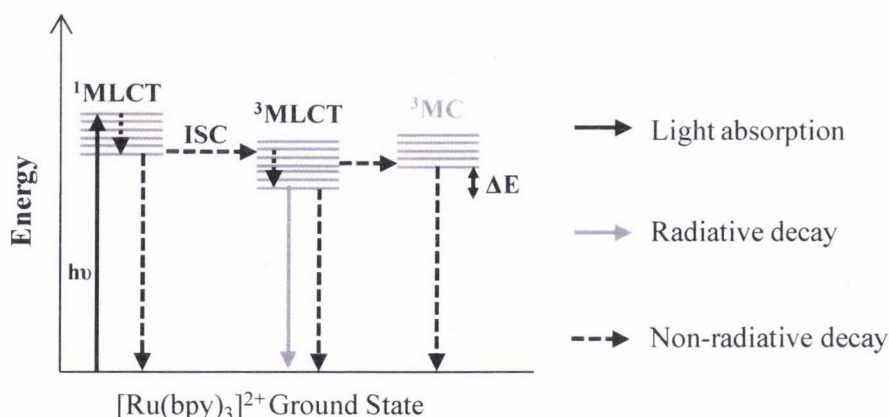


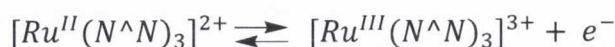
Figure 2.3: Jablonski energy level diagram showing excited state decay pathways for  $[\text{Ru}(\text{bpy})_3]^{2+}$  complexes.

For  $[\text{Ru}(\text{bpy})_3]^{2+}$  complexes, absorption of a photon of light populates a high energy  $^1\text{MLCT}$  excited state (Figure 2.3). This may relax *via* non-radiative decay to the ground

state or it may decay rapidly *via* InterSystem Crossing (ISC) to form a  $^3\text{MLCT}$  state. The high spin-orbit coupling constant of the heavy Ru(II) centre permits this spin-forbidden mixing of singlet and triplet molecular orbitals.<sup>85</sup> Luminescence from  $[\text{Ru}(\text{bpy})_3]^{2+}$  occurs from the  $^3\text{MLCT}$  state after very rapid (and efficient) population *via* ISC. The  $^3\text{MLCT}$  emission occurs in the orange-red spectral region with a luminescence band maximum of  $\lambda$  615 nm and an excited state lifetime  $\tau$  1.1  $\mu\text{s}$  ( $\text{CH}_3\text{CN}$ , room temperature).<sup>80,86</sup> If the  $^3\text{MC}$  (d-d) state is low enough in energy and is thermally accessible, the  $^3\text{MLCT}$  state may decay *via* crossover to the metal-centred excited state. In this excited state, the molecule will undergo fast radiationless deactivation to the ground state and no luminescence will be observed (Figure 2.3).<sup>78</sup> Ru(II) complexes of the tridentate 2,2':6',2''-terpyridine ligand,  $[\text{Ru}(\text{tpy})_2]^{2+}$ , have weaker ligand field strength and consequently a lower energy MC state than observed in  $[\text{Ru}(\text{bpy})_3]^{2+}$  complexes, as a direct result of the bite angle of the ligand.<sup>87</sup> Therefore, the thermally activated process from  $^3\text{MLCT}$  to a higher lying  $^3\text{MC}$  state is more efficient in  $[\text{Ru}(\text{tpy})_2]^{2+}$  and the excited state is rapidly deactivated by non-radiative decay processes. Accordingly, at room temperature in  $\text{CH}_3\text{CN}$ ,  $[\text{Ru}(\text{tpy})_2]^{2+}$  is essentially non-luminescent and its excited state lifetime measures just 250 ps.<sup>88</sup>

### 2.1.3 Electrochemical behaviour of $[\text{Ru}(\text{bpy})_3]^{2+}$

The first oxidation process of Ru(II) polypyridyl complexes involves the removal of an electron from the HOMO which is typically a metal-centred  $\pi_{\text{M}}$  ( $t_{2g}$ ) orbital. This process interconverts the low-spin Ru(II)  $d^6$  and Ru(III)  $d^5$  ions and is fully reversible as both oxidation states are inert to ligand substitution. For  $[\text{Ru}(\text{bpy})_3]^{2+}$ , the Ru(II/III) potential measures +1.33 V vs. SCE.<sup>86</sup>



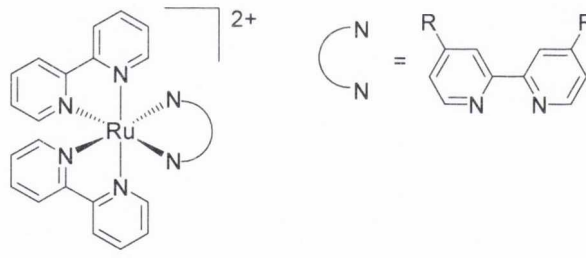
The first reduction process of Ru(II) polypyridine complexes is typically ligand-centred. The promoted electron is localised on one ligand, with the first reduction process located on the ligand which is easiest to reduce. These complexes usually exhibit at least two reversible ligand-centred reduction processes. The first reduction generally takes place on a low-energy  $\pi^*_{\text{L}}$  orbital, the LUMO. The first reduction potential of  $[\text{Ru}(\text{bpy})_3]^{2+}$  measures -1.29 V vs. SCE.<sup>86</sup>



### 2.1.4 Tuning of optical and redox properties of $[\text{Ru}(\text{bpy})_3]^{2+}$ analogues

A significant body of research has focused on tuning the excited state and redox properties of Ru(II) *tris*-diimine complexes by variation in energy of the HOMO (Ru(II)  $\pi_{\text{M}}$  orbital) and the LUMO (bipyridine-based  $\pi_{\text{L}}^*$  orbital).<sup>89</sup> This can be achieved by synthetic modification of bipyridine ligands or by functionalisation of the ligands employed to incorporate electron-donating or electron-withdrawing substituents.

This chapter focuses on heteroleptic Ru(II) polypyridyl complexes of formula  $[\text{Ru}(\text{bpy})_2(\text{L})]^{2+}$ . The UV-Visible absorption spectra of heteroleptic complexes of this type typically exhibit two distinct absorption bands due to charge transfer transitions to the two types of ligand. In this class of complex, non-radiative decay pathways normally lead to a single, lowest energy emissive  $^3\text{MLCT}$  excited state, usually located on the ligand containing the lowest energy  $\pi^*$  molecular orbital.<sup>89</sup> In Figure 2.4, some examples are presented showing the effect of varying the electronic demand of substituents on one ligand, L, on the emission energy in a series of heteroleptic complexes.



$[\text{Ru}(\text{bpy})_2(\text{L})]^{2+}$	$\lambda_{\text{MLCT}}^{\text{Abs}}$ nm	$\lambda_{\text{MLCT}}^{\text{Em}}$ nm
R = H	452	615
R = CH <sub>3</sub>	445	615
R = C(CH <sub>3</sub> ) <sub>3</sub>	450	625
R = Ph	458	628
R = Cl	448	645

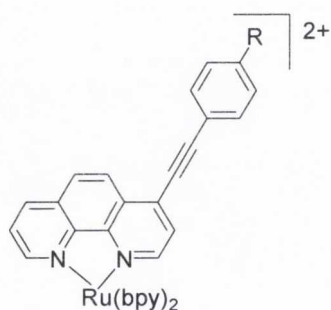
Figure 2.4: The effect of substituents on the lowest energy  $^1\text{MLCT}$  absorption band ( $\lambda_{\text{MLCT}}^{\text{Abs}}$ ) and the  $^3\text{MLCT}$  emission energy ( $\lambda_{\text{MLCT}}^{\text{Em}}$ )/nm.

Incorporation of an electron-releasing substituent (such as *tert*-butyl group or a phenyl ring) destabilises the  $\pi_{\text{M}}$  orbital (the HOMO located on the Ru(II)) to a greater degree than the ligand-based LUMO ( $\pi_{\text{L}}^*$ ), resulting in a reduced HOMO-LUMO gap and a reduced emission energy of the  $^3\text{MLCT}$  state relative to  $[\text{Ru}(\text{bpy})_3]^{2+}$ .<sup>89-90</sup> Taking the opposite approach, the electron-withdrawing chlorine substituent on one bipyridine ligand stabilises the  $\pi^*$  orbital localised on the Cl<sub>2</sub>-bpy ligand more than the metal-based HOMO ( $\pi_{\text{M}}$ ) resulting in a red-shifted luminescence emission maximum.<sup>91</sup> In keeping with the energy gap law, reduction of emission energy corresponds in general with a reduction in excited state lifetime ( $\tau$ , 298 K, CH<sub>3</sub>CN:  $[\text{Ru}(\text{bpy})_3]^{2+}$  1.1  $\mu\text{s}$ ;  $[\text{Ru}(\text{bpy})_2(4,4'\text{-Cl}_2\text{bpy})]^{2+}$  0.42  $\mu\text{s}$ ).<sup>89</sup>

Increasing the delocalisation and structural rigidity in the acceptor ligand (with the lowest energy  $\pi^*_L$  orbital) and incorporating alternative heterocyclic ligands have also been successfully adopted as techniques to tune the excited state properties.<sup>28,89,92</sup>

#### 2.1.4.1 Simultaneous $^3\text{MLCT}$ emission from two excited states

As mentioned earlier, Ru(II) polypyridyl complexes containing mixed ligands generally emit exclusively from the lowest energy  $^3\text{MLCT}$  excited state. A recent series of Ru(II) heteroleptic complexes prepared by Tor *et al.* appear to contradict this generalisation.<sup>93</sup> The complexes, of formula  $[\text{Ru}(\text{bpy})_2(\text{L})]^{2+}$ , contain a 1,10-phenanthroline ligand (phen) as acceptor ligand, L, whose  $\pi$ -conjugation has been extended by incorporation of aryl-acetylene substituents (Figure 2.5).



$[\text{Ru}(\text{bpy})_2(\text{L})]^{2+}$	$\lambda_{\text{max}}^{\text{Em}}$ nm	$\tau/\mu\text{s}$ (%) <sup>1</sup>	$\Phi_{\text{em}}$
$[\text{Ru}(\text{bpy})_2(\text{phen})]^{2+}$	610	0.80 (100)	0.060
(a) R = H	660 <sup>2</sup>	6.55 (98), 1.21 (2)	0.023
(b) R = OCH <sub>3</sub>	662 <sup>2</sup>	11.50 (93), 1.06 (7)	0.016
(c) R = CF <sub>3</sub>	675 <sup>2</sup>	6.56 (97), 1.30 (3)	0.021

<sup>1</sup> Fraction of biexponential decay fitting, ( $\lambda_{\text{exc}}$  455 nm),  
<sup>2</sup> Broad emission peak profile

Figure 2.5: Structure and spectroscopic data of dual emissive heteroleptic Ru(II) complexes, L = functionalized 1,10-phenanthroline ligand ( $\text{CH}_3\text{CN}$ , 298 K).<sup>93</sup>

The parent complex,  $[\text{Ru}(\text{bpy})_2(\text{phen})]^{2+}$ , emits at  $\lambda$  610 nm and has an excited state lifetime of 0.80  $\mu\text{s}$  for a single emissive excited state (or two very similar states in thermal equilibrium). The luminescence band maxima of aryl-acetylene phenanthroline complexes (Figure 2.5, complexes (a)-(c)), were significantly red-shifted with very broad emission profiles relative to the unsubstituted parent complex. The luminescence decay was found to be biexponential with the slow-decaying component contributing a larger percentage at lower energy, although the two discrete excited state energies could not be resolved in the emission spectra. This was attributed to the presence of two emissive  $^3\text{MLCT}$  excited states localised on two different ligands. The short-lived, higher energy component is assigned as bipyridine-based and the longer-lived, lower energy component localised on



the conjugated phenanthroline ligand. This dual emission was found to be sensitive to the degree of  $\pi$ -conjugation and substituent position and was more prevalent in complexes with asymmetric acceptor ligands.

#### 2.1.4.2 Re-ordering of excited states: $^3\text{IL}$ emission from Ru(II) heteroleptic complexes

An alternative approach has been used to generate Ru(II) bipyridine-based heteroleptic complexes which are luminescent at room temperature. Coordination of a functionalised diimine ligand where the substituent is a highly conjugated polyaromatic subunit has a dramatic effect on the excited state properties. The  $^3\pi\pi^*$  excited state localised on this highly electron-delocalised ligand is lower in energy than the lowest energy  $^3\text{MLCT}$  state, and exclusive long-lived  $^3\text{IL}$  (intra-ligand) phosphorescence is observed at room temperature.<sup>94</sup> This is a relatively rare feature in Ru(II) polypyridyl complexes whose emissive excited states are almost entirely dominated by  $^3\text{MLCT}$ -based luminescence.<sup>78</sup> The  $\pi$ -conjugated polyaromatic subunit pyrene has been employed to induce this re-ordering of the excited states in several Ru(II) heteroleptic complexes.<sup>94-96</sup> For example, an ethynyl-pyrene substituted  $[\text{Ru}(\text{bpy})_3]^{2+}$  complex prepared by Castellano and co-workers exhibits very long, room temperature phosphorescence (53.1  $\mu\text{s}$ ) consistent with emission from a pure  $^3\text{IL}$  excited state localised on the pyrene moiety (Figure 2.6).<sup>94</sup>

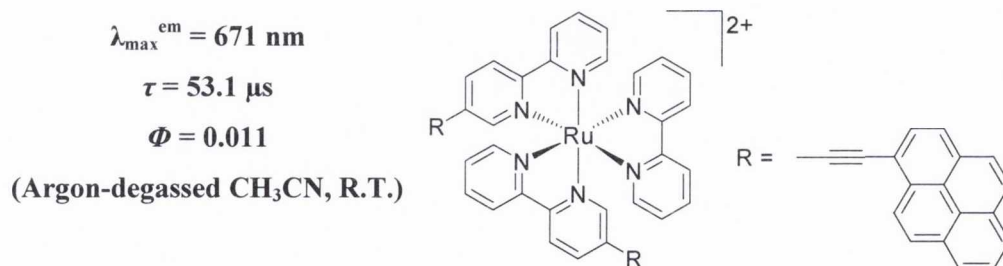


Figure 2.6: Ethynylpyrene-substituted Ru(II) heteroleptic tris-diimine complex displaying long-lived room temperature phosphorescence.<sup>94</sup>

#### 2.1.5 Selected applications of Ru(II) polypyridine complexes

The existence of an extensive library of Ru(II) polypyridine complexes in the literature has been driven by the very wide range of possible applications that such compounds have demonstrated.<sup>77</sup> The majority of these applications rely on their well-defined and predictable photophysical and redox properties which may be fine-tuned by synthetic

modification. Several properties of Ru(II) polypyridine complexes render them suitable for incorporation into photonic and optoelectronic devices.<sup>16,78</sup> In general, complexes absorb strongly throughout the entire visible spectral region ( $\lambda$  380-750 nm), which can extend to the near-infrared ( $> \lambda$  750 nm). This feature is key to light-harvesting efficiency for solar cell application as it facilitates maximum absorption of sunlight photons of all visible light wavelengths. Secondly, the absorption spectra and excited state photophysical and redox properties may be tuned by judicious choice of ligands. The stability of Ru(II) complexes in the ground state, excited state and redox states is yet another desirable attribute. Consequently, Ru(II) polypyridine complexes have been successfully used in a variety of energy conversion devices such as optical sensors (for the detection of O<sub>2</sub>,<sup>97</sup> CO<sub>2</sub>,<sup>98</sup> pH<sup>99</sup> changes and in anion sensing<sup>100</sup>) and in electroluminescent displays.<sup>77,101</sup>

One of the most important applications involving Ru(II) polypyridine complexes relates to the development of dye-sensitized solar cells (DSSCs). This work was pioneered by Michael Grätzel with the first such device appearing in the early 1990s.<sup>102</sup> DSSCs employ a redox-active molecule as dye which is covalently attached to a semi-conductor surface with a redox mediator present in the electrolyte. In a typical cell, a Ru(II) polypyridine complex acts as the dye which is anchored to the host matrix (for example TiO<sub>2</sub> as a wide band-gap semi-conductor) *via* a carboxylate (-O-(C=O)-) linkage in the presence of I<sub>2</sub>/I<sub>3</sub><sup>-</sup> as electron donor/acceptor.<sup>16</sup> Optical excitation of the dye with visible light promotes the complex to an excited state where electrons are injected into the conduction band of the TiO<sub>2</sub> layer. The electrons are collected and pass through an external circuit to arrive at the counter electrode. The oxidised complex is reduced back to the ground state by the redox mediator. The net effect of this process is the driving of an electron through an external circuit, i.e. the direct conversion of sunlight to electricity. One of the Ru(II) complexes with the best performance is [Ru(dcbpy)<sub>2</sub>(NCS)<sub>2</sub>] (dcbpy = 4,4'-dicarboxyl-bipyridine). It exhibits an incident photon-to-current conversion efficiency (IPCE) of ~90 % between  $\lambda$  500-600 nm and the corresponding photoelectrochemical device gives an overall solar-to-electric conversion efficiency of 10 %.<sup>103</sup>

Photoactive Ru(II) polypyridyl complexes have also found application in biological systems. In particular, much interest has focused on the interaction of ruthenium polypyridyl complexes with nucleic acids.<sup>104</sup> The complex [Ru(bpy)<sub>2</sub>(dppz)]<sup>2+</sup> (dppz =

dipyrido[3,2-a:2',3'-c]phenazine) is essentially non-luminescent in water ( $\tau$  200 ps) due to deactivation of the excited state by water through hydrogen-bonding with the dppz ligand.<sup>105</sup> Upon introduction of double-stranded DNA, intense photoluminescence is observed ( $\tau$  200 ns). The planar dppz functionality inserts and stacks (intercalates) between the base pairs of double-stranded DNA in the major groove of the double helix. The fact that emission is observed reflects the relative shielding of the intercalating ligand from the bulk solvent. This phenomenon is known as the “molecular light switch” effect.<sup>105</sup> Indeed, the strength and nature of binding of Ru(II) polypyridyl complex to DNA may be modified by careful choice of acceptor ligand. The parent complex  $[\text{Ru}(\text{bpy})_3]^{2+}$  has been shown to bind weakly to DNA *via* electrostatic interactions with the negatively charged helix whereas the more planar heteroaromatic ligands in  $[\text{Ru}(\text{phen})_3]^{2+}$  facilitate the partial intercalation of the complex.<sup>106</sup>

### 2.1.6 Project Goals: Heteroleptic Ru(II) complexes with asymmetric, sterically-hindered ligands

This chapter describes the preparation of a series of Ru(II) heteroleptic complexes incorporating four of the asymmetrically functionalised-bipyridines whose synthesis was discussed in Chapter 1 (Figure 2.7). The simple ligands 6-(4-*tert*-butyl-phenylethynyl)-2,2'-bipyridine (**1**) and 6-(4-trifluoromethyl-phenylethynyl)-2,2'-bipyridine (**2**) were employed in order to compare the effects of electron-donating (**1**) and electron-withdrawing groups (**2**) as substituents on one bipyridine chelate system on the optical properties of the corresponding Ru(II) complexes  $[\text{Ru}(\text{bpy})_2(\mathbf{1})]^{2+}$  (**33**) and  $[\text{Ru}(\text{bpy})_2(\mathbf{2})]^{2+}$  (**34**) (Figure 2.7). In addition, the effect of a systematic increase in the degree of steric congestion imposed by the third ligand on the lowest energy metal-to-ligand charge transfer emission energy was investigated. This was achieved by the coordination of 6-(3,6-dimethyl-2,4,5-triphenylbenz-1-ene)-2,2'-bipyridine (**3**) and the larger ligand, 1-(2,2'-bipyrid-6-yl)-2,3,4,5-tetra-(4-*tert*-butylphenyl)benzene (**4**), to a Ru(II) metal centre, producing complexes  $[\text{Ru}(\text{bpy})_2(\mathbf{3})]^{2+}$  (**35**) and  $[\text{Ru}(\text{bpy})_2(\mathbf{4})]^{2+}$  (**36**) (Figure 2.7).

Despite the wealth of Ru(II) polypyridine complexes that have been prepared over the last fifty years, relatively little attention has been directed towards complexes with asymmetric bidentate diimine ligands. It would be anticipated that locating the substituent directly adjacent to the pyridine ring nitrogen would have a significant influence on the octahedral

arrangement of the three bipyridyl ligands about the Ru(II) metal centre. As a consequence, the photophysical properties of the complexes would be expected to be quite different from those observed in the prototype complex  $[\text{Ru}(\text{bpy})_3]^{2+}$ . This effect should be most pronounced in complexes **35** and **36**, in which the third ligand is composed of a sterically encumbered polyphenylene moiety appended  $\alpha$  to a coordinated nitrogen (Figure 2.7). The variation of electronic demand and the increase in  $\pi$ -electronic delocalisation within the aryl-acetylene ligands in complexes **33** and **34** should affect the energies of the HOMO ( $\pi_M$ ) and the LUMO ( $\pi^*_L$ ) to afford relatively intense, low-energy photoluminescence profiles.

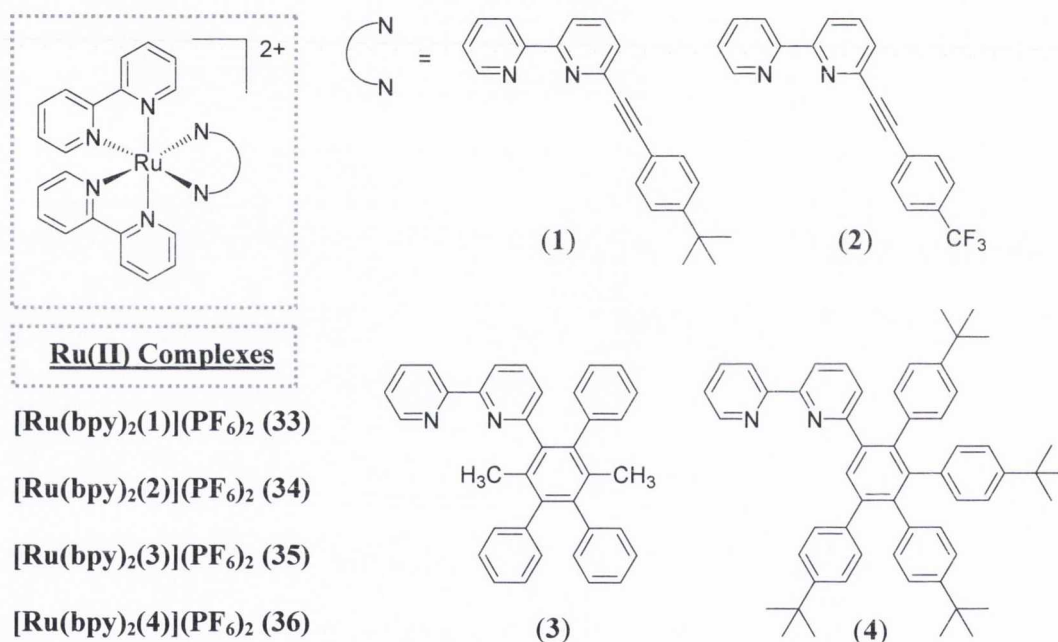


Figure 2.7: Heteroleptic Ru(II) complexes incorporating asymmetric bipyridine ligands substituted  $\alpha$  to the pyridine ring nitrogen.

## 2.2 Synthesis of heteroleptic $[\text{Ru}(\text{bpy})_2(\text{L})](\text{PF}_6)_2$ complexes

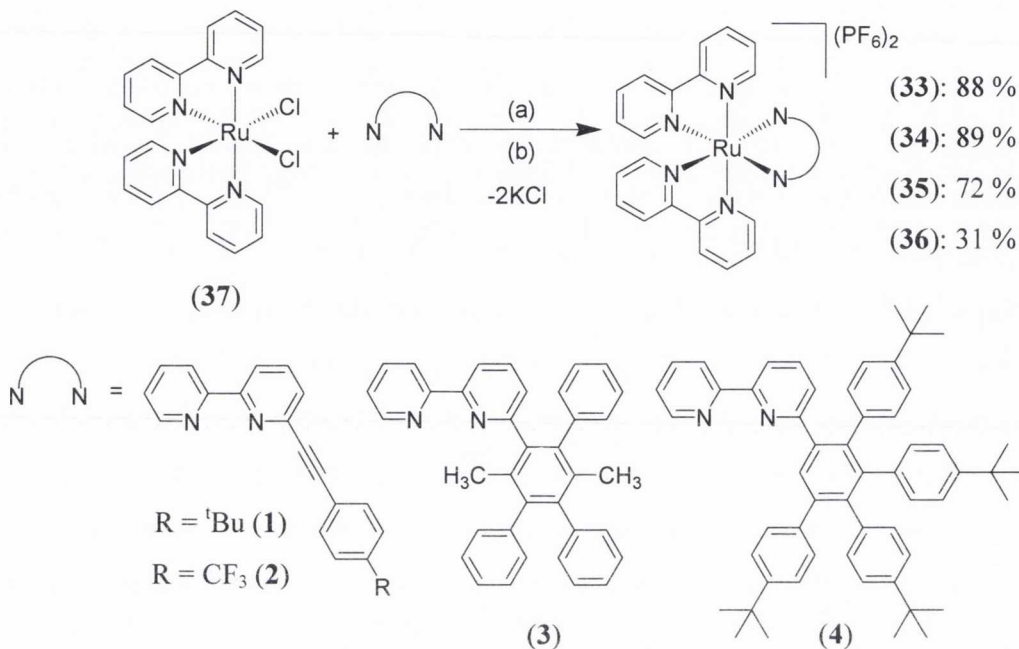
The ligand field in Ru(II) is considerably larger than that of first row metals with the result that ligand exchange reactions require elevated temperatures and correspondingly high boiling point solvents.<sup>77</sup> This enhanced stability of Ru(II) complexes is a consequence of the symmetric  $t_{2g}^6$  configuration. Ru(II) heteroleptic complexes, of general formula  $[\text{Ru}(\text{bpy})_2(\text{L})]^{2+}$ , are typically prepared by refluxing the ligand, L, with a suitable ruthenium salt in a high boiling polar solvent under inert conditions. Ethylene glycol, with a boiling point of 197 °C, is classically used as solvent in these reactions.<sup>107</sup> *Cis*- $\text{Ru}(\text{bpy})_2\text{Cl}_2$  (**37**) was employed as a starting material for the four complexes prepared.<sup>108</sup> Isolation of the complexes as their hexafluorophosphate ( $\text{PF}_6^-$ ) salts facilitated their characterisation and optical measurement in standard organic chlorinated solvents. The relative insolubility of metal complexes with  $\text{PF}_6^-$  counterions in aqueous solution and their extensive use as non-coordinating anions in metal complexes are valuable properties that have resulted in their widespread application in transition-metal coordination complexes.

### 2.2.1 Synthesis of $[\text{Ru}(\text{bpy})_2(\mathbf{1})](\text{PF}_6)_2$ (**33**), $[\text{Ru}(\text{bpy})_2(\mathbf{2})](\text{PF}_6)_2$ (**34**), $[\text{Ru}(\text{bpy})_2(\mathbf{3})](\text{PF}_6)_2$ (**35**) and $[\text{Ru}(\text{bpy})_2(\mathbf{4})](\text{PF}_6)_2$ (**36**)

The syntheses of heteroleptic ruthenium(II) complexes **33** (Ru-<sup>t</sup>Bu), **34** (Ru-CF<sub>3</sub>) and **35** (Ru-Me<sub>2</sub>) were achieved *via* similar synthetic procedures (Scheme 2.1). In order to aid solubilisation, the desired ligand (**1**, **2** or **3**) (1.05 eq.) was sonicated in ethylene glycol for 10 minutes and degassed *via* argon bubbling for 20 minutes. The Ru(II) precursor, *cis*- $[\text{Ru}(\text{bpy})_2\text{Cl}_2]$  (**37**, 1 eq.) was added and the reaction mixture heated at 110-130 °C under argon overnight. The colour change after several hours from purple, (due to the presence of *cis*- $[\text{Ru}(\text{bpy})_2\text{Cl}_2]$  (**37**)), to orange-red, characteristic of *tris*-diimine Ru(II) complexes, was indicative of the progress of the reaction.

Preparation of the complex containing the more sterically encumbered ligand  $[\text{Ru}(\text{bpy})_2(\mathbf{4})](\text{PF}_6)_2$  (**36**) required more forcing conditions. Polyphenylene ligand **4** is insoluble in ethylene glycol even at high temperatures (130 °C). Diethylene glycol monoethyl ether as a less polar but related solvent was used instead. The reaction mixture was heated at 170-180 °C for 3 days under argon. After this time, thin layer chromatography (TLC) indicated that neither the Ru(II) starting material nor the ligand had been entirely consumed. In order to force the reaction to completion, some ethylene glycol

was added to the reaction mixture which was heated for a further 24 hours. At this point, all traces of the purple *cis*-[Ru(bpy)<sub>2</sub>Cl<sub>2</sub>] (**37**) were absent *via* TLC and thus the reaction was deemed to have gone to completion.



Scheme 2.1: Synthesis of [Ru(bpy)<sub>2</sub>(**1**)](PF<sub>6</sub>)<sub>2</sub> (**33**), [Ru(bpy)<sub>2</sub>(**2**)](PF<sub>6</sub>)<sub>2</sub> (**34**), [Ru(bpy)<sub>2</sub>(**3**)](PF<sub>6</sub>)<sub>2</sub> (**35**) and [Ru(bpy)<sub>2</sub>(**4**)](PF<sub>6</sub>)<sub>2</sub> (**36**). **33**, **34**, **35**: (a) Ethylene glycol, 24 hours, under Ar, 110-130 °C, (b) Sat. aq. KPF<sub>6</sub>. **36**: (a) diethylene glycol monoethyl ether, ethylene glycol, 4 days, under Ar, 170-180 °C. (b) Sat. aq. KPF<sub>6</sub>.

In the case of *tert*-butyl substituted [Ru(bpy)<sub>2</sub>(**1**)](PF<sub>6</sub>)<sub>2</sub> (**33**), simple addition of excess saturated KPF<sub>6</sub> solution to the cooled reaction mixture produced the desired product as a bright orange precipitate (Scheme 2.1). This was removed *via* filtration and washed with water (to remove traces of the Ru(II) starting material and KCl) and diethyl ether (to remove traces of unreacted ligand and to aid drying of the complex). No further purification was required and the product was obtained in 88 % yield. The simple isolation of this complex is quite unusual for Ru(II) polypyridyl complexes as they usually require arduous column chromatography.

For the other three complexes [Ru(bpy)<sub>2</sub>(**2**)](PF<sub>6</sub>)<sub>2</sub> (**34**), [Ru(bpy)<sub>2</sub>(**3**)](PF<sub>6</sub>)<sub>2</sub> (**35**) and [Ru(bpy)<sub>2</sub>(**4**)](PF<sub>6</sub>)<sub>2</sub> (**36**) the addition of excess saturated KPF<sub>6</sub> solution to the cooled reaction mixture also produced a bright orange precipitate (Scheme 2.1). Unlike **33**, this was not completely pure and required purification *via* column chromatography on silica,

eluting with a mixture of acetonitrile:saturated KNO<sub>3</sub> solution:water (10:0.5:1.5 v/v). The solvent was removed *in vacuo* from the product fractions. Excess nitrate salt from the solvent system was removed by redissolution of the residue in CH<sub>2</sub>Cl<sub>2</sub> and washing with water. After removal of the solvent from the organic layer, excess saturated KPF<sub>6</sub> solution was added to an ethylene glycol solution of the complex to obtain a precipitate. This was removed *via* filtration and washed with water and diethyl ether. Each product was obtained as an orange powder in moderate to excellent yield - **34** (Ru-CF<sub>3</sub>) 89 %, **35** (Ru-Me<sub>2</sub>) 72 %, **36** (Ru-Ar<sub>5</sub>) 31 % yield.

The four complexes were fully characterised using <sup>1</sup>H and <sup>13</sup>C {<sup>1</sup>H} NMR spectroscopy, elemental analysis and infrared spectroscopy. Complex **34** was further characterised using <sup>19</sup>F NMR spectroscopy. X-ray crystal structures of **33** (Ru-<sup>t</sup>Bu) and **35** (Ru-Me<sub>2</sub>) were also obtained.

The electrospray mass spectra of all four complexes in CH<sub>3</sub>CN reveals a major peak that corresponds to the [M-2(PF<sub>6</sub>)]<sup>2+</sup> cation where the two PF<sub>6</sub><sup>-</sup> counterions have dissociated from the cationic species. These peaks show the expected Ru(II) isotopic distribution pattern, with ½ m.u. intervals confirming the 2+ charge on the molecular ion. A second peak is observed for both complexes for the [M-(PF<sub>6</sub>)]<sup>+</sup> ion where just one counterion has dissociated. The mass spectral data is summarised in Table 2.1.

Table 2.1: Electrospray mass spectral data for complexes **33**, **34**, **35** and **36** (*m/z* in *m.u.*).

	<b>Molecular Ion</b>	<b>Formula</b>	<b>Found <i>m/z</i> (%)</b>	<b>Calculated <i>m/z</i></b>
<b>33</b>	[M-2(PF <sub>6</sub> )] <sup>2+</sup>	[C <sub>42</sub> H <sub>36</sub> N <sub>6</sub> Ru] <sup>2+</sup>	363.1022 (100)	363.1023
	[M-(PF <sub>6</sub> )] <sup>+</sup>	[C <sub>42</sub> H <sub>36</sub> N <sub>6</sub> F <sub>6</sub> RuP] <sup>+</sup>	871.1414 (25)	871.1426
<b>34</b>	[M-2(PF <sub>6</sub> )] <sup>2+</sup>	[C <sub>39</sub> H <sub>27</sub> N <sub>6</sub> F <sub>3</sub> Ru] <sup>2+</sup>	369.0065 (100)	369.0089
	[M-(PF <sub>6</sub> )] <sup>+</sup>	[C <sub>39</sub> H <sub>27</sub> N <sub>6</sub> F <sub>9</sub> PRu] <sup>2+</sup>	883.0941 (32)	883.0935
<b>35</b>	[M-2(PF <sub>6</sub> )] <sup>2+</sup>	[C <sub>56</sub> H <sub>44</sub> N <sub>6</sub> Ru] <sup>2+</sup>	451.1345 (100)	451.1336
	[M-(PF <sub>6</sub> )] <sup>+</sup>	[C <sub>56</sub> H <sub>44</sub> N <sub>6</sub> F <sub>6</sub> PRu] <sup>+</sup>	1047.2273 (25)	1047.2313
<b>36</b>	[M-2(PF <sub>6</sub> )] <sup>2+</sup>	[C <sub>76</sub> H <sub>76</sub> N <sub>6</sub> Ru] <sup>2+</sup>	587.2565 (100)	587.2588
	[M-(PF <sub>6</sub> )] <sup>+</sup>	[C <sub>76</sub> H <sub>76</sub> N <sub>6</sub> F <sub>6</sub> PRu] <sup>+</sup>	1319.4418 (10)	1319.4775

### 2.2.2 X-Ray Crystallography: 33.2CHCl<sub>3</sub>.CH<sub>2</sub>Cl<sub>2</sub> and 35.2CHCl<sub>3</sub>.CH<sub>2</sub>Cl<sub>2</sub>

Single crystals of [Ru(bpy)<sub>2</sub>(**1**)](PF<sub>6</sub>)<sub>2</sub> (**33**) suitable for X-ray diffraction were grown by layering hexane on a CH<sub>2</sub>Cl<sub>2</sub>/CHCl<sub>3</sub> solution of the complex. This was left to stand in the fridge for one week to produce large deep-red wafer-like crystals. The complex crystallizes in the monoclinic space group *C2/c*. The asymmetric unit of **33** contains one molecule of **33**, two PF<sub>6</sub><sup>-</sup> counteranions, two chloroform molecules and one dichloromethane molecule. The crystal structure of a single molecule of **33** is shown in Figure 2.8.

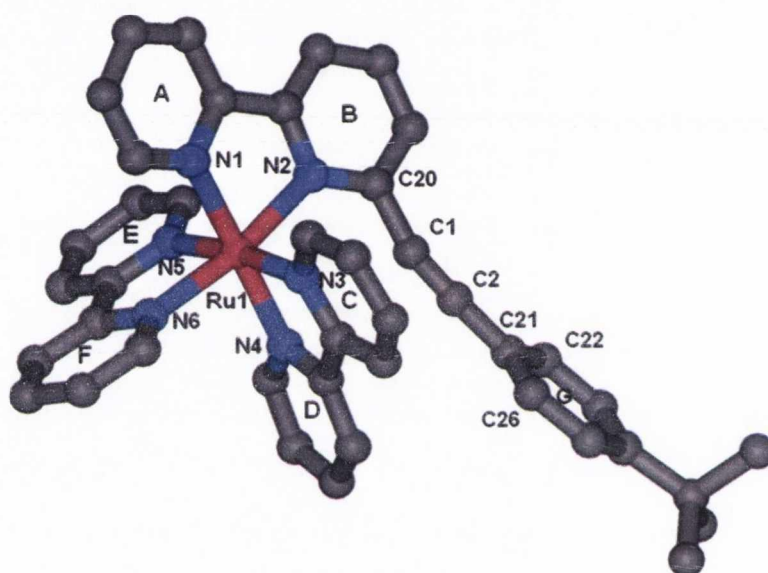


Figure 2.8: Perspective view of the crystal structure of **33** with selected atom and aromatic ring labelling. Solvent molecules, PF<sub>6</sub><sup>-</sup> counterions and hydrogens have been removed for clarity.

Single crystals of [Ru(bpy)<sub>2</sub>(**3**)](PF<sub>6</sub>)<sub>2</sub> (**35**) suitable for X-ray diffraction were grown by slow diffusion of hexane into a CH<sub>2</sub>Cl<sub>2</sub>/CHCl<sub>3</sub> solution of the complex. This was left to stand in the fridge for 4 days after which time large deep-red cubic crystals were obtained. The complex crystallises in the triclinic *P1* space group. The asymmetric unit contains one molecule of **35**, two PF<sub>6</sub><sup>-</sup> counterions, two molecules of CHCl<sub>3</sub> and one molecule of CH<sub>2</sub>Cl<sub>2</sub>.



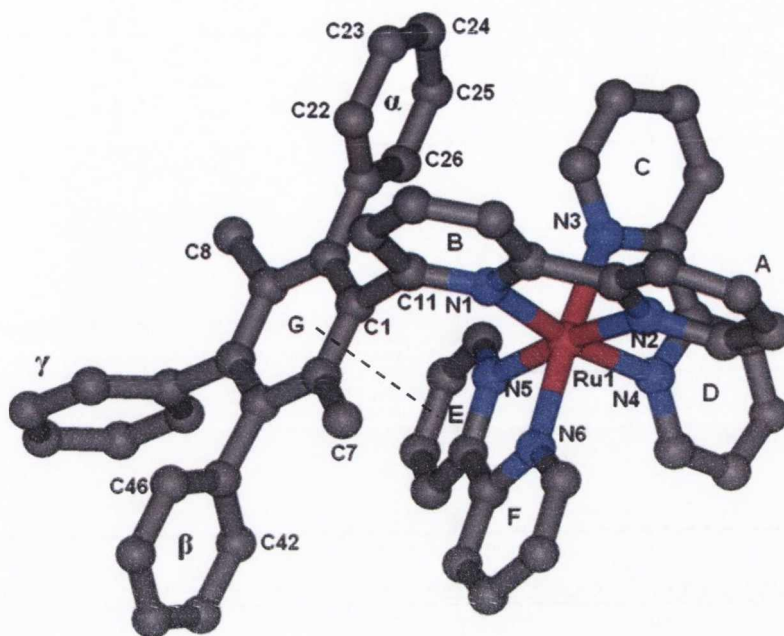


Figure 2.9: Perspective view of the crystal structure of **35** with selected atom and aromatic ring labelling. Solvent molecules,  $\text{PF}_6^-$  counterions and hydrogens have been removed for clarity. Intermolecular interaction indicated by dashed line.

In both crystal structures, the three bipyridine ligands are coordinated in a slightly distorted octahedral arrangement about the Ru(II) metal centre. Each of the three ligand moieties deviate slightly from planarity. In **33** (Ru-<sup>t</sup>Bu), the mean plane of ring A is tilted  $10.4^\circ$  from that of ring B and tilt angles between C and D and between E and F of  $6.9$  and  $6.0^\circ$  respectively are measured (Table 2.2). Similarly, for **35** (Ru-Me<sub>2</sub>) the tilt angles between the mean planes calculated for the two pyridine rings located on the same ligand are between  $6.6$ - $10.9^\circ$  (Table 2.2).

In keeping with the octahedral arrangement, it would be anticipated that the angle between pyridine ring nitrogens located *trans* to each other through the Ru(II) centre should approach  $180^\circ$ . This is essentially true in **33** (Ru-<sup>t</sup>Bu) for N(1)-Ru(1)-N(4) and N(3)-Ru(1)-N(5) ( $176.13(18)^\circ$ ,  $172.23(16)^\circ$ ), both comparable to the *trans* angle in  $[\text{Ru}(\text{bpy})_3](\text{PF}_6)_2$  itself ( $173^\circ$ ).<sup>109</sup> However, a slight deviation is observed for N(2)-Ru(1)-N(6) which measures  $169.28(16)^\circ$ . Similarly, in **35** (Ru-Me<sub>2</sub>), the greatest deviation is observed for the angle involving the polyphenylene-substituted pyridine ring (B) where the angle N(1)-Ru(1)-N(4) measures  $170.9(2)^\circ$ . This deviation is due to the steric bulk of the aromatic functional group which forces B to deviate more significantly from linearity.

This effect is not observed in other heteroleptic Ru(II) bipyridyl complexes where one ligand is substituted on one ring at the 6-position.<sup>70,110</sup> An examination of the bond angles about the acetylene in **33** also sheds light on this effect. The angle between C(2)-C(1)-C(20) measures 164.5(6)° which is quite a significant deviation from the expected 180° for an acetylene moiety (Table 2.2). The close proximity of these moieties to the sterically congested [Ru(bpy)<sub>2</sub>]<sup>2+</sup> core forces the acetylene to point out of the plane. In contrast, the more linear angle of 177.2(6)° measured for the second portion of the alkyne fragment, C(1)-C(2)-C(21), is a consequence of a greater distance from the Ru(II) coordination sphere.

Table 2.2: Selected bond lengths (Å) bond angles (°) and tilt angles (°) for **33** and **35**.

Bond	Bond Length (Å)	Bond Angle	Angle (°)	Tilt Angles between aromatic rings (°)
<b>33 (Ru-<sup>t</sup>Bu)</b>				
Ru(1)-N(1)	2.052(4)	N(3)-Ru(1)-N(4)	79.12(17)	A-B: 10.4 <sup>a</sup>
Ru(1)-N(2)	2.093(4)	N(1)-Ru(1)-N(2)	78.37(17)	C-D: 6.9
Ru(1)-N(3)	2.054(4)	N(5)-Ru(1)-N(6)	78.72(17)	E-F: 6.0
Ru(1)-N(4)	2.064(4)	N(1)-Ru(1)-N(4)	176.13(18)	A/B – G: 46.9 <sup>b</sup>
Ru(1)-N(5)	2.087(4)	N(3)-Ru(1)-N(5)	172.23(16)	
Ru(1)-N(6)	2.066(4)	N(2)-Ru(1)-N(6)	169.28(16)	
C(1)-C(2)	1.200(8)	C(2)-C(1)-C(20)	164.5(6)	
C(1)-C(20)	1.436(8)	C(1)-C(2)-C(21)	177.2(6)	
C(2)-C(21)	1.434(8)			
<b>35 (Ru-Me<sub>2</sub>)</b>				
Ru(1)-N(1)	2.129(5)	N(3)-Ru(1)-N(4)	78.6(2)	A-B: 9.4 <sup>a</sup>
Ru(1)-N(2)	2.061(6)	N(1)-Ru(1)-N(2)	78.6(2)	C-D: 6.6
Ru(1)-N(3)	2.057(5)	N(5)-Ru(1)-N(6)	79.1(2)	E-F: 10.9
Ru(1)-N(4)	2.064(5)	N(1)-Ru(1)-N(4)	170.9(2)	G – α: 61.7
Ru(1)-N(5)	2.065(5)	N(3)-Ru(1)-N(6)	174.3(3)	G – β: 73.2
Ru(1)-N(6)	2.064(5)	N(2)-Ru(1)-N(5)	173.1(2)	G – γ: 75.2
C(1)-C(11)	1.502(7)			A/B – G: 87.6 <sup>b</sup>

For example: <sup>a</sup> Angle between the mean planes calculated for ring A and ring B; <sup>b</sup> Angle between the A/B mean ligand plane and the calculated plane for benzene ring G.

Ruthenium-nitrogen bond lengths in Ru(II) *tris*-bipyridyl complexes are usually comparable to those of the parent [Ru(bpy)<sub>3</sub>](PF<sub>6</sub>)<sub>2</sub> complex (2.056(6) Å).<sup>109</sup> In complex **33**, ruthenium-nitrogen bond lengths are similar (2.052(4)-2.066(4) Å) with two marginal exceptions (Table 2.2). Ru(1)-N(5) is slightly longer with a value of 2.087(4) Å. More significantly, the bond between the metal centre and the pyridine with the pendant phenyl substituent (Ru(1)-N(2)) measures 2.093(4) Å. The same feature is evident in complex **35** (Ru-Me<sub>2</sub>) for substituted pyridine ring B, where the Ru(1)-N(1) bond is significantly longer (2.129(5) Å) than the other Ru-N distances which fall between 2.057(5) and 2.065(5) Å. This is predominantly a steric effect, where elongation is caused by the steric hindrance of the adjacent aryl functional group. This bond weakening is typical of Ru(II) structures containing any group attached at the 6-position on a bipyridyl ligand moiety.<sup>70,110-112</sup> Additionally, another contributing factor may be the extra electron density from the aryl-acetylene which enhances  $\pi$ -electron conjugation on ring B resulting in a relative weakening of the Ru-N bond.

In **35** (Ru-Me<sub>2</sub>), the N-Ru-N bite angles on each ligand fall between 78.6(2) and 79.1(2)° which is in good agreement with the measured range 78.37(17)-79.12(17)° for [Ru(bpy)<sub>2</sub>(**1**)](PF<sub>6</sub>)<sub>2</sub> (**33**). These values also correspond with literature values for the parent complex [Ru(bpy)<sub>3</sub>](PF<sub>6</sub>)<sub>2</sub> itself and with analogous heteroleptic *tris*-bipyridyl ruthenium(II) complexes, where one ligand is substituted in one or both 6-positions (adjacent to the pyridine ring nitrogen).<sup>70,109-112</sup>

In **35** (Ru-Me<sub>2</sub>), the dihedral angles between the central phenyl ring on the substituted bipyridine (G, Figure 2.9) and each of the appended phenyl rings ( $\alpha$ ,  $\beta$  and  $\gamma$ ) are given in Table 2.2. The three phenyl substituents are twisted at angles between 61.7 and 75.2° from the plane of the central benzene ring G. These features are quite typical of propeller-like polyphenylenes synthesised previously within the group and are also evident in the structures of two Pt(II) polyphenylene complexes in Chapter 4.<sup>31,73</sup> In **33** (Ru-<sup>t</sup>Bu), ring G on the aryl-acetylene is tilted quite significantly out of the mean plane of the coordinated A-B bipyridine ring (46.9°).

An intramolecular interaction is evident in the crystal structure of **35**. Weak  $\pi$ -stacking is observed between ring G on the extended bipyridine ligand and ring E on one of the unsubstituted bipyridines with a distance of 3.705 Å between centroids calculated for E

and G. The two aromatic rings are almost parallel to each other (with an angle of  $20^\circ$  between mean planes calculated for each ring system).

### 2.2.2.1 Packing of $33.2\text{CHCl}_3 \cdot \text{CH}_2\text{Cl}_2$ and $35.2\text{CHCl}_3 \cdot \text{CH}_2\text{Cl}_2$ in the crystal

The molecules of **33** arrange in an offset head-to-tail fashion. The  $\text{CH}_2\text{Cl}_2$  and  $\text{CHCl}_3$  solvent molecules and the hexafluorophosphate ions play a key role in the packing of the molecule in the solid state (Figure 2.10).

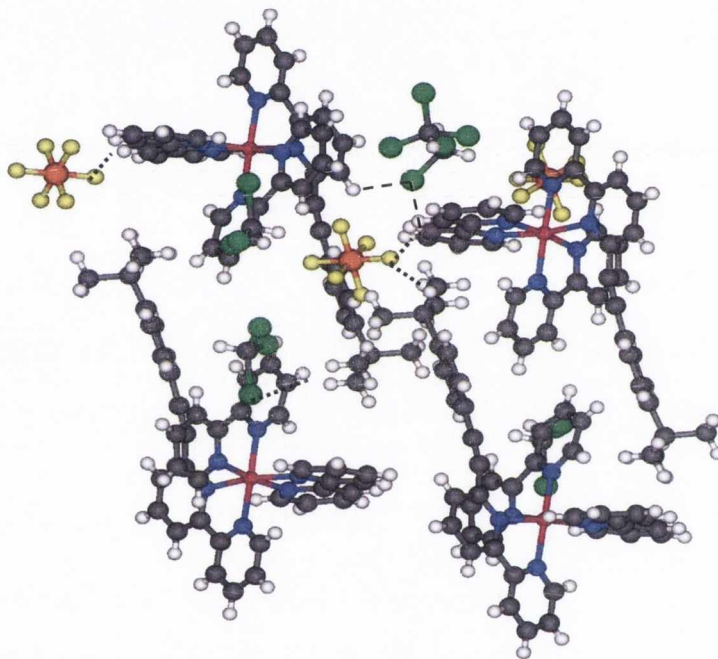


*Figure 2.10: Packing of molecules of **33** showing interactions between solvent and counterion molecules with the complex,  $\text{C-H}\cdots\text{Cl}$  and  $\text{C-H}\cdots\text{F}$  bonds.*

Specific interactions are observed between the chlorine atoms on the solvent molecules and hydrogens located on unsubstituted bipyridine ligands (interactions shown in Figure 2.10). For example, an interaction is evident between a chlorine on a chloroform molecule and hydrogens located on pyridine rings ( $\text{C-Cl}\cdots\text{H}$ ) of two adjacent molecules of **33**. In the crystal these distances measure  $\text{Cl}\cdots\text{H}$  2.75-2.91 Å and are shorter than the sum of the Van der Waals radii for H and Cl atoms (2.95 Å).<sup>113</sup> These interactions align the molecules of the complex in a row with the same orientation (Row A, Figure 2.11). Further weak non-covalent interactions involve the  $\text{PF}_6^-$  ions (interactions shown in Figure 2.10) which link together the two rows of molecules of **33** of opposite orientations (rows A and B, Figure 2.11). Weak  $\text{P-F}\cdots\text{H}$  interactions are evident between the hexafluorophosphate fluorine

atom and both bipyridyl hydrogen atoms and hydrogen atoms on pendant phenyl ring G (with  $F\cdots H$  distance varying between 2.37-2.66 Å). These are slightly less than the sum of the Van der Waals radii for F and H atoms (2.67 Å) and indicating a weak non-covalent interaction.

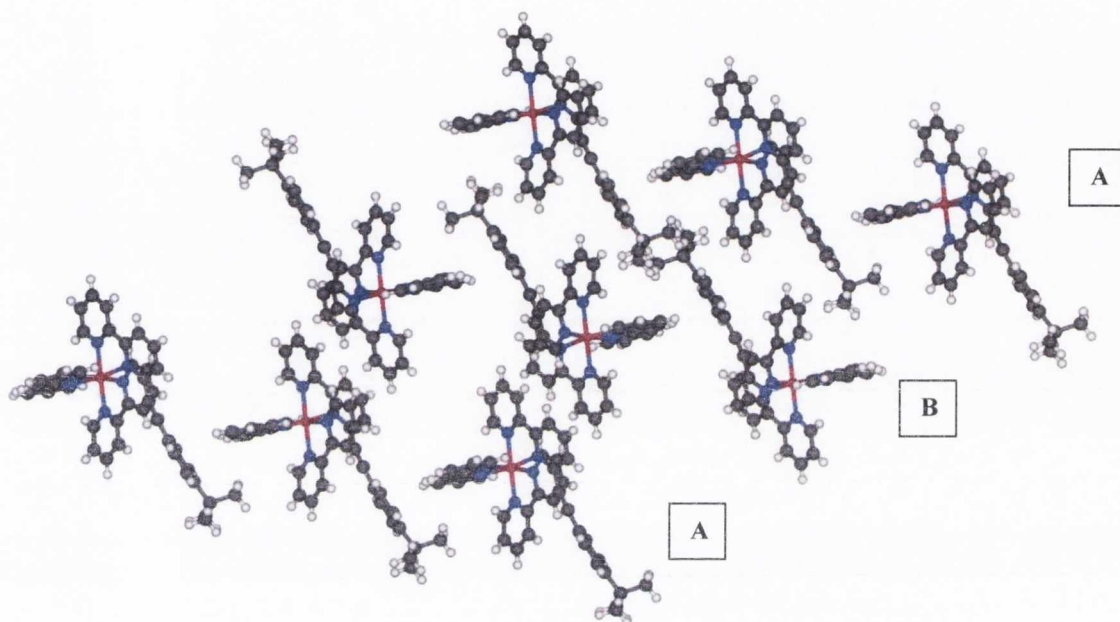


Figure 2.11: Expanded crystal packing in **33** viewed along the *b*-axis.  $PF_6^-$  counterions and solvent molecules have been omitted for clarity.

The packing arrangement of  $[Ru(bpy)_2(\mathbf{3})](PF_6)_2$  (**35**) in the crystal lattice is shown in Figure 2.12. The molecules undergo self-assembly to pack into unidirectional sheets where the voids are filled by solvent molecules and  $PF_6^-$  counterions. These sheets are held together by multiple non-covalent Van der Waals interactions and hydrogen-bonds involving  $CHCl_3$ ,  $CH_2Cl_2$  molecules and  $PF_6^-$  counterions. These interactions include  $P\cdots F\cdots H$  ( $F\cdots H$  2.33-2.48 Å) and  $C\cdots Cl\cdots H$  ( $Cl\cdots H$  2.67-2.88 Å) between solvent/counterions and bipyridyl ring hydrogens, where the interactions are shorter than the sum of the respective Van der Waals radii involved.<sup>113</sup>

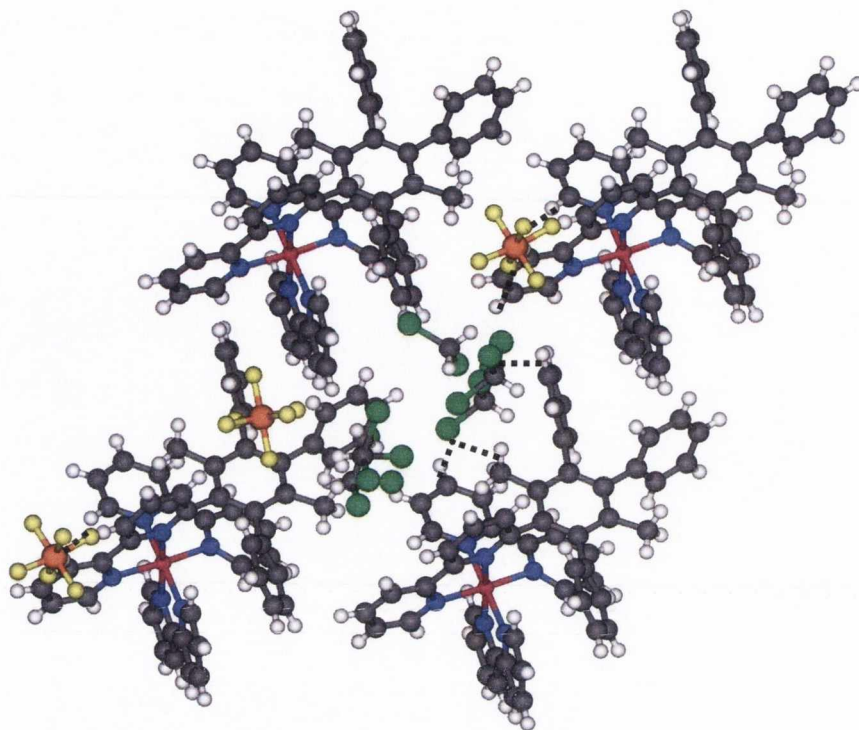


Figure 2.12: Packing of molecules of **35** in the crystal lattice as viewed along the *a* axis, showing interactions between the complex and solvent molecules ( $C-Cl \cdots H$ ) and counterions ( $P-F \cdots H$ ) (black dashed lines).

### 2.2.3 NMR Spectroscopic Characterisation of **33**, **34**, **35** and **36**

The characterisation by NMR spectroscopy of  $[Ru(bpy)_2(\mathbf{1})](PF_6)_2$  (**33**),  $[Ru(bpy)_2(\mathbf{2})](PF_6)_2$  (**34**),  $[Ru(bpy)_2(\mathbf{3})](PF_6)_2$  (**35**) and  $[Ru(bpy)_2(\mathbf{4})](PF_6)_2$  (**36**) by NMR spectroscopy proved to be particularly challenging. Coordination of one asymmetric bipyridine ligand to the  $[Ru(bpy)_2]^{2+}$  metal centre results in a complex with such low symmetry that none of the signals appear in identical chemical environments. Consequently, each of the four pyridine rings on the unsubstituted bipyridine moieties in addition to the two pyridines and the aryl ring on the asymmetric ligand appear as separate signals in the extremely complex NMR spectrum. Despite this, the NMR spectra ( $^1H$  and  $^{13}C \{^1H\}$ ) have been fully assigned by using multiple NMR (1D and 2D) experiments.

### 2.2.3.1 $^1\text{H}$ and $^{13}\text{C}$ $\{^1\text{H}\}$ NMR spectra of **33** and **34**

The spectroscopic characterisation of complexes  $[\text{Ru}(\text{bpy})_2(\mathbf{1})](\text{PF}_6)_2$  (**33**) and  $[\text{Ru}(\text{bpy})_2(\mathbf{2})](\text{PF}_6)_2$  (**34**) containing the simple aryl-acetylene bipyridyl ligands, are discussed separately from complexes **35** and **36** incorporating larger polyaryl ligands.

The numbering scheme applied to complexes **33** ( $\text{Ru}-^t\text{Bu}$ ) and **34** ( $\text{Ru}-\text{CF}_3$ ) is given in Figure 2.13. Unsubstituted bipyridine ligands are designated (b) and (c). Each pyridine ring is differentiated on the basis of primed numbers, for example the two protons in the 6 position of ligand (b) are called Hb6 and Hb6'. The unique ligand is called ligand (a). Ligand (a) has one four-spin system (a') and one three-spin system (a).  $\text{C}_\alpha$  is the acetylenic carbon closest to the bipyridyl moiety and  $\text{C}_\beta$  is closest to the pendant aryl. The aryl ring is labelled *i*, *o*, *m* and *p* for *ipso*, *ortho*, *meta* and *para* positions. For each of the four complexes, the signals were identified *via* the same methods. As an example, the in-depth details of NMR signal assignment are discussed for complex **33**.

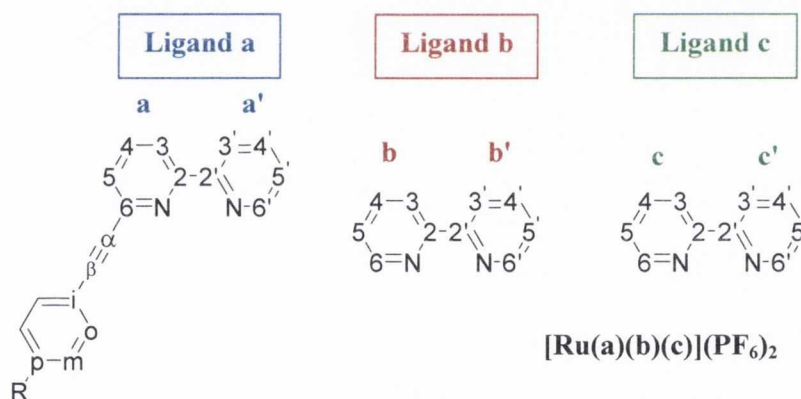


Figure 2.13: NMR numbering scheme for  $[\text{Ru}(\text{bpy})_2(\mathbf{1})](\text{PF}_6)_2$  (**33**) and  $[\text{Ru}(\text{bpy})_2(\mathbf{2})](\text{PF}_6)_2$  (**34**). ( $R = ^t\text{Bu}$ , (**33**),  $R = \text{CF}_3$  (**34**)).

#### 2.2.3.1.1 $^1\text{H}$ NMR spectrum of $[\text{Ru}(\text{bpy})_2(\mathbf{1})](\text{PF}_6)_2$ (**33**)

The fully assigned  $^1\text{H}$  NMR spectrum of **33** is given in Figure 2.14. The integration value for each of the peaks (number of protons per signal) is given underneath the spectrum.

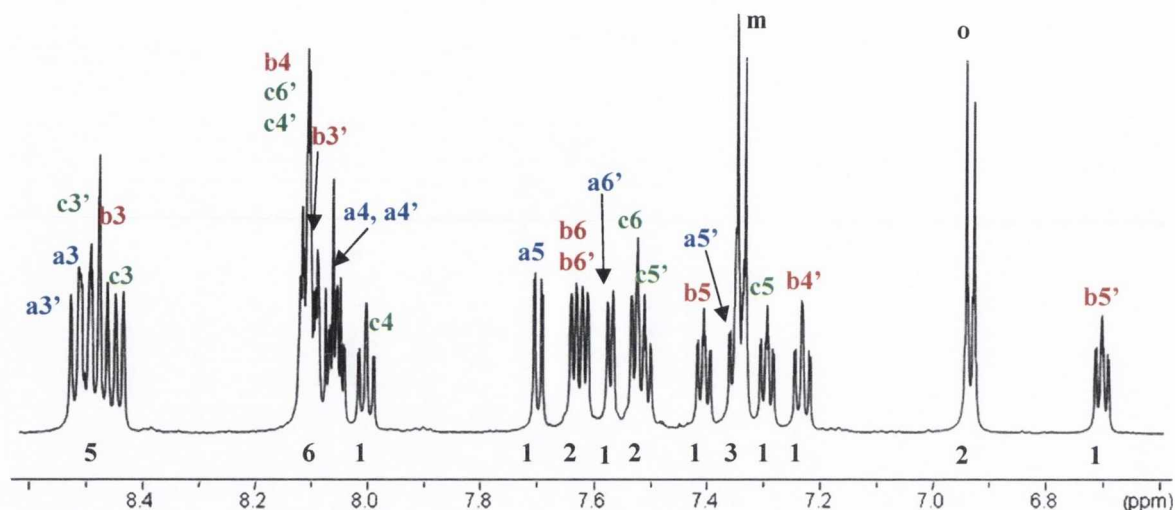


Figure 2.14:  $^1\text{H}$  NMR spectrum of **33** in  $\text{CD}_3\text{CN}$  (600.1 MHz, R.T). Atom labelling as in Figure 2.13.

A significant degree of overlap is evident in the spectrum. In general, the signals located on the same ring can be identified using a  $^1\text{H}$ - $^1\text{H}$  COSY (TOCSY) experiment, which correlates all the proton signals located on the same spin system (Figure 2.15). The four-spin system indicated by the green dashed arrows in Figure 2.15 is particularly informative (ring c). This identifies the deshielded doublet at  $\delta$  8.44 ppm ( $^3J_{\text{HH}} = 8.0$  Hz) and the doublet at  $\delta$  7.54 ppm ( $^3J_{\text{HH}} = 6.0$  Hz) as being on the same ring system and belonging to c3 and c6 protons respectively. These can be distinguished on the basis of their coupling constants, with the smaller coupling constant characteristic of the proton adjacent to the nitrogen on a pyridine ring. The other two signals on this ring appear as doublets of doublets (ddd) at  $\delta$  7.29 ppm ( $^3J_{\text{HH}} = 6.9, 6.4$  Hz,  $^4J_{\text{HH}} = 1.3$  Hz) and at  $\delta$  8.0 Hz ( $^3J_{\text{HH}} = 7.8$  Hz,  $^4J_{\text{HH}} = 1.5$  Hz). Again coupling constants facilitate identification of these signals. The more shielded of the signals, at  $\delta$  7.29 ppm, with the smaller geminal three-bond coupling constants ( $^3J$ ), is indicative of proximity to the pyridine ring nitrogen. This is identified as c5 (three-bond coupling to c4 and c6 and long-range through four-bonds coupling to c3) and the downfield signal is assigned as c4. As the odd one out, the ring on which the three-spin system is located on ligand (a) is easily identified. The doublet of doublets at  $\delta$  7.70 ppm (blue dashed arrow) is on the same ring as a signal appearing in the multiplet at  $\delta$  8.03-8.13 ppm and another in the most downfield multiplet between  $\delta$  8.46-8.53 ppm.



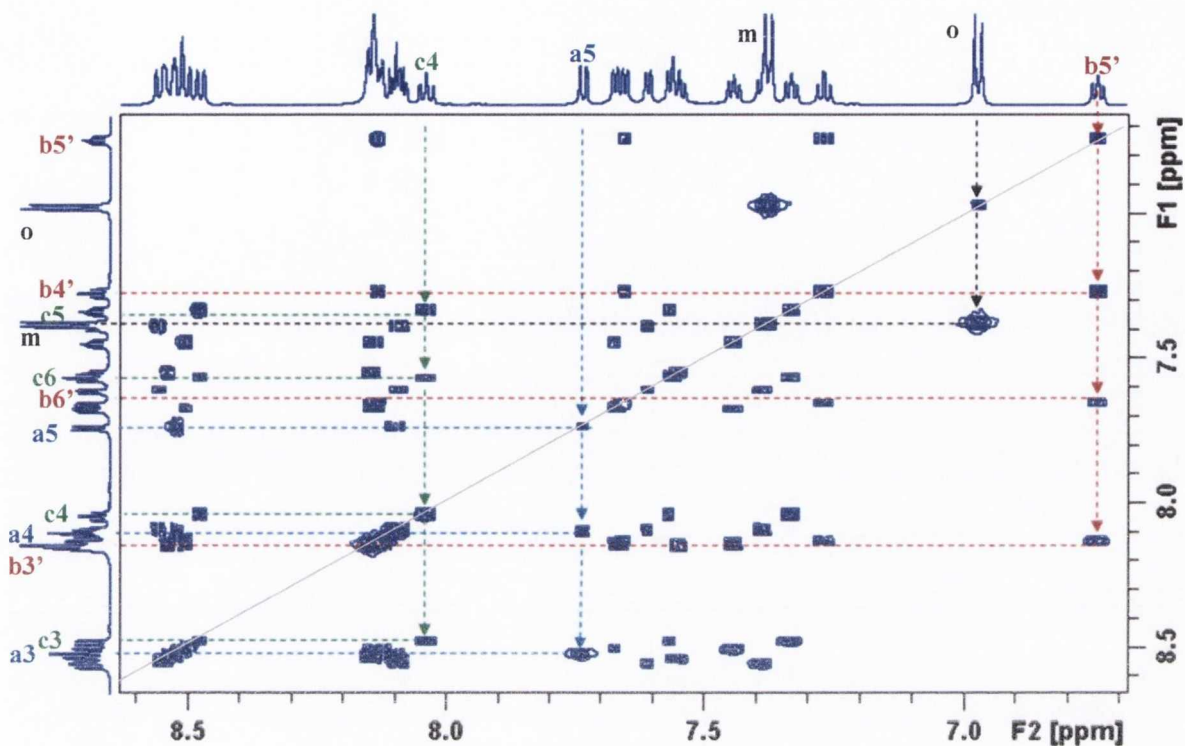


Figure 2.15:  $^1\text{H}$ - $^1\text{H}$  COSY experiment of **33** showing through bond correlations for several of the pyridine ring systems (atom labelling and colours as per Figure 2.13).

The trend in chemical shifts in the  $^1\text{H}$  NMR of **33** (Figure 2.14) holds in general for each of the pyridine rings. The protons in the three position appear as the most downfield signals in a multiplet at  $\delta$  8.46–8.53 ppm, with the four-position protons occurring in general in the multiplet between  $\delta$  8.03–8.13 ppm. For each of the pyridine rings, the proton in the 5-position is the most upfield of the ring system. The signals on one ring, specifically the b' ring on one of the unsubstituted bipyridines, are significantly more shielded than the other pyridine heterocycles (Figure 2.15, red-dashed arrow). This occurs for one ring in one of the unsubstituted bipyridine ligands in each of the four Ru(II) complexes prepared in this chapter. This general trend in chemical shifts,  $\text{H3} > \text{H4} > \text{H6} > \text{H5}$ , which is observed for complex **33** and in turn for **34**, **35** and **36**, is well established for Ru(II) *tris*-bipyridyl complexes.<sup>114</sup>

The AB spin system attributable to the pendant phenyl ring on ligand (a) is one of the most obvious features of the  $^1\text{H}$  NMR (Figure 2.14), with one doublet appearing at  $\delta$  6.93 ppm ( $^3J_{\text{HH}} = 8.8$  Hz) and the other overlapping another signal at  $\delta$  7.37 ppm. The through bond cross peak which identifies the two signals as adjacent to each other is seen in the  $^1\text{H}$ - $^1\text{H}$

COSY experiment (Figure 2.15, black dashed arrow). A 2D long-range  $^1\text{H}$ - $^{13}\text{C}$  correlation spectrum (HMBC, Heteronuclear Multi-Bond Connectivity) is optimised to detect  $^1\text{H}$ - $^{13}\text{C}$  correlation over two/three bonds and can be used to distinguish Ho from Hm (Figure 2.16).

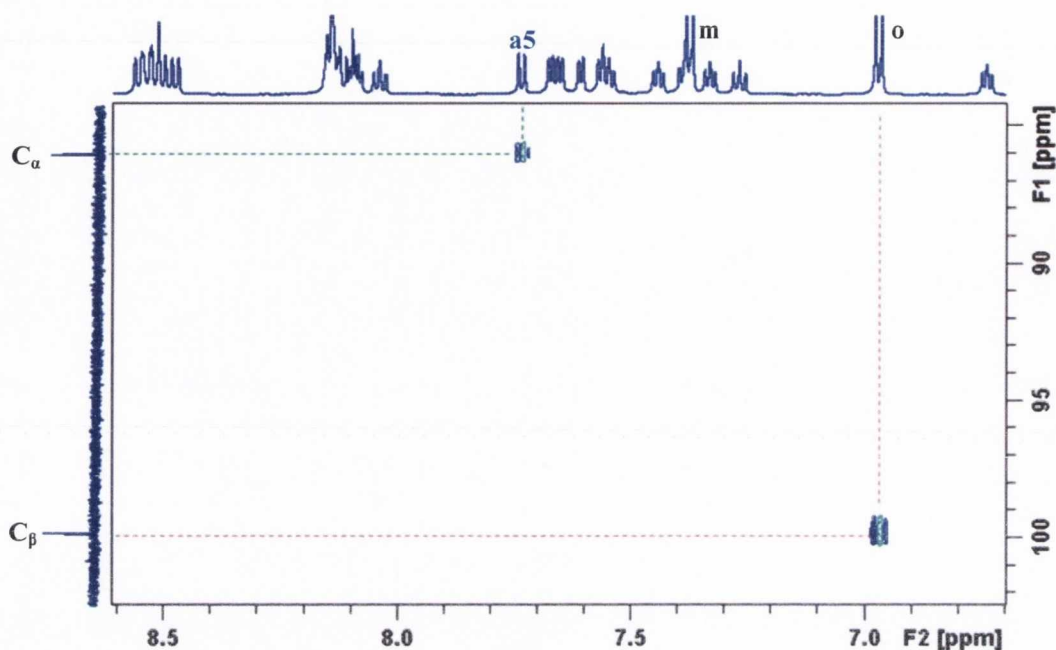


Figure 2.16:  $^1\text{H}$ - $^{13}\text{C}$  HMBC experiment of **33** showing long-range links to the acetylenic carbons. (Atom labelling as per Figure 1.13).

A link between the doublet at  $\delta$  6.93 ppm and an acetylenic carbon at  $\delta$  88.86 ppm is evident whereas the doublet at  $\delta$  7.37 ppm displays no correlation (Figure 2.16). Hence the more upfield doublet must be Ho closest to the acetylene moiety and the acetylenic carbon signal must be  $\text{C}_\beta$  closest to the pendant phenyl ring. The other acetylenic carbon,  $\text{C}_\alpha$ , at  $\delta$  86.05 ppm experiences one through three-bonds link to the doublet of doublets at  $\delta$  7.70 ppm, which has been assigned to the 3-spin system of ring (a) (Figure 2.13). This confirms the identity of the doublet of doublets as Ha5 closest to the acetylene ( $^3J_{\text{H5H4}}$ ,  $^4J_{\text{H5H3}} = 8.0$ , 1.3 Hz). Finally, an additional singlet at  $\delta$  1.31 ppm integrating for 9H corresponds to the *tert*-butyl group in the *para* position on ligand (a).

### 2.2.3.1.2 $^{13}\text{C}$ $\{^1\text{H}\}$ NMR Spectrum of $[\text{Ru}(\text{bpy})_2(\mathbf{1})](\text{PF}_6)_2$ (**33**)

The  $^{13}\text{C}$   $\{^1\text{H}\}$  DEPT 90 spectrum of  $[\text{Ru}(\text{bpy})_2(\mathbf{1})](\text{PF}_6)_2$  (**33**) is shown in Figure 2.17. The DEPT-90 spectrum is considerably simpler than the full  $^{13}\text{C}$   $\{^1\text{H}\}$  spectrum as it displays CH signals as positive peaks and the quaternary carbon signals are absent. The methine carbon signals were assigned fully using a 2D HSQC ( $^1\text{H}$ - $^{13}\text{C}$  COSY) NMR experiment

(Heteronuclear Single Quantum Coherence). A HSQC experiment correlates direct one-bond links between  $^1\text{H}$  and  $^{13}\text{C}$  nuclei.

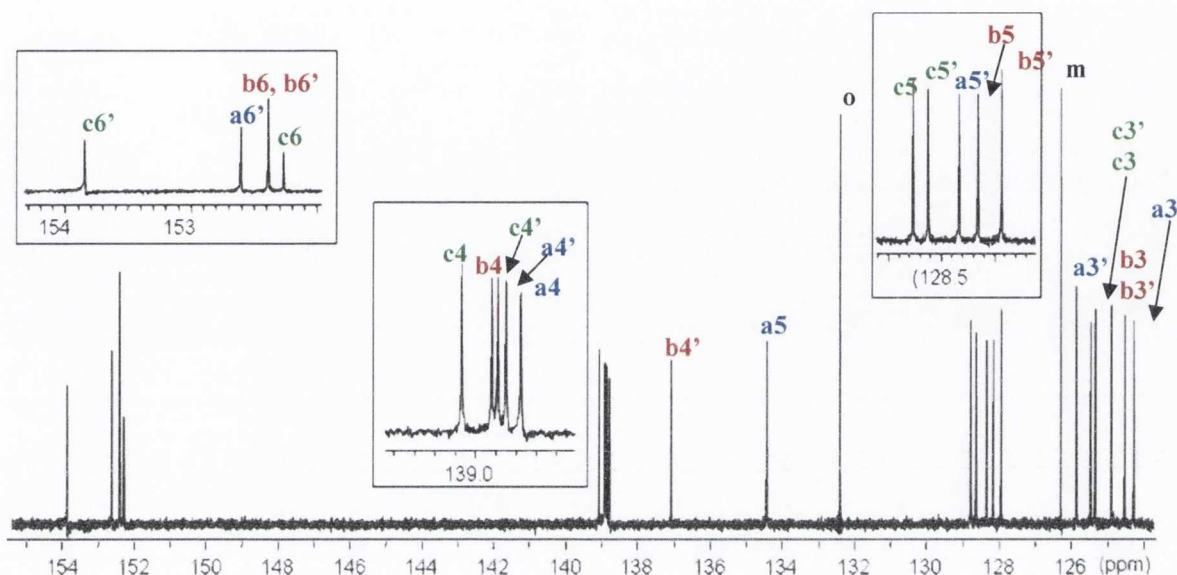


Figure 2.17: Aromatic region of the  $^{13}\text{C} \{^1\text{H}\}$  NMR DEPT 90 spectrum of **33** in  $\text{CD}_3\text{CN}$  (150.9 MHz, R.T.). (Atom labelling as Figure 2.13).

The carbon signals in the 6-positions on the bipyridine rings always appear as the most downfield of the resonances, occurring for complex **33** between  $\delta$  152.33-153.91 ppm (Figure 2.17). The next set of signals, between  $\delta$  137.13-139.13 ppm, are attributable to the methine carbon signals in the 4-position. The CH signals located at the 5-position occur for the most part between  $\delta$  127.99-128.82 ppm. Finally, the 3-positioned CH signals appear together between  $\delta$  124.34-125.91 ppm. One obvious deviation from this is the methine signal attributed to a5 ( $\delta$  134.48 ppm), the three-spin pyridine ring on ligand (a). Ca5 is located in close proximity to the acetylene moiety. The magnetic anisotropy of the acetylene group, a consequence of an induced  $\pi$ -electron secondary magnetic field, results in a shielding and a deshielding area about the triple bond. The methine signal must fall into the deshielding region and so appears more downfield of the other 3-positioned methine carbons. A similar effect is observed in the  $^1\text{H}$  NMR spectrum for Ha5 ( $\delta$  7.70 ppm) which is again located more downfield of similarly located protons. The trends observed for the chemical shifts of the pyridine rings hold for each of the four complexes prepared in this chapter.

Finally, the HMBC experiment (Figure 2.18) was used to link each of the pyridine rings together, i.e. determine which 4-spin system is ring (a) and which is ring (a'). The first step to achieve this was to identify the quaternary carbon at the 2-position on each ring, i.e. at the link between the two rings. This was achieved using the HMBC experiment. The 2-positioned carbons all appear most deshielded of the carbon signals in the  $^{13}\text{C} \{^1\text{H}\}$  NMR, between  $\delta$  157.53-158.94 ppm. Each of these quaternary carbons “see” the H3 (through two bonds), H4 and H6 (both through three bonds) on one ring system. In general, no correlation (or very weak) is observed to the proton at the 5-position which, at four bonds distance, is furthest away.

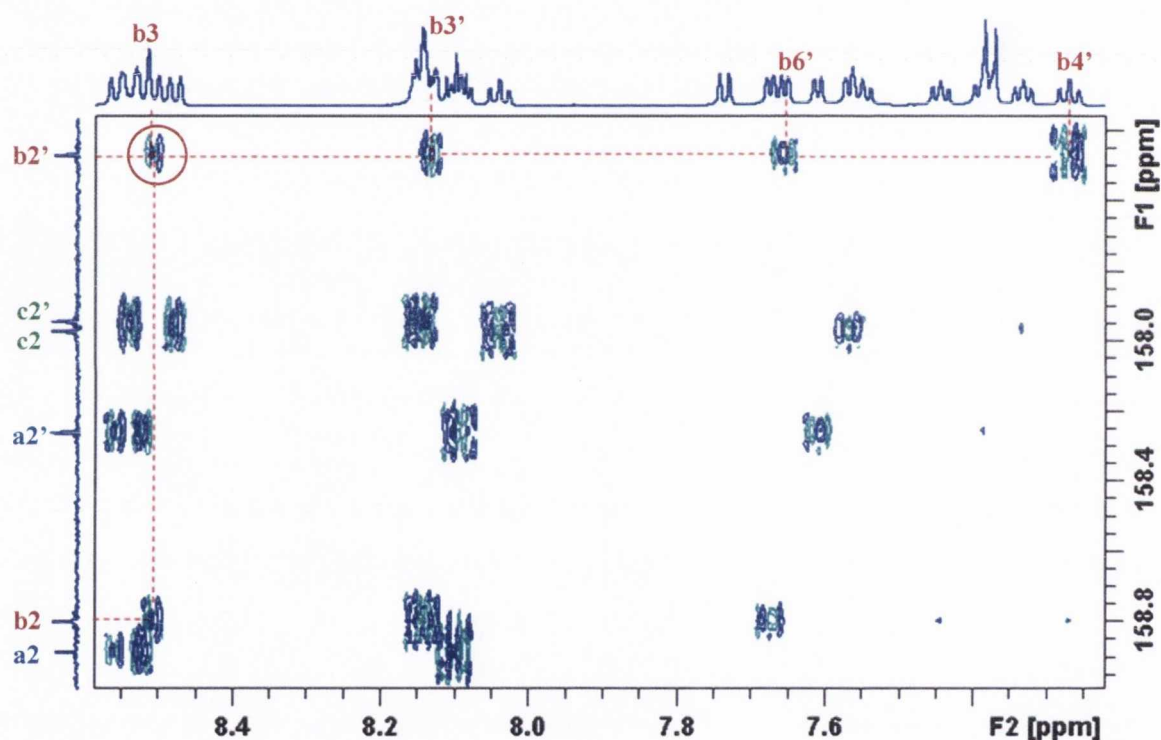


Figure 2.18: HMBC experiment of **33** showing links between the 2-positioned quaternary carbons on bipyridine ligand (**b**). Atom labelling as in Figure 2.13.

For example, a strong cross peak is observed between the quaternary carbon at  $\delta$  157.53 ppm and the protons on the b' ring, specifically b3', b4' and b6', and can be assigned to b2' (Figure 2.18). Most significantly, a correlation for this signal is also observed to another 3-positioned proton signal in the multiplet at  $\delta$  8.50 ppm. This is identified as b3 on the connected pyridine ring. From the same spectrum, a long-range correlation is seen for this signal to the quaternary carbon at  $\delta$  158.86 ppm which must be the carbon at b2. By this method, the complete assignment of each of the three bipyridine ligands is

achieved. The general trend in  $^{13}\text{C}$   $\{^1\text{H}\}$  chemical shifts,  $\text{C2} > \text{C6} > \text{C4} > \text{C5} > \text{C3}$ , holds for all the complexes **33-36** and is commonly observed in  $\text{Ru}(\text{bpy})_3]^{2+}$  derivatives.<sup>114</sup>

### 2.2.3.1.3 $^1\text{H}$ NMR Spectrum of $[\text{Ru}(\text{bpy})_2(\mathbf{2})](\text{PF}_6)_2$ (**34**)

The  $^1\text{H}$  NMR spectrum of  $[\text{Ru}(\text{bpy})_2(\mathbf{2})](\text{PF}_6)_2$  (**34**) was assigned using the same techniques described in Section 2.2.3.1.1 for the structurally similar tert-butyl substituted complex  $[\text{Ru}(\text{bpy})_2(\mathbf{1})](\text{PF}_6)_2$  (**33**). The fully assigned spectrum is presented in Figure 2.19. The full spectrum integrates for a total of 27 protons, 8H for unsubstituted ligands (b) and (c), 7H on the bipyridyl rings of ligand (a) with a further 4H attributable to the pendant aryl ring (the integration values for each signal are given underneath).

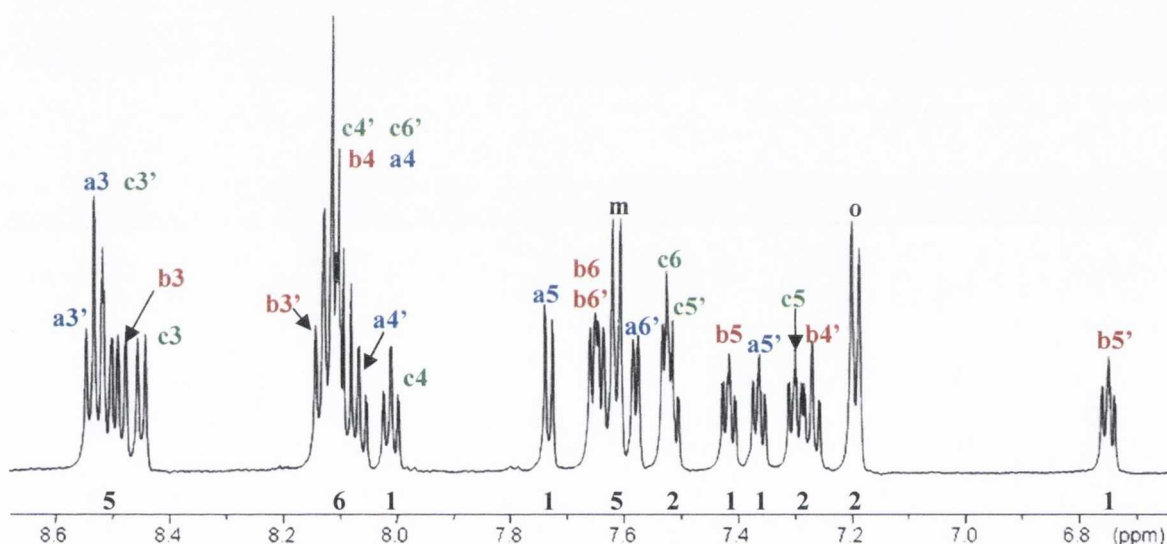


Figure 2.19:  $^1\text{H}$  NMR spectrum of **34** in  $\text{CD}_3\text{CN}$  (600.1 MHz, R.T.). Atom labelling as per Figure 2.13.

In general, the trends observed in the  $^1\text{H}$  NMR spectrum of **33** (Figure 2.14) are also observed in complex **34**. The protons located in the 3-position on each of the three ligands are the most downfield signals on their respective rings. The majority of these occur as a series of overlapping doublets (i.e. in a multiplet) between  $\delta$  8.45-8.55 ppm. Similarly, the protons in the 5-positions on the three ligands are the most upfield on their respective pyridine heterocycles. A H5 signal typically appears as a doublet of doublets of doublets (ddd), with two vicinal (3 bond) couplings to H4 and H6 (which are in non-chemically equivalent environments) and sometimes a more distant four-bond long-range coupling with H3. For example, the signal at a5' has this multiplicity (ddd) and correspondingly three distinct coupling constants -  $^3J_{\text{H5}'\text{H4}'}$ ,  $^3J_{\text{H5}'\text{H6}'}$ ,  $^4J_{\text{H5}'\text{H3}'}$  = 6.8, 6.6, 1.1 Hz. As observed

for *tert*-butyl substituted complex **33**, the b' protons of ligand (b) have anomalous chemical shifts – they are notably more shielded than for any of the other pyridine rings in the complex.

Table 2.3: Comparative  $^1\text{H}$  and  $^{13}\text{C}$  NMR chemical shifts and signal multiplicity for complexes **33** and **34** in  $\text{CD}_3\text{CN}$  (multiplicity). Atom labelling as per Figure 2.13.

Complex	$^1\text{H}$ NMR ( $\delta$ , ppm)					$^{13}\text{C}$ NMR ( $\delta$ , ppm) ( $\text{C}_\alpha \equiv \text{C}_\beta$ )
	<i>ortho</i> (o)	<i>meta</i> (m)	a5	a4	a3	
<b>33</b>	6.93 (d)	7.37 (d)	7.70 (dd)	8.10 (m)	8.50 (m)	$\alpha$ : 86.05, $\beta$ : 99.86
<b>34</b>	7.20 (d)	7.61 (d)	7.73 (dd)	8.10 (m)	8.52 (m)	$\alpha$ : 88.05, $\beta$ : 97.31

Selected  $^1\text{H}$  and  $^{13}\text{C}$  NMR chemical shifts are presented in Table 2.3. The proton chemical shifts of the AB ring system (Ho and Hm) of the pendant aryl substituent on ligand (a) in both complexes **33** and **34** are significantly affected by the R group in the para position (labelling shown in Figure 2.13). In complex **34** where R is the electron-withdrawing trifluoromethyl substituent, Ho and Hm are much more deshielded than in complex **33** (where R is an electron-rich *tert*-butyl functional group). Additionally, in complex **34** the Hm signal appears more downfield as it is subject to the inductive withdrawal effect of the  $\text{CF}_3$  group more greatly than its neighbouring Ho. The more upfield position of Ho is also a result of the proximity of the electron-delocalised acetylene functionality.

#### 2.2.3.1.4 $^{13}\text{C}$ $\{^1\text{H}\}$ NMR Spectrum of $[\text{Ru}(\text{bpy})_2(\mathbf{2})](\text{PF}_6)_2$ (**34**)

The  $^{13}\text{C}$   $\{^1\text{H}\}$  NMR spectrum of **34** was fully assigned using 2D NMR correlation experiments as described in Section 2.2.3.1.2. A portion of the aromatic region of the spectrum, between  $\delta$  121-134 ppm, is shown in Figure 2.20.

The pendant trifluoromethyl-substituted aryl ring on ligand (a) in complex **34** contributes an additional degree of complexity to the spectroscopic characterisation of the complex. The  $^{19}\text{F}$  NMR active nucleus (100 % natural abundance, spin  $\frac{1}{2}$ ) in the molecule results in  $^{13}\text{C}$ - $^{19}\text{F}$  heteronuclear coupling, as observed in the NMR spectroscopic characterisation of the free ligand **2** ( $\text{CF}_3$ ) in Chapter 1. In Figure 2.20, the coloured circles illustrate the quartet resulting from  $^{13}\text{C}$ - $^{19}\text{F}$  couplings,  $^1J_{\text{CF}}$  and  $^2J_{\text{CF}}$ .

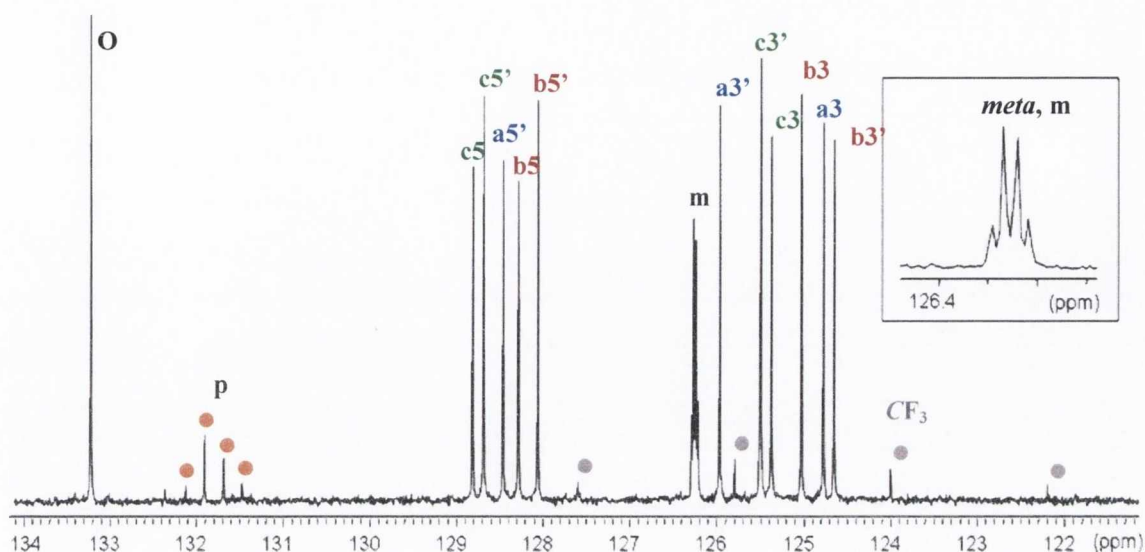


Figure 2.20:  $^{13}\text{C} \{^1\text{H}\}$  NMR spectrum ( $\text{CD}_3\text{CN}$ , 150.9 MHz, R.T.) showing the aromatic region of **34** between  $\delta$  121–134 ppm. Atom labelling as per inset Figure 2.13.

The carbon directly attached to the fluorine atoms, i.e. on the  $\text{CF}_3$  group itself ( $\delta$  124.90 ppm), appears as a quartet as predicted and has the largest through bond coupling constant,  $^1J_{\text{CF}} = 286$  Hz. Moving one bond further away from the fluorine atoms, the *para* quaternary carbon signal ( $\delta$  131.80 ppm) is also a quartet with a carbon-fluorine coupling constant which is almost an order of magnitude smaller,  $^2J_{\text{CF}} = 32$  Hz. The quartet at  $\delta$  126.25 ppm can be assigned to the *m* (*meta*) methine signal on the phenyl ring and has a coupling constant of  $^3J_{\text{CF}} = 3$  Hz. All measured carbon-fluorine coupling constants are in good agreement with other related systems.<sup>68,115</sup>

In the  $^{13}\text{C} \{^1\text{H}\}$  NMR spectrum, the chemical shift of the quaternary alkynyl carbon signals can reflect the electron demand from the metal centre through the  $\sigma$ -framework and essentially describes the degree of electron delocalisation in the ground state.<sup>93</sup> The carbon resonance for  $\text{C}_\alpha$ , the acetylenic carbon closest to the coordinated bipyridine unit, are more shielded than  $\text{C}_\beta$  signals due to proximity of the coordinated electron rich Ru(II) centre. In **33** (Ru- $^t\text{Bu}$ ),  $\text{C}_\alpha$  ( $\delta$  86.05 ppm) is more upfield than in **34** (Ru- $\text{CF}_3$ ) ( $\delta$  88.05 ppm) possibly due to the electron-donating *tert*-butyl substituent having a shielding effect on  $\text{C}_\alpha$  in **33** and the inductive withdrawal effect of the  $\text{CF}_3$  group deshielding the  $\text{C}_\alpha$  signal in complex **34**. In contrast, the protons on the three-spin system of ligand (a) are not affected by changing the R group. This may indicate that the effect of varying the electronic demand of the

substituent on the pendant aryl ring does not extend through the  $\sigma$ -framework as far as the bipyridine.

### 2.2.3.1.5 $^{19}\text{F}$ NMR Spectrum of $[\text{Ru}(\text{bpy})_2(2)](\text{PF}_6)_2$ (**34**)

The  $^{19}\text{F}$  NMR spectrum of **34** is shown in Figure 2.21. The signal that appears as a singlet at  $\delta$  -63.5 ppm can be attributed to fluorine on the  $\text{CF}_3$  functional group. The signal is a singlet because each of the three  $^{19}\text{F}$  nuclei within the  $\text{CF}_3$  unit are chemically equivalent. This resonance appears in the typical region for trifluoromethyl groups attached to an aryl ring.<sup>116-117</sup> An additional more upfield signal which occurs at  $\delta$  -72.9 ppm is assigned to the  $(\text{PF}_6)^-$  counterion. This is a doublet due to coupling of the  $^{19}\text{F}$  nucleus with the  $^{31}\text{P}$  NMR active nucleus (100 % abundance,  $I=1/2$ ) with a coupling constant  $^1J_{\text{PF}} = 704$  Hz.

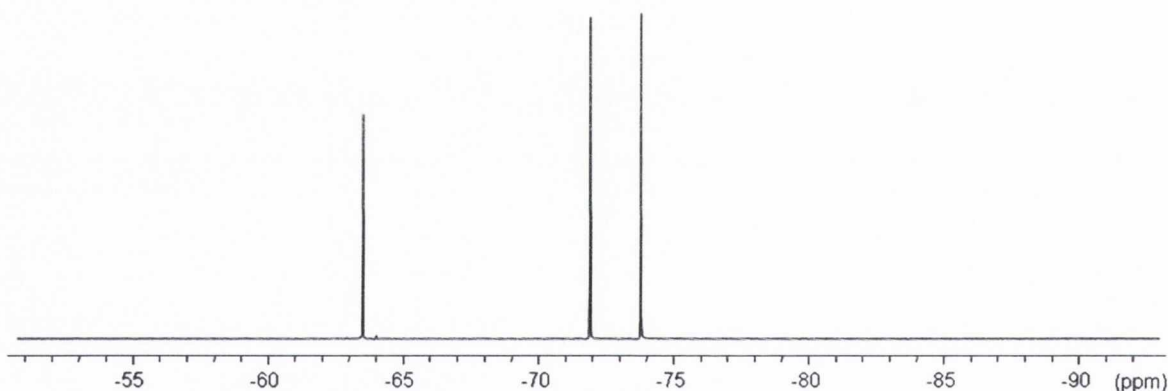


Figure 2.21:  $^{19}\text{F}$  NMR of **34** in  $\text{CD}_3\text{CN}$  (376.6 MHz, R.T.).

### 2.2.3.2 NMR Spectroscopic Characterisation of **35** and **36**

The NMR numbering scheme for complexes **35** and **36** containing polyphenylene substituents is shown in Figure 2.22. The additional polyphenylene rings add an extra layer of complexity to the NMR spectra that was not seen in complexes **33** and **34** with pendant aryl-acetylene moieties.

$^1\text{H}$  and  $^{13}\text{C}$   $\{^1\text{H}\}$  NMR spectra of both **35** and **36** have been fully assigned.  $^1\text{H}$  NMR spectra are presented in Sections 2.2.3.2.1 (**35**) and 2.2.3.2.2 (**36**).  $^{13}\text{C}$   $\{^1\text{H}\}$  NMR spectra are very similar to those described for aryl-acetylene complexes **33** and **34** and are not shown here, but full characterisation is detailed in Chapter 5 – Experimental.



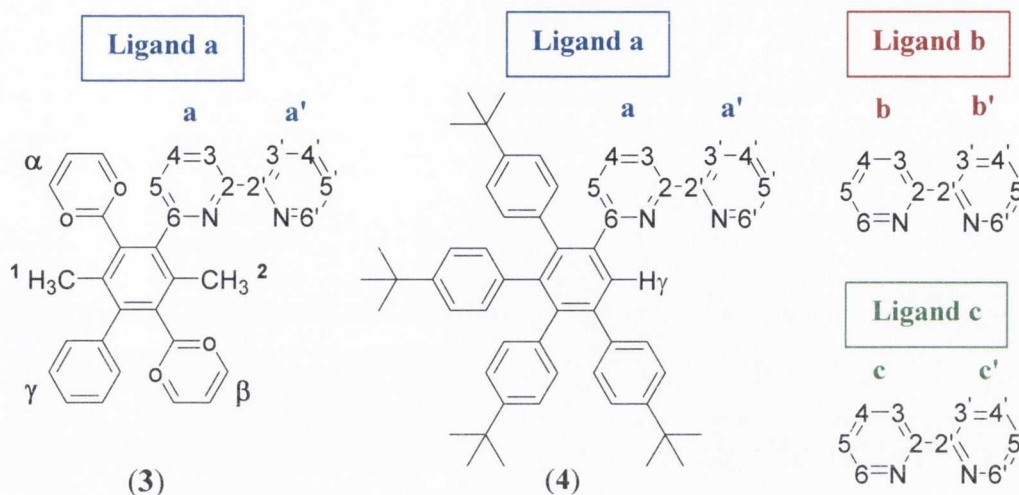


Figure 2.22: NMR numbering scheme for  $[Ru(a)(b)(c)](PF_6)_2$  complexes -  $[Ru(3)(bpy)_2](PF_6)_2$  (**35**) and  $[Ru(4)(bpy)_2](PF_6)_2$  (**36**). Key: Ligand (a) = (3)  $\rightarrow$   $[Ru(3)(bpy)_2](PF_6)_2$  (**35**), Ligand (a) = (4)  $\rightarrow$   $[Ru(4)(bpy)_2](PF_6)_2$  (**36**).

### 2.2.3.2.1 $^1H$ NMR Spectrum of **35**

The  $^1H$  NMR spectrum of **35** in deuterated  $CD_3CN$  is presented in Figure 2.23. The spectrum was assigned using the same methods described for  $[Ru(1)(bpy)_2](PF_6)_2$  (**33**). Initially a 2-D TOCSY experiment ( $^1H$ - $^1H$  correlation) was employed to identify all the protons on the same spin system. On the basis of coupling constants and chemical shift (in both  $^1H$  and  $^{13}C$  NMR spectra), it was possible to assign signals to their respective pyridine ring positions.

As observed in the spectra of **33** (Figure 2.14) and **34** (Figure 2.19), the most downfield signals are attributable to protons in the 3 (and 3') positions on the pyridine rings. These appear as a series of six doublets between  $\delta$  8.29-8.55 ppm, that are coupled through three bonds to the adjacent H4 (or H4') with typical coupling constants  $^3J_{H_3H_4} = 8.0$  Hz. In general, the most shielded of the signals on each pyridine ring system occurs for the proton in the 5 position. There is one noticeable exception. Hc6 appears particularly upfield at  $\delta$  6.66 ppm ( $^3J_{H_6H_5} = 5.2$  Hz). It is suggested that this proton is located in the 6 position on ring E (see crystal structure, Figure 2.9) which is involved in the weak  $\pi$ -interaction with the central benzene ring G. Hc6 "feels" more electron density as it points into a shielding region of the anisotropic field induced by the ring current on G.

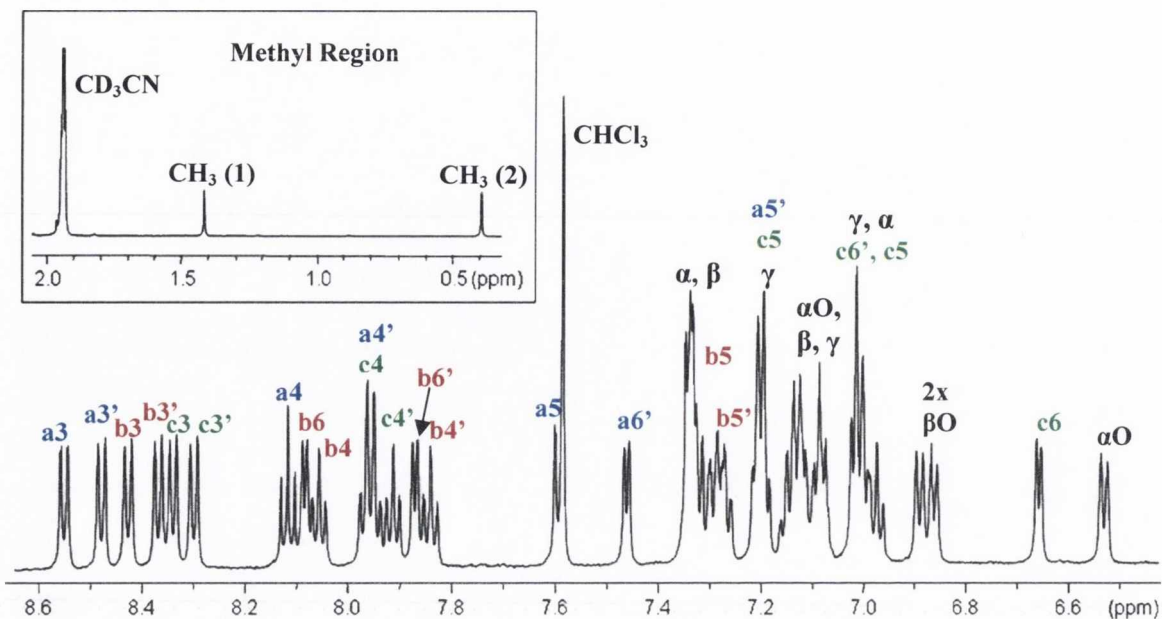


Figure 2.23:  $^1\text{H}$  NMR spectrum of **35** in  $\text{CD}_3\text{CN}$  (600.1 MHz, R.T.). Atom labelling as Figure 2.22, (a) = (3).

In complex **33**, the two pyridine rings located on the same coordinated ligand were identified using long-range  $^1\text{H}$ - $^{13}\text{C}$  correlation experiments (HMBC). In the case of **35**, an alternative method was employed. A two-dimensional ROESY (Rotating frame Overhauser Effect Spectroscopy) experiment allows the through-space interaction between multiple nuclei to be mapped. A ROESY spectrum showing a portion of the aromatic region of complex **35** is shown in Figure 2.24. From this spectrum, H3 and H3' on the two pyridine rings of one ligand moiety show a through-space correlation to each other. For example, the doublet at  $\delta$  8.55 ppm which is on the three spin system, Ha3, is in close proximity through space to the doublet which appears at  $\delta$  8.48 ppm which can be thus assigned as Ha3' (blue dashed line, Figure 2.24). Ligands b and c can be similarly assigned. For each H3 signal, a shorter distance and therefore a stronger cross-peak, is evident between H3 and the adjacent H4 signal on the same ring system.

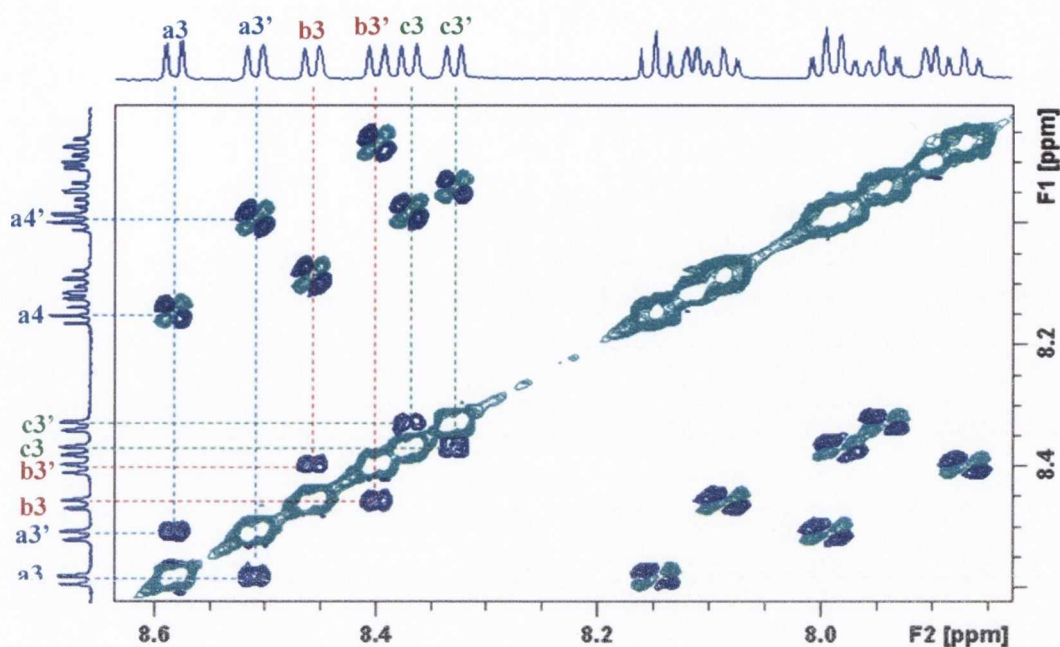


Figure 2.24: ROESY experiment for **35** showing through-space interactions between 3-position protons on adjacent pyridine rings.

As seen in the crystal structure, the two CH<sub>3</sub> signals occur in very different chemical environments. The methyl group at C7 in the crystal structure (Figure 2.9), points directly into the high electronic density of the Ru(bpy)<sub>3</sub><sup>2+</sup> coordination sphere. In contrast, the C8 methyl group points away from this region. In the <sup>1</sup>H NMR, the same effect is observed with one methyl group considerably more shielded ( $\delta$  0.39 ppm) than the other ( $\delta$  1.42 ppm). By comparing the two, the CH<sub>3</sub> signal at  $\delta$  0.39 ppm can be assigned as Me2 (Figure 2.22) or as the group at C7 in the crystal structure. Similarly, Me1 (or the CH<sub>3</sub> at C8) appears at  $\delta$  1.42 ppm.

Proton signals that are attributable to the three phenyl rings ( $\alpha$ ,  $\beta$  and  $\gamma$ , Figure 2.22) occur in general in a series of multiplets between  $\delta$  6.9–7.4 ppm. In consultation with the X-ray crystal structure of **35**, it is possible to assign the signals to the correct phenyl ring, and in some cases, to the correct position, by focusing on the two methyl signals in the <sup>1</sup>H NMR spectrum. In a selective NOE (Nuclear Overhauser effect) experiment, irradiation of a signal at its resonance frequency will produce an NOE enhancement for spins that are close in space to the inverted (i.e. irradiated) spin. Selective NOE experiments were carried out on **35**, irradiating at the resonance frequency of the two methyl signals (Figure 2.25).

In spectrum (ii) (Figure 2.25), the positive signal observed for the most downfield of the aromatic signals ( $\delta$  6.53 ppm) indicates that it is close in space to the methyl group at  $\delta$  1.42 ppm and must be located on either the  $\alpha$  or  $\gamma$  phenyl ring. On the basis of the closer proximity of the  $\alpha$  ring to the electron rich coordination centre compared to  $\gamma$  (i.e. signal is quite shielded) and the fact that it is a doublet, this proton is assigned as an *ortho* proton on the  $\alpha$  ring (Figure 2.22). Using a selective NOE on this signal at  $\delta$  6.53 ppm, the other protons on the  $\alpha$  ring may be assigned. Irradiation of the upfield methyl resonance at  $\delta$  0.39 ppm (Figure 2.25, (iii)) produces a signal enhancement at  $\delta$  6.89 ppm which can be assigned as the  $\beta$ -*ortho* proton by examination of the crystal structure of **35**. A second positive signal at  $\delta$  7.59 ppm which is attributable to Ha5 confirms the proximity of the methyl group to the coordination sphere.

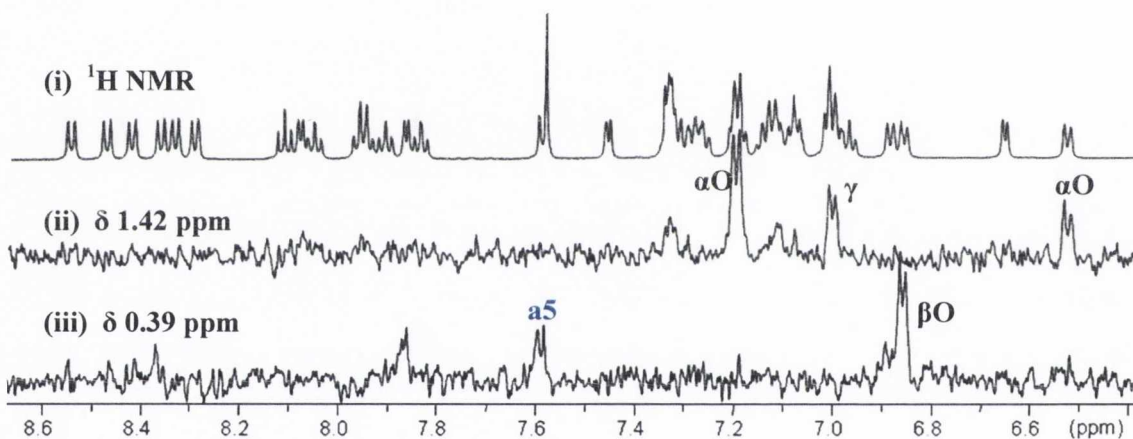


Figure 2.25: Comparative  $^1\text{H}$  NMR spectra (i) and two selective NOE experiments (ii, iii) for **35** recorded in  $\text{CD}_3\text{CN}$ . Atom labelling as per Figure 2.22.

#### 2.2.3.2.2 $^1\text{H}$ NMR Spectrum of **36**

The fully assigned  $^1\text{H}$  NMR spectrum of  $[\text{Ru}(\text{bpy})_2(\mathbf{4})](\text{PF}_6)_2$  (**36**) is presented in Figure 2.26. The assignment of proton signals located on the three bipyridine ligands was achieved using analogous methods to those described for  $[\text{Ru}(\text{bpy})_2(\mathbf{3})](\text{PF}_6)_2$  (**35**) and the two aryl-acetylene complexes  $[\text{Ru}(\text{bpy})_2(\mathbf{1})](\text{PF}_6)_2$  (**33**) and  $[\text{Ru}(\text{bpy})_2(\mathbf{2})](\text{PF}_6)_2$  (**34**). In contrast to the changes in some of the proton chemical shifts from complex to complex, it was found that the resonances of the carbon signals in the  $^{13}\text{C}$   $\{^1\text{H}\}$  spectrum had a commonality in each complex. Consequently, the assignments of the proton signals in complex **36** were checked against the corresponding carbon signal using a 2D  $^1\text{H}$ - $^{13}\text{C}$  COSY experiment (HSQC).

The increase in the steric bulk of ligand **a** (Figure 2.22) in complex **36** adds a further complication to the complete assignment of the NMR spectrum. Signals that can be attributed to *tert*-butyl phenyl rings appear across the aromatic region of the spectrum (Figure 2.26). In some ideal cases, two doublets each integrating for 2H (i.e. a simple AB ring system) are observed for a ring (e.g. between  $\delta$  6.3-7.1 ppm, Figure 2.26). In others however, four signals are observed for a single ring system, some signals appear as broad peaks on the spectrum (e.g.  $\delta$  6.1, 6.6 ppm) and signals may appear considerably downfield of the region typically expected for simple phenyl ring protons (for example the series of doublets between  $\delta$  8.54-8.66 ppm). These phenomena make it very difficult to accurately integrate the signals due to the phenyl rings in the  $^1\text{H}$  NMR spectrum. The purity of the complex is however not in question with both mass spectral and elemental analysis confirming both the presence and purity of complex **36**.

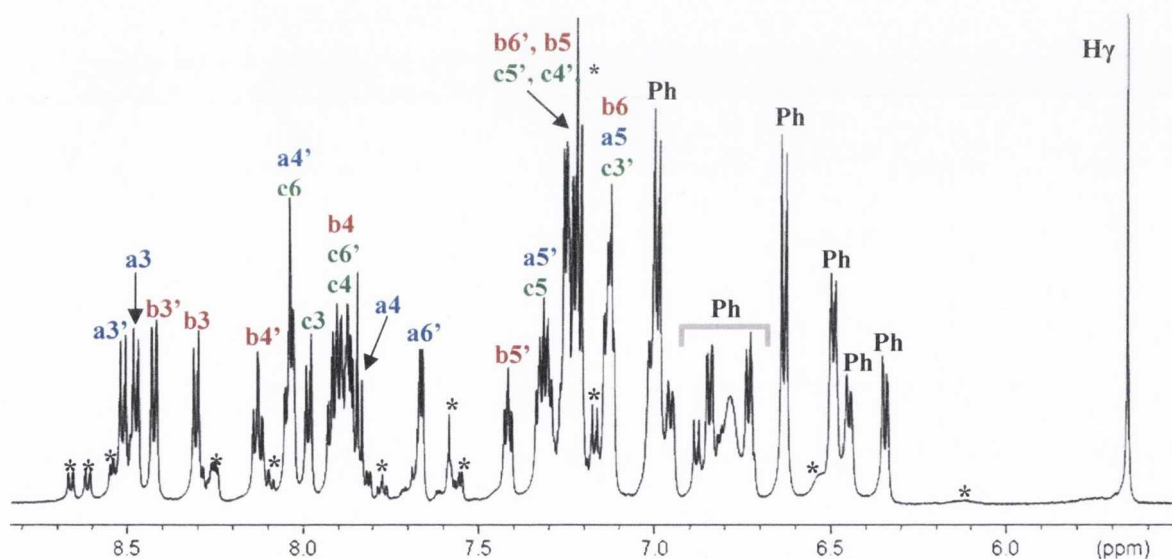


Figure 2.26:  $^1\text{H}$  NMR spectrum of **36** recorded in  $\text{CD}_3\text{CN}$  (150.9 MHz, R.T.). Atom labelling as per Figure 2.22. (\* denotes protons on *tert*-butyl phenyl rings).

It appears that at least two of the *tert*-butyl phenyl rings on the polyphenylene diimine ligand (**4**) in  $[\text{Ru}(\text{bpy})_2(\mathbf{4})](\text{PF}_6)_2$  (**36**) experience significant steric hindrance and cannot freely rotate about the central phenyl ring resulting in the unusual behaviour described above. In this  $^1\text{H}$  NMR spectrum, rotation of some of the *tert*-butyl phenyl rings about the central phenyl ring is essentially frozen on the NMR timescale, giving rise to both broadened signals and more signals than expected for a given *tert*-butyl phenyl ring. This is as a result of intramolecular steric constraints caused by the additional steric bulk of

multiple aromatic substituents. This feature is also observed in Chapter 4 throughout a series of Pt(II) complexes incorporating this diimine polyaromatic ligand (**4**).

## 2.3 UV-Visible Absorption Spectra

### 2.3.1 Aryl-acetylene and polyphenylene-substituted bipyridine ligands **1**, **2**, **3** and **4**

The UV-visible absorption spectra of 6-(4-*tert*-butyl-phenylethynyl)-2,2'-bipyridine (**1**), 6-(4-trifluoromethyl-phenylethynyl)-2,2'-bipyridine (**2**), 6-(3,6-dimethyl-2,4,5-triphenyl benzene)-2,2'-bipyridine (**3**) and the larger ligand 1-(2,2'-bipyrid-6-yl)-2,3,4,5-tetra(4-*tert*-butylphenyl) benzene (**4**) are presented in Figure 2.27 with relevant data in Table 2.4.

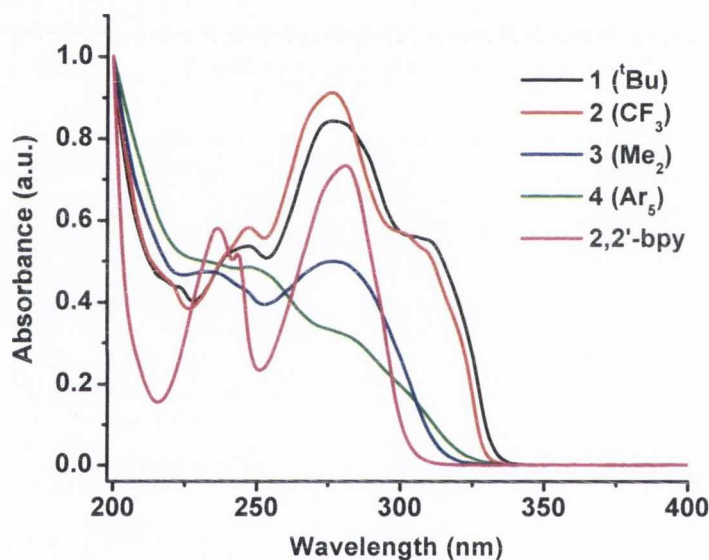


Figure 2.27: Normalised UV-Visible absorption spectra of asymmetric ligands **1**, **2**, **3** and **4** and 2,2'-bipyridine in  $\text{CH}_3\text{CN}$  ( $\sim 10^{-5} \text{ M}$ ).

The absorption spectra of the four new ligands **1-4** and 2,2'-bipyridine feature strong bands in the near UV-region of the spectrum (Figure 2.27). In general, the absorptions are quite broad which is indicative of nearly free rotation of the attached arene rings along the molecular axis and of rotation about the 2,2' carbon-carbon bond of the bipyridyl moiety.<sup>118-119</sup> In 2,2'-bipyridine, these bands have been assigned as spin-allowed ligand centred (LC)  $\pi\text{-}\pi^*$  transitions (at  $\lambda$  185, 236, 280 nm).<sup>118</sup> Correspondingly, the intense absorption bands of the four asymmetric ligands centred at  $\lambda$  280 nm (Table 2.4) are assigned as  $\pi\text{-}\pi^*$  in origin involving pyridyl and phenyl aromatic rings with extinction coefficients indicative of the spin allowed nature of the transition ( $\epsilon > 1000 \text{ M}^{-1} \text{ cm}^{-1}$ ).<sup>120-121</sup>

Table 2.4: Room temperature UV-Visible Spectral Data for Ligands **1**, **2**, **3** and **4** and their heteroleptic Ru(II) complexes **33**, **34**, **35** and **36** in CH<sub>3</sub>CN (~10<sup>-5</sup>M).

Compound	$\lambda_{\max}$ [nm] ( $\epsilon \times 10^{-4}$ [M <sup>-1</sup> cm <sup>-1</sup> ])
<b>1</b> ( <sup>t</sup> Bu)	222 (5.20), 239 <i>sh</i> (6.13), 247 (6.39), 277 (9.99), 309 (6.61), 323 <i>sh</i> (3.57)
<b>2</b> (CF <sub>3</sub> )	219 (4.45), 238 <i>sh</i> (5.02), 247 (5.75), 276 (9.02), 301 (5.60), 307 (5.20), 319 <i>sh</i> (3.23)
<b>3</b> (Me <sub>2</sub> )	232 (3.87), 245 <i>sh</i> (3.56), 280 (4.05), 299 <i>sh</i> (2.19)
<b>4</b> (Ar <sub>5</sub> )	230 (4.44), 247 (4.31), 256 <i>sh</i> (4.05), 278 (2.89), 301 (1.73)
[Ru(bpy) <sub>2</sub> ( <b>1</b> )](PF <sub>6</sub> ) <sub>2</sub> ( <b>33</b> )	245 (4.28), 255 (4.42), 288 (7.23), 330 <i>sh</i> (1.63), 420 <i>sh</i> (0.76), 451 (0.89), 526 (0.26)
[Ru(bpy) <sub>2</sub> ( <b>2</b> )](PF <sub>6</sub> ) <sub>2</sub> ( <b>34</b> )	246 (3.70), 253 (3.76), 287 (6.71), 322 <i>sh</i> (1.87), 422 <i>sh</i> (0.79), 450 (0.94), 520 (0.26)
[Ru(bpy) <sub>2</sub> ( <b>3</b> )](PF <sub>6</sub> ) <sub>2</sub> ( <b>35</b> )	246 (4.51), 255 (4.53), 289 (7.63), 348 <i>sh</i> (0.57), 423 <i>sh</i> (0.80), 451 (1.05), 519 (0.09)
[Ru(bpy) <sub>2</sub> ( <b>4</b> )](PF <sub>6</sub> ) <sub>2</sub> ( <b>36</b> )	258 (6.25), 288 (8.48), 349 <i>sh</i> (0.81), 424 <i>sh</i> (0.80), 452 (1.07), 525 (0.08)

Aryl-acetylene ligands **1** and **2** both possess red-shifted absorption bands (**1**,  $\lambda$  309 nm; **2**  $\lambda$  307 nm) that are not evident in the spectra of **3** and **4**. The attached aryl-acetylene facilitates an enhancement of  $\pi$ -electron conjugation in the system resulting in a bathochromic shift in the lowest energy absorption band. This effect is commonly observed in 2,2'-bipyridyl phenyl-ethynylene molecules.<sup>119,122-123</sup> The occurrence of this absorption band at slightly lower energy ( $\Delta E = 2$  nm) in **1** (<sup>t</sup>Bu) than in **2** (CF<sub>3</sub>) corresponds to an increase in electron density on the  $\pi$ -orbital (the HOMO) of ligand **1**. This results in destabilization of the orbital and overall a smaller HOMO-LUMO gap in **1** than in **2**, where the electron-withdrawing substituent stabilizes (i.e. lowers the energy of) the energy of the HOMO to produce a hypsochromic shift. In contrast, the absorption spectra of ligands **3** and **4** do not possess this red-shifted absorption band. Their spectra are even broader and less structured than those of the simpler bipyridine ligands **1** and **2**

(Figure 2.27). They are typical of polyphenylene derivatives such as hexaphenylbenzene which have no effective conjugation between the rings and where steric hindrance in the ground state imposes a non-planar configuration on the chromophore.<sup>124-125</sup>

In Table 2.5, the absorption maximum of the lowest energy absorption band for each of the four ligands **1**, **2**, **3** and **4** is presented. It is clear that each exhibits only a very minor dependence on solvent polarity. This has been observed for 2,2'-bipyridine and is characteristic of the assignment of the transition as spin-allowed  $\pi$ - $\pi^*$  in origin.<sup>118</sup> "Pure"  $\pi$ - $\pi^*$  transitions usually exhibit negligible to marginal solvent dependencies as they involve a redistribution of electron density within the same  $\pi$  framework.<sup>126</sup>

Table 2.5: UV-Visible Absorption maxima ( $\lambda$ , nm) of lowest energy absorption band for ligands **1-4** in  $\text{CH}_3\text{CN}$ , THF and diisopropylether solutions ( $\sim 10^{-5}$  M).

	$\text{CH}_3\text{CN}$	THF	( <sup>i</sup> Pr) <sub>2</sub> O
<b>1</b> ( <sup>t</sup> Bu)	309	311	310
<b>2</b> ( $\text{CF}_3$ )	307	308	308
<b>3</b> ( $\text{Me}_2$ )	280	282	282
<b>4</b> ( $\text{Ar}_5$ )	278	278	278

### 2.3.2 Heteroleptic Ru(II) bipyridyl complexes **33**, **34**, **35** and **36**

The absorption spectra of Ru(II) heteroleptic complexes  $[\text{Ru}(\text{bpy})_2(\mathbf{1})](\text{PF}_6)_2$  (**33**),  $[\text{Ru}(\text{bpy})_2(\mathbf{2})](\text{PF}_6)_2$  (**34**),  $[\text{Ru}(\text{bpy})_2(\mathbf{3})](\text{PF}_6)_2$  (**35**) and  $[\text{Ru}(\text{bpy})_2(\mathbf{4})](\text{PF}_6)_2$  (**36**) are presented in Figure 2.28 with absorption maxima and corresponding extinction coefficients listed in Table 2.4.

Assignment of the absorption bands in these complexes may be undertaken by comparison with the thoroughly investigated prototype of this class of compounds,  $[\text{Ru}(\text{bpy})_3]^{2+}$  (**32**).<sup>78,89</sup> The band at  $\sim \lambda$  288 nm (Table 2.4) which is essentially coincident from the parent complex to the derivatives reported here can be assigned as originating from LC spin-allowed  $\pi$ - $\pi^*$  transitions. The absorption is noticeably broader on going from  $[\text{Ru}(\text{bpy})_3]^{2+}$  to complexes **33-36** most likely as a result of the contribution of intraligand transitions located on both 2,2'-bipy and the asymmetric bipyridine ligand. At slightly



longer wavelengths, the shoulders in the UV spectra between  $\lambda$  320–340 nm which are evident in each complex are suggested to arise from metal-centred d-d transitions.<sup>80</sup>

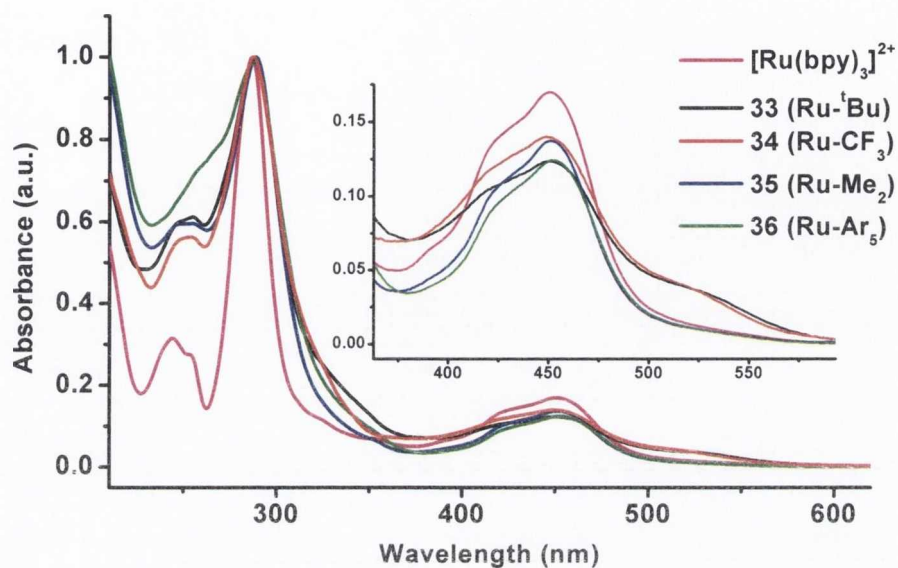


Figure 2.28: Normalised UV-Visible absorption spectra of Ru(II) heteroleptic complexes **33**, **34**, **35** and **36** and  $[\text{Ru}(\text{bpy})_3]^{2+}$  in  $\text{CH}_3\text{CN}$  ( $\sim 10^{-5}$  M), with inset enlarged MLCT region.

The most interesting feature arises from the two intense bands in the visible region of the spectrum (inset, Figure 2.28). The first occurs between  $\lambda$  420–424 nm ( $[\text{Ru}(\text{bpy})_3]^{2+}$ ,  $\lambda$  422 nm) and the second between  $\lambda$  450–452 nm ( $[\text{Ru}(\text{bpy})_3]^{2+}$ ,  $\lambda$  450 nm). These transition have been assigned as spin-allowed metal-to-ligand charge transfer (MLCT),  $[\text{d}(\text{Ru}) \rightarrow \pi^*(\text{N}^{\wedge}\text{N})]$ , and have typical extinction coefficients of  $\epsilon \sim 1 \times 10^4 \text{ M}^{-1} \text{ cm}^{-1}$ .<sup>78,89,118</sup> The MLCT region of the absorption spectra of polyphenylene-substituted complexes **35** and **36** matches almost perfectly the absorption profile of the prototype complex (Figure 2.28). This suggests that polyphenylene substitution at the 6-position on the bipyridine ligand has almost negligible effect on the energy of the transition such that the charge transfer to 2,2'-bpy and charge transfer to polyphenylene-bipy (**35** or **36**) transitions are of similar energy and most likely coincident and co-populated upon excitation.

For the aryl-acetylene complexes **33** and **34**, an additional red-shifted band is observed that is not evident in the spectra of  $[\text{Ru}(\text{bpy})_3]^{2+}$ , **35** or **36** (Figure 2.28). The band appears at  $\lambda$  526 nm in *tert*-butyl complex **33** and at  $\lambda$  520 nm in  $\text{CF}_3$ -substituted complex **34** (for both complexes,  $\epsilon = 2600 \text{ M}^{-1} \text{ cm}^{-1}$ ). This is assigned as an MLCT transition localised on the acetylene-bpy (**1** or **2**),  $[\text{d}(\text{Ru}) \rightarrow \pi^*(\text{R}-\text{C} \equiv \text{C}-\text{bpy})]$ . The increase in conjugation in the

ancilliary ligand in complexes **33** and **34** lowers the energy of the  $\pi^*(bpy)$  orbital resulting in a red-shifted absorption band. Furthermore, the occurrence of the transition at lower energy for **33** (Ru-<sup>t</sup>Bu) than for **34** (Ru-CF<sub>3</sub>) is indicative of the relative stabilization of the d(Ru) orbitals in **34** as a result of the electron-withdrawing group. Correspondingly, the HOMO-LUMO gap, [d(Ru)→ $\pi^*(bpy)$ ], is greater in **34** than in **33**.

The UV-visible absorption spectra of the four Ru(II) heteroleptic complexes **33-36** were recorded in three solvents with decreasing polarity, CH<sub>3</sub>CN, CH<sub>3</sub>OH, THF, and the maxima of the lowest energy bands are presented in Table 2.6.

*Table 2.6: UV-Visible Absorption maxima ( $\lambda$ , nm) of the lowest energy absorption bands for complexes **33-36** in CH<sub>3</sub>CN, CH<sub>3</sub>OH and THF solutions ( $\sim 10^{-5}$  M).*

	CH <sub>3</sub> CN	CH <sub>3</sub> OH	THF
[Ru(bpy) <sub>2</sub> ( <b>1</b> )](PF <sub>6</sub> ) <sub>2</sub> ( <b>33</b> )	288, 451, 526	289, 449, 526	298, 449, 528
[Ru(bpy) <sub>2</sub> ( <b>2</b> )](PF <sub>6</sub> ) <sub>2</sub> ( <b>34</b> )	287, 450, 520	288, 447, 520	288, 449, 521
[Ru(bpy) <sub>2</sub> ( <b>3</b> )](PF <sub>6</sub> ) <sub>2</sub> ( <b>35</b> )	289, 451	290, 451	291, 454
[Ru(bpy) <sub>2</sub> ( <b>4</b> )](PF <sub>6</sub> ) <sub>2</sub> ( <b>36</b> )	288, 452	290, 452	290, 454

In general, the absorption profiles and maxima are slightly dependent on solvent polarity, undergoing small red-shifts in less polar solvents ( $\Delta E \sim 1-3$  nm), i.e. a slight negative solvatochromic effect. The essentially negligible effect for the  $\pi-\pi^*$  transition at  $\lambda$  288 nm was also observed for the free ligands (Table 2.5). Absorptions derived from MLCT transitions are known to be sensitive to the nature of the solvent.<sup>80</sup> Promoting an electron from a metal-centred d-orbital to a ligand-centred  $\pi^*$  orbital involves a large change in dipole moment. As a result, for a charge-transfer transition the ground state of the molecule will be stabilized by a polar solvent relative to the excited state. This results in a larger energy difference between the ground and excited states and accordingly a blue-shift in polar solvent. In a non-polar solvent, the MLCT state energy decreases as the ground state is destabilized relative to the excited state resulting in a shift to longer wavelengths of the MLCT band. The prototype complex, [Ru(bpy)<sub>3</sub>]<sup>2+</sup>, displays comparable negative solvatochromic shifts to those observed for complexes **33-36**.<sup>127</sup> For example, the MLCT maximum undergoes a red-shift from  $\lambda$  450.1 to 451.1 nm moving from water to methanol/acetonitrile. Further decreasing solvent polarity results in a further bathochromic

shift to  $\lambda$  452.7 nm in  $\text{CH}_2\text{Cl}_2$ . Notably, the solvatochromic nature of the additional lowest energy band in complexes **33** and **34** confirms their assignment as MLCT in origin.

## 2.4 Electrochemical Properties of Ligands 1-4 and heteroleptic Ru(II) complexes 33-36

Cyclic voltammetric (CV) studies were carried out on 1 mM solutions of the ligands (**1**, **2**, **3** and **4**) and complexes (**33**, **34**, **35** and **36**) in  $\text{CH}_3\text{CN}$  (0.1 M  $n\text{Bu}_4\text{NPF}_6$ ). The results are summarised in Table 2.7. Cyclic voltammograms were carried out using a Ag/AgCl electrode as reference electrode, a Pt wire counter electrode and a glassy carbon working electrode. Potentials are quoted *versus* the  $\text{Fc}/\text{Fc}^+$  couple (0.0 V) and referenced to internal ferrocene added at the end of each experiment (potentials were converted to  $\text{Fc}/\text{Fc}^+$  scale by subtraction of 0.40 V).

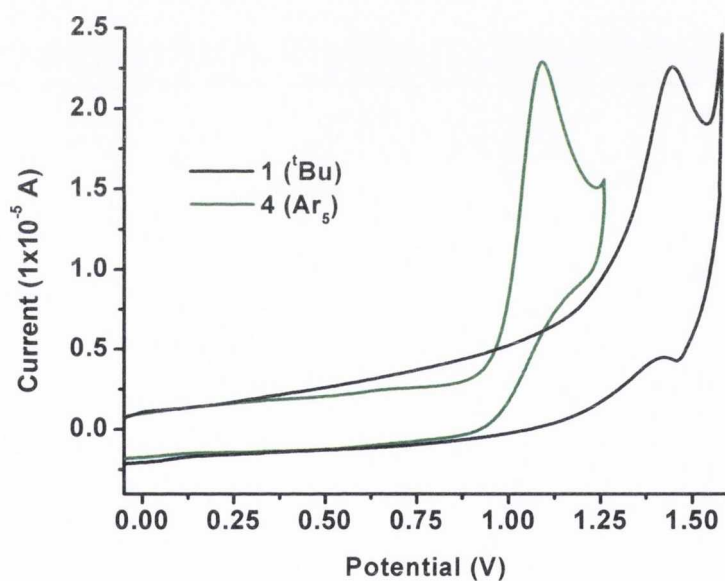


Figure 2.29: Cyclic voltammograms of ligands **1** and **4** showing the ligand-based oxidation process. (1 mM in  $\text{CH}_3\text{CN}$ , V vs.  $\text{Fc}/\text{Fc}^+$ ).

The oxidation wave for each bipyridyl ligand (**1-4**) exhibits one irreversible oxidation process between +1.17 and +1.49 V (Table 2.7). From Figure 2.29, the oxidation of **4** occurs at +1.17 V whilst the same process on *tert*-butyl ligand **1** occurs at a potential of +1.43 V. Clearly, the degree of conjugation in the ligand has a significant effect on the oxidation potential and in general, the oxidation process on aryl-acetylene substituted bipyridines (**1** and **2**) occurs at significantly more positive potentials than for polyphenylene-substituted bipyridines (**3** and **4**). It is more difficult to remove an electron

from the HOMO, a  $\pi$  orbital on the bipyridine, in the more conjugated ligands than in the polyphenylene derivatives. Secondly, as would be anticipated, oxidation of the ligand is more facile on the acetylene-bipy containing the electron-releasing substituent **1** (<sup>t</sup>Bu) than on the electron-withdrawing bipy (**2**, +1.49 V). It also appears that **4** (Ar<sub>5</sub>) is more electron-rich and therefore easier to reduce than **3** (Me<sub>2</sub>), whose oxidation potential is noticeably more positive (+1.31 V).

Table 2.7: Electrochemical data for ligands 1-4 and Ru(II) complexes 33-36.<sup>a</sup>

Compound	Oxid.	Oxid.	Reduction	$\Delta E_{1/2}/V$ ( $E_{ox}-E_{red}$ )
	$E_{1/2}/V$ [ $\Delta E_p/mV$ ] <sup>d</sup> Ru(II)-(III)	$E_{pa}/V$ <sup>b</sup> (N <sup>^</sup> N)	$E_{1/2}/V$ [ $\Delta E_p/mV$ ] <sup>d</sup> (N <sup>^</sup> N)	
<b>1</b> ( <sup>t</sup> Bu)	-	+1.43	-1.95 [257] <sup>c</sup>	
<b>2</b> (CF <sub>3</sub> )	-	+1.49	-1.86 [145] <sup>c</sup>	
<b>3</b> (Me <sub>2</sub> )	-	+1.31	-2.13 [228] <sup>c</sup>	
<b>4</b> (Ar <sub>5</sub> )	-	+1.17	-1.96 [335] <sup>c</sup>	
[Ru(b) <sub>2</sub> ( <b>1</b> )](PF <sub>6</sub> ) <sub>2</sub> ( <b>33</b> )	+0.93 [75]	+1.44	-1.68 [40], -1.89 [75], -2.20 [77]	2.60
[Ru(b) <sub>2</sub> ( <b>2</b> )](PF <sub>6</sub> ) <sub>2</sub> ( <b>34</b> )	+0.93 [78]	+1.42	-1.28 [95], -1.85 [111], -2.21 [85]	2.21
[Ru(b) <sub>2</sub> ( <b>3</b> )](PF <sub>6</sub> ) <sub>2</sub> ( <b>35</b> )	+0.95 [85]	-	-1.70 [49], -1.93 [71], -2.23 [79]	2.64
[Ru(b) <sub>2</sub> ( <b>4</b> )](PF <sub>6</sub> ) <sub>2</sub> ( <b>36</b> )	+0.93 [69]	-	-1.69 [32], -1.93 [75], -2.24 [81]	2.63

<sup>a</sup> In deoxygenated acetonitrile (0.1 M, <sup>n</sup>Bu<sub>4</sub>NPF<sub>6</sub>) at 298K, scan rate = 100 mVs<sup>-1</sup>, reported vs. Fc/Fc<sup>+</sup>; <sup>b</sup> Irreversible/quasi-reversible oxidation process,  $E_{pa}/V$  (anodic peak potential) quoted; <sup>c</sup> Return oxidation wave associated with this reduction poorly defined; <sup>d</sup>  $\Delta E_p = E_{pa}-E_{pc}$ , peak potential separation.

The first oxidation process on the Ru(II) heteroleptic complexes (**33-36**) occurs between +0.93 and +0.95 V (Figure 2.30). The small peak potential separations,  $\Delta E_p$ , measuring between 69-85 mV, are indicative of a kinetically reversible oxidation process (Table 2.7).

(Ideal  $\Delta E_p = E_{pa} - E_{pc} \sim 60$  mV for a completely reversible process involving the transfer of one electron).<sup>128</sup> This oxidation process is metal-centred and arises from the reversible oxidation of Ru(II) to Ru(III), resulting in the formation of a low spin Ru(III)  $d^5$  metal ion from a Ru(II)  $d^6$  ion. The Ru(II)/(III) couple appear in a very narrow range, indicating that the inductive effects from the various ligand substituents are quite similar across the series.<sup>129</sup> In fact, the Ru(II) oxidation potentials of the four complexes **33-36** are not markedly different from that of  $[\text{Ru}(\text{bpy})_3]^{2+}$  itself whose oxidation potential is +0.93 V vs.  $\text{Fc}/\text{Fc}^+$  (measured against SCE, converted to  $\text{Fc}/\text{Fc}^+$  scale by subtraction of 0.40 V).<sup>86</sup> In general, complexes **33** and **34** with a coordinated aryl-acetylene functionalized bipyridine are marginally easier to oxidize than their polyphenylene analogues **35** and **36**. This first oxidation process correlates to the removal of an electron from the HOMO involved in the lowest energy transition seen in the UV-Visible spectra of the complexes (Figure 2.28).

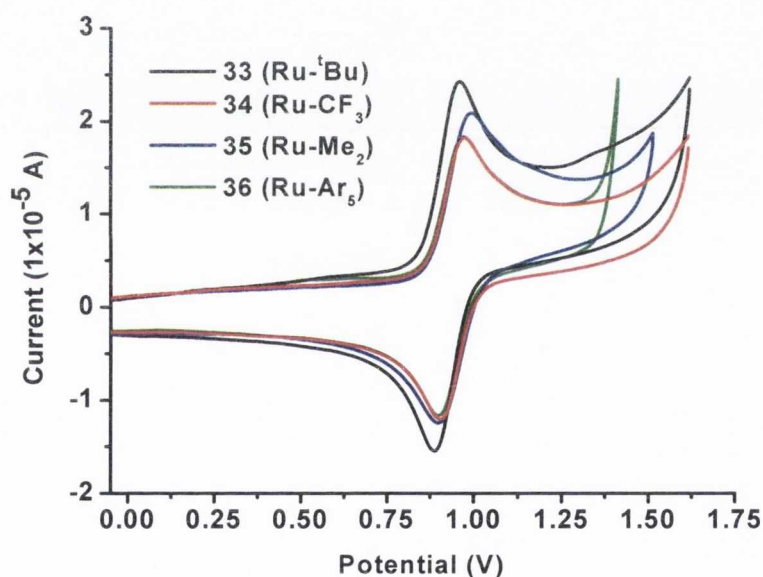


Figure 2.30: Cyclic voltammograms of **33**, **34**, **35** and **36** showing the Ru(II)-Ru(III) reversible oxidation processes. (1 mM in  $\text{CH}_3\text{CN}$ , V vs.  $\text{Fc}/\text{Fc}^+$ ).

Several reduction processes are evident for each of the four ligands investigated here and for their corresponding Ru(II) heteroleptic complexes. In general, reductions on the uncoordinated ligands occur between -1.86 and -2.13 V (Table 2.7) and are only partially reversible, as indicated by the large peak potential separations which fall between 145-335 mV. (The return wave associated with each of these reductions is diminished which implies chemical irreversibility). Addition of an electron to the  $\pi^*$  orbital is easiest for **2**

(CF<sub>3</sub>), where the electron-withdrawing substituent stabilizes (and therefore lowers) the energy of the LUMO.

In contrast, the reduction waves of the cyclic voltammograms recorded for Ru(II) complexes **33-36** are characterised by three essentially reversible peaks (Figure 2.31). In general, these ligand reductions occur at more positive potentials when coordinated to the metal centre than in the free ligand. This is as a result of the partial loss of negative charge by the ligand upon coordination which occurs via  $\sigma$ -donation by the chelating nitrogen atoms.<sup>130</sup> Peak potential separations ( $\Delta E_p = 32$ -111 mV, Table 2.7) confirm the reversibility of the majority of these reduction peaks. Note: for some complexes, the first reduction wave is less defined than expected as a result of an impurity in the electrolyte, which is also evident in the CVs of the other complexes. The impurity has been identified as water, which remained despite arduous drying of the electrolyte under vacuum and heat. (The standard reduction potential of water is -0.828 V vs. SCE (-1.228 V vs. Fc/Fc<sup>+</sup>),  $2\text{H}_2\text{O} + e^- \rightleftharpoons \text{H}_{2(\text{g})} + 2\text{OH}^-$ ).

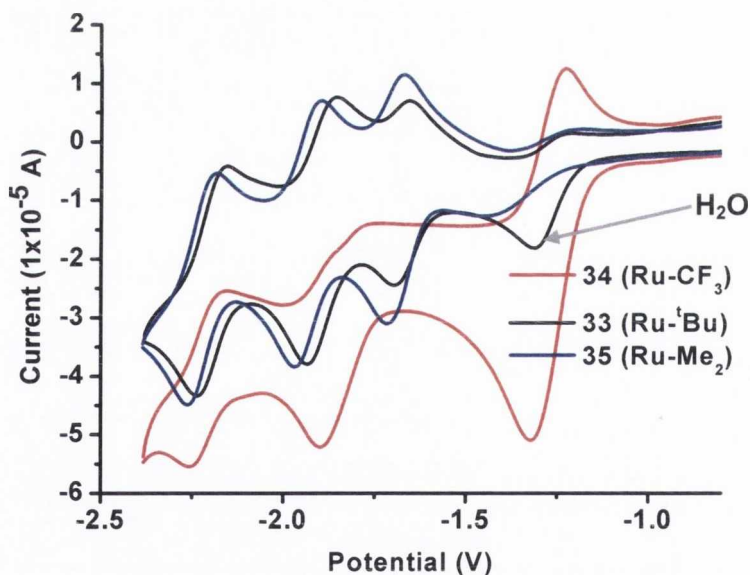


Figure 2.31: Cyclic voltammograms of Ru(II) complexes **33**, **34** and **35** showing ligand-centred reversible reduction processes (1 mM in CH<sub>3</sub>CN, V vs. Fc/Fc<sup>+</sup>).

With the knowledge that the added electron in the first reduction process in Ru(II) tris-bipyridyl complexes is localised on one ligand, specifically on the bipyridine ligand which is easiest to reduce, assignment of reduction peaks to specific ligands is relatively straightforward.<sup>78,89</sup> In keeping with the trend in the free ligands, the first reduction (-1.28

V) on **34** (Ru-CF<sub>3</sub>) occurs on ligand **2** (CF<sub>3</sub>), which has a low lying  $\pi^*$  orbital which is easiest to reduce. This is coincident with reduction of water in the electrolyte and results in a distorted reduction peak shape and peak potential separation (Figure 2.31). The next more facile reduction (-1.68 V) occurs on **33** (Ru-<sup>t</sup>Bu) and is attributed to reduction on **1** (<sup>t</sup>Bu). The first reductions on polyphenylene complexes **35** (Ru-Me<sub>2</sub>) and **36** (Ru-Ar<sub>5</sub>) occur at similar potentials, -1.70 V (**35**) and -1.69 V (**36**) respectively, comparable to a value of -1.70 V for the first reduction potential on [Ru(bpy)<sub>3</sub>]<sup>2+</sup> (reported vs. SCE, converted to Fc/Fc<sup>+</sup> scale by subtraction of 0.40 V).<sup>131</sup> For each of the four complexes, the second and third reduction peaks occur at similar voltages (2<sup>nd</sup>  $\approx$  -1.90 V, 3<sup>rd</sup>  $\approx$  -2.22 V, Table 2.7), confirming their assignment as localised on unsubstituted bipyridine moieties. These values are consistent with literature values for the second and third bpy reductions on prototype [Ru(bpy)<sub>3</sub>]<sup>2+</sup>, which occur at -1.88 V and -2.13 V vs. Fc/Fc<sup>+</sup> respectively.<sup>131</sup> Interestingly, the second reduction on complexes **33** and **34** occurs at marginally less negative potentials (-1.89 V, -1.85 V) than for polyphenylene complexes **35** and **36**. This implies that electron delocalization on the aryl-acetylene ligand may extend across the metal centre to influence reduction on a second bipyridine ligand. This effect has also been observed in a related series of heteroleptic Ru(II) complexes [Ru(bpy)<sub>2</sub>(L)]<sup>2+</sup>, where L is a 2,2'-bipyridine ligand substituted in the 6-position by a thiophene heterocycle.<sup>132</sup>

It is well established for Ru(II) polypyridine complexes that the  $\pi^*$  orbital involved in the first electrochemical reduction is the same as that involved in the MLCT absorption (and emission) processes.<sup>80</sup> In general, the more facile first reduction on aryl-acetylene complexes **33** and **34** than on polyphenylene complexes **35** and **36** corresponds to the trend observed in the UV-Visible spectra (Figure 2.28). From the absorption spectra, it is clear that aryl-acetylene substituted bipyridines **1** and **2** introduce a low lying  $\pi^*$  orbital into the manifold which accounts for a more facile reduction process for these complexes (and indeed in the free ligands). The absence of this conjugation in polyphenylene-substituted complexes **35** and **36** means that the  $\pi^*$  is higher in energy than those on **33** and **34**, rendering them overall more difficult to reduce. The energy gap,  $\Delta E_{1/2}$ , which measures the difference in potential between the one electron Ru(II)/(III) oxidation and the first reduction potential on the complex, should give an indication of the HOMO-LUMO energy gap of the complexes and correlate with the MLCT in both absorption and emission spectra (Table 2.7).<sup>80,89</sup> In general, **34** (Ru-CF<sub>3</sub>) (and **33** (Ru-<sup>t</sup>Bu)) have the lowest energy absorption bands (**33**  $\lambda$  526 nm, **34**  $\lambda$  520 nm) and would therefore be expected to have the

smallest HOMO-LUMO gap as calculated from CV data. This is true of **34** ( $\Delta E_{1/2} = 2.21$  V) but is not observed for **33** ( $\Delta E_{1/2} = 2.60$  V). Conversely, complexes **35** and **36** with higher energy MLCT bands (**35**  $\lambda$  451 nm, **36**  $\lambda$  452 nm) have larger HOMO-LUMO gaps ( $\Delta E_{1/2} = 2.64, 2.63$  V).

## 2.5 Emission Properties of Bipyridine Ligands and their heteroleptic Ru(II) complexes

The photoluminescence properties of 6-(4-*tert*-butyl-phenylethynyl)-2,2'-bipyridine (**1**), 6-(4-trifluoromethyl-phenylethynyl)-2,2'-bipyridine (**2**), 6-(3,6-dimethyl-2,4,5-triphenyl benzene)-2,2'-bipyridine (**3**) and the larger ligand 1-(2,2'-bipyrid-6-yl)-2,3,4,5-tetra(4-*tert*-butylphenyl) benzene (**4**) are discussed separately from their corresponding heteroleptic complexes, [Ru(bpy)<sub>2</sub>(**1**)](PF<sub>6</sub>)<sub>2</sub> (**33**), [Ru(bpy)<sub>2</sub>(**2**)](PF<sub>6</sub>)<sub>2</sub> (**34**), [Ru(bpy)<sub>2</sub>(**3**)](PF<sub>6</sub>)<sub>2</sub> (**35**) and [Ru(bpy)<sub>2</sub>(**4**)](PF<sub>6</sub>)<sub>2</sub> (**36**).

### 2.5.1 Emission properties of bipyridyl ligands **1**, **2**, **3** and **4**

Table 2.8 summarises the relevant photoluminescence data for aryl-acetylene ligands **1** and **2** and polyphenylene ligands **3** and **4** in argon-degassed CH<sub>3</sub>CN solution and in solid state at 298K and 77K, including lifetimes and quantum yields.



Table 2.8: Emission data for ligands **1**, **2**, **3** and **4** in solid state and in solution ( $\text{CH}_3\text{CN}$ ) at 298 K and 77K.

	Medium (T[K])	$\lambda_{\text{em}}[\text{nm}]$ ( $\lambda_{\text{exc}}[\text{nm}]$ )	$\tau$ [ns] ( $\lambda_{\text{exc}}[\text{nm}] / \lambda_{\text{em}}[\text{nm}]$ ) <sup>b</sup>	$\Phi_{\text{em}}$ <sup>c</sup>
<b>1</b> <b><sup>t</sup>Bu</b>	Solid (298)	355 <sub>sh</sub> , 364 <sub>max</sub> , 387 <sub>sh</sub> (300)	28 (60 %), 55 (40 %) (295 / 365) 796 (64 %), 39 (36 %) (295 / 390)	
	Solid (77)	359 <sub>max</sub> , 391 <sub>sh</sub> (300)		
	$\text{CH}_3\text{CN}$ (298) <sup>a</sup>	352 (300), 430 (360)	1 (66 %), 38 (34 %) (295 / 352) 73 (74 %), 10 (26 %) (370 / 430)	0.398
	$\text{CH}_3\text{CN}$ (77)	347 <sub>max</sub> , 379 <sub>sh</sub> , 486 <sub>wk</sub> (300)	37 (79 %), 16 (21 %) (295 / 350)	
<b>2</b> <b><math>\text{CF}_3</math></b>	Solid (298)	366 <sub>max</sub> , 386 <sub>sh</sub> , 435 <sub>sh</sub> (305)	31 (67 %), 65 (33 %) (295 / 368) 683 (65 %), 38 (35 %) (295 / 388)	
	Solid (77)	370 <sub>sh</sub> , 385 <sub>max</sub> , 420 <sub>sh</sub> (330)		
	$\text{CH}_3\text{CN}$ (298) <sup>a</sup>	341 <sub>max</sub> , 355 <sub>sh</sub> (300), 510 (340)	1 (78 %), 24 (21 %) (295 / 340) 60 (81 %), 11 (19 %) (370 / 510)	0.110
	$\text{CH}_3\text{CN}$ (77)	342 <sub>max</sub> , 371 <sub>sh</sub> , 486 <sub>wk</sub> (300)	31 (76 %), 2 (24 %) (295 / 345)	
<b>3</b> <b><math>\text{Me}_2</math></b>	Solid (298)	365 <sub>max</sub> , 390 <sub>sh</sub> , 489 (300)	46 (76 %), 19 (24 %) (295 / 365) 1,100 (81 %), 200 (19 %) (370 / 492)	
	Solid (77)	366 <sub>max</sub> , 389 <sub>sh</sub> , 491, 511 <sub>sh</sub> (320)		
	$\text{CH}_3\text{CN}$ (298) <sup>a</sup>	333, 352, 374 <sub>max</sub> 395 <sub>sh</sub> , 497 (300)	7 (57 %), 29 (43 %) (295 / 375) 44 (71 %), 8 (29 %) (370 / 496)	0.007
	$\text{CH}_3\text{CN}$ (77)	361, 463 <sub>max</sub> (308)	40 (84 %), 19 (16 %) (295 / 361) 488 (81 %), 62 (19 %) (360 / 463)	
<b>4</b> <b><math>\text{Ar}_5</math></b>	Solid (298)	365 <sub>max</sub> , 512 (315)	41 (65 %), 16 (35 %) (295 / 365) 1,400 (79 %), 300 (21 %) (370 / 512)	
	Solid (77)	360 <sub>max</sub> , 508, 554 <sub>sh</sub> (300)		
	$\text{CH}_3\text{CN}$ (298) <sup>a</sup>	376 <sub>max</sub> (300), 479 (380)	7 (53 %), 24 (47 %) (295 / 380) 34 (61 %), 12 (39 %) (370 / 480)	0.012
	$\text{CH}_3\text{CN}$ (77)	357 <sub>max</sub> , 478 (300)	39 (86 %), 19 (14 %) (295 / 360) 561 (91 %), 80 (9 %) (370/480)	

<sup>a</sup> Argon-degassed solutions,  $\sim 10^{-5}$  M (unless otherwise stated); <sup>b</sup> Estimated uncertainty on  $\tau \pm 10\%$ ;

<sup>c</sup> Measured using quinine sulfate as a standard, average of three measurements.<sup>133</sup>

### 2.5.1.1 Room temperature and 77 K in solid state

The emission spectra of ligands **1**, **2**, **3** and **4** in solid state at room temperature are presented in Figure 2.32. The spectra of the four ligands resemble each other and are dominated by an intense, high energy broad band centred at  $\sim\lambda$  365 nm. This emission features excited state lifetimes in the nanosecond region which are marginally longer for aryl-acetylene bipyridines **1** and **2** (**1**  $\tau$ : 55 ns (40 %), 28 ns (60 %)) than for polyphenylene ligands **3** and **4** (**3**  $\tau$ : 46 ns (76 %), 19 ns (24 %)). A mirror symmetry is evident between the excitation spectrum of **1** (as also observed for the other three ligands) and the corresponding emission spectrum with a narrow Stokes shift (18 nm) between the lowest energy excitation band ( $\lambda$  337 nm) and the onset of fluorescence. A small Stokes shift indicates that only small geometric changes occur between the ground state ( $S_0$ ) and the singlet excited state ( $S_1$ ).<sup>120</sup> The nanosecond lifetimes and small Stokes shifts allow the assignment of the emission as fluorescence from the bipyridine chromophore ( $^1\pi\pi^*$ ). This fluorescence is a feature of the emission spectra of all of the Ru(II) complexes prepared in this chapter and is characteristic of polyphenylene/bipyridine derivatives in general. A series of aryl-acetylene substituted bipyridine derivatives prepared by Klemm *et al.* display an identical emission profile with Stokes shifts of similar magnitude.<sup>122</sup>

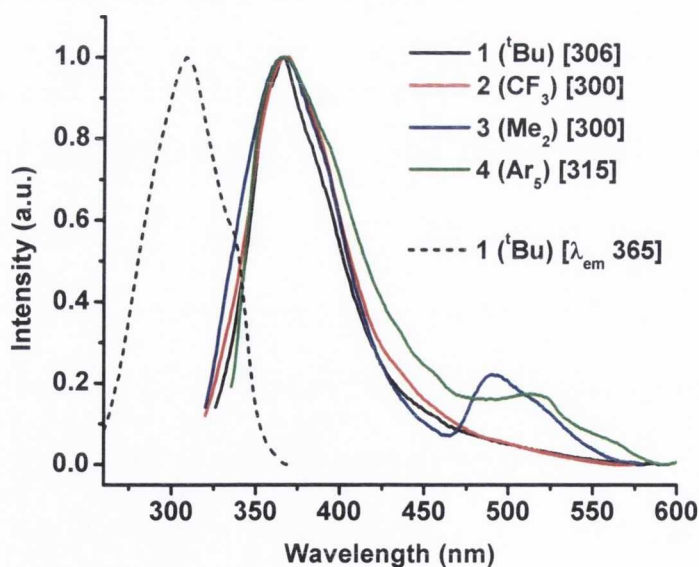


Figure 2.32: Normalised emission spectra of ligands **1-4** [ $\lambda_{exc}/nm$ ] and excitation spectrum of **1** [ $\lambda_{em}/nm$ ] in solid state at 298 K.

For polyphenylene ligands **3** and **4**, an additional lower energy emission band is evident which appears at  $\lambda$  489 nm (**3**) and  $\lambda$  512 nm (**4**) (Figure 2.32). The measured excited state lifetimes for these bands are significantly longer than for the higher energy emission,

measuring 1.1  $\mu\text{s}$  (81 %), 0.2  $\mu\text{s}$  (19 %) for **3** and 1.4  $\mu\text{s}$  (79 %), 0.3  $\mu\text{s}$  (21 %) for **4**. Although no such defined band is observed for ligands **1** and **2**, both possess a shoulder at  $\lambda$  386 nm (and an extended tail on the emission band to  $\lambda$  550 nm) which have similarly extended lifetimes (Table 2.8). This emission is likely composed of some phosphorescent character from the bipyridine ligand ( $^3\pi\pi^*/^3n\pi^*$ ), on the basis of extended lifetimes and the larger Stokes shift.

Several changes are observed on recording the emission spectra at 77 K (Figure 2.33). In general, the spectra are less smooth than the room temperature spectra due to bubbles in the liquid nitrogen used to cool the sample. Each of the four ligands exhibit the same broad high energy fluorescence band evident at room temperature. **3** ( $\text{Me}_2$ ) undergoes a significant enhancement in  $^3\pi\pi^*$  phosphorescence relative to fluorescence at 77 K with a marginal increase observed for **4**. At low temperature, the rate of non-radiative deactivation of the triplet excited state (by oxygen quenching) is much lower than at room temperature due to the relative immobilisation of the deactivating species in a more rigid matrix. Correspondingly, an enhancement in spin-forbidden emission from the  $T_1$  state is observed.

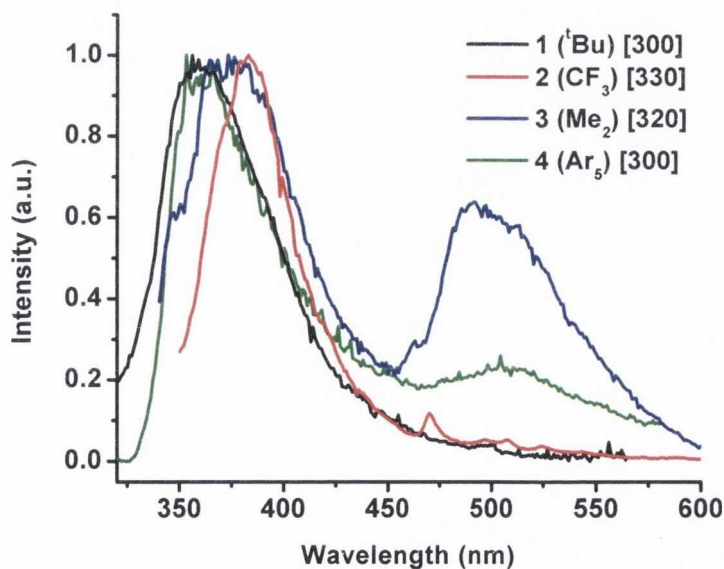


Figure 2.33: Normalised emission spectra of ligands **1-4** in solid state at 77 K [ $\lambda_{\text{exc}}/\text{nm}$ ].

### 2.5.1.2 Room temperature ( $\text{CH}_3\text{CN}$ solution) and 77 K in frozen $\text{CH}_3\text{CN}$ ( $10^{-5}$ M)

In argon-degassed  $\text{CH}_3\text{CN}$  ( $10^{-5}$  M) solution, emission from ligands **1**, **2** and **3** is excitation wavelength dependent (Figure 2.34). Excitation at high energy ( $\lambda_{\text{exc}}$  300 nm) induces a

strong high energy emission ( $\lambda_{\max}$ : **1**, 352; **2**, 341; **3**, 374; **4**, 376 nm) which have excited state lifetimes of nanosecond magnitude (Table 2.8). The variation in emission maximum can be attributed to the effect of electron-donicity on the  $\pi$ -orbital, the HOMO. The  $\pi$  orbital is the most stabilized and therefore has the lowest energy for the bipyridine with the electron-withdrawing  $\text{CF}_3$  group (**2**), resulting in a larger HOMO-LUMO energy gap ( $\pi \rightarrow \pi^*$ ) and a blue-shifted emission maximum. At the opposite end of the spectrum, the HOMO on polyaromatic electron-rich **4** ( $\text{Ar}_5$ ) is destabilized relative to **2** and correspondingly has a smaller HOMO-LUMO gap and a red-shifted emission. Interestingly, emission from **3** ( $\text{Me}_2$ ) is quite highly structured and exhibits a vibronic progression of  $\sim 1650 \text{ cm}^{-1}$ , typical of C=C and C=N stretching modes. Upon excitation at lower energy, a less-intense red-shifted band is observed for ligands **1**, **2** and **4** (Figure 2.34). A lower energy emission band is also seen for **3** ( $\text{Me}_2$ ) but it is excitation wavelength independent. For each ligand, excited state lifetimes for this lower energy band are approximately twice those recorded for the high energy emission (Table 2.8).

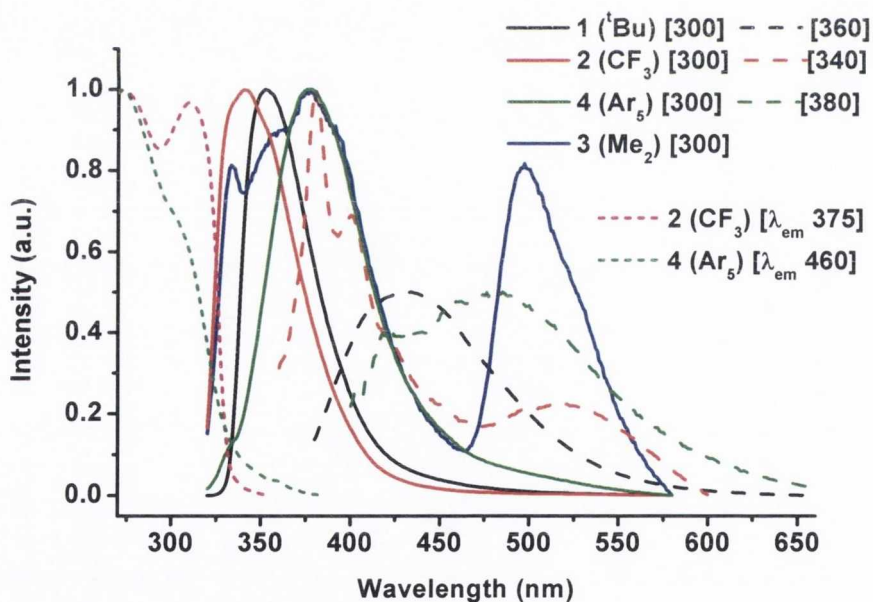


Figure 2.34: Normalised emission spectra of ligands **1-4** [ $\lambda_{\text{exc}}/\text{nm}$ ] and excitation spectra of **2** and **4** [ $\lambda_{\text{em}}/\text{nm}$ ] in argon-degassed  $\text{CH}_3\text{CN}$  at 298 K ( $\sim 10^{-5} \text{ M}$ ).

At 77 K in frozen  $\text{CH}_3\text{CN}$ , the emission profiles of ligands **1**, **2**, **3** and **4** are essentially identical to those measured in the solid state at low temperature (Figure 2.33). Emission from the four ligands is composed of both a higher energy ( $\lambda_{\max}$ : **1**, 347; **2**, 342; **3**, 361; **4**, 357 nm) and a lower energy band with a phosphorescent component (Table 2.8). In

general, from room temperature solution to low temperature, a blue-shift of emission maximum is observed for each of the four ligands. This is quite a common phenomenon and is called the “rigidochromic effect”. The rigidity of the frozen matrix restricts distortion of the excited state to relieve strain. This has also been attributed to solvent-solute interactions in fluid solution which can stabilise the excited state.<sup>134</sup>

A general trend from solid state to solution measurements can also be established. At room temperature, emission maxima tend to occur at slightly higher energy in the solid state than in solution. In solution, the compound has the freedom to distort so that a lower energy conformation is possible, whereas in the solid state the rigidity of the matrix prevents this and so the same emission band appears at higher energy. The excitation spectra (shown for **2** and **4** as examples, Figure 2.34) coincide with the corresponding absorption spectral profiles (Figure 2.27), precluding the involvement of aggregate effects in the emissive profile of the ligands in solution. As observed in the solid state, this emission band can be attributed to  $^1\pi\pi^*$  fluorescence from the bipyridine/polyphenylene chromophores on the basis of its short excited state lifetimes and small Stokes shifts.

For the four ligands studied in this chapter (and indeed for the majority of the other polyphenylene ligands and complexes in the remainder of this work), the excited state lifetimes are fit to biexponential decays. In almost every case, monoexponential decays yield a poor fit ( $0.75 > \chi^2 > 1.25$ ; Durbin-Watson parameter  $> 2.4$ ;  $> 15\%$  standard deviation on the fitted lifetimes;  $< 50\%$  of residuals within one standard deviation of the fitted line). Recording the lifetimes at slightly lower and higher energy ( $\pm 5$  nm) than the fluorescence maximum ( $\lambda_{em}^{max}/nm$ ) also yielded biexponential lifetimes, but with components of different proportions (e.g. at lower energy, the slower decaying component lifetime contributed a greater percentage to the fit). The short lifetime component is most likely localised on the bipyridine moiety in this case (bipyridine itself has a lifetime of  $\sim 1$  ns)<sup>80</sup> and the longer component is located on the polyphenylene component of the ligand unit.

### 2.5.1.3 Quantum Yields

Quantum yields of emission ( $\Phi$ ) were measured for each bipyridyl ligand **1-4** (Table 2.8) using the method of Demas and Crosby by employing a suitable reference compound whose quantum yield is accurately known.<sup>135</sup> Quinine sulfate in 0.5 M H<sub>2</sub>SO<sub>4</sub> solution

( $\lambda_{\text{exc}}$  310 nm,  $\Phi_{\text{em}}$  0.546) was used as the reference because its emission profile is analogous to the ligands.<sup>133,136</sup> Corrections were made for the difference in refractive indices of the media used for the standard and the sample. Quantum yields were measured using the equation –

$$\Phi_{F(x)} = \frac{A_s}{A_x} \cdot \frac{F_x}{F_s} \cdot \frac{(\eta_x)^2}{(\eta_s)^2} \cdot \Phi_{F(s)}$$

where s and x refer to the standard and the unknown respectively, A is the absorbance at the excitation wavelength, F is the area under the corrected emission curve and  $\eta$  is the refractive index of the solvents used.<sup>137</sup> All quantum yields reported in this work are an average of three repeat measurements for each complex. Measured using this method, aryl-acetylene substituted **1** and **2** display particularly high quantum yields ( $\Phi_{\text{em}}$  0.398 (**1**), 0.110 (**2**)) which are significantly higher than those measured for ligands **3** and **4** ( $\Phi_{\text{em}}$  0.007 (**3**), 0.012 (**4**)). Population of the  $S_1$  state by absorption of a photon of light leads to very efficient radiative decay from the singlet excited state (fluorescence,  $S_1 \rightarrow S_0$ ) and from the triplet (phosphorescence,  $T_1 \rightarrow S_0$ ). For the polyphenylene ligands, it seems that the excited state is subject to quite extensive radiationless decay from  $S_1$ . These have also been shown to undergo intersystem crossing to populate the  $T_1$  excited state which is highly sensitive to oxygen quenching and collisional deactivation by solvent molecules at room temperature.<sup>80</sup>

In the literature, a comprehensive study of bipyridine and phenanthroline derivatives substituted in the 4,4', 5,5' and 6,6' positions by “manisyl” groups (4-methoxy-2,6-dimethylphenyl) revealed that the 5-position is optimal to achieve high quantum yields ( $\Phi$  0.87), followed by the 4-position ( $\Phi$  0.15) with in general only marginal quantum yields achievable in the 6-position ( $\Phi$  0.02).<sup>138</sup> A series of bipyridines substituted in the 5-position by aryl-acetylene substituents possess very high quantum yields with values for 5,5'-substituted bis-alkynyl derivatives approaching unity.<sup>123</sup> For a family bearing aryl-acetylene functionalities in the 4 position, slightly poorer quantum yields than achieved in this work are recorded ( $\Phi_{\text{em}}$  0.2-12 % in  $\text{CH}_3\text{CN}$ ).<sup>119</sup> In general, the quantum yields achieved for **1** and **2** are exceptionally high for 6-position substituted bipyridines and are most likely a consequence of an enhancement in  $\pi$ -electron conjugation within the system.

### 2.5.2 Emission Properties of Ru(II) heteroleptic complexes

Table 2.9 summarises the relevant photoluminescence data for heteroleptic Ru(II) complexes, [Ru(bpy)<sub>2</sub>(**1**)](PF<sub>6</sub>)<sub>2</sub> (**33**), [Ru(bpy)<sub>2</sub>(**2**)](PF<sub>6</sub>)<sub>2</sub> (**34**), [Ru(bpy)<sub>2</sub>(**3**)](PF<sub>6</sub>)<sub>2</sub> (**35**) and [Ru(bpy)<sub>2</sub>(**4**)](PF<sub>6</sub>)<sub>2</sub> (**36**) in argon-degassed CH<sub>3</sub>CN solution and in the solid state at 298 K and 77 K, including lifetimes (at 298 K) and quantum yields.

Table 2.9: Emission data for Ru(II) heteroleptic complexes **33**, **34**, **35** and **36** in solid state and in solution (CH<sub>3</sub>CN) at 298 K and 77 K.

	Medium (T[K])	$\lambda_{em}$ [nm] ( $\lambda_{exc}$ [nm])	$\tau$ [ns] ( $\lambda_{exc}$ [nm] / $\lambda_{em}$ [nm]) <sup>b</sup>	$\Phi_{em}$ <sup>c</sup>
<b>33</b> <b><sup>t</sup>Bu</b>	Solid (298)	363 <sub>max</sub> (305), 615, 667 <sub>sh</sub> (475)	30 (64 %), 62 (36 %) (295 / 363) 2,730 (74 %), 480 (26 %) (370 / 614)	
	Solid (77)	360 <sub>max</sub> (300), 617 <sub>max</sub> , 663 (470)	4,030 (75 %), 660 (25 %) (370 / 617)	
	CH <sub>3</sub> CN (298) <sup>a</sup>	359 (310), 499 <sub>wk</sub> (360), 613 <sub>max</sub> , 665 <sub>sh</sub> (460)	28 (40 %), 6 (60 %) (295 / 360) 1,150 (79 %), 240 (21 %) (370 / 612)	0.008
	CH <sub>3</sub> CN (77)	362 <sub>wk</sub> (300), 594 <sub>max</sub> , 636 <sub>sh</sub> , 699 <sub>sh</sub> (300)	2,190 (77 %), 390 (23 %) (370 / 595)	
<b>34</b> <b>CF<sub>3</sub></b>	Solid (298)	363 <sub>max</sub> , 391 <sub>sh</sub> (305), 610 <sub>max</sub> , 665 <sub>sh</sub> (470)	28 (59 %), 57 (41 %) (295 / 363) 2,160 (75 %), 430 (25 %) (370 / 612)	
	Solid (77)	360 (300), 612 <sub>max</sub> , 661 <sub>sh</sub> (470)	3,910 (70 %), 760 (30 %) (370 / 612)	
	CH <sub>3</sub> CN (298) <sup>a</sup>	334 <sub>sh</sub> , 354 <sub>max</sub> , 388 <sub>sh</sub> (300), 496 <sub>wk</sub> (360), 623 <sub>max</sub> , 668 <sub>sh</sub> (465)	30 (59 %), 3 (41 %) (295 / 354) 1,280 (78 %), 240 (22 %) (370 / 620)	0.010
	CH <sub>3</sub> CN (77)	360 <sub>wk</sub> (300), 592 <sub>max</sub> , 638 <sub>sh</sub> , 694 <sub>sh</sub> (450)	2,360 (73 %), 440 (27 %) (370 / 595)	
<b>35</b> <b>Me<sub>2</sub></b>	Solid (298)	365 <sub>max</sub> , 390 <sub>sh</sub> (310), 615 <sub>max</sub> , 664 <sub>sh</sub> (475)	48 (70 %), 22 (30 %) (295 / 365) 2,620 (75 %), 490 (25 %) (370 / 615)	
	Solid (77)	361 <sub>wk</sub> (300), 611 <sub>max</sub> , 660 <sub>sh</sub> (465)	4,650 (72 %), 920 (28 %) (370 / 611)	
	CH <sub>3</sub> CN (298) <sup>a</sup>	377 <sub>max</sub> , 504 (300), 505, 608, 662 <sub>sh</sub> (420)	48 (57 %), 11 (43 %) (295 / 370) 1,140 (77 %), 230 (23 %) (370 / 510) 1,400 (76 %), 310 (24 %) (370 / 606)	0.007
	CH <sub>3</sub> CN (77)	370 <sub>wk</sub> (300), 588 <sub>max</sub> , 636 <sub>sh</sub> (455)	2,970 (76 %), 560 (24 %) (370 / 590)	

<b>36</b> <b>Ar<sub>5</sub></b>	Solid (298)	363 <sub>max</sub> , 390 <sub>sh</sub> (305), 619 <sub>max</sub> , 661 <sub>sh</sub> (485)	52 (52 %), 27 (48 %) (295 / 363) 2,370 (75 %), 460 (25 %) (370 / 620)	
	Solid (77)	359 <sub>max</sub> (300), 611 <sub>max</sub> , 661 <sub>sh</sub> (300)	4,520 (75 %), 1,210 (25 %) (370 / 611)	
	CH <sub>3</sub> CN (298) <sup>a</sup>	382 <sub>max</sub> , 488 (300), 619 <sub>max</sub> , 664 <sub>sh</sub> (430)	31 (72 %), 4 (28 %) (295 / 380) 990 (82 %), 150 (18 %) (370 / 488) 1,240 (78 %), 260 (22 %) (370 / 619)	0.009
	CH <sub>3</sub> CN (77)	366 <sub>wk</sub> (300), 589 <sub>max</sub> , 637 <sub>sh</sub> , 664 <sub>sh</sub> (425)	2,630 (75 %), 440 (25 %) (370 / 590)	

<sup>a</sup> Argon-degassed solutions,  $\sim 10^{-5}$  M (unless otherwise stated); <sup>b</sup> Estimated uncertainty on  $\tau \pm 11\%$ ;

<sup>c</sup> Measured using [Ru(bpy)<sub>3</sub>]<sup>2+</sup> as a standard, based on an average of three measurements.<sup>139</sup>

### 2.5.2.1 Solid State at 298 K and 77 K

The normalised emission spectra of heteroleptic Ru(II) complexes **33-36** in the solid state at 298 K are presented in Figure 2.35. For each complex, an essentially identical emission profile is recorded. A high energy band centred at  $\lambda$  363 nm (for **33**, **34** and **36**) and  $\lambda$  365 nm (for **35**) is observed (Table 2.9). Lifetimes for this band are typically of nanosecond magnitude (for example for **33** (Ru-<sup>t</sup>Bu):  $\tau$  30 ns (64 %), 62 ns (36 %)) and by comparison with the free ligand (Figure 2.32), this emission can be attributed to fluorescence from the bipyridine ligand, specifically  $^1\pi\pi^*$ .

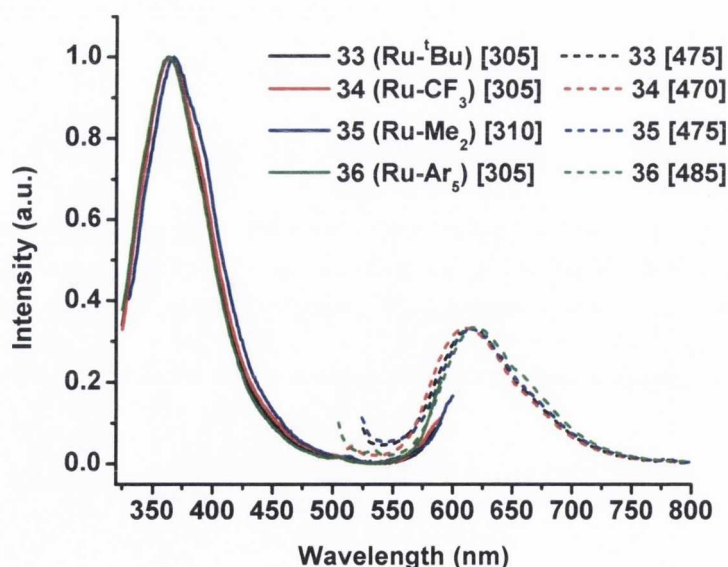


Figure 2.35: Normalised emission spectra of complexes **33-36**, solid state 298 K [ $\lambda_{exc}/nm$ ].

For each complex, a second emissive band at much lower energy is observed ( $\lambda_{max}$ : **33**, 615; **34**, 610; **35**, 615; **36**, 619 nm). The peak is excitation-wavelength-independent and



appears on excitation into either the higher energy  $\pi \rightarrow \pi^*$  absorption bands ( $< 300$  nm) or by direct excitation into the  $^1\text{MLCT}$  absorption manifold ( $\sim \lambda$  420-450 nm). This luminescence is derived from a  $^3\text{MLCT}$  state, or more accurately from a cluster of closely spaced  $^3\text{MLCT}$  levels  $^3[\text{d}(\text{Ru}) \rightarrow \pi^*(\text{bpy})]$  which is characteristic of the prototype complex  $[\text{Ru}(\text{bpy})_3]^{2+}$  ( $\lambda_{\text{max}}$  615 nm,  $\text{CH}_3\text{CN}$ ).<sup>78,85</sup> The relatively long lifetimes recorded for this low energy band for each of the complexes **33-36** (Table 2.9) confirm the assignment of the emission as triplet in origin with a two-component fit for the lifetimes, the major component ( $\sim 75$  %) with a lifetime between 2.2-2.7  $\mu\text{s}$  and the faster decaying, minor component excited state lifetime of  $\sim 0.4$   $\mu\text{s}$  (25 %).

At low temperature in the solid state (Figure 2.36), only very weak ligand-centred fluorescence ( $\sim \lambda$  360 nm) is observed for each of the four complexes (Table 2.9). The emission spectrum exhibits an intense highly structured luminescence band in the orange-red spectral region ( $\lambda_{\text{max}}$ /nm **1, 2, 3, 4** – 617, 612, 611, 611 nm). This band is composed of significant vibrational fine structure which can be assigned to a vibrational progression ( $1200$   $\text{cm}^{-1}$  energy spacing) that is characteristic of C=N and C=C stretching bands of the aromatic rings. The emission profile is typical of low temperature  $^3\text{MLCT}$  emission from  $[\text{Ru}(\text{bpy})_3]^{2+}$  itself and analogous complexes.

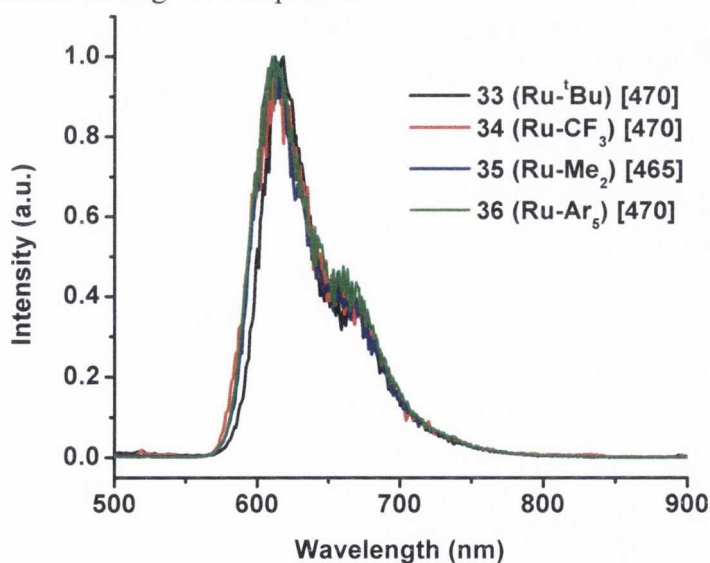


Figure 2.36: Normalised emission spectra of complexes **33-36** in solid state at 77 K [ $\lambda_{\text{exc}}$ /nm].

Notably, approximately a two-fold enhancement in lifetime is observed from room temperature to low temperature in the solid state (Table 2.9). Temperature dependence of the lifetime is characteristic of a  $^3\text{MLCT}$  excited state and is commonly observed in Ru(II)

polypyridine complexes. The dependence of the emission quantum yield on temperature has also been investigated for this class of complexes and is found to decrease with increasing temperature.<sup>85,89</sup>

Excited state lifetimes calculated for the high energy ligand-centred fluorescence are again fitted to biexponential decays, with contributions from excited states localised on the substituted bipyridine, the polyphenylene substituent and the unsubstituted bipyridine. For the <sup>3</sup>MLCT low energy emission, the appearance of a clearly biexponential decay may be attributed to the presence of (at least) two emissive <sup>3</sup>MLCT states [d(Ru)→π\*(N<sup>^</sup>N)] in close energetic proximity, one on the unsubstituted bipyridine and the other on the asymmetric ligand centre.

### 2.5.2.2 Room temperature (CH<sub>3</sub>CN solution) and 77 K in frozen CH<sub>3</sub>CN (10<sup>-5</sup> M)

The emission spectra of complexes **33-36** in argon-degassed CH<sub>3</sub>CN are presented in Figure 2.37. Although not shown in this figure, polyphenylene-bipyridine centred <sup>1</sup>π-π\* fluorescence is observed for each of the complexes with a luminescence band maximum between λ 354-382 nm and nanosecond lifetimes (Table 2.9). In addition, the complexes exhibit a relatively weak emissive band which by comparison with the free ligand and on examination of the lifetimes, can be attributed to <sup>3</sup>ππ\*/<sup>3</sup>nπ\* on the bipyridine chromophore (λ<sup>em</sup> 499 (**33**), 496 (**34**), 504 (**35**), 488 (**36**) nm). In the case of **35** (Ru-Me<sub>2</sub>), this phosphorescence is significantly more intense than observed in the free ligand. The high spin orbit coupling of the heavy Ru(II) metal centre induces enhanced mixing of singlet and triplet excited states. As a result, coordination of the heavy metal to the bipyridine ligands facilitates enhanced inter-system crossing (ISC) to populate a triplet excited state and afford long-lived phosphorescent emission.

At low energy, the emission spectra of the four complexes are dominated by a relatively intense, broad and quite unstructured emission band (λ<sub>max</sub><sup>em</sup> 613 (**33**), 623 (**34**), 608 (**35**), 619 (**36**) nm). The lifetimes measured for this family of complexes are similar, with values in general of ~1.3 μs (~78 %), ~0.25 μs (~22 %) across the series under these conditions (Table 2.9). Additionally, the luminescence excitation spectra are in good agreement with the corresponding absorption spectra (Figure 2.28) ruling out complications due to intermolecular interactions or aggregates in the excited state. Both the emission profile

and room temperature lifetimes are comparable to those obtained for the prototype complex,  $[\text{Ru}(\text{bpy})_3]^{2+}$  ( $\lambda_{\text{max}}^{\text{em}}$  615 nm,  $\tau$  1.1  $\mu\text{s}$ ) and in accordance with this, the emission band is assigned to  ${}^3\text{MLCT} [\text{d}(\text{Ru}) \rightarrow \pi^*(\text{bpy})]$ .<sup>80,86</sup>

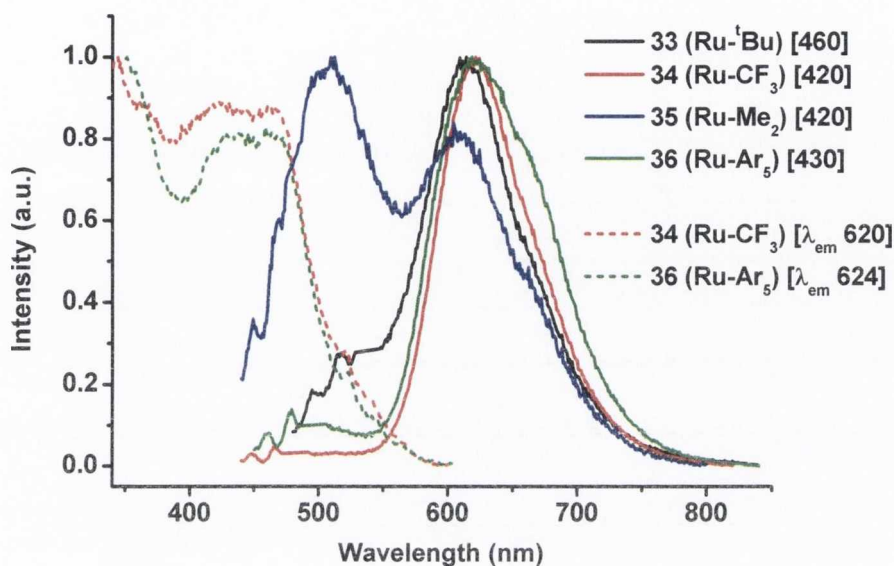


Figure 2.37: Normalised excitation spectra for complexes **34** and **36** [ $\lambda_{\text{em}}/\text{nm}$ ] and emission spectra for complexes **33-36** [ $\lambda_{\text{exc}}/\text{nm}$ ] in degassed  $\text{CH}_3\text{CN}$  ( $\sim 10^{-5} \text{ M}$ ).

It is quite difficult to discern a trend among the luminescence band maxima of complexes **33-36**. Based on the absorption spectral trends (Figure 2.28), the  $\lambda_{\text{max}}^{\text{em}}$  for polyphenylene complexes **35** and **36** would have been expected to be essentially coincident with that of  $[\text{Ru}(\text{bpy})_3]^{2+}$ . Within the margin of error, it is possible that this holds for these two complexes. In accordance with the red-shifted  ${}^1\text{MLCT}$  absorption band evident for aryl-acetylene complexes **33** and **34**, slightly red-shifted  ${}^3\text{MLCT}$  emission bands would be anticipated compared to  $[\text{Ru}(\text{bpy})_3]^{2+}$ . While this may be true for **34** ( $\text{Ru-CF}_3$ ), it is not for **33** ( $\text{Ru-tBu}$ ), whose emission band maximum is closer to  $[\text{Ru}(\text{bpy})_3]^{2+}$  itself.

Finally, in frozen  $\text{CH}_3\text{CN}$ , the emission profiles of the four complexes are almost identical to those in the solid state at 77 K (Figure 2.38). The luminescence band maximum undergoes a significant “rigidochromic” blue-shift in the rigid medium as is characteristic of  ${}^3\text{MLCT}$  phosphorescence ( $\lambda_{\text{max}}^{\text{em}}$  594 (**33**), 592 (**34**), 588 (**35**), 589 (**36**) nm). In addition, an almost two-fold enhancement in lifetime is observed for the complexes, with average values  $\sim 2.5 \mu\text{s}$  (75 %),  $0.4 \mu\text{s}$  (25 %). These are much shorter than  $[\text{Ru}(\text{bpy})_3]^{2+}$  which has a reported lifetime of 5  $\mu\text{s}$  in  $\text{CH}_3\text{CN}$  at 77 K.<sup>78</sup>

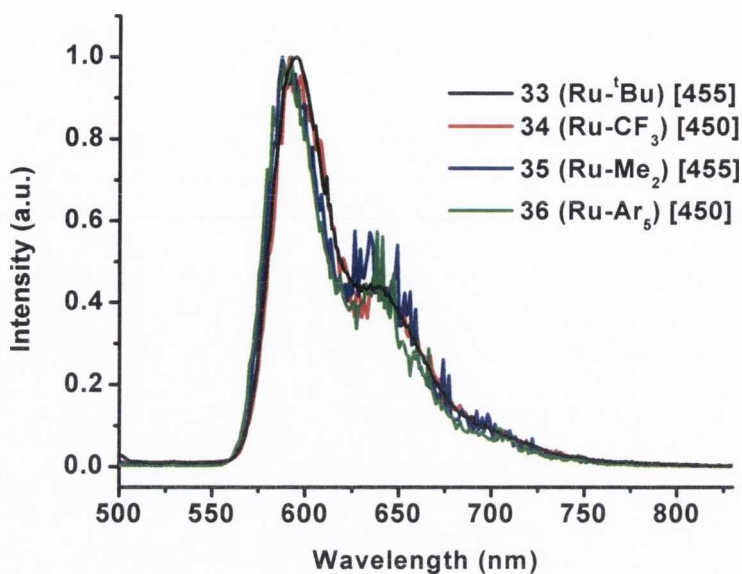


Figure 2.38: Normalised emission spectra of complexes 33-36 in  $\text{CH}_3\text{CN}$  ( $\sim 10^{-5}\text{M}$ ) at 77 K [ $\lambda_{\text{exc}}/\text{nm}$ ].

### 2.5.3 Nature of the emissive excited states in Ru(II) complexes 33, 34, 35 and 36

The estimated energies of the excited states as calculated from the absorption and room temperature solution emission spectra are depicted in Figure 2.39. ( $^1\pi\pi^*$  energies calculated from  $\lambda_{\text{max}}^{\text{fl}}$  in the emission spectra as  $\pi\pi^*$  absorptions are spread across the spectrum for each complex).

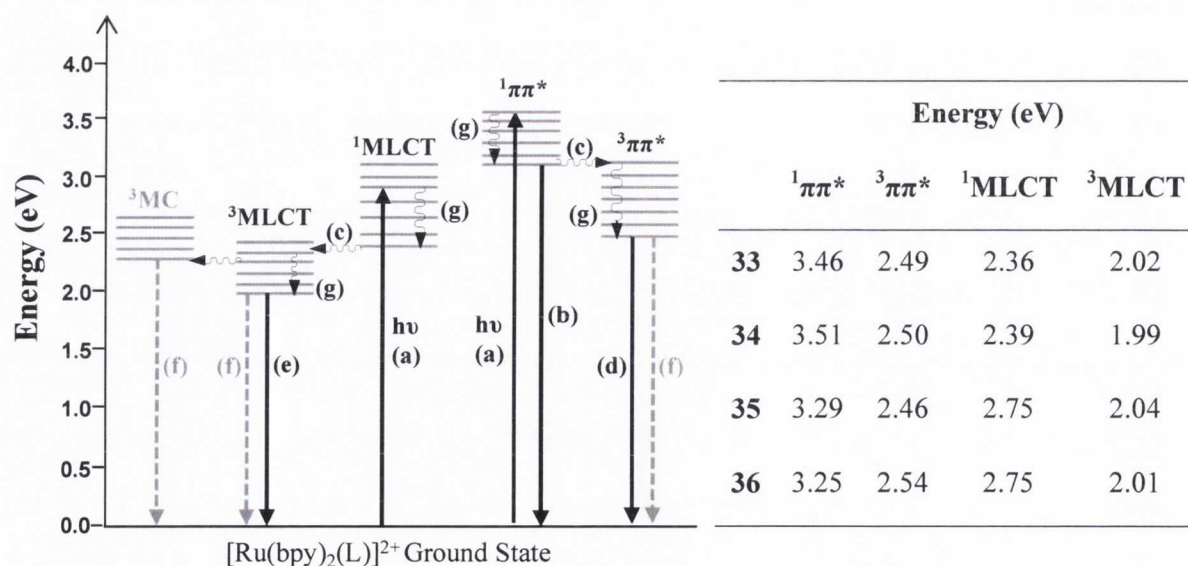


Figure 2.39: Jablonski energy level diagram for complexes 33-36 showing photoinduced radiative processes and inset, calculated approximate energies (eV) of excited states (from 298 K  $\text{CH}_3\text{CN}$  solution measurements). (a) Absorption; (b), (d), (e) Radiative decay; (c) Intersystem crossing; (f) Radiationless decay; (g) Internal conversion.

Excitation into any absorption band of complexes **33-36** (Figure 2.39, a), results in population of both the  $^1\pi\pi^*$  excited state and the  $^1\text{MLCT}$  excited state. For all complexes, high energy emission from the  $^1\pi\pi^*$  excited state is observed (Figure 2.39, b,  $\sim 3.3\text{-}3.5$  eV). The remainder of the absorbed photon of light may relax *via* non-radiative decay from this state or may populate a lower lying triplet excited state by intersystem crossing (Figure 2.39, c). Phosphorescence from this  $^3\pi\pi^*$  state is observed for the three complexes (Figure 2.39, d, 3.5 eV), but its relatively poor intensity (with the exception of **35**) indicates that the rate of intersystem crossing is less competitive with radiative or radiationless decay of the  $^1\pi\pi^*$  excited state.

No emission from the  $^1\text{MLCT}$  excited state is observed. The heavy Ru(II) metal induces high spin-orbit coupling and singlet-triplet state mixing, such that the  $^3\text{MLCT}$  state is formed typically in high yield. At this point, the  $^3\text{MLCT}$  state has three major decay pathways. Each complex undergoes radiative decay to the ground state (Figure 2.39, e),  $\sim 2.0$  eV) but this emission is of particularly low efficiency, as evidenced by poor quantum yields ( $\Phi_{\text{em}}: \leq 0.01$ , Table 2.9). These are significantly lower than the quantum yield of  $[\text{Ru}(\text{bpy})_3]^{2+}$  which measures  $\Phi_{\text{em}} = 0.07$  at room temperature.<sup>86</sup> It is clear that the  $^3\text{MLCT}$  excited state in complexes of this class is highly susceptible to deactivation. This may occur *via* two routes (Figure 2.39, f) – energy may decay non-radiatively to the ground state from the  $^3\text{MLCT}$  state itself, or it may cross over into nearby, thermally accessible d-d (metal-centred, MC) states.<sup>80,89</sup> These d-d excited states are strongly distorted with respect to ground state geometry and accordingly are subject to very fast radiationless decay.

The dramatic decrease in quantum yield from the prototype complex,  $[\text{Ru}(\text{bpy})_3]^{2+}$  to complexes **33-36**, is most likely a direct consequence of steric hindrance induced by a substituent in the 6-position.<sup>140</sup> The crystal structures of complexes **33** and **35** both revealed an elongated (weakened) Ru-N bond for the aryl-substituted pyridine ring (**33** 2.093(4) Å, **35** 2.129(5) Å). The consequent distortion of octahedral geometry reduces the ligand field strength and lowers the energy of the triplet  $^3\text{d-d}$  (MC) states. Accordingly, population of MC states is more facile and provides a more rapid deactivation pathway for the excited  $^3\text{MLCT}$  state, reducing the quantum efficiency of emission.<sup>140-142</sup> This effect is analogous to that observed for  $[\text{Ru}(\text{tpy})_2]^{2+}$  incorporating the tridentate terpyridine ligand (Section 2.1.2).<sup>87-88</sup> Although steric hindrance is the key factor responsible for the poor

emission intensity of 6-substituted heteroleptic Ru(II) complexes, separate studies have shown that functionalisation of one pyridine ring in either the 4-, 5- or 6- position by attachment of a phenyl (or tolyl) group causes very little change in the spectral profile, emission band maximum or excited state lifetime relative to  $[\text{Ru}(\text{bpy})_3]^{2+}$ .<sup>140,143-144</sup>

## 2.6 Summary and Conclusions

This chapter describes the synthesis and characterisation of a series of Ru(II) heteroleptic complexes, containing an asymmetric ligand functionalised in the 6-position. The electronic demand of the third ligand was varied in complexes **33** and **34** and the size of the substituent was significantly increased in complexes **35** and **36**. To date, the latter two complexes are some of the largest reported mononuclear heteroleptic Ru(II) bipyridyl complexes containing a pendant functional group located  $\alpha$  to a pyridine ring nitrogen.

These complexes were fully characterised by NMR spectroscopy, mass spectrometry and elemental analysis. The asymmetric third ligand in the four complexes added a significant degree of complexity to the NMR spectra by ensuring that every proton on each ligand possessed a separate signal. The additional steric encumbrance encountered in complex **36** resulted in broadened signals for the *tert*-butyl phenyl rings which appeared throughout the aromatic region of the spectrum. Single crystal X-ray structures of **33** and **35** revealed slightly distorted octahedral geometries about the Ru(II) centres with an elongated Ru-N bond located on the pyridine ring containing the substituent.

The increased  $\pi$ -conjugation within aryl-acetylene ligands **1** and **2** was confirmed by red-shifted UV-Visible absorption bands relative to polyphenylene ligands **3** and **4**. This also appeared in the UV spectra of the corresponding complexes (**33** and **34**) which exhibited a <sup>1</sup>MLCT absorption band which was more bathochromically shifted than complexes **35**, **36** and the parent complex,  $[\text{Ru}(\text{bpy})_3]^{2+}$  (**32**). In terms of electrochemical behaviour, Ru(II) oxidation potentials of the four complexes are not markedly different from that of the prototype complex, suggesting that the energy of the HOMO is similar in complexes **33-36** and  $[\text{Ru}(\text{bpy})_3]^{2+}$ . In keeping with the UV-Visible trends, the first ligand-based reduction process is easier for aryl-acetylene complexes **33** and **34** which implies a lower  $\pi^*$  (LUMO) orbital for these complexes relative to **35**, **36** and  $[\text{Ru}(\text{bpy})_3]^{2+}$ . Unfortunately, this trend does not extend into the emissive properties of the complexes. In general,

emission in the solid state and in solution at room temperature is almost identical to that of  $[\text{Ru}(\text{bpy})_3]^{2+}$ , with slightly shorter lifetimes and significantly reduced quantum yields. The origin of this decrease is most likely structural rather than electronic and may be ascribed to a reduction in ligand field strength as a result of the distorted octahedral geometry induced by the steric bulk of the 6-positioned substituent. Accordingly, deactivating d-d orbitals are much more thermally accessible and the  $^3\text{MLCT}$  state is subject to very rapid radiationless decay, giving rise to significantly reduced quantum yields relative to  $[\text{Ru}(\text{bpy})_3]^{2+}$ . The similarity in lifetime from the parent complex to complexes **33-36** in this work suggests that the lowest lying  $^3\text{MLCT}$  excited state is localised on an unsubstituted bipyridine ligand.





## **Chapter 3**

# **Phosphorescent Pt(II) $\sigma$ -acetylide complexes from polyaromatic ligands**



### 3.1 Introduction

Acetylene-functionalities are often employed as highly-conjugated spacer groups which can facilitate a wide range of photorelated processes and promote strong electronic communication between two chromophores.<sup>56</sup> The functionalisation of polyphenylene compounds with acetylene substituents results in an overall extension of  $\pi$ -conjugation within the system. Additionally, this confers significant ligand functionality on the material with the potential to form metal-carbon bonds.<sup>145</sup> Metal-alkynyl complexes have consequently been employed as building blocks in molecular wires, polymeric materials and supramolecular assemblies.<sup>146-147</sup>

The polyaromatic acetylene-substituted hexaphenylbenzene and hexa-*peri*-hexabenzocoronene derivatives described in Chapter 1 are synthetically accessible compounds that offer the opportunity to further extend the family of metal-organic polyphenylene complexes. In particular, ethynyl-hexaphenylbenzene (**6**) and ethynyl-HBC (**7**) have been employed in this chapter as polyaromatic  $\sigma$ -acetylide ligands coordinated to a Pt(II) metal centre. Attachment of a heavy metal to the polyphenylene core *via* an acetylene linker would be anticipated to significantly influence the optical properties of the system.

#### 3.1.1 Metal-alkynyl bonding

The interaction of alkynes with a metal centre is electronically analogous to that of  $\text{CN}^-$ , CO and  $\text{N}_2$  ligands which can have  $\sigma$ -donating,  $\pi$ -donating and  $\pi$ -accepting character. However, it is known that metal-carbon  $\pi$  back-bonding into the empty  $\pi^*(\text{C}\equiv\text{CR})$  orbitals in general plays only a small role in the bonding interaction, so the interaction between transition metal centres and alkynes can be regarded as predominantly  $\sigma$ -donating in character, from the anionic  $\text{C}\equiv\text{CH}$  moiety into empty metal-centred orbitals.<sup>148</sup> Alkynes can be considered as “strong-field” ligands in the spectrochemical series, inducing a large splitting between filled and empty metal d-orbitals. Acetylide coordination raises the energy of metal-centred d-d states so that they are less thermally accessible and non-radiative decay *via* this pathway is less facile.<sup>149</sup> This also introduces high lying filled acetylide-localised  $\pi$ -orbitals, whose energy may be tuned by careful choice of alkynyl-substituent.<sup>150</sup>

### 3.1.2 Organic and organometallic $\pi$ -conjugated materials

$\pi$ -conjugated organic materials, frequently incorporating structurally rigid acetylenes as the spacer unit between two active centres, have been the subject of significant interest over the last twenty years. Their ease of fabrication and structural modification, high electronic conductivity and often high fluorescence quantum yields has resulted in their application as organic semiconductors, in polymer light emitting devices (PLEDs) and in plastic lasers.<sup>151-153</sup> The introduction of heavy transition metals *via* metal-alkynyl bonds into the organic conjugated framework has significant effects on the optical and electronic properties of the materials.<sup>154-155</sup> The high spin-orbit coupling constant of the metal centre facilitates singlet-triplet mixing with the result that spin-forbidden phosphorescence processes may be observed. Consequently, optoelectronic devices based on  $\pi$ -conjugated transition-metal containing materials as triplet emitters display enhanced electrical luminescence quantum efficiencies.<sup>156-157</sup> This is because excitons in both singlet and triplet states formed upon electrical excitation may be harvested.

### 3.1.3 Pt-acetylide complexes: Monomers, oligomers, dendrimers and polymers

Some of the first reports describing photoluminescence in Pt(II) acetylide systems attributed the emission to a metal-to-ligand charge transfer state [ $d(\text{Pt}) \rightarrow \pi^*(\text{C}\equiv\text{CR})$ ] for simple mononuclear *trans*-[Pt(C $\equiv$ CR)<sub>2</sub>(PEt<sub>3</sub>)<sub>2</sub>] (R = Ph, H).<sup>158-159</sup> Twenty years later, intensive investigations into the photophysical properties of Pt-acetylide containing monomers, oligomers and polymers has produced a class of materials with properties that may be both tuned and predicted by control of the molecular structure.<sup>146,160</sup>

In-depth studies by Schanze *et al.* and the Raithby groups have examined how the structure of a Pt-acetylide oligomer or polymer may control its optical properties, with particular focus on the properties of the triplet excited state. In a series of Pt-acetylide oligomers (PAOs) (Figure 3.1, (a)), with increasing oligomer length the lowest energy absorption band, attributable to a long-axis  $\pi$ - $\pi^*$  transition, and the high energy fluorescence band, red-shift with increasing chain length, indicating that the singlet excited state ( $S_1$ ) is considerably delocalised over several repeat units.<sup>160-161</sup> In contrast, the phosphorescence maximum red-shifts only marginally over the same number of chain units. This reveals that the triplet excited state ( $T_1$ ) is considerably less delocalised than  $S_1$  and is spatially confined to just one or two phenylene rings.<sup>162</sup> It has also been shown that decreasing the

Pt-acetylide content in the polymer chain results in an increase in fluorescence efficiency, a decrease in the quantum efficiency of intersystem crossing ( $S_1 \rightarrow T_1$ ) and an overall decrease in phosphorescence.<sup>160</sup>

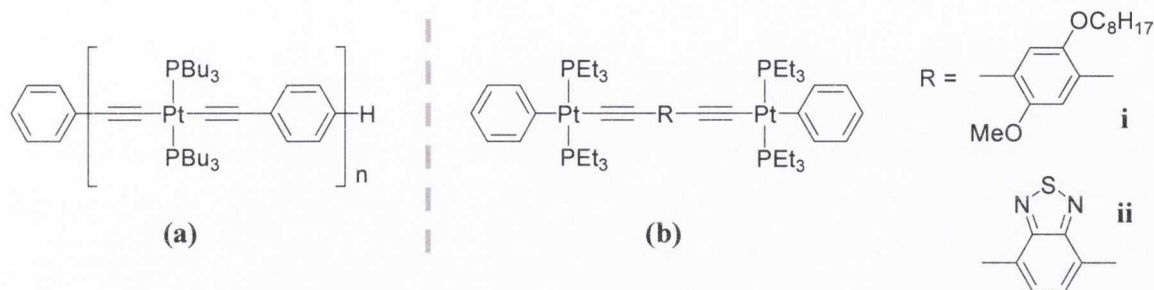


Figure 3.1: Structures of Pt-acetylide oligomers. [a]  $n=1-7$ ,<sup>161</sup>  $n=\infty$ ,<sup>162</sup>].

A series of rigid dinuclear Pt(II) acetylides (Figure 3.1, (b)) with extended conjugation through aromatic and heteroaromatic linker units show substantial donor-acceptor interactions, from the electron-rich Pt metal centre to electron-accepting chromophores.<sup>163</sup> Fluorescence, phosphorescence and absorption energy decrease with increasing electronegativity of the spacer groups, i.e. from 1-(2-ethylhexyloxy)-4-methoxybenzene (i) to 2,1,3-benzothiadiazole (ii, BTD) (Figure 3.1, (b)). In addition to these detailed luminescence surveys, platinum-acetylide polymeric materials have found varying degrees of application in non-linear optics and as liquid crystalline materials.<sup>145,164-165</sup> More recently, donor-acceptor  $\pi$ -conjugated chromophores have been incorporated as active materials for organic solar cells.<sup>166</sup>

Platinum-acetylide moieties have been employed as building blocks in the synthesis of nano-sized organometallic molecules.<sup>167-168</sup> These hyperbranched dendrimers contain metal atoms in every generation and giant Pt-acetylide molecules containing 198 Pt atoms have been prepared.<sup>167</sup> On a smaller scale, Yam and co-workers have shown that by incorporating different alkynyl moieties into the periphery of a branched alkynyl core, the nature of the lowest energy emissive state can be tuned.<sup>169-170</sup> Photoluminescence from a tolyl-substituted complex (Figure 3.2, (a)) is attributed to predominantly  $^3\pi\pi^*$  localised on the central core whereas  $^3\pi\pi^*$  centred on the naphthalene alkynyl moieties dominates the emission profile of the naphthyl-functionalised complex (Figure 3.2, (b)).

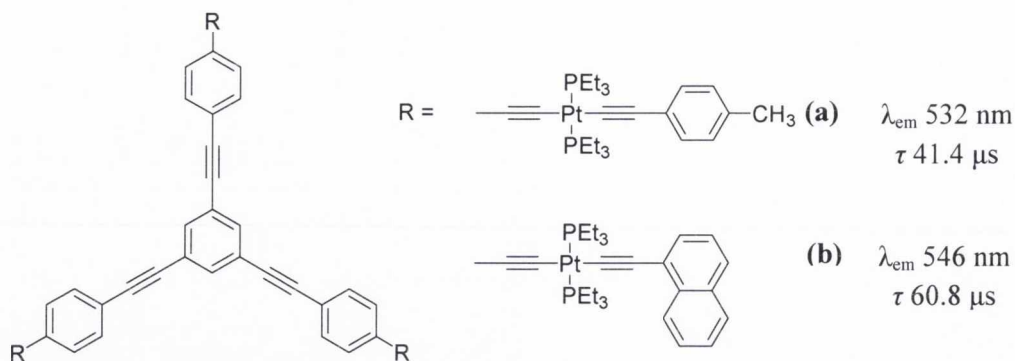


Figure 3.2: Structure and luminescence properties ( $\text{CH}_2\text{Cl}_2$  solution, 298 K) of branched-alkynyl Pt(II)-acetylide complexes.

### 3.1.4 Pt-acetylide hexa-*peri*-hexabenzocoronenes & HBC complexes

Hexa-*peri*-hexabenzocoronene (HBC) and its derivatives possess valuable properties induced by their highly conjugated  $\pi$ -electron delocalised systems. As molecular graphite-like discs, they have been shown to demonstrate liquid crystallinity and very high charge carrier mobilities.<sup>7,12</sup> Additionally, they are known to aggregate significantly in both solution and the solid state due to their tendency to form columnar stacks held together by  $\pi$ - $\pi$  interactions.<sup>5-6,171</sup> In their own right, propeller-like polyphenylene precursors to HBC have been studied as molecular scaffolds for multichromophoric arrays, as ligands for encapsulated metal complexes and in organometallic molecules and in supramolecular host-guest frameworks.<sup>40,42-44</sup> Extension of the  $\pi$ -conjugated polyaromatic framework by combining HBC derivatives and their propeller-like precursors with metal-acetylide moieties would be expected to provide a strong pathway for energy transfer and electronic communication across the molecular axis. Schanze *et al.*, and Müllen and co-workers have provided the three known examples of compounds that couple a HBC platform to a Pt(II) metal centre (Figure 3.3).<sup>172-173</sup>

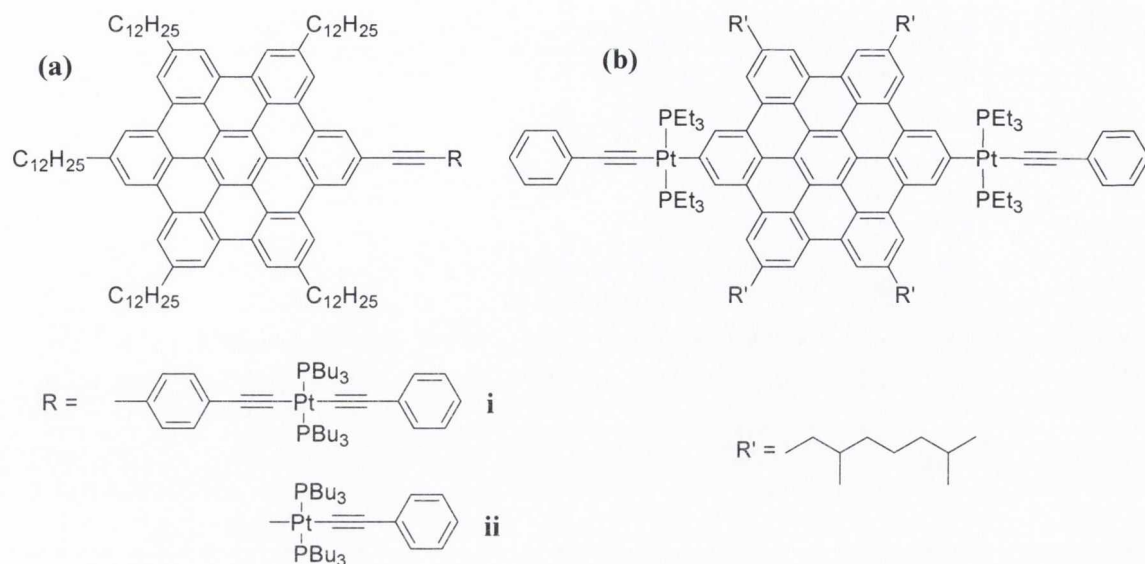


Figure 3.3: Structures of Pt(II)-acetylide HBC complexes prepared to date.

The high spin-orbit coupling introduced by the Pt-acetylide into the HBC core facilitates efficient population (*via* intersystem crossing) of the triplet excited state ( $^3\pi\pi^*$ ) centred on the graphene and correspondingly the observation of very long-lived room-temperature phosphorescence for the three complexes ( $>20 \mu s$ ). The strong tendency of the HBC chromophores towards aggregation is retained in the Pt-HBC complexes. This is observed in complexes (i) and (ii) (Figure 3.3, (a)) in non-polar solution which leads to quenching of the triplet excited state – an effect which manifests itself in a reduction of phosphorescence lifetime, reduced quantum yield of emission and an overall broadening of the emission profile.<sup>173</sup>

To date, no other Pt(II) HBC complexes have been reported and relatively few such metal-graphene compounds have been described in the literature. The only other organometallic complexes incorporating hexa-*peri*-hexabenzocoronenes appear to be a  $\eta^6$ -bound  $Cr(CO)_3$  complex and a series of  $Co_2(CO)_8$ -functionalised derivatives.<sup>10,174</sup> A greater number of nitrogen-containing HBC coordination complexes are known. The first of these were prepared by the Draper group and arise from the coordination of nitrogen-doped HBCs (N-HSB, Section 1.1.3) with  $[Ru(bpy)_2]^{2+}$  (Figure 3.4, (a)) and  $[Pd(\eta^3-C_3H_5)]^{2+}$ .<sup>27-28</sup> An extended PAH derivative of N-HSB coordinated to Ru(II) was later prepared by Müllen (Figure 3.4, (b)) who also synthesised a giant Cu(II)-coordinated phthalocyanine complex with four fused HBC units on the periphery.<sup>175</sup> Finally, a HBC core with an appended

pyridine ring which was subsequently coordinated to a Ru(II) metal centre in a phthalocyanine has also been synthesised (Figure 3.4, (c)).<sup>176</sup>

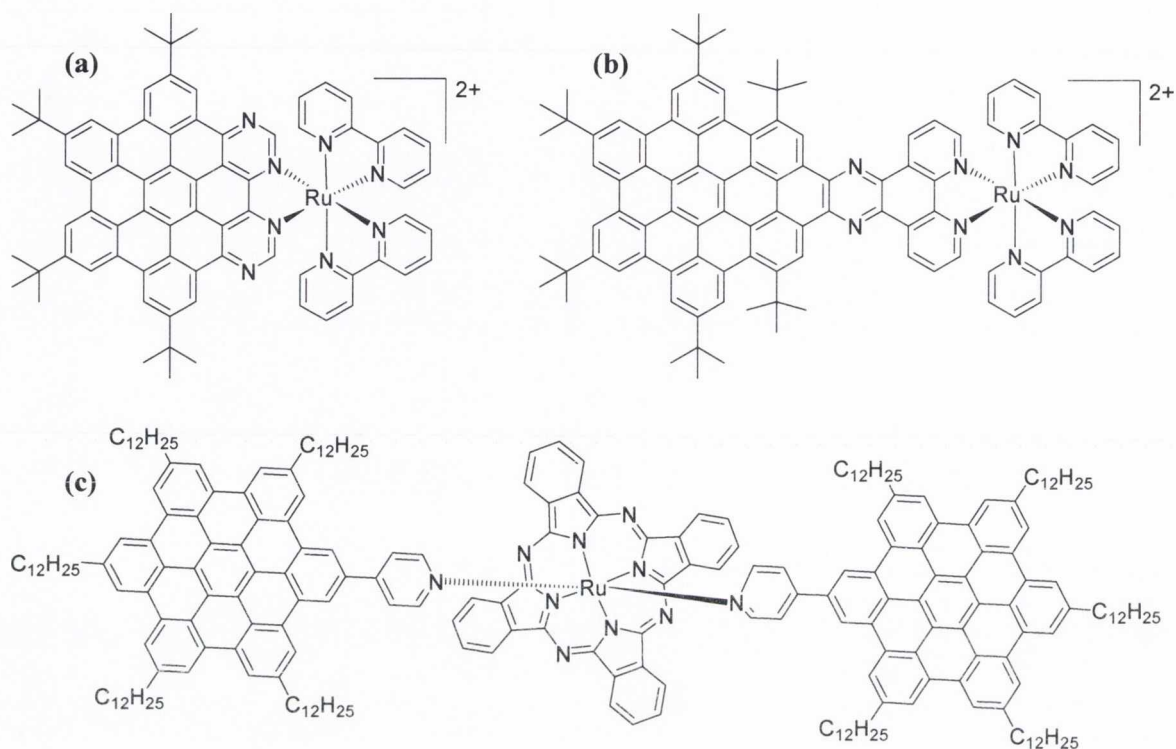


Figure 3.4: Ru(II) coordination complexes of nitrogen-doped and pyridine-appended HBC derivatives.

### 3.1.5 Target Molecules: *Cis* and *Trans* Pt-acetylide complexes

This chapter describes the preparation of four novel platinum(II) bis-acetylide complexes, two in *cis* square-planar geometry and two in *trans*. These incorporate either uncyclised polyphenylene ligand ethynyl-hexaphenylbenzene (**6**) or fused ligand ethynyl-HBC (**7**), the syntheses and characterisation of which are detailed in Chapter 1, in addition to the monodentate or bidentate phosphines employed as auxiliary ligands (Figure 3.5).

Each of the four super-aromatic complexes is composed of two graphene subunits. The attachment of the additional extended polyphenylene core allows an increase in steric bulk of the complex while still retaining the desirable properties induced by the transition metal. It is anticipated that this two-fold enhancement in molecule size should facilitate the extension of the  $\pi$ -conjugated molecular axis.



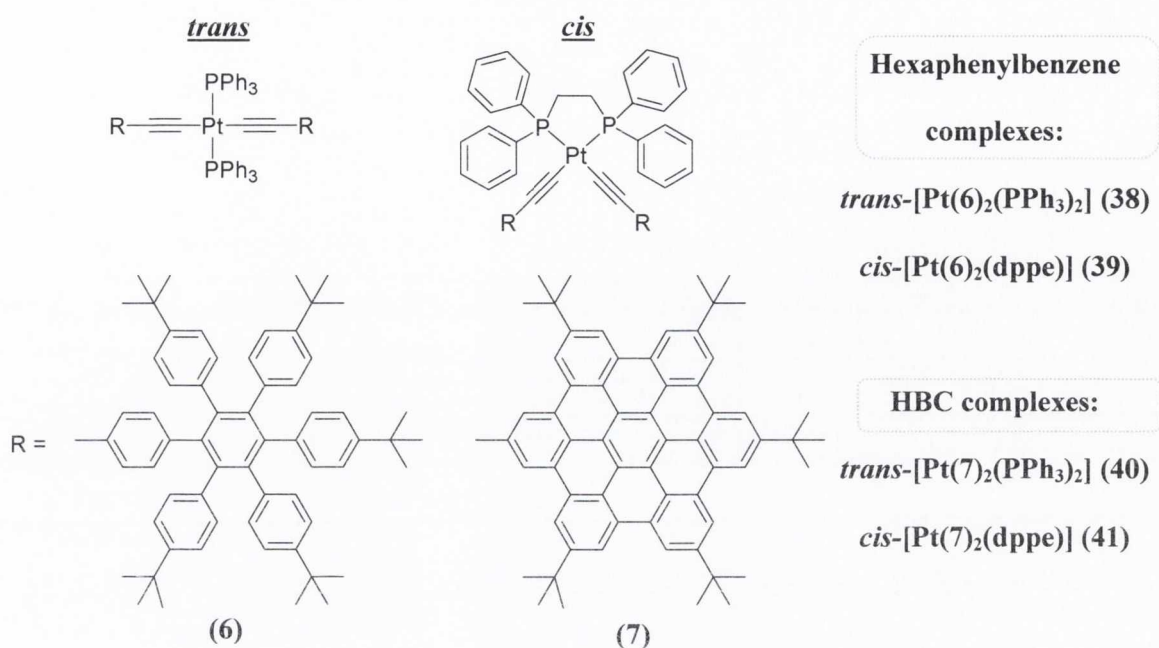


Figure 3.5: *Cis* and *trans* Pt(II)-acetylide complexes, incorporating hexaphenylbenzene and hexa-*peri*-hexabenzocoronene PAHs.

Owing to the general preference of Pt(II) to adopt a square planar configuration, two geometric arrangements of the two alkynyl-HBCs about the metal centre are possible. The preparation of both *cis* and *trans* isomers was undertaken in order to examine the effect on intramolecular electronic delocalisation of changing the coordination geometry of the acetylides at the metal centre.<sup>177</sup> In addition, the application of an unfused polyphenylene alkynyl as  $\sigma$ -acetylide in contrast to a highly electron-delocalised planar graphene subunit would be expected to produce systems with dramatically different optical properties. This combination of a heavy metal and strong-field polyaromatic acetylides should result in significantly enhanced optical properties at room temperature and allow for an examination of the structural, electronic and optical consequences of a second coordinated HBC unit to a Pt(II) metal centre for the first time.

### 3.2 Synthesis of *cis* and *trans* Pt(II) complexes of acetylene-hexaphenylbenzene (6) and acetylene-HBC (7)

The synthesis of platinum(II) acetylide complexes in the literature uses a modification of the method originally developed by Hagihara and Sonogashira in the 1970's, a copper(I)-catalysed dehydrohalogenation of metal halides in an amine solvent.<sup>178</sup> In a subsequent paper, the authors report the selective syntheses of *cis*- and *trans*-Pt(II) acetylide complexes of the type  $[(R_3P)_2Pt(C\equiv CR')_2]$  but note that the thermodynamic instability of *cis* isomers relative to *trans* results in the slow isomerisation of the *cis* to the *trans* form in solution, an effect accelerated by catalytic amounts of cuprous halides.<sup>179</sup> This instability may be overcome by carrying out reactions at -20 °C to yield the pure *cis* complex, whereas a 50:50 mixture of *cis:trans* isomers is obtained at higher temperature.<sup>179</sup> The incorporation of chelating auxiliary ligands, such as phosphines or diimines, is more typically employed as a synthetic method towards the preparation of *cis* complexes, an additional benefit being the consequent inhibition of the slow conversion of *cis* back to the *trans* isomer.<sup>180-181</sup>

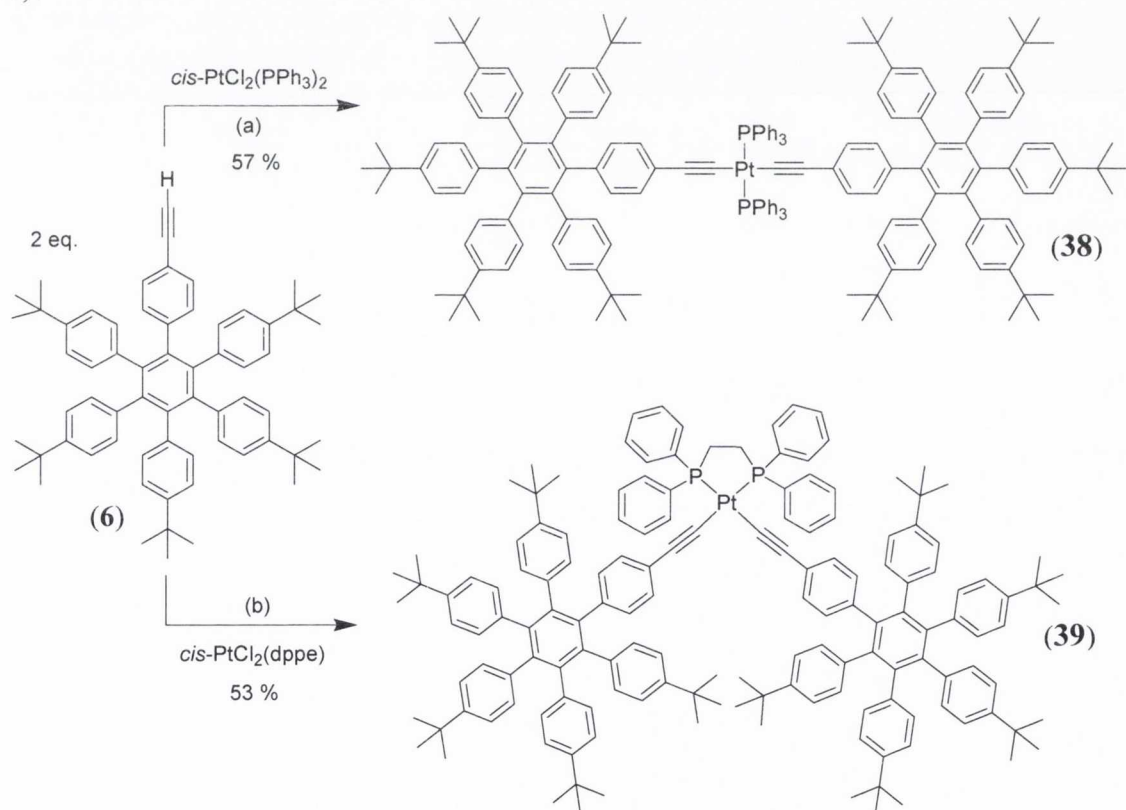
In this work, Sonogashira-Hagihara coupling reactions were similarly used to prepare *cis* complexes *cis*-[Pt(6)<sub>2</sub>(dppe)] (39) and *cis*-[Pt(7)<sub>2</sub>(dppe)] (41) and *trans* complexes *trans*-[Pt(6)<sub>2</sub>(PPh<sub>3</sub>)<sub>2</sub>] (38) and *trans*-[Pt(7)<sub>2</sub>(PPh<sub>3</sub>)<sub>2</sub>] (40). In general, this required the use of copper(I) iodide as catalyst, with diisopropylamine (<sup>i</sup>Pr<sub>2</sub>NH) as base, CH<sub>2</sub>Cl<sub>2</sub> as an additional solvent, a suitable Pt(II) metal precursor and a slight excess of the terminal alkyne, ethynyl-HPB (6) or ethynyl-HBC (7). Complexes in *trans* configuration were prepared using *cis*-PtCl<sub>2</sub>(PPh<sub>3</sub>)<sub>2</sub> as the metal precursor.<sup>182</sup> In order to avoid the thermodynamic instability of *cis* isomers, the bidentate phosphine bridging ligand 1,2-bis(diphenylphosphino)ethane (dppe) was used to prepare *cis*-[PtCl<sub>2</sub>(dppe)], the metal precursor employed to prepare both *cis* complexes.<sup>183</sup>

### 3.2.1 Syntheses of *trans*-[Pt(6)<sub>2</sub>(PPh<sub>3</sub>)<sub>2</sub>] (38) and *cis*-[Pt(6)<sub>2</sub>(dppe)] (39):

#### Ethynyl-hexaphenylbenzene (6) as $\sigma$ -acetylide.

The two complexes incorporating ethynyl-hexaphenylbenzene (6) as an acetylide, specifically *trans* complex [Pt(6)<sub>2</sub>(PPh<sub>3</sub>)<sub>2</sub>] (38, *trans*-HPB) and *cis* configured complex [Pt(6)<sub>2</sub>(dppe)] (39, *cis*-HPB), were prepared *via* the conventional Sonogashira-Hagihara cross-coupling route (Scheme 3.1).<sup>179</sup>

The synthesis of 38 (*trans*-HPB) employed *cis*-PtCl<sub>2</sub>(PPh<sub>3</sub>)<sub>2</sub> as the platinum starting material (1 eq.), ethynyl-hexaphenylbenzene (2 eq.) and CuI as catalyst which were stirred in darkness under argon at room temperature for 36 hours in a solvent mixture of still-dried, argon-degassed CH<sub>2</sub>Cl<sub>2</sub>:<sup>i</sup>Pr<sub>2</sub>NH (Scheme 3.1). The same method, but using *cis*-Pt(dppe)Cl<sub>2</sub> (1 eq.) as Pt(II) precursor salt, was used to synthesise 39 (*cis*-HPB) (Scheme 3.1).



Scheme 3.1: Syntheses of *trans*-[Pt(6)<sub>2</sub>(PPh<sub>3</sub>)<sub>2</sub>] (38) and *cis*-[Pt(6)<sub>2</sub>(dppe)] (39).  
 (a) CH<sub>2</sub>Cl<sub>2</sub>:<sup>i</sup>Pr<sub>2</sub>NH (5:1 v/v), CuI (7 mol%), R.T., 36 hours; (b) CH<sub>2</sub>Cl<sub>2</sub>:<sup>i</sup>Pr<sub>2</sub>NH (3:1 v/v), CuI (9 mol%), R.T., 36 hours.

For both complexes, when the reaction had reached completion (i.e. when starting materials had been consumed, as indicated by TLC), the solvent was removed *in vacuo* and

the residue redissolved in  $\text{CH}_2\text{Cl}_2$  and washed with water (x3) in order to remove diisopropyl-ammonium salts formed as side-products. For *trans* complex **38**, purification was achieved by column chromatography on silica. Elution with hexane: $\text{CH}_2\text{Cl}_2$  (2:1 v/v), followed by precipitation from a stirring excess of methanol afforded **38** as an off-white powder in 57 % yield. For *cis* complex **39**, column chromatography on silica eluting with  $\text{CH}_2\text{Cl}_2$ :hexane (1:1 v/v) afforded the desired *cis*-configured complex **39** as a pale yellow solid in 53 % yield.

The two products were characterised by  $^1\text{H}$ ,  $^{13}\text{C}$   $\{^1\text{H}\}$  and  $^{31}\text{P}$   $\{^1\text{H}\}$  NMR spectroscopy, elemental analysis and infrared spectroscopy. A MALDI-TOF mass spectrum for **38** (*trans*-HPB) was obtained which consisted of a peak centred at  $m/z = 2394.2241$  m.u. for  $[\text{M}]^+$ , which is in good agreement with the calculated value of 2394.2269 m.u. for  $[\text{C}_{164}\text{H}_{168}\text{P}_2\text{Pt}]^+$ . For **39** (*cis*-HPB), the peak at  $m/z = 2268.1777$  m.u. in the MALDI-TOF mass spectrum corresponds to  $[\text{M}]^+$ , which matches well to the calculated value of  $m/z = 2268.1800$  m.u. for  $[\text{C}_{154}\text{H}_{162}\text{P}_2\text{Pt}]^+$ .

### 3.2.1.1 $^1\text{H}$ NMR spectroscopic characterisation of **38**

The  $^1\text{H}$  NMR spectrum of *trans*- $[\text{Pt}(\mathbf{6})_2(\text{PPh}_3)_2]$  (**38**) is shown in Figure 3.6. The molecule is highly symmetric, with 2 axes of symmetry evident (inset, Figure 3.6), which considerably simplifies the NMR spectrum of the complex. As a result, only one quarter of the total proton signals in the molecule appear in the spectrum and the integration calculated for each signal is correspondingly four times greater than is evident.

The most downfield signals in the  $^1\text{H}$  NMR spectrum of complex **38** ( $\delta$  7.65 ppm) are due to the protons located on the  $\text{PPh}_3$  phenyl rings. The most deshielded of these can be assigned to the *ortho* protons which integrates for 12H in total, resulting from 6 protons on each of two triphenylphosphine groups. The signal appears as a multiplet, coupling initially with the adjacent *meta* proton and also with the NMR active  $^{31}\text{P}$  nucleus. The signal assigned to the *para* protons ( $\delta$  7.21 ppm) can be differentiated from that assigned to the *meta* protons on the  $\text{PPh}_3$  moiety (both of which appear as a triplet,  $^3J_{\text{HH}} = 7.3$  Hz), on the basis of its integration (6H) compared to that of  $\delta$  7.14 ppm (*meta*) (12H). The hexaphenylbenzene ligands account for the series of doublets between  $\delta$  5.7-6.9 ppm for four chemically inequivalent AB ring systems.

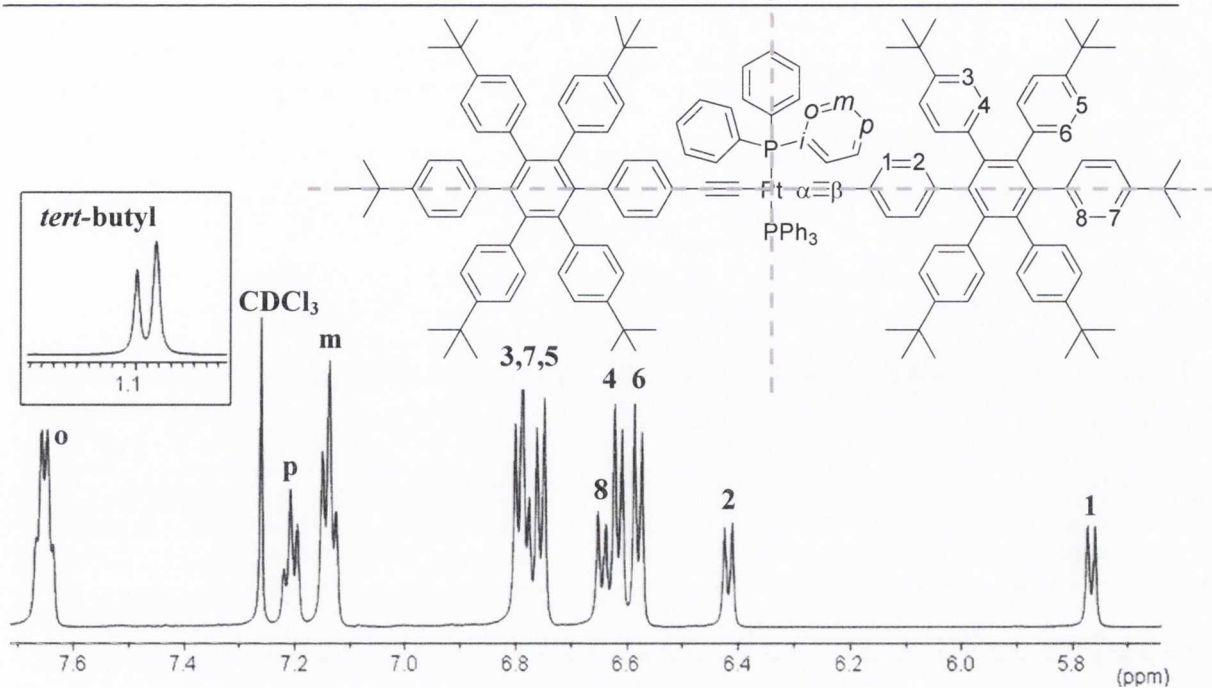


Figure 3.6:  $^1\text{H}$  NMR spectrum of **38** in  $\text{CDCl}_3$  (600.1 MHz, R.T.) showing the aromatic region, with inset *tert*-butyl region. Atom labelling as per inset figure.

H1 and H2 located on the phenyl ring closest to the acetylene moiety were identified by selective one dimensional NOE “through-space” NMR experiments (Figure 3.7). Irradiation at the corresponding resonance frequency for the signal occurring at  $\delta$  5.76 ppm (Figure 3.7, B) results in an NOE enhancement on adjacent spin systems through space, indicating that these protons must be located close *in space* to the irradiated spin. In this case, the strongest positive signal occurs at  $\delta$  6.42 ppm indicating that this doublet is adjacent to the doublet at  $\delta$  5.76 ppm (the irradiated signal appears inverted on the NOE spectrum). This suggests that these two doublets constitute a phenyl ring AB system, which can be confirmed by a  $^1\text{H}$ - $^1\text{H}$  COSY experiment. The converse is observed upon irradiation at  $\delta$  6.42 ppm (Figure 3.7, C). More interestingly, positive signals are seen for the protons on the phosphine moieties upon irradiation at  $\delta$  5.76 ppm which are only very weakly observed upon  $\delta$  6.42 ppm irradiation. This indicates that H1 occurs at the more upfield position ( $\delta$  5.76 ppm) as it is closest in space to the phosphine co-ligand and the more downfield signal can be assigned to H2. An additional effect shown in C (Figure 3.7) is that irradiation at  $\delta$  6.42 ppm also produces positive results at  $\delta$  6.79 and 6.62 ppm. This allows us to identify these signals as located on the phenyl ring adjacent to the H1-H2 ring, i.e. containing H3 and H4.

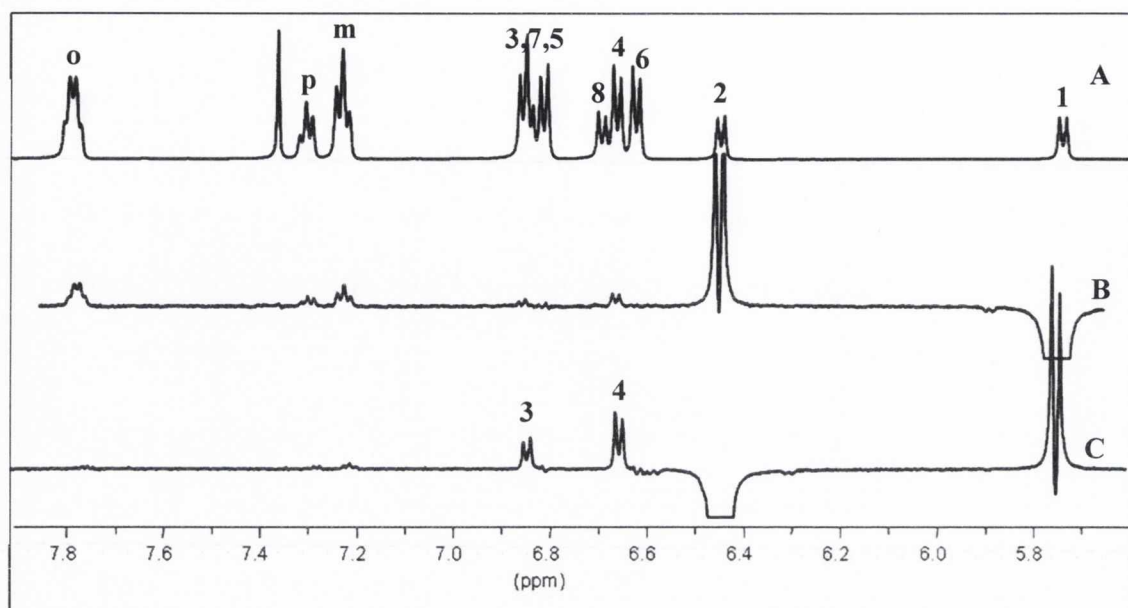


Figure 3.7: Compiled  $^1\text{H}$  NMR experiments for **38** (in  $\text{CDCl}_3$ ): A)  $^1\text{H}$  NMR spectrum (aromatic region); B) Selective 1D NOE experiment, irradiating at 3,456 Hz ( $\delta$  5.76 ppm); C) Selective 1D NOE experiment, irradiating at 3,852 Hz ( $\delta$  6.42 ppm).

The appearance of H1 and H2 on **38** at such upfield positions demonstrates the dramatic change in the chemical shifts experienced upon attachment of the electron-rich Pt-acetylide moiety, in contrast to that observed in the free ligand, ethynyl-hexaphenylbenzene (**6**), where H1 and H2 are the most downfield shifts (H1:  $\delta$  6.99 ppm; H2:  $\delta$  6.84 ppm).

In each of the five phenyl rings that are substituted in the *para* position by a *tert*-butyl group, selective NOE experiments irradiating at the frequency of either one of the *tert*-butyl groups ( $\delta$  1.08-1.10 ppm, the signals are too close in chemical shift to be able to selectively irradiate one signal), give positive signals for protons located between  $\delta$  6.75-6.80 ppm. This identifies H3, H5 and H7 closest to the *tert*-butyl moieties. By  $^1\text{H}$ - $^1\text{H}$  COSY, the adjacent proton on each of the three ring systems can be identified. Finally, the H5/H6 phenyl ring and the H7/H8 phenyl ring can be differentiated on the basis that H7 and H8 have an integration value half of that of H5 and H6. Specifically, the doublet at  $\delta$  6.64 ppm must be attributed to H8.

### 3.2.1.2 $^{13}\text{C}$ NMR spectroscopic characterization of **38**

The  $^{13}\text{C}$  NMR DEPT 45 experiment for *trans*-[Pt(**6**)<sub>2</sub>(PPh<sub>3</sub>)<sub>2</sub>] (**38**) is shown in Figure 3.8. Quaternary carbons do not appear in DEPT 45 NMR experiments and so the spectrum is simplified, displaying only CH, CH<sub>3</sub> (and CH<sub>2</sub>) signals.

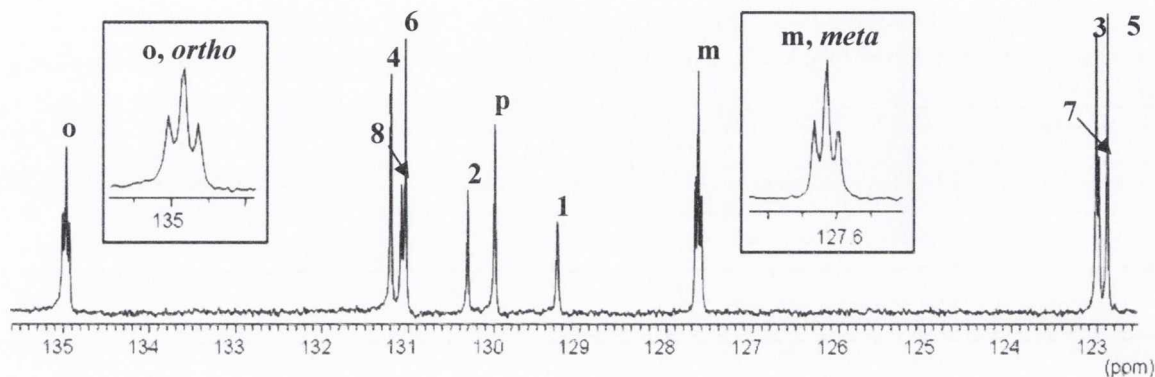


Figure 3.8:  $^{13}\text{C}$   $\{^1\text{H}\}$  DEPT 45 experiment for **38** ( $\text{CDCl}_3$ , 150.9 MHz, R.T.) showing the aromatic region with atom labelling as per inset Figure 3.6.

The two aromatic CH signals attributable to each of the *tert*-butyl phenyl rings are easily assigned *via* HSQC  $^1\text{H}$ - $^{13}\text{C}$  correlation spectroscopy (Heteronuclear Single Quantum Coherence). CH signals in the 3, 7 and 5 positions closest to the *tert*-butyl substituents are the most upfield of the methine signals, occurring quite close together at  $\delta$  123.00, 122.97 and 122.87 ppm respectively. Their adjacent methine signals, 4, 8 and 6 also appear in close proximity to each other, between  $\delta$  131.01-131.18 ppm (Figure 3.8).

The most interesting feature of this spectrum is the heteronuclear coupling of *ortho* and *meta* carbon signals on the PPh<sub>3</sub> ligands to the nearby NMR active  $^{31}\text{P}$  nucleus (100 % abundance, spin =  $\frac{1}{2}$ ). The *ortho* CH signal appears as a *pseudo*-triplet at  $\delta$  134.96 ppm with a coupling constant ( $J_{\text{PC}}$ ) of 7 Hz due to coupling of the  $^{13}\text{C}$ - $^{31}\text{P}$  nuclei (Figure 3.8). Similarly, the *meta* methine signal occurs at  $\delta$  127.61 ppm with  $J_{\text{PC}} = 6$  Hz. In contrast, the CH signal in the *para* position on the phosphine phenyl ring is a singlet, too distant from the  $^{31}\text{P}$  to experience a coupling effect. The reason for *ortho* and *meta* carbons appearing as *pseudo*-triplets is not immediately obvious. In the *ortho* case, the carbon atom can couple to one  $^{31}\text{P}$  nucleus through two bonds, which should result in the carbon signal being split into a doublet. However, the attached platinum atom three bonds away from the *o*-CH also has a spin active nucleus ( $^{195}\text{Pt}$  33.8 % abundance, spin =  $\frac{1}{2}$ ) and another

phosphorus atom is located four bonds away, one or both of which must have an effect on the magnetic environment about the methine signal. A similar effect is observed for the *meta* carbon. In addition, the *meta*  $J_{\text{PC}}$  coupling constant would be expected to be an order of magnitude less than that of the *ortho* carbon as the  $^{31}\text{P}$  nucleus is three bonds away. Similar coupling of the *ortho* and *meta* phenyl ring carbons bond to phosphorus has been reported, for example for a series of *cis*-[Pt(dppe)(C≡CAr)<sub>2</sub>] complexes and for the complex *trans*-[Pt(PPh<sub>3</sub>)<sub>2</sub>(C≡C-*p*-Ph-Ph-*p*-C≡CH)(C≡C-Ph-*p*-NO<sub>2</sub>)].<sup>181,184</sup> The *ipso* quaternary carbon which directly attaches the phenyl rings to the phosphine atom (not evident in the DEPT spectrum), should appear as a doublet due to P-C coupling, but partially overlaps with the signal for C4 ( $C_i$ ;  $\delta$  131.37 ppm).

The  $^{13}\text{C}$  { $^1\text{H}$ } NMR spectrum of **38** exhibits two quaternary carbon signals at  $\delta$  113.42 and 114.08 ppm, which can be attributed to  $C_\alpha$  and  $C_\beta$  of the C≡C moiety attached to the Pt(II) metal centre. It is typically possible to distinguish  $C_\alpha$  (closest to the Pt centre) from  $C_\beta$  by means of an examination of their coupling constants with the adjacent NMR spin-active  $^{195}\text{Pt}$  nucleus (33.8 % spin-active abundance). The closer proximity of  $C_\alpha$  than  $C_\beta$  to the metal centre usually results in a larger Pt-C coupling constant (1 bond coupling > geminal 2-bond coupling), i.e.  $^1J_{\text{Pt-C}\alpha} > ^2J_{\text{Pt-C}\beta}$ .<sup>115,134</sup> Unfortunately, despite long accumulation times it was not possible to extract coupling constants and thereby distinguish  $C_\alpha$  from  $C_\beta$  by this method for any of the four complexes (**38-41**). An alternative method was employed to identify the signals. Long-range  $^1\text{H}$ - $^{13}\text{C}$  correlation spectroscopy (HMBC) shows that H1 experiences a long-range coupling to the signal at  $\delta$  114.08 ppm, which is correspondingly assigned as  $C_\beta$  (coupling through three bonds), and a weaker long-range coupling to the signal at  $\delta$  113.42 ppm, assigned as  $C_\alpha$  (coupling through four bonds).

### 3.2.1.3 $^1\text{H}$ NMR characterisation of **39**

The  $^1\text{H}$  NMR spectrum of *cis*-[Pt(**6**)<sub>2</sub>(dppe)] (**39**) in CDCl<sub>3</sub> is shown in Figure 3.9. Two features simplify the spectrum of **39**. The first of these is a plane of symmetry drawn vertically through the centre of the molecule (inset, Figure 3.9). Secondly, free rotation of each hexaphenylbenzene core about the acetylene renders protons on either side of the dashed line chemically equivalent (Figure 3.9).



The proton closest to the Pt(II)-acetylide, H1, is the most upfield of the aromatic signals, appearing as a doublet at  $\delta$  6.55 ppm ( $^3J_{\text{HH}} = 8.3$  Hz) in *cis* complex **39**. The proximity of the electron-rich metal-alkynyl moiety has a shielding effect on the magnetic environment of H1, an effect also observed for *trans* complex **38** (H1:  $\delta$  5.76 ppm). H2 is the next more downfield signal, overlapping with other signals in a multiplet at  $\delta$  6.60 ppm. The remainder of the phenyl ring signals appear as two multiplets between  $\delta$  6.60-6.80 ppm (Figure 3.9). The signals relating to H1 and H2 were assigned by comparison with **38** (*trans*-HPB) and a process of elimination using selective NOE experiments. One signal is observed at  $\delta$  1.09 ppm (multiplet) that integrates for 90H for ten *tert*-butyl groups. Irradiation at the resonance frequency of this *tert*-butyl signal produced positive results in the two multiplets between  $\delta$  6.63-6.80 ppm, but none at  $\delta$  6.55 ppm (H1) or for the signal on the edge of the more upfield multiplet, specifically at  $\delta$  6.60 ppm (H2). This reaffirms the assignment of H1 and H2 by indicating there is no through-space interaction with a *tert*-butyl group for these signals, i.e. they are not due to protons on a *tert*-butyl phenyl ring.

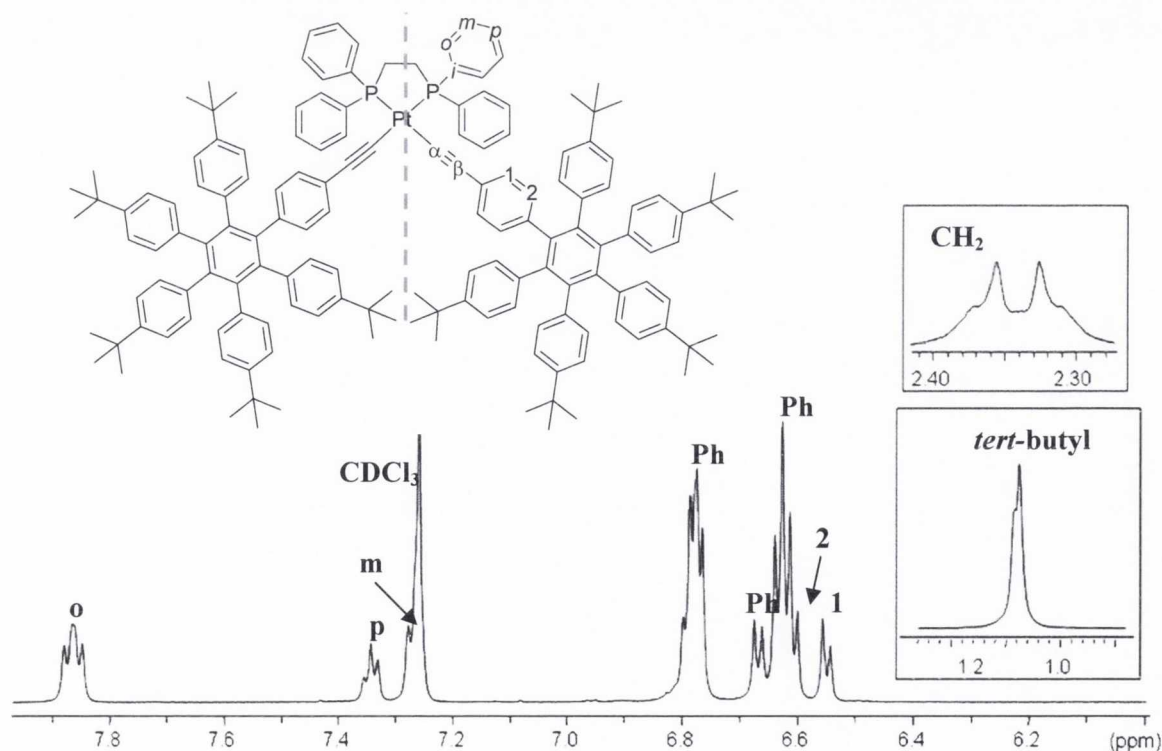


Figure 3.9:  $^1\text{H}$  NMR spectrum of **39** ( $\text{CDCl}_3$ , 600.1 MHz, R.T.) showing the aromatic region, with inset portions of aliphatic region. Atom labelling as per inset figure.

As observed for **38** (*trans*-HPB), the *ortho* phenyl ring signals on the phosphine moiety are the most downfield, appearing as a multiplet at  $\delta$  7.86 ppm. The *para* signal appears as a triplet centred at  $\delta$  7.34 ppm, whose coupling to two equivalent *meta* protons splits the signal with  $^3J_{\text{HH}} = 8$  Hz. The chemical shift of *meta*-positioned protons is the most upfield of the phosphine signals and is coincident with that of the residual  $\text{CDCl}_3$  peak so its multiplicity was not defined (Figure 3.9). An additional peak at  $\delta$  2.34 ppm can be attributed to the methylenic protons of the dppe group,  $\text{P}(\text{CH}_2)_2\text{P}$  ( $\text{CH}_2$  inset, Figure 3.9). The signal appears as a multiplet due to coupling of the proton signal with the adjacent  $^{31}\text{P}$  nucleus.

#### 3.2.1.4 The *trans* influence: effects on $^1\text{H}$ NMR chemical shifts of *cis*(**39**) vs. *trans*(**38**)

The *trans* influence is a common phenomenon in platinum(II) square-planar coordination chemistry and has been much investigated since early studies by Pidcock *et al.* in 1966.<sup>185</sup> It is a thermodynamic effect resulting from the fact that ligands which are mutually *trans* to each other about the metal centre share the same set of molecular orbitals. It is essentially dominated by metal-ligand  $\sigma$ -bonding, where  $\sigma$ -donation of a ligand into the empty anti-bonding metal d-orbital(s) results in the relative weakening of the metal-ligand bond located *trans*. Consequently, the ground state properties of the *trans* ligand can be affected, e.g. NMR chemical shifts and coupling constants, metal-ligand bond lengths (and correspondingly bond strengths) and IR stretching frequencies. As a result, *cis* and *trans* isomers of the same compound can display significantly different properties. One of the most famous examples of this involves  $\text{Pt}(\text{NH}_3)_2\text{Cl}_2$ , whose *cis* isomer “cisplatin” is an effective anti-cancer drug but the *trans* isomer possesses no such activity.<sup>186-188</sup>

Anionic acetylide ligands ( $\text{C}\equiv\text{CAr}$ ) possess strong  $\sigma$ -donor (and relatively weak  $\pi$ -acceptor) functionality and exert a higher *trans* influence in their  $d^8$  transition-metal complexes than neutral phosphines.<sup>189</sup> They correspondingly have a greater influence on electron density at the Pt(II) metal centre. In *trans*- $[\text{Pt}(\mathbf{6})_2(\text{PPh}_3)_2]$  (**38**), the  $\text{PPh}_3$  moieties are located mutually *trans* to each other. In contrast, in *cis*- $[\text{Pt}(\mathbf{6})_2(\text{dppe})]$  (**39**), an acetylide and a phosphine moiety share metal orbitals along the molecular axis.

Table 3.1 presents selected  $^1\text{H}$  NMR data for *cis* and *trans* complexes **39** and **38**. H1 and H2 protons are considerably more shielded in **38** (*trans*-HPB) than in **39** (*cis*-HPB). In **38**,

the *trans* acetylide ligands both strongly  $\sigma$ -donate into the empty Pt  $d_{x^2-y^2}$  orbital (and both simultaneously receiving a degree of electron density *via*  $\pi$ -back donation into empty  $p\pi^*$  ( $C\equiv CAr$ ) orbitals). The significant increase in electron density at the metal centre and along the [acetylide-Pt-acetylide] axis results in considerably more shielded H1 and H2 protons in *trans* complex (**38**) than in *cis*. Examining the chemical shifts of the phosphine phenyl rings, the effect of locating a  $PPh_3$  and an acetylide on opposite sides on the coordination centre in *cis* complex (**39**) is to cause a downfield shift of *ortho*, *meta* and *para* protons relative to those in *trans* (**38**).

Table 3.1:  $^1H$  NMR spectroscopic data and assignments of H1, H2 and phosphine protons in complexes **38** and **39** reported in  $CDCl_3$ . Chemical shifts ( $\delta$ ) in ppm.

Complex	Proton				
	H1	H2	<i>ortho</i> (o)	<i>meta</i> (m)	<i>para</i> (p)
<i>trans</i> -[Pt( <b>6</b> ) <sub>2</sub> ( $PPh_3$ ) <sub>2</sub> ] ( <b>38</b> )	5.76	6.42	7.65	7.14	7.21
<i>cis</i> -[Pt( <b>6</b> ) <sub>2</sub> (dppe)] ( <b>39</b> )	6.55	6.60	7.86	7.28	7.34

The effect of this *trans* influence will be encountered again in the comparison of NMR chemical shifts in *trans* and *cis* complexes (**40** and **41**) containing cyclised HBC ligands and in an examination of  $^{31}P$  NMR spectra for the four complexes.

### 3.2.1.5 $^{13}C$ $\{^1H\}$ NMR Characterisation of **39**

The  $^{13}C$   $\{^1H\}$  NMR spectrum of *cis* complex **39** is displayed in Figure 3.10. A simple 2D  $^1H$ - $^{13}C$  correlation experiment (HSQC) was used to identify and assign the carbon NMR signals.

As observed for *trans* complex **38**, *ortho* and *meta* methine signals both appear as *pseudo*-triplets due to coupling with the  $^{31}P$  NMR active nucleus (*ortho*:  $\delta$  133.49 ppm; *meta*:  $\delta$  128.54 ppm) and the *para* CH appears as a singlet ( $\delta$  130.87 ppm). Once again these display quite similar coupling constants (*ortho*:  $J_{PC} = 6$  Hz; *meta*:  $J_{PC} = 5$  Hz), despite the fact that the *ortho* carbon is located two bonds away from the phosphorus atom while the *meta* carbon is located three bonds away.<sup>181,184</sup> An interesting feature in this spectrum is the presence of a *pseudo*-doublet for the *ipso* carbon directly attached to the phosphorus

atom ( $\delta$  129.92 ppm, Figure 3.10). Heteronuclear coupling of this carbon to the P nucleus splits the signal into a doublet with  $J_{PC} = 54$  Hz, with the greater coupling constant compared to *ortho* and *meta* carbons indicative of a closer interaction. This value falls within the range expected for one-bond coupling constants between  $^{13}\text{C}$  and  $^{31}\text{P}$ .<sup>67</sup>

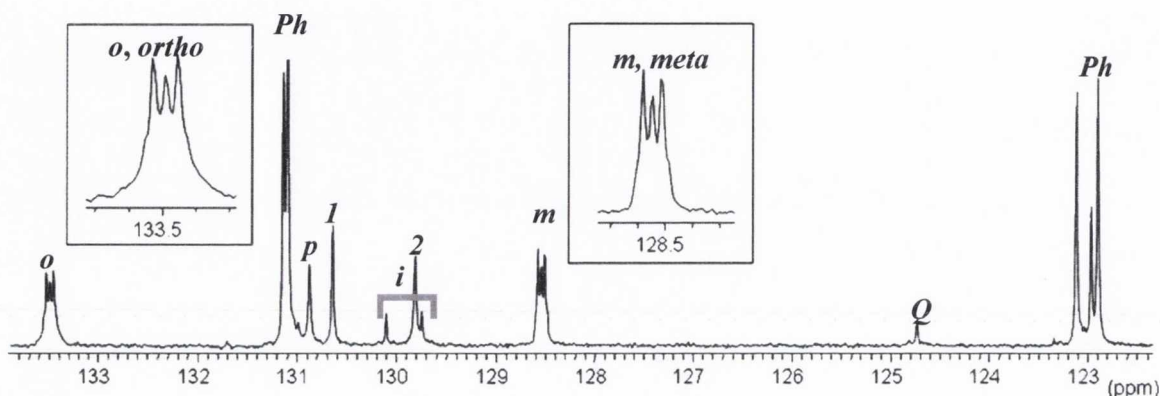


Figure 3.10:  $^{13}\text{C}$  NMR spectrum of *cis*-[Pt(6)<sub>2</sub>(dppe)] (**39**) showing a section of the aromatic region ( $\text{CDCl}_3$ , 150.9 MHz, R.T.). Atom labelling as per inset Figure 3.9 (*Q* = quaternary carbon signal).

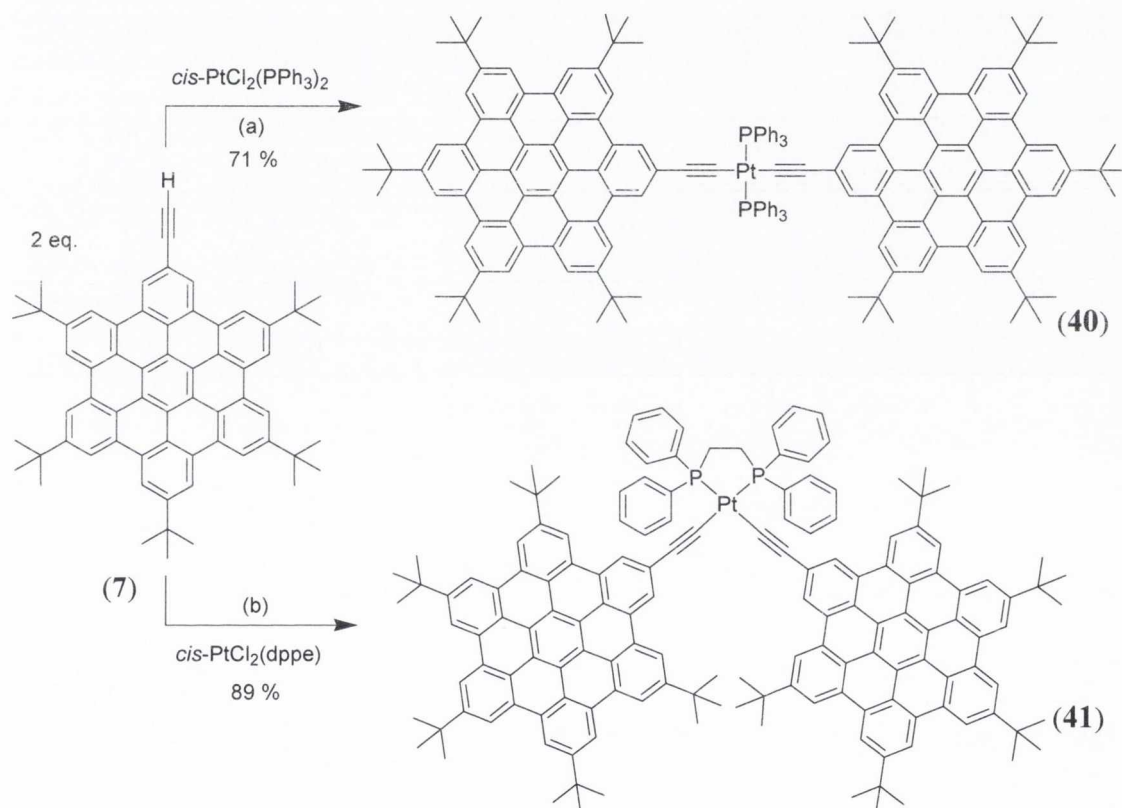
In the aliphatic region of the  $^{13}\text{C}$  spectrum, the methylene group of the dppe ligand appears as a multiplet at  $\delta$  27.76 ppm, again affected by the  $^{13}\text{C}$ - $^{31}\text{P}$  heteronuclear coupling. Two signals at  $\delta$  31.26 and 31.19 ppm can be assigned to the *tert*-butyl substituents on the polyphenylene ligands. Finally, the two alkynyl carbon signals ( $-\text{C}_\alpha\equiv\text{C}_\beta-$ ) occur at  $\delta$  112.98 and 112.75 ppm. The signal due to  $\text{C}_\alpha$  was distinguished from the  $\text{C}_\beta$  signal using a  $^1\text{H}$ - $^{13}\text{C}$  HMBC experiment, as detailed for **38** (*trans*-HPB).

### 3.2.2 Syntheses of *trans*-[Pt(7)<sub>2</sub>(PPh<sub>3</sub>)<sub>2</sub>] (**40**) and *cis*-[Pt(7)<sub>2</sub>(dppe)] (**41**):

#### Ethynyl-HBC as $\sigma$ -acetylide.

The syntheses of HBC-containing complexes *trans*-[Pt(7)<sub>2</sub>(PPh<sub>3</sub>)<sub>2</sub>] (**40**, *trans*-HBC) and *cis*-[Pt(7)<sub>2</sub>(dppe)] (**41**, *cis*-HBC) were undertaken using copper(I)-catalysed Sonogashira-Hagihara coupling reactions (Scheme 3.2).<sup>179</sup> In both cases, CuI was employed as catalyst with two equivalents of ethynyl-hexa-*peri*-hexabenzocoronene (**7**) as terminal acetylene and a suitable Pt(II) metal precursor salt. The reactions were carried out in dry, degassed  $\text{CH}_2\text{Cl}_2$ : $^i\text{Pr}_2\text{NH}$ , stirring under argon in darkness for two days.

For both reactions, the solvent was removed to dryness under vacuum and the residue redissolved in a mixture of  $\text{CH}_2\text{Cl}_2$  and  $\text{CHCl}_3$  and washed with water. Purification of **40** was achieved by column chromatography on silica, using petroleum ether: $\text{CH}_2\text{Cl}_2$  as eluent, followed by precipitation from excess methanol to afford the product as a deep yellow powder in 71 % yield. Complex **41** was filtered off as a bright yellow powder following precipitation from methanol and was washed with copious amounts of cold methanol (89 % yield). The higher yield of **41** (*cis*-HBC) is due to its insolubility relative to **40** (*trans*-HBC).



Scheme 3.2: Synthesis of *trans*-[Pt(7)<sub>2</sub>(PPh<sub>3</sub>)<sub>2</sub>] (**40**) and *cis*-[Pt(7)<sub>2</sub>(dppe)] (**41**).  
 (a)  $\text{CH}_2\text{Cl}_2$ : $i\text{-Pr}_2\text{NH}$  (2.5:1 v/v), CuI (10 mol%), R.T.; (b)  $\text{CH}_2\text{Cl}_2$ : $i\text{-Pr}_2\text{NH}$  (3:1 v/v), CuI (7 mol%), R.T.

The two products, **40** (*trans*-HBC) and **41** (*cis*-HBC) were fully characterised using  $^1\text{H}$ ,  $^{13}\text{C}$  { $^1\text{H}$ } and  $^{31}\text{P}$  { $^1\text{H}$ } NMR spectroscopy, elemental analyses and infrared spectroscopy. The MALDI-TOF mass spectrum of **40** displays a peak centred at  $m/z = 2371.0386$  m.u. for  $[\text{M}+\text{H}]^+$  which corresponds well to the calculated value of 2371.0469 mass units for  $[\text{C}_{164}\text{H}_{145}\text{P}_2\text{Pt}]^+$ . Similarly, the presence of **41** is confirmed in its MALDI-TOF mass spectrum, with a peak with  $m/z = 2244.9922$  m.u. for  $[\text{M}+\text{H}]^+$  which is in excellent agreement with the calculated value  $m/z = 2245.0000$  m.u.  $[\text{C}_{154}\text{H}_{139}\text{P}_2\text{Pt}]^+$ .

3.2.2.1  $^1\text{H}$  NMR spectroscopic characterization of **40** and **41**

The  $^1\text{H}$  NMR spectra of *trans*-[Pt(**7**)<sub>2</sub>(PPh<sub>3</sub>)<sub>2</sub>] (**40**) and *cis*-[Pt(**7**)<sub>2</sub>(dppe)] (**41**) are very similar and are shown together in Figure 3.11.

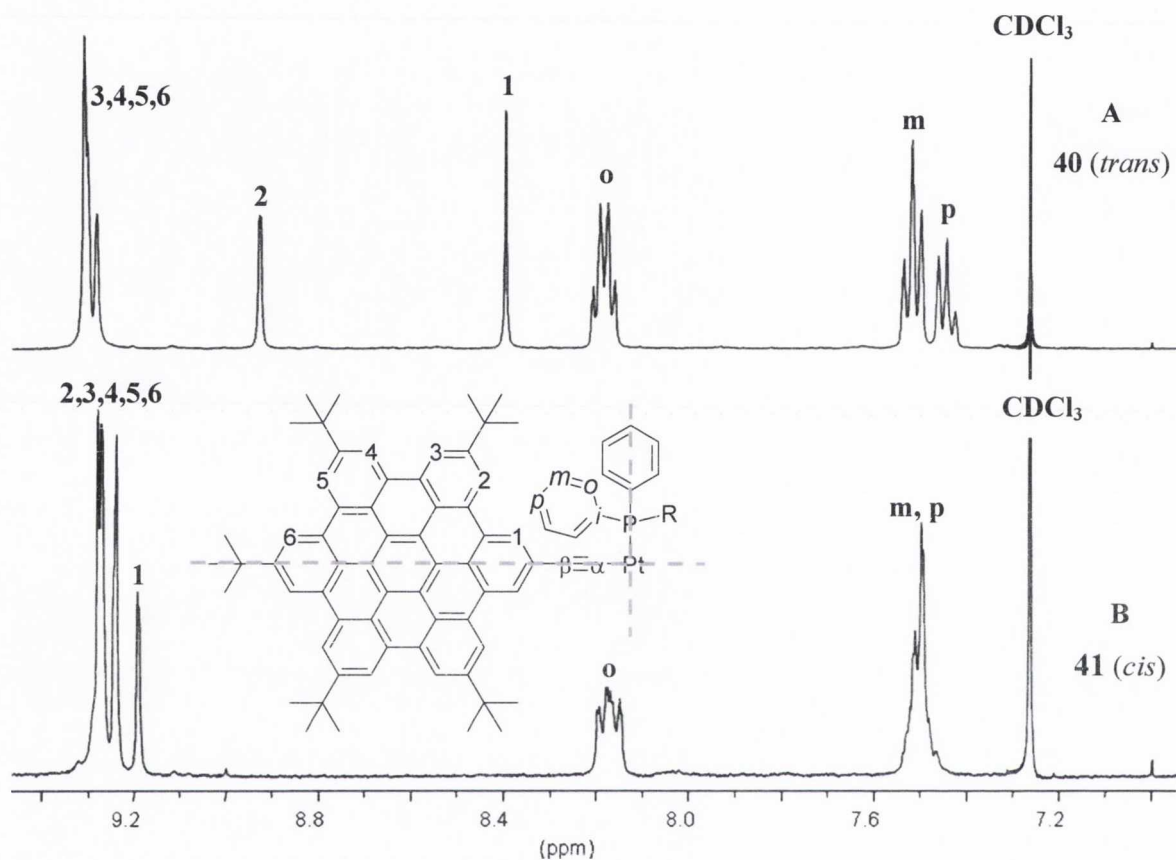


Figure 3.11: Aromatic region of the  $^1\text{H}$  NMR spectra of **40** (600.1 MHz, R.T.) and **41** (400.1 MHz, R.T.) in  $\text{CDCl}_3$  showing the aromatic regions. Atom labelling as per partial inset figure (**40**:  $R=\text{Phenyl}$ , **41**:  $R=\text{CH}_2$ ), full complex structures inset Scheme 3.2.

Complexes *trans*-[Pt(**7**)<sub>2</sub>(PPh<sub>3</sub>)<sub>2</sub>] (**40**) and *cis*-[Pt(**7**)<sub>2</sub>(dppe)] (**41**) exhibit the same symmetry as their uncyclised analogues. Six singlets due to the HBC unit would be anticipated in the spectra of the two complexes. The effect of complexation upon the  $^1\text{H}$  NMR chemical shifts of the HBC protons is quite dramatic on comparison of the spectra in Figure 3.11 to the  $^1\text{H}$  NMR spectrum of free cyclised HBC ligand **7** (which consists of 6 singlets between between  $\delta$  8.6–9.2 ppm). The HBC protons occur significantly downfield of the phosphine phenyl ring signals and were assigned with the aid of long-range  $^1\text{H}$ - $^1\text{H}$  COSY experiments (TOCSY). These are considerably downfield in comparison to complexes **38** and **39** containing hexaphenylbenzenes as a result of the enhanced electron

delocalisation and aromaticity of the HBC platforms. Specifically, the HBC protons are deshielded as a result of the magnetic anisotropic ring current of the graphene core.<sup>5,67</sup>

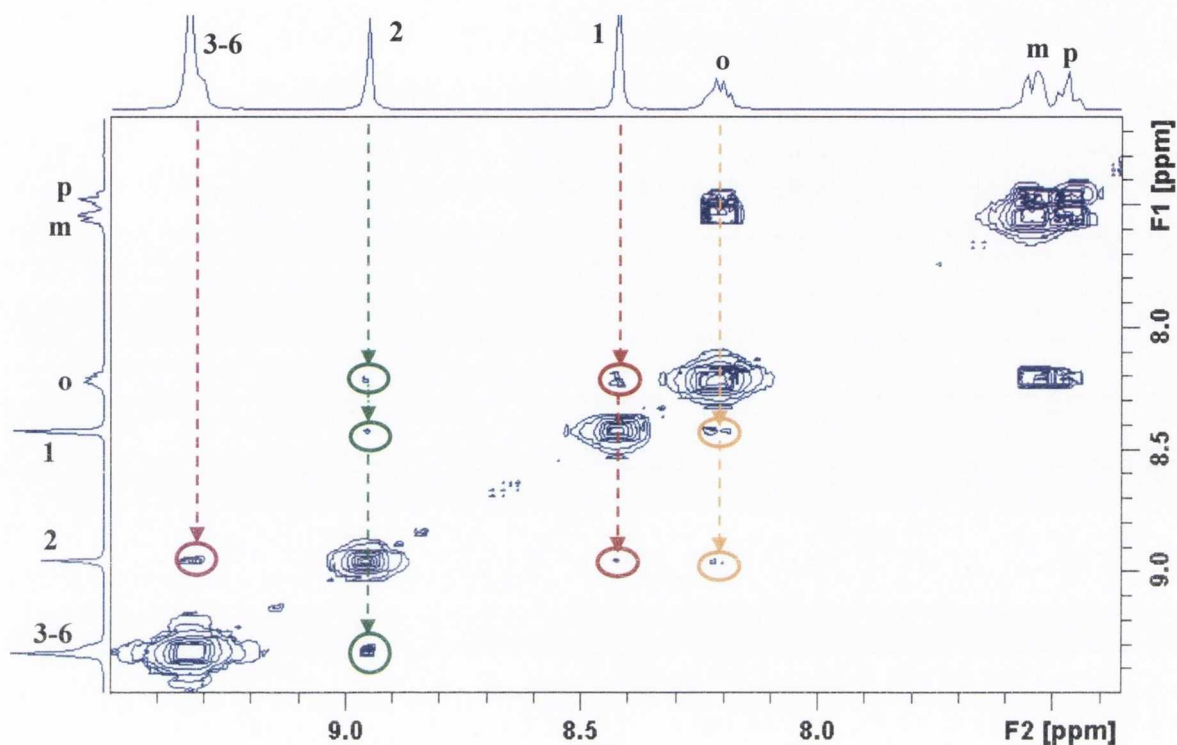


Figure 3.12: Long-range  $^1\text{H}$ - $^1\text{H}$  COSY experiment for **40** (*trans*-HBC) in  $\text{CDCl}_3$  showing H1 and H2 interactions with *ortho*-protons on phosphine phenyl ring.

The long-range  $^1\text{H}$ - $^1\text{H}$  COSY experiment for **40** (*trans*-HBC) is shown in Figure 3.12. The singlet at  $\delta$  8.40 ppm, the most shielded of the HBC protons, has a long-range correlation with the *ortho* protons on the phosphine and also with the singlet at  $\delta$  8.93 ppm. In contrast, the singlet at  $\delta$  8.93 ppm has a much weaker interaction with the *ortho* signal indicating that it is located further away from the phosphine, and also interacts with the multiplet at  $\delta$  9.28-9.31 ppm, which does not interact with either the *ortho* protons or the singlet at  $\delta$  8.40 ppm. On this basis, H1 and H2 closest to the Pt(II) acetylide are assigned as the most upfield of the singlets (H1:  $\delta$  8.40 ppm; H2:  $\delta$  8.92 ppm) and H3, H4, H5 and H6 signals overlap to appear as a multiplet between  $\delta$  9.28-9.31 ppm, integrating in total for 16H. An additional signal in **41** for the  $\text{CH}_2$  group of the (diphenylphosphino)ethane appears at  $\delta$  2.56 ppm.

Similarly, the majority of the HBC protons in **41** (*cis*-HBC) are located in two multiplets between  $\delta$  9.24-9.28 ppm. In contrast, H1 and H2 located closest to the acetylide axis are

considerably more upfield in **40** compared to **41** (where H1 appears at  $\delta$  9.19 ppm). This can once again be explained by the *trans* influence. In **40** (*trans*-HBC), two electron-rich HBC sheets are located mutually *trans* to each other through the Pt coordination centre. The resulting increase in electron density along the molecular axis has a shielding effect on H1 and H2 located closest to the metal centre. In **41**, a much more electron-poor PPh<sub>3</sub> is located opposite an acetylide-HBC and so the six non-equivalent aromatic protons appear in very similar magnetic environments.

In contrast, resonances for the phosphine phenyl ring aromatic proton signals are almost identical in **40** (*trans*-HBC) and **41** (*cis*-HBC), *para* and *meta* signals are more shielded relative to *ortho* signals. For both complexes, the *ortho* signal can be clearly identified on the basis of its multiplicity – its close proximity to the NMR active <sup>31</sup>P nucleus results in heteronuclear coupling between <sup>1</sup>H and <sup>31</sup>P atoms. In contrast, *meta* and *para* protons in this series of complexes are not affected by the phosphorus, and both appear as triplets in **40** (although *para* with half the integration value of that of the *meta* protons). In **41**, *meta* and *para* proton signals overlap to appear as a multiplet centred at  $\delta$  7.50 ppm. In general, this is analogous to the trend observed for complexes **38** and **39** containing uncyclised ligands.

### 3.2.2.2 Concentration and temperature dependence of <sup>1</sup>H NMR chemical shifts of **41**

The self-assembly of hexa-*peri*-hexabenzocoronene and related polyaromatic graphene subunits into aggregates held together by  $\pi$ -stacking between the electron-delocalised sheets is well known. Indeed this property has been frequently exploited in the study of HBCs as materials with high charge carrier mobility and as discotic liquid crystals, where the discs form columnar stacks in solution which in turn arrange into a two-dimensional array.<sup>12</sup> Similarly, the influence of the steric demand of flexible alkyl chains and rigid polyphenylene dendrons on the aggregation properties of HBC discs in solution has been thoroughly investigated.<sup>5,7,171</sup>

<sup>1</sup>H NMR spectroscopy is one of the techniques commonly used to investigate the self-assembly of polyaromatic graphene subunits in solution. The aromatic protons of hexa-*peri*-hexabenzocoronene derivatives are known to exhibit considerable temperature and concentration dependence.<sup>5,171</sup>



The relatively poor solubility of *cis*-[Pt(7)<sub>2</sub>(dppe)] (**41**) compared to *trans*-[Pt(7)<sub>2</sub>(PPh<sub>3</sub>)<sub>2</sub>] (**40**) suggested that the *cis* configured complex must be subject to considerable aggregation effects. This prompted the measurement of a series of temperature and concentration dependent <sup>1</sup>H NMR spectra of **41**. The spectra were recorded in deuterated tetrachloroethane (d<sub>2</sub>-C<sub>2</sub>D<sub>2</sub>Cl<sub>4</sub>) whose higher boiling point relative to chloroform facilitated the recording of higher temperature NMR spectra. Temperature-dependent spectra (Figure 3.13) were recorded from 20-60 °C and concentration-dependent spectra were recorded over a concentration range of 0.1 mM – 10 mM (chemical shifts reported in Table 3.2).

The temperature-dependent spectra of the HBC protons in complex **41** (*cis*-HBC) are shown in Figure 3.13. In general, with increasing temperature a downfield shift is observed for the aromatic signals. For example, the resonance of H1 shifts from δ 9.24 ppm at 20 °C to δ 9.27 ppm at 60 °C (Table 3.2). This downfield shift with increasing temperature is also observed for the two multiplets containing HBC protons (labeled HBC(A) and HBC(B)) and for *ortho*, *meta* and *para* protons on the phenyl rings of the PPh<sub>3</sub> auxiliary ligand. Similarly, with decreasing concentration (100-fold), the aromatic HBC protons become more deshielded (H1: δ 9.23 ppm, 10 mM; δ 9.25 ppm, 0.1 mM). *Ortho* phosphine protons exhibit the same effect but the *meta/para* multiplet is only marginally affected (Table 3.2).

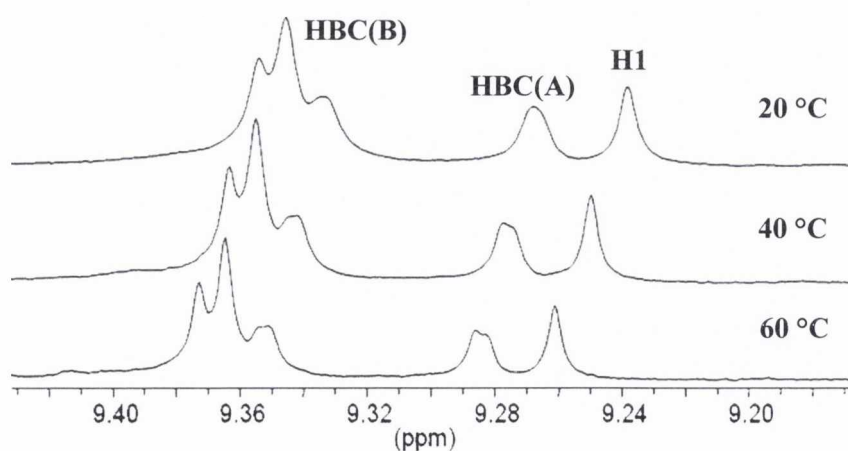


Figure 3.13: Temperature-dependent <sup>1</sup>H NMR spectra of **41** showing the HBC platform protons in d<sub>2</sub>-C<sub>2</sub>D<sub>2</sub>Cl<sub>4</sub> solution (600.1 MHz), labelled A and B.

Table 3.2:  $^1\text{H}$  NMR chemical shifts of **41** ( $\delta$ , ppm) of aromatic protons as determined from temperature and concentration dependent NMR spectra,  $d_2\text{-C}_2\text{D}_2\text{Cl}_4$ . (*o*, *m*, *p* = ortho, meta and para protons on phosphine phenyl rings; HBC(A), HBC(B) = multiplets due to HBC protons).

Proton \ Condition	Temperature			Concentration (R.T.)		
	20 °C	40 °C	60 °C	0.1 mM	1 mM	10 mM
H1	9.24	9.25	9.27	9.25	9.24	9.23
HBC(A)	9.27	9.28	9.30	9.29	9.27	9.26
HBC(B)	9.34	9.36	9.37	9.36	9.34	9.33
<i>o</i>	8.21	8.23	8.26	8.18	8.20	8.20
<i>m/p</i>	7.61	7.61	7.62	7.60	7.60	7.59

The downfield shift of  $^1\text{H}$  NMR chemical shifts with increasing temperature and increasing dilution is a result of a reduction in stacking of the HBC platforms in solution. Fewer molecules in solution or providing the species with the energy to break the strong interactions holding them together (by increasing the temperature), lessens the degree of intermolecular self-assembly. By further decreasing the concentrations under investigation, it has been shown that it is also possible to measure the association constants of the interacting units.<sup>5,171,190</sup>

These trends are typical of HBC derivatives and have been observed for numerous disc-like PAHs.<sup>3,5,7,12</sup> However, the magnitude of downfield shifts of the  $^1\text{H}$  NMR signals with increasing temperature and dilution (and over the same range as measured here) are usually in the order of 0.4-0.6 ppm for HBC units substituted with flexible long chains.<sup>5</sup> It has been noted that aromatic  $\pi$ - $\pi$  interactions are partially suppressed as the molecules are prevented from approaching each other when the periphery of the platform is substituted with bulky *tert*-butyl groups.<sup>3,28</sup> This explains the slightly smaller degree of change in chemical shift observed for **41** (*cis*-HBC). Similar concentration and temperature dependence measurements for **40** (*trans*-HBC) revealed that it undergoes self-assembly in solution to a lesser extent than **41** as evidenced by only marginal changes in proton resonance frequency.

### 3.2.2.3 $^{13}\text{C}\{^1\text{H}\}$ NMR spectroscopic characterization of **40** and **41**

The aromatic region of the  $^{13}\text{C}\{^1\text{H}\}$  DEPT 90 experiment, displaying only the CH signals, of *trans*-[Pt(**7**)<sub>2</sub>(PPh<sub>3</sub>)<sub>2</sub>] (**40**) is shown in Figure 3.14. The carbon signals were assigned using a 2D  $^1\text{H}$ - $^{13}\text{C}$  correlation experiment (HSQC).

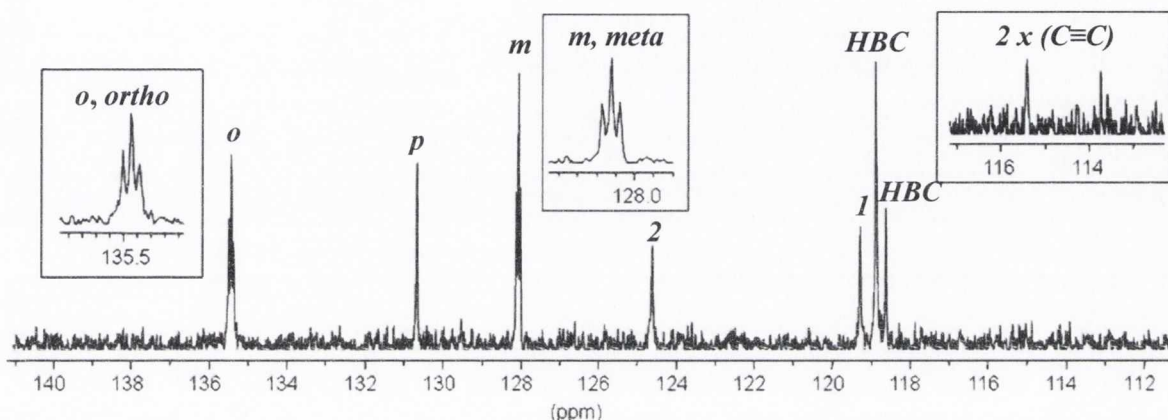


Figure 3.14:  $^{13}\text{C}\{^1\text{H}\}$  DEPT 90 experiment for **40** ( $\text{CDCl}_3$ , 150.9 MHz, R.T.) showing the aromatic region with atom labelling as per inset Figure 3.11. Inset acetylenic carbon region from  $^{13}\text{C}$  spectrum.

Similar patterns in the multiplicity and chemical shift of carbon signals due to the phosphine phenyl rings are observed for *trans*-[Pt(**7**)<sub>2</sub>(PPh<sub>3</sub>)<sub>2</sub>] (**40**) and *cis*-[Pt(**7**)<sub>2</sub>(dppe)] (**41**) and in general from *cis* to *trans* complexes in this series. These are summarised in Table 3.3.

Table 3.3: Comparative  $^{13}\text{C}$  NMR chemical shifts of complexes **38-41**, showing PPh<sub>3</sub> and quaternary acetylenic carbon signals,  $\text{CDCl}_3$ , room temperature. [ $\delta$ , ppm ( $J_{\text{PC}}$ , Hz)].

Complex	Ortho (o)	Meta (m)	Para (p)	Ipsos (i) <sup>a</sup>	C≡C
<i>trans</i> -[Pt( <b>6</b> ) <sub>2</sub> (PPh <sub>3</sub> ) <sub>2</sub> ] ( <b>38</b> )	134.96 (7)	127.61 (6)	129.97	131.37 <sup>b</sup>	114.08, 113.42
<i>trans</i> -[Pt( <b>7</b> ) <sub>2</sub> (PPh <sub>3</sub> ) <sub>2</sub> ] ( <b>40</b> )	133.45 (6)	128.07 (5)	130.68	131.27 (pt, 29)	115.41, 113.74
<i>cis</i> -[Pt( <b>6</b> ) <sub>2</sub> (dppe)] ( <b>39</b> )	133.49 (6)	128.54 (5)	130.87	129.92 (pd, 54)	112.98, 112.75
<i>cis</i> -[Pt( <b>7</b> ) <sub>2</sub> (dppe)] ( <b>41</b> )	133.62 (6)	128.76 (5)	131.27	130.01 (pd, 55)	113.55, 112.79

<sup>a</sup> pt = pseudo-triplet, pd = pseudo-doublet,  $^{31}\text{P}$ - $^{13}\text{C}$  coupling; <sup>b</sup> overlaps with CH signals.

For all four complexes, *ortho* and *meta* carbon signals appear as *pseudo*-triplets due to heteronuclear coupling between  $^{13}\text{C}$  and  $^{31}\text{P}$  (Table 3.3). *Ortho* carbons exhibit coupling constants ( $J_{\text{PC}}$ ) between 6-7 Hz, with *trans* marginally larger than those measured for *cis* complexes. *Meta* coupling constants are generally slightly smaller ( $J_{\text{PC}} = 5\text{-}6$  Hz), but would be expected to be significantly smaller than calculated, as the  $^{31}\text{P}$  nucleus is located three bonds away compared to two for the *ortho* position.<sup>181,184</sup> The *ortho* methine signal is always the most downfield of the  $\text{PPh}_3$  carbon resonances. The fact that the *para* CH appears as a singlet reflects the progressive distance of the *para* position from the  $^{31}\text{P}$  nucleus – it is too far away to interact with its magnetic field.

For each complex, two quaternary alkynyl carbon signals are observed for  $\text{C}_\alpha\equiv\text{C}_\beta$  of the acetylide (Table 3.3). For the *trans* complexes (**38**:  $\delta$  114.08, 113.42 ppm; **40**:  $\delta$  115.41, 113.74 ppm), these signals are shifted slightly downfield relative to the *cis* complexes (**39**:  $\delta$  112.98, 112.75 ppm; **41**:  $\delta$  113.55, 112.79 ppm) due to the *trans* influence of the  $\text{C}\equiv\text{C}$ . As discussed for complex **38** (*trans*-HPB) (Section 3.2.1.5), despite long accumulation times it was not possible to extract  $^{195}\text{Pt}$ - $^{13}\text{C}$  coupling constants for the acetylenic carbons and thereby distinguish  $\text{C}_\alpha$  from  $\text{C}_\beta$ .

### 3.2.3 Confirmation of *cis* and *trans* configurations (38-41): $^{31}\text{P}$ NMR and infrared spectroscopic analysis

$^{31}\text{P}$   $\{^1\text{H}\}$  NMR spectroscopy was a useful tool in confirming the *cis/trans* configuration of the polyphenylene acetylides about the Pt(II) coordination centre. As a result of the symmetry of all four complexes, the two phosphorus atoms present are in equivalent environments, to give rise to one  $^{31}\text{P}$   $\{^1\text{H}\}$  signal in the spectrum of each complex. However, as each phosphorus atom is directly attached to a Pt(II) metal centre ( $^{195}\text{Pt}$ , spin =  $\frac{1}{2}$ , 33.8 % abundance), the  $^{31}\text{P}$  nucleus will couple to the NMR active  $^{195}\text{Pt}$  resulting in a doublet separated by  $^1J_{\text{P-Pt}}$  centred around a single peak. This is shown in the  $^{31}\text{P}$   $\{^1\text{H}\}$  spectra of **38** and **39** shown in Figure 3.15.

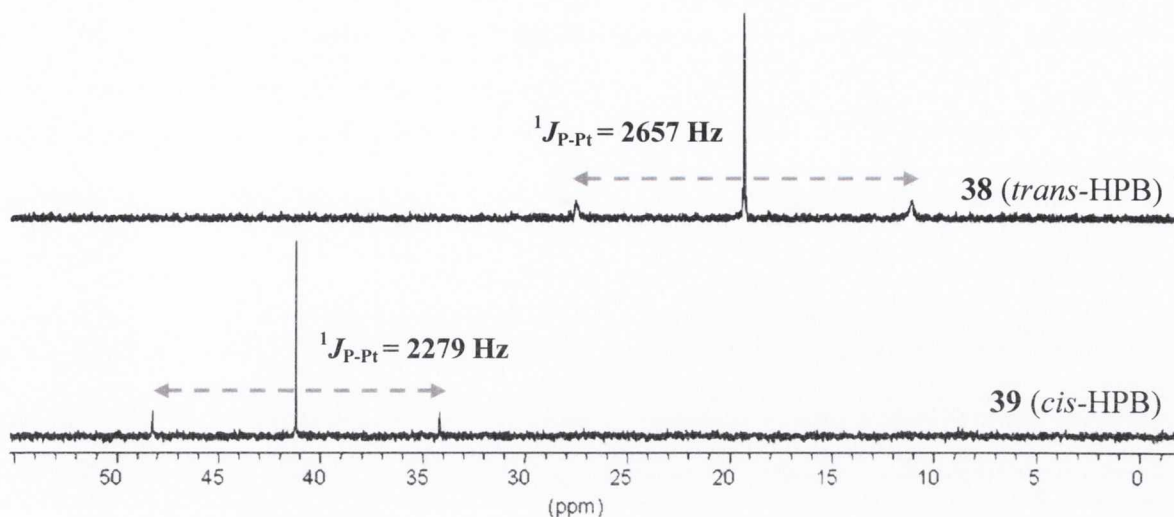


Figure 3.15:  $^{31}\text{P}\{^1\text{H}\}$  NMR spectra of **38** and **39** ( $\text{CDCl}_3$ , 162 MHz, R.T.) showing  $^{195}\text{Pt}$  satellites.

For **38** (*trans*-HPB) and **40** (*trans*-HBC), the  $^{31}\text{P}\{^1\text{H}\}$  signal (**38**,  $\delta$  19.3 ppm, **40**,  $\delta$  19.0 ppm) appears as a singlet with platinum satellites and typical *trans* coupling constants  $J_{\text{Pt-P}}$  = 2657 Hz (**38**) and  $J_{\text{Pt-P}}$  = 2625 Hz (**40**) (Table 3.4).<sup>191-192</sup> In the case of the *cis* complexes **39** (*cis*-HPB) and **41** (*cis*-HBC), the coupling constants were considerably smaller, with a value of 2279 Hz for both **39** and **41**.<sup>181,193-195</sup> The *cis*  $^{31}\text{P}\{^1\text{H}\}$  signals (**39**,  $\delta$  41.3 ppm, **41**,  $\delta$  41.2 ppm) appear at quite deshielded chemical shifts compared to those of the corresponding *trans* isomers.

Table 3.4:  $^{31}\text{P}\{^1\text{H}\}$  NMR and IR spectroscopic data for **38**, **39**, **40** and **41**

	$^{31}\text{P}\{^1\text{H}\}^{\text{a}}$ [ $\delta$ , ppm] ( $^1J_{\text{P-Pt}}$ , Hz)	IR [ $\nu(\text{C}\equiv\text{C})$ , $\text{cm}^{-1}$ ]
<i>trans</i> -[Pt( <b>6</b> ) <sub>2</sub> (PPh <sub>3</sub> ) <sub>2</sub> ] ( <b>38</b> )	19.3 (2657)	2110
<i>trans</i> -[Pt( <b>7</b> ) <sub>2</sub> (PPh <sub>3</sub> ) <sub>2</sub> ] ( <b>40</b> )	19.0 (2625)	2093
<i>cis</i> -[Pt( <b>6</b> ) <sub>2</sub> (dppe)] ( <b>39</b> )	41.3 (2279)	2106, 2118 (sh) <sup>b</sup>
<i>cis</i> -[Pt( <b>7</b> ) <sub>2</sub> (dppe)] ( <b>41</b> )	41.2 (2279)	2104, 2109

<sup>a</sup>  $^{31}\text{P}\{^1\text{H}\}$  NMR ( $\text{CDCl}_3$ , RT, 162 MHz); <sup>b</sup> sh = shoulder.

The greater *trans*-influence of the polyaromatic acetylide compared to the phosphine ligands explains both the larger coupling constants and upfield chemical shifts in the *trans*

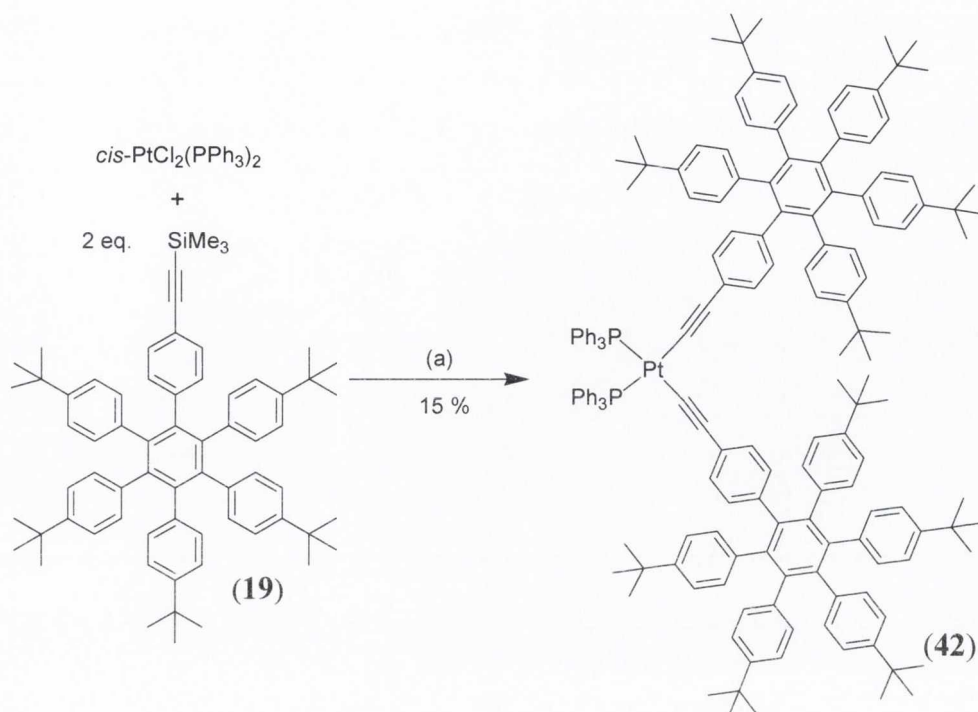
complexes. When a  $\text{PPh}_3$  is located *trans* to an acetylide (*cis* configuration), the Pt-P bond is weakened due to the greater *trans* influence exerted by the acetylide. The lower values of  $J_{\text{Pt-P}}$  are consistent with a *cis*-square planar complex with a weakened Pt-P bond compared to the *trans* isomer. Correspondingly, the magnitude of the  $^{195}\text{Pt}$ - $^{31}\text{P}$  coupling constant can be considered as an estimate of the bond strength between the two nuclei.<sup>196-198</sup>

IR spectroscopy was also employed to confirm the coordination geometry of the complexes. The  $\nu(\text{C}\equiv\text{C})$  stretching frequency is diagnostic of metal-ethynyl complexes. For a vibration to be IR active, a change in the electric dipole moment of the molecule must occur.

$\text{C}_{2v}$  – symmetric *cis*-dialkynyl complexes give rise to two  $\nu(\text{C}\equiv\text{C})$  bands, corresponding to two infra-red active stretching modes (symmetric and asymmetric) of the alkynyl moiety. The two *cis* configured complexes, **39** (*cis*-HPB) and **41** (*cis*-HBC) both exhibit two  $\nu(\text{C}\equiv\text{C})$  bands (**39**, 2106, 2118 (shoulder)  $\text{cm}^{-1}$ ; **41**, 2104, 2109  $\text{cm}^{-1}$ ). In contrast, only one stretching mode is IR active for *trans*-dialkynyl complexes, which has  $\text{D}_{2h}$  symmetry. As anticipated, **38** (*trans*-HPB) and **40** (*trans*-HBC) both exhibit a single  $\nu(\text{C}\equiv\text{C})$  absorption band at 2110  $\text{cm}^{-1}$  (**38**) and 2093  $\text{cm}^{-1}$  (**40**). The  $\nu(\text{C}\equiv\text{C})$  band wavenumbers are in good agreement with analogous Pt(II) bis-acetylide phosphine complexes in the literature.<sup>181,191,194</sup>

### 3.2.4 An alternative route to *trans*-[Pt(**6**)<sub>2</sub>(PPh<sub>3</sub>)<sub>2</sub>] (**38**) and a new product: *cis-trans* isomerisation in action

An alternative synthetic route to *trans*-[Pt(**6**)<sub>2</sub>(PPh<sub>3</sub>)<sub>2</sub>] (**38**) was undertaken and is described in Scheme 3.3. It was anticipated that this method could reduce by one the number of synthetic steps in the synthesis of **38** (*trans*-HPB) and be employed as the synthetic pathway to all four Pt(II) bis-acetylide complexes described. The reaction involves the *in-situ* deprotection of trimethylsilylethynyl-hexaphenylbenzene (**19**) to form ethynyl-hexaphenylbenzene (**6**) which immediately undergoes a Sonogashira cross-coupling reaction with *cis*-PtCl<sub>2</sub>(PPh<sub>3</sub>)<sub>2</sub>, once again using CuI as catalyst (10 mol%).<sup>199</sup>



Scheme 3.3: Attempted preparation of **38** – actual synthesis of  $\text{cis-}[\text{Pt}(\mathbf{6})_2(\text{PPh}_3)_2]$  (**42**).  
 (a)  $\text{CH}_2\text{Cl}_2:\text{CH}_3\text{OH}$  (4:1 v/v),  $\text{KF}$  (4.5 eq.),  $\text{CuI}$  (9 mol%), R.T.

KF is present to afford deprotection of TMS-ethynyl-hexaphenylbenzene (**19**), facilitating the formation of the platinum-carbon bond. The reaction was stirred under argon in darkness for 18 hours. When the reaction was deemed to have reached completion (i.e. the starting materials were consumed as evidenced by TLC), the reaction mixture was washed with water to remove unreacted KF and by-product salts formed during the cross-coupling reaction. The product (**42**) was obtained in 15 % yield following purification *via* column chromatography on silica eluting with petroleum ether: $\text{CH}_2\text{Cl}_2$  (3:2 v/v) and subsequent precipitation from methanol.

#### 3.2.4.1 Characterisation of (**42**)

The product was characterised using  $^1\text{H}$  and  $^{31}\text{P}$   $\{^1\text{H}\}$  NMR spectroscopy, infrared spectroscopy and mass spectrometry. A peak at  $m/z = 2394.2245$  m.u. in the MALDI-TOF mass spectrum of **42** for  $[\text{M}]^+$  is in good agreement with the calculated value  $m/z = 2394.2269$  m.u. for  $[\text{C}_{164}\text{H}_{168}\text{P}_2\text{Pt}]^+$ . This mass matches that calculated for  $\text{trans-}[\text{Pt}(\mathbf{6})_2(\text{PPh}_3)_2]^+$  (**38**).

The  $^1\text{H}$  NMR spectrum of **42** is shown in Figure 3.16 (B). This is clearly very different from the NMR spectrum of **38** (*trans*-HPB) (Figure 3.16, A). H1 and H2 protons are significantly more deshielded in complex **42** (H1,  $\delta$  6.14 ppm; H2,  $\delta$  6.43 ppm) than in **38**. The proton signals attributable to the phosphine phenyl rings all appear more upfield than seen in **38**. However, the integration values match perfectly to those calculated for the target complex **38** (*trans*-HPB).

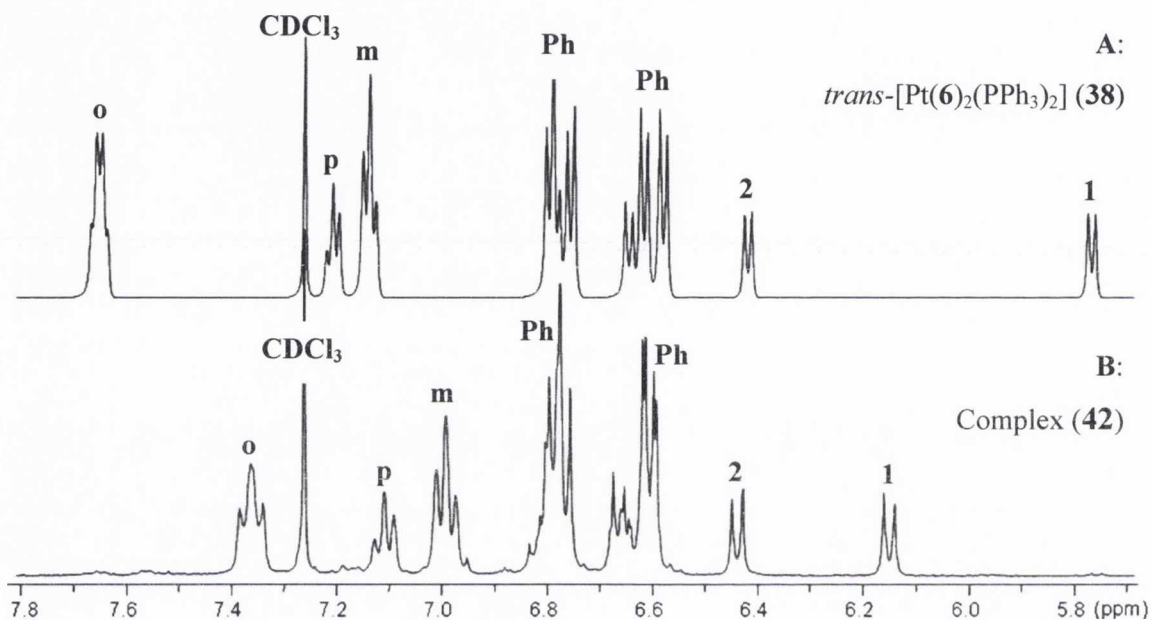


Figure 3.16:  $^1\text{H}$  NMR spectra of *trans* complex (**38**) (600.1 MHz, R.T.) and complex (**42**) (400.1 MHz, R.T.) showing the aromatic regions ( $\text{CDCl}_3$ ). Atom labelling as per inset Figure 3.6.

The  $^{31}\text{P}$   $\{^1\text{H}\}$  NMR spectrum of **42** reveals a peak centred at  $\delta$  18.0 ppm which has satellites as expected due to coupling with the  $^{195}\text{Pt}$  nucleus, with a coupling constant  $^1J_{\text{P-Pt}} = 2318$  Hz. By comparison with the P-Pt coupling constant calculated for complexes **38-41**, it is clear that **42** is in *cis*-configuration. The matching mass spectral result to that obtained for **38** indicates that the product isolated from this reaction is the *cis*-isomer of **38**, specifically *cis*-[Pt(**6**)<sub>2</sub>(PPh<sub>3</sub>)<sub>2</sub>] (**42**, Scheme 3.3).

This reaction was undertaken several times, employing extended reaction times in an attempt to facilitate the formation of the thermodynamic product, **38** (*trans*-HPB), from the kinetic *cis* product **42**, however the only product ever isolated *via* this synthetic method was **42**. As a result, this route was abandoned in favour of the classic Sonogashira pathway described in Scheme 3.1.



### 3.3 UV-Visible Absorption Spectra

#### 3.3.1 Ethynyl-hexaphenylbenzene (**6**) and uncyclised **39** (*cis*-HPB) and **38** (*trans*-HPB) complexes

The UV-Visible absorption spectra of polyphenylene ligand ethynyl-hexaphenylbenzene (**6**) and its corresponding **39** (*cis*-HPB) and **38** (*trans*-HPB) complexes are presented in Figure 3.17.

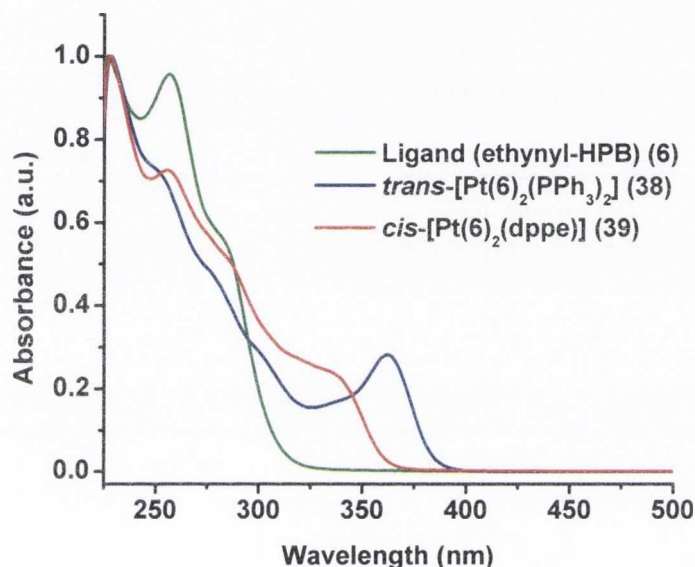


Figure 3.17: Normalised UV-Visible absorption spectra of **6**, **38** and **39** in  $\text{CH}_2\text{Cl}_2$  ( $10^{-5}$  M).

The absorption spectrum of ethynyl-hexaphenylbenzene ligand (**6**) is quite broad and relatively featureless as is typical of polyphenylene derivatives with no effective conjugation between the rings (Figure 3.17).<sup>124-125</sup> In the ground state, steric hindrance is expected to impose a non-planar configuration on the chromophore resulting in a mostly structureless electronic absorption.<sup>124</sup> It features strong bands centred in the near UV region ( $\lambda_{\text{max}}$  257 nm, Table 3.5) which can be assigned to ligand-centred transitions (e.g.  $\pi$ - $\pi^*$ ).

Table 3.5: Room temperature UV-Visible Spectral Data for Ligands **6** and **7** and their *cis* (**39**, **41**) and *trans* (**38**, **40**) complexes in CH<sub>2</sub>Cl<sub>2</sub> (~10<sup>-5</sup>M).

Compound	$\lambda_{\max}$ [nm] ( $\epsilon \times 10^{-4}$ [M <sup>-1</sup> cm <sup>-1</sup> ])
Ethynyl-HPB ( <b>6</b> )	227 (6.53), 257 (6.25), 284 <i>sh</i> (3.58)
<i>cis</i> -[Pt( <b>6</b> ) <sub>2</sub> (dppe)] ( <b>39</b> )	228 (15.6), 256 (11.3), 284 (8.1), 337 (3.7)
<i>trans</i> -[Pt( <b>6</b> ) <sub>2</sub> (PPh <sub>3</sub> ) <sub>2</sub> ] ( <b>38</b> )	228 (17.2), 253 (12.1), 279 <i>sh</i> (8.0), 299 (5.1), 362 (4.8)
Ethynyl-HBC ( <b>7</b> )	230 (23.1), 243 (20.3), 260 <i>sh</i> (5.3), 267 <i>sh</i> (4.6), 317 (2.1), 331 (4.0), 345 (10.4), 363 (24.3), 373 <i>sh</i> (9.4), 393 (7.1), 404 (3.1), 442 (0.3), 450 (0.2)
<i>cis</i> -[Pt( <b>7</b> ) <sub>2</sub> (dppe)] ( <b>41</b> )	229 (44.4), 242 (33.9), 265 (14.2), 319 (5.7), 333 (8.7), 349 (20.8), 365 (40.6), 396 (14.5), 414 (6.3), 443 (0.8), 451 (0.6), 459 (0.3), 470 (0.2)
<i>trans</i> -[Pt( <b>7</b> ) <sub>2</sub> (PPh <sub>3</sub> ) <sub>2</sub> ] ( <b>40</b> )	232 (34.7), 242 (33.3), 265 <i>sh</i> (11.3), 319 (4.6), 333 (6.9), 349 (16.1), 367 (31.6), 384 <i>sh</i> (18.2), 398 (15.9), 419 (9.1), 445 (0.7), 452 (0.5), 460 (0.2), 472 (0.2)

**39** (*cis*-HPB) and **38** (*trans*-HPB) uncyclised complexes also exhibit intense absorption bands in the near-UV region of the spectrum (Figure 3.17). By comparison with polyphenylene ligand **6**, these can be assigned as predominantly ligand-centred  $\pi$ - $\pi^*$  transitions. The two complexes exhibit an additional red-shifted band (**39**,  $\lambda$  337 nm, **38**,  $\lambda$  362 nm) due to the coordinated Pt(II) centre (Table 3.5). The appearance of this band implies that electron density located on the hexaphenylbenzene chromophore is delocalised across the molecule, mediated by  $d\pi(\text{Pt})$  orbitals.<sup>177</sup> The fact that this absorption band occurs at longer wavelengths (by 25 nm) for **38** (*trans*-HPB) than for **39** (*cis*-HPB) suggests that electronic communication through the Pt(II) centre is more effective in the *trans* configuration. This observation is in good agreement with previous reports in related *cis* and *trans* configured bis(alkynyl)platinum complexes.<sup>177,179,181,200</sup> This lowest energy band observed in complexes **38** and **39** can be assigned as a predominantly  $[\pi(\text{C}\equiv\text{C})\rightarrow\pi^*(\text{C}\equiv\text{C})]$  transition with some charge transfer character as a result of mixing between the alkynyl and the metal orbitals.<sup>201-202</sup>

No concentration effects are observed for polyphenylene ligand (**6**) or for its corresponding *cis* or *trans* complexes between  $10^{-4}$  –  $5 \times 10^{-7}$  M, and the Beer-Lambert law holds over this concentration range. The absorption bands of hexaphenylbenzene (**6**) are almost entirely invariant to changes in solvent polarity (Table 3.6). Marginal changes such as these are quite typical of electronic transitions which are purely  $\pi$ - $\pi^*$  in origin as the transition does not involve a significant change in dipole moment.<sup>126</sup> In contrast, the lowest energy band in both **39** (*cis*-HPB) and **38** (*trans*-HPB) exhibits a negative solvatochromic effect, undergoing a red-shift in solvents of decreased polarity (Table 3.6). For example, in *cis*-[Pt(**6**)<sub>2</sub>(dppe)] (**39**) the band occurs at  $\lambda$  333 nm in THF but at  $\lambda$  342 nm in non-polar toluene solution. This suggests that the ground state is more polar than the excited state, confirming the assignment of the lowest energy transition as possessing some charge transfer character. The  $\pi$ - $\pi^*$  absorption has gained some solvent dependency as a result of mixing with metal-based orbitals.<sup>126</sup> A polar solvent will stabilise a polar ground state relative to its excited state, resulting in a hypsochromic shift of the absorption band. Conversely, a non-polar solvent will destabilise a polar ground state, reducing the energy gap between it and the corresponding excited state, with a consequent bathochromic shift of the electronic absorption band.

Table 3.6: UV-Visible Absorption maxima ( $\lambda$ , nm) of lowest energy absorption band for ligand **6** and complexes **38** and **39** in THF, CH<sub>2</sub>Cl<sub>2</sub> and Toluene solutions ( $\sim 10^{-5}$  M).

	THF	CH <sub>2</sub> Cl <sub>2</sub>	Diisopropyl ether/Toluene
Ethynyl-HPB ( <b>6</b> )	256	257	257
<i>cis</i> -[Pt( <b>6</b> ) <sub>2</sub> (dppe)] ( <b>39</b> )	333	337	342
<i>trans</i> -[Pt( <b>6</b> ) <sub>2</sub> (PPh <sub>3</sub> ) <sub>2</sub> ] ( <b>38</b> )	360	362	365

### 3.3.2 Ethynyl-HBC (**7**) and cyclised **41** (*cis*-HBC) and **40** (*trans*-HBC) complexes

Figure 3.18 shows the normalised UV-Visible absorption spectra of the cyclised ligand (**7**) and complexes *cis*-[Pt(**7**)<sub>2</sub>(dppe)] (**41**) and *trans*-[Pt(**7**)<sub>2</sub>(PPh<sub>3</sub>)<sub>2</sub>] (**40**) in CH<sub>2</sub>Cl<sub>2</sub> solution. In contrast to the broad, featureless absorption spectrum of **6** (Figure 3.17), the increased planarity and rigidity of cyclised ligand **7** results in the appearance of well-resolved bands with significant fine structure, characteristic of hexa-*peri*-hexabenzocoronenes, with an observed  $\lambda_{\text{max}}$  363 nm (Figure 3.18).<sup>203-204</sup> According to the nomenclature employed by Clar to describe the electronic transitions of HBCs and of polyaromatic hydrocarbons

(PAHs) in general, this  $\lambda_{\max}$  can be assigned as the  $\beta$ -band, which corresponds to the electronic interaction between benzenoid rings.<sup>17</sup> The transition centred at  $\lambda$  393 nm for ethynyl-HBC (**7**), designated as the p-band, involves the localisation of electrons in the excited state.<sup>17</sup>

Absorption spectra for cyclised complexes **41** (*cis*-HBC) and **40** (*trans*-HBC) are dominated by the typical HBC bands but with slight red-shifts observed, the  $\beta$ -band which occurs at 363 nm for ethynyl-HBC is visible at  $\lambda$  365 nm for **41** and  $\lambda$  367 nm for **40** (Figure 3.18). This observation corresponds to an increase in electronic interaction by extending the  $\pi$ -conjugated system.<sup>17,204</sup> The red-shifts observed from ligand to *cis* to *trans* complexes for both cyclised and uncyclised systems indicate that  $\pi$ -conjugation along the molecular axis is more efficient when the acetylides are arranged *trans* to each other about the Pt(II) metal centre.<sup>177</sup>

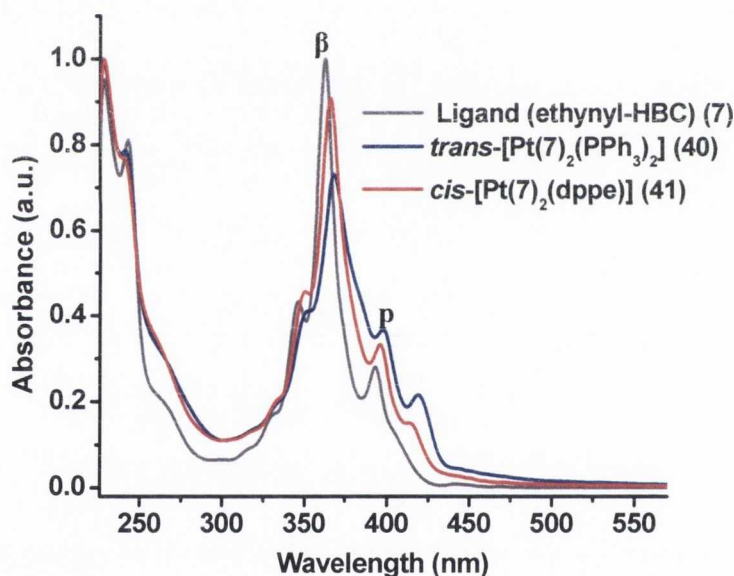


Figure 3.18: Normalised UV-Visible absorption spectra of **7**, **40** and **41** in  $\text{CH}_2\text{Cl}_2$  ( $\sim 10^{-5} \text{M}$ ).

An additional electronic absorption band is observed for **41** (*cis*-HBC) and **40** (*trans*-HBC) (**41**,  $\lambda$  414 nm; **40**,  $\lambda$  419 nm) that was not evident in ethynyl-HBC (**7**) (Figure 3.18). The effect of coordination of a fused, highly electron-delocalised graphene to a metal centre is to introduce a low-lying  $\pi^*$  orbital centred on the HBC sub-unit into the excited state manifold.<sup>173</sup> As a result, this transition may be considered to be as a result of predominantly intra-ligand character ( $\pi$ - $\pi^*$ ) with some contribution from a metal-to-ligand charge transfer transition (MLCT) due to perturbation by the coordinated Pt centre. The appearance of this additional band has been previously attributed to the fact that

attachment of the Pt-acetylide breaks the symmetry of the HBC and facilitates the extension of electron delocalisation along the molecular axis.<sup>173</sup> The characteristic HBC transitions and the low energy band in complexes **40** and **41** experience a negative solvatochromic behaviour that is essentially absent in ethynyl-HBC (**7**) (Table 3.7). This reinforces the assignment of these absorption bands in the HBC complexes as intra-ligand HBC absorption mixed with some charge-transfer character which contributes to the solvatochromic behaviour observed.<sup>126</sup>

Table 3.7: UV-Visible Absorption maxima ( $\lambda$ , nm) of  $\beta$ ,  $p$  and lowest energy absorption band for HBC ligand **7** and complexes **40** and **41** in THF, CH<sub>2</sub>Cl<sub>2</sub> and Toluene solutions ( $\sim 10^{-5}$  M).

	THF	CH <sub>2</sub> Cl <sub>2</sub>	Toluene
Ethynyl-HBC ( <b>7</b> )	363, 392	363, 393	364, 393
<i>cis</i> -[Pt( <b>7</b> ) <sub>2</sub> (dppe)] ( <b>41</b> )	363, 392, <sup>a</sup>	365, 396, 414	367, 398, 417
<i>trans</i> -[Pt( <b>7</b> ) <sub>2</sub> (PPh <sub>3</sub> ) <sub>2</sub> ] ( <b>40</b> )	368, 398, 419	367, 398, 419	370, 399, 421

<sup>a</sup> Broad, undefined band with extended tail due to poor solubility in THF.

### 3.4 Electrochemical properties of uncyclised and cyclised ligands and *cis* and *trans* complexes

Cyclic voltammetric (CV) studies were carried out on 1 mM solutions of the ligands (**6**, **7**) and complexes (**38**, **39** and **41**) in CH<sub>2</sub>Cl<sub>2</sub> (0.1 M <sup>n</sup>Bu<sub>4</sub>NPF<sub>6</sub>). The results are summarised in Table 3.8. Poor solubility of *trans*-[Pt(**7**)<sub>2</sub>(PPh<sub>3</sub>)<sub>2</sub>] (**40**) at suitable concentrations precluded CV measurement in this case. Cyclic voltammograms were measured using a standard calomel electrode (SCE) as reference electrode, with potentials quoted vs. the Fc/Fc<sup>+</sup> couple (0.0 V) and referenced to internal ferrocene added at the end of each experiment.

Table 3.8: Electrochemical data for ligands **6**, **7**, for *cis* complexes **39**, **41**, *trans* **38** and related Pt-HBC complex.<sup>173</sup>

Compound <sup>a</sup>	Oxidation $E_{1/2}/V$ [ $\Delta E_p/mV$ ] <sup>e</sup>	Reduction $E_{1/2}/V$ <sup>d</sup>
Ethynyl-HPB ( <b>6</b> )	- <sup>b</sup>	-1.93
<i>cis</i> -[Pt( <b>6</b> ) <sub>2</sub> (dpppe)] ( <b>39</b> )	0.66 <sup>c</sup> , 0.96 <sup>c</sup>	-1.92
<i>trans</i> -[Pt( <b>6</b> ) <sub>2</sub> (PPh <sub>3</sub> ) <sub>2</sub> ] ( <b>38</b> )	0.60 <sup>c</sup> , 0.99 <sup>c</sup>	-1.90
Ethynyl-HBC ( <b>7</b> )	0.57 [91], 0.83 [145]	-1.96
<i>cis</i> -[Pt( <b>7</b> ) <sub>2</sub> (dpppe)] ( <b>41</b> )	0.49 <sup>c</sup> , 0.87 [101]	-1.93
<b>Pt(HBC)</b> <sup>173, f</sup>	0.8 <sup>c</sup>	

<sup>a</sup> In CH<sub>2</sub>Cl<sub>2</sub> (0.1 M, <sup>n</sup>Bu<sub>4</sub>NPF<sub>6</sub>) at 298K, scan rate = 100 mV s<sup>-1</sup>, reported vs. Fc/Fc<sup>+</sup>; <sup>b</sup> No oxidation process observed within 0.0-2.0 V spectral window; <sup>c</sup> Irreversible/*quasi*-reversible oxidation process,  $E_{pa}/V$  (anodic peak potential) quoted; <sup>d</sup> Return oxidation wave associated with this reduction poorly defined; <sup>e</sup>  $\Delta E_p = E_{pa} - E_{pc}$ , peak potential separation; <sup>f</sup> Structure of complex given in Figure 3.3 (a)-ii.

The redox behaviour of polyphenylene ligand **6** is significantly different from that observed for HBC ligand **7**. **6** displays no oxidation process within the solvent window (+0.0 V to +2.0 V, Table 3.8), whereas one reversible and one quasi-reversible oxidation process are evident for **7** ( $\Delta E_p$  91, 145 mV),<sup>128</sup> appearing at +0.57 and +0.83 V (Figure 3.19). This is quite typical of HBC derivatives, for example 2,5,8,11,14,17-hexa-*tert*-butylhexa-*peri*-hexabenzocoronene displays two mainly reversible oxidation processes at +0.50 and +1.02 V vs. Fc/Fc<sup>+</sup> (measured against SCE, converted to Fc/Fc<sup>+</sup> scale by subtraction of 0.40 V).<sup>10</sup>

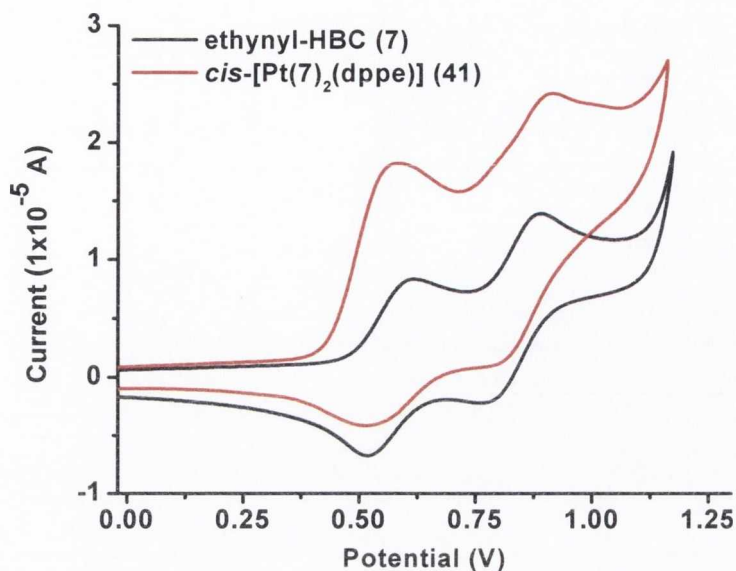


Figure 3.19: Cyclic voltammograms of **7** and **41** showing the Pt(II) and ligand-based oxidation processes. (1 mM in  $\text{CH}_2\text{Cl}_2$ , V vs.  $\text{Fc}/\text{Fc}^+$ ).

The three Pt(II) complexes measured exhibit a *quasi*-reversible/irreversible oxidation wave between +0.49 and +0.66 V (Table 3.8) which can be attributed to the metal-centred oxidation of Pt(II) to Pt(III) and corresponds to the removal of an electron from the HOMO.<sup>205</sup> These potentials are noticeably less positive than that recorded by Schanze *et al.* for a HBC platinum acetylide (+0.8 V vs. SCE).<sup>173</sup> The incorporation of an additional aromatic subunit significantly increases the electronic density at the metal centre rendering the metal centre more electron rich resulting in a less difficult oxidation process.

In general, oxidation of the Pt centre occurs at less positive potentials for complexes with cyclised ligands than for those with uncyclised appendages. Similarly, **38** (*trans*-HPB) is more easily oxidised than **39** (*cis*-HPB) (Figure 3.20). This observation is in agreement with the red-shift of the lowest charge-transfer energy bands in the UV-Visible spectra from uncyclised to cyclised complexes and from *cis* to *trans* configurations ( $\lambda$ : **39** (*cis*-HPB) 337 nm; **38** (*trans*-HPB) 362 nm, **41** (*cis*-HBC): 414 nm, Table 3.5). The enhanced electron density due to the electron-rich HBC platform facilitates a more facile electron removal. Similarly, the  $E_{\text{pa}}$  of **38** is less positive than that of **39**, indicating that a more efficient  $\pi$ -electron delocalization along the molecular axis in **38** increases the electron density at the metal centre, resulting in an easier oxidation from Pt(II) to Pt(III).

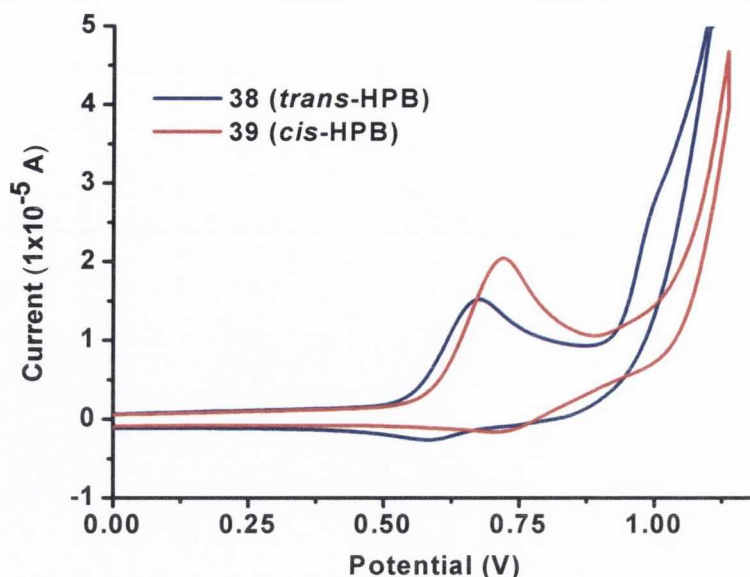


Figure 3.20: Cyclic voltammograms of **38** and **39** showing the Pt(II) oxidation process.

The two reversible oxidation peaks seen in ethynyl-HBC (**7**) are also seen in *cis*-[Pt(**7**)<sub>2</sub>(dppe)] (**41**). However, in **41** the irreversible Pt(II)/Pt(III) oxidation is coincident with the first oxidation on the ligand and so this oxidation peak appears as a broadened signal on the CV (Figure 3.19). A reversible reduction is observed between -1.9 and -2.0 V for both ligands and complexes, however the reverse oxidation process associated with this reduction appears as a relatively broad peak, implying a degree of *quasi*-reversibility.

### 3.5 Photophysical properties of ligands **6** and **7**, *cis* complexes **39** and **41** and *trans* complexes **38** and **40**

The photophysical properties of ethynyl-hexaphenylbenzene (**6**) and its corresponding *cis*-[Pt(**6**)<sub>2</sub>(dppe)] (**39**) and *trans*-[Pt(**6**)<sub>2</sub>(PPh<sub>3</sub>)<sub>2</sub>] (**38**) complexes are discussed separately from the analogous cyclised complexes - ethynyl-HBC (**7**), *cis*-[Pt(**7**)<sub>2</sub>(dppe)] (**41**) and *trans*-[Pt(**7**)<sub>2</sub>(PPh<sub>3</sub>)<sub>2</sub>] (**40**).

#### 3.5.1 Emission properties of uncyclised ligand **6** and complexes **38** and **39**

Table 3.9 summarises the relevant photoluminescence data for uncyclised ligand **6** and its corresponding *cis* and *trans* complexes, **39** (*cis*-HPB) and **38** (*trans*-HPB), in argon-degassed CH<sub>2</sub>Cl<sub>2</sub> solution and in solid state at 298K and 77K, including lifetimes (at 298K) and quantum yields.



Table 3.9: Emission data for ligand **6** and complexes **38** (*trans*-HPB) and **39** (*cis*-HPB) in solid state and in solution ( $\text{CH}_2\text{Cl}_2$ ) at 298 K and 77 K.

	Medium (T[K])	$\lambda_{\text{em}}[\text{nm}]$ ( $\lambda_{\text{exc}}[\text{nm}]$ )	$\tau$ [ns] ( $\lambda_{\text{exc}} / \lambda_{\text{em}}$ nm) <sup>b</sup>	$\Phi_{\text{em}}$ <sup>c</sup>
<b>6</b> <b>L</b>	Solid (298)	354 (305)	36 (88 %), 8 (12%) (295 / 355)	
	Solid (77)	350 <sub>max</sub> , 455, 488 (305)		
	$\text{CH}_2\text{Cl}_2$ (298) <sup>a</sup>	362 (280), 465 (360)	19 (61 %), 6 (39 %) (295 / 370) 7 (73 %), 15 (27 %) (370 / 460)	<0.001
	$\text{CH}_2\text{Cl}_2$ (77)	345 <sub>max</sub> , 447, 479 (285)		
<b>39</b> <i>cis</i>	Solid (298)	377 <sub>max</sub> , 482, 513 <sub>sh</sub> (315)	40 (89 %), 15 (11 %) (295 / 375) 1,100 (80 %), 200 (20 %) (370 / 480)	
	Solid (77)	481 <sub>max</sub> , 540 (350)		
	$\text{CH}_2\text{Cl}_2$ (298) <sup>a</sup>	368 (282), 375 <sub>sh</sub> , 395 (350) 444, 465 <sub>sh</sub> (390)	20 (56 %), 7 (44 %) (295 / 370) 23 (67 %), 7 (33 %) (370 / 460)	0.022
	$\text{CH}_2\text{Cl}_2$ (77)	467 <sub>max</sub> , 494, 516 <sub>sh</sub> (330)		
<b>38</b> <i>trans</i>	Solid (298)	372 <sub>max</sub> , 386, 481, 518 (315)	51 (44 %), 31 (56 %) (295 / 375) 4,400 (74 %), 600 (26 %) (370 / 480)	
	Solid (77)	477 <sub>max</sub> , 521 (360)		
	$\text{CH}_2\text{Cl}_2$ (298) <sup>a</sup>	355 <sub>sh</sub> , 374 <sub>max</sub> (286), 433, 458, 478 <sub>max</sub> , 508 <sub>sh</sub> (380)	24 (69 %), 7 (31 %) (295 / 370) 39 (38 %), 8 (62 %) (370 / 460)	0.005
	$\text{CH}_2\text{Cl}_2$ (77)	471 <sub>max</sub> , 512 (365)		

<sup>a</sup> Argon-degassed solutions,  $\sim 10^{-5}$  M (unless otherwise stated); <sup>b</sup> Estimated uncertainty on  $\tau \pm 12$  %;

<sup>c</sup> Measured using quinine sulfate as a standard, based on an average of three repeat measurements.<sup>133</sup>

### 3.5.1.1 Room temperature ( $\text{CH}_2\text{Cl}_2$ solution) and 77 K in frozen $\text{CH}_2\text{Cl}_2$ ( $10^{-5}$ M)

In degassed  $\text{CH}_2\text{Cl}_2$  ( $10^{-5}$  M) solution (Figure 3.21), emission from **6**, **39** (*cis*-HPB) and **38** (*trans*-HPB) is dependent on excitation wavelength. Excitation at high energies ( $\lambda \sim 280$  nm) induces strong emission (**6**  $\lambda_{\text{max}}$  362 nm, **39**  $\lambda_{\text{max}}$  368 nm, **38**  $\lambda_{\text{max}}$  374 nm) which possess excited state lifetimes of nanosecond magnitude (Table 3.9). This emission band can be attributed to fluorescence derived from the polyphenylene chromophore ( $^1\pi\pi^*$ ) on the basis of its short excited state lifetimes and small Stokes shifts from the lowest energy

absorption bands in its corresponding spectra (Figure 3.17). This high energy emission is a feature of propeller-like polyphenylene emission and features also in Chapter 2 and Chapter 4 where the unfused polyaryl-substituted bipyridine ligands display a similar photoluminescence profile.<sup>124-125</sup> For the three complexes, the excitation spectra match the absorption spectra (Figure 3.17), indicating the absence of excited state intermolecular aggregates or interactions. Interestingly, a series of polyphenylene dendrimers composed of tens or hundreds of out-of-plane twisted phenyl units, display an analogous strong emission profile with a fluorescence centred at  $\lambda_{\text{max}}$  365 nm.<sup>206</sup> With increasing dendrimer generation, only marginal bathochromic shifts of the emission band are observed.

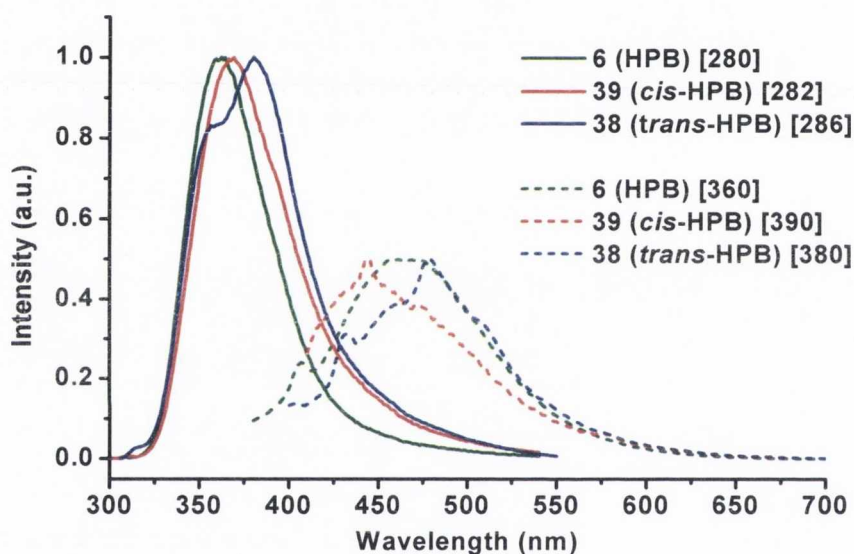


Figure 3.21: Normalised Emission spectra showing the two emission bands (excitation wavelength dependent) of ethynyl-hexaphenylbenzene (**6**), *cis*-[Pt(**6**)<sub>2</sub>(dppe)] (**39**) and *trans*-[Pt(**6**)<sub>2</sub>(PPh<sub>3</sub>)<sub>2</sub>] (**38**) in argon-degassed CH<sub>2</sub>Cl<sub>2</sub> at 298K [ $\lambda_{\text{exc}}$ /nm].

Upon excitation at lower energy, a less-intense red-shifted band is observed (Figure 3.21). For the complexes, this lower energy emission is significantly more structured than the higher energy band. In **38** (*trans*-HPB), it shows a vibronic progression of  $\sim 2200$  cm<sup>-1</sup> consistent with the involvement of the C $\equiv$ C unit in the electronic transition. Lifetimes for each of these emission bands are in the nanosecond region and slightly enhanced on moving from ligand to complex. For example, for the lower energy band, the lifetime of *cis*-[Pt(**6**)<sub>2</sub>(dppe)] (**39**) ( $\tau$ : 23 ns (67 %), 7 (33 %)) is noticeably greater than that measured for polyphenylene ligand (**6**) is ( $\tau$ : 7 ns (73 %), 15 ns (27 %)).

At 77K in DCM glass (Figure 3.22), emission from ligand (**6**) is composed of both a higher energy ( $\lambda_{\text{max}}$  345 nm) and a lower energy  $^3\pi\pi^*$  component ( $\lambda$  447, 479 nm). For **39** (*cis*-HPB) and **38** (*trans*-HPB), no  $^1\pi\pi^*$  fluorescence emission is evident and only a lower energy band is observed (**39**  $\lambda_{\text{max}}$  467 nm, **38**  $\lambda_{\text{max}}$  471 nm) which may be attributed to phosphorescence due to hexaphenylbenzene-derived  $^3\pi\pi^*$  with some effect by mixing from d(Pt) orbitals.

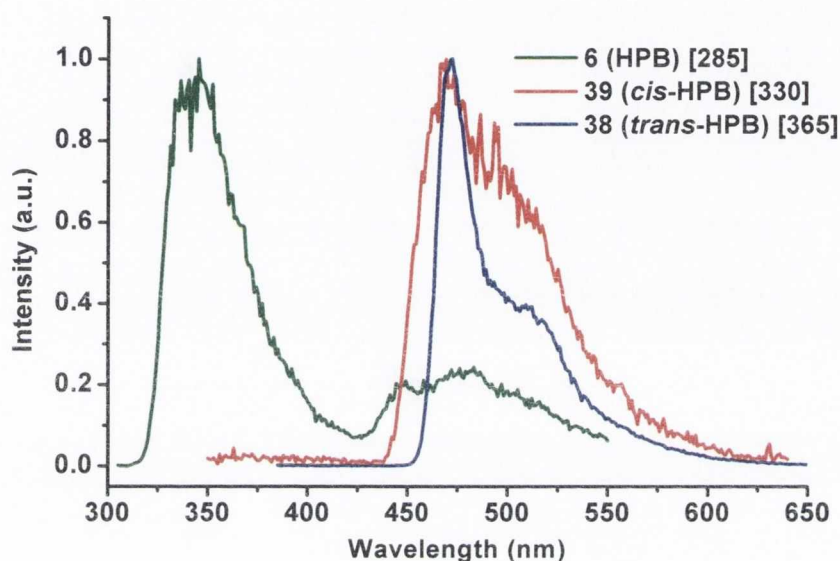


Figure 3.22: Normalised emission spectra of ethynyl-hexaphenylbenzene (**6**), *cis*-[Pt(**6**)<sub>2</sub>(dppe)] (**39**) and *trans*-[Pt(**6**)<sub>2</sub>(PPh<sub>3</sub>)<sub>2</sub>] (**38**) in frozen CH<sub>2</sub>Cl<sub>2</sub> at 77 K [ $\lambda_{\text{exc}}$ /nm].

### 3.5.1.2 Solid state at 298 K and 77 K

In the solid state, emission from ethynyl-hexaphenylbenzene (**6**) appears at room temperature as a broad band ( $\lambda_{\text{max}}$  354 nm) with an extended tail (Figure 3.23). Excitation of uncyclised **39** (*cis*-HPB) and **38** (*trans*-HPB) at 315 nm results in significantly more red-shifted emission bands (**39**  $\lambda_{\text{max}}$  377 nm, **38**  $\lambda_{\text{max}}$  372 nm, Figure 3.23) and slight lifetime enhancement on going from ligand-(**6**) (36, 8 ns) to **39** (40, 15 ns) to **38** (51, 31 ns). This is consistent with the Pt(II) centre affecting  $^1\pi\pi^*$  polyphenylene emission by causing an extension of  $\pi$ -conjugation along the molecular axis. As observed in solution (Figure 3.21), **39** (*cis*-HPB) and **38** (*trans*-HPB) complexes exhibit an additional broad lower energy emission band in the solid state (**39**  $\lambda$  482 nm, **38**  $\lambda$  481 nm) with significantly enhanced lifetimes (**39** 1.1  $\mu\text{s}$  (80 %), 0.2  $\mu\text{s}$  (20 %); **38** 4.4  $\mu\text{s}$  (74 %), 0.6  $\mu\text{s}$  (26 %)) due to phosphorescence facilitated by the high spin-orbit coupling of the metal centre.

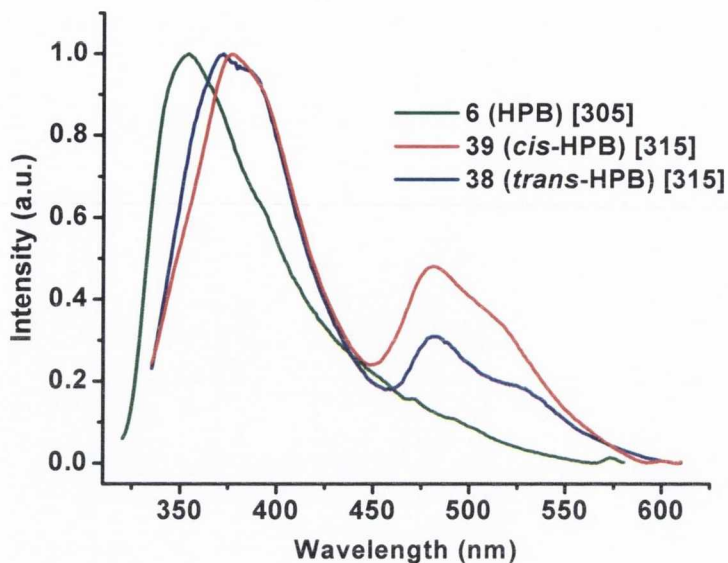


Figure 3.23: Normalised solid state emission spectra of ligand **6** and complexes **38** and **39** at room temperature [ $\lambda_{exc}/nm$ ].

At 77K in the solid state (Figure 3.24), as observed in frozen  $\text{CH}_2\text{Cl}_2$  (Figure 3.22), emission from **6** is composed of both a higher energy ( $\lambda_{max}$  350 nm) and a lower energy  $^3\pi\pi^*$  component ( $\lambda$  455, 488 nm). For both **39** (*cis*-HPB) and **38** (*trans*-HPB) there is no evident  $^1\pi\pi^*$  fluorescence and only a lower energy phosphorescence (**39**  $\lambda_{max}$  481 nm, **38**  $\lambda_{max}$  477 nm) attributed to  $^3\pi\pi^*$  with some Pt(II) influence.

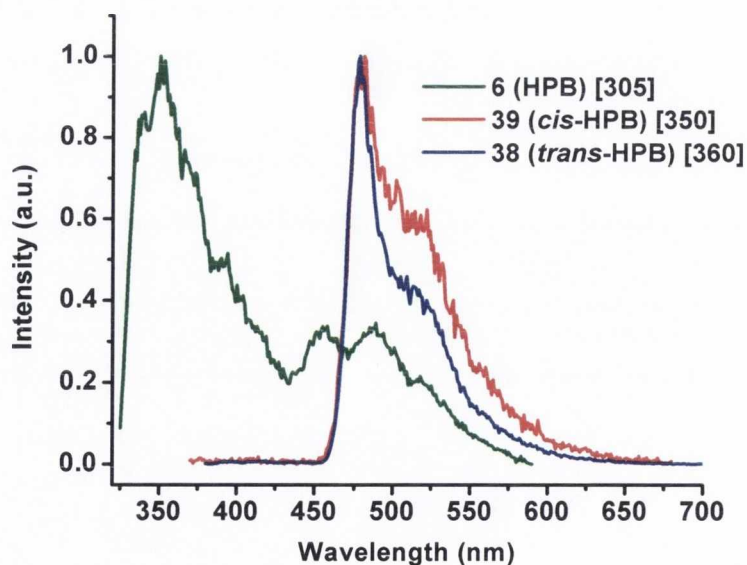


Figure 3.24: Normalised solid state emission spectra of ligand **6** and complexes **38** and **39** at 77 K [ $\lambda_{exc}/nm$ ].

### 3.5.1.3 Nature of the emissive excited states in **6**, **38** and **39**

The Jablonski diagram depicted in Figure 3.25 is consistent with the observed photophysical behaviour of ethynyl-hexaphenylbenzene (**6**) and its corresponding *cis*-[Pt(**6**)<sub>2</sub>(dppe)] (**39**) and *trans*-[Pt(**6**)<sub>2</sub>(PPh<sub>3</sub>)<sub>2</sub>] (**38**) complexes in CH<sub>2</sub>Cl<sub>2</sub> solution at 298 K.

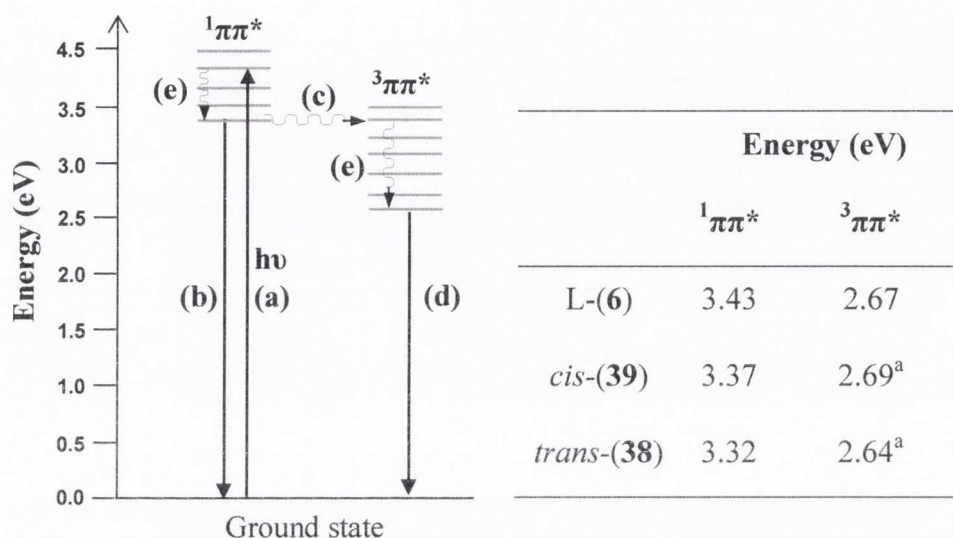


Figure 3.25: Jablonski energy level diagram for ligand **6** and **38** (*trans*-HPB) and **39** (*cis*-HPB) complexes showing photoinduced radiative processes and inset, calculated approximate energies (eV) of excited states (from 298 K CH<sub>2</sub>Cl<sub>2</sub> solution measurements).

<sup>a</sup> Combined  $^3\pi\pi^*$  with some Pt(II) contribution. (a) Absorption; (b) & (d) Emission; (c) Intersystem crossing; (e) Internal conversion.

Absorption of light (Figure 3.25, (a)) forms the  $^1\pi\pi^*$  excited state. The lowering in energy of this excited state from ligand (3.43 eV) to *cis* (3.37 eV) to *trans* (3.32 eV) is consistent with the delocalisation of electron density through the metal centre in the complexes, with most effective  $\pi$ -conjugation observed when the polyphenylene ligands are mutually *trans* to each other about the Pt(II) centre.<sup>177</sup>

Radiative decay from this  $^1\pi\pi^*$  state (Figure 3.25, (b)) is quite efficient. Additionally, the  $^1\pi\pi^*$  excited state can relax *via* inter-system crossing (Figure 3.25, (c)) to form the  $^3\pi\pi^*$  excited state. Ligand **6** exhibits weak emission (phosphorescence) from this excited state in solution at room temperature (Figure 3.21) and at low temperature (Figure 3.22) and its emission profile is essentially dominated by  $^1\pi\pi^*$  fluorescence. In contrast, at low temperature, **39** (*cis*-HPB) and **38** (*trans*-HPB) display almost exclusive phosphorescence from this  $^3\pi\pi^*$  excited state (Figure 3.25, (d)). The spin-orbit coupling introduced by the

Pt allows mixing of singlet and triplet states and facilitates strong intersystem crossing and population of the  $^3\pi\pi^*$  excited state.

Interestingly, the phosphorescence band maxima are very similar from ligand to complexes (Figure 3.25, 2.64-2.69 eV). This implies that the  $^3\pi\pi^*$  excited state is essentially localised on a single ligand, in contrast to the  $\pi$ -electron delocalised  $^1\pi\pi^*$  excited state, and is quite independent of coordination geometry. This effect was also observed by Schanze *et al.* for *cis* and *trans* Pt(II) stilbene bis-phosphine complexes.<sup>177</sup> Further to this, the localisation of the triplet excited state on a single repeat unit in platinum-acetylide polymers has been well established.<sup>160-162</sup>

### 3.5.2 Emission properties of HBC ligand 7 and complexes 40 and 41

The photoluminescent properties of ethynyl-HBC (**7**) and its corresponding *cis* and *trans* complexes *cis*-[Pt(**7**)<sub>2</sub>(dppe)] (**41**) and *trans*-[Pt(**7**)<sub>2</sub>(PPh<sub>3</sub>)<sub>2</sub>] (**40**) are summarised in Table 3.10, for data recorded in argon-degassed CH<sub>2</sub>Cl<sub>2</sub> solution at 298 K and at 77 K, and in solid state at 298K and 77K, including lifetimes (at 298K) and quantum yields.

Table 3.10: Emission data for HBC-ligand **7** and complexes *trans*-(**40**) and *cis*-(**41**) in solid state and in solution ( $\text{CH}_2\text{Cl}_2$ ) at 298 K and 77K.

	Medium (T[K])	$\lambda_{\text{em}}[\text{nm}]$ ( $\lambda_{\text{exc}}[\text{nm}]$ )	$\tau$ [ns] ( $\lambda_{\text{exc}} / \lambda_{\text{em}}$ nm) <sup>c</sup>	$\Phi_{\text{em}}$ <sup>d</sup>
<b>7</b>	Solid (298)	483, 509 <sub>max</sub> , 546, 580 <sub>sh</sub> (420)	1,100 (81 %), 200 (19 %) (370 / 508)	
<b>HBC</b>	Solid (77)	483, 512 <sub>max</sub> , 546, 581 <sub>sh</sub> (420)		
	$\text{CH}_2\text{Cl}_2$ (298) <sup>a</sup>	460 <sub>wk</sub> , 471 <sub>max</sub> , 481, 490, 500, 524, 535, 545 <sub>sh</sub> , 563 <sub>wk</sub> (335)	12 (3 %), 24 (97 %) (370 / 470) 18 (68 %), 6 (32 %) (370 / 500)	0.093
	$\text{CH}_2\text{Cl}_2$ (298) <sup>b</sup>	460 <sub>wk</sub> , 471 <sub>max</sub> , 481, 491, 500, 525, 535, 545 <sub>sh</sub> , 565 <sub>wk</sub> (390)		0.079
	$\text{CH}_2\text{Cl}_2$ (77)	463 <sub>sh</sub> , 475 <sub>max</sub> , 486, 497, 506, 534, 544, 579, 636 <sub>wk</sub> (420)		
<b>41</b> <i>cis</i>	Solid (298)	482 <sub>sh</sub> , 508 <sub>max</sub> , 542 <sub>sh</sub> , 590 <sub>sh</sub> (425)	4,800 (74 %), 600 (26 %)(370 / 510)	
	Solid (77)	512, 577 <sub>max</sub> , 625, 657 <sub>wk</sub> (425)		
	$\text{CH}_2\text{Cl}_2$ (298) <sup>a</sup>	473, 481, 492, 502, 526, 536 <sub>wk</sub> , 577 <sub>max</sub> , 625, 656 <sub>wk</sub> (420)	19 (85 %), 6 (15 %) (370 / 470) 18,300 (100 %) (370 / 578)	0.021
	$\text{CH}_2\text{Cl}_2$ (298) <sup>b</sup>	453 <sub>wk</sub> , 473, 483, 493 <sub>max</sub> , 502, 515 <sub>sh</sub> , 527, 538, 548 <sub>sh</sub> , 567 <sub>wk</sub> , 575 <sub>wk</sub> , 616 <sub>sh</sub> (405)		0.095
	$\text{CH}_2\text{Cl}_2$ (77)	471 <sub>wk</sub> , 481 <sub>wk</sub> , 491 <sub>wk</sub> , 500 <sub>wk</sub> , 526 <sub>wk</sub> , 573 <sub>max</sub> , 582 <sub>sh</sub> , 621, 631, 653 <sub>wk</sub> (400)		
<b>40</b> <i>trans</i>	Solid (298)	506 <sub>max</sub> , 540, 591 <sub>sh</sub> (400)	12,400 (79 %), 1,100 (21 %) (370 / 505)	
	Solid (77)	506, 542 <sub>sh</sub> , 577 <sub>max</sub> , 625, 633 <sub>wk</sub> (420)		
	$\text{CH}_2\text{Cl}_2$ (298) <sup>a</sup>	471, 481, 491, 501, 525 <sub>wk</sub> , 536 <sub>wk</sub> , 578 <sub>max</sub> , 626, 636 <sub>sh</sub> , 657 <sub>wk</sub> (405)	23 (85 %), 14 (15 %) (370 / 472) 30,900 (100 %) (370 / 578)	0.018
	$\text{CH}_2\text{Cl}_2$ (298) <sup>b</sup>	473, 482, 493, 503 <sub>max</sub> , 527, 536, 577 <sub>wk</sub> (408)		0.032
	$\text{CH}_2\text{Cl}_2$ (77)	491 <sub>wk</sub> , 574 <sub>max</sub> , 623, 633 <sub>sh</sub> , 654 <sub>wk</sub> (420)		

<sup>a</sup> Argon-degassed solutions,  $\sim 10^{-5}$  M; <sup>b</sup> Oxygenated solutions,  $\sim 10^{-5}$  M; <sup>c</sup> Estimated uncertainty on  $\tau \pm 10$  %;

<sup>d</sup> Measured using 4',6-diamidino-2-phenylindole dihydrochloride as a standard, based on an average of three repeat measurements.<sup>207</sup>

### 3.5.2.1 Solid State at 298 K and 77 K

In the solid state at room temperature, emission from cyclised ethynyl-HBC (**7**) appears as a broad quite structured band in the range  $\lambda$  480-650 nm with  $\lambda_{\text{max}}$  509 nm (Figure 3.26). An almost identical luminescence profile is observed for **41** (*cis*-HBC) and **40** (*trans*-HBC) (**41**  $\lambda_{\text{max}}$  508 nm, **40**  $\lambda_{\text{max}}$  506 nm). Significant differences are evident however upon comparison of the lifetimes. As observed for the uncyclised family, lifetimes ( $\lambda_{\text{em}} \sim 505$  nm) are enhanced considerably from ligand to complex enabled by the attached metal centre and again from *cis* to *trans* complex due to more efficient electronic delocalisation (ethynyl-HBC (**7**) 1.1  $\mu\text{s}$  (81 %), 0.2  $\mu\text{s}$  (19 %); **41** (*cis*-HBC) 4.8  $\mu\text{s}$  (74 %), 0.6  $\mu\text{s}$  (26 %); **40** (*trans*-HBC) 12.4  $\mu\text{s}$  (79 %), 1.1  $\mu\text{s}$  (21 %)).

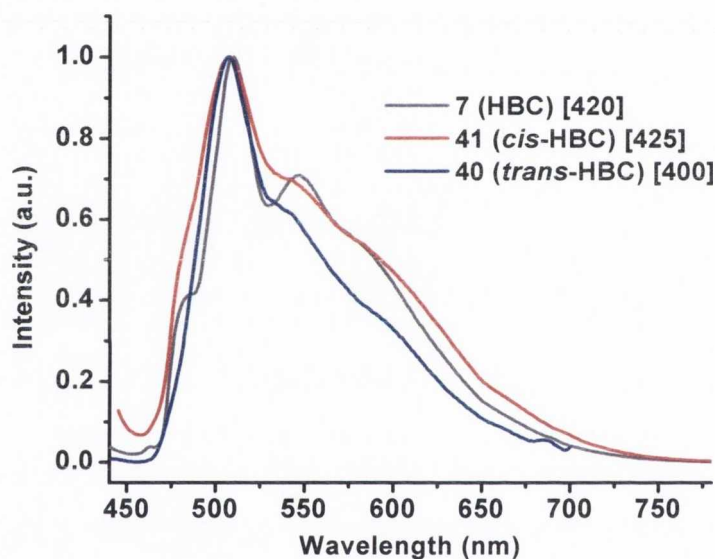


Figure 3.26: Normalised solid state emission spectra of ligand **7** and complexes **40** and **41** at room temperature [ $\lambda_{\text{exc}}/\text{nm}$ ].

The emission of ethynyl-HBC (**7**) is almost identical at 298K and 77K (Figure 3.26 and Figure 3.27). Substantial differences, however, are observed for **41** (*cis*-HBC) and **40** (*trans*-HBC) on moving to lower temperature. A quite broad and unstructured HBC-based emission can be identified for both complexes, but the spectra at 77K are dominated by an intense very narrow band-width emission centred at  $\lambda$  577 nm with an additional vibronic band at 625 nm. This has been previously assigned to phosphorescence from the HBC-chromophore facilitated by the attached platinum(II) acetylide.<sup>172-173</sup> Here enhanced Inter-System Crossing (ISC) occurs due to the high spin-orbit coupling constant of the



coordinated heavy metal which allows population of the  $T_1$  excited state and correspondingly radiative decay from the triplet state.

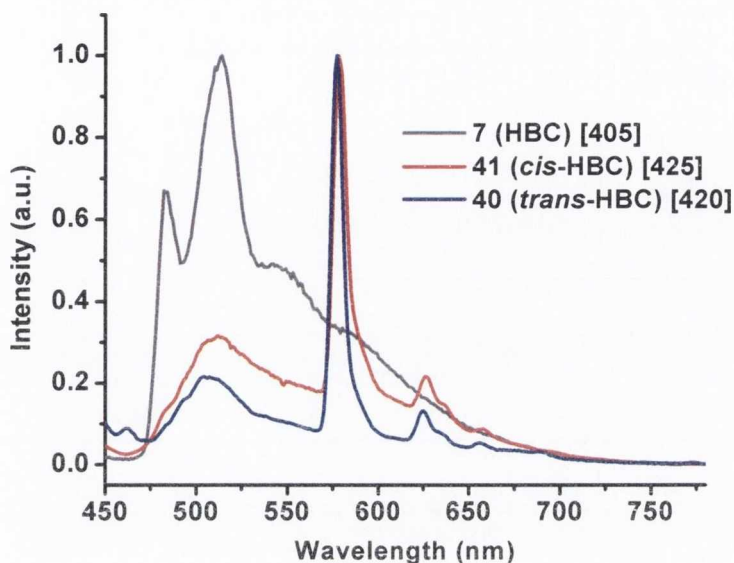


Figure 3.27: Normalised solid state emission spectra of ligand **7** and complexes **40** and **41** at 77 K [ $\lambda_{exc}/nm$ ].

### 3.5.2.2 Room temperature ( $CH_2Cl_2$ solution) and 77 K in frozen $CH_2Cl_2$ ( $10^{-5}$ M)

The emission spectra of ethynyl-HBC (**7**) in argon-degassed  $CH_2Cl_2$  solution is composed of an extended band with a complex vibronic structure between  $\lambda$  450-590 nm ( $\lambda_{max}$  471 nm;  $\tau$  24 ns (97 %), 12 ns (3 %), Figure 3.28). This profile varies little with solvent, aeration or temperature (at 77K, the  $\lambda_{max}$  is red-shifted slightly to  $\lambda$  475 nm, Table 3.10). The shape of the emission band is characteristic of singlet emission ( $^1\pi\pi^*$ ) derived from the hexa-*peri*-hexabenzocoronene chromophore.<sup>74,203-204</sup> The excitation spectrum of ethynyl-HBC (**7**) matches well with the recorded absorption spectrum (Figure 3.18) and is given in Figure 3.28. A noticeable Stokes shift is evident between the onset of absorption and fluorescence ( $\sim 40$  nm). This was also observed by Schanze and co-workers, who suggest that the radiative decay from the lowest singlet excited state to the ground state is symmetry forbidden, which gives rise to very weak emission at  $\lambda$  460 nm, a large Stokes shift and relatively long fluorescence lifetimes (Table 3.10).<sup>173</sup>

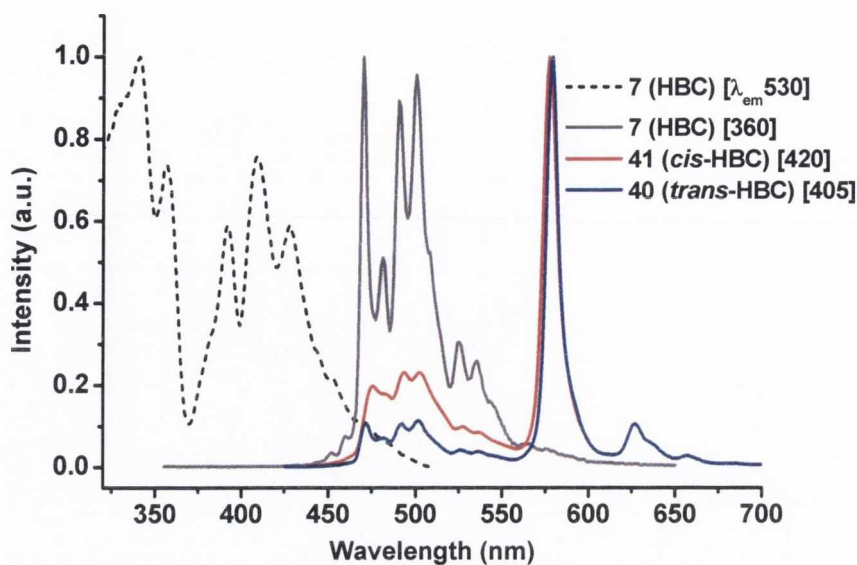


Figure 3.28: Normalised Emission spectra of **7**, **41** and **40**, and excitation spectrum of **7**, in argon-degassed  $\text{CH}_2\text{Cl}_2$  ( $\sim 10^{-5} \text{ M}$ ) at 298K [ $\lambda_{\text{exc}}/\text{nm}$ ].

In Ar-degassed  $\text{CH}_2\text{Cl}_2$  solution, narrow band-width phosphorescence from the HBC chromophore is the dominant feature of the emission spectra of both **41** (*cis*-HBC) and **40** (*trans*-HBC) (**41**  $\lambda_{\text{max}}$  577 nm, **40**  $\lambda_{\text{max}}$  578 nm, Figure 3.28). The onset of typical HBC fluorescence occurs as expected at 470 nm (mimicking that observed for ligand **7**) and the lifetimes recorded for ligand and complexes at this emission maximum are comparable ( $\sim 20$  ns,  $\sim 10$  ns). The ratio of phosphorescence:HBC fluorescence is large in both cases (**41** (*cis*-HBC) 5:1, **40** (*trans*-HBC) 20:1), with **40** experiencing the effect of the attached metal centre considerably more than **41**. The recorded lifetimes for the phosphorescent band ( $\lambda$  578 nm) observed in the emission spectra of both **40** and **41** are remarkably long ( $\lambda_{\text{exc}}$  370 nm: **41** 30.9  $\mu\text{s}$  (100 %); **40** 18.3  $\mu\text{s}$  (100 %)). Such very long-lived lifetimes correspond to the assignment of this emission as being derived from a triplet excited state located on the HBC chromophore.<sup>172-173</sup> The population of this state is allowed as a result of spin-orbit coupling of the attached heavy metal. The marked difference in triplet lifetime observed between **40** (*trans*-HBC) and **41** (*cis*-HBC) affirms our conclusion that  $\pi$ -conjugation is most efficient when the acetylide ligands are coordinated *trans*.<sup>177</sup>

In oxygenated  $\text{CH}_2\text{Cl}_2$  solutions, only the vibronic fine structure of fluorescence from the HBC platform is evident from both *cis*-[Pt(**7**)<sub>2</sub>(dppe)] (**41**) and *trans*-[Pt(**7**)<sub>2</sub>(PPh<sub>3</sub>)<sub>2</sub>] (**40**), with solely residual fluorescence from the ligand evident at 578 nm (Figure 3.29). The high oxygen sensitivity of the narrow emissive band at  $\lambda$  578 nm confirms its assignment

as phosphorescence ( ${}^3\pi\pi^*$ ) derived from the HBC platform and facilitated by the attached heavy metal. The opposite effect is observed for both complexes at 77K in frozen  $\text{CH}_2\text{Cl}_2$  (Figure 3.29) – the intensity of HBC fluorescence drops further relative to phosphorescence, which is blue-shifted slightly for both complexes (**41** (*cis*-HBC)  $\lambda_{\text{max}}$  573 nm, **40** (*trans*-HBC)  $\lambda_{\text{max}}$  574 nm). Specifically, the ratio of phosphorescence:fluorescence increases to 25:1 for **41** and 131:1 for **40**.

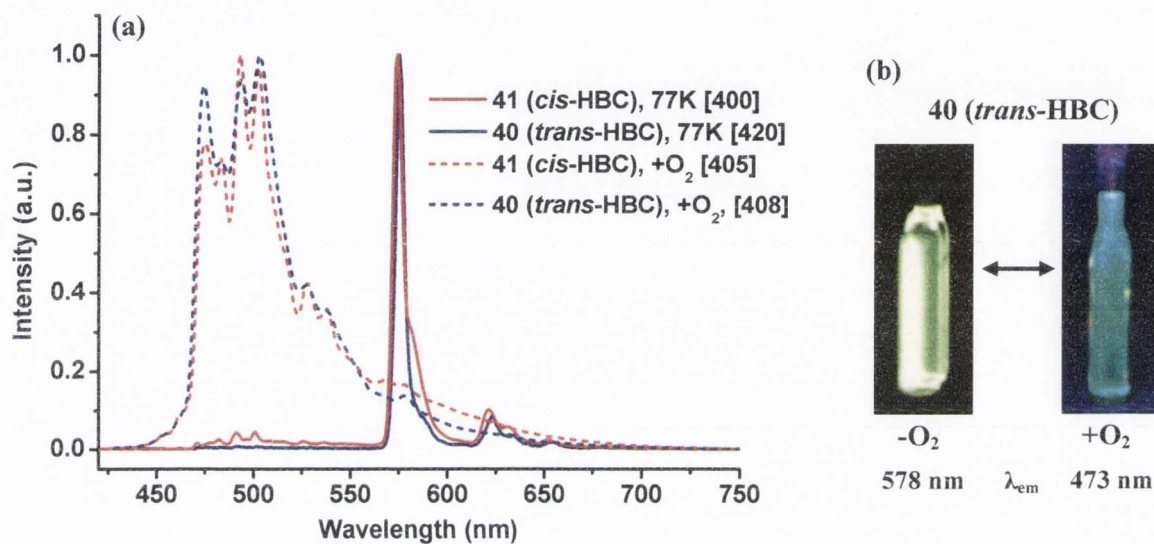


Figure 3.29: (a) Normalised emission spectra of **40** and **41** in  $\text{CH}_2\text{Cl}_2$  at 77 K (solid lines) and in oxygenated solution at 298 K (dashed lines). [ $\lambda_{\text{exc}}/\text{nm}$ ]. (b) Images of deoxygenated and oxygenated  $\text{CH}_2\text{Cl}_2$  solutions (298 K) of **40** ( $\lambda_{\text{exc}} \sim 360 \text{ nm}$ ).

### 3.5.2.3 Emission profile of **40** and **41** at room temperature in toluene ( $10^{-5} \text{ M}$ )

The photophysical properties of Pt-acetylide HBC complexes have been shown to exhibit significant solvent sensitivity.<sup>173</sup> In particular, it was found that the emission spectrum recorded in hexane was considerably broadened as a result of aggregation between the HBC chromophores.<sup>173</sup> With this in mind, the emission spectra of **41** (*cis*-HBC) and **40** (*trans*-HBC) were recorded in argon-degassed toluene solution, a significantly less polar solvent than  $\text{CH}_2\text{Cl}_2$ . (The complete insolubility of **40** (*trans*-HBC) and **41** (*cis*-HBC) in hexane precluded their measurement in this solvent).

Approximately 1:1 phosphorescence:fluorescence is observed for **41** (*cis*-HBC) at room temperature in degassed toluene (Figure 3.30). In contrast, the narrow emissive band at 578 nm dominates the corresponding **40** (*trans*-HBC) spectrum (13:1). In both cases, a

greater degree of fluorescence (relative to phosphorescence) from the HBC chromophore is observed in toluene solution than in the more polar  $\text{CH}_2\text{Cl}_2$ , indicating that the rate of intersystem crossing for the complexes is less in the less polar solvent. Ultimately, the observed emission profile is almost the same indicating that the excited state is not strongly affected by aggregation in these two solvents. However, a second consideration must be that in addition to its properties as a non-polar solvent, toluene may be used to perturb aggregation between fused graphene subunits. For example, in the NMR characterisation of  $[\text{Ru}(\text{bpy})_2(\text{N-HSB})](\text{PF}_6)_2$ , benzene was employed as a competing stacking molecule to off-set intermolecular aggregation between the polyaromatic cores.<sup>28</sup> It is likely that this property outweighs its non-polarity to influence the emissive properties of **40** and **41**.

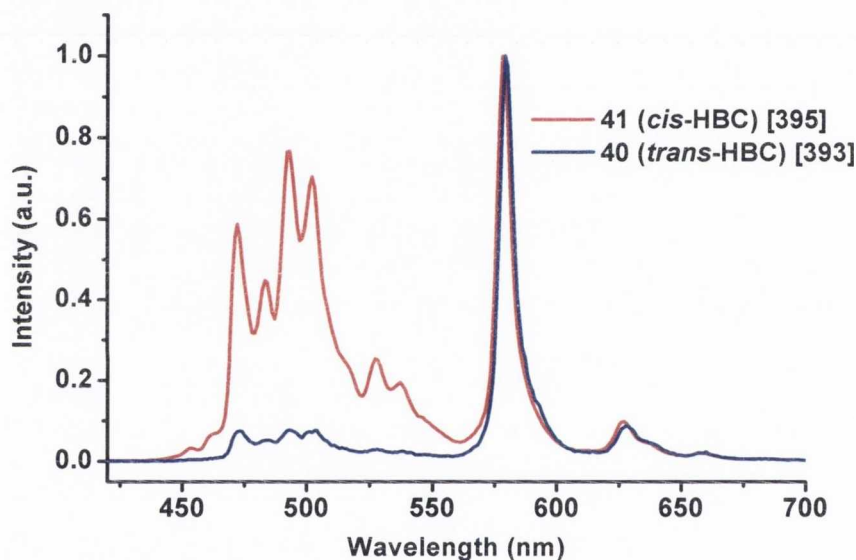


Figure 3.30: Normalised emission spectra of **40** and **41** in argon-degassed toluene solution ( $\sim 10^{-5}$  M) [ $\lambda_{\text{exc}}/\text{nm}$ ].

#### 3.5.2.4 Nature of the emissive excited states in **7**, **40** and **41**

In Figure 3.31, a Jablonski energy level diagram is shown, illustrating the photoinduced electronic transitions of ethynyl-HBC (**7**) and its corresponding *cis*-[Pt(**7**)<sub>2</sub>(dppe)] (**41**) and *trans*-[Pt(**7**)<sub>2</sub>(PPh<sub>3</sub>)<sub>2</sub>] (**40**) complexes in  $\text{CH}_2\text{Cl}_2$  solution at 298 K. (The energy of the  $^1\pi\pi^*$  state calculated from the onset of allowed fluorescence is  $\sim \lambda$  470 nm).

For both ligand **7** and complexes **40** and **41**, the absorption of light (Figure 3.31, (a)) forms the  $^1\pi\pi^*$  excited state ( $S_1$ ) which has an energy of  $\sim 2.6$  eV. As indicated in the absorption spectrum (Figure 3.18), the red-shifts of the most intense absorption band from ligand to

*cis* to *trans* complex are consistent with firstly the delocalisation of electron density through the metal centre in the complexes, and secondly with a more efficient extension of  $\pi$ -conjugation along the molecular axis when the HBC ligands are mutually *trans*.<sup>177</sup>

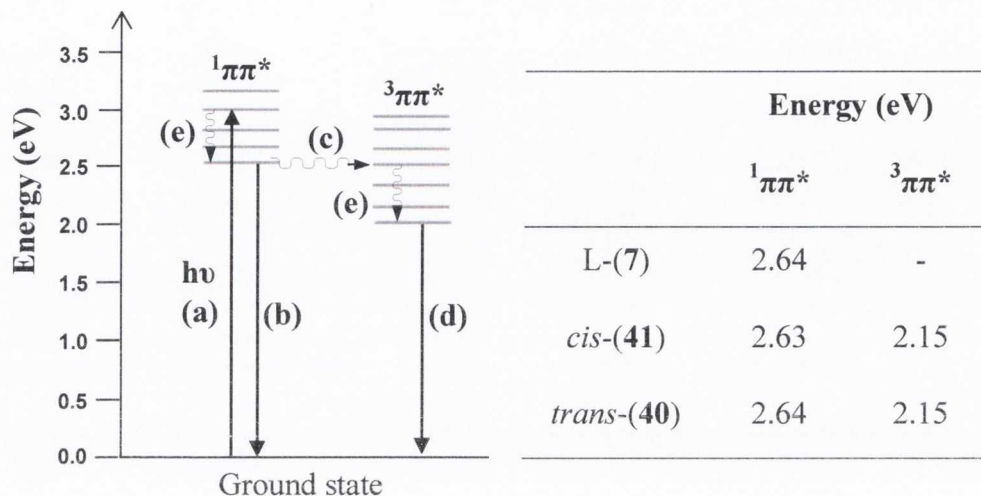


Figure 3.31: Jablonski energy level diagram for ethynyl-HBC ligand (7) and **40** (*trans*-HBC) and **41** (*cis*-HBC) complexes showing photoinduced radiative processes and inset, calculated approximate energies (eV) of excited states (from 298 K  $\text{CH}_2\text{Cl}_2$  solution measurements). (a) Absorption; (b) & (d) Emission; (c) Intersystem crossing; (e) Internal conversion.

Ethynyl-HBC (**7**) emits only from this  $^1\pi\pi^*$  state (Figure 3.31, (b)) with a quantum yield,  $\Phi_{\text{em}} = 0.093$  (0.079 in oxygenated solution). In the case of the HBC complexes **40** and **41**, the incorporation of the heavy Pt(II) metal facilitates intersystem crossing from the  $^1\pi\pi^*$  excited state to the  $^3\pi\pi^*$  ( $T_1$ ) excited state (c) from which phosphorescent radiative decay occurs (Figure 3.31, (d)). On the basis of emission measurements, the energy of this triplet state ( $^3\pi\pi^*$ ) on the HBC chromophore is located at  $\sim 2.15$  eV and the singlet-triplet splitting ( $S_1-T_1$ ) is 0.5 eV. This is comparable to that observed by Schanze ( $T_1$ : 2.14 eV,  $\Delta E$ : 0.6 eV) and Müllen (2.15 eV  $\Delta E$ : 0.5 eV) for their Pt-HBC complexes.<sup>172-173</sup>

The ratio of phosphorescence:fluorescence provides an estimate for the efficiency of intersystem crossing between  $S_1$  and  $T_1$  excited states. For **41** (*cis*-HBC), in both argon-degassed  $\text{CH}_2\text{Cl}_2$  at room-temperature (Figure 3.28) and 77 K (Figure 3.29), proportionally more fluorescence is observed relative to **40** (*trans*-HBC). This effect was also observed in the two original Pt(II) acetylide complexes (Figure 3.3, (a)) prepared by Schanze *et al.*<sup>173</sup> In complex (i) where the Pt-acetylide is directly attached to the HBC chromophore, almost exclusive phosphorescence was observed at room temperature, indicating very

rapid intersystem crossing from singlet ( $^1\pi\pi^*$ ) to triplet ( $^3\pi\pi^*$ ) excited states. In contrast, in complex (ii) where a phenyl ring separates the Pt-alkynyl from the HBC subunit, the fluorescence is considerably stronger (~3:2 phosphorescence:HBC fluorescence), analogous to *cis*-[Pt(**7**)<sub>2</sub>(dppe)] (**41**) prepared in this work. This indicates that the rate of intersystem crossing is less competitive with radiative decay of the  $^1\pi\pi^*$  excited state.

The measured quantum yields for **7** are comparable to those available in the literature and increase from oxygenated to deoxygenated solution, as would be anticipated.<sup>173</sup> In addition, a decrease in  $\Phi_{em}$  on moving from ligand to complex is observed, a trend also observed in the two other reported examples of Pt(II)-acetylide functionalised HBCs.<sup>172-173</sup> A reduction in quantum yield on moving from oxygenated to degassed solutions is also observed. The removal of oxygen removes a pathway of non-radiative decay of the triplet excited state with a corresponding enhancement in radiative decay and so the intensity of broad ligand-centred fluorescence decreases relative to narrow-band width phosphorescence, resulting in a reduction in measured area relative to that of the quantum yield standard employed, 4',6-diamidino-2-phenylindole dihydrochloride.

### 3.6 Summary and Conclusions

This work details the synthesis of four novel Pt(II)  $\sigma$ -acetylide molecular systems incorporating uncyclised propeller ligand **6** and its corresponding fully cyclised HBC **7**. Complexes in both *cis* and *trans* geometries were successfully prepared by careful choice of platinum(II) precursor using either monodentate or bidentate phosphine auxiliary ligand. All the complexes were fully characterised by spectroscopic and analytical methods.

As anticipated, the optical properties of uncyclised **6** and planarised ligand **7** are very different. The appearance of highly structured red-shifted bands in the UV-visible spectrum of **7** occurs as a result of enhanced  $\pi$ -electron delocalisation within the molecule and its enforced planarity. In non-planar polyphenylene **6**, no effective conjugation between the rings means that such features are entirely absent. Similarly, the photoluminescence spectra of **6** and **7** reveal that emission from **6** is quite broad and featureless ( $\lambda_{max}$  370 nm) as is typical of non-planar polyphenylene compounds, whereas the emission from ethynyl-HBC (**7**) is red-shifted (onset at  $\lambda$  470 nm) and is composed of significant vibronic fine structure. **7** displays notably longer emission lifetimes in both

solution and in the solid state and improved quantum yields as is characteristic of hexa-*peri*-hexabenzocoronenes.

Both uncyclised and cyclised sets of Pt(II) compounds are dual-luminescent. They each possess a higher energy ligand-based fluorescence emission, slightly red-shifted and with longer lifetimes than the corresponding free ligand. In both cyclised and uncyclised compounds, strong spin-orbit coupling induced by the heavy metal Pt(II) centre promotes intersystem crossing to populate the  $T_1$  excited state on the acetylide ligand.<sup>181</sup> As a result, the lower energy bands have significant phosphorescent character, as evidenced by the longer lifetimes recorded. HBC complexes **41** (*cis*-HBC) and **40** (*trans*-HBC) exhibit remarkably long lifetimes in degassed  $\text{CH}_2\text{Cl}_2$  (**40** 30.9  $\mu\text{s}$ ; **41** 18.3  $\mu\text{s}$ ) for the sharp phosphorescent band at 578 nm (a feature that is absent in HBC ligand (**7**)). Moving from *cis* to *trans* complexes, less positive Pt(II)/Pt(III) oxidation potentials, slightly enhanced fluorescence lifetimes, red-shifted absorption bands in the UV spectra and notably extended phosphorescence lifetimes (particularly in the case of **41** (*cis*-HBC) and **40** (*trans*-HBC)) are observed. In combination, these results clearly demonstrate that the *trans* arrangement of acetylide ligands on the Pt(II) centre is optimal for  $\pi$ -conjugation along the molecular axis. This could have consequences for opto-electronic applications which involve tapping into the energy of long-lived excited states, or into the design of polymeric chromophores.





## Chapter 4

**[Pt(N<sup>^</sup>N)(σ-acetylide)<sub>2</sub>]:**

**Synthesis, Structure and Photophysics**



## 4.1 Introduction

In continuation of the work described in Chapter 3 on *cis* and *trans* Pt(II) alkynyl complexes incorporating unfused polyphenylene and planar hexa-*peri*-hexabenzocoronenes, this chapter adds a further layer of complexity to the manifold of emissive excited states by combining the bipyridyl ligand, 1-(2,2'-bipyrid-6-yl)-2,3,4,5-tetra-(4-*tert*-butylphenyl)benzene (**4**), with Pt(II) acetylides. This combination of oligopyridines and platinum acetylides would be expected to yield a series of complexes with fascinating optical properties, tunable by modification of the acetylides attached to the platinum metal core.

Ligand **4** is designed such that two potential coordination modes to a metal centre are possible (Figure 4.1). The first, bidentate bipyridyl coordination to a transition metal (Figure 4.1, (a)), is anticipated to be the most facile and indeed was employed in Chapter 2 to synthesise the heteroleptic complex [Ru(bpy)<sub>2</sub>(**4**)](PF<sub>6</sub>)<sub>2</sub> (**36**). The second coordination mode involves CH activation on the free site on the central phenyl ring – specifically deprotonation at this position to form a C<sup>-</sup> anion. This renders the ligand overall anionic in nature and facilitates *pseudo*-terpyridine coordination [N<sup>^</sup>N<sup>^</sup>C<sup>-</sup>] (Figure 4.1, (b)). Whereas bipyridines and terpyridines are considered to be weak-field ligands, a ligand which has the coordination mode [N<sup>^</sup>N<sup>^</sup>C<sup>-</sup>] has both π-acceptor (on the pyridine ring) and σ-donor (through the C<sup>-</sup>) properties and exerts a strong ligand field influence on the metal centre. As a result, the photophysical properties of structurally related terpyridine [N<sup>^</sup>N<sup>^</sup>N] and cyclometallated [N<sup>^</sup>N<sup>^</sup>C<sup>-</sup>] complexes are often dramatically different.<sup>208</sup>

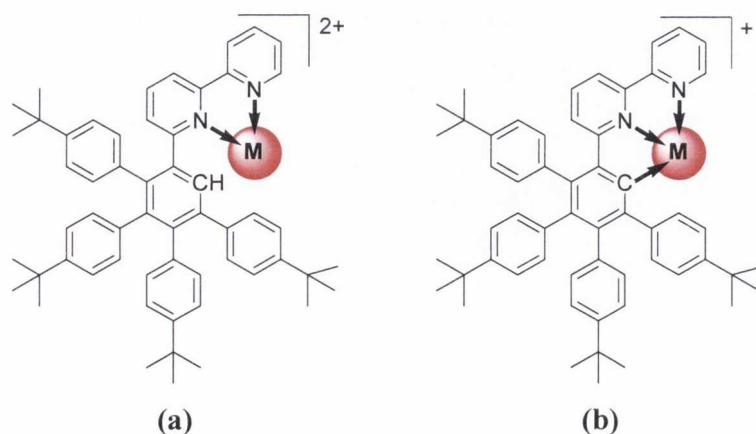


Figure 4.1: Bidentate (N<sup>^</sup>N) and tridentate (N<sup>^</sup>N<sup>^</sup>C) coordination modes of ligand **4** to a metal centre (M<sup>2+</sup>).

This project initially aimed to prepare a class of compounds where **4** is bound to Pt(II) as an N<sup>^</sup>N<sup>^</sup>C cyclometallated ligand, resulting in a series of complexes of general formula, [Pt(N<sup>^</sup>N<sup>^</sup>C)(C≡C-R)], (where (C≡C-R) is a series of substituted aryl acetylide co-ligands). Unfortunately, N<sup>^</sup>N<sup>^</sup>C coordination of ligand **4** could not be achieved in reasonable yield despite trying multiple synthetic methods. However, bidentate N<sup>^</sup>N coordination to the Pt(II) metal centre did occur and the complex [Pt(**4**)Cl<sub>2</sub>] ([Pt(N<sup>^</sup>N)Cl<sub>2</sub>], **44**) was employed as the precursor to a series of [Pt(N<sup>^</sup>N)(C≡C-R)<sub>2</sub>] complexes. There is significant precedent for complexes of both classes ([Pt(N<sup>^</sup>N<sup>^</sup>C)(C≡CR)] and [Pt(N<sup>^</sup>N)(C≡CR)<sub>2</sub>]) in the literature. The incorporation of strong-field ligands, such as acetylides or cyclometallating ligands, into the coordination sphere of Pt(II) polypyridyl complexes has a dramatic effect on room temperature photoluminescence. These ligands induce a larger splitting between the filled and empty d-orbitals on the metal centre, such that that non-radiative decay via metal-centred d-d states is reduced as they are less thermally accessible and emission at room temperature is observable.<sup>149</sup>

This chapter describes the synthesis and characterisation of a series of bipyridyl platinum(II) complexes incorporating polyaromatic ligand **4** (Ar<sub>5</sub>-Bpy). The electronic properties of these were modified *via* the attachment of σ-acetylide moieties to the platinum centre, where the electronic demand or the extent of π-electronic delocalisation of the acetylide is varied (i.e. from an electron-withdrawing CF<sub>3</sub> substituent to an electron-rich HBC acetylide). A full photophysical and electrochemical examination has revealed significant complexity in the nature of the emissive states of these complexes.

#### 4.1.1 Room Temperature emission from [Pt(N<sup>^</sup>N)Cl<sub>2</sub>] vs. [Pt(N<sup>^</sup>N<sup>^</sup>C)Cl]

Pt(II) complexes have a preference for square-planar geometry and as a result possess an unoccupied  $d_{x^2-y^2}$  orbital which is strongly anti-bonding (Figure 4.2, (a)). Diimine ligands (such as 2,2'-bipyridine) exert a relatively weak ligand field on the metal centre and so the HOMO and LUMO are both located on metal orbitals. Excitation of [Pt(N<sup>^</sup>N)X<sub>2</sub>] complexes (X=halide), results in the population of the  $d_{x^2-y^2}$  orbital and as a result, efficient non-radiative decay via ligand field (d-d) excited states (Figure 4.2, (a)). Correspondingly, simple Pt(II) bipyridyl complexes with halide co-ligands are in general non-emissive in solution at room temperature.<sup>149,209</sup>

In contrast,  $[\text{Pt}(\text{N}^{\wedge}\text{N}^{\wedge}\text{C})\text{Cl}]$  complexes are highly emissive at room temperature. As a strong-field ligand, the energy of the deactivating d-d states are raised relative to emissive metal-to-ligand charge transfer (MLCT) states and they are less thermally accessible (Figure 4.2, (b)). As a result, the simple complex  $[\text{Pt}(\text{N}^{\wedge}\text{N}^{\wedge}\text{C})\text{Cl}]$  (Figure 4.2, (b)  $\text{N}^{\wedge}\text{N}^{\wedge}\text{CH} = 6\text{-phenyl-2,2'-bipyridine}$ ) exhibits long-lived  $^3\text{MLCT}$  emission, with a lifetime of  $0.51\ \mu\text{s}$ .<sup>210-211</sup>

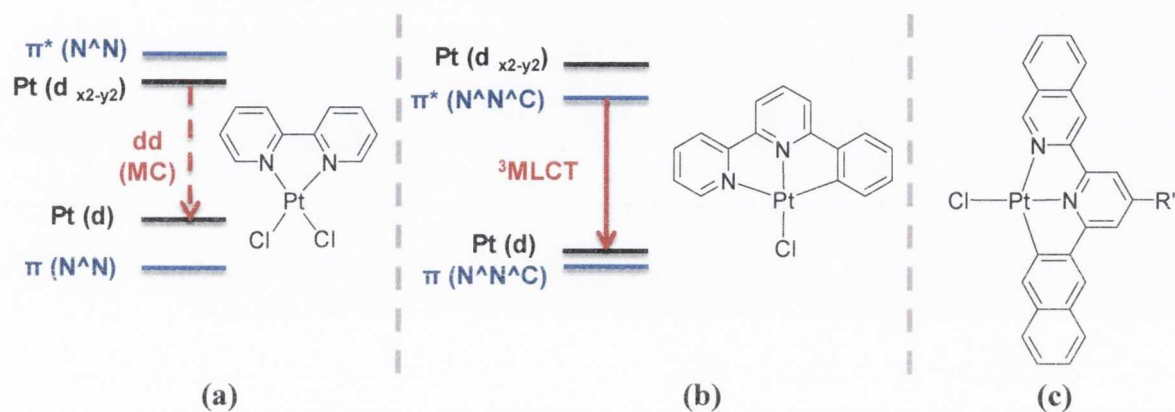


Figure 4.2: Relative energy level diagrams showing room temperature excited states of  $[\text{Pt}(\text{bpy})\text{Cl}_2]$  (a) and  $[\text{Pt}(\text{N}^{\wedge}\text{N}^{\wedge}\text{C})\text{Cl}]$  (b) (Dashed red arrow = non-radiative decay, solid red arrow = radiative decay).<sup>211</sup> Structure of WOLED-incorporated complex (c,  $\text{R}' = \text{H}, (\text{CF}_3)_2\text{C}_6\text{H}_3$ ).<sup>212</sup>

$[\text{Pt}(\text{N}^{\wedge}\text{N}^{\wedge}\text{C})]^+$  coordination complexes, often in conjunction with acetylide co-ligands in the fourth coordination site, have found application in a variety of fields. The high thermal stability, microsecond lifetimes and emission tunability (*via* ligand modification) of simple  $[\text{Pt}(\text{N}^{\wedge}\text{N}^{\wedge}\text{C})(\text{C}\equiv\text{CR})]$  complexes and  $[\text{Pt}(\text{N}^{\wedge}\text{N}^{\wedge}\text{C})\text{Cl}]$  complexes with extended  $\pi$ -conjugation (Figure 4.2, (c)) has seen them incorporated into both yellow-red emitting OLEDs and white OLEDs (WOLEDs) as charge-transfer phosphors.<sup>212-215</sup>  $[\text{Pt}(\text{N}^{\wedge}\text{N}^{\wedge}\text{C})(\text{C}\equiv\text{CR})]$  chromophores (and analogous  $[\text{Pt}(\text{N}^{\wedge}\text{N}^{\wedge}\text{N})(\text{C}\equiv\text{CR})]^+$  systems) have recently been employed as sensitizers in cobalt-catalysed, visible light-driven  $\text{H}_2$  production.<sup>216</sup> They have also found application as protein binding probes in live cell imaging, intercalating/minor-groove binding agents for DNA and as cytotoxic materials for several carcinoma cell lines.<sup>217-218</sup>

#### 4.1.2 Highly emissive $[\text{Pt}(\text{N}^{\wedge}\text{N})(\text{C}\equiv\text{CR})_2]$ complexes

The first diimine Pt(II) bis-acetylide was prepared by Che in 1994 and initiated a surge of interest in the field.<sup>219</sup> The highly emissive complex,  $[\text{Pt}(\text{phen})(\text{C}\equiv\text{C-Ph})_2]$ , displaying a

broad, structureless red-shifted emission band at room temperature (relative to  $[\text{Pt}(\text{phen})_2]^{2+}$ ), was assigned to a  $[\text{d}(\text{Pt}) \rightarrow \pi^*(\text{phen})]$   $^3\text{MLCT}$  excited state and was prepared *via* displacement of the labile 1,5-cyclooctadiene (cod) group by a phenanthroline ligand from the Pt precursor  $[\text{Pt}(\text{cod})(\text{C}\equiv\text{CPh})_2]$ .

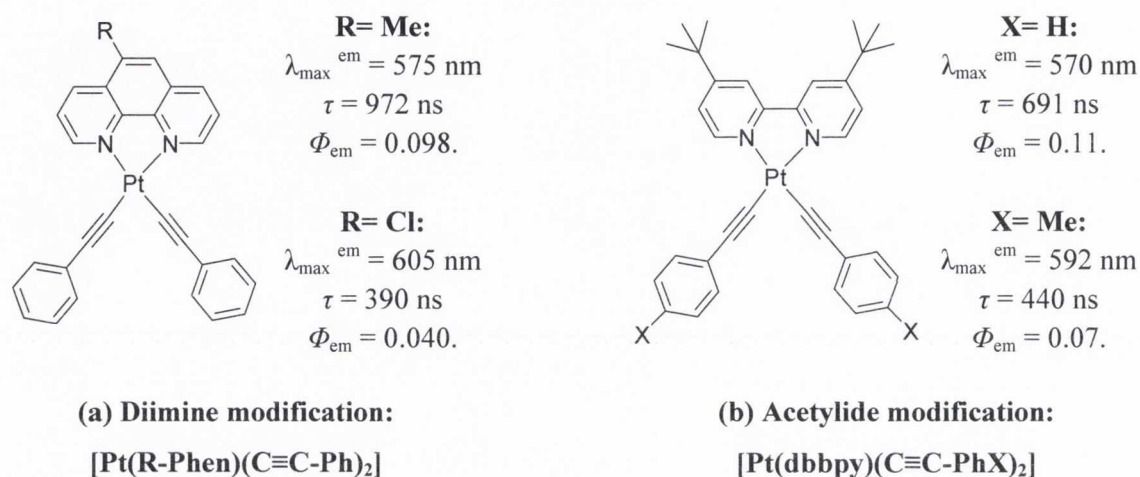


Figure 4.3: Effect of varying the diimine and acetylide on the photophysical properties of  $[\text{Pt}(\text{N}^{\wedge}\text{N})(\text{C}\equiv\text{CAr})_2]$  systems (dbbpy = 4,4'-di(tert-butyl)bipyridine).<sup>220</sup>

Several years later, the Eisenberg group published a comprehensive study examining the nature of the emissive states in diimine Pt(II) bis-acetylides.<sup>220</sup> In one series of complexes, the aryl-acetylides were kept constant while the substituents on the diimine were varied (Figure 4.3, (a)). A bathochromic shift in emission maximum was observed as the electron-withdrawing ability of the diimine increased, corresponding to the stabilisation of a diimine-based LUMO. Conversely, in the second series of complexes the diimine was held constant while the donor ability of the aryl acetylide was varied (Figure 4.3, (b)). A red-shift in emission energy was recorded with increasing electron density on the acetylide, corresponding to the destabilisation of a metal-based HOMO. Almost concurrently, Schanze *et al.* and Che and co-workers published two similar investigations that also demonstrated emission tunability using diimine/acetylide substituents and also assigned the emissive state as  $^3\text{MLCT}$   $[\text{d}(\text{Pt}) \rightarrow \pi^*(\text{N}^{\wedge}\text{N})]$ .<sup>221-222</sup>

More recent analyses of the emissive properties in conjunction with DFT calculations on Pt(II) diimine bis-acetylide complexes have revealed that the HOMO in such systems often contains substantial contributions from  $\pi(\text{acetylide})$  orbitals in addition to  $\text{d}(\text{Pt})$  orbitals.<sup>150,223</sup> This would render the lowest emissive excited state a mixture of MLCT

[d(Pt)→π\*(bpy)] and L'LCT, ligand-to-ligand charge transfer [π(acetylide)→π\*(bpy)]. One of the only differentiating features, in terms of optical properties, of mixed MLCT/L'LCT states compared to pure MLCT is the partial structuring of emission bands sometimes observed in MLCT/L'LCT.<sup>150</sup> There are now many articles reporting aryl-acetylide Pt(II) diimine, terpyridine or their cyclometallated analogues in which the lowest energy emissive excited state is assigned to a mixed <sup>3</sup>MLCT/<sup>3</sup>L'LCT, sometimes referred to <sup>3</sup>(ML)LCT.<sup>224-226</sup> For example, in a structurally related series of complexes prepared by Yam *et al.* of general formula [Pt(N^N)(C≡CAr)<sub>2</sub>] incorporating a functionalized bipyridine ligand (4,4'-dicarboxy-2,2'-bipyridine), the photophysical properties match those observed in earlier work by Eisenberg and Schanze.<sup>227</sup> The authors therefore assign the lowest energy transition as a spin-allowed, metal-perturbed [π(acetylide)→π\*(bpy)], essentially a mixture of MLCT/L'LCT, on the basis of a thorough electrochemical and photophysical examination and DFT calculations.

#### 4.1.3 Applications of [Pt(diimine)(C≡CAr)<sub>2</sub>]

Pt(II) diimine bis-acetylides have been tested as electrophosphorescent emitters in OLEDs although their application in this field is limited as they readily decompose during vapour deposition.<sup>213,221</sup> Very recently, their performance as chromophores in dye-sensitized solar cells (DSSCs) was evaluated but they showed quite low overall power conversion efficiencies (1.8 %).<sup>227</sup> However, Pt(II) diimine σ-acetylides have found quite extensive application as vapoluminescent materials (Figure 4.4), e.g. in the sensing of volatile organic compounds (VOCs) containing one carbon atom such as CH<sub>2</sub>Cl<sub>2</sub>, CHCl<sub>3</sub> and CH<sub>3</sub>I (not observed for larger hydrocarbons).<sup>228-229</sup>

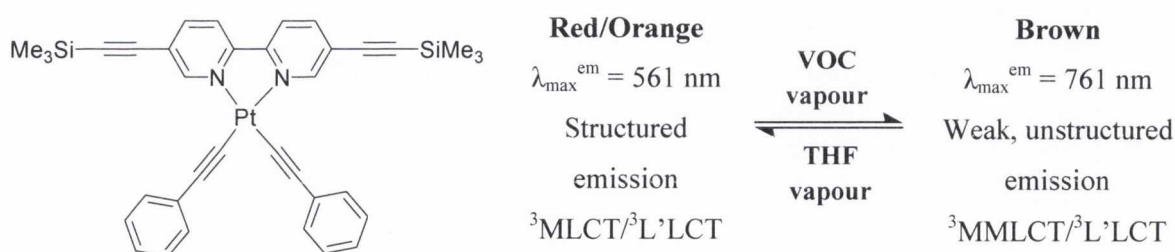


Figure 4.4: Vapoluminescent behaviour of a Pt(II) diimine bis-acetylide complex towards small volatile organic compounds.<sup>229</sup>

As shown in Figure 4.4, a simple acetylene-substituted bipyridyl-Pt(II) complex undergoes a striking red-shift in emission energy and a colour change upon VOC exposure ( $\text{CH}_2\text{Cl}_2$ ,  $\text{CHCl}_3$  or  $\text{CH}_3\text{I}$ ), as a result of the formation of Pt-Pt interactions in the vapour-exposed form of the complex.<sup>229</sup> With the aid of DFT calculations and X-ray crystal structures, this has been attributed to the reversible conversion of a  ${}^3\text{MLCT}/{}^3\text{L}'\text{LCT}$  [ $\text{d}(\text{Pt}) \rightarrow \pi^*(\text{bpy})$ ] / [ $\pi(\text{acetylide}) \rightarrow \pi^*(\text{bpy})$ ] emissive excited state to a  ${}^3\text{MMLCT}/{}^3\text{L}'\text{LCT}$  [ $\text{d}(\text{Pt})/\text{d}(\text{Pt}) \rightarrow \pi^*(\text{bpy})$ ] / [ $\pi(\text{acetylide}) \rightarrow \pi^*(\text{bpy})$ ] state upon exposure to saturated VOC vapour.

Eisenberg and co-workers have undertaken extensive studies on the incorporation of Pt(II) diimine bis-acetylide systems as the charge-transfer chromophore in two and three component systems (dyads and triads) containing donor and acceptor moieties with the aim of promoting long-range photoinduced charge separation.<sup>230</sup> Recently, a photochromic bis-alkynyl complex containing a dithienyl-functionalised phenanthroline has been prepared by Yam, which demonstrates photosensitized photochromism, triggering reversible photocyclisation of the dithienyl ligand and a switch of emissive excited state from  ${}^3\text{MLCT}/{}^3\text{LLCT}$  (open) to  ${}^3\text{IL}$  (closed).<sup>231</sup> The emission band of the photocyclised product is red-shifted as a result of increased  $\pi$ -conjugation in the closed form (Figure 4.5).

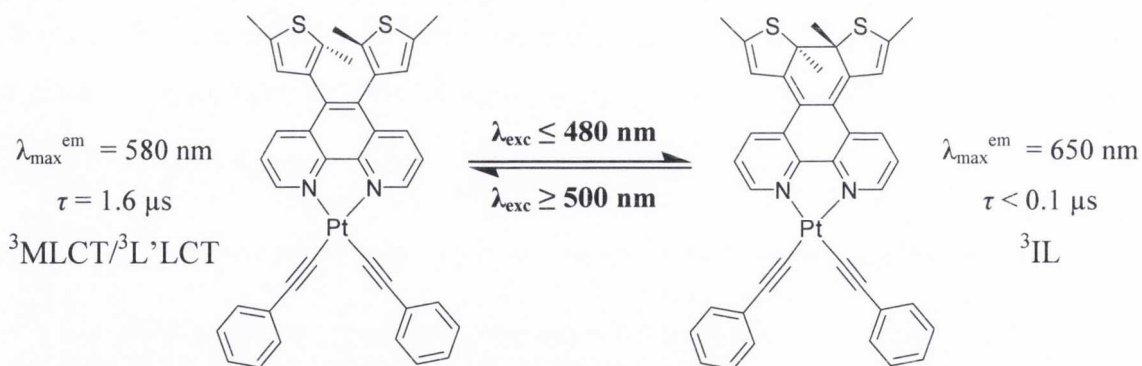


Figure 4.5: Photochromic bis-alkynyl Pt(II) diimine complex and photophysical properties.<sup>231</sup>

## 4.2 Synthesis: $[\text{Pt}(\text{N}^{\wedge}\text{N}^{\wedge}\text{C})\text{Cl}]$ (43) and $[\text{Pt}(\text{N}^{\wedge}\text{N})\text{Cl}_2]$ (44) as precursors

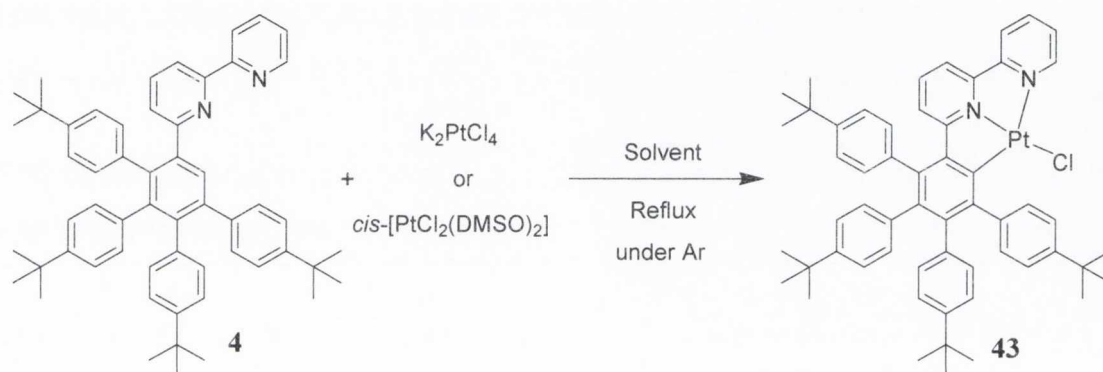
The considerably enhanced redox and photophysical properties of cyclometallated Pt(II) complexes compared to those of bidentate nitrogen-coordinated complexes encouraged us to undertake initially the preparation of  $[\text{Pt}(\text{4:N}^{\wedge}\text{N}^{\wedge}\text{C})\text{Cl}]$  (43). CH activation and subsequent deprotonation to produce an anionic  $\text{N}^{\wedge}\text{N}^{\wedge}\text{C}$  ligand has been achieved in the



literature *via* relatively facile means. Correspondingly, few synthetic difficulties were anticipated in the case of **43** despite the hindered nature of the ligand.

#### 4.2.1 Synthetic procedure: 1 Step Method

Initial attempts to produce cyclometallated complex **43** involved heating a solution of **4** ( $\text{Ar}_5\text{-Bpy}$ ) and  $\text{K}_2\text{PtCl}_4$  to reflux under an inert atmosphere for several hours (Scheme 4.1). A variety of solvents were used for this purpose. From reactions refluxing in water:acetonitrile, ethanol or water:THF for several days, free ligand alone was recovered.<sup>232-233</sup>



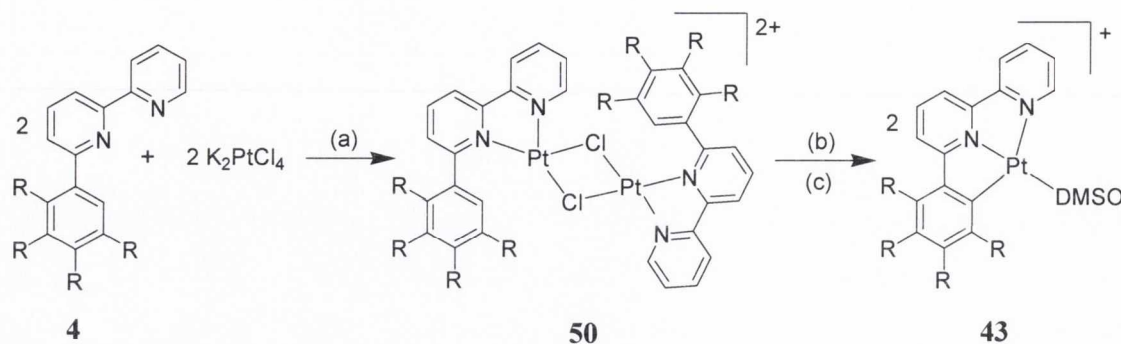
Scheme 4.1: General synthetic route to  $[\text{Pt}(\text{N}^{\wedge}\text{N}^{\wedge}\text{C})\text{Cl}]$  (**43**).

An alternative route employing  $\text{cis-}[\text{PtCl}_2(\text{DMSO})_2]$  as Pt precursor with diimine ligand **4** in refluxing chloroform yielded a yellow powder product in 77 % yield. (The use of  $[\text{cis-}\text{PtCl}_2(\text{DMSO})_2]$  was required as it is more soluble than  $\text{K}_2\text{PtCl}_4$  in less polar organic solvents such as  $\text{CHCl}_3$  and  $\text{CH}_2\text{Cl}_2$ ). The same yellow product was obtained *via* one of the most common routes towards CH activation, specifically reflux of  $\text{K}_2\text{PtCl}_4$  with the desired ligand in glacial acetic acid.<sup>234</sup>

#### 4.2.2 Synthetic procedure: 2 Step Method

Preparation of  $[\text{Pt}(\text{N}^{\wedge}\text{N}^{\wedge}\text{C})\text{Cl}]$  (**43**) was also attempted *via* a two-step route, adapted from a literature procedure for the synthesis of a bis-cyclometallated  $[\text{Pt}(\text{C}^{\wedge}\text{N}^{\wedge}\text{C})\text{X}]$  complex (Scheme 4.2).<sup>235-236</sup> The first step involves refluxing the ligand with  $\text{K}_2\text{PtCl}_4$  in glacial acetic acid to yield a dichloro-bridged dimer (**50**). The second step employs water to induce CH activation and formation of the Pt-C bond. Dissolution of the filtrate in

minimum hot DMSO and precipitation from water should yield a DMSO-substituted derivative of **43**.



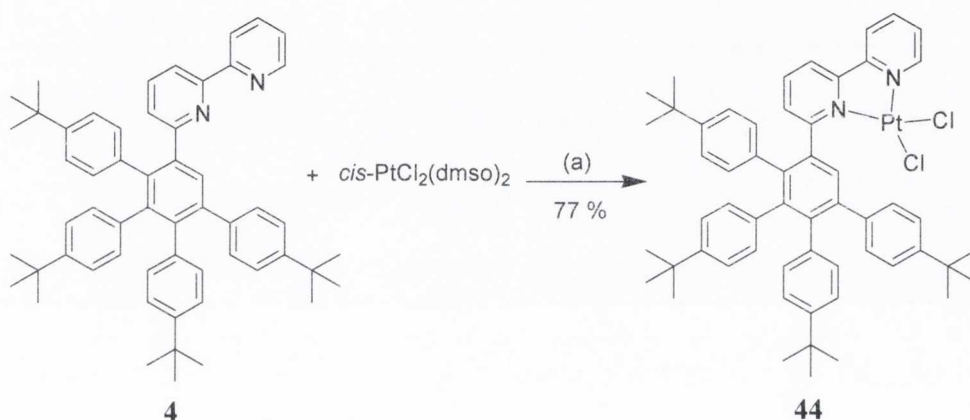
*Scheme 4.2: Proposed 2-step synthesis of dichloro-bridged dimer (**50**) and subsequent reaction to form cyclometallated **43** ( $R=4\text{-tert-butylphenyl}$ ). a)  $\text{AcOH}$ , Reflux, under  $\text{Ar}$ ; b)  $\text{DMSO}$ ; c)  $\text{H}_2\text{O}$ .*

The yellow products obtained from both one step and two step methods proved to be the same compound, which was identified by NMR spectroscopy and mass spectrometry as the bidentate  $\text{N}^{\wedge}\text{N}$  coordinated complex of **4**,  $[\text{Pt}(\text{N}^{\wedge}\text{N})\text{Cl}_2]$  (**44**). An electrospray mass spectrum of this complex showed a peak centred at  $m/z$  1048.3693 m.u., which corresponds to the calculated value for **44** plus a sodium cation  $[\text{M}+\text{Na}]^+$  with a calculated  $m/z = 1048.3679$  m.u. for  $[\text{C}_{56}\text{H}_{60}\text{N}_2\text{Cl}_2\text{Pt}+\text{Na}]^+$ . The NMR spectroscopic analysis of this complex is discussed in Section 4.2.4.

### 4.2.3 The serendipitous synthesis of $[\text{Pt}(\text{N}^{\wedge}\text{N}^{\wedge}\text{C})\text{Cl}]$ (**43**)

Despite the variety of methods employed, the synthesis of cyclometallated **43** proved to be very difficult. However, during attempts to obtain a crystal structure of  $[\text{Pt}(\text{N}^{\wedge}\text{N})\text{Cl}_2]$  (**44**), successful crystallisation of cyclometallated-**43** was achieved. **44** was dissolved in chloroform, a layer of ethanol placed on top and was left to stand for several weeks. The fine orange needles obtained were suitable for single-crystal X-ray diffraction (Section 4.2.5). NMR and mass spectral data on **43** were obtained by dissolving the orange crystals. An electrospray mass spectrum of an orange crystal shows a peak at  $m/z$  954.4332 m.u. corresponding to **43** but without the coordinated chloride ion  $[\text{M}-\text{Cl}]^+$  due to the fragmentation process in the mass spectrometer. This is in good agreement with the calculated  $m/z$  value 954.4326 m.u. for  $[\text{C}_{56}\text{H}_{59}\text{N}_2\text{Pt}]^+$ .

Unfortunately, attempts to prepare cyclometallated complex **43** on a large scale were unsuccessful. Recrystallisation of  $[\text{Pt}(\text{N}^{\wedge}\text{N})\text{Cl}_2]$  (**44**) from chloroform/ethanol resulted in the recovery of predominantly **44** with traces of cyclometallated **43**, but in yields of <10 %. In contrast,  $[\text{Pt}(\text{N}^{\wedge}\text{N})\text{Cl}_2]$  (**44**) can be reliably prepared by simply refluxing ligand **4** in chloroform with one equivalent of *cis*- $[\text{PtCl}_2(\text{DMSO})_2]$  under argon for 2 days until all traces of the ligand are gone (monitored by TLC). Reduction of the solvent *in vacuo*, followed by precipitation of the product as a yellow powder from excess methanol produces bidentate complex **44** in 77 % yield (Scheme 4.3).



Scheme 4.3: Synthesis of  $[\text{Pt}(\text{N}^{\wedge}\text{N})\text{Cl}_2]$  (**44**). (a)  $\text{CHCl}_3$ , 55 °C, under Ar, 48 hours.

#### 4.2.4 $^1\text{H}$ NMR Characterisation of $[\text{Pt}(\text{N}^{\wedge}\text{N})\text{Cl}_2]$ (**44**) and $[\text{Pt}(\text{N}^{\wedge}\text{N}^{\wedge}\text{C})\text{Cl}]$ (**43**)

The  $^1\text{H}$  NMR spectra of  $[\text{Pt}(\text{N}^{\wedge}\text{N})\text{Cl}_2]$  (**44**) and  $[\text{Pt}(\text{N}^{\wedge}\text{N}^{\wedge}\text{C})\text{Cl}]$  (**43**) in  $\text{CDCl}_3$  are presented in Figure 4.6. Comparative chemical shifts ( $\delta$ , ppm) for the bipyridine and H $\gamma$  on the central benzene ring on diimine ligand **4**,  $[\text{Pt}(\text{N}^{\wedge}\text{N})\text{Cl}_2]$  (**44**) and  $[\text{Pt}(\text{N}^{\wedge}\text{N}^{\wedge}\text{C})\text{Cl}]$  (**43**) are given in Table 4.1. The full assignment of **43** and **44** was facilitated using 2D TOCSY ( $^1\text{H}$ - $^1\text{H}$ ), HSQC ( $^1\text{H}$ - $^{13}\text{C}$ ) and HMBC (long-range  $^1\text{H}$ - $^{13}\text{C}$ ) NMR correlation experiments.

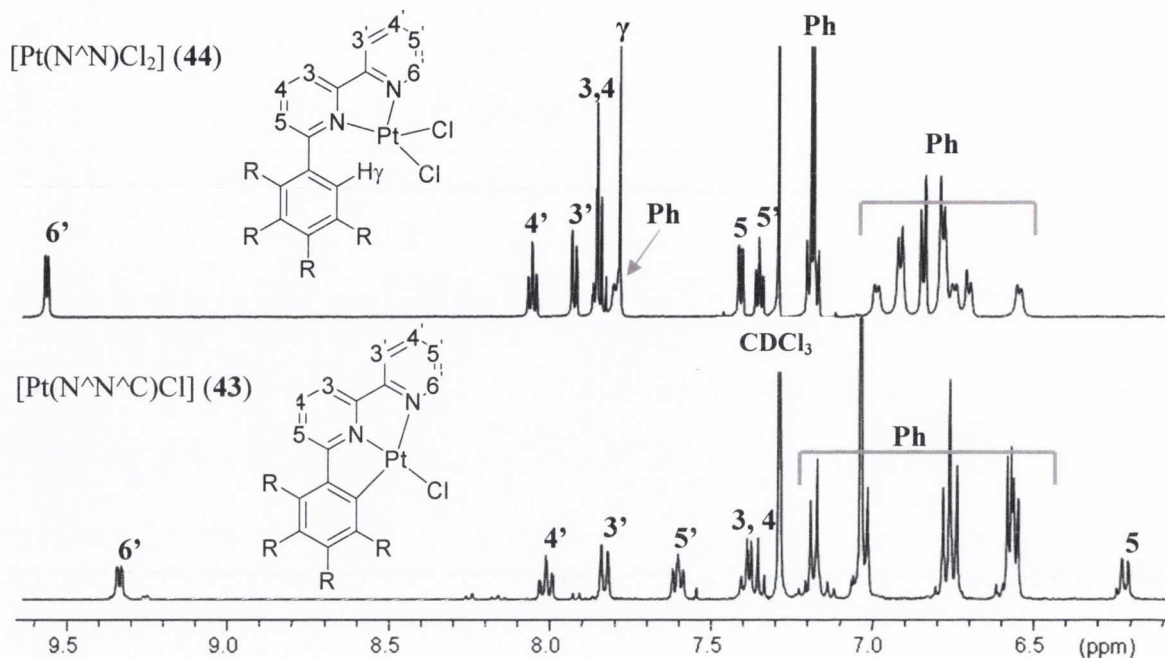


Figure 4.6:  $^1\text{H}$  NMR spectra of **44** (600.1 MHz, R.T.) and **43** (400.1 MHz, R.T.) in  $\text{CDCl}_3$ . Atom labelling as per inset figures.  $R = 4\text{-tert-butylphenyl}$ .

A key difference between the  $^1\text{H}$  NMR spectra of **43** and **44** is the absence of a singlet at  $\delta$  7.75 ppm in cyclometallated **43**, attributable to the proton in the  $\gamma$  position on the central phenyl ring (Figure 4.6). The deprotonation of  $\text{H}_\gamma$  in  $[\text{Pt}(\text{N}^{\wedge}\text{N}^{\wedge}\text{C})\text{Cl}]$  (**43**) to form a strong  $\sigma$ -donating  $\text{C}^-$  moiety facilitates the formation of the Pt-C bond and causes a significant upfield shift of all of the protons,  $\text{H}_3$ ,  $\text{H}_4$  and  $\text{H}_5$ , on the 3-spin pyridine ring. In particular,  $\text{H}_5$  located closest to  $\text{C}_\gamma$  shifts from  $\delta$  7.38 ppm in  $[\text{Pt}(\text{N}^{\wedge}\text{N})\text{Cl}_2]$  (**44**) to  $\delta$  6.19 ppm in cyclometallated-**43** (Table 4.1). A marginal upfield shift of  $\text{H}_\gamma$  from diimine ligand (**4**) to  $[\text{Pt}(\text{N}^{\wedge}\text{N})\text{Cl}_2]$  (**44**) ( $\delta$  7.87 to 7.75 ppm) can be explained by the proximity of the electron-rich Pt metal centre.

Table 4.1:  $^1\text{H}$  NMR spectroscopic data and assignments of bipyridine protons in ligand **4** and complexes **43** and **44** reported in  $\text{CDCl}_3$ . Chemical shifts in ppm.

Complex	Proton							
	$\text{H}_\gamma$	$\text{H}_{6'}$	$\text{H}_{5'}$	$\text{H}_{4'}$	$\text{H}_{3'}$	$\text{H}_5$	$\text{H}_4$	$\text{H}_3$
L ( <b>4</b> )	7.87	8.60	7.22	7.65	8.05	7.10	7.56	8.14
$[\text{Pt}(\text{N}^{\wedge}\text{N})\text{Cl}_2]$ ( <b>44</b> )	7.75	9.53	7.32	8.03	7.89	7.38	7.8	7.8
$[\text{Pt}(\text{N}^{\wedge}\text{N}^{\wedge}\text{C})\text{Cl}]$ ( <b>43</b> )	-	9.31	7.58	7.99	7.80	6.19	7.32	7.36

In general for Pt(II) complexes **43** and **44**, H6' is the most downfield signal on the  $^1\text{H}$  NMR spectrum (Table 4.1, atom labelling as per inset Figure 4.6). It appears as a doublet with a smaller vicinal coupling constant than the other bipyridine resonances ( $^3J_{\text{H6}'\text{H5}'} = 5.1$  Hz (**43**), 6.0 Hz (**44**)). H6' undergoes a marked downfield shift upon complexation, from  $\delta$  8.60 ppm in ligand (**4**) to  $\delta$  9.31-9.53 ppm (**43**, **44**). The square planar nature of the Pt(II) complexes means that the coordinated chloride ligand lies in close proximity to H6' and its strong electronegativity results in a more deshielded chemical shift for the resonance of this proton.<sup>66</sup> H5 and H5' are the most shielded protons on their respective pyridine rings in both ligand and complexes, with H5' becoming slightly more deshielded upon coordination for both complexes. In contrast, H3' becomes marginally more shielded (Table 4.1). In  $[\text{Pt}(\text{N}^{\wedge}\text{N})\text{Cl}_2]$  (**44**) and  $[\text{P}(\text{N}^{\wedge}\text{N}^{\wedge}\text{C})\text{Cl}]$  (**43**), H5' (and H4') appears as a doublet of doublets of doublets (ddd), due to vicinal coupling with adjacent H6' and H4' protons and a long-range coupling with H3' (e.g.  $[\text{Pt}(\text{N}^{\wedge}\text{N})\text{Cl}_2]$  (**44**):  $^3J_{\text{H5}'\text{H4}'/\text{H6}'} = 6.6$  Hz,  $^4J_{\text{H5}'\text{H3}'} = 1.5$  Hz).

The  $^1\text{H}$  NMR spectra of **43** and **44** are quite complex as a result of the asymmetric nature of the ligand employed and the four hindered *tert*-butyl phenyl substituents. In both cases, two doublets, each integrating for 2H, for an AB substitution pattern would be anticipated for each *tert*-butyl phenyl substituent as a result of free rotation. This is the case for  $[\text{Pt}(\text{N}^{\wedge}\text{N}^{\wedge}\text{C})\text{Cl}]$  (**43**) (Figure 4.6), where the phenyl rings occur as a series of linked doublets between  $\delta$  6.5-7.2 ppm (typically  $^3J_{\text{HH}} = 7.9$  Hz). However,  $[\text{Pt}(\text{N}^{\wedge}\text{N})\text{Cl}_2]$  (**44**) exhibits considerably different behaviour (Figure 4.6). There are more proton resonances attributable to phenyl rings than would be expected and several of these appear as broad doublets with  $^3J_{\text{HH}} = 7.3$  Hz (assigned *via* HMBC, HSQC and NOE experiments). Some of the proton signals for the phenyl rings appear much more downfield than would be expected. Steric constraints within the molecule prohibit the free rotation of one or more of the *tert*-butyl phenyl substituents and as a result four phenyl proton resonances instead of two are observed. Attempts to obtain a crystal structure of **44** were unsuccessful, however a crystal structure of a subsequent complex based on this Pt precursor provided further information on this steric hindrance (Section 4.3.1.5).

### 4.2.5 X-Ray Crystal Structure of 43.H<sub>2</sub>O

Crystals of **43** suitable for single-crystal X-ray diffraction analysis were grown from a chloroform/ethanol solution of [Pt(N<sup>^</sup>N)Cl<sub>2</sub>] (**44**) at room temperature as orange needles. [Pt(N<sup>^</sup>N<sup>^</sup>C)Cl] crystallises in the monoclinic space group *C2/c* with one molecule of **43** and one water molecule in the asymmetric unit.

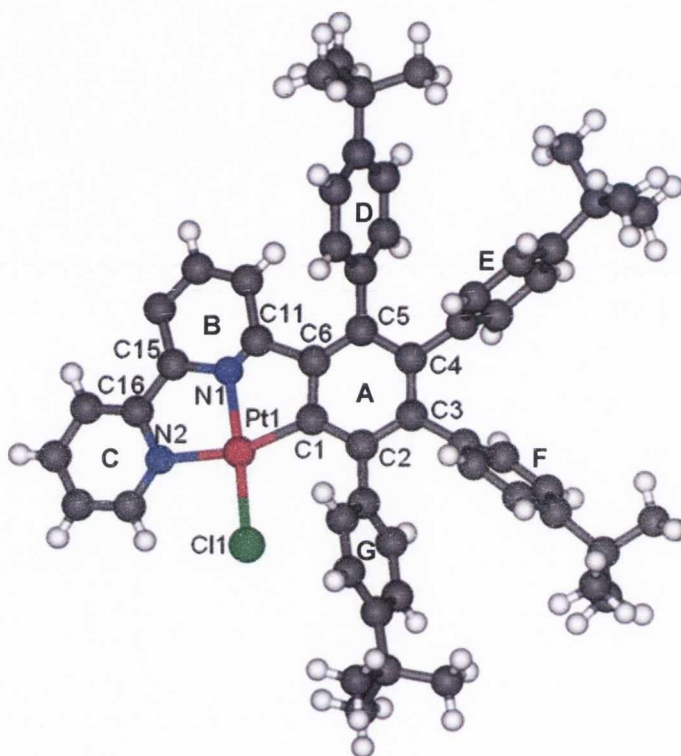


Figure 4.7: Perspective view of **43**, with selected atomic numbering shown. Solvent molecules have been removed for clarity. Selected bond lengths and angles are contained in Table 4.1.

C-Pt-Cl angles for related simple N<sup>^</sup>N<sup>^</sup>C Pt(II) complexes are typically  $\sim 100^\circ$  and N-Pt-C approximately  $82^\circ$ .<sup>121,237-238</sup> The geometry of the ligands about the Pt centre in **43** can be described as distorted square-planar, where the C(1)-Pt(1)-Cl(1) angle measures  $105.6(9)^\circ$  and N(1)-Pt(1)-C(1) is  $76.7(11)^\circ$  (Table 4.2). This distortion arises as a result of the geometric constraints of the [N<sup>^</sup>N<sup>^</sup>C] *pseudo*-terpyridine unit and the extended polyphenylene substituents on the central phenyl ring, particularly involving ring G. The dihedral angles between the central phenyl ring (Figure 4.7, A) and each of the aromatic rings (B and C on the N<sup>^</sup>N<sup>^</sup>C ligand subunit, D-G on the polyphenylene core) are given in Table 4.2. The ligand moiety is almost planar with the mean planes of B and C tilted  $10.8$  and  $11.9^\circ$  respectively from that of ring A. The four phenyl substituents are twisted at

angles between 73.8 and 85.8° from the plane of the central benzene ring A. These features are quite typical of propeller-like polyphenylenes synthesised previously within the group.<sup>31</sup>

Table 4.2: Selected bond lengths (Å) and bond angles (°) for **43**.

Bond	Bond Length (Å)	Bond Angle	Angle (°)	Tilt Angle of pyridine rings w.r.t. A (°)	Tilt Angle of <sup>t</sup> Bu-Phenyl rings w.r.t. A (°)
Pt(1)-C(1)	2.008(2)	C(1)-Pt(1)-N(1)	76.7(11)	<b>B:</b> 10.8	<b>D:</b> 73.8
Pt(1)-N(2)	2.112(2)	N(1)-Pt(1)-N(2)	84.9(10)	<b>C:</b> 11.9	<b>E:</b> 85.8
Pt(1)-N(1)	2.044(3)	C(1)-Pt(1)-Cl(1)	105.6(9)		<b>F:</b> 79.4
Pt(1)-Cl(1)	2.319(10)	N(2)-Pt(1)-Cl(1)	92.9(8)		<b>G:</b> 75.3

The Pt(1)-N(2) bond length is slightly longer (2.112(2) Å) than the Pt(1)-N(1) bond (2.044(3) Å), a feature arising from the *trans* influence (Table 4.2).<sup>121,237-238</sup> Pt(1)-N(2) is *trans* to the orthometallated phenyl ring, whereas Pt(1)-N(1) is *trans* to a chloride. The greater *trans* influence of the phenyl substituent (strong  $\sigma$ -donor) relative to the chloride results in a longer and weaker Pt(1)-N(2) bond. As expected, the Pt-Cl distance is significantly longer than the Pt-C or Pt-N bonds (2.319(10) Å).

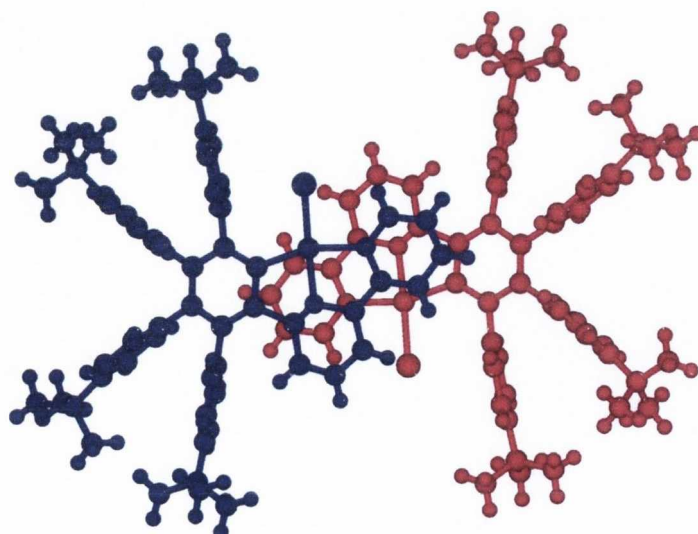


Figure 4.8: A packing diagram of **43** along the *b*-axis, showing  $\pi$ -interactions. Solvent molecules omitted for clarity.

The crystal structure shows the formation of dimeric pairs of molecules arranged in a head-to-tail fashion (Figure 4.8). In this interaction, ring C on the ligand moiety of one molecule undergoes an off-set face-to-face pi-packing interaction with the ring containing N1 (ring B) on the adjacent molecule in the dimer, with distances of 3.249 Å and 3.416 Å between N1 and a centroid calculated for ring C (Figure 4.9).

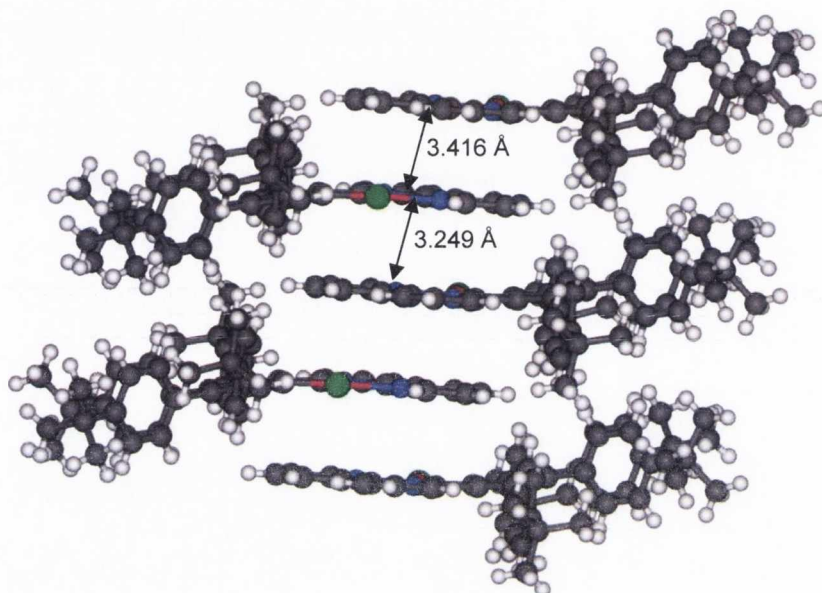


Figure 4.9: Packing arrangement of **43** viewed down the *c*-axis. Solvent molecules are omitted for clarity.

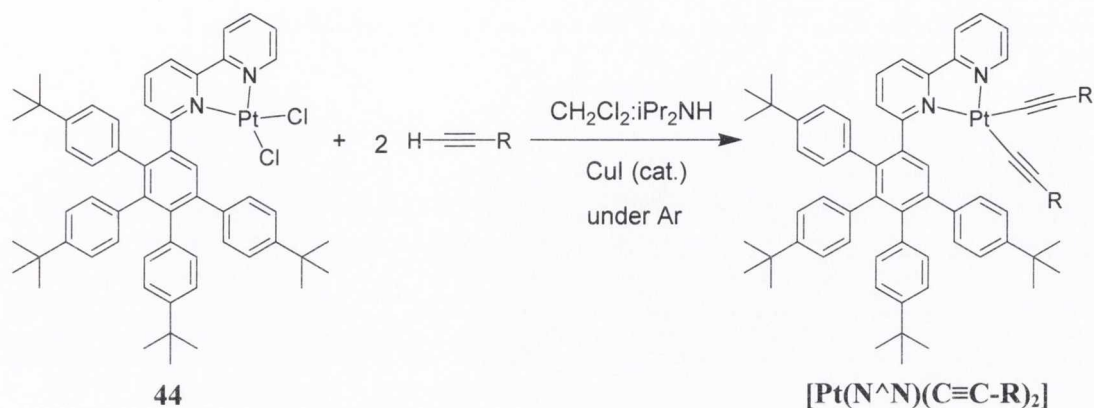
### 4.3 Synthesis and Characterisation of [Pt(N<sup>^</sup>N)(C≡C-R)<sub>2</sub>]

The synthesis of [Pt(N<sup>^</sup>N)Cl<sub>2</sub>] (**44**) proved to proceed in reliable yields (77 %) and as a result was chosen as the Pt(II) oligopyridine precursor for the preparation of a family of platinum(II)  $\sigma$ -acetylides, of general formula [Pt(N<sup>^</sup>N)(C≡C-R)<sub>2</sub>]. The prepared class of compounds contain two strong-field acetylide ligands and were expected to possess desirable photophysical properties.

[Pt(N<sup>^</sup>N)(C≡C-R)<sub>2</sub>] complexes are well known in the literature and are synthesised *via* well established methods. The most straightforward and commonly used is the CuI-catalysed dehydrohalogenative reaction of a platinum(II) diimine precursor with two equivalents of the required terminal alkyne in the presence of an amine base, essentially a Sonogashira cross-coupling reaction.<sup>178,219,239</sup> Hence reactions were carried out in



diisopropylamine ( $i\text{Pr}_2\text{NH}$ ) as base and  $\text{CH}_2\text{Cl}_2$  as solvent using a catalytic amount of  $\text{CuI}$  (5-7 mol%), stirring under argon in the dark over several days (Scheme 4.4).



Scheme 4.4: General reaction scheme for the synthesis of the family of diimine  $\text{Pt}(\text{II})$  bis  $\sigma$ -acetylides (chosen terminal acetylenes shown in Figure 4.10).

In the series of compounds prepared, the diimine ligand is held constant while the electronic and steric demands of the aryl acetylide co-ligands are altered by changing the acetylide substituent  $\text{R}$ , which may be an electron donating, withdrawing or delocalising group. In this work,  $[\text{Pt}(\text{N}^{\wedge}\text{N})(4\text{-}i\text{tert-butylphenyl acetylene})_2]$  (**45**) and  $[\text{Pt}(\text{N}^{\wedge}\text{N})(\text{ethynyl-hexaphenylbenzene})_2]$  (**48**) represent complexes with electron-donating acetylides,  $[\text{Pt}(\text{N}^{\wedge}\text{N})(4\text{-ethynyl-}\alpha,\alpha,\alpha\text{-trifluorotoluene})_2]$  (**46**) an electron-withdrawing acetylide and  $[\text{Pt}(\text{N}^{\wedge}\text{N})(\text{ethynyl-HBC})_2]$  (**49**) and  $[\text{Pt}(\text{N}^{\wedge}\text{N})(1\text{-ethynylpyrene})_2]$  (**47**) incorporate highly electron-delocalised acetylides (Figure 4.10).

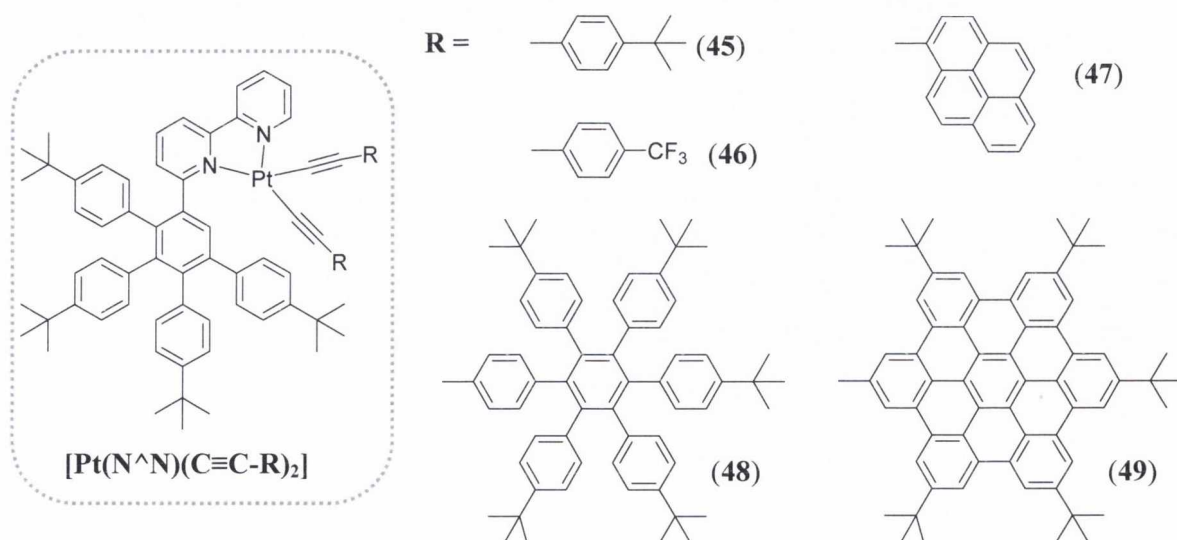


Figure 4.10: Acetylide substituents used in generating a family of compounds of general formula  $[\text{Pt}(\text{N}^{\wedge}\text{N})(\text{C}\equiv\text{C}-\text{R})_2]$ .

### 4.3.1 Synthesis of **45** and **46**

[Pt(**4**)(4-*tert*-butylphenyl acetylene)<sub>2</sub>] (**45**, (<sup>t</sup>Bu)) and [Pt(**4**)(4-ethynyl- $\alpha,\alpha,\alpha$ -trifluorotoluene)<sub>2</sub>] (**46**, (CF<sub>3</sub>)) were prepared *via* the CuI-catalysed chloride to alkyne metathesis reaction detailed in Scheme 4.4. For both complexes, the terminal alkyne (2.5 eq.) was added to a solution of [Pt(N<sup>^</sup>N)Cl<sub>2</sub>] (**44**) in still-dried and argon degassed CH<sub>2</sub>Cl<sub>2</sub>:iPr<sub>2</sub>NH (~4:1, v/v) in the presence of a catalytic amount of CuI. For **45**, 4-*tert*-butylphenyl acetylene was employed as the terminal alkyne and for CF<sub>3</sub>-substituted **46**, the terminal alkyne was 4-ethynyl- $\alpha,\alpha,\alpha$ -trifluorotoluene. Purification of **45** was achieved by concentration of the solvent *in vacuo* and precipitation from methanol. Excess terminal acetylene was removed by washing the resultant yellow powder with excess methanol and the desired product was obtained in 62 % yield. **46** was purified *via* column chromatography on silica eluting with CHCl<sub>3</sub>, followed by removal of solvent *in vacuo*, to obtain the desired product in 55 % yield.

Both complexes were characterised using <sup>1</sup>H and <sup>13</sup>C {<sup>1</sup>H} NMR spectroscopy and <sup>19</sup>F NMR spectroscopy was employed for complex **46**. Infrared spectroscopy and elemental analysis were also used. A MALDI-TOF mass spectrum for **45** (<sup>t</sup>Bu) reveals a peak at *m/z* 1269.6469 m.u. (100 %) which corresponds to [M]<sup>+</sup>, whose calculated mass of *m/z* = 1269.6439 m.u. matches well to [C<sub>80</sub>H<sub>86</sub>N<sub>2</sub>Pt]<sup>+</sup>. The electrospray mass spectrum of **46** (CF<sub>3</sub>) shows a major peak at 1315.4767 mass units for the [M+Na]<sup>+</sup> cation (100 %), in good agreement with the calculated value for C<sub>74</sub>H<sub>67</sub>N<sub>2</sub>F<sub>6</sub>PtNa (*m/z* = 1315.4754 m.u.). A second peak corresponding to the ionised product [Pt(N<sup>^</sup>N)+H]<sup>+</sup> (10 %), where **46** has ionised by losing the acetylide co-ligands in the mass spectrometer, is also observed.

#### 4.3.1.1 <sup>1</sup>H NMR Spectroscopic Characterisation of **45** and **46**

The <sup>1</sup>H NMR spectra of **45** (<sup>t</sup>Bu) and **46** (CF<sub>3</sub>) in CDCl<sub>3</sub> are presented together in Figure 4.11. Selected <sup>1</sup>H NMR chemical shifts of bipyridyl protons and H<sub>γ</sub> in complexes **45** and **46** are presented in Table 4.3. For each complex, the asymmetric nature of the diimine ligand means that the two acetylide ligand moieties are in slightly different chemical environments and as a result possess two separate sets of NMR signals. The AB systems on acetylide co-ligands, A1/B1 and A2/B2, are arbitrarily assigned for complexes **45** and

46. As an example for all complexes in this family, the process of identification of HA and HB on [Pt(N<sup>^</sup>N)(C≡C-C<sub>6</sub>H<sub>4</sub>-<sup>t</sup>Bu)<sub>2</sub>] (**45**) is discussed in Section 4.3.1.2.

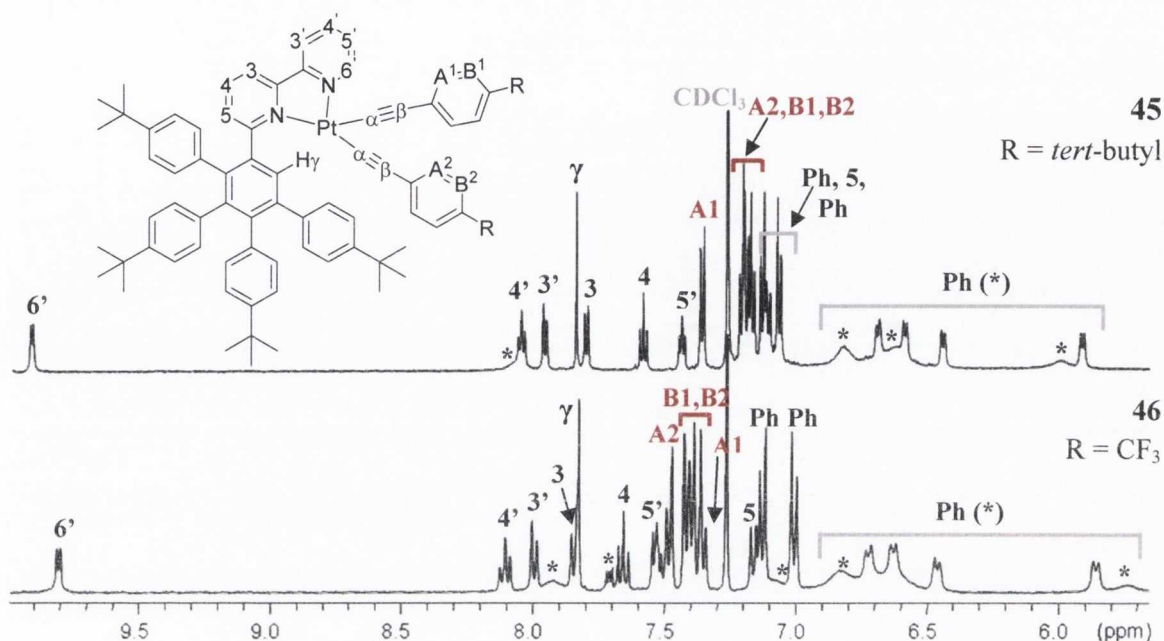


Figure 4.11: <sup>1</sup>H NMR spectra of the aromatic regions of **45** (<sup>t</sup>Bu) and **46** (CF<sub>3</sub>) in CDCl<sub>3</sub> (600.1 MHz, R.T.). Atom labelling as per inset figures, R = <sup>t</sup>Bu (**45**), CF<sub>3</sub> (**46**). \* indicates broad, unresolved proton signals due to unlabelled phenyl rings.

In general, the signals for the 4-spin pyridine ring (3'-6') and for the 3-spin pyridine ring system (3-5) appear at very similar chemical shifts from **45** (<sup>t</sup>Bu) to **46** (CF<sub>3</sub>) (Table 4.3). Some signals (such as H<sub>4</sub>, H<sub>5</sub> and H<sub>5'</sub>) undergo slight downfield shifts on moving from **45**, where R on the acetylide co-ligand is an electron-rich *tert*-butyl substituent, to **46**, where R is an electron-withdrawing CF<sub>3</sub> group.

Table 4.3: <sup>1</sup>H NMR spectroscopic data and assignments of bipyridine protons in complexes **45** and **46** reported in CDCl<sub>3</sub>. Chemical shifts (δ) in ppm.

Complex	Proton							
	H <sub>γ</sub>	H <sub>6'</sub>	H <sub>5'</sub>	H <sub>4'</sub>	H <sub>3'</sub>	H <sub>5</sub>	H <sub>4</sub>	H <sub>3</sub>
[Pt(N <sup>^</sup> N)(C≡C-C <sub>6</sub> H <sub>4</sub> - <sup>t</sup> Bu) <sub>2</sub> ] ( <b>45</b> )	7.83	9.88	7.39	8.03	7.96	7.1	7.55	7.80
[Pt(N <sup>^</sup> N)(C≡C-C <sub>6</sub> H <sub>4</sub> -CF <sub>3</sub> ) <sub>2</sub> ] ( <b>46</b> )	7.83	9.81	7.52	8.10	7.98	7.17	7.65	7.83

H<sub>6'</sub> is the most downfield of the aromatic protons in complexes **45** (δ 9.88 ppm) and **46** (δ 9.81 ppm), occurring as a doublet slightly more deshielded than observed in [Pt(N<sup>^</sup>N)Cl<sub>2</sub>]

(**44**), where H6' resonates at  $\delta$  9.53 ppm. H $\gamma$  occurs as a singlet at  $\delta$  7.83 ppm in both [Pt(N $\wedge$ N)(C $\equiv$ C-C<sub>6</sub>H<sub>4</sub>-<sup>t</sup>Bu)<sub>2</sub>] (**45**) and [Pt(N $\wedge$ N)(C $\equiv$ C-C<sub>6</sub>H<sub>4</sub>-CF<sub>3</sub>)<sub>2</sub>] (**46**), similar to H $\gamma$  in precursor **44** ( $\delta$  7.75 ppm). H5' and H5 are the most shielded of the protons on each of the pyridyl rings in both **45** and **46**.

The <sup>1</sup>H NMR signals of the phenyl rings on the acetylide co-ligands (A and B) undergo changes from electron-poor **46** (CF<sub>3</sub>) to electron-rich **45** (<sup>t</sup>Bu). HA signals appear at  $\delta$  7.48 and 7.35 ppm and HB at  $\delta$  7.40 ppm on the CF<sub>3</sub>-substituted acetylides in **46**. In contrast, HA and HB are both considerably more upfield in **45** (HA:  $\delta$  7.34 ppm, 7.20 ppm; HB:  $\delta$  7.15-7.21 ppm). These changes, achieved by simply replacing a *tert*-butyl group with a trifluoromethyl group, are quite significant and indicate large differences in the distribution of electrons within the complexes. <sup>1</sup>H NMR data alone suggest that the photophysical properties of **45** and **46** might be markedly different.

The *tert*-butyl phenyl rings on the diimine ligand in both **45** and **46** display similar behaviour to that observed for [Pt(N $\wedge$ N)Cl<sub>2</sub>] (**44**, Figure 4.6). Signals that can be attributed to *tert*-butyl phenyl rings appear throughout the aromatic region of the spectrum and do not always comprise of the expected two doublets, each integrating for 2H (i.e. a simple AB ring system). Instead, four signals can be observed for a single ring system or are too broad for coupling to be assigned. It is clear that at least two of the *tert*-butyl phenyl rings on the diimine ligand in both complexes experience significant steric hindrance and cannot freely rotate about the central phenyl ring. The unhindered phenyl ring protons appear in general between between  $\delta$  7.0-7.15 ppm as two sets of doublets for two AB substitution patterns. This unusual behaviour can be explained by the geometry of the ligands about the metal centre, as visualised in the X-ray crystal structure of **45** (Section 4.3.1.5) and can be probed by variable-temperature NMR studies (Section 4.3.1.6).

In the aliphatic region of **45** (<sup>t</sup>Bu), four *tert*-butyl resonances are observed. Three of these integrate for 9H and each corresponds to one *tert*-butyl group ( $\delta$  1.14, 1.13, 1.08 ppm) while the fourth signal is a multiplet integrating for 27H ( $\delta$  1.26 ppm). This accounts for three overlapping *tert*-butyl signals. In **46** (CF<sub>3</sub>), three aliphatic *tert*-butyl resonances are observed, one of which is due to two *tert*-butyl signals ( $\delta$  1.26, 1.14 and 1.10 ppm).

### 4.3.1.2 $^{13}\text{C}$ $\{^1\text{H}\}$ NMR Spectroscopic Characterisation of **45**

The  $^{13}\text{C}$   $\{^1\text{H}\}$  NMR spectrum of  $[\text{Pt}(\text{N}^{\wedge}\text{N})(\text{C}\equiv\text{C}-\text{C}_6\text{H}_4-\text{tBu})_2]$  (**45**) is extremely complex as a result of the asymmetric nature of the compound. The majority of the signals are quaternary in nature: the molecule possesses 20 aromatic quaternary carbons, 4 acetylide quaternary carbons and 6 aliphatic quaternary carbons due to the six *tert*-butyl substituents in **45**. Examination of a DEPT-90° experiment for **45** displays only methine carbon signals (-CH) in the aromatic region and so considerably simplifies the spectrum (Figure 4.12).

All CH signals were assigned with the aid of  $^1\text{H}$ - $^{13}\text{C}$  correlation spectroscopy (HSQC). C6' is the most downfield of the methine signals ( $\delta$  151.20 ppm). C4' and C4 occur at quite similar chemical shifts ( $\delta$  137.87, 135.91 ppm respectively), as do C3' and C3 ( $\delta$  122.26, 119.49 ppm). C5 appears considerably downfield from C5' ( $\delta$  132.59, 126.25 ppm) a feature that will emerge to be quite common in this family of complexes.

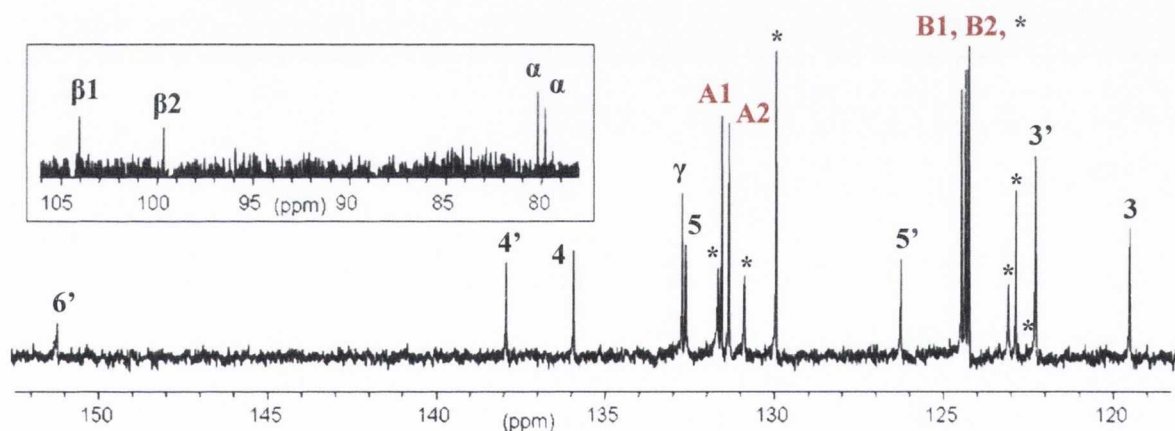


Figure 4.12: Aromatic region of the  $^{13}\text{C}$  DEPT-90 experiment for **45** ( $\text{CDCl}_3$ , 100.6 MHz, R.T.) with atom labelling as per inset figure in Figure 4.11. Inset plot illustrates acetylenic carbon region of  $^{13}\text{C}$  NMR spectrum. \* indicates methine signals attributable to phenyl rings.

For each aryl acetylide ligand, two acetylenic carbons are evident (inset  $^{13}\text{C}$   $\{^1\text{H}\}$  spectrum, Figure 4.12). In the literature  $\text{C}_\alpha$  and  $\text{C}_\beta$  are typically distinguished from one another by means of an examination of their coupling constants with the adjacent NMR spin-active  $^{195}\text{Pt}$  nucleus ( $^1J_{\text{Pt}-\text{C}_\alpha} > ^2J_{\text{Pt}-\text{C}_\beta}$ ).<sup>115,134</sup> Unfortunately, despite long accumulation times it was not possible to extract coupling constants and thereby distinguish  $\text{C}_\alpha$  from  $\text{C}_\beta$  by this method for any of the complexes prepared in this chapter. Instead for each complex long-range  $^1\text{H}$ - $^{13}\text{C}$  correlation spectroscopy (HMBC) was used to identify the CH

signals of the aryl acetylide ligands, on the basis that HA on each ligand is coupled through three bonds to  $C_{\beta}$  (Figure 4.13). Taking this approach, it was possible to identify  $C_{\beta}$ , HA and  $C_{\alpha}$  (by a process of elimination of the acetylenic carbon signals). From this information, a  $^1\text{H}$ - $^1\text{H}$  correlation experiment (TOCSY) was used to identify HB adjacent to HA on each of the ligands. For **45** ( $^t\text{Bu}$ ), this indicates that the carbons directly attached to the platinum metal centre ( $C_{\alpha}$ :  $\delta$  80.19, 79.82 ppm) feel significantly more electron density and so appear upfield of the alkynyl carbons closest to the AB ring system ( $C_{\beta 2}$ :  $\delta$  104.01;  $C_{\beta 1}$ :  $\delta$  99.63).

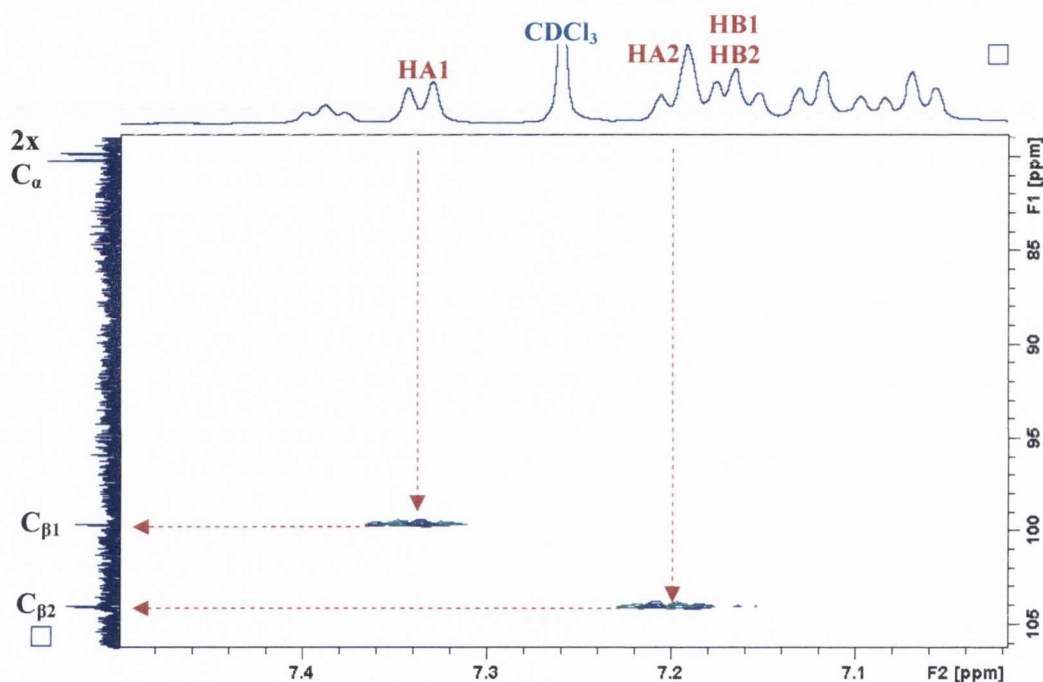


Figure 4.13: HMBC spectrum of **45** between  $\delta$  7.0-7.5 ppm ( $^1\text{H}$ ), and  $\delta$  80-106 ppm ( $^{13}\text{C}$ ).

#### 4.3.1.3 $^{13}\text{C}$ $\{^1\text{H}\}$ NMR Spectrum of **46**

The  $^{13}\text{C}$   $\{^1\text{H}\}$  NMR spectrum of  $[\text{Pt}(\text{N}^{\wedge}\text{N})(\text{C}\equiv\text{C}-\text{C}_6\text{H}_4-\text{CF}_3)_2]$  (**46**) exhibits  $^{13}\text{C}$ - $^{19}\text{F}$  heteronuclear coupling, that was not seen in **45** ( $^t\text{Bu}$ ), due to coupling to the  $^{19}\text{F}$  NMR active nucleus. A portion of the aromatic region of the  $^{13}\text{C}$  NMR spectrum of **46**, between  $\delta$  121-128 ppm, is shown in Figure 4.14. The coloured circles illustrate the quartets resulting from  $^1J_{\text{CF}}$  and  $^2J_{\text{CF}}$  couplings and full details are given in Table 4.4.

Table 4.4: Comparative  $^{13}\text{C}$  NMR chemical shifts and coupling constants for carbon-fluorine through bond interactions in **46**.

	$^{13}\text{C}$ NMR Chemical Shift: $\delta$ (ppm)	Coupling Constant: $J$ (Hz)
-CF <sub>3</sub>	124.59 (●)	$^1J_{\text{CF}} = 271$ Hz
	124.34 (●)	$^1J_{\text{CF}} = 272$ Hz
C <sub>i</sub> -CF <sub>3</sub>	126.75 (●)	$^2J_{\text{CF}} = 33$ Hz
	125.69 (●)	$^2J_{\text{CF}} = 32$ Hz

The largest through bond coupling constants are found for the carbon of the CF<sub>3</sub> group ( $^1J_{\text{CF}} = 271, 272$  Hz). Moving one bond further away, the quaternary ipso carbons have smaller carbon-fluorine coupling constants ( $^2J_{\text{CF}} = 33$  Hz, 32 Hz, Table 4.4). The multiplet which appears at  $\delta$  124.4 ppm can be assigned to the B methine signals on the acetylide co-ligands. As B1 and B2 CH signals overlap, it is not possible to extract  $^3J_{\text{CF}}$  coupling constant values but would be expected to fall between 2-8 Hz, as seen in Chapter 2.<sup>68</sup> All measured  $^{13}\text{C}$ - $^{19}\text{F}$  coupling constants are in good agreement with related systems.<sup>68,115</sup>

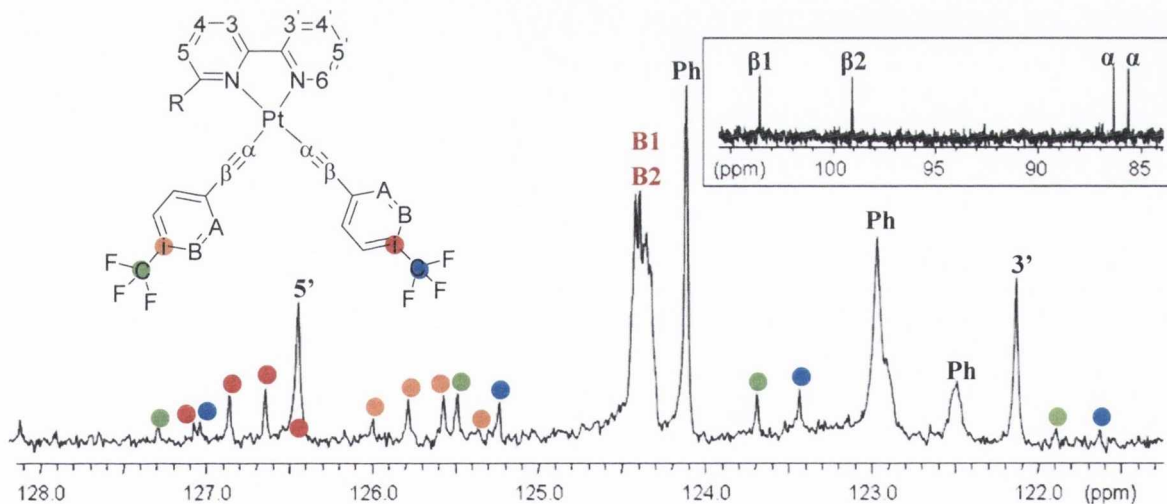


Figure 4.14:  $^{13}\text{C}$  NMR spectrum ( $\text{CDCl}_3$ , 150.9 MHz, R.T.) showing a portion of the aromatic region of **46** between  $\delta$  122-128 ppm, with inset acetylenic carbon region ( $\delta$  85-105 ppm). Atom labelling as per inset figure.

The acetylenic carbon region of the  $^{13}\text{C}$  NMR spectrum of **46** is also shown in Figure 4.14.  $\beta 1$  and  $\beta 2$  signals, i.e. those furthest from the Pt(II) metal centre, are most deshielded whereas the two  $\alpha$  alkynyl carbons are more shielded due to their proximity to the metal centre. These were identified *via* their long-range coupling with HA proton signals on the pendant aryl ring, as described for **45** (Section 4.3.1.2).

#### 4.3.1.4 $^{19}\text{F}$ NMR Spectrum of **46**

The  $^{19}\text{F}$  NMR spectrum of  $[\text{Pt}(\text{N}^{\wedge}\text{N})(\text{C}\equiv\text{C}-\text{C}_6\text{H}_4-\text{CF}_3)_3]$  (**46**) is shown in Figure 4.15. Two signals are observed, occurring at  $\delta$  -62.6 and -62.8 ppm respectively, which can be attributed to each of the two  $\text{CF}_3$  functional groups on the acetylide ligands. These signals appear in the typical region for trifluoromethyl groups attached to an aryl ring.<sup>116-117</sup> The signals are singlets because the three fluorine atoms within each  $\text{CF}_3$  unit are chemically equivalent.

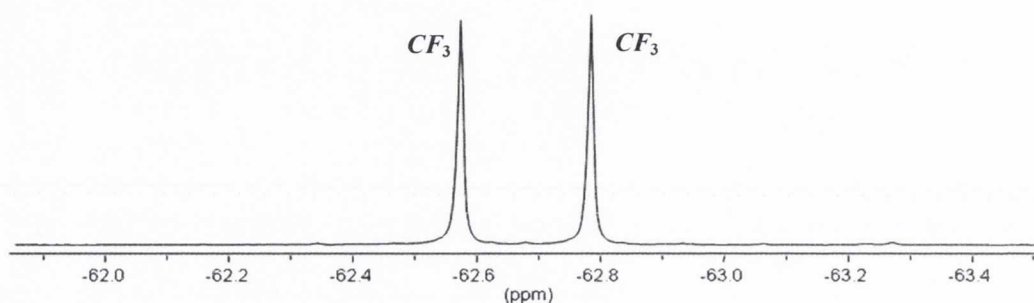


Figure 4.15:  $^{19}\text{F}$  NMR spectrum of **46** in  $\text{CDCl}_3$  (376 MHz, R.T.).

#### 4.3.1.5 X-Ray Crystal Structure of **45**. $\text{CH}_3\text{OH}$ . $3\text{H}_2\text{O}$

Crystals of  $[\text{Pt}(\text{N}^{\wedge}\text{N})(\text{C}\equiv\text{C}-\text{C}_6\text{H}_4-\text{tBu})_2]$  (**45**) suitable for single crystal X-ray crystallography were grown from a solution of **45** in  $\text{CH}_2\text{Cl}_2$  layered with methanol. This solution was left to stand at room temperature over 3 days, after which time yellow needles had formed. **45** crystallises in the tetragonal space group  $I4_1/a$ . The asymmetric unit contains one molecule of **45**, one molecule of methanol and three water molecules.

The geometry of the ligand about the Pt(II) metal centre can be described as distorted square-planar (Figure 4.16). The twist angle between the  $\text{Pt}(\text{N}^{\wedge}\text{N})$  plane and the  $\text{C}(7)\text{-Pt}(1)\text{-C}(9)$  plane is  $7.4^\circ$ . In addition, the bipyridyl moiety of the ligand itself deviates slightly from planarity, with a tilt angle of  $10.6^\circ$  between pyridine rings B and C, a feature that is also seen in other Pt(II) bipyridyl bis-acetylides. The dihedral angles between the central phenyl ring on the  $\text{N}^{\wedge}\text{N}$  ligand (Figure 4.16) and each of the aromatic rings (B and C on the bipyridyl moiety, D-G on the polyphenylene core) are given in Table 4.5 and fall in the range  $49.5\text{-}65.5^\circ$ . The bite angles of the ligands arranged about the Pt(II) metal centre deviate slightly from those observed in similar systems in the literature. The  $\text{C}(9)\text{-Pt}(1)\text{-C}(7)$  measured for **45**,  $86.2(7)^\circ$ , is slightly smaller than anticipated (typically  $89\text{-}$



$94^\circ$ ).<sup>228,240-241</sup> In addition, N(2)-Pt(1)-C(9) measures  $99.6(4)^\circ$  which is marginally outside the standard range ( $94-97^\circ$ ).<sup>228,240-241</sup> The bulk of the polyphenylene pushes the acetylide ligands closer together leaving the N-Pt-C angles larger than expected.

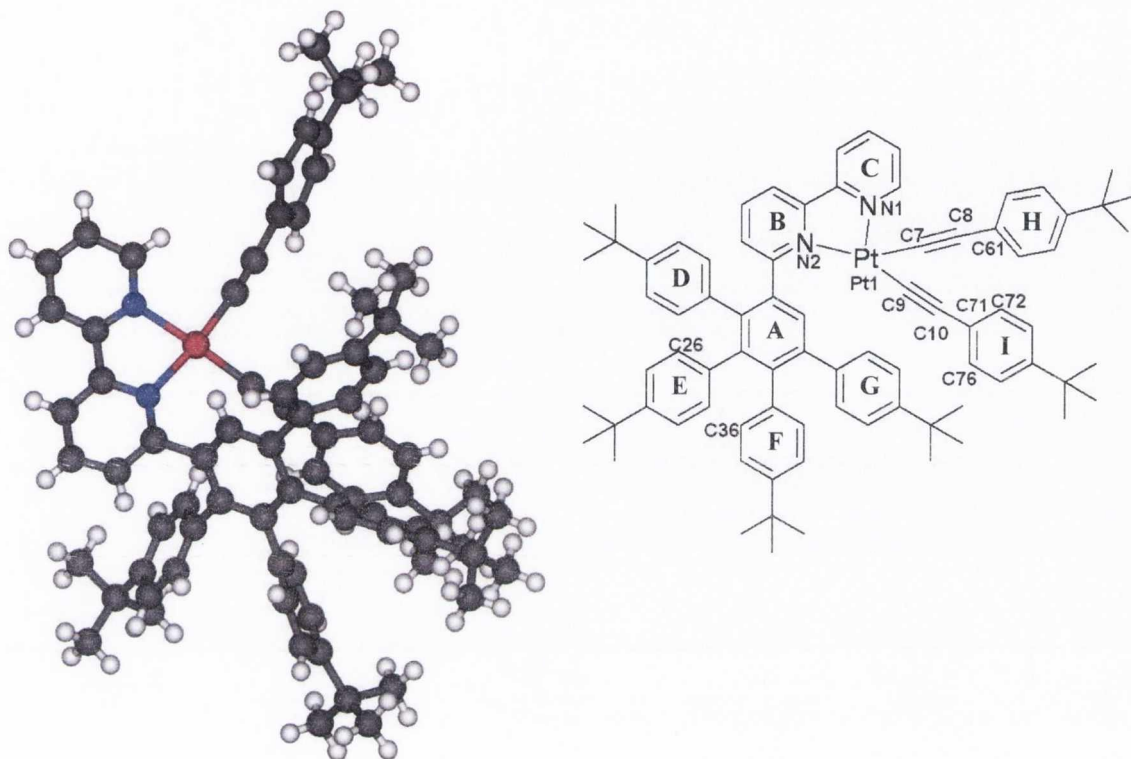


Figure 4.16: Perspective view of **45** (inset diagram-selected atomic numbering and aromatic ring labelling). Solvent molecules have been removed for clarity. Selected bond lengths and angles are contained in Table 4.5.

The phenyl rings of the acetylides are tilted quite significantly out of the Pt(II) coordination plane (ring H:  $67.6^\circ$ ; ring I:  $59.4^\circ$ ). Comparable systems composed of a simple *tert*-butyl substituted bipyridine and either two phenyl acetylides or two pyridyl acetylides display an almost perfectly planar arrangement about the metal centre.<sup>228,241</sup> In complex **45**, this deviation occurs because of severe steric hindrance: the acetylide phenyl rings must twist in order to accommodate the expanded polyphenylene core. This also explains the deviation of the ethynyl moieties from linearity, with bond angles in the range  $169.1(11)-178(2)^\circ$  (Table 4.5). In particular, the C(9)-C(10) acetylide containing *tert*-butyl phenyl ring I (Figure 4.16), experiences the greatest deviation from  $180^\circ$ . As a result of its close proximity to the diimine ligand, it is forced to point out of the plane. However, the bond lengths between the acetylenic carbons and the distance between the acetylenic carbons and the attached phenyl rings are in good agreement with other diimine containing bis-acetylide structures.<sup>228,241</sup>

Table 4.5: Selected bond lengths (Å) and bond angles (°) for **45** (*t*Bu).

Bond	Bond Length (Å)	Bond Angle	Angle (°)	Tilt Angle of aromatic rings w.r.t. A (°)
Pt(1)-C(9)	1.941(14)	C(9)-Pt(1)-C(7)	86.2(7)	<b>B:</b> 54.6
Pt(1)-C(7)	1.96(2)	N(1)-Pt(1)-N(2)	78.7(4)	<b>C:</b> 49.5
Pt(1)-N(1)	2.084(10)	N(1)-Pt(1)-C(7)	95.1(7)	<b>D:</b> 62.2
Pt(1)-N(2)	2.095(10)	N(2)-Pt(1)-C(9)	99.6(4)	<b>E:</b> 65.5
C(7)-C(8)	1.12(2)	Pt(1)-C(9)-C(10)	169.1(11)	<b>F:</b> 61.1
C(8)-C(61)	1.56(3)	Pt(1)-C(7)-C(8)	174(2)	<b>G:</b> 55.2
C(9)-C(10)	1.230(17)	C(7)-C(8)-C(61)	178(2)	
C(10)-C(71)	1.428(18)	C(9)-C(10)-C(71)	172.7(13)	

Generally for  $[\text{Pt}(\text{N}^{\wedge}\text{N})(\text{C}\equiv\text{CR})_2]$  complexes, Pt-C bond lengths are typically  $\sim 1.95$  Å and Pt-N bond lengths fall within the range of  $\sim 2.05$ - $2.07$  Å.<sup>199,221,228,240-241</sup> For **45**, Pt-C bond lengths are in good agreement with the literature and Pt-N bond lengths are only marginally longer, measuring 2.084(10) and 2.095(10) Å respectively. These values are noticeably longer than the Pt(1)-N(1) distance measured in  $[\text{Pt}(\text{N}^{\wedge}\text{N}^{\wedge}\text{C})\text{Cl}]$  (**43**, 2.044(3) Å), where a chloride ligand is located *trans* to the bond. The elongated bond in **45** (*t*Bu) can be explained by the greater *trans* influence of the phenylacetylide as a strong  $\sigma$ -donor ligand compared to the chloride ligand. In contrast, Pt-N bond distances in **45** are very close to the Pt(1)-N(2) bond distance in cyclometallated **43** (2.112(2)°), where the strongly sigma-donating  $\text{C}^-$  functionality with a strong *trans* influence results in a considerably elongated Pt-N bond.

It is clear that there is a significant degree of steric strain within the molecule. Several intramolecular interactions can be seen, particularly involving the acetylide ligand containing ring I and *tert*-butyl phenyl rings E and F (Figure 4.17). The distance between C76 on an acetylide moiety and C36 on phenyl ring F measures 3.663 Å and the distance between C72 on acetylide containing ring I and C26 on phenyl ring E measures 3.517 Å. These distances are only slightly larger than the sum of the van der Waals radii of two carbon atoms (3.40 Å).<sup>113</sup> The short distances are indicative of a very hindered molecule and it could be anticipated that phenyl rings E and F might experience reduced rotational

ability. Thus it is suggested that phenyl rings E and F are responsible for the abnormal behaviour of some of the aromatic signals in the  $^1\text{H}$  NMR spectra of **45** ( $t\text{Bu}$ ), and by analogy **46** ( $\text{CF}_3$ ) (Section 4.3.1.1). As a result of the proximity of acetylide I, phenyl rings E and F are not free to rotate about the central phenyl ring. The protons on each of these rings appear in four different chemical environments and correspondingly as four separate signals on the  $^1\text{H}$  NMR spectrum. The broadness of the second phenyl ring on the NMR spectrum can also be explained by this steric strain.

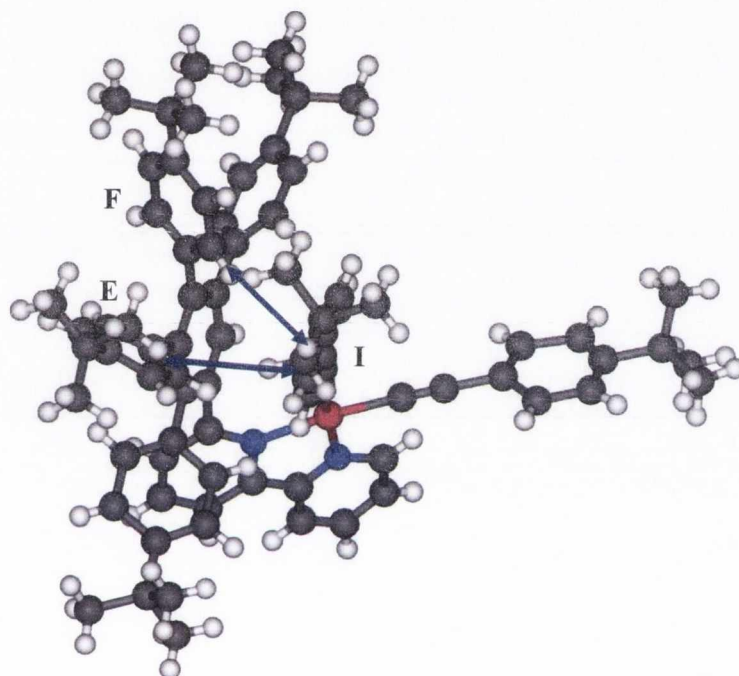


Figure 4.17: Perspective view of **45** showing intramolecular interactions (marked with a blue arrow, showing closest points of contact). Solvent molecules are omitted for clarity.

Few significant interactions arise from packing arrangements within the crystal. Some weak Van der Waals interactions between *tert*-butyl groups hold the crystal together.

#### 4.3.1.6 Variable Temperature $^1\text{H}$ NMR Spectra of **46**

The persistent phenomenon where the *tert*-butyl phenyl rings in **45** and **46** impose steric strain on the complex may be further examined using a series of variable temperature  $^1\text{H}$  NMR experiments. These were carried out for complex **46** in deuterated dimethylsulfoxide ( $d_6$ -DMSO) as the boiling point ( $189\text{ }^\circ\text{C}$ ) is suitably high. The resulting  $^1\text{H}$  NMR spectrum at room temperature is quite different in Figure 4.18 compared to that

obtained in the much less polar solvent  $\text{CDCl}_3$  (Figure 4.11). The variable temperature  $^1\text{H}$  NMR behaviour of complex **45** is analogous to that of **46**.

Variable temperature NMR is most commonly used by lowering the temperature of a sample in order to reduce fluxional behaviour at room temperature. This procedure makes it possible to study conformational interchange, identify different rotational isomers of a given molecule and calculate activation barriers to this rotation.<sup>46,242-243</sup> However in the case of this family of sterically encumbered complexes,  $[\text{Pt}(\text{N}^{\wedge}\text{N})(\text{C}\equiv\text{CR})_2]$ , at room temperature rotation of some of the *tert*-butyl phenyl rings about the central phenyl ring is slowed sufficiently on the NMR timescale to give rise to broadened signals and/or more signals than expected for a given *tert*-butyl phenyl ring. This is as a result of intramolecular steric constraints caused by the proximity of one of the acetylide co-ligands to two of the *tert*-butyl phenyl rings (specifically rings E and F, inset atom labelling Figure 4.16). As the interactions causing the restricted rotation of the *tert*-butyl phenyl rings are predominantly intramolecular (as evidenced by the crystal structure discussed in Section 4.3.1.5), concentration dependent NMR studies are not useful in this case.

The  $^1\text{H}$  NMR spectra of  $[\text{Pt}(\text{N}^{\wedge}\text{N})(\text{C}\equiv\text{C}-\text{C}_6\text{H}_4-\text{CF}_3)_2]$  (**46**) from 20-100 °C showing the phenyl ring section of the aromatic region is shown in Figure 4.18. In general, the protons of both the four and the three spin pyridine ring systems and  $\text{H}_\gamma$  undergo relatively small ( $<0.1$  ppm) downfield or upfield shifts on increasing temperature from 20 to 100 °C and so are not shown here. The most changed feature of Figure 4.18 involves the doublet at  $\delta$  5.72 ppm (20 °C, \*), which broadens and shifts downfield ( $\delta$  5.82 ppm) at 40 °C until at 60 °C, it appears only as a broad signal at  $\delta$  5.92 ppm. Similar behaviour is observed for doublets at  $\delta$  6.76 ( $\diamond$ ), 6.52 ( $\bullet$ ) and 6.59 ppm ( $\bullet$ ) (on the 20 °C spectrum) and the broad signal at 6.89 ppm ( $\blacksquare$ ). An average of free rotation and hindered rotation is observed firstly as these doublets initially broaden (see 40 °C and 60 °C). At high temperatures (80 and 100 °C), these signals have shifted significantly downfield and have become resolved doublets, in addition to the appearance of a newly resolved doublet ( $\circ$ ) at  $\delta$  7.4 ppm ( $\geq$  60°C). It is clear that increasing the temperature provides enough energy to overcome intramolecular steric constraints.<sup>244</sup> As a result, inward and outward facing protons on the same *tert*-butyl phenyl ring (see crystal structure, Figure 4.17) become equivalent at high temperature, so that only two doublets for an AB system on each phenyl ring are observed.

In contrast, *tert*-butyl phenyl ring signals between  $\delta$  7.05-7.20 ppm remain essentially unchanged with increasing temperature. This indicates fast rotation of the ring on the NMR timescale and correspondingly that these aromatic rings are not subjected to restricted rotation.<sup>244</sup>

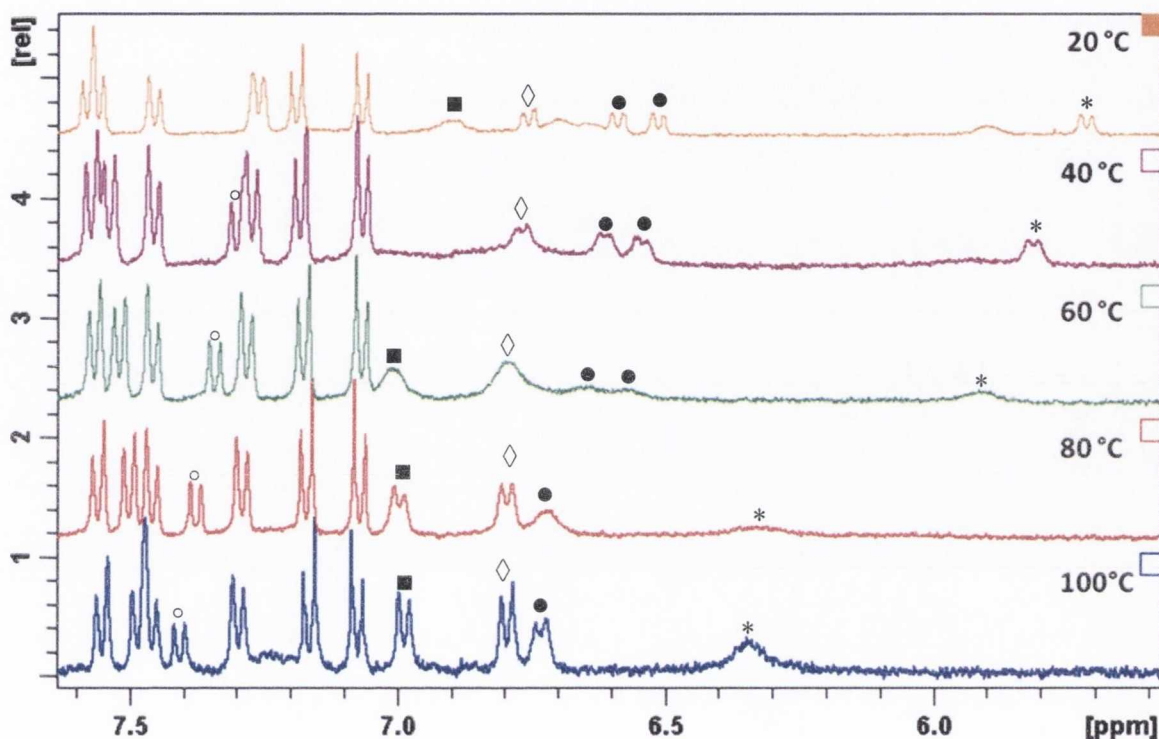


Figure 4.18: Variable temperature  $^1\text{H}$  NMR spectra of **46** in  $d^6$ -DMSO from 20-100  $^\circ\text{C}$ , showing part of the aromatic region from  $\delta$  6.6-7.6 ppm (600.1 MHz).

The downfield shift of signals observed with increasing temperature can be attributed to protons located in close proximity to, and therefore in the shielding region of, nearby aromatic rings that are becoming less shielded as they gain enough energy to freely rotate about the central phenyl ring.

Increasing the temperature induces significant changes in the  $^1\text{H}$  NMR chemical shifts of the *tert*-butyl groups themselves for complex **46**. With increasing temperature, the *tert*-butyl signals undergo a marked downfield shift. This low-field shift with increasing temperature indicates increased vibrational and rotational motion within the molecule and an overall reduction in the steric encumbrance of the geometry of **46**.

### 4.3.2 Synthesis of the larger members of the $[\text{Pt}(\text{N}^{\wedge}\text{N})(\text{C}\equiv\text{CR})_2]$ series: **47**, **48** and **49**

$[\text{Pt}(\text{N}^{\wedge}\text{N})(1\text{-pyrenyl acetylene})_2]$  (**47**),  $[\text{Pt}(\text{N}^{\wedge}\text{N})(\text{ethynyl-hexaphenylbenzene})_2]$  (**48**) and  $[\text{Pt}(\text{N}^{\wedge}\text{N})(\text{ethynyl-HBC})_2]$  (**49**) were synthesised according to the general synthetic procedure outlined in Scheme 4.4. A solution of  $[\text{Pt}(\text{N}^{\wedge}\text{N})\text{Cl}_2]$  (**44**, 1 eq.), and the required terminal acetylene (1-ethynyl pyrene (towards complex **47**), ethynyl-hexaphenylbenzene (towards complex **48**) or ethynyl-HBC (towards complex **49**)), and CuI (cat.) were stirred in a mixture of still-dried and argon degassed  $\text{CH}_2\text{Cl}_2:\text{}^i\text{Pr}_2\text{NH}$  under argon for two days in darkness. The progress of each reaction was monitored by TLC. In each case, two new spots were evident after 2 days, most likely due to the formation of both the “half-on” complex with one attached acetylene ( $[\text{Pt}(\text{N}^{\wedge}\text{N})(\text{C}\equiv\text{CR})\text{Cl}]$ ) and the target product with two attached acetylides. For each complex, it was necessary to add additional terminal acetylene (~10 mol %) to the reaction mixture in order to push it to completion. After two further days, only 1 product spot was evident by TLC for each complex.

The anticipated significant steric congestion of target complexes **47**, **48** and **49** provides an explanation for the relative difficulty in preparation of the complex (i.e. long reaction times, excess of the acetylene reagent). In contrast, an analogous complex in the literature  $[\text{Pt}(\text{dbbpy})(1\text{-pyrenyl acetylene})_2]$  (where  $\text{dbbpy} = 4,4'\text{-di}(\text{tert-butyl})\text{-2,2'-bipyridine}$ ) employing the same acetylene reagent as in complex **47** but a significantly smaller diimine ligand is reported with a reaction time of 24 hours.<sup>245</sup>

Purification of  $[\text{Pt}(\text{N}^{\wedge}\text{N})(\text{C}\equiv\text{C-Pyr})_2]$  (**47**) was achieved by column chromatography on silica, followed by precipitation from diethyl ether to obtain the bright yellow product in 31 % yield.  $[\text{Pt}(\text{N}^{\wedge}\text{N})(\text{C}\equiv\text{C-HPB})_2]$  (**48**) was also purified by column chromatography on silica, after which removal of the solvent *in vacuo* afforded complex **48** as a pale orange/pink powder in 29 % yield. Finally,  $[\text{Pt}(\text{N}^{\wedge}\text{N})(\text{C}\equiv\text{C-HBC})_2]$  (**49**) was obtained by reduction of the solvent *in vacuo*, which was then added to an excess of stirring methanol. The product was obtained as an orange/brown precipitate following filtration in 77 % yield.

$[\text{Pt}(\text{N}^{\wedge}\text{N})(\text{C}\equiv\text{C-Pyr})_2]$  (**47**) and  $[\text{Pt}(\text{N}^{\wedge}\text{N})(\text{C}\equiv\text{C-HPB})_2]$  (**48**) were characterised using  $^1\text{H}$  and  $^{13}\text{C}$   $\{^1\text{H}\}$  NMR spectroscopy and their purities confirmed using elemental analysis and mass spectrometry.  $[\text{Pt}(\text{N}^{\wedge}\text{N})(\text{C}\equiv\text{C-HBC})_2]$  (**49**) was characterised using  $^1\text{H}$  NMR

spectroscopy, mass spectrometry and elemental analysis. The product is poorly soluble in most common organic solvents, a factor which severely restricted its characterisation. As a result, despite very long accumulation times and high temperature NMR experiments, it was not possible to obtain a  $^{13}\text{C}$  NMR spectrum of **49**. The intramolecular steric congestion observed in all other members of this family of complexes,  $[\text{Pt}(\text{N}^{\wedge}\text{N})(\text{C}\equiv\text{CR})_2]$ , is compounded by the attachment of two bulky electron-rich aromatic HBC sheets. The exceptionally poor solubility of **49** is likely due to intermolecular aggregation.

The mass spectral data for **47** (Pyr), **48** (HPB) and  $[\text{Pt}(\text{N}^{\wedge}\text{N})(\text{HBC})_2]$  (**49**) is summarised in Table 4.6. The MALDI-TOF mass spectra of complexes **47** and **48** in  $\text{CH}_3\text{CN}$  and **49** in toluene reveal a major peak that corresponds to the  $[\text{M}]^+$  molecular ion for each compound. These found values are in good agreement with their respective calculated masses. A second peak for **49** (HBC) is observed for the  $[\text{M}+\text{Cu}]^+$  ion, where **49** has become ionised by picking up a  $\text{Cu}^+$  cation either in the mass spectrometer or from the reaction mixture.

Table 4.6: HR MALDI-TOF mass spectral data for complexes **47**, **48** and **49** ( $m/z$  in m.u.).

	Molecular Ion	Formula	Found $m/z$ (%)	Calculated $m/z$
<b>47</b>	$[\text{M}]^+$	$[\text{C}_{92}\text{H}_{78}\text{N}_2\text{Pt}]^+$	1405.5841 (100)	1405.5813
<b>48</b>	$[\text{M}]^+$	$[\text{C}_{184}\text{H}_{198}\text{N}_2\text{Pt}]^+$	2630.5161 (100)	2630.5203
<b>49</b>	$[\text{M}]^+$	$[\text{C}_{184}\text{H}_{174}\text{N}_2\text{Pt}]^+$	2606.3408 (100)	2606.3325
<b>49</b>	$[\text{M}+\text{Cu}]^+$	$[\text{C}_{184}\text{H}_{174}\text{N}_2\text{PtCu}]^+$	2669.2783 (60)	2669.2621

#### 4.3.2.1 $^1\text{H}$ NMR spectra of **47**, **48** and **49**

The  $^1\text{H}$  NMR spectra of  $[\text{Pt}(\text{N}^{\wedge}\text{N})(\text{C}\equiv\text{C-Pyr})_2]$  (**47**) and  $[\text{Pt}(\text{N}^{\wedge}\text{N})(\text{C}\equiv\text{C-HPB})_2]$  (**48**) are shown together in Figure 4.19. These spectra were recorded in  $\text{CDCl}_3$  at room temperature. In contrast, the  $[\text{Pt}(\text{N}^{\wedge}\text{N})(\text{C}\equiv\text{C-HBC})_2]$  (**49**) is poorly soluble in  $\text{CDCl}_3$  and it was necessary to use a high boiling solvent, deuteriated  $\text{d}_2\text{-C}_2\text{D}_2\text{Cl}_4$ , and to record the spectrum at higher temperature (40 °C) in order to improve the spectral resolution. This spectrum is shown in Figure 4.20. Since the spectrum is poorly resolved, the spinning sidebands of the  $\text{C}_2\text{D}_2\text{Cl}_4$  can be observed (#).

The  $^1\text{H}$  NMR spectra of **47**, **48** and **49** are considerably more complex than that of **45** ( $^t\text{Bu}$ ) or **46** ( $\text{CF}_3$ ). In **47** (Pyr), the aromatic region alone accounts for 42 protons – 9 on each of the pyrene moieties and 7 bipyridyl protons, one  $\text{H}_\gamma$  and 16 *tert*-butyl phenyl ring protons on the diimine ligand (**4**). The spectrum of **48** (HPB) contains 24 protons on the diimine ligand and an additional 24 protons on each of the ethynyl-hexaphenylbenzene co-ligands which totals 72 protons in the aromatic region. Finally in complex **49** (HBC), 12 protons per HBC subunit, each appearing as a singlet and integrating for one proton, plus the diimine protons are expected.

The pattern of chemical shifts for the bipyridyl protons in complex **47**, **48** and **49** are in agreement with those of the simpler family members. Once again,  $\text{H6}'$  is the most downfield of all the proton signals. In complexes **47** and **49** where the acetylide is an electron-delocalised co-ligand,  $\text{H6}'$  appears at very downfield chemical shift (**47**  $\delta$  10.12 ppm; **49**  $\delta$  10.26 ppm) compared to uncyclised polyphenylene complex **48** ( $\delta$  9.63 ppm).  $\text{H6}'$  may fall in the deshielded region of the anisotropic ring current induced in the HBC or pyrene electron-delocalised core by the magnetic field of the NMR spectrometer. Several signals display this trend (Table 4.7; e.g.  $\text{H5}'$ ,  $\text{H5}$ ,  $\text{H4}$ ,  $\text{H3}$ ), appearing more deshielded in complexes **47** and **49** compared to  $[\text{Pt}(\text{N}^{\wedge}\text{N})(\text{HPB})_2]$  (**48**).

Table 4.7:  $^1\text{H}$  NMR spectroscopic data and assignments of bipyridine protons in complexes **47**, **48** ( $\text{CDCl}_3$ , R.T.) and **49** ( $\text{C}_2\text{D}_2\text{Cl}_4$ , 40 °C). Chemical shifts in ppm.

Complex	Proton							
	$\text{H}_\gamma$	$\text{H6}'$	$\text{H5}'$	$\text{H4}'$	$\text{H3}'$	$\text{H5}$	$\text{H4}$	$\text{H3}$
$[\text{Pt}(\text{N}^{\wedge}\text{N})(\text{C}\equiv\text{C}\text{-Pyr})_2]$ ( <b>47</b> )	7.55	10.12	7.48	7.97	7.70	7.60	7.73	7.97
$[\text{Pt}(\text{N}^{\wedge}\text{N})(\text{C}\equiv\text{C}\text{-HPB})_2]$ ( <b>48</b> )	7.72	9.63	7.19	7.85	7.76	7.10	7.46	7.62
$[\text{Pt}(\text{N}^{\wedge}\text{N})(\text{C}\equiv\text{C}\text{-HBC})_2]$ ( <b>49</b> )	7.77	10.26	7.56	8.18	8.00	7.31	7.8	7.92



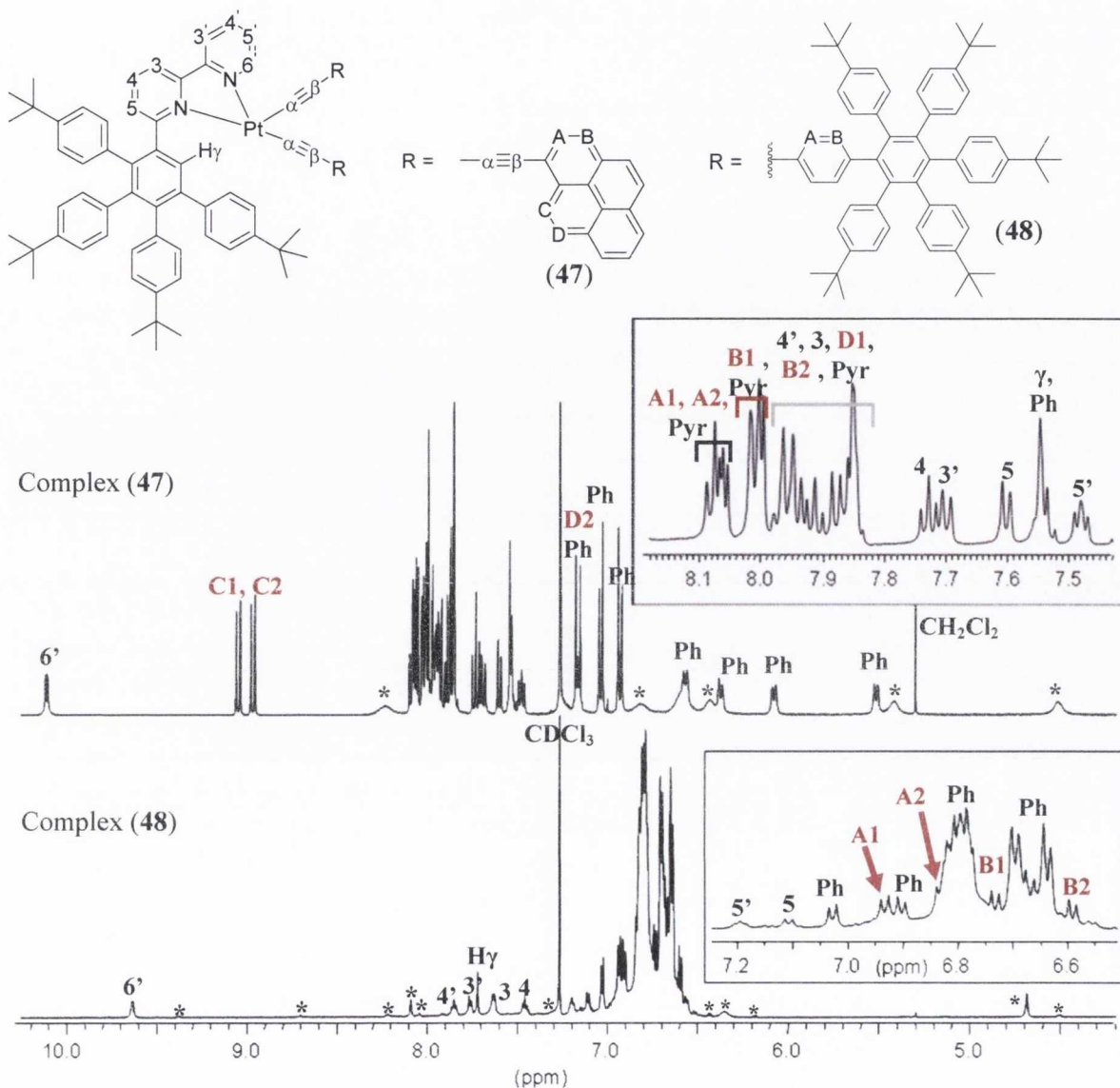


Figure 4.19:  $^1\text{H}$  NMR spectrum showing the aromatic regions of **47** and **48** ( $\text{CDCl}_3$ , 600.1 MHz, R.T.). Atom labelling as per inset figure. \* indicates broad, unresolved proton signals attributed to phenyl rings.

The chemical shift of Hy is dependent on the steric bulk and  $\pi$ -conjugation of the coordinated acetylide co-ligand. In complexes **45** ( $^t\text{Bu}$ ) and **46** ( $\text{CF}_3$ ), it has a resonance at  $\delta$  7.83 ppm. Increasing the bulk of the acetylide has a shielding effect on Hy. This is most evident in **47** (Pyr), where Hy occurs at  $\delta$  7.55 ppm. A less pronounced effect is observed in **48** ( $\delta$  7.72 ppm) and **49** ( $\delta$  7.77 ppm). In **49** Hy would be expected to undergo a shielding effect of similar magnitude as **47** but the chemical shifts cannot be absolutely compared here as the spectrum of **49** was recorded under different conditions.

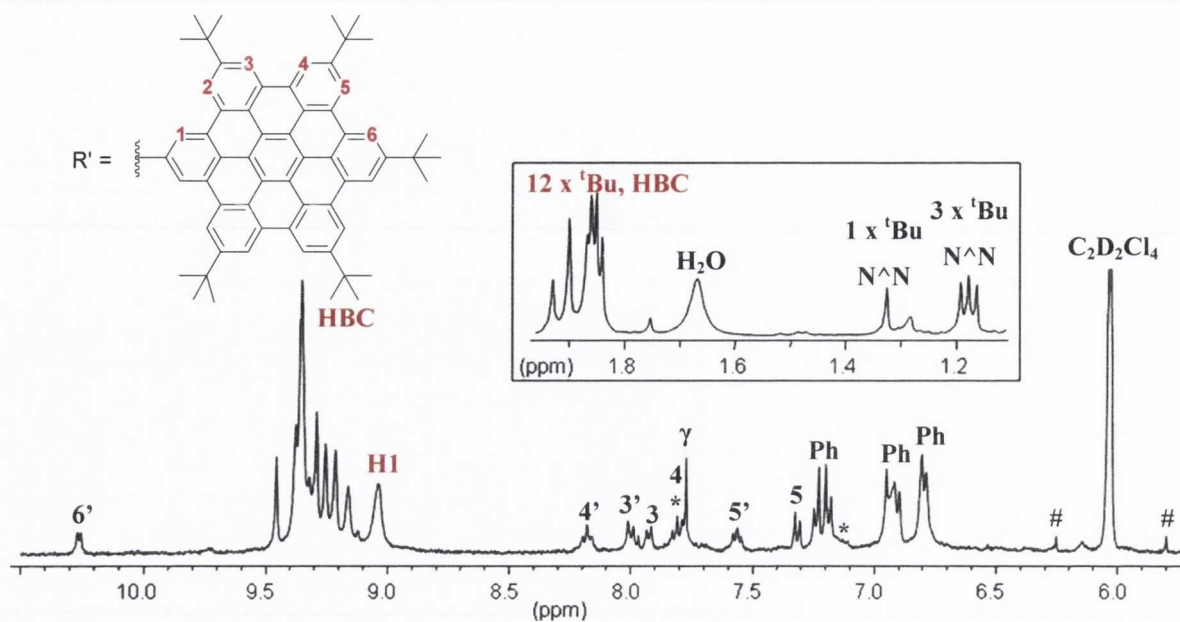


Figure 4.20:  $^1\text{H}$  NMR spectrum of **49** ( $\text{C}_2\text{D}_2\text{Cl}_4$ , 400.1 MHz, 40  $^\circ\text{C}$ ) showing the aromatic region, with inset aliphatic region of the spectrum. Atom labelling as per inset Figure 4.19, R group inset figure above. ( $\text{C}_2\text{D}_2\text{Cl}_4$  spinning side bands marked as #).

In each complex (**47**, **48** and **49**), the additional proton signals due to the polyaromatic acetylide co-ligands dominate the aromatic region of the  $^1\text{H}$  NMR spectra. In pyrenyl-complex **47**, HA1/HB1 and HA2/HB2 acetylide protons were identified using long-range  $^1\text{H}$ - $^{13}\text{C}$  correlation spectra (HMBC), as discussed for **45** ( $^t\text{Bu}$ ) (Section 4.3.1.2). Additionally, two very deshielded doublets that can be attributed to the pyrene co-ligands appear at  $\delta$  9.05 and 8.97 ppm respectively (much more downfield than observed in the free ligand, 1-ethynyl pyrene).<sup>246</sup> As HA protons are closer to the metal centre, it would have been expected that HA would have undergone the most significant changes in chemical shift upon complexation. However, as these have been unambiguously assigned, HC protons, as the next closest to the acetylide moiety, should undergo the most dramatic change in chemical environment when coordinated to the Pt(II) metal centre. Correspondingly, these downfield doublets are tentatively assigned to the HC proton on the two pyrene cores, on the basis of their close proximity to the metal centre. The remainder of the pyrene protons appear in multiplet ( $\delta$  7.8-8.1 ppm). The broad, poorly resolved signals due to *tert*-butyl phenyl ring protons observed in complexes **45** ( $^t\text{Bu}$ ) and **46** ( $\text{CF}_3$ ) is also evident in the spectrum of **47**. This was investigated by variable-temperature  $^1\text{H}$  NMR spectroscopy to study the effect of temperature on the restricted rotation of the *tert*-butyl phenyl rings (Section 4.3.2.2).

The  $^1\text{H}$  NMR spectrum of **48** (HPB) is dominated by a large multiplet between  $\delta$  6.5-6.9 ppm which can be assigned to *tert*-butyl phenyl protons located on both the diimine ligand and on the hexaphenylbenzene acetylides (Figure 4.19). As observed before, there is a significant amount of steric hindrance, as evidenced by the appearance of broad signals across the spectrum attributable to *tert*-butyl phenyl protons on the diimine ligand. Unfortunately, variable temperature  $^1\text{H}$  NMR experiments were unsuccessful for this complex. The complex exhibits quite poor solubility in  $\text{d}_6$ -DMSO even at elevated temperatures - changing the solvent would render comparisons between other complexes in the family invalid.

In **49** (HBC), 12 protons per HBC subunit, each appearing as a singlet and integrating for one proton, would be anticipated due the presumed restricted rotation of the HBC acetylides about the Pt-C bond. The HBC protons overlap significantly and all appear quite downfield as a multiplet between  $\delta$  9.45 and 9.04 ppm. On the basis of the  $^1\text{H}$  NMR of [*cis*-Pt(C $\equiv$ C-HBC) $_2$ (dppe)] (**41**), the broad singlet at  $\delta$  9.04 ppm can be assigned to one or more of the four H1 protons on the HBC core, that is the protons closest to the acetylide bond. It is not possible to determine any broad *tert*-butyl phenyl ring proton signals in Figure 4.20 and consequently the integration for the phenyl ring proton signals are lower than would be expected (only 14 protons can be accounted for instead of the calculated 16).

In the aliphatic region of the  $^1\text{H}$  NMR spectrum of **48** (Figure 4.21), four *tert*-butyl groups on the diimine ligand and in total ten *tert*-butyl groups on the two hexaphenylbenzene acetylene co-ligands must be accounted for, each integrating for 9H. Four of these appear as singlets ( $\delta$  1.22, 1.19, 1.15, 1.00 ppm) and the remaining 90 protons are overlapping in a multiplet  $\delta$  1.07-1.10 ppm. In the aliphatic region of **49**, the *tert*-butyl groups on the HBC ligands appear significantly more downfield ( $\delta$  1.84-1.93 ppm) than those on the diimine ligand ( $\delta$  1.17-1.33 ppm). This is characteristic of HBC platforms compared to unfused polyphenylene derivatives and was also observed in Chapter 3, from fused to unfused *cis* and *trans* Pt(II) complexes.

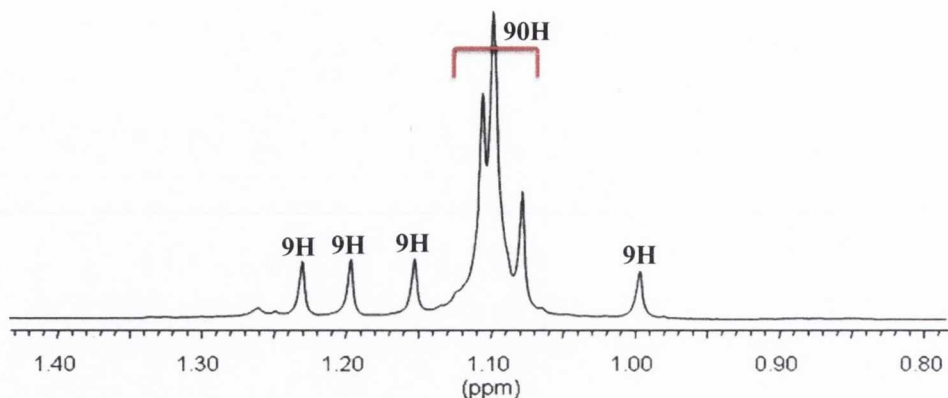


Figure 4.21:  $^1\text{H}$  NMR spectrum of  $[\text{Pt}(\text{N}^{\wedge}\text{N})(\text{HPB})_2]$  (**48**) ( $\text{CDCl}_3$ , 600.1 MHz, R.T.) showing the aliphatic region with integration values for each peak.

#### 4.3.2.2 Variable Temperature $^1\text{H}$ NMR spectra of **47**

The  $^1\text{H}$  NMR spectrum of  $[\text{Pt}(\text{N}^{\wedge}\text{N})(\text{C}\equiv\text{C}\text{-Pyr})_2]$  (**47**) as seen in Figure 4.19 demonstrates characteristic behaviour of the *tert*-butyl phenyl rings on the diimine ligand. The appearance of a broad signal at  $\delta$  4.55 ppm, extremely upfield for an aromatic proton, which can be identified *via*  $^1\text{H}^1\text{H}$ -COSY as belonging to a *tert*-butyl phenyl ring, indicates that the effect is even more pronounced in this complex. (The most shielded protons in **45** ( $^t\text{Bu}$ ) (Figure 4.11) resonated at  $\delta$  5.91 ppm and in **46** ( $\text{CF}_3$ ) (Figure 4.11) at  $\delta$  5.7 ppm). This dramatic upfield shift can be rationalised by the large increase in size (and correspondingly steric congestion) and electronic density as a result of changing a simple aryl acetylide for a pyrenyl acetylide.

The  $^1\text{H}$  NMR spectra (recorded in  $d_6$ -DMSO) of part of the aromatic region of **47** (Pyr) is shown in Figure 4.22. This illustrates the sections of the spectra where the *tert*-butyl phenyl ring proton signals are predominant. In general, protons on the four or three spin pyridine rings and pyrene-based protons undergo marginal shifts upon increasing the temperature from 20–90  $^\circ\text{C}$  and so are not shown in this figure.

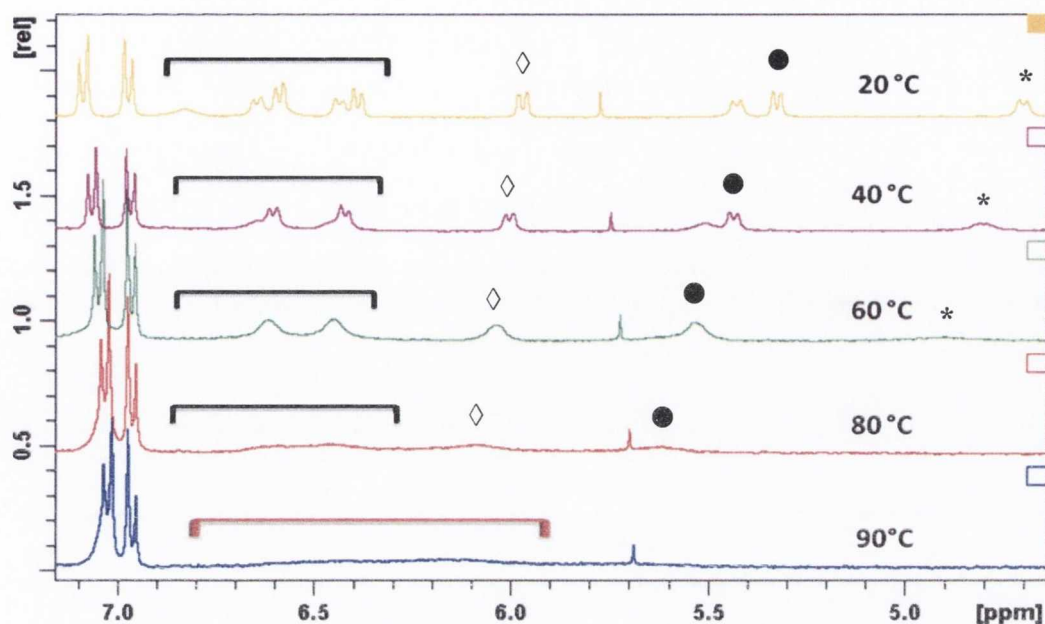


Figure 4.22: Variable temperature  $^1\text{H}$  NMR spectra of **47** in  $d_6$ -DMSO from 20-90  $^\circ\text{C}$ , showing part of the aromatic region from  $\delta$  4.5-7.1 ppm.

With increasing temperature, broad signals at  $\delta$  4.71, 5.33, 5.43, 5.98 and between 6.4-6.9 ppm (20  $^\circ\text{C}$ ) gradually shift downfield and broaden even further. By 90  $^\circ\text{C}$ , these signals appear to have coalesced to very broad featureless signals between  $\delta$  5.9-6.8 ppm. In complex **45**, the phenyl ring signals shifted downfield and broadened until over 60  $^\circ\text{C}$  when the signals sharpened with increasing temperature as the rings could freely rotate. The broadening of the phenyl ring proton signals occurs as the molecule gradually receives enough energy to be able to cross the rotational barrier imposed by steric congestion. At 90  $^\circ\text{C}$  in **47**, the molecule has not reached the point of free rotation of the rings. The additional steric bulk of the pyrenyl acetylides results in even more restricted internal rotations than observed for simple phenyl acetylides.

#### 4.3.2.3 $^{13}\text{C}$ NMR Spectra of **47** and **48**

The  $^{13}\text{C}$   $\{^1\text{H}\}$  NMR spectrum of **47** and **48** were fully assigned using HSQC and long-range HMBC experiments. Poor solubility precluded the measurement of the  $^{13}\text{C}\{^1\text{H}\}$  NMR spectrum of **49**. In both **47** and **48**, the spectra are extremely complex. In the aromatic region of the spectrum, 7 methine peaks for the bipyridyl rings are expected and one for H $\gamma$ . As it is uncertain which, and how many, *tert*-butyl phenyl rings in the complex

experience restricted rotation, the number of CH signals expected for each ring cannot be predicted. The chemical shifts of the bipyridyl carbon signals are in agreement with those of the other members of the  $[\text{Pt}(\text{N}^{\wedge}\text{N})(\text{C}\equiv\text{CR})_2]$  family. Table 4.8 summarises the  $^{13}\text{C}\{^1\text{H}\}$  chemical shifts of the bipyridyl and C $\gamma$  methine signals for each complex in the series.

Table 4.8:  $^{13}\text{C}\{^1\text{H}\}$  NMR spectroscopic data and assignments of bipyridine methine signals and C $\gamma$  in complexes **47**, **48** ( $\text{CDCl}_3$ , R.T.) and **49** ( $\text{C}_2\text{D}_2\text{Cl}_4$ , 40 °C). Chemical shifts ( $\delta$ ) in ppm.

	C $\gamma$	C6'	C5'	C4'	C3'	C5	C4	C3
Ligand <b>4</b>	130.47	148.30	122.99	136.15	121.29	124.58	135.76	117.74
NNC ( <b>43</b> )	-	148.51	126.46	138.68	121.04	124.51	136.24	116.56
<b>44</b> ( $\text{Cl}_2$ )	130.98	149.45	125.63	138.32	122.37	131.42	136.87	119.66
<b>45</b> ( $^t\text{Bu}$ )	132.71	151.20	126.25	137.87	122.26	132.59	135.91	119.49
<b>46</b> ( $\text{CF}_3$ )	132.52	150.98	126.44	138.15	122.13	132.52	136.23	119.43
<b>47</b> (Pyr)	136.21	151.45	126.68	138.02	122.14	124.43	125.41	124.03
<b>48</b> (HPB)	132.39	150.74	125.98	137.56	122.29	132.25	136.00	119.62

The bipyridyl  $^{13}\text{C}$  chemical shifts in  $[\text{Pt}(\text{N}^{\wedge}\text{N})(\text{C}\equiv\text{C-Pyr})_2]$  (**47**) deviate significantly from the trend for the other members of the series (Table 4.8). C $\gamma$  and C3 are more deshielded than in the other complexes, whereas C5 and C4 resonate at much more upfield chemical shift than is typical of the trend. This is a consequence of attaching the highly  $\pi$ -electron conjugated ethynyl-pyrene platform as co-ligand. As observed in the  $^1\text{H}$  NMR chemical shifts of **47** (Table 4.7), the co-ligand both enhances electron delocalisation within the molecule through bonds and affects the magnetic environments of individual atoms through space *via* the inherent ring current induced in the polyaromatic platform in the magnetic field of the NMR spectrometer.

### 4.3.3 IR Spectroscopy of $[\text{Pt}(\text{N}^{\wedge}\text{N})(\text{C}\equiv\text{CR})_2]$

The family of compounds  $[\text{Pt}(\text{N}^{\wedge}\text{N})(\text{C}\equiv\text{CR})_2]$  may be considered only as *pseudo cis*-configured bis(acetylide) complexes, as the asymmetric diimine ligand renders the two acetylide co-ligands inequivalent. Hence for each complex, two  $\nu(\text{C}\equiv\text{C})$  absorption bands at approximately  $2100\text{ cm}^{-1}$  for two infrared active stretching modes (symmetric and asymmetric) would be expected.<sup>179</sup>

Table 4.9 lists the  $\nu(\text{C}\equiv\text{C})$  and  $\nu(\text{C}\equiv\text{C}-\text{H})$  infrared bands in the family of complexes  $[\text{Pt}(\text{N}^{\wedge}\text{N})(\text{C}\equiv\text{CR})_2]$  and their component free terminal acetylenes (i.e. for complex **45**, the terminal acetylene is 4-*tert*-butylphenyl acetylene). The acetylene ligands exhibit two bands of interest, one at higher wavenumbers,  $\sim 3290\text{ cm}^{-1}$ , due to the  $\equiv\text{C}-\text{H}$  stretching in the terminal  $\text{C}\equiv\text{CH}$  unit, and one at lower wavenumbers,  $\sim 2100\text{ cm}^{-1}$ , due to  $\nu(\text{C}\equiv\text{C})$  stretching.

Table 4.9: Selected IR Spectroscopic absorption bands of  $[\text{Pt}(\text{N}^{\wedge}\text{N})(\text{C}\equiv\text{CR})_2]$  complexes and corresponding free acetylene co-ligands (solid state).

Complex	Acetylene Ligand		Pt(NN)(L) <sub>2</sub>
	$[\nu(\text{C}\equiv\text{C}-\text{H})\text{ cm}^{-1}]$	$\nu(\text{C}\equiv\text{C}),\text{ cm}^{-1}]$	$[\nu(\text{C}\equiv\text{C}),\text{ cm}^{-1}]$
<b>45</b> ( <sup>t</sup> Bu)		2109 <sup>247</sup>	2128, 2112
<b>46</b> (CF <sub>3</sub> )	3300 <sup>248</sup>	2112 (wk) <sup>248</sup>	2130, 2114
<b>47</b> (Pyr)	3295	2095 (wk)	2131 (sh), 2104
<b>48</b> (HPB)	3288	2107 (wk)	2130 (sh), 2115
<b>49</b> (HBC)	3289	2106 (wk)	2114 (sh), 2108

Each member of this family of complexes shows two infrared bands for  $\nu(\text{C}\equiv\text{C})$ , due to a different stretching frequency for each of the alkynyl ligands about the Pt(II) metal centre. The complexes are structurally very similar to *cis*-configured Pt(diimine) bis-acetylide complexes and the values obtained are in good agreement with complexes of this type.<sup>220,241,249</sup> In contrast, in analogous bis-acetylide complexes where the “*cis*” configuration is imposed by a chelating phosphine ligand, e.g. dppe, the  $\nu(\text{C}\equiv\text{C})$  absorption bands tend to occur at slightly lower wavenumber (lower energy).<sup>181,250</sup> (In *cis*- $[\text{Pt}(\text{C}\equiv\text{C}-\text{HBC})_2(\text{dppe})]$  (**41**) and *cis*- $[\text{Pt}(\text{C}\equiv\text{C}-\text{HPB})_2(\text{dppe})]$  (**39**),  $\nu(\text{C}\equiv\text{C})$  stretching frequencies occur at 2109, 2104  $\text{cm}^{-1}$  and 2118, 2106  $\text{cm}^{-1}$  respectively.) The strong  $\sigma$ -donation ability of phosphine ligands relative to bipyridines results more electron density residing on the Pt(II) metal orbitals, which facilitates an increase in  $\pi$ -back donation towards the  $\pi^*$  on the acetylide co-ligands. As a result,  $\text{C}\equiv\text{C}$  bonds are weakened and  $\nu(\text{C}\equiv\text{C})$  infrared absorption bands appear at lower wavenumbers. The same phenomenon was observed for a series of homoleptic Pt(II) alkynyl complexes containing four acetylides.<sup>115</sup> In this case, the anionic complexes  $[\text{Pt}(\text{C}\equiv\text{CAr})_4]^{2-}$  are more electron rich as a result of the coordination of four, instead of two,  $\sigma$ -donor acetylide subunits.

#### 4.4 The UV-Visible Absorption spectra of ligand **4** & complexes of general formula $[\text{Pt}(\text{N}^{\wedge}\text{N})(\text{C}\equiv\text{CR})_2]$

The UV-Visible absorption spectra of polyaromatic diimine ligand **4**, Pt(II) dichloride precursor complex  $[\text{Pt}(\text{N}^{\wedge}\text{N})\text{Cl}_2]$  (**44**) and the series of acetylide complexes,  $[\text{Pt}(\text{N}^{\wedge}\text{N})(\text{C}\equiv\text{CR})_2]$  (**45-49**), were recorded in  $\text{CH}_2\text{Cl}_2$  solution ( $10^{-5}$  M). The corresponding spectral data is presented in Table 4.10. None of the compounds display concentration dependence over the range ( $10^{-4} - 5 \times 10^{-7}$  M).

Table 4.10: Room temperature UV-Visible Spectral Data for diimine ligand **4**,  $[\text{Pt}(\text{N}^{\wedge}\text{N})\text{Cl}_2]$  (**44**) and related acetylide complexes,  $\text{Pt}(\text{N}^{\wedge}\text{N})(\text{C}\equiv\text{CR})_2$  in  $\text{CH}_2\text{Cl}_2$  ( $\sim 10^{-5}$  M).

Complex	$\lambda_{\text{max}}$ [nm] ( $\epsilon \times 10^{-4}$ [ $\text{M}^{-1} \text{cm}^{-1}$ ])
$\text{N}^{\wedge}\text{N}$ ( <b>4</b> )	234 (5.3), 250 (5.1), 279 (3.8), 304 <i>sh</i> (2.2)
<b>44</b> ( $\text{Cl}_2$ )	250 (5.6), 278 (4.6), 337 (1.6), 380 (0.8), 418 <i>sh</i> (0.3), 481 (0.02)
<b>45</b> ( <sup>t</sup> Bu)	261 (8.9), 292 <i>sh</i> (5.8), 356 (1.6), 416 (0.7), 465 <i>sh</i> (0.3)
<b>46</b> ( $\text{CF}_3$ )	257 (7.3), 267 (7.4), 283 (7.0), 302 <i>sh</i> (5.4), 357 (1.4), 401 (0.8)
<b>47</b> (Pyr)	232 (14.4), 248 <i>sh</i> (11.3), 280 (8.1), 291 (9.6), 347 <i>sh</i> (4.7), 364 (7.4), 384 (6.9), 397 (5.2), 462 (0.8)
<b>48</b> (HPB)	251 (15.7), 279 (10.9), 313 (6.1), 446 (0.6)
<b>49</b> (HBC)	231 (34.8), 241 (31.0), 260 (14.3), 317 (6.1), 332 (8.3), 348 (16.5), 364 (31.0), 395 (11.7), 414 (5.0), 443 (1.4)

##### 4.4.1 UV-Visible Absorption Spectra of ligand **4** and $[\text{Pt}(\text{N}^{\wedge}\text{N})\text{Cl}_2]$ (**44**)

The UV-Visible absorption spectra of diimine ligand **4**,  $[\text{Pt}(\text{N}^{\wedge}\text{N})\text{Cl}_2]$  (**44**) and *tert*-butyl phenyl acetylide complex **45** (<sup>t</sup>Bu) are presented in Figure 4.23. The absorption spectrum of diimine ligand **4** is quite broad and featureless, with a maximum absorbance at  $\lambda$  234 nm (Table 4.10). This typical feature of non-planar polyphenylene derivatives was also observed for oligophenylene bipyridine ligands (**1**, **2**, **3** and **4** in  $\text{CH}_2\text{Cl}_2$  solution) in Chapter 2 and subsequently for ethynyl-hexaphenylbenzene (**6**) in Chapter 3.<sup>124-125</sup> The



band can be attributed to ligand-centred  $\pi\text{-}\pi^*$  transitions of the pyridine and phenyl rings in addition to  $n\text{-}\pi^*$  transitions due to the presence of heteroatoms within the framework.

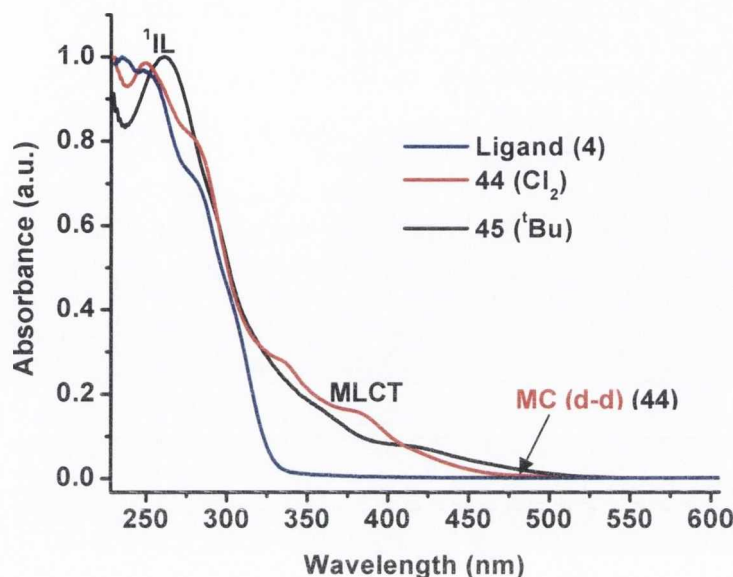


Figure 4.23: Normalised UV-Visible absorption spectra of **4**, **44** and **45** in  $\text{CH}_2\text{Cl}_2$  ( $10^{-5} \text{ M}$ ).

In the absorption spectrum of  $[\text{Pt}(\text{N}^{\wedge}\text{N})\text{Cl}_2]$  (**44**) (Figure 4.23), high energy transitions ( $\lambda$  230-280 nm) occur in the same region as ligand-centred absorptions in the free ligand (Table 4.10). Coordination to the Pt(II) metal centre introduces several new bands which occur at  $\lambda$  337 and 380 nm with a shoulder at  $\lambda$  418 nm. These absorptions are assigned as metal-to-ligand charge transfer ( $^1\text{MLCT}$ )  $[\text{d}(\text{Pt}) \rightarrow \pi^*(\text{N}^{\wedge}\text{N})]$  transitions with some contribution from  $^3\text{MLCT}$ . This feature is commonly observed in Pt(II) diimine dihalide complexes.<sup>209,251-252</sup> An additional weak band appears in the broad tail at  $\lambda$  481 nm ( $\epsilon$   $0.02 \text{ M}^{-1} \text{ cm}^{-1}$ ). It is well understood for  $[\text{Pt}(\text{bpy})\text{Cl}_2]$  systems that the lowest energy band originates from a metal-centred transition (MC), where a d-d excited state is the lowest energy excited state (also known as ligand field state, LF).<sup>209,251</sup> The bands' intensity is weak because the d-d transition is spin-allowed but Laporte forbidden.

#### 4.4.2 UV-Visible Absorption Spectra of complexes $[\text{Pt}(\text{N}^{\wedge}\text{N})(\text{C}\equiv\text{CR})_2]$ (**45-49**)

Figure 4.24 shows the normalised UV-Visible absorption spectra of the five  $[\text{Pt}(\text{N}^{\wedge}\text{N})(\text{C}\equiv\text{CR})_2]$  complexes **45-49** in  $\text{CH}_2\text{Cl}_2$  solution. All five complexes exhibit high energy absorption bands between  $\lambda$  200-300 nm, attributable to diimine and acetylide-based intra-ligand transitions (Table 4.10).<sup>220</sup> Complexes composed of the larger acetylide

co-ligands, specifically **47** (Pyr), **48** (HPB) and **49** (HBC), display notably more intense absorption bands in this region ( $\lambda$  240-250 nm: **47**,  $\epsilon$   $11.3 \times 10^4$ ; **48**,  $\epsilon$   $15.7 \times 10^4$ ; **49**,  $\epsilon$   $31.0 \times 10^4$   $\text{M}^{-1}\text{cm}^{-1}$ ). These absorptions were also visible in the electronic absorption spectra of ethynyl-hexaphenylbenzene (**6**) and ethynyl-HBC (**7**) discussed in Chapter 3 and are due to intra-ligand ( $\pi$ - $\pi^*$ ) absorptions based on the polyaromatic acetylene.<sup>74</sup>

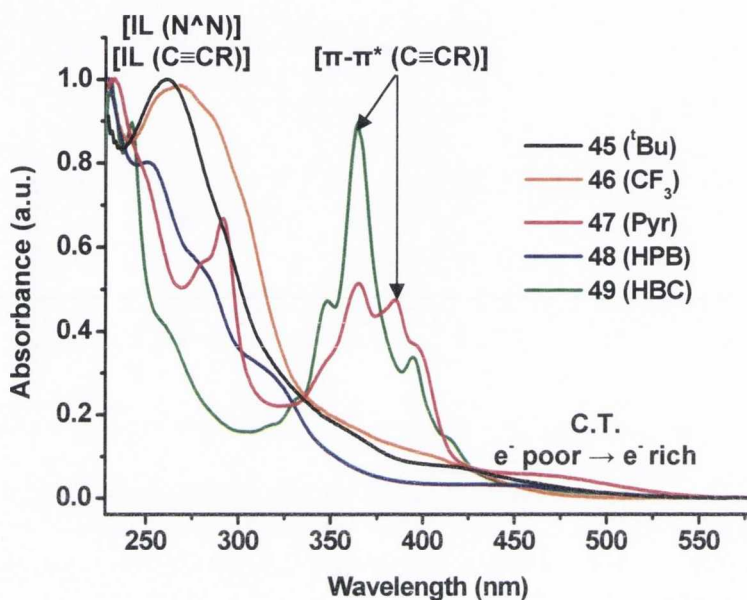


Figure 4.24: Normalised UV-Visible absorption spectra of Pt(II) diimine bis-acetylide complexes (**45-49**) in  $\text{CH}_2\text{Cl}_2$  ( $10^{-5}$  M).

By comparing  $[\text{Pt}(\text{N}^{\wedge}\text{N})\text{Cl}_2]$  (**44**) and **45** ( $^t\text{Bu}$ ) in Figure 4.23, it is reasonable to assume that the bands of intermediate energy, for example at  $\lambda$  356 nm for complex **45**, originate from  $^1\text{MLCT}$  transitions  $[\text{d}(\text{Pt}) \rightarrow \pi^*(\text{N}^{\wedge}\text{N})]$ . By analogy, absorptions in this region of the spectrum for all five complexes are likely composed of some MLCT character (Figure 4.24). Both **47** (Pyr) and **49** (HBC) possess additional intense well-resolved, highly structured absorption bands between  $\lambda$  340-420 nm that are not seen in the other complexes in this family. These may be attributed to  $\pi$ - $\pi^*$  transitions on the appended planar chromophore and in the case of **49**, were also observed in Chapter 3 for ethynyl-HBC (**7**) and its corresponding **41** (*cis*-HBC) and **40** (*trans*-HBC) complexes.<sup>203,245</sup> The absorption bands are slightly red-shifted from their free acetylene-polyaromatic moiety due to  $\sigma$ -donation from the acetylide onto the Pt(II) metal centre.<sup>173,245</sup> The additional low energy absorption band observed in **41** (*cis*-HBC) and **40** (*trans*-HBC) (which was absent in the free ligand), appears in the UV spectrum of complex  $[\text{Pt}(\text{N}^{\wedge}\text{N})(\text{C}\equiv\text{C}\text{-HBC})_2]$  (**49**) ( $\lambda$  414 nm), at exactly the same wavelength as for **41**. Once again, this may be considered to be

composed of some intra-ligand character perturbed by the Pt(II) with some contribution from an MLCT transition.<sup>173</sup>

The most significant feature of the absorption spectra of all five complexes (Figure 4.24) is a low energy absorption band that varies in energy from complex to complex as a result of the substituent on the aryl acetylide (Table 4.11). This low energy band, (absent in ligand **4** and [Pt(N<sup>^</sup>N)Cl<sub>2</sub>] (**44**)), appears at highest energy in **46** (CF<sub>3</sub>) (λ 401 nm), at λ 416 nm in **45** (<sup>t</sup>Bu) and moves to sequentially lower energies from **49** (HBC), to **48** (HPB) to **47** (Pyr) where the absorption band is observed at λ 462 nm, i.e. the transition involved moves to lower energy as the electron-donating properties of the acetylide increases.

*Table 4.11: UV-Visible Absorption wavelengths (λ, nm) of lowest energy absorption bands of complexes **45** to **49** in order of decreasing energy.*

<b>46</b> (CF <sub>3</sub> )	<b>45</b> ( <sup>t</sup> Bu)	<b>49</b> (HBC)	<b>48</b> (HPB)	<b>47</b> (Pyr)
401 nm	416 nm	443 nm	446 nm	462 nm


#### 4.4.3 Solvent polarity: Solvatochromism

An analysis of the solvatochromic behaviour of the compounds prepared in this work was undertaken by recording their absorption spectra in solvents of different polarity, from polar CH<sub>3</sub>CN to less polar toluene solution.

##### 4.4.3.1 Solvatochromism in ligand **4** and [Pt(N<sup>^</sup>N)Cl<sub>2</sub>]

An examination of the solvatochromic behaviour of **44** (Table 4.12) reveals that the lowest energy transition (λ 481 nm) is relatively insensitive to changes in solvent polarity. This is typical of d-d states.<sup>80</sup> The intermediate energy absorption bands (λ 337, 380, 418 nm, in CH<sub>2</sub>Cl<sub>2</sub> solution) experience noticeable hypsochromic shifts in polar solvents and bathochromic shifts in non-polar solvents. This negative solvatochromic behaviour is characteristic of a charge-transfer transition.<sup>251</sup> In this case the bands are most likely MLCT [d(Pt)→π\*(N<sup>^</sup>N)] in origin as diimine ligands are known π acceptor ligands with low-lying π\* orbitals.<sup>80</sup>

Table 4.12: Lower energy absorption bands ( $\lambda$ , nm) of  $[Pt(N^{\wedge}N)Cl_2]$  (**44**) in  $CH_3CN$ ,  $CH_2Cl_2$  and toluene solutions ( $\sim 10^{-5}$  M).

	Solvent	$\lambda_{max}$ [nm]
Decreasing polarity 	$CH_3CN$	332, 367, 408, 480
	$CH_2Cl_2$	337, 380, 418, 481
	Toluene	348, 396, 436, 481

#### 4.4.3.2 Solvatochromism in $[Pt(N^{\wedge}N)(C\equiv CR)_2]$ complexes (**45-49**)

The intra-ligand bands in  $[Pt(N^{\wedge}N)(C\equiv C-Pyr)_2]$  (**47**) and  $[Pt(N^{\wedge}N)(C\equiv C-HBC)_2]$  (**49**) ( $\lambda$  340-420 nm) exhibit slight negative solvatochromic effects (Table 4.13), becoming slightly red-shifted with decreasing solvent polarity.

Table 4.13: Lowest energy absorption bands ( $\lambda$ , nm) for complexes **45-49** in  $CH_3CN$ , THF and Toluene solutions ( $\sim 10^{-5}$  M).

	$CH_3CN$	THF	Toluene
<b>45</b> ( <sup>t</sup> Bu)	402	425	442
<b>46</b> ( $CF_3$ )	392	409	426
<b>47</b> (Pyr)	362, <sup>a</sup> 397, <sup>a</sup> 448	366, <sup>a</sup> 398, <sup>a</sup> 467	367, <sup>a</sup> 399, <sup>a</sup> 493
<b>48</b> (HPB)	421	453	472
<b>49</b> (HBC)	360, <sup>b</sup> 390, <sup>b</sup> 402	- <sup>c</sup>	366, <sup>b</sup> 396, <sup>b</sup> 416

<sup>a</sup> Correspond to pyrene IL transitions; <sup>b</sup> Correspond to HBC IL transitions; <sup>c</sup> complex **49** is insoluble in THF.

In **47**, a red-shift of 5 nm for the most intense absorption band ( $\sim \lambda$  362 nm) is recorded from the most polar solvent  $CH_3CN$  to the least polar, toluene (Figure 4.25). Similarly, **49** displays a red-shift of 6 nm for a  $\lambda_{max}$  360 nm under the same conditions. These relatively small bathochromic shifts were also observed in uncoordinated ethynyl-HBC (**7**) (Chapter 3) and are typical of changes in solvent polarity on states which are  $\pi-\pi^*$  in origin.<sup>126,171</sup> It is also likely that these absorption bands are not “pure”  $\pi\rightarrow\pi^*$  in origin but are mixed with some MLCT transitions (of weaker intensity) which may also contribute to the solvatochromic behaviour observed.<sup>126</sup>

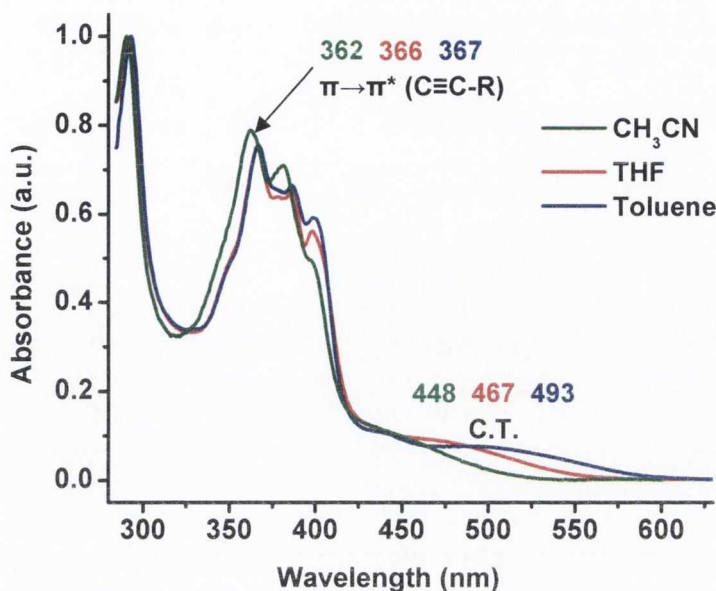


Figure 4.25: Normalised UV-Visible absorption spectra of solutions of  $[Pt(N^N)(C\equiv C-Pyr)_2]$  (**47**) in  $CH_3CN$ , THF and toluene ( $\sim 10^{-5}$  M).

#### 4.4.3.3 Solvatochromism of the lowest energy absorption band in complexes 45-49

The lowest energy transition is particularly sensitive to solvent polarity (Table 4.13). In all cases, it exhibits a significant degree of negative solvatochromism, suggesting that the ground state is more polar than the excited state. For example in **47** (Pyr), the transition appears at  $\lambda$  448 nm in acetonitrile but in non-polar toluene solution it has undergone a bathochromic shift to appear at  $\lambda$  493 nm (Figure 4.25). Similarly in the most blue-shifted of all the complexes **46** ( $CF_3$ ), the band undergoes a 34 nm red-shift from acetonitrile solution to toluene solution (Table 4.13). The extent of the solvent dependency of this low energy band suggests the involvement of charge transfer in the lowest energy transition.<sup>225</sup> This observed red-shift of the lowest energy absorption band from electron-withdrawing to electron-donating or  $\pi$ -conjugated acetylides has also been observed in several series of Pt(II) complexes in the literature, containing bipyridine, terpyridine or phenanthroline-based polypyridyl or  $N^C$  cyclometallated ligands.<sup>134,220-222,225,253</sup>

#### 4.4.4 Nature of lowest energy excited state

The substitution of weak-field halides for strong-field acetylides in Pt(II) diimine complexes has several consequences (Figure 4.26). The introduction of strong field acetylides results in a larger splitting between the filled and empty d-orbitals on the metal

centre, raising the energy of the lowest unoccupied d orbital ( $d_{x^2-y^2}$ ) most likely above that of the lowest lying empty  $\pi^*$  on the diimine ligand (diimines are good  $\pi$  acceptor ligands and are known to have low lying  $\pi^*$  orbitals). As a result, non-radiative decay via metal-centred d-d states is reduced as they are less thermally accessible and emission at room temperature is observable.<sup>149</sup> Concurrently, the highest occupied Pt metal d orbital is lowered in energy and the acetylides provide relatively high-lying filled  $\pi$  orbitals. As a result of this re-ordering of orbitals, the lowest unoccupied molecular orbital (LUMO) is centred on the diimine [ $\pi^*(N^{\wedge}N)$ ] and the highest occupied molecular orbital is either metal-centred (Figure 4.26, A), centred on the acetylide co-ligand [ $\pi(C\equiv CAr)$ ] (Figure 4.26, B) or is composed of a mixture of both.

When the HOMO is metal-centred, the lowest available energy transition is metal-to-ligand charge transfer, MLCT [ $d(Pt) \rightarrow \pi^*(N^{\wedge}N)$ ] (Figure 4.26, A). A HOMO centred on the acetylide co-ligand results in a lowest energy transition that is ligand-to-ligand charge transfer, from the highest filled  $\pi$  orbital on the acetylide to the lowest  $\pi^*$  on the diimine [ $\pi(C\equiv CAr) \rightarrow \pi^*(N^{\wedge}N)$ ] (Figure 4.26, B).<sup>150</sup>

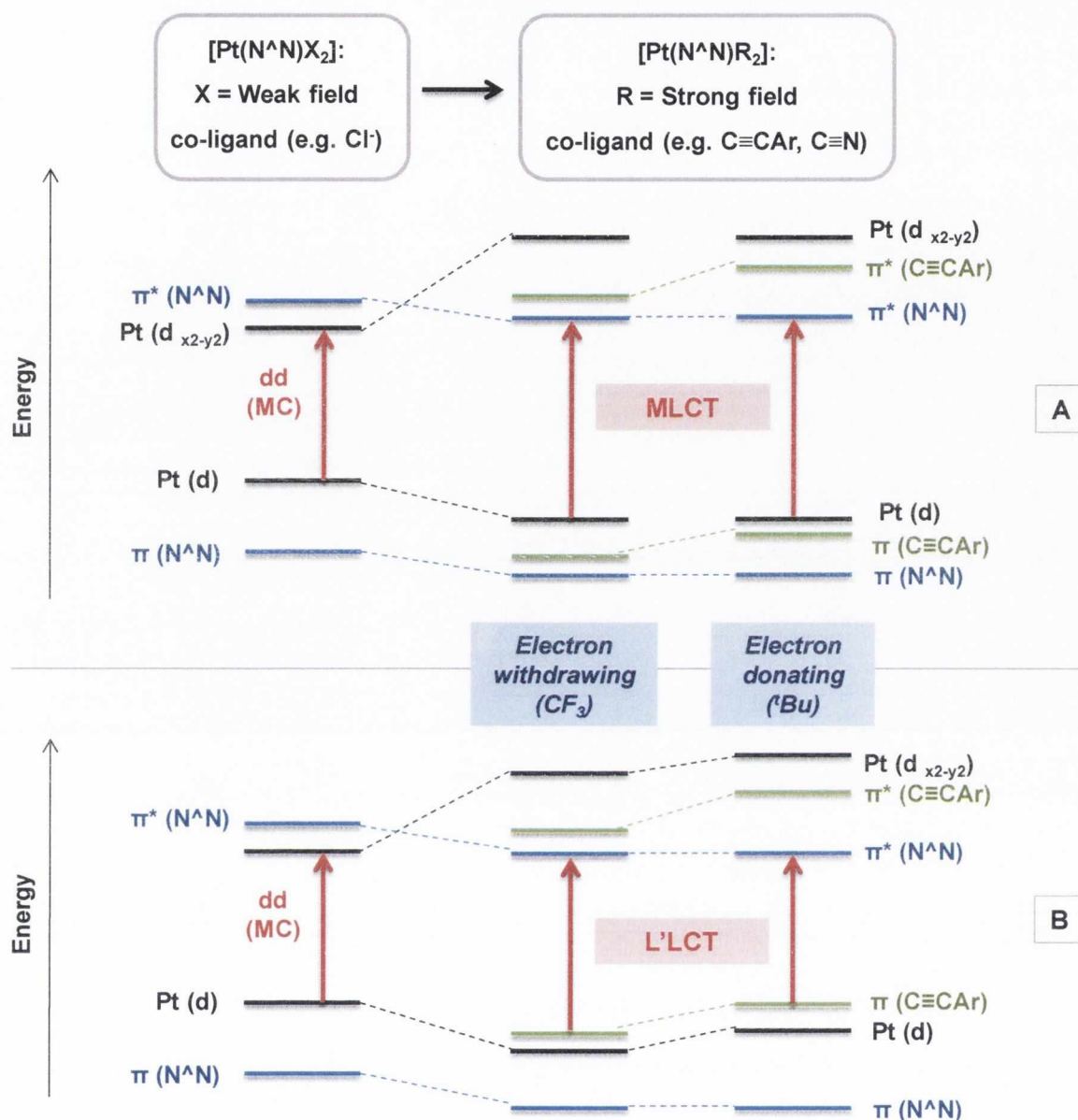


Figure 4.26: Qualitative molecular orbital diagram for  $[\text{Pt}(\text{N}^{\wedge}\text{N})\text{Cl}_2]$  (**44**) and  $[\text{Pt}(\text{N}^{\wedge}\text{N})(\text{C}\equiv\text{CAr})_2]$  (**45-49**) illustrating the effect of introducing strong-field co-ligands on Pt(II) diimine complexes. A) Pt(d) metal-centred HOMO; B)  $\pi(\text{C}\equiv\text{C})$  acetylide-centred HOMO.

Electron-withdrawing substituents on the acetylide (for example as in complex **46** ( $\text{CF}_3$ )) will stabilise the highest energy filled  $\pi$  orbital on the acetylide but have little effect on the  $\pi^*$  on the diimine. Similarly, electron-donating substituents (e.g. **45** ( $^t\text{Bu}$ )) will raise the energy of  $\pi(\text{C}\equiv\text{CAr})$ . If the transition was purely MLCT in origin (Figure 4.26, A) with the HOMO centred on the metal (and with no contribution from the acetylide filled orbitals - this would affect the electron density at the metal centre), then the HOMO-LUMO energy

gap would be almost identical for complexes **45** and **46**. This is not the case – the band is red-shifted from **46** (CF<sub>3</sub>) to **45** (<sup>t</sup>Bu) by 15 nm.

If the HOMO is centred on the acetylide (Figure 4.26, B), an electron-withdrawing group will lower the energy of the  $\pi(\text{C}\equiv\text{C}\text{Ar})$ , therefore the energy gap between the HOMO and LUMO increases, causing a hypsochromic shift of this band. Alternatively, an electron-donating group will destabilise the  $\pi(\text{C}\equiv\text{C}\text{Ar})$ , raising its energy and reducing the energy gap between the HOMO and the LUMO, resulting in a bathochromically shifted lowest energy transition. This transition is designated ligand-to-ligand charge transfer (L'LCT) and corresponds to the red-shift with increasing electron donicity observed in the family of complexes described in this work.

However, the close electronic coupling between acetylide orbitals and 5d Pt metal orbitals means that the introduction of an electron-withdrawing group onto the acetylide will lower the energy of the  $\pi(\text{C}\equiv\text{C}\text{Ar})$  and simultaneously lower the 5d(Pt) energy. As a result, the HOMO is most likely composed of a mixture of both 5d(Pt) orbitals and  $\pi(\text{C}\equiv\text{C}\text{Ar})$ . The HOMO in this case could be described as metal-perturbed  $\pi(\text{C}\equiv\text{C}\text{Ar})$ , and the HOMO-LUMO transition as (metal-ligand)-to-ligand charge transfer (ML)LCT [ $\text{Pt}(\text{d})/\pi(\text{C}\equiv\text{C}\text{Ar}) \rightarrow \pi^*(\text{N}^{\wedge}\text{N})$ ].<sup>134,150</sup> They display very similar behaviour to that of a series of Pt(II) diimine dithiolate complexes where the electronic demand of both diimine and dithiolate were systematically varied.<sup>254-255</sup> The authors designated the transition as essentially a mixture of MLCT/L'LCT.

#### 4.5 Electrochemical properties of $[\text{Pt}(\text{N}^{\wedge}\text{N})(\text{C}\equiv\text{C}\text{Ar})_2]$

Cyclic voltammetric studies were carried out on 1 mM solutions of the ligands and complexes in CH<sub>2</sub>Cl<sub>2</sub> (0.1 M <sup>n</sup>Bu<sub>4</sub>NPF<sub>6</sub> as electrolyte) and the results obtained are summarised in Table 4.14. A standard calomel electrode (SCE) was used as reference electrode, with potentials quoted *versus* the Fc/Fc<sup>+</sup> couple (0.0 V) and referenced to internal ferrocene added at the end of each experiment.



Table 4.14: Electrochemical Data for ligand **4**, [Pt(N<sup>^</sup>N)Cl<sub>2</sub>] (**44**) and complexes **45-49**<sup>a</sup>

Compound	Oxidation	Oxidation	Reduction
	$E_{pa}/V$ <sup>b</sup> Pt(II)-Pt(III)	$E_{pa}/V$ <sup>b</sup> (N <sup>^</sup> N)/(C≡CR)	$E_{1/2}/V$ [ $\Delta E_p/mV$ ] <sup>d</sup> (N <sup>^</sup> N)/(C≡CR)
N <sup>^</sup> N ( <b>4</b> )	-	+1.07	-1.96 [273] <sup>c</sup>
[Pt(N <sup>^</sup> N)Cl <sub>2</sub> ] ( <b>44</b> )	+0.70	+1.01	-1.74 [169]
[Pt(N <sup>^</sup> N)(C≡C- <sup>t</sup> Bu) <sub>2</sub> ] ( <b>45</b> )	+0.56	+1.01	-1.90 [101]
[Pt(N <sup>^</sup> N)(C≡C-CF <sub>3</sub> ) <sub>2</sub> ] ( <b>46</b> )	+0.87	-	-1.85 [191]
[Pt(N <sup>^</sup> N)(C≡C-Pyr) <sub>2</sub> ] ( <b>47</b> )	+0.37	+0.83	-1.86 [85]
[Pt(N <sup>^</sup> N)(C≡C-HPB) <sub>2</sub> ] ( <b>48</b> )	+0.58	-	-1.92 [104] , -2.20 [43]
[Pt(N <sup>^</sup> N)(C≡C-HBC) <sub>2</sub> ] ( <b>49</b> )	+0.45	+0.80	-1.90 [81]

<sup>a</sup> In deoxygenated dichloromethane (0.1 M, <sup>n</sup>Bu<sub>4</sub>NPF<sub>6</sub>) at 298K, scan rate = 100 mVs<sup>-1</sup>, reported vs. Fc/Fc<sup>+</sup>; <sup>b</sup> Irreversible/*quasi*-reversible oxidation process,  $E_{pa}/V$  (anodic peak potential) quoted; <sup>c</sup> Return oxidation wave associated with this reduction poorly defined; <sup>d</sup>  $\Delta E_p = E_{pa} - E_{pc}$ , peak potential separation.

The first oxidation process observed for all six Pt(II) complexes is a *quasi*-reversible/irreversible oxidation wave between +0.37 and +0.87 V (Table 4.14). It can be attributed to the metal-centred oxidation of Pt(II) to Pt(III) and corresponds to the removal of an electron from the HOMO.<sup>205</sup> Comparing **45** (<sup>t</sup>Bu) and **46** (CF<sub>3</sub>) (Figure 4.27), Pt(II) oxidation occurs at less positive potentials on electron rich *tert*-butyl acetylide complex **45** (+0.56 V) than for **46** (+0.87 V). The metal centre in **46** (CF<sub>3</sub>) is the most difficult to oxidise, whereas as pyrenyl complex **47** (Pyr) is the easiest. In general, the Pt(II)-Pt(III) oxidation potential becomes less positive as the electron-donating ability of the acetylide substituents increase – it is easier to remove an electron from the HOMO when it has more electron density. This is in good agreement with the red-shift of the lowest energy band in the UV-Visible spectra of the complexes from electron-withdrawing substituents to electron-rich substituents, where **46** was the most blue-shifted and **47** the most red-shifted (Table 4.11). The dependence of the Pt(II) oxidation potential on the alkynyl co-ligand substituent is further evidence of the participation of both the  $\pi(C\equiv CAr)$  and 5d(Pt) in the HOMO and reinforces the assignment of the lowest energy transition as (ML)LCT. In the

majority of Pt(II) complexes, at more positive potentials than the Pt(II)-Pt(III) oxidation process a second *quasi*-reversible/irreversible oxidation process is evident, attributable to an oxidation on the diimine or to an irreversible oxidation process on the alkyne. In the case of **46**, the very positive Pt(II)-Pt(III) oxidation process is coincident with the diimine oxidation and as a result the oxidation peak appears as a broad signal on the CV (Figure 4.27).

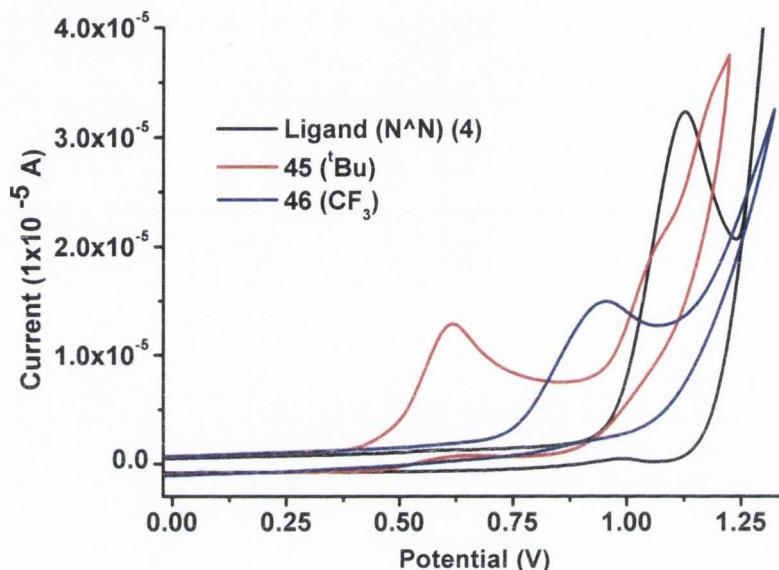


Figure 4.27: Cyclic voltammograms of **4**, **45** and **46** showing the Pt(II) and ligand-based oxidation processes. (1 mM in  $\text{CH}_2\text{Cl}_2$ , V vs.  $\text{Fc}/\text{Fc}^+$ ).

The two essentially reversible oxidation processes on ethynyl-HBC (**7**) (+0.50, +1.02 V; Figure 4.28) are also evident in **49** (HBC). As observed for *cis*-[Pt(C≡C-HBC)<sub>2</sub>(dppe)] (**41**) in Chapter 3 (E: +0.49, +0.87 V), the Pt(II)/Pt(III) oxidation is coincident with the first oxidation on the HBC platform (Figure 4.28). However, for **49** the reverse wave associated with this first oxidation is broadened and unstructured – a consequence of the partially irreversible oxidation process and the relatively poor solubility of the complex.

In general, the ligand and each complex displays one reduction process within the solvent window on the diimine (Table 4.14). The reduction on ligand **4** occurs at -1.96 V and is chemically irreversible, indicated by a diminished return wave associated with this reduction and a large anodic-to-cathodic peak separation of  $\Delta E_p = 273$  mV. (In general, for similar Pt(II) polypyridyl acetylide complexes, an oxidation or reduction with a  $\Delta E_p$  of approximately 90 mV or less is considered to be a chemically reversible process).<sup>256-257</sup>

This diimine-centred reduction on  $[\text{Pt}(\text{N}^{\wedge}\text{N})\text{Cl}_2]$  (**44**) and on all  $[\text{Pt}(\text{N}^{\wedge}\text{N})(\text{C}\equiv\text{CR})_2]$  complexes occurs at a less negative potential than in the free ligand. Coordination of the bipyridyl ligand to the positively-charged Pt metal centre renders the ligand overall more electron accepting and consequently easier to reduce.

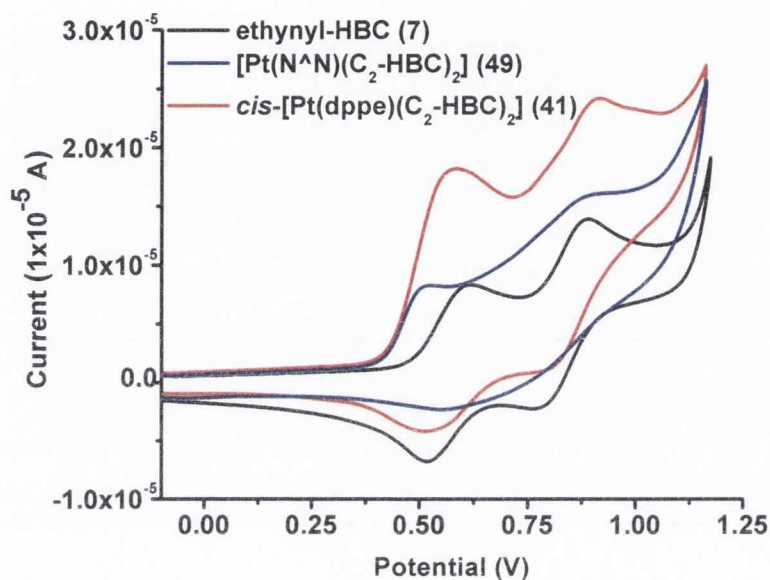


Figure 4.28: Cyclic voltammograms of ethynyl-HBC (**7**),  $[\text{cis-Pt}(\text{dppe})(\text{C}\equiv\text{C-HBC})_2]$  (**41**) and  $[\text{Pt}(\text{N}^{\wedge}\text{N})(\text{C}\equiv\text{C-HBC})_2]$  (**49**) showing the Pt(II) and ligand-based oxidation processes. (1 mM in  $\text{CH}_2\text{Cl}_2$ , V vs.  $\text{Fc}/\text{Fc}^+$ ).

Comparing the simple acetylide complexes, the reduction on **45** ( $^t\text{Bu}$ ) occurs at -1.90 V whereas **46** ( $\text{CF}_3$ ) is slightly easier to reduce, undergoing a reduction at -1.85 V. These complexes are identical apart from the substituent in the *para* position on the acetylide moieties. In contrast, a significantly larger  $\Delta E_p$  for **46** (191 mV) than for **45** (101 mV) indicates that the processes underlying the reductions are different, with the reduction on **45** largely reversible but that on **46** less so (Table 4.14). The reduction on *tert*-butyl **45** can most likely be attributed to a reduction process on the diimine. The larger anodic-cathodic peak potential separation for **46** suggests that this reduction is composed of two coincident *quasi*-reversible processes, one localised on the diimine and the other on the acetylide itself.<sup>258</sup> The more electron-rich acetylide on **45** will be significantly more difficult to reduce than  $\text{CF}_3$ -substituted acetylide in **46** and a reduction process centred on the *tert*-butyl acetylide most likely appears at more negative potentials than available in the solvent window. Similarly, the reductions that are recorded for **49** (HBC) (-1.90 V), **48** (HPB)

(-1.92 V) and **47** (Pyr) (-1.86 V) are probably composed of both a reversible diimine reduction and *quasi*-reversible alkynyl-based reduction. The free ligands ethynyl-hexaphenylbenzene (**6**) and ethynyl-HBC (**7**) were previously shown to have reduction peaks at -1.93 V and -1.96 V respectively.

## 4.6 Photoluminescence Properties of **4**, [Pt(N<sup>^</sup>N)Cl<sub>2</sub>] (**44**) and [Pt(N<sup>^</sup>N)(C≡CR)<sub>2</sub>] (**45-49**)

The photoluminescence spectra of of bipyridyl ligand **4**, precursor complex [Pt(N<sup>^</sup>N)Cl<sub>2</sub>] (**44**) and the series of complexes [Pt(N<sup>^</sup>N)(C≡CR)<sub>2</sub>] (**45-49**) were recorded in the solid state and in argon-degassed CH<sub>2</sub>Cl<sub>2</sub> solution at 298 K and 77K (including lifetimes (at 298 K) and quantum yields (in solution at 298 K)). Firstly, the emission of the precursors, ligand **4** and Pt(II) precursor **44**, are discussed.

### 4.6.1 Emission properties of bipyridyl ligand **4**

The emission profile of bipyridyl ligand **4** in the solid state (298 K and 77 K) and in CH<sub>3</sub>CN solution (10<sup>-5</sup> M, 298 K and 77 K) are discussed in detail in Chapter 2. The emission spectra of the ligand were also recorded in CH<sub>2</sub>Cl<sub>2</sub> solution (10<sup>-5</sup> M) to ensure accurate comparison with complexes [Pt(N<sup>^</sup>N)(C≡CR)<sub>2</sub>] in this work (Table 4.15).

In CH<sub>2</sub>Cl<sub>2</sub> solution at room temperature and at low temperature (Figure 4.29), emission from diimine **4** is composed of both a higher energy (298 K:  $\lambda_{\text{max}}$  375 nm, 77 K:  $\lambda_{\text{max}}$  358 nm at 77 K) and a lower energy component (298K:  $\lambda_{\text{max}}$  507 nm, 77 K:  $\lambda_{\text{max}}$  490 nm). Both present lifetimes in the nano-second region. Excitation of ligand **4** at  $\lambda_{\text{exc}}$  368 nm produces a structured emission band with vibronic fine structure and a spacing interval of  $\sim 1250$  cm<sup>-1</sup> (Figure 4.29). This corresponds to the C=C and C=N vibronic frequencies of the aromatic rings.<sup>134</sup> The excitation spectrum ( $\lambda_{\text{em}}$  406 nm) matches well to the absorption spectrum of **4** indicating the absence of intermolecular interactions or aggregates in the excited state. The higher energy band can be assigned as <sup>1</sup> $\pi\pi^*/n\pi^*$  fluorescence and the lower energy as <sup>3</sup> $\pi\pi^*/^3n\pi^*$  phosphorescence.

Table 4.15: Emission data for ligand **4** (298 K, 77K) in solid state and in solution ( $\text{CH}_2\text{Cl}_2$ ,  $10^{-5}$  M).

	Medium (T[K])	$\lambda_{\text{em}}[\text{nm}]$ ( $\lambda_{\text{exc}}[\text{nm}]$ )	$\tau$ [ns] ( $\lambda_{\text{exc}} / \lambda_{\text{em}}$ nm) <sup>b</sup>	$\Phi_{\text{em}}$ <sup>c</sup>
<b>4</b>	Solid (298)	365 <sub>max</sub> , 512 (315)	41 (65 %), 16 (35 %) (295 / 365)	
	NN		1,400 (79 %), 300 (21 %) (370 / 512)	
	Solid (77)	360 <sub>max</sub> , 508, 554 <sub>sh</sub> (300)		
	$\text{CH}_2\text{Cl}_2$ (298) <sup>a</sup>	375 <sub>max</sub> , 502 (315),	15 (47 %), 5 (53 %) (295 / 375)	<10 <sup>-3</sup>
		477, 487, 497, 507 <sub>max</sub> , 531 <sub>sh</sub> (368)	20 (68 %), 12 (32 %) (370 / 504)	
	$\text{CH}_2\text{Cl}_2$ (77)	358 <sub>max</sub> , 490 (315)		

<sup>a</sup> Argon-degassed solution,  $10^{-5}$  M; <sup>b</sup> Estimated error on  $\tau \pm 10$  %; <sup>c</sup> Measured using quinine sulfate as a standard, based on three repeat measurements.<sup>133</sup>

This emission profile is analogous to that recorded in Chapter 2 for **4** in  $\text{CH}_3\text{CN}$  solution and is unaffected by concentration ( $10^{-3}$ - $10^{-6}$  M). In general, it is characteristic of uncyclised polyphenylene derivatives, from the simple aryl acetylide bipyridines (<sup>t</sup>Bu-Bpy (**1**),  $\text{CF}_3$ -Bpy (**2**)) in Chapter 2 to ethynyl-hexaphenylbenzene (**6**) whose emission features are detailed in Chapter 3.

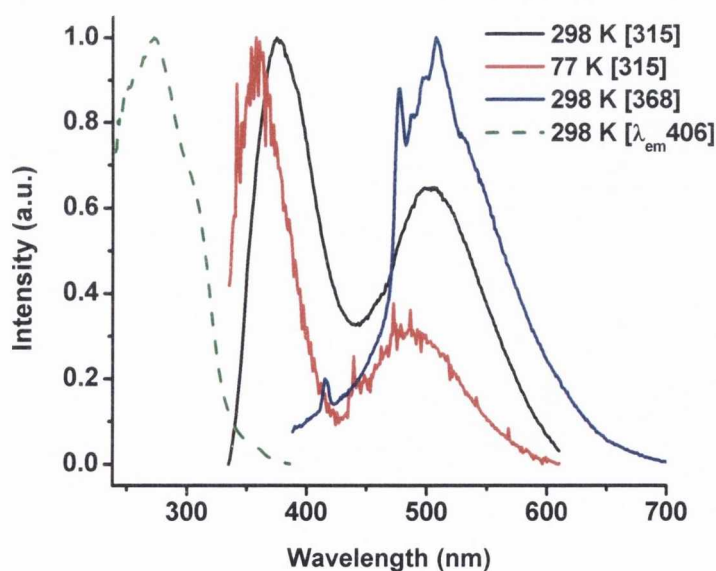


Figure 4.29: Normalised emission (solid line) and excitation (dashed line) spectra of **4** in  $\text{CH}_2\text{Cl}_2$  solution at 298 K and 77 K [ $\lambda_{\text{exc}}/\text{nm}$ ].

### 4.6.2 Emission spectra of [Pt(N<sup>^</sup>N)Cl<sub>2</sub>] (**44**)

The full emission data of [Pt(N<sup>^</sup>N)Cl<sub>2</sub>] (**44**) is detailed in Table 4.16. It is essentially non-emissive in the solid state. At 77 K, an emission band is observed at  $\lambda_{\text{max}}$  362 nm, attributable to diimine intra-ligand fluorescence, but it is too weak to measure its excited state lifetime. In CH<sub>2</sub>Cl<sub>2</sub> solution at room temperature, a dual emission is evident ( $\lambda_{\text{max}}$  353, 474 nm) but its intensity is 10-fold less than that observed for free ligand **4** ( $\lambda_{\text{max}}$  353, 474 nm – note spectrum in Figure 4.30 has been normalised). The poor luminescence profile of **44** is as a result of facile non-radiative decay *via* low-lying d-d excited states. The emission profile of **44** does not change with concentration ( $10^{-3}$ - $10^{-6}$  M).

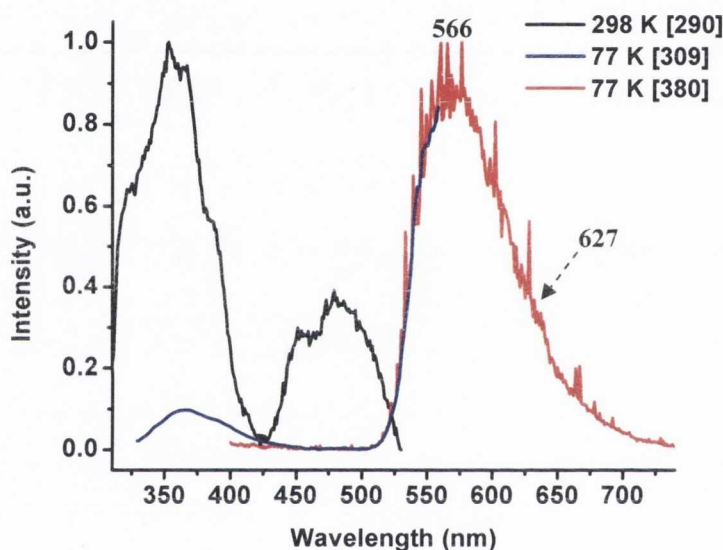


Figure 4.30: Normalised emission spectra of [Pt(N<sup>^</sup>N)Cl<sub>2</sub>] (**44**) in CH<sub>2</sub>Cl<sub>2</sub> solution at 298 K and 77 K [ $\lambda_{\text{exc}}/\text{nm}$ ].

In contrast, at 77 K in frozen CH<sub>2</sub>Cl<sub>2</sub>, a broad structureless emission band is observed at  $\lambda_{\text{max}}$  566 nm, significantly red-shifted from both singlet and triplet bipyridine-related luminescence. It is also much more intense than the higher energy diimine fluorescence observed at  $\lambda$  360 nm. There are two possible assignments for this emission band. Comprehensive studies on Pt(II) diimine dihalide complexes [Pt(N<sup>^</sup>N)Cl<sub>2</sub>] incorporating bipyridine, phenanthroline or simple methyl or *tert*-butyl derivatised bipyridines have assigned the broad, Gaussian-shaped orange emission which occurs in a glassy/frozen matrix at 10 K (or in the solid state at low temperature) to a <sup>3</sup>d-d metal-centred band. This is centred state at  $\sim \lambda$  625 nm in the majority of cases.<sup>209,251</sup> The emission band is symmetric, devoid of any fine structure, solvent insensitive and narrows upon cooling.

The second possible assignment is  $^3\text{MLCT}$ . This is the case in  $[\text{Pt}(3,3'-(\text{CH}_3\text{OCO})_2\text{-bpy})\text{Cl}_2]$ , where the emission band is asymmetrical with an onset at  $\lambda$  535 nm (centre of band  $\sim \lambda$  575 nm) and some broad vibronic structure.<sup>209</sup> (At low temperature in a frozen matrix, emission from a  $^3\text{MLCT}$  may become observable as a result of energy re-ordering of orbitals and the inhibition of structural distortions that may promote non-radiative decay). The emission spectrum of complex **44** is quite broad and there is little evidence of fine structure, however the band is not entirely symmetric. There appears to be a shoulder at  $\sim \lambda$  627 nm and an extended tail into the red region of the spectrum. The emission in this case is tentatively assigned to a mixture of  $^3\text{MLCT}$  ( $\lambda$  566 nm) and  $^3\text{d-d}$  ( $\lambda$  627 nm).

Table 4.16: Emission data for complex  $[\text{Pt}(\text{N}^{\wedge}\text{N})\text{Cl}_2]$  (**44**) in solid state and in solution ( $\text{CH}_2\text{Cl}_2$ ) at 298 K and 77K.

	Medium (T[K])	$\lambda_{\text{em}}[\text{nm}]$ ( $\lambda_{\text{exc}}[\text{nm}]$ )	$\tau$ [ns] ( $\lambda_{\text{exc}} / \lambda_{\text{em}}$ nm) <sup>c</sup>	$\Phi_{\text{em}}$ <sup>d</sup>
<b>44</b> Cl <sub>2</sub>	Solid (298) <sup>a</sup>	Non-emissive	Non-emissive	
	Solid (77) <sup>a</sup>	362 <sub>wk</sub> (310)		
	CH <sub>2</sub> Cl <sub>2</sub> (298) <sup>b</sup>	353 <sub>max</sub> , 367, 386, 451, 482 (290), 449 <sub>sh</sub> , 474 <sub>max</sub> , 505, 541 <sub>sh</sub> (360)	15 (82 %), 7 (18 %) (370 / 474) 20 (46 %), 9 (54 %) (370 / 504)	0.002
	CH <sub>2</sub> Cl <sub>2</sub> (77)	360 <sub>wk</sub> , 566 <sub>max</sub> , 627 <sub>sh</sub> (309)		

<sup>a</sup> Poorly emissive in solid state; <sup>b</sup> Argon-degassed solution,  $10^{-5}$  M; <sup>c</sup> Estimated error on  $\tau \pm 8\%$ ; <sup>d</sup> Measured using 4',6-diamidino-2-phenylindole dihydrochloride (DAPI) as a standard, based on an average of three measurements.<sup>207</sup>

### 4.6.3 Photoluminescence of $[\text{Pt}(\text{N}^{\wedge}\text{N})(\text{C}\equiv\text{CR})_2]$ complexes (**45-49**)

The photoluminescence properties of the series of Pt(diimine) bis-acetylide complexes can be divided into two groups. The emission of **45** (<sup>t</sup>Bu), **46** (CF<sub>3</sub>) and **48** (HPB) are compared (Group 1) and **47** (Pyr) and **49** (HBC) are discussed separately (Group 2).

#### 4.6.3.1 Group 1: Photoluminescence of **45**, **46** and **48**

Complexes **46** (CF<sub>3</sub>), **45** (<sup>t</sup>Bu) and **48** (HPB) exhibit analogous photophysical behaviour and are discussed together, firstly in the solid state and then in CH<sub>2</sub>Cl<sub>2</sub> solution. Table 4.17 details the photoluminescence data for **45**, **46** and **48** in argon-degassed CH<sub>2</sub>Cl<sub>2</sub> solution and in the solid state at 298 K and at 77 K.

Table 4.17: Emission data for **45**, **46** and **48** in solid state and solution ( $\text{CH}_2\text{Cl}_2$ ) at 298 K and 77K.

	Medium (T[K])	$\lambda_{\text{em}}$ [nm] ( $\lambda_{\text{exc}}$ [nm])	$\tau$ [ns] ( $\lambda_{\text{exc}} / \lambda_{\text{em}}$ nm) <sup>b</sup>	$\Phi_{\text{em}}$ <sup>c</sup>
<b>45</b> <sup>t</sup> Bu	Solid (298)	358 <sub>wk</sub> , 543 <sub>max</sub> (316)	2,500 (77 %), 400 (23 %) (370 / 543)	0.016
	Solid (77)	537 <sub>max</sub> , 574 (360)		
	$\text{CH}_2\text{Cl}_2$ (298) <sup>a</sup>	357, 375, 386 <sub>sh</sub> , 502, 604 <sub>max</sub> (325), 476, 487, 496, 508, 604 <sub>max</sub> , 668 <sub>sh</sub> (425)	20 (70 %), 6 (30 %) (295 / 373) 134 (13 %), 20 (87 %) (370 / 500) 945 (87 %), 159 (13 %) (370 / 600)	
	$\text{CH}_2\text{Cl}_2$ (77)	360 <sub>wk</sub> , 517 <sub>max</sub> , 542 <sub>sh</sub> , 572 <sub>sh</sub> (290-390)		
<b>46</b> $\text{CF}_3$	Solid (298)	362 <sub>wk</sub> , 524 <sub>max</sub> , 561 <sub>sh</sub> (315)	2,800 (75 %), 500 (25 %) (370 / 524)	0.017
	Solid (77)	488, 524, 559 <sub>sh</sub> (360)		
	$\text{CH}_2\text{Cl}_2$ (298) <sup>a</sup>	355, 374, 387 <sub>sh</sub> , 476 <sub>sh</sub> , 533 <sub>max</sub> (360), 477, 487, 508, 545 <sub>max</sub> , 607 <sub>sh</sub> (425)	22 (71 %), 14 (29 %) (370 / 476) 363 (33 %), 19 (67 %) (370 / 506) 1,300 (79 %), 300 (21 %) (370 / 550)	
	$\text{CH}_2\text{Cl}_2$ (77)	363 <sub>wk</sub> (295), 480 <sub>max</sub> , 514, 545, 592 <sub>sh</sub> (400)		
<b>48</b> HPB	Solid (298)	361 (305), 599 <sub>max</sub> (470)	2,600 (77 %), 400 (23 %) (370 / 599)	0.076
	Solid (77)	360 <sub>wk</sub> (295), 600 <sub>max</sub> , 647 (482)		
	$\text{CH}_2\text{Cl}_2$ (298) <sup>a</sup>	395 <sub>max</sub> , 413, 472, 502, 609 (345) 477, 496 <sub>sh</sub> , 506, 609 <sub>max</sub> , 661 <sub>sh</sub> (434)	21 (65 %), 13 (35 %) (370 / 473) 241 (16 %), 19 (84 %) (370 / 502) 735 (89 %), 72 (11 %) (370 / 609)	
	$\text{CH}_2\text{Cl}_2$ (77)	365 <sub>wk</sub> , 541 <sub>max</sub> (300), 539 <sub>max</sub> , 578 <sub>sh</sub> , 613 <sub>sh</sub> (440)		

<sup>a</sup> Argon-degassed solutions,  $\sim 10^{-5}$  M (unless otherwise stated); <sup>b</sup> Estimated error on  $\tau \pm 10\%$ ; <sup>c</sup> Measured using 4',6-diamidino-2-phenylindole dihydrochloride (DAPI) as a standard., based on an average of 3 measurements.<sup>207</sup>

#### 4.6.3.1.1 Solid state emission spectra of **45**, **46** and **48**

The solid state emission spectra of **46** ( $\text{CF}_3$ ), **45** (<sup>t</sup>Bu) and **48** (HPB), shown in Figure 4.31, are dominated by broad, structureless emission bands over  $\lambda$  470-700 nm ( $\Delta E = 6,990 \text{ cm}^{-1}$ ). Complex **46** containing the electron-withdrawing substituent on the acetylide is most blue-shifted ( $\lambda_{\text{max}}^{\text{em}}$  524 nm) and the band becomes more red-shifted with substituents



of increasing electron density (**45** (<sup>t</sup>Bu)  $\lambda_{\text{max}}^{\text{em}}$  543 nm; **48** (HPB)  $\lambda_{\text{max}}^{\text{em}}$  599 nm). The measured excited state lifetimes for this emission band in all three complexes are similar (**45**, **46** and **48**: 2.5-2.8  $\mu\text{s}$  (75-77 %), 0.4-0.5  $\mu\text{s}$  (23-25 %), Table 4.17). Notably, these are double that recorded for  $^3\pi\pi^*$  emission from **4** in the solid state (1.4  $\mu\text{s}$  (79 %), 0.3  $\mu\text{s}$  (21 %)). The characteristic polyphenylene <sup>1</sup>IL emission band centred at  $\sim\lambda$  360 nm is also evident as a weak intensity emission in the spectra of **46**, **45** and **48** (Figure 4.31).

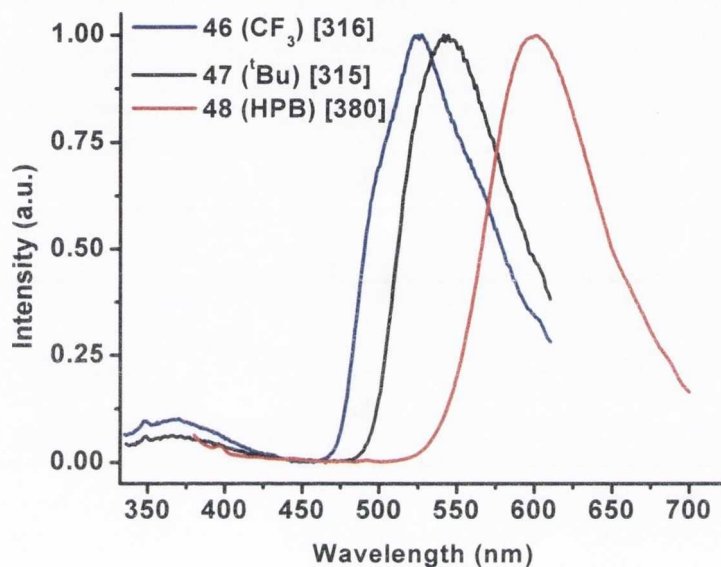


Figure 4.31: Normalised solid state emission spectra of **45**, **46** and **48** at 298 K [ $\lambda_{\text{exc}}/\text{nm}$ ].

At 77 K, the emission profiles of **46** ( $\text{CF}_3$ ), **45** (<sup>t</sup>Bu) and **48** (HPB) in the solid state are asymmetric and considerably sharper than at room temperature (Figure 4.32). All three spectra have a shoulder at slightly longer wavelength than the emission maximum, with an energy difference between the two peaks indicative of the involvement of the diimine (C=C, C=N) in the emissive excited state ( $\nu/\text{cm}^{-1}$ : 1298 (**46**), 1200 (**45**) and 1212 (**48**)). Marginal blue-shifts of emission peak maxima from room temperature to low temperature are evident for **46** (298 K:  $\lambda_{\text{max}}$  524 nm; 77 K:  $\lambda_{\text{max}}$  488/524 nm) but for other two complexes the energy of the band does not change. This is anticipated for solid state measurements, in which temperature should have a minimal effect as molecules do not have the freedom to undergo distortion to relieve strain in the excited state.

At 77 K, the shift to lower energy on increasing the electron donicity of the substituent on the aryl acetylide is once again evident. This trend parallels that observed in the UV-Visible absorption spectra (Figure 4.24) and the cyclic voltammetric data (Table 4.14) for this family of complexes. An electron-donating substituent on the Pt acetylide will

increase the energy of the  $\pi(\text{C}\equiv\text{C-R})$  orbital (consequently destabilising the  $5d(\text{Pt})$  orbital), reducing the HOMO-LUMO gap [ $\text{Pt}(d)/\pi(\text{C}\equiv\text{CAr}) \rightarrow \pi^*(\text{N}^{\wedge}\text{N})$ ] of the (ML)LCT state resulting in a red-shift of the emission band. The considerably longer lifetimes and separation between the lowest energy absorption and this emission band are indicative of triplet state phosphorescence.

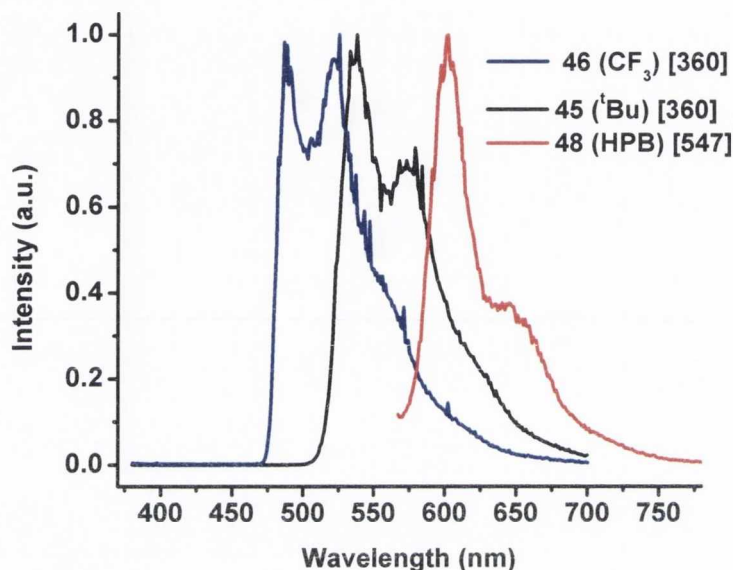


Figure 4.32: Normalised solid state emission spectra of **45**, **46** and **48** at 77 K [ $\lambda_{\text{exc}}/\text{nm}$ ].

#### 4.6.3.1.2 Photoluminescence of **45**, **46** and **48** in $\text{CH}_2\text{Cl}_2$ solution (298 K)

The photoluminescence spectra of complexes **45**, **46** and **48** were recorded in optically dilute argon-degassed  $\text{CH}_2\text{Cl}_2$  solution ( $\sim 10^{-5}$  M). No concentration effects were observed for these three complexes, ruling out the influence of aggregates on the excited state properties (within the concentration range  $10^{-3} - 10^{-5}$  M). Several emissive states are evident for complexes **45**, **46** and **48** in degassed  $\text{CH}_2\text{Cl}_2$  solution (Figure 4.33). These are a high energy  $^1\pi\pi^*$  diimine fluorescence ( $\sim \lambda$  360 nm), an intermediate energy  $^3\pi\pi^*/^3n\pi^*$  diimine phosphorescence ( $\sim \lambda$  500 nm) and a low energy  $^3\text{L}'\text{LCT}/^3\text{MLCT}$  emission ( $\lambda$  545-609 nm).

The high energy  $^1\text{IL}$  fluorescence seen in the uncoordinated bipyridine ligand, occurring at  $\lambda$  360 nm, is once again evident in the spectra of complexes **45** and **46** (Figure 4.33). The high energy region of **48** (HPB) is quite different. Excitation of **48** at high energies ( $\lambda$  345 nm) produces a spectrum dominated by a very intense, broad band between  $\sim \lambda$  370-460 nm ( $\lambda_{\text{max}}$  395 nm). This is probably derived from several emissive excited states – diimine

$^1\text{IL}$  fluorescence and intraligand  $^1\pi\pi^*$  fluorescence and  $^3\pi\pi^*$  phosphorescence on the ethynyl-hexaphenylbenzene chromophore itself (as observed for *cis*-[Pt(C $\equiv$ C-HPB) $_2$ (dppe)] (**39**) and *trans*-[Pt(C $\equiv$ C-HPB) $_2$ (PPh $_3$ ) $_2$ ] (**38**) in Chapter 3). For all three complexes, the excited state lifetimes for these high energy bands are in the nanosecond region – indicating that they are derived from singlet excited states as anticipated (Table 4.17).

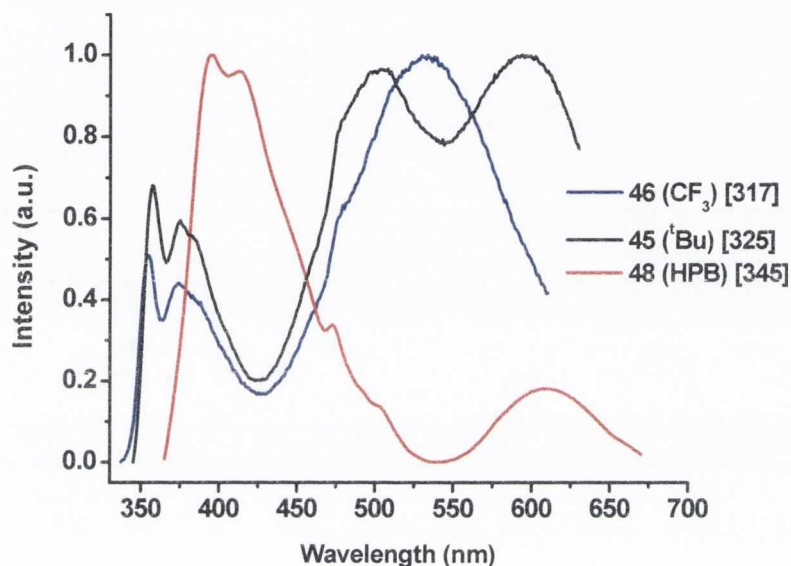


Figure 4.33: Emission spectra of **45**, **46** and **48** in  $\text{CH}_2\text{Cl}_2$  solution at 298 K,  $\lambda_{\text{exc}} < 350$  nm [ $\lambda_{\text{exc}}/\text{nm}$ ].

Photoluminescence bands of intermediate energy are observed for the three complexes **45** ( $t\text{Bu}$ ), **46** ( $\text{CF}_3$ ) and **48** (HPB) (Figure 4.33). At  $\sim\lambda$  500 nm, complexes both **46** and **48** exhibit some fine structure on the shoulders of more intense emission bands which cannot be identified in this spectrum (Figure 4.33). An additional band is observed for **45** ( $t\text{Bu}$ ) ( $\lambda$  501 nm) which is quite broad and featureless when excited at this higher energy wavelength. Excitation of complexes **45**, **46** and **48** at longer wavelengths ( $\lambda_{\text{exc}} \sim 430$  nm) improves the resolution of the emission profile of this band and is shown in Figure 4.34. An almost identical highly resolved emission appears at  $\lambda$  477-508 nm for each of the three complexes, showing for each a vibronic progression of  $1240\text{ cm}^{-1}$ , consistent with the involvement of C=C and C=N in the electronic transition (Figure 4.34). This corresponds to the  $^3\text{IL}$  emission observed from diimine ligand **4** (Figure 4.29). Taking **45** as an example, the excited state lifetime of this band has two components - 20 ns (87 %) and a significantly longer 134 ns (13 %). A similar trend in excited state lifetimes for this emission band is seen for complexes **46** and **48**. In contrast, the excited state lifetimes of

the lower energy band in ligand **4** and in ethynyl-hexaphenylbenzene (**6**) are both  $\sim 20$  ns. Most likely, this emission can be attributed to  $^3\pi\pi^*$  from the diimine ligand with some Pt(II) influence and some additional MLCT character [Pt(d) $\rightarrow \pi^*(N^{\wedge}N)$ ] of weak intensity.

The final, lowest energy emission band from each of the three complexes **45** ( $^t\text{Bu}$ ), **46** ( $\text{CF}_3$ ) and **48** (HPB) is quite broad and considerably red-shifted (Figure 4.34). It appears at highest energy for **46** at  $\lambda$  545 nm ( $\tau$ : 1.3  $\mu\text{s}$  (79 %), 0.3  $\mu\text{s}$  (21 %)). Increasing the electron-donicity of the aryl acetylide shifts this emission band to lower energy, occurring at  $\lambda$  604 nm (**45**) and  $\lambda$  609 nm (**48**). This trend corresponds to that observed in the solid state (298 K and 77 K), the absorption spectra and in electrochemical data. The long excited state lifetimes (**45**:  $\tau$  945 (87 %), 159 (13 %) **48**:  $\tau$  735 ns (89 %), 72 ns (11 %)) and large Stokes shifts of this emission band from the lowest energy absorption band suggest that the transitions involved in this emission band are triplet in origin,  $^3(\text{ML})\text{LCT}$ .

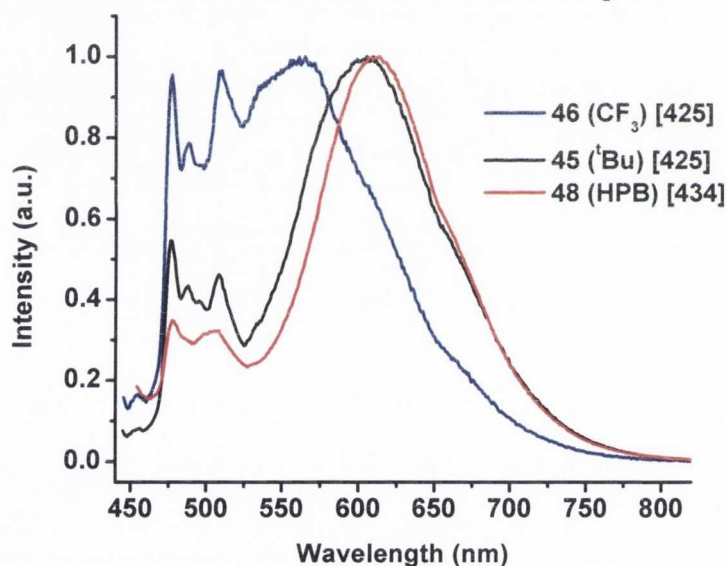


Figure 4.34: Emission spectra of **45**, **46** and **48** in  $\text{CH}_2\text{Cl}_2$  solution at 298 K,  $\lambda_{\text{exc}} > 420$  nm [ $\lambda_{\text{exc}}/\text{nm}$ ].

The decrease in excited state lifetimes with decreasing emission energy corresponds to the energy gap law, which essentially states that the larger the energy gap between the ground and the excited state, the less efficient are deactivation processes (i.e. the non-radiative decay rate constant,  $k_{\text{nr}}$ , decreases exponentially with increasing emission energy).<sup>259</sup> Consequently, a larger HOMO-LUMO gap should result in longer excited state lifetimes.<sup>222,260</sup> This feature has been observed in many of the Pt(II) diimine series, containing bis-acetylides and dithiolates, prepared in the literature.<sup>220,222,254</sup>

#### 4.6.3.1.3 Photoluminescence of 45, 46 and 48 in CH<sub>2</sub>Cl<sub>2</sub> solution (77 K)

The emission spectra of **45**, **46** and **48** in CH<sub>2</sub>Cl<sub>2</sub> solution (10<sup>-5</sup> M) at 77 K are displayed in Figure 4.35. The emission maxima of each of the three complexes undergo large rigidochromic shifts from 298 K to 77 K. In **45** (<sup>t</sup>Bu),  $\lambda_{\text{max}}^{\text{em}}$  blue shifts from  $\lambda$  600 nm (at 298 K) to  $\lambda$  517 nm, a thermally induced Stokes shift ( $\Delta E_s$ ) of 2675 cm<sup>-1</sup> (at 77 K, Figure 4.35). Similarly, **48** (HPB) emits at  $\lambda$  609 nm at room temperature but at  $\lambda$  541 nm at low temperature ( $\Delta E_s = 2064$  cm<sup>-1</sup>). These large thermally induced Stokes shifts observed for **45**, **46** and **48** are characteristic of charge-transfer emission.<sup>126,222,253</sup> At low temperature, the emission spectrum of **46** is significantly fine-structured with a vibronic progression of 1380 cm<sup>-1</sup>, confirming the diimine ligand involvement in the emissive excited state. Although **45** is not as highly structured as **46** at 77 K, its emission has two lower energy shoulders (at  $\lambda$  542 and 572 nm respectively) separate from the emission maximum which correspond to a similar vibronic spacing to that observed for **46** (Figure 4.35). This is also evident in **48** (HPB).

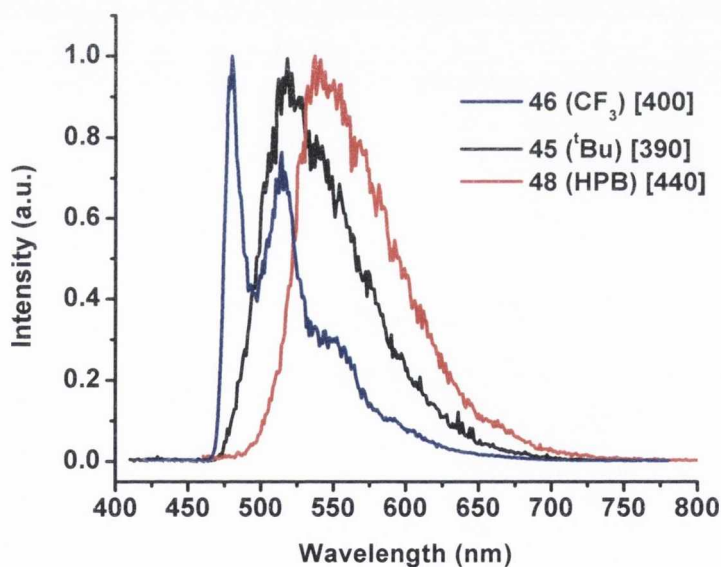


Figure 4.35: Emission spectra of **45**, **46** and **48** in CH<sub>2</sub>Cl<sub>2</sub> solution at 77 K [ $\lambda_{\text{exc}}/\text{nm}$ ].

The tendency of the emission energy to decrease with increasing electronic-donicity of the aryl acetylide co-ligand holds also in CH<sub>2</sub>Cl<sub>2</sub> solution at 77 K (Figure 4.35). All emission, absorption and electrochemical measurements prove that increasing the electron density on the  $\pi(\text{C}\equiv\text{Ar})$  (and correspondingly on the 5d(Pt) orbitals) results in a smaller HOMO-LUMO gap and gives further merit to the assignment of this transition as (ML)LCT [Pt(d)/ $\pi(\text{C}\equiv\text{CAr}) \rightarrow \pi^*(\text{N}^{\wedge}\text{N})$ ] (essentially metal-perturbed L'LCT).

## 4.6.3.2 Group 2: Photoluminescence of 47 and 49

The photoluminescence spectra of  $[\text{Pt}(\text{N}^{\wedge}\text{N})(\text{C}\equiv\text{C-Pyr})_2]$  (**47**) and  $[\text{Pt}(\text{N}^{\wedge}\text{N})(\text{C}\equiv\text{C-HBC})_2]$  (**49**) are considerably different from those of **45** (<sup>t</sup>Bu), **46** (CF<sub>3</sub>) and **48** (HPB) in solution at 298 K and 77 K. **47** and **49** are discussed together, firstly in the solid state and then in CH<sub>2</sub>Cl<sub>2</sub> solution. Full spectroscopic details are provided in Table 4.18.

Table 4.18: Emission data for **47** and **49** in solid state and solution (CH<sub>2</sub>Cl<sub>2</sub>) at 298 K, 77K.

	Medium (T[K])	$\lambda_{\text{em}}[\text{nm}]$ ( $\lambda_{\text{exc}}[\text{nm}]$ )	$\tau$ [ns] ( $\lambda_{\text{exc}} / \lambda_{\text{em}}$ nm) <sup>d</sup>	$\Phi_{\text{em}}$ <sup>e</sup>
<b>47</b>	Solid (298) <sup>b</sup>	360 (310)	Poorly emissive	
Pyr	Solid (77) <sup>b</sup>	355 <sub>wk</sub> (310)		
	CH <sub>2</sub> Cl <sub>2</sub> 10 <sup>-5</sup> M (298) <sup>a</sup>	395, 415, 449 <sub>max</sub> , 478, 495 <sub>sh</sub> , 644 <sub>sh</sub> , 663, 679 <sub>sh</sub> (360)	28 (82 %), 5 (18 %) (370 / 448) 23 (64 %), 6 (36 %) (370 / 477) 4,650 (370 / 661)	0.042
	CH <sub>2</sub> Cl <sub>2</sub> 10 <sup>-3</sup> M (298) <sup>a</sup>	662 <sub>max</sub> , 719, 738 <sub>sh</sub> (545)	730 (370 / 662)	
	CH <sub>2</sub> Cl <sub>2</sub> (77)	484, 501, 540 <sub>sh</sub> , 660, 674 <sub>sh</sub> , 715, 734 (448)		
<b>49</b>	Solid (298) <sup>b</sup>	372 (312), 472, 493, 593 (360) <sup>b</sup>	Poorly emissive	
HBC	Solid (77) <sup>b</sup>	367 (309), 558, 583 <sub>max</sub> , 638 (390-505) <sup>b</sup>		
	CH <sub>2</sub> Cl <sub>2</sub> (298) <sup>a</sup>	452 <sub>sh</sub> , 473 <sub>max</sub> , 481 <sub>sh</sub> , 491, 501, 525, 536, 545 <sub>sh</sub> , 560 <sup>c</sup> (360)	15 (57 %), 21 (43 %) (370 / 475) 21 (71 %), 12 (29 %) (370 / 504)	0.077
	CH <sub>2</sub> Cl <sub>2</sub> (77)	477, 509, 524 <sub>sh</sub> , 551 <sub>sh</sub> , 572 <sub>max</sub> , 618, 630 <sub>sh</sub> , 667 <sub>sh</sub> (402)		

<sup>a</sup> Argon-degassed solutions, ~10<sup>-5</sup> M (unless otherwise stated); <sup>b</sup> Poorly emissive in solid state; <sup>c</sup> Tail of emission band extends to  $\lambda$  700 nm; <sup>d</sup> Estimated error on  $\tau \pm 10$  %; <sup>e</sup> Measured using 4',6-diamidino-2-phenylindole dihydrochloride (DAPI) as a standard., based on an average of 3 measurements.<sup>207</sup>

## 4.6.3.2.1 Solid state emission spectra of 47 and 49

$[\text{Pt}(\text{N}^{\wedge}\text{N})(\text{C}\equiv\text{C-Pyr})_2]$  (**47**) and  $[\text{Pt}(\text{N}^{\wedge}\text{N})(\text{C}\equiv\text{C-HBC})_2]$  (**49**) are essentially non-emissive in the solid state at both room temperature and low temperature (Table 4.18). This can be

attributed to aggregation (e.g.  $\pi$ - $\pi$  stacking) due to the extended alkynyl  $\pi$ -conjugated platforms which appears to quench almost all luminescence. In pyrenyl complex **47**, the only luminescence observed is a very weak intra-ligand (N<sup>N</sup>) fluorescence ( $\sim\lambda$  360 nm) at 298 K and 77 K. This is also observed at both temperatures for HBC complex **49**. Traces of intra-ligand fluorescence from the HBC chromophore are also evident at both temperatures (Table 4.18) but this emission is quite poorly resolved and difficult to distinguish from the baseline noise in the emission spectrum.

#### 4.6.3.2.2 Photoluminescence of **47** and **49** in CH<sub>2</sub>Cl<sub>2</sub> solution (298 K)

The photoluminescence spectra of complexes **47** and **49** were recorded in optically dilute argon-degassed CH<sub>2</sub>Cl<sub>2</sub> solution ( $\sim 10^{-5}$  M). The argon-degassed CH<sub>2</sub>Cl<sub>2</sub> solution emission spectra of **47** and **49** at 298 K are dominated by emission from their respective highly conjugated aromatic co-ligands (Figure 4.36). Luminescence from both complexes appears as an extended band with a complex vibronic structure. In neither case is intra-ligand emission (either of singlet or triplet origin) from the diimine ligand evident, in contrast to **45**, **46** and **48** (Table 4.18). For both complexes, the absorption and excitation spectra were superimposable, excluding the possibility of intermolecular interaction effects (at  $10^{-5}$  M concentrations).

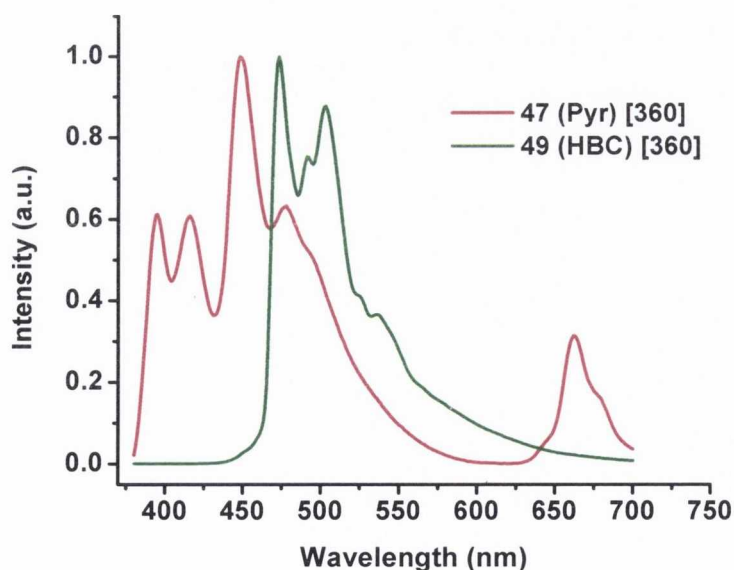


Figure 4.36: Normalised emission spectra of **47** and **49** at 298 K in CH<sub>2</sub>Cl<sub>2</sub> solution ( $10^{-5}$  M) [ $\lambda_{exc}$ /nm].

The emission spectrum of HBC complex **49** is very similar to that recorded for the free ethynyl-HBC ligand (**7**) as seen in Chapter 3.<sup>74</sup> The emission band has an onset at  $\lambda$  473 nm and extends to  $\lambda$  600 nm (Figure 4.36) and excited state lifetimes measured at two maximum emission bands are in nanoseconds, indicative of the singlet nature of the excited state transition (Table 4.18). This band can be assigned as  $^1\pi\pi^*$  on the hexa-*peri*-hexabenzocoronene chromophore. The emission spectrum of **49** displays no evidence of the narrow band-width phosphorescent band at  $\lambda$  578 nm that was a feature of the *cis* and *trans* Pt(II) HBC complexes discussed in Chapter 3. In *cis*-[Pt(C $\equiv$ C-HBC)<sub>2</sub>(dppe)] (**41**) and *trans*-[Pt(C $\equiv$ C-HBC)<sub>2</sub>(PPh<sub>3</sub>)<sub>2</sub>] (**40**), the appearance of this  $^3\pi\pi^*$  (C $\equiv$ C-HBC) emission was found to be extremely sensitive to quenching by oxygen, however despite very thorough argon-degassing of [Pt(N $\wedge$ N)(C $\equiv$ C-HBC)<sub>2</sub>] (**49**), no phosphorescence from the HBC chromophore could be detected.

The ethynyl-pyrene chromophores in **47** (Pyr) are largely responsible for the highly structured emission spectrum observed in Figure 4.36, with an onset at  $\lambda$  395 nm (Table 4.18). Excitation into the pyrenyl  $\pi\pi^*$  absorption bands ( $\lambda_{\text{exc}}$  360 nm) produces dual emission from **47**: a higher energy structured emission between  $\lambda$  395-500 nm and a lower energy band centred at 663 nm. The relatively short lifetimes ( $\tau$ : 28 ns (82 %), 5 ns (18 %), ( $\lambda_{\text{max}}^{\text{em}}$  448 nm)) support the assignment of the higher energy band as derived from singlet  $^1\pi\pi^*$  transitions on the pyrene subunit. The lower energy band has a greatly enhanced lifetime of 4.65  $\mu$ s and confirms the assignment of this transition as phosphorescence originating from a triplet intra-ligand state on the pyrene chromophore ( $^3\pi\pi^*$ (C $\equiv$ C-Pyrene)). The high spin orbit coupling of the attached heavy metal Pt centre facilitates room temperature triplet state emission from the pyrene acetylide. (Uncoordinated ethynyl-pyrene requires a heavy atom dopant, ethyl iodide, in order to undergo  $^3\pi\pi^*$  emission).<sup>245</sup> An identical emission profile has been observed for a related pyrenyl complex, [Pt(dbbpy)(C $\equiv$ C-Pyr)<sub>2</sub>] (dbbpy = 4,4'-di(*tert*-butyl)-2,2'-bipyridine).<sup>245</sup> The paper also noted that [Pt(dbbpy)(C $\equiv$ C-Pyr)<sub>2</sub>] and *trans*-[Pt(PBu<sub>3</sub>)<sub>2</sub>(C $\equiv$ C-Pyr)<sub>2</sub>] possess identical emission spectra, despite the absence of both a diimine ligand and the change in geometry of the pyrene subunits about the Pt centre from *cis* to *trans* in the latter complex. It is suggested that the two pyrenyl chromophores do not interact within the molecule.



The self-quenching of solid-state emission in **47** (Pyr) prompted us to undertake the measurement of a CH<sub>2</sub>Cl<sub>2</sub> solution of the complex at a higher concentration. In the absorption spectrum of **47**, no concentration effects are observed over the range 10<sup>-4</sup> - 5x10<sup>-7</sup> M (Section 4.4.2) and so a 10-fold increase in concentration to 10<sup>-3</sup> M was chosen. The relatively poor solubility of **49** (HBC) precluded a similar examination of concentration-dependent emissive properties.

Inspection of the emission spectrum of **47** (Pyr) at 10<sup>-3</sup> M concentration reveals that all fluorescence from the pyrene-acetylide chromophore has been entirely quenched (Table 4.18). However, phosphorescence originating from the triplet  $\pi\pi^*$  state on the pyrenyl acetylide is still present ( $\lambda_{\text{max}}$  662 nm) and the band shape and energy location is essentially identical from 10<sup>-5</sup> - 10<sup>-3</sup> M. A noticeable decrease in phosphorescence lifetime (0.73  $\mu$ s,  $\lambda_{\text{exc}}$  662 nm) is also evident. The UV-visible absorption spectrum of the complex at 10<sup>-3</sup> M was comparable to those at lower concentrations, indicating the complex does not show any ground state aggregation effects.

It is clear that at 10<sup>-3</sup> M, [Pt(N<sup>^</sup>N)(C $\equiv$ C-Pyr)<sub>2</sub>] (**47**) self-quenches in solution, most likely by  $\pi$  stacking of pyrene chromophores. This aggregation has little effect on the electronic structure of the triplet excited state (similar band shape and  $\lambda_{\text{max}}^{\text{em}}$ ) but it results in a shortening of the triplet excited state lifetime, an effect also observed in the first Pt(II) hexa-*peri*-hexabenzocoronene acetylide.<sup>173</sup>

#### 4.6.3.2.3 Photoluminescence of 47 and 49 in CH<sub>2</sub>Cl<sub>2</sub> solution (77 K)

The emission spectra of [Pt(N<sup>^</sup>N)(C≡C-Pyr)<sub>2</sub>] (**47**) and [Pt(N<sup>^</sup>N)(C≡C-HBC)<sub>2</sub>] (**49**) in frozen CH<sub>2</sub>Cl<sub>2</sub> at 77 K are presented in Figure 4.37. In **49**, fluorescence arising from the HBC chromophore is evident with an onset at λ 477 nm. An additional narrow band-width emission is observed at λ<sub>max</sub> 572 nm and a shoulder at λ 618 nm. This corresponds to a triplet excited state located on the HBC platform, <sup>3</sup>ππ\* (C≡C-HBC).<sup>172-173</sup> The heavy metal Pt(II) centre induces strong-spin orbit coupling to stabilize the triplet excited state on the acetylide ligand, as observed for both *cis* and *trans* Pt(II) HBC complexes in Chapter 3.

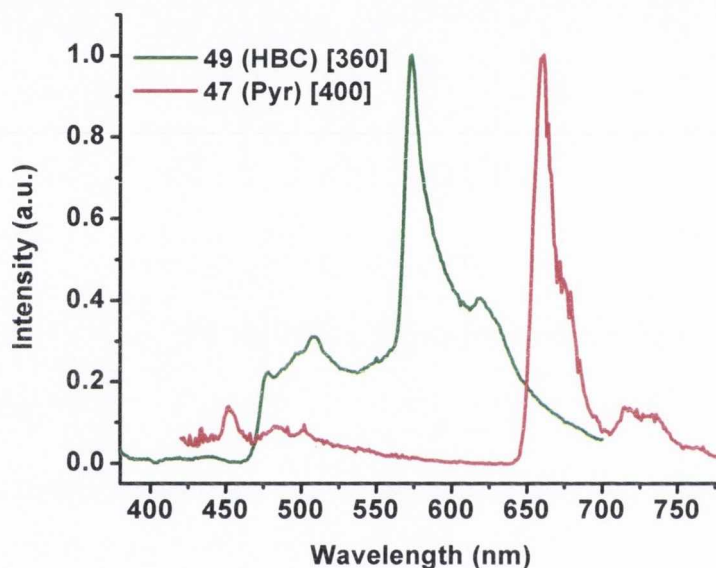


Figure 4.37: Normalised emission spectra of **47**&**49** in CH<sub>2</sub>Cl<sub>2</sub> (10<sup>-5</sup> M) at 77 K [ $\lambda_{exc}/nm$ ].

At low temperature, the <sup>1</sup>ππ\* fluorescence yield of **47** (Pyr) is very low. Instead, <sup>3</sup>ππ\* phosphorescence from the pyrene chromophore itself dominates the emission spectrum as expected, with a maximum at λ 660 nm. This thermally-induced Stokes shift ( $\Delta E_s = 69 \text{ cm}^{-1}$ ) is extremely small, in contrast with the dramatic shifts observed in complexes **45**, **46** and **48**. This indicates that emission from **47** and **49** is not derived from a charge-transfer excited state and is instead within the range expected for <sup>3</sup>ππ\* emissive state.<sup>245,253</sup>

#### 4.6.4 Emission Quantum Yields

All emission quantum yields were measured using the Demas and Crosby method discussed in Chapter 2.<sup>135</sup> The quantum yield of emission for polyphenylene diimine ligand **4** was measured using quinine sulfate as a standard (0.5 M H<sub>2</sub>SO<sub>4</sub>,  $\Phi_{em} = 0.546$ ,  $\lambda_{exc}$

310 nm) and found to be  $< 0.1\%$  (Table 4.15).<sup>133</sup> This is typical of non-planar polyphenylene derivatives and has been observed previously for unsubstituted hexaphenylbenzene, ethynyl-hexaphenylbenzene (**6**) in Chapter 3 and dimethyl-bipyridyl ligand **3** (Chapter 2).<sup>125</sup>

The quantum yields of emission for complexes **44-49** were measured relative to 4',6-diamidino-2-phenylindole dihydrochloride, DAPI ( $\text{H}_2\text{O}$ ,  $\Phi_{\text{em}} = 0.043$ ,  $\lambda_{\text{exc}} 350\text{ nm}$ ).<sup>207</sup> Unsurprisingly, the quantum yield of  $[\text{Pt}(\text{N}^{\wedge}\text{N})\text{Cl}_2]$  (**44**) is the lowest of all the complexes measured (0.2 %) as a result of the population of low-lying non-emissive metal-centred states (Table 4.16). For the bis-acetylide complexes,  $\Phi_{\text{em}}$  values fall between 1.6 – 7.7 % (Table 4.17, Table 4.18). These values are comparable to those reported previously for diimine Pt(II) bis-acetylide systems.<sup>220,222,245,261</sup> Low quantum yields in general for this class of compounds indicate that excited state decay is governed by non-radiative processes. The highest quantum yields are noted for  $[\text{Pt}(\text{N}^{\wedge}\text{N})(\text{C}\equiv\text{C-Pyr})_2]$  (**47**),  $[\text{Pt}(\text{N}^{\wedge}\text{N})(\text{C}\equiv\text{C-HPB})_2]$  (**48**) and  $[\text{Pt}(\text{N}^{\wedge}\text{N})(\text{C}\equiv\text{C-HBC})_2]$  (**49**) ( $\Phi_{\text{em}}$  4.2 %, 7.6 % and 7.7 %). This is a result of the intense polyaromatic platform-centred fluorescence and phosphorescence observed for these complexes.

#### 4.6.5 A comparison: The photoluminescence of Group 1 (**45**, **46**, **48**) vs. Group 2 (**47**, **49**)

The emissive properties of **47** (Pyr) and **49** (HBC) differ from those of **45** (<sup>t</sup>Bu), **46** ( $\text{CF}_3$ ) and **48** (HPB) as a result of the appended highly aromatic, electron-delocalised chromophores. The (ML)LCT excited state which dominates photoluminescence from the latter three complexes cannot explain the excited state behaviour of the pyrenyl and HBC complexes. The photoluminescence of complexes **47** (Pyr) and **49** (HBC) is entirely independent of the coordinated diimine ligand. The observed phosphorescence from both complexes is almost identical to that of analogous systems containing phosphine ligands instead of bipyridyl, namely *cis*- $[\text{Pt}(\text{C}\equiv\text{C-HBC})_2(\text{dppe})]$  (**41**), *trans*- $[\text{Pt}(\text{C}\equiv\text{C-HBC})_2(\text{PPh}_3)_2]$  (**40**) and the literature complex *trans*- $[\text{Pt}(\text{PBU}_3)_2(\text{C}\equiv\text{C-Pyr})_2]$ .<sup>245</sup> This phosphorescence is evidently derived from a  $^3\pi\pi^*$  excited state located on the extended aromatic chromophore. The effect of extending the  $\pi$ -conjugation of the acetylide is to introduce an energetically accessible  $^3\pi\pi^*$  excited state localized on the alkynyl moiety that is lower in energy than that of  $^3(\text{ML})\text{LCT} [\text{Pt}(\text{d})/\pi(\text{C}\equiv\text{CAr}) \rightarrow \pi^*(\text{N}^{\wedge}\text{N})]$ .<sup>213,245</sup>

There are many examples of this in the literature for related complexes. Castellano *et al.* have prepared two Pt(II) diimine complexes containing  $\pi$ -conjugated polyaromatic platforms (specifically anthracene and perylene) whose lowest emissive excited states are phosphorescent intraligand  $^3\pi\pi^*(C\equiv CR)$  in nature.<sup>262</sup> Schanze and co-workers have reported a sequence of Pt(II) complexes with two appended stilbene-acetylide moieties and either a bidentate phosphine or a bipyridine chelating ligand.<sup>177</sup> In both cases, emission is derived entirely from the triplet  $\pi\pi^*$  emissive state located on the acetylide (in fact, a single acetylide subunit) and in the case of the bipyridine complex, MLCT absorption bands are able to sensitise  $^3\pi\pi^*$  emission.

#### 4.7 Summary and Conclusions

This chapter describes the synthesis of a series of Pt(II) diimine bis-acetylide complexes, incorporating a polyphenylene-functionalised bipyridine ligand and a range of  $\sigma$ -alkynyl co-ligands of varying electronic demand and  $\pi$ -electronic delocalisation. Complexes were characterised using NMR spectroscopy, mass spectrometry, elemental analysis and infra-red spectrometry.  $^1\text{H}$  NMR spectroscopy of precursor complex  $[\text{Pt}(\text{N}^{\wedge}\text{N})\text{Cl}_2]$  (**44**) suggests that steric constraints within the molecule prohibit the free rotation of one or more of the *tert*-butyl phenyl substituents, an effect which is observed to increase significantly upon coordination of  $\sigma$ -acetylide auxiliary ligands to the metal centre. Single crystal X-ray diffraction on  $[\text{Pt}(\text{N}^{\wedge}\text{N})(\text{C}\equiv\text{C}-\text{C}_6\text{H}_4-\text{tBu})_2]$  (**45**) confirms this, suggesting that intramolecular interactions between an acetylide subunit and two of the *tert*-butyl phenyl rings on the diimine ligand result in restricted rotation of these two rings.

The nature of the emissive states of the  $[\text{Pt}(\text{N}^{\wedge}\text{N})(\text{C}\equiv\text{CR})_2]$  series of complexes has been investigated by UV-visible absorption spectroscopy, cyclic voltammetry and photoluminescence studies. The lowest energy absorption band in the UV spectrum of the acetylide complexes undergoes a systematic bathochromic shift as the electron donating properties of the acetylide co-ligand increases, such that **46** ( $\text{CF}_3$ ) is the most blue-shifted and **47** (Pyr) the most red-shifted. This electronic absorption band exhibits significant negative solvatochromic behaviour, shifting to lower energy in low polarity solvents, indicating that the excited state responsible is charge transfer in nature. Furthermore, the Pt(II)-Pt(III) oxidation potential becomes less positive as the electronic donicity of the alkynyl auxiliary increases - **46** containing the electron-withdrawing substituent is the most

difficult to oxidise, whereas as **47** is the easiest. In general, this is in agreement with the red-shift of the lowest energy band in the UV-visible spectra of the complexes from electron-withdrawing substituents to electron-rich substituents. The dependence of the Pt(II) oxidation potential on the electron donicity of the appended acetylide, in addition to the trend observed in the UV-visible spectra, is evidence of the participation of both the  $\pi(\text{C}\equiv\text{CAr})$  and  $5d(\text{Pt})$  in the HOMO and reinforces the assignment of the lowest energy transition as (metal-ligand)-to-ligand charge transfer (ML)LCT [ $\text{Pt}(d)/\pi(\text{C}\equiv\text{CR})\rightarrow\pi^*(\text{N}^{\wedge}\text{N})$ ].

Photoluminescence from this family of Pt(II) bis-acetylides is complex with a variety of emissive states observed. The Pt(II) precursor [ $\text{Pt}(\text{N}^{\wedge}\text{N})\text{Cl}_2$ ] (**44**) is essentially non-emissive in the solid state and in room temperature solution, but at 77 K in frozen  $\text{CH}_2\text{Cl}_2$ , an intense emission is observed which is tentatively assigned to a mixture of  $^3d-d$  and  $^3\text{MLCT}$  emission. In addition to diimine-centred fluorescence and phosphorescence, Group 1 complexes **45** ( $^t\text{Bu}$ ), **46** ( $\text{CF}_3$ ) and **48** (HPB), exhibit a broad, red-shifted emission profile with lifetimes in the microsecond range (R.T. solid and in solution). The emission maximum shifts to lower energy as the aryl acetylide becomes more electron donating. At 77 K, the band becomes more resolved and undergoes a rigidochromic shift (thermally induced Stokes shift  $\Delta E_s > 2000 \text{ cm}^{-1}$ ). This combination of vibronic fine structure and blue-shifted low temperature emission along with the decrease in emissive energy with increasing electron donicity and room temperature lifetimes in the microsecond range, confirm the nature of the emissive state as charge transfer and reaffirms the assignment of the excited state as (ML)LCT. The phosphorescent  $^3(\text{ML})\text{LCT}$  emission observed is facilitated by spin-orbit coupling of the attached heavy Pt centre.

The emission profiles of the Group 2 complexes [ $\text{Pt}(\text{N}^{\wedge}\text{N})(\text{C}\equiv\text{C-Pyr})_2$ ] (**47**) and [ $\text{Pt}(\text{N}^{\wedge}\text{N})(\text{C}\equiv\text{C-HBC})_2$ ] (**49**) are very different from **45**, **46** and **48**. Highly structured, narrow bandwidth emission from **47** and **49** is observed which undergoes quite small thermally induced Stokes shifts ( $\Delta E_s < 100 \text{ cm}^{-1}$ ). This is attributed to population of an energetically accessible  $^3\pi\pi^*$  excited state localised on the acetylide, a state made accessible as a consequence of the introduction of highly conjugated alkynyl co-ligands. This phosphorescent  $^3\pi\pi^*(\text{C}\equiv\text{CAr})$  excited state is lower in energy than the triplet metal-perturbed L'LCT excited state described for complexes **45**, **46** and **48**.

## 4.8 Future work

### 4.8.1 [Pt(N^N)( $\sigma$ -acetylide)<sub>2</sub>] complexes: Diimine variation

The weak emission intensity of polyaromatic bipyridine **4** ( $\Phi_{em} < 0.001$ ) was a contributing factor to the corresponding relatively poor quantum yields ( $\Phi_{em}$  0.002-0.077) recorded for the series of complexes, [Pt(**4**)(C $\equiv$ CR)<sub>2</sub>], detailed in Chapter 4 (in argon-degassed CH<sub>2</sub>Cl<sub>2</sub> solution at room temperature). In this series of complexes, the diimine ligand was held constant while the electronic demand or aromaticity of the  $\sigma$ -acetylide co-ligand was varied. Incorporation of a diimine ligand with greater luminescence intensity would be expected to improve the emission quantum yields of corresponding complexes.

With this in mind, the preparation of a new series of Pt(II) diimine complexes is proposed (Figure 4.38), incorporating the highly emissive aryl-acetylene bipyridine ligands, 6-(4-*tert*-butyl-phenylethynyl)-2,2'-bipyridine (**1**,  $\Phi_{em}$  0.398) or 6-(4-trifluoromethyl-phenylethynyl)-2,2'-bipyridine (**2**,  $\Phi_{em}$  0.110), whose photoluminescence properties were discussed in Chapter 2. In order to probe the trend of increasing quantum yield with electron donating substituents, a Pt(II) coordination complex of the novel ligand 6-(4-methoxy-phenylethynyl)-2,2'-bipyridine will be synthesised (Figure 4.38, (a-iii)).

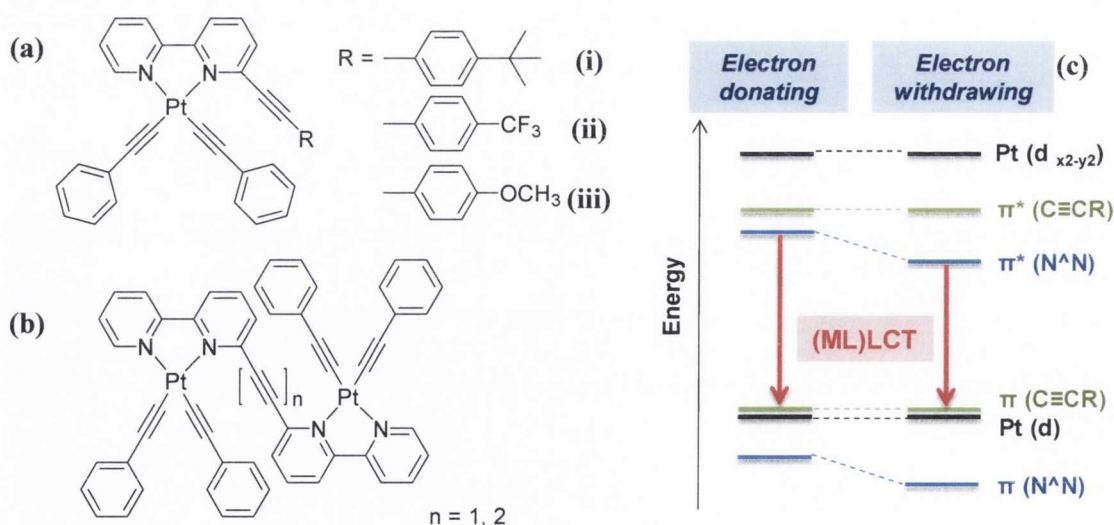


Figure 4.38: Structural variation of the bipyridyl ligand in [Pt(N^N)(C $\equiv$ CPh)<sub>2</sub>] complexes (a, b), and qualitative molecular orbital diagram illustrating the effect of these changes on the emission profile (c).

In a similar vein to the original work by Eisenberg and co-workers (Figure 4.3), a series of complexes  $[\text{Pt}(\text{N}^{\wedge}\text{N})(\text{C}\equiv\text{C}-\text{Ph})_2]$ , will be prepared in which the bipyridyl ligand substituent is varied as the acetylide ligand is held constant (Figure 4.38, (a)).<sup>220</sup> It is expected that an electron-withdrawing substituent will induce a bathochromic shift in emission maximum as the LUMO,  $\pi^*(\text{N}^{\wedge}\text{N})$ , is lowered in energy. Increasing the  $\pi$ -electronic conjugation within the system by connecting two bipyridine units *via* either one or two acetylene linkers will also be investigated (Figure 4.38, (b)). It is hoped that these two complexes may exhibit significantly different optical properties, potentially switching from emission derived from a  $^3(\text{ML})\text{LCT}$  excited state ( $^3\text{L}'\text{LCT}/^3\text{MLCT}$ ) to metal-perturbed ligand-centred  $^3\pi\pi^*(\text{N}^{\wedge}\text{N})$  luminescence, or displaying a mixture of both. The second coordinated Pt(II) centre may introduce an additional complexity to the manifold of excited states *via* Pt(d)-Pt(d) interaction along the  $\pi$ -conjugated network.

#### 4.8.2 Extension of the bipyridyl polyaromatic substituent

Building on the synthesis of bipyridyl and acetylene functionalised polyphenylene ligands described in Chapter 1, insertion of an acetylene link between the 2,2'-bipyridine and the hexaphenylbenzene molecular scaffold would be expected to enhance  $\pi$ -electronic communication, and consequently the optical properties, of the corresponding compound. This has been shown for a 2,2':6',2''-terpyridine-functionalised HBC platform, in which insertion of an acetylene between the terpy and the polyaromatic core allows more efficient energy transfer between the two components.<sup>74</sup>

The synthesis of the ethynyl-bipyridyl polyphenylenes described in Figure 4.39 will be undertaken *via* Sonogashira Pd(0) cross-coupling reactions between 6-bromo-2,2'-bipyridine (**10**) and ethynyl-hexaphenylbenzene (**6**), ethynyl-HBC (**7**) or *para*-diethynyl-hexaphenylbenzene (**8**) to yield molecules (**a**), (**b**) and (**c**) respectively. It is anticipated that these novel compounds will combine the desirable structural and electronic properties of their individual components - bipyridine, acetylene and oligophenylene. Their corresponding metal complexes should give rise to a variety of metallo-supramolecular nanostructures of defined geometry and porosity and with a rigid, shape-persistent framework.

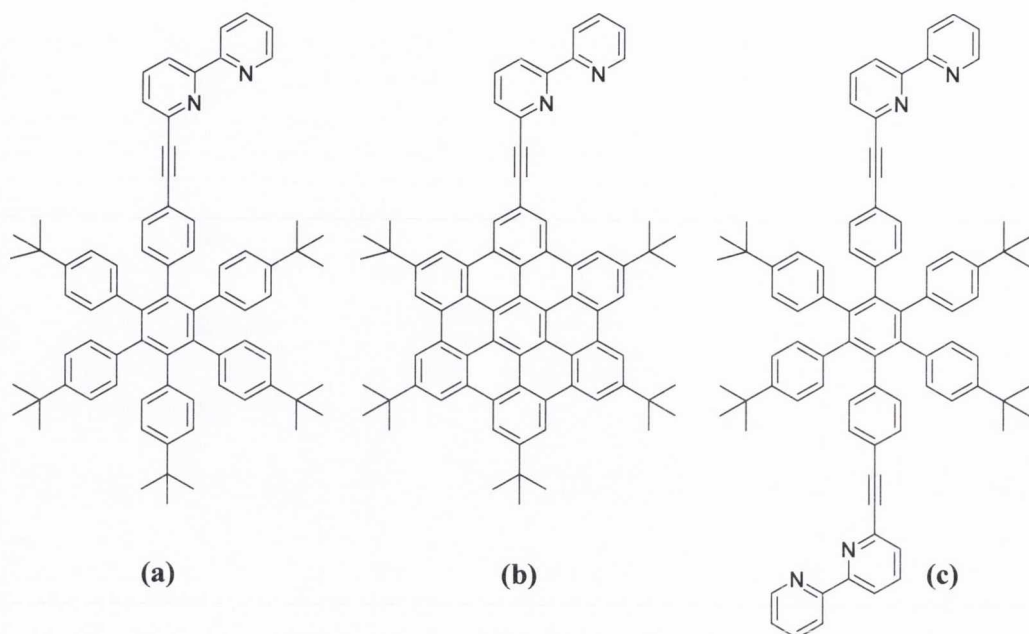


Figure 4.39: Ethynyl-bipyridine functionalised hexaphenylbenzenes (a, c) and HBC (b).

#### 4.8.3 *Cis* and *Trans* Pt(II)-acetylide HBC complexes

In highly  $\pi$ -conjugated molecules, a reduction in the excited state lifetime of the triplet state has been reported as a result of aggregation, an effect that would have been anticipated for HBC complexes *cis*-[Pt(HBC)<sub>2</sub>(dppe)] (41) and *trans*-[Pt(HBC)<sub>2</sub>(PPh<sub>3</sub>)<sub>2</sub>] (40) discussed in Chapter 3.<sup>173</sup> However, no aggregation was observed for these complexes under photophysical examination or *via* NMR spectroscopic studies. It is suggested that the *tert*-butyl substituents on the HBC suppresses such stacking effects.<sup>5</sup>

In order to counteract this, the preparation of analogous *cis* and *trans* acetylide-HBC complexes substituted along the periphery of the graphene core with long alkyl chains (n-C<sub>12</sub>H<sub>25</sub>) will be undertaken (Figure 4.40). It is anticipated that the graphene discs will then be able to approach in solution and undergo self-association into columnar stacks with the aliphatic moieties filling the inter-columnar space.<sup>12</sup> In this way, a more thorough and systematic investigation of the effect of aggregation on the triplet excited state of these super-aromatic systems may be achieved. Flexible long-chained HBC molecules and Pt-acetylide oligomeric systems have separately found application as liquid crystalline materials and it is hoped that the combination of both will produce systems with valuable and enhanced self-aggregation characteristics.



Additionally, the synthesis of a homoleptic tetra-alkynyl Pt(II) system with a long-chain HBC as  $\sigma$ -acetylide will be undertaken (Figure 4.40, (d)). This complex is not expected to undergo  $\pi$ -stacking of the aromatic platforms in solution as the four attached bulky HBCs will be unable to achieve simultaneous co-planarity. However, the giant organometallic molecule would be expected to possess fascinating optical properties as the final member of the series of super-aromatic complexes, in which  $\pi$ -electronic communication may be extended, *via* the rigid acetylene spacer unit, across the entire molecule.

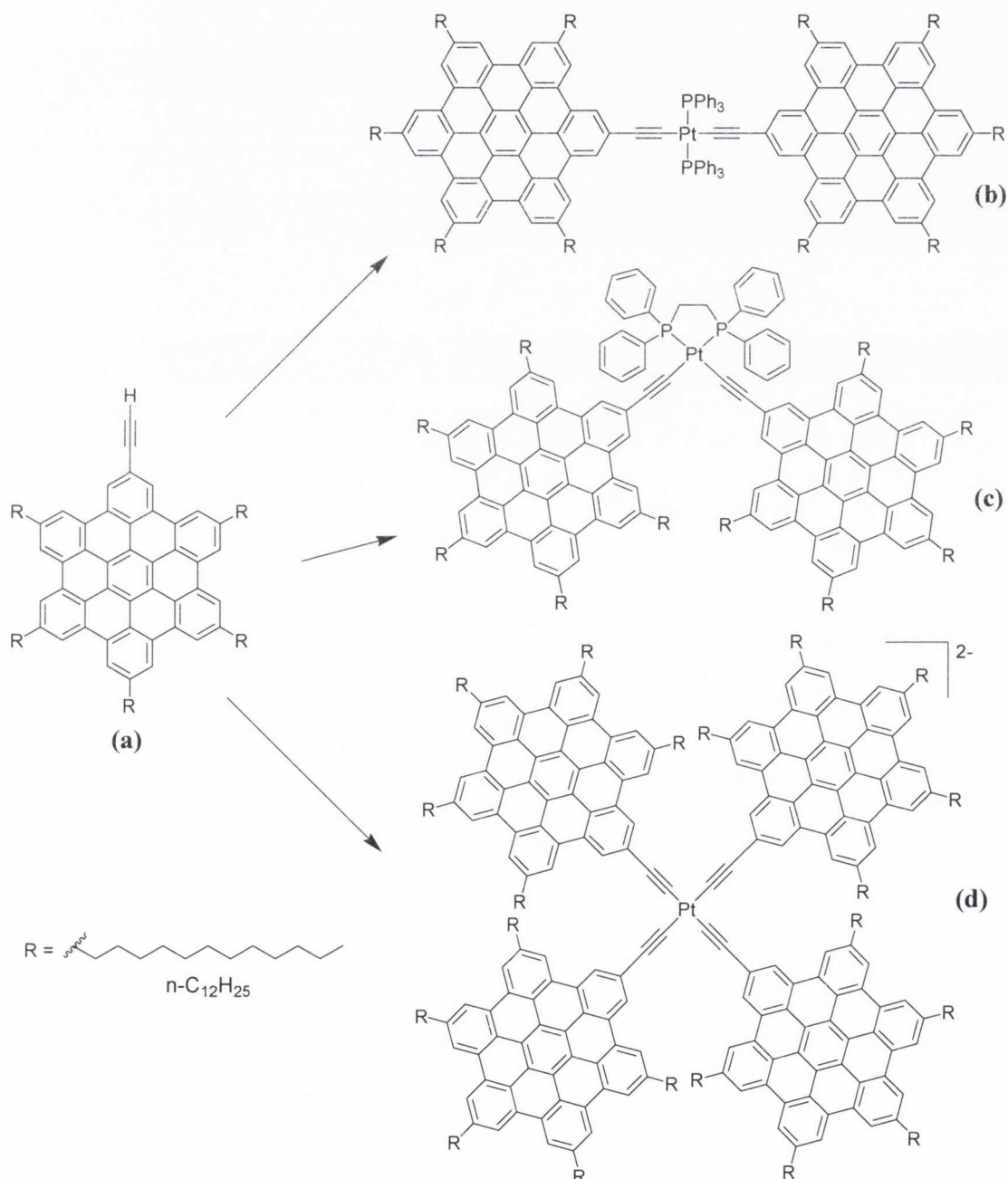


Figure 4.40: *Cis*-[Pt(HBC)<sub>2</sub>(dppe)] (b), *Trans*-[Pt(HBC)<sub>2</sub>(PPh<sub>3</sub>)<sub>2</sub>] (b) and homoleptic tetra-alkynyl [Pt(HBC)<sub>4</sub>]<sup>2-</sup> complexes (d) of long-chain ethynyl-HBC derivative (a, HBC).



**Chapter 5**  
**Experimental**



## 5.1 General Methods

Unless otherwise stated, all reactions were carried out under an inert atmosphere of either nitrogen or argon using standard Schlenk and vacuum line techniques. Solvents were dried using appropriate drying agents and distilled under a nitrogen atmosphere; diisopropylamine and dichloromethane distilled over  $\text{CaH}_2$  and THF and toluene over sodium wire/benzophenone. Flash chromatography was performed using silica gel (Aldrich) as the stationary phase. Starting materials ethynyltrimethylsilane,  $\text{CuI}$ ,  $\text{Pd}(\text{PPh}_3)_4$ , 2,2'-bipyridine,  $\text{PPh}_3$ , 1,2-bis(diphenylphosphino)ethane, diphenylacetylene (**26**) and 1,3-diphenylacetone (**23**) (Sigma-Aldrich) and 1-ethynyl pyrene (Alfa Aesar) and standard solvents were used without further purification.  $\text{RuCl}_3 \cdot x\text{H}_2\text{O}$  and  $\text{K}_2\text{PtCl}_4$  were purchased from Alfa Aesar. The known compounds 1,4-dimethylpiperazine-2,3-dione (DMPD),<sup>72</sup> 6-bromo-2,2'-bipyridine (**10**),<sup>65</sup> bis(4-*tert*-butylphenyl)acetylene (**22**),<sup>10</sup> 4-iodo-4'-*tert*-butylphenylacetylene (**17**),<sup>74</sup> *cis*- $\text{PdCl}_2(\text{PPh}_3)_3$ ,<sup>263</sup> *cis*- $\text{PtCl}_2(\text{PPh}_3)_2$ <sup>182</sup>, *cis*- $\text{Pt}(\text{dppe})\text{Cl}_2$ <sup>183</sup>, *cis*- $\text{PtCl}_2(\text{DMSO})_2$ ,<sup>264</sup> and *cis*- $\text{Ru}(\text{bpy})_2\text{Cl}_2 \cdot 2\text{H}_2\text{O}$  (**37**)<sup>108</sup> were synthesised according to literature procedures.

NMR spectra were recorded in  $\text{CDCl}_3$ ,  $\text{CD}_3\text{CN}$  or  $\text{C}_2\text{D}_2\text{Cl}_4$  on: (i) Bruker Avance DPX-400 MHz spectrometer (operating at 400.13 MHz for  $^1\text{H}$ , 100.6 MHz for  $^{13}\text{C}$ ); (ii) Bruker AV-600 MHz spectrometer (600.1 MHz for  $^1\text{H}$ , 150.6 MHz for  $^{13}\text{C}$ ); (iii) Bruker AV-400 MHz spectrometer (162.0 MHz for  $^{31}\text{P}$ , 376.5 MHz for  $^{19}\text{F}$ ).  $^1\text{H}$  and  $^{13}\text{C}$  NMR spectra were referenced relative to TMS ( $\delta$  0.00 ppm),  $^{31}\text{P}$  NMR spectra relative to  $\text{H}_3\text{PO}_4$  and  $^{19}\text{F}$  spectra relative to  $\text{CFCl}_3$  as an external standard.  $^{13}\text{C}$  and  $^{31}\text{P}$  NMR spectra were proton decoupled. Chemical shifts ( $\delta$ ) are reported in ppm and coupling constants ( $J$ ) in Hertz.  $^{13}\text{C}$  NMR chemical shifts are quoted to two decimal places due to the complex, overlapping nature of signals in the spectra. For the NMR characterisation of the complexes, *i*, *o*, *m* and *p* refer to the *ipso*, *ortho*, *meta* and *para* carbons on the indicated phenyl ring, *br* a broad signal, *pt* a *pseudo*-triplet and *pd* a *pseudo*-doublet respectively. IR spectra (reported in  $\text{cm}^{-1}$ ) were made as neat samples and were recorded on a Perkin-Elmer Spectrum-One FT-IR spectrometer equipped with a Universal-ATR sampling accessory. Electrospray mass spectra were recorded on a Micromass-LCT spectrometer. MALDI-TOF mass spectra were recorded on a Waters MALDI-QTOF Premier spectrometer using an  $\alpha$ -cyano-4-hydroxy cinnamic acid matrix. Accurate mass spectra were referenced against leucine enkephalin ( $555.6 \text{ g mol}^{-1}$ ) or  $[\text{Glu}^1]\text{-Fibrinopeptide B}$  ( $1570.6 \text{ g mol}^{-1}$ ) and reported to

within 5 ppm. Elemental analyses were performed in the Microanalytical Laboratory, University College Dublin.

**Electrochemical Measurements.** Cyclic voltammetry was performed using a CH Instruments Electrochemical Analyser Model 600B. Cyclic voltammograms were measured on 1 mM solutions of ligands and complexes in  $\text{CH}_2\text{Cl}_2$  or  $\text{CH}_3\text{CN}$  using tetra-n-butylammonium hexafluorophosphate ( $\text{TBAPF}_6$ , 0.1 M) as supporting electrolyte. A standard three electrode cell was employed with a glassy carbon working electrode, a Pt wire counter electrode and a reference electrode (SCE or an Ag/AgCl (sat. KCl)). Potentials are quoted versus the ferrocene-ferrocenium couple (0.0 V) and all potentials were referenced to internal ferrocene added at the end of each experiment. Solutions were degassed for several minutes by nitrogen bubbling before the experiments were performed and a flow of nitrogen was maintained over the solution for the duration of the experiment.

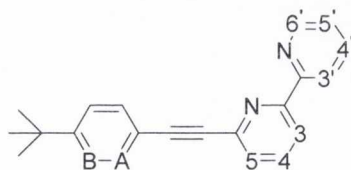
**Photophysical Measurements.** UV-Visible absorption spectra were recorded as optically dilute solutions ( $10^{-4} - 5 \times 10^{-7}$  M) in  $1 \times 1 \text{ cm}^2$  quartz cuvettes on a Shimadzu UV-2450 spectrophotometer. Corrected steady-state solution ( $10^{-3}$ - $10^{-5}$  M) and solid-state emission spectra at 298K and 77K were recorded on a Horiba-Jobin-Yvon Fluorolog 3-22 spectrometer with double grating emission and excitation monochromators. A Jobin Yvon FluoroHub single photon counting controller fitted with a 295 nm or a 370 nm Jobin Yvon NanoLED was used to measure lifetimes which were determined from the observed decays using DataStation v2.4. Emission quantum yields of the solutions were measured by the Demas and Crosby<sup>135</sup> method and were measured relative to quinine sulfate in 0.5M  $\text{H}_2\text{SO}_4$  ( $\Phi_{\text{em}} = 0.546$ ),<sup>133</sup> 4',6-diamidino-2-phenylindole dihydrochloride (DAPI) in water ( $\Phi_{\text{em}} = 0.043$ )<sup>207</sup> or  $[\text{Ru}(\text{bpy})_3]^{2+}$  in water ( $\Phi_{\text{em}} = 0.042$ ).<sup>139</sup> Corrections were made for the difference in refractive index of the sample and reference solutions.<sup>137</sup>

**X-Ray Crystallography.** Crystal and structural experimental data are summarised in Tables 1 and 2 in the Annex. Selected bond lengths and angles are given in the discussion. The remaining angles, distances, atom coordinates in addition to anisotropic displacement parameters and hydrogen atom coordinates are on the enclosed CD. The single-crystal analyses were performed by Dr. Tom McCabe and Dr. LongSheng Wang in Trinity College with a Bruker SMART APEX CCD diffractometer (compounds **33** and **35**) or a

Rigaku Saturn-724 CCD diffractometer (compounds **43** and **45**) at the temperatures given in tables. Data integration and reduction were carried out using Bruker Saint+ Version 6.45 software and corrected for absorption and polarization effects using SADABS Version 2.10 software. Space group determination, structure solution and refinement were obtained using Shelxtl\* ver. 6.14 software. \*Software Reference Manual, version 5.625, Bruker Analytical X-Ray Systems Inc., Madison, WI, 2001. Sheldrick, G. M. SHELXTL, An Integrated System for Data Collection, Processing, Structure Solution and Refinement, Bruker Analytical X-Ray Systems Inc., Madison, WI, 2001. The four structures converged to reasonable R factors. All the non-hydrogen atoms were refined anisotropically, and the hydrogen atoms were fixed from the residual electron density using appropriate HFIX commands. Intermolecular interactions were computed using the PLATON program. The crystal structure of **45** contains solvent accessible voids and the compound may contain additional solvent molecules.

## 5.2 Synthesis of Bipyridyl and Acetylene-based polyphenylene Ligands

### 6-(4-*tert*-butylphenylethynyl)-2,2'-bipyridine (**1**)

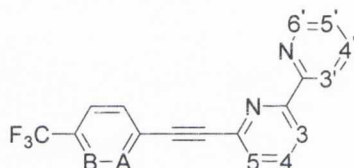


A solution of 6-bromo-2,2'-bipyridine (300.2 mg; 1.277 mmol) in still-dried THF:<sup>i</sup>Pr<sub>2</sub>NH (2:1 v/v, 20 mL:10 mL) was degassed twice. PdCl<sub>2</sub>(PPh<sub>3</sub>)<sub>2</sub> (57.4 mg; 6 mol%) and CuI (14.6 mg; 6 mol%) were added to the Schlenk flask and the mixture was degassed once more *via* freeze-pump-thaw. 4-*tert*-butylphenyl acetylene (254 μL; 1.405 mmol) was added *via* syringe over 5 minutes and the reaction mixture was left to stir for 18 hours at room temperature under nitrogen.

The volume of solvent was reduced *in vacuo* and the residue re-dissolved in CHCl<sub>3</sub> (~150 mL). This organic layer was washed with water (3x150 mL), dried over MgSO<sub>4</sub> and activated charcoal, filtered off and the solvent removed once again. The product was purified by column chromatography on silica using hexane:ethyl acetate (3:1 v/v) as eluent. The product was obtained as an off-white/yellow solid. (295 mg; 0.943 mmol; 74 %). **m.p.** 142-144 °C. <sup>1</sup>H NMR (CDCl<sub>3</sub>, 400.1 MHz): δ 8.69 (d, 1H, <sup>3</sup>J<sub>HH</sub> = 4.5 Hz, H<sup>6'</sup>), 8.50 (d, 1H, <sup>3</sup>J<sub>HH</sub> = 8.0 Hz, H<sup>3'</sup>), 8.35 (d, 1H, <sup>3</sup>J<sub>HH</sub> = 8.0 Hz, H<sup>3</sup>), 7.81 (m, 2H, H<sup>4</sup>, H<sup>4'</sup>),

7.56 (m, 3H, H<sub>A</sub>, H<sup>5</sup>), 7.40 (d, 2H, <sup>3</sup>J<sub>HH</sub> = 8.5 Hz, H<sub>B</sub>), 7.33 (m, 1H, H<sup>5</sup>), 1.34 (s, 9H, C(CH<sub>3</sub>)<sub>3</sub>). <sup>13</sup>C {<sup>1</sup>H} NMR (CDCl<sub>3</sub>, 100.6 MHz): δ 156.57 (C<sub>quat</sub>), 155.60 (C<sub>quat</sub>), 152.34 (C<sub>quat</sub>), 149.14 (CH, C<sup>6</sup>), 143.10 (C<sub>quat</sub>), 137.06 (CH, C<sup>4</sup> or C<sup>4'</sup>), 136.97 (CH, C<sup>4</sup> or C<sup>4'</sup>), 131.87 (2C, CH, C<sub>A</sub>), 127.35 (CH, C<sup>5</sup>), 125.44 (2C, CH, C<sub>B</sub>), 123.99 (CH, C<sup>5</sup>), 121.62 (CH, C<sup>3</sup>), 120.18 (CH, C<sup>3</sup>), 119.30 (C<sub>quat</sub>), 89.34 (C<sub>quat</sub>, C≡C), 88.42 (C<sub>quat</sub>, C≡C), 34.91 (C<sub>quat</sub>, C(CH<sub>3</sub>)<sub>3</sub>), 31.18 (9C, C(CH<sub>3</sub>)<sub>3</sub>). **MS** (*m/z*-ES-MS, THF): Found: 313.1717 [M+H]<sup>+</sup>, calculated for [C<sub>22</sub>H<sub>21</sub>N<sub>2</sub>]<sup>+</sup>: 313.1705. **Anal. Calcd.** For C<sub>22</sub>H<sub>20</sub>N<sub>2</sub>·2(H<sub>2</sub>O): C, 82.21; H, 6.59; N, 8.72. Found: C, 82.58; H, 6.33; N, 8.44. **IR** ν (cm<sup>-1</sup>): 3055 (s), 2963 (s), 2931 (m), 2910 (m), 2866 (m), 2205 (m, C≡C), 1590 (w), 1576 (m), 1558 (s), 1517 (m), 1506 (m), 1468 (m), 1450 (s), 1429 (s), 1408 (m), 1384 (m), 1257 (s), 1165 (m), 1111 (m), 987 (m), 827 (s), 779 (s), 744 (m), 692 (m).

#### 6-(4-trifluoromethyl-phenylethynyl)-2,2'-bipyridine (2)



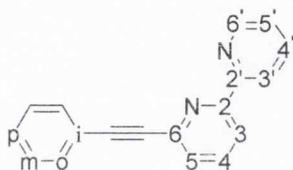
A solution of 6-bromo-2,2'-bipyridine (251.9 mg; 1.072 mmol) in still-dried THF:<sup>i</sup>Pr<sub>2</sub>NH (3:1 v/v, 24 mL:8 mL) was degassed twice. PdCl<sub>2</sub>(PPh<sub>3</sub>)<sub>2</sub> (37.1 mg; 5 mol%) and CuI (9.6 mg; 5 mol%) were added to the Schlenk flask and the mixture was degassed once more *via* freeze-pump-thaw. The reaction mixture was left to stir for 18 hours at room temperature under nitrogen. At this point 4-ethynyl- $\alpha,\alpha,\alpha$ -trifluorotoluene (190.0  $\mu$ L; 1.169 mmol) was added *via* syringe to the flask. This was left to stir overnight under argon at room temperature.

The volume of solvent was reduced *in vacuo* and the residue re-dissolved in CH<sub>2</sub>Cl<sub>2</sub> (~150 mL). This organic layer was washed with water (3x150 mL), dried over MgSO<sub>4</sub> and filtered off and the solvent removed once again to dryness. The product was purified by column chromatography on silica using hexane:ethyl acetate (2:1 v/v) as eluent. The product was obtained as a yellow solid. (326 mg; 1.004 mmol; 94 %). **m.p.** 106-108 °C. <sup>1</sup>H NMR (CDCl<sub>3</sub>, 400.1 MHz): δ 8.69 (d, 1H, <sup>3</sup>J<sub>HH</sub> = 4.0 Hz, H<sup>6</sup>), 8.48 (d, 1H, <sup>3</sup>J<sub>HH</sub> = 8.0 Hz, H<sup>3</sup>), 8.40 (d, 1H, <sup>3</sup>J<sub>HH</sub> = 8.0 Hz, H<sup>3</sup>), 7.84 (m, 2H, H<sup>4</sup>, H<sup>4'</sup>), 7.73 (d, 2H, <sup>3</sup>J<sub>HH</sub> = 8.0 Hz, H<sub>A</sub>), 7.64 (d, 2H, <sup>3</sup>J<sub>HH</sub> = 8.0 Hz, H<sub>B</sub>), 7.57 (d, 1H, <sup>3</sup>J<sub>HH</sub> = 7.5 Hz, H<sup>5</sup>), 7.33 (m, 1H, H<sup>5</sup>). <sup>13</sup>C {<sup>1</sup>H} NMR (CDCl<sub>3</sub>, 100.6 MHz): δ 156.77 (C<sub>quat</sub>), 155.32 (C<sub>quat</sub>), 149.18 (CH, C<sup>6</sup>), 142.18 (C<sub>quat</sub>), 137.17 (CH, C<sup>4</sup>), 136.96 (CH, C<sup>4'</sup>), 132.28 (2C, CH, C<sub>A</sub>), 130.61 (q, C<sub>quat</sub>,



$^2J_{CF} = 33$  Hz, C-CF<sub>3</sub>), 127.45 (CH, C<sup>5</sup>), 126.21 (C<sub>quat</sub>), 125.31 (q, 2C, CH,  $^3J_{CF} = 4$  Hz, C<sub>B</sub>), 124.08 (CH, C<sup>5</sup>), 123.87 (q, C<sub>quat</sub>,  $^1J_{CF} = 271$  Hz, -CF<sub>3</sub>), 121.50 (CH, C<sup>3</sup>), 120.81 (CH, C<sup>3</sup>), 90.97 (C<sub>quat</sub>, C≡C), 87.15 (C<sub>quat</sub>, C≡C).  **$^{19}\text{F}$  NMR** (CDCl<sub>3</sub>, 376.5 MHz):  $\delta$  -63.3 (CF<sub>3</sub>). **MS** (*m/z*-ES-MS, THF): Found: 325.0952 [M+H]<sup>+</sup>, calculated for [C<sub>19</sub>H<sub>12</sub>N<sub>2</sub>F<sub>3</sub>]<sup>+</sup>: 325.0953. **Anal. Calcd.** For C<sub>19</sub>H<sub>11</sub>F<sub>3</sub>N<sub>2</sub>·¼(H<sub>2</sub>O): C, 69.40; H, 3.53; N, 8.52. Found: C, 69.31; H, 3.25; N, 8.31. **IR**  $\nu$  (cm<sup>-1</sup>): 3059 (s), 3024 (m), 2926 (m), 2198 (w, C≡C), 1922 (w), 1611 (m), 1578 (m), 1559 (m), 1456 (m), 1429 (m), 1320 (s, br), 1159 (s), 1115 (s), 1102 (s), 1063 (s), 1010 (m), 989 (m), 842 (s), 826 (m), 777 (s), 745 (m), 737 (m), 695(m).

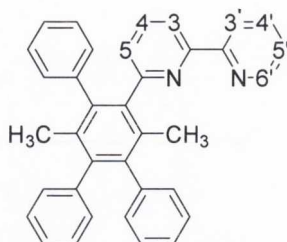
### 6-phenylethynyl-2,2'-bipyridine (11)



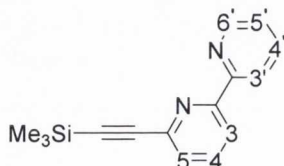
6-bromo-2,2'-bipyridine (301.0 mg; 1.280 mmol) was dissolved in still-dried THF:Pr<sub>2</sub>NH (3:1 v/v, 20 mL:10 mL). The solution was degassed twice *via* freeze-pump-thaw. PdCl<sub>2</sub>(PPh<sub>3</sub>)<sub>2</sub> (52.4 mg; 6 mol%) and CuI (15.0 mg; 6 mol%) were added to the Schlenk flask and the reaction mixture was degassed once more. At this point phenylacetylene (150.0  $\mu$ L; 1.408 mmol) was added *via* syringe to the flask. The reaction mixture was left to stir at room temperature overnight under nitrogen.

The solvents were removed *in vacuo* and the residue redissolved in CH<sub>2</sub>Cl<sub>2</sub> (~100 mL). This was washed with water (3x100 mL) and the organic layer dried over MgSO<sub>4</sub>, filtered and the solvent removed once again. The product was purified by column chromatography on silica using hexane:ethyl acetate (3:1 v/v) as eluent. The product was obtained as a yellow/brown oil. (255 mg; 0.995 mmol; 78 %).  **$^1\text{H}$  NMR** (CDCl<sub>3</sub>, 600.1 MHz):  $\delta$  8.68 (d, 1H,  $^3J_{\text{HH}} = 4.1$  Hz, H<sup>6</sup>), 8.50 (d, 1H,  $^3J_{\text{HH}} = 7.9$  Hz, H<sup>3</sup>), 8.37 (d, 1H,  $^3J_{\text{HH}} = 7.9$  Hz, H<sup>3</sup>), 7.81 (m, 2H, H<sup>4</sup>, H<sup>4'</sup>), 7.64 (m, 2H, H<sub>o</sub>), 7.56 (d, 1H,  $^3J_{\text{HH}} = 7.5$  Hz, H<sup>5</sup>), 7.38 (m, 3H, H<sub>m</sub>, H<sub>p</sub>), 7.32 (m, 1H, H<sup>5</sup>).  **$^{13}\text{C}$  { $^1\text{H}$ } NMR** (CDCl<sub>3</sub>, 150.9 MHz):  $\delta$  156.60 (C<sub>quat</sub>, C<sup>2</sup>), 155.53 (C<sub>quat</sub>, C<sup>2</sup>), 149.11 (CH, C<sup>6</sup>), 142.86 (C<sub>quat</sub>, C<sup>6</sup>), 137.05 (CH, C<sup>4</sup>), 136.92 (CH, C<sup>4'</sup>), 132.08 (CH, C<sub>o</sub>), 128.94 (CH, C<sub>p</sub>), 128.37 (CH, C<sub>m</sub>), 127.30 (CH, C<sup>5</sup>), 123.97 (CH, C<sup>5</sup>), 122.37 (C<sub>quat</sub>, C<sub>i</sub>), 121.56 (CH, C<sup>3</sup>), 120.32 (CH, C<sup>3</sup>), 88.94 (2C, C<sub>quat</sub>, C≡C). **MS** (*m/z*-ES-MS, THF): Found: 257.1077 [M+H]<sup>+</sup>, calculated for [C<sub>18</sub>H<sub>13</sub>N<sub>2</sub>]<sup>+</sup>: 257.1079.

## 6-(3,6-dimethyl-2,4,5-triphenylbenz-1-ene)-2,2'-bipyridine (3)

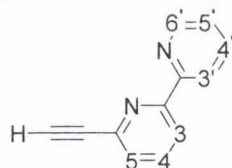


6-phenylethynyl-2,2'-bipyridine (**11**) (167.8 mg; 0.6547 mmol) and the 2,5-dimethyl-3,4-diphenylcyclopentadienone dimer (162.1 mg; 0.3118 mmol) were heated in a benzophenone melt (~1.0 g; ~5.5 mmol) for 3 hours at 150-180 °C, followed by a further 6 hours at 280-300 °C. The compound was purified by column chromatography on silica eluting firstly with CH<sub>2</sub>Cl<sub>2</sub> (to remove benzophenone) and then increasing polarity to CH<sub>2</sub>Cl<sub>2</sub>:MeOH (5:1 v/v). The pure product was obtained as a pale brown solid following further column chromatography using a silica plug and hexane:ethyl acetate (2:1 v/v) as eluent. (220 mg; 0.451 mmol; 69 %). **m.p.** 272-274 °C. **<sup>1</sup>H NMR** (CDCl<sub>3</sub>, 400.1 MHz): δ 8.63 (d, 1H, <sup>3</sup>J<sub>HH</sub> = 4.9 Hz, H<sup>6'</sup>), 8.29 (d, 1H, <sup>3</sup>J<sub>HH</sub> = 8.8 Hz, H<sup>3'</sup>), 8.07 (d, 1H, <sup>3</sup>J<sub>HH</sub> = 7.8 Hz, H<sup>3</sup>), 7.77 (ddd, 1H, <sup>3</sup>J<sub>HH</sub>, <sup>4</sup>J<sub>HH</sub> = 7.8, 2.0 Hz, H<sup>4'</sup>), 7.57 (dd, 1H, <sup>3</sup>J<sub>HH</sub> = 7.8 Hz, H<sup>4</sup>), 7.28 (m, 1H, H<sup>5'</sup>), 6.98-7.18 (m, 16H, H<sup>5</sup>, H<sub>phenyl</sub>), 1.90 (s, 3H, CH<sub>3</sub>), 1.85 (s, 3H, CH<sub>3</sub>). **<sup>13</sup>C {<sup>1</sup>H} NMR** (CDCl<sub>3</sub>, 100.6 MHz): δ 159.53 (C<sub>quat</sub>), 156.57 (C<sub>quat</sub>), 155.10 (C<sub>quat</sub>), 148.95 (CH, C<sup>6'</sup>), 141.85 (C<sub>quat</sub>), 141.38 (C<sub>quat</sub>), 141.18 (C<sub>quat</sub>), 140.96 (C<sub>quat</sub>), 140.52 (C<sub>quat</sub>), 139.82 (C<sub>quat</sub>), 136.73 (CH, C<sup>4'</sup>), 136.20 (CH, C<sup>4</sup>), 131.71 (C<sub>quat</sub>), 131.47 (C<sub>quat</sub>), 130.57 (CH), 130.33 (CH), 130.15 (CH), 129.90 (CH), 127.64 (CH), 127.40 (CH), 126.06 (CH), 125.88 (CH), 125.72 (CH, C<sup>5</sup>), 123.47 (CH, C<sup>5'</sup>), 121.66 (CH, C<sup>3'</sup>), 118.31 (CH, C<sup>3</sup>), 19.45 (1C, CH<sub>3</sub>), 19.14 (1C, CH<sub>3</sub>). **MS** (*m/z*-ES-MS, THF): Found: 489.2321 [M+H]<sup>+</sup>, calculated for [C<sub>36</sub>H<sub>29</sub>N<sub>2</sub>]<sup>+</sup>: 489.2331. **Anal. Calcd.** For C<sub>36</sub>H<sub>28</sub>N<sub>2</sub>: C, 88.49; H, 5.78; N, 5.73. Found: C, 88.80; H, 5.49; N, 5.61. **IR** ν (cm<sup>-1</sup>): 3055 (m), 3024 (m), 2922 (w), 1741 (w), 1601 (m), 1580 (m), 1566 (s), 1496 (m), 1475 (m, br), 1443 (m), 1428 (s), 1411 (s), 1381 (w, br), 1254 (m), 1223 (m, br), 1150 (w), 1095 (m), 1069 (m), 1026 (m), 987 (s), 790 (m), 779 (s), 755 (s), 745 (s), 695 (s), 668 (m).

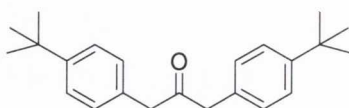
6-(trimethylsilyl)ethynyl-2,2'-bipyridine (13a)<sup>70</sup>

A solution 6-bromo-2,2'-bipyridine (749.1 mg; 3.187 mmol) in a mixture of still-dried THF:<sup>1</sup>Pr<sub>2</sub>NH (~3:1eq., 60 mL:20 mL) was degassed twice *via* freeze-pump-thaw. PdCl<sub>2</sub>(PPh<sub>3</sub>)<sub>2</sub> (135.4 mg; 6 mol%) and CuI (37.8 mg; 6 mol%) were added to the Schlenk flask and the reaction mixture degassed again. Trimethylsilylacetylene (0.8 mL; 4.954 mmol) was added by syringe over a few minutes and the reaction mixture was left to stir overnight. After 18 hours, the solvent was removed and the residue redissolved in CH<sub>2</sub>Cl<sub>2</sub> (~150 mL). This was washed with water (3x150 mL). Activated charcoal was added to the organic layer to adsorb any palladium(0) waste. The solution was dried over MgSO<sub>4</sub>, filtered off and the solvent removed *in vacuo*. The product was purified by column chromatography on silica using hexane:ethyl acetate (3:1 v/v) as the eluent, affording a brown semi-solid. (699 mg; 2.77 mmol; 87 %). <sup>1</sup>H NMR (CDCl<sub>3</sub>, 400.1 MHz): δ 8.68 (d, 1H, <sup>3</sup>J<sub>HH</sub> = 4.5 Hz, H<sup>6'</sup>), 8.50 (d, 1H, <sup>3</sup>J<sub>HH</sub> = 8.0 Hz, H<sup>3'</sup>), 8.38 (d, 1H, <sup>3</sup>J<sub>HH</sub> = 7.5 Hz, H<sup>3</sup>), 7.81 (m, 2H, H<sup>4</sup>, H<sup>4'</sup>), 7.52 (d, 1H, <sup>3</sup>J<sub>HH</sub> = 7.5 Hz, H<sup>5</sup>), 7.34 (m, 1H, H<sup>5'</sup>), 0.32 (s, 9H, -Si(CH<sub>3</sub>)<sub>3</sub>).

### 6-ethynyl-2,2'-bipyridine (13)<sup>70</sup>

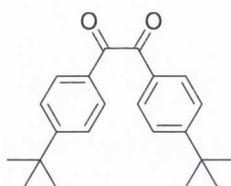


6-(trimethylsilyl)ethynyl-2,2'-bipyridine (698.5 mg; 2.771 mmol) was dissolved in a mixture of methanol and THF (1:1 v/v, 25 mL:25 mL). KF (804.9 mg; 13.853 mmol) was added and the reaction mixture was stirred under argon overnight. The solvent was removed and the residue redissolved in CH<sub>2</sub>Cl<sub>2</sub> (~150 mL). This was washed with water (3x150 mL) to remove both unreacted KF and the side-product Me<sub>3</sub>SiF. The organic layer was dried over MgSO<sub>4</sub>, filtered off and the solvent removed to yield the desired product as a semi-solid. (419 mg; 2.32 mmol; 84 %). <sup>1</sup>H NMR (CDCl<sub>3</sub>, 400.1 MHz): δ 8.70 (d, 1H, <sup>3</sup>J<sub>HH</sub> = 4.0 Hz, H<sup>6'</sup>), 8.50 (d, 1H, <sup>3</sup>J<sub>HH</sub> = 8.0 Hz, H<sup>3'</sup>), 8.43 (d, 1H, <sup>3</sup>J<sub>HH</sub> = 8.0 Hz, H<sup>3</sup>), 7.83 (m, 2H, H<sup>4</sup>, H<sup>4'</sup>), 7.54 (d, 1H, <sup>3</sup>J<sub>HH</sub> = 7.5 Hz, H<sup>5</sup>), 7.35 (m, 1H, H<sup>5'</sup>), 3.22 (s, 1H, -C≡CH). MS (*m/z*-ES-MS, THF): Found: 181.0771 [M+H]<sup>+</sup>, calculated for [C<sub>12</sub>H<sub>9</sub>N<sub>2</sub>]<sup>+</sup>: 181.0766.

**1,3-bis(4-*tert*-butylphenyl)propan-2-one (14)**<sup>71</sup>

Ca(OH)<sub>2</sub> (4.0310 g; 54.42 mmol) and (tBu)<sub>4</sub>NHSO<sub>4</sub> (2.3101 g; 6.803 mmol) were stirred under argon in CH<sub>2</sub>Cl<sub>2</sub>:water (60 mL:60 mL) with Ar bubbling through the solution. 4-*tert*-butyl-benzylbromide (5.00 mL; 27.21 mmol) was added dropwise into the solution. Fe(CO)<sub>5</sub> (1.8 mL; 13.61 mmol) was then added dropwise to the solution. This was stirred vigorously with Ar bubbling through over several hours and was left to stir under an Ar atmosphere overnight.

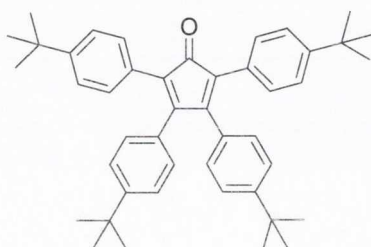
10% HCl solution (~100 mL) was added to the CH<sub>2</sub>Cl<sub>2</sub>:water solution and air was bubbled through the solution for 2 hours until a colour change from deep red to brown/orange was observed. The product was then extracted into CH<sub>2</sub>Cl<sub>2</sub>, washed with water (x2) and dried over MgSO<sub>4</sub>. The solvent was removed and the product purified by column chromatography on silica eluting with CH<sub>2</sub>Cl<sub>2</sub>:hexane (3:1 v/v). Recrystallisation from hexane yielded the product as a white powder. (2.96 g; 9.19 mmol; 68 %). <sup>1</sup>H NMR (CDCl<sub>3</sub>, 400.1 MHz): δ 7.34 (d, 4H, <sup>3</sup>J<sub>HH</sub> = 8.5 Hz, H<sub>phenyl</sub>), 7.10 (d, 4H, <sup>3</sup>J<sub>HH</sub> = 8.5 Hz, H<sub>phenyl</sub>), 3.70 (s, 4H, CH<sub>2</sub>), 1.32 (s, 18H, C(CH<sub>3</sub>)<sub>3</sub>). MS (*m/z*-ES-MS, THF): Found: 345.2209 [M+Na]<sup>+</sup>, calculated for [C<sub>23</sub>H<sub>30</sub>O<sub>2</sub>Na]<sup>+</sup>: 345.2194.

**1,2-bis-(4-*tert*-butylphenyl)ethane-1,2-dione (15)**<sup>72</sup>

A solution of 1-bromo-4-*tert*-butylbenzene (6.0 mL; 34.80 mmol) in THF (30 mL) was degassed three times and cooled to -78 °C for 30 minutes in an ethanol ice bath. N-butyl lithium (24 mL of a 1.6 M solution in hexanes; 37.8 mmol) was added directly to the Schlenk flask and the solution was stirred at -78 °C for 1 hour. A second flask containing DMPD (2.1515 g; 15.13 mmol) in THF (100 mL) was degassed three times, sonicated for ~20 minutes and cooled to -78 °C. The lithiated solution was transferred *via* cannula into this flask. The pale yellow solution was stirred at -78 °C for an hour and was then allowed to slowly warm to room temperature overnight.

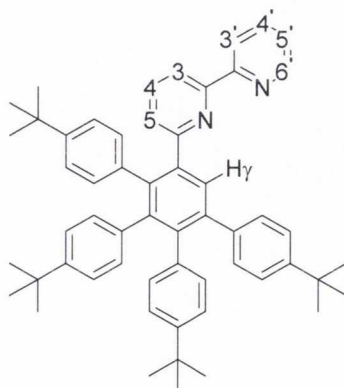
10% HCl solution (100 mL) was added to quench the reaction and the organic product was extracted into dichloromethane/chloroform. This was washed with water (x3), the organic layer separated out, dried over  $\text{MgSO}_4$  and the solvent removed. The product was obtained as a pale yellow crystalline solid after recrystallisation from hexane and filtration. (4.278 g; 13.28 mmol; 88 %).  $^1\text{H NMR}$  ( $\text{CDCl}_3$ , 400.1 MHz):  $\delta$  7.91 (d, 4H,  $^3J_{\text{HH}} = 8.5$  Hz,  $\text{H}_{\text{phenyl}}$ ), 7.51 (d, 4H,  $^3J_{\text{HH}} = 8.6$  Hz,  $\text{H}_{\text{phenyl}}$ ), 1.34 (s, 18H,  $\text{C}(\text{CH}_3)_3$ ). **MS** ( $m/z$ -ES-MS, THF): Found: 345.1836  $[\text{M}+\text{Na}]^+$ , calculated for  $[\text{C}_{22}\text{H}_{26}\text{O}_2\text{Na}]^+$ : 345.1831.

### 2,3,4,5-tetra-(4-*tert*-butylphenyl)cyclopenta-2,4-dienone (16)<sup>265</sup>

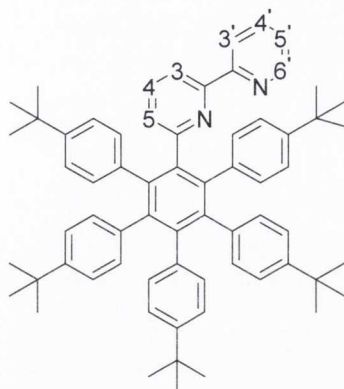


1,2-bis-(4-*tert*-butylphenyl)ethane-1,2-dione (200.8 mg; 0.623 mmol) and 1,3-bis(4-*tert*-butylphenyl)propan-2-one (201.0 mg; 0.623 mmol) were heated to reflux in ethanol (1.5 mL). KOH (18.0 mg; 0.321 mmol) was dissolved in ethanol (1.5 mL). The KOH solution was added in two portions to the flask. This was heated at reflux for a further hour and was then cooled in ice for an hour. The purple precipitate obtained was filtered off, washed with cold ethanol and dried thoroughly. (243 mg; 0.399 mmol; 64 %).  $^1\text{H NMR}$  (400.1 MHz,  $\text{CDCl}_3$ ):  $\delta$  7.19-7.26 (m, 8H,  $\text{H}_{\text{phenyl}}$ ), 7.14 (d, 4H,  $^3J_{\text{HH}} = 8.8$  Hz,  $\text{H}_{\text{phenyl}}$ ), 6.82 (d, 4H,  $^3J_{\text{HH}} = 8.8$  Hz,  $\text{H}_{\text{phenyl}}$ ), 1.29 (s, 18H,  $\text{C}(\text{CH}_3)_3$ ), 1.27 (s, 18H,  $\text{C}(\text{CH}_3)_3$ ). **MS** ( $m/z$ -ES-MS, Acetone): Found: 609.4092  $[\text{M}+\text{H}]^+$ , calculated for  $[\text{C}_{45}\text{H}_{53}\text{O}]^+$ : 609.4096.

### 1-(2,2'-bipyrid-6-yl)-2,3,4,5-tetra-(4-*tert*-butylphenyl) benzene (4)



6-ethynyl-2,2'-bipyridine (150.1 mg; 0.832 mmol) and 2,3,4,5-tetra-(4-*tert*-butylphenyl)cyclopenta-2,4-dienone (505.0 mg; 0.829 mmol) were heated in benzophenone (~1.0 g; 5.5 mmol) in a sand-bath at 150-200 °C under argon for 6 hours. The temperature was then increased to 280-300 °C and the reaction mixture heated for a further 18 hours under argon. The solid was purified by column chromatography on silica eluting firstly with CH<sub>2</sub>Cl<sub>2</sub>:hexane (4:1 v/v) to remove unreacted cyclopentadienone and benzophenone. The solvent system was then changed to CH<sub>2</sub>Cl<sub>2</sub>:ethyl acetate to elute the product. Removal of solvent *in vacuo* furnished the desired product as a pale brown crystalline solid. (518 mg; 0.680 mmol; 84 %). **m.p.** 237-240 °C. **<sup>1</sup>H NMR** (CDCl<sub>3</sub>, 400.1 MHz): δ 8.60 (d, 1H, <sup>3</sup>J<sub>HH</sub> = 4.9 Hz, H<sup>6</sup>), 8.14 (d, 1H, <sup>3</sup>J<sub>HH</sub> = 6.9 Hz, H<sup>3</sup>), 8.05 (d, 1H, <sup>3</sup>J<sub>HH</sub> = 7.8 Hz, H<sup>3'</sup>), 7.87 (s, 1H, H<sub>γ</sub>), 7.65 (dd, 1H, <sup>3</sup>J<sub>HH</sub> = 7.8 Hz, H<sup>4</sup>), 7.56 (dd, 1H, <sup>3</sup>J<sub>HH</sub> = 7.8 Hz, H<sup>4</sup>), 7.22 (m, 1H, H<sup>5</sup>), 7.08-7.17 (m, 5H, H<sup>5</sup>, H<sub>phenyl</sub>), 6.91 (m, 4H, H<sub>phenyl</sub>), 6.83 (d, 2H, <sup>3</sup>J<sub>HH</sub> = 8.8 Hz, H<sub>phenyl</sub>), 6.80 (d, 2H, <sup>3</sup>J<sub>HH</sub> = 7.8 Hz, H<sub>phenyl</sub>), 6.70 (d, 2H, <sup>3</sup>J<sub>HH</sub> = 8.8 Hz, H<sub>phenyl</sub>), 6.64 (d, 2H, <sup>3</sup>J<sub>HH</sub> = 8.8 Hz, H<sub>phenyl</sub>), 1.26 (s, 9H, C(CH<sub>3</sub>)<sub>3</sub>), 1.15 (s, 9H, C(CH<sub>3</sub>)<sub>3</sub>), 1.11 (s, 9H, C(CH<sub>3</sub>)<sub>3</sub>), 1.10 (s, 9H, C(CH<sub>3</sub>)<sub>3</sub>). **<sup>13</sup>C {<sup>1</sup>H} NMR** (CDCl<sub>3</sub>, 100.6 MHz): δ 158.65 (C<sub>quat</sub>), 156.00 (C<sub>quat</sub>), 154.73 (C<sub>quat</sub>), 148.35 (C<sub>quat</sub>), 148.30 (CH, C<sup>6</sup>), 147.75 (C<sub>quat</sub>), 147.65 (C<sub>quat</sub>), 147.28 (C<sub>quat</sub>), 141.92 (C<sub>quat</sub>), 140.45 (C<sub>quat</sub>), 140.34 (C<sub>quat</sub>), 138.95 (C<sub>quat</sub>), 138.81 (C<sub>quat</sub>), 138.46 (C<sub>quat</sub>), 136.90 (C<sub>quat</sub>), 136.83 (C<sub>quat</sub>), 136.67 (C<sub>quat</sub>), 136.15 (CH, C<sup>4</sup>), 135.76 (CH, C<sup>4</sup>), 130.66 (CH, C<sub>phenyl</sub>), 130.58 (CH, C<sub>phenyl</sub>), 130.54 (CH, C<sub>phenyl</sub>), 130.47 (CH, C<sub>γ</sub>), 129.22 (CH, C<sub>phenyl</sub>), 124.58 (CH, C<sup>5</sup>), 123.80 (CH, C<sub>phenyl</sub>), 123.26 (CH, C<sub>phenyl</sub>), 122.99 (CH, C<sub>phenyl</sub>, C<sup>5'</sup>), 122.67 (CH, C<sub>phenyl</sub>), 121.29 (CH, C<sup>3'</sup>), 117.74 (CH, C<sup>3</sup>), 33.89 (C<sub>quat</sub>, C(CH<sub>3</sub>)<sub>3</sub>), 33.70 (2C, C<sub>quat</sub>, C(CH<sub>3</sub>)<sub>3</sub>), 33.63 (C<sub>quat</sub>, C(CH<sub>3</sub>)<sub>3</sub>), 30.85 (3C, C(CH<sub>3</sub>)<sub>3</sub>), 30.75 (9C, C(CH<sub>3</sub>)<sub>3</sub>). **MS** (*m/z*-ES-MS, THF): Found: 761.4841 [M+H]<sup>+</sup>, calculated for [C<sub>56</sub>H<sub>61</sub>N<sub>2</sub>]<sup>+</sup>: 761.4835. **Anal. Calcd.** For C<sub>56</sub>H<sub>60</sub>N<sub>2</sub>: C, 88.37; H, 7.95; N, 3.68. Found: C, 88.11; H, 8.04; N, 3.64. **IR** ν (cm<sup>-1</sup>): 3056 (w), 2965 (s), 2904 (m), 2866 (m), 1665 (w), 1584 (m), 1565 (s), 1516 (m, br), 1476 (m), 1463 (s), 1424 (s), 1395 (m), 1363 (m), 1269 (s, br), 1174 (w), 1117 (m), 1016 (m), 833 (m, br), 823 (m), 781 (s), 763 (m), 750 (m), 680 (m).

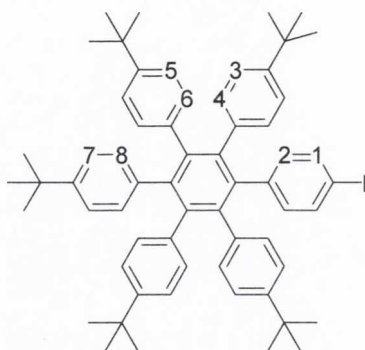
1-(2,2'-bipyrid-6-yl)-2,3,4,5,6-penta-(4-*tert*-butylphenyl) benzene (5)

6-(4-*tert*-butylphenylethynyl)-2,2'-bipyridine (200.2 mg; 0.641 mmol) and 2,3,4,5-tetra-(4-*tert*-butylphenyl)cyclopenta-2,4-dienone (354.5 mg; 0.582 mmol) were heated at 180-200 °C for 6 hours in benzophenone (~1.0 g; ~5.5 mmol) under argon. The temperature was increased to 300 °C and the reaction mixture was continued for a further 18 hours. At this point, TLC indicated that all the acetylene had reacted so the reaction was stopped.

The solid was purified by column chromatography on silica, eluting first with petroleum ether:toluene (2:1 v/v) and then petroleum ether:toluene:CH<sub>2</sub>Cl<sub>2</sub> (1:1:0.1 v/v) to remove benzophenone, unreacted cyclopentadienone and side-products. The desired product was eluted using toluene:CH<sub>2</sub>Cl<sub>2</sub> (3:1 v/v) and then decreasing toluene concentration gradually to use pure CH<sub>2</sub>Cl<sub>2</sub> as eluent. The product was obtained as a pale yellow solid. (308 mg; 0.345 mmol; 59 %). **m.p.** 286-289 °C. <sup>1</sup>H NMR (CDCl<sub>3</sub>, 600.1 MHz): δ 8.52 (d, 1H, <sup>3</sup>J<sub>HH</sub> = 4.2 Hz, H<sup>6'</sup>), 7.74 (d, 1H, <sup>3</sup>J<sub>HH</sub> = 7.9 Hz, H<sup>3</sup>), 7.53 (ddd, 1H, <sup>3</sup>J<sub>HH</sub>, <sup>4</sup>J<sub>HH</sub> = 7.5, 1.5 Hz, H<sup>4'</sup>), 7.43 (d, 1H, <sup>3</sup>J<sub>HH</sub> = 7.9 Hz, H<sup>3'</sup>), 7.29 (dd, 1H, <sup>3</sup>J<sub>HH</sub> = 7.5 Hz, H<sup>4</sup>), 7.15 (m, 1H, H<sup>5'</sup>), 6.81-6.87 (m, 13H, H<sup>5</sup>, H<sub>phenyl</sub>), 6.70-6.73 (m, 5H, H<sub>phenyl</sub>), 6.65 (br d, 2H, H<sub>phenyl</sub>), 6.58 (br d, 1H, H<sub>phenyl</sub>), 1.11 (s, 27H, C(CH<sub>3</sub>)<sub>3</sub>), 1.04 (s, 18H, C(CH<sub>3</sub>)<sub>3</sub>). <sup>13</sup>C {<sup>1</sup>H} NMR (CDCl<sub>3</sub>, 150.9 MHz): δ 159.06 (C<sub>quat</sub>), 156.79 (C<sub>quat</sub>), 154.48 (C<sub>quat</sub>), 148.34 (CH, C<sup>6'</sup>), 147.59 (2C, C<sub>quat</sub>), 147.41 (2C, C<sub>quat</sub>), 141.58 (C<sub>quat</sub>), 140.69 (2C, C<sub>quat</sub>), 140.03 (2C, C<sub>quat</sub>), 138.89 (C<sub>quat</sub>), 137.67 (2C, C<sub>quat</sub>), 137.55 (2C, C<sub>quat</sub>), 136.13 (CH, C<sup>4'</sup>), 134.88 (CH, C<sup>4</sup>), 131.50 (CH), 131.03 (CH), 130.90 (CH), 130.75 (CH), 130.21 (CH), 127.08 (CH, C<sup>5</sup>), 123.45 (CH), 122.88-123.05 (m, 7C, CH, C<sup>5'</sup>), 122.03 (CH, C<sup>3'</sup>), 117.39 (CH, C<sup>3</sup>), 33.91 (4C, C<sub>quat</sub>, C(CH<sub>3</sub>)<sub>3</sub>), 31.04 (9C, C(CH<sub>3</sub>)<sub>3</sub>), 30.97 (6C, C(CH<sub>3</sub>)<sub>3</sub>). **MS** (*m/z*-ES-MS, THF): Found: 893.5803 [M+H]<sup>+</sup>, calculated for [C<sub>66</sub>H<sub>73</sub>N<sub>2</sub>]<sup>+</sup>: 893.5774. **Anal. Calcd.** For C<sub>66</sub>H<sub>72</sub>N<sub>2</sub>·3(H<sub>2</sub>O): C, 83.68; H, 8.30; N, 2.96. Found: C, 83.64; H, 8.28; N, 2.80. **IR** ν (cm<sup>-1</sup>): 3029 (w), 2958 (m, br), 2903 (m), 2865 (w), 1665 (w), 1583 (m), 1561 (s), 1513

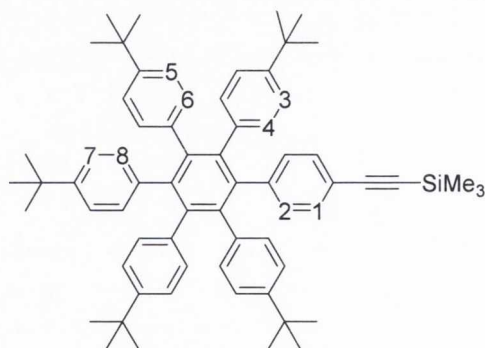
(s), 1459 (s), 1427 (m), 1394 (m), 1366 (s), 1262 (s, br), 1163 (m), 1147 (m), 1119 (m), 1105 (s), 1084 (m), 1021 (s), 861 (m), 835 (s), 773 (s), 689 (m), 636 (m).

### 1-(4-iodophenyl)-2,3,4,5,6-penta-*tert*-butylphenyl-benzene (18)<sup>74</sup>



4-iodo-4'-*tert*-butylphenylacetylene (315.4 mg; 0.876 mmol) and 2,3,4,5-tetra-(4-*tert*-butylphenyl)cyclopenta-2,4-dienone (507.6 mg; 0.834 mmol) were heated to 200°C in benzophenone (~1.5 g; 9 eq.) under argon for 2 hours. After this time the temperature was increased to 300 °C and the reaction was left to reflux for 16 hours. The mixture was cooled and then dissolved in CH<sub>2</sub>Cl<sub>2</sub> (~2 mL). The product was precipitated from excess methanol (~50 mL), filtered and washed with cold methanol (3x25 mL portions) to remove any traces of benzophenone. The desired compound was obtained as an off-white powder. (632 mg; 0.671 mmol; 81 %). <sup>1</sup>H NMR (CDCl<sub>3</sub>, 400.1 MHz): δ 7.15 (d, 2H, <sup>3</sup>J<sub>HH</sub> = 8.0 Hz, H<sup>1</sup>), 6.84 (d, 4H, <sup>3</sup>J<sub>HH</sub> = 8.5 Hz, H<sup>3</sup>), 6.78-6.81 (m, 6H, H<sup>5</sup>, H<sup>7</sup>), 6.63-6.67 (m, 10H, H<sup>4</sup>, H<sup>6</sup>, H<sup>8</sup>), 6.58 (d, 2H, <sup>3</sup>J<sub>HH</sub> = 8.5 Hz, H<sup>2</sup>), 1.13 (s, 18H, C(CH<sub>3</sub>)<sub>3</sub>), 1.09 (s, 27H, C(CH<sub>3</sub>)<sub>3</sub>). MS (*m/z*-MALDI-TOF, CH<sub>2</sub>Cl<sub>2</sub>): Found: 940.4470 [M]<sup>+</sup>, calculated for [C<sub>62</sub>H<sub>69</sub>I]<sup>+</sup>: 940.4444.

### 1-(4-trimethylsilylethynylphenyl)-2,3,4,5,6-penta-(4-*tert*-butylphenyl)benzene (19)

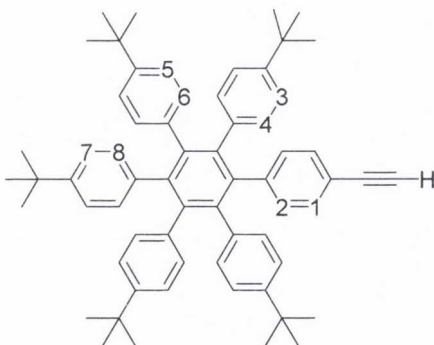


1-(4-iodophenyl)-2,3,4,5,6-penta-*tert*-butylphenyl-benzene (731.4 mg, 0.777 mmol) was dissolved in still-dried THF (90 mL) and <sup>1</sup>Pr<sub>2</sub>NH (30 mL). The solution was degassed *via*



freeze-pump-thaw (x2). PdCl<sub>2</sub>(PPh<sub>3</sub>)<sub>2</sub> (32.9 mg; 6 mol%) and CuI (9.3 mg; 6 mol%) were added rapidly and the reaction mixture was degassed once more. Ethynyltrimethylsilane (0.33 ml; 2.331 mmol) was added *via* syringe to the Schlenk flask and the reaction was left to stir under nitrogen at room temperature over 3 days. After this time, the solvent was removed and CH<sub>2</sub>Cl<sub>2</sub> (~5 mL) was added to the residue to form a suspension. This was added to a stirring excess of methanol (~100 mL). The product was obtained *via* filtration as an off-white powder. (665 mg; 0.730 mmol; 94 %). <sup>1</sup>H NMR (CDCl<sub>3</sub>, 600.1 MHz): δ 6.98 (d, 2H, <sup>3</sup>J<sub>HH</sub> = 8.0 Hz, H<sup>1</sup>), 6.77-6.83 (m, 12H, H<sup>3</sup>, H<sup>2</sup>, H<sup>5</sup>, H<sup>7</sup>), 6.61-6.68 (m, 10H, H<sup>4</sup>, H<sup>6</sup>, H<sup>8</sup>), 1.12 (s, 18H, C(CH<sub>3</sub>)<sub>3</sub>), 1.09 (s, 27H, C(CH<sub>3</sub>)<sub>3</sub>), 0.18 (s, 9H, Si(CH<sub>3</sub>)<sub>3</sub>). <sup>13</sup>C {<sup>1</sup>H} NMR (CDCl<sub>3</sub>, 100.6 MHz): δ 147.87 (C<sub>quat</sub>), 147.60 (C<sub>quat</sub>), 147.51 (C<sub>quat</sub>), 142.04 (C<sub>quat</sub>), 140.90 (C<sub>quat</sub>), 140.17 (C<sub>quat</sub>), 138.96 (C<sub>quat</sub>), 137.89 (C<sub>quat</sub>), 137.65 (C<sub>quat</sub>), 135.61 (C<sub>quat</sub>), 133.73 (C<sub>quat</sub>), 131.68 (CH, C<sup>2</sup>), 131.17 (CH, C<sup>4</sup>/C<sup>6</sup>), 131.09 (CH, C<sup>8</sup>, C<sup>4</sup>/C<sup>6</sup>), 130.44 (CH, C<sup>1</sup>), 123.48 (CH, C<sup>3</sup>/C<sup>5</sup>), 123.20 (CH, C<sup>7</sup>), 123.14 (CH, C<sup>3</sup>/C<sup>5</sup>), 119.25 (C<sub>quat</sub>), 106.03 (C<sub>quat</sub>, C≡C), 93.05 (C<sub>quat</sub>, C≡C), 34.26 (2C, C<sub>quat</sub>, C(CH<sub>3</sub>)<sub>3</sub>), 34.18 (3C, C<sub>quat</sub>, C(CH<sub>3</sub>)<sub>3</sub>), 31.32 (15C, C(CH<sub>3</sub>)<sub>3</sub>), 0.12 (3C, Si(CH<sub>3</sub>)<sub>3</sub>). MS (*m/z*-ES-MS, THF): Found: 933.5785 [M+Na]<sup>+</sup>, calculated for [C<sub>67</sub>H<sub>78</sub>NaSi]<sup>+</sup>: 933.5771.

### 1-(4-ethynylphenyl)-2,3,4,5,6-penta-(4-*tert*-butylphenyl)benzene (ethynyl-HPB; **6**)

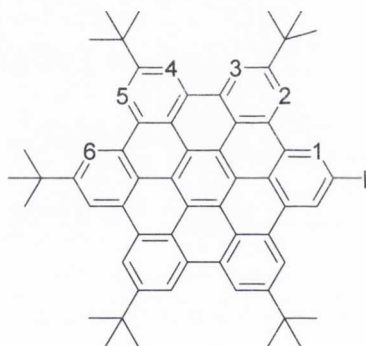


**19** (665.1 mg, 0.730 mmol) was dissolved in a mixture of THF: CH<sub>2</sub>Cl<sub>2</sub> (150 mL:100 mL). KF (412.0 mg, 7.091 mmol) in excess methanol (150 mL) was added to the reaction mixture which was then left to stir overnight under nitrogen. The solvent was removed *in vacuo* and the residue was dissolved in excess CH<sub>2</sub>Cl<sub>2</sub> (~300 mL). This was washed with water (3x200 mL). The organic layer was reduced in volume (~5 mL) and the product was obtained as an off-white powder by filtration after it was precipitated from methanol (~150 mL). (554 mg; 0.661 mmol; 91 %). **m.p.** >200 °C (decomp.) <sup>1</sup>H NMR (CDCl<sub>3</sub>, 400.1 MHz): δ 6.99 (d, 2H, <sup>3</sup>J<sub>HH</sub> = 8.5 Hz, H<sup>1</sup>), 6.78-6.84 (m, 12H, H<sup>2</sup>, H<sup>3</sup>, H<sup>5</sup>, H<sup>7</sup>), 6.62-6.68 (m, 10H, H<sup>4</sup>, H<sup>6</sup>, H<sup>8</sup>), 2.92 (s, 1H, C≡CH), 1.12 (s, 18H, C(CH<sub>3</sub>)<sub>3</sub>), 1.09 (s, 27H, C(CH<sub>3</sub>)<sub>3</sub>). <sup>13</sup>C

**$\{^1\text{H}\}$  NMR** ( $\text{CDCl}_3$ , 150.9 MHz):  $\delta$  147.80 ( $\text{C}_{\text{quat}}$ ), 147.49 ( $\text{C}_{\text{quat}}$ ), 147.43 ( $\text{C}_{\text{quat}}$ ), 142.16 ( $\text{C}_{\text{quat}}$ ), 140.83 ( $\text{C}_{\text{quat}}$ ), 140.72 ( $\text{C}_{\text{quat}}$ ), 140.02 ( $\text{C}_{\text{quat}}$ ), 138.88 ( $\text{C}_{\text{quat}}$ ), 137.77 ( $\text{C}_{\text{quat}}$ ), 137.73 ( $\text{C}_{\text{quat}}$ ), 137.50 ( $\text{C}_{\text{quat}}$ ), 131.61 (1C, CH,  $\text{C}^2$ ), 131.04 (CH,  $\text{C}^4/\text{C}^6$ ), 130.99 (CH,  $\text{C}^8$ ), 130.98 (CH,  $\text{C}^4/\text{C}^6$ ), 130.31 (1C, CH,  $\text{C}^1$ ), 123.32 (CH,  $\text{C}^3/\text{C}^5$ ), 123.06 (CH,  $\text{C}^7$ ), 123.02 (CH,  $\text{C}^3/\text{C}^5$ ), 118.15 ( $\text{C}_{\text{quat}}$ ), 84.33 ( $\text{C}_{\text{quat}}$ ,  $\text{C}\equiv\text{CH}$ ), 76.05 (CH,  $\text{C}\equiv\text{CH}$ ), 34.10 (2C,  $\text{C}_{\text{quat}}$ ,  $\text{C}(\text{CH}_3)_3$ ), 34.04 (1C,  $\text{C}_{\text{quat}}$ ,  $\text{C}(\text{CH}_3)_3$ ), 34.02 (2C,  $\text{C}_{\text{quat}}$ ,  $\text{C}(\text{CH}_3)_3$ ), 31.18 (m, 15C,  $\text{C}(\text{CH}_3)_3$ ).

**MS** ( $m/z$ -ES-MS, THF): Found: 861.5387  $[\text{M}+\text{Na}]^+$ , calculated for  $[\text{C}_{64}\text{H}_{70}\text{Na}]^+$ : 861.5375. **Anal. Calcd.** For  $\text{C}_{64}\text{H}_{70}$ : C, 91.59; H, 8.41. Found: C, 91.72; H, 8.29. **IR**  $\nu$  ( $\text{cm}^{-1}$ ): 3288 (m,  $\text{C}\equiv\text{C}-\text{H}$ ), 3034(w), 2961(s), 2900(m), 2865(m), 2107 ( $\text{C}\equiv\text{C}$ ), 1658(w), 1611(w), 1513(s), 1464(s), 1389(s), 1355(s), 1270(s), 1197(m), 1150(m), 1118(m), 1105(m), 1020(m, br), 860(m), 832(s), 780(m), 674(m).

### 2-iodo-5,8,11,14,17-penta-*tert*-butylhexa-*peri*-hexabenzocoronene (20)<sup>74</sup>

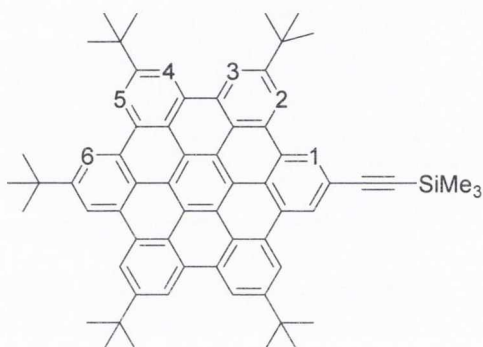


1-(4-iodophenyl)-2,3,4,5,6-penta-(4-*tert*-butylphenyl)benzene (250.5 mg; 0.266 mmol) in still-dried  $\text{CH}_2\text{Cl}_2$  (100 mL) was degassed *via* freeze-pump-thaw (x3). A solution of iron (III) chloride (1.11 g; 6.64 mmol) in dry, degassed nitromethane (5 mL) was added slowly *via* syringe to the  $\text{CH}_2\text{Cl}_2$  solution. Nitrogen was bubbled through this solution for 20 hours until the pH of the gas emerging from the flask was no longer acidic (monitored using litmus paper). Methanol (~150 mL) was added to quench the reaction and dark yellow precipitate was obtained. This was filtered off and washed with methanol (3x50 mL). The precipitate was redissolved in minimum  $\text{CH}_2\text{Cl}_2$  (~10 mL) and was passed through a short silica column using  $\text{CH}_2\text{Cl}_2$  as eluent in order to remove iron impurities. The solvent was reduced in volume under vacuum and excess methanol (~100 mL) was added to the flask with stirring to produce a dark yellow precipitate. This was filtered off, washed with methanol (3x50 mL) and dried under vacuum. (240 mg; 0.258 mmol; 97 %).

**$\{^1\text{H}\}$  NMR** ( $\text{CDCl}_3$ , 400.1 MHz):  $\delta$  9.19 (s, 2H,  $\text{H}^6$ ), 9.13 (s, 2H,  $\text{H}^5$ ), 9.06 (s, 2H,  $\text{H}^4$ ), 8.96

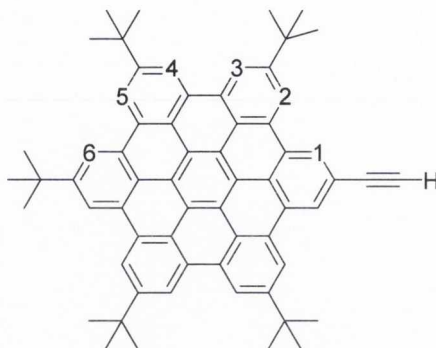
(s, 2H, H<sup>3</sup>), 8.87 (s, 2H, H<sup>1</sup>), 8.70 (s, 2H, H<sup>2</sup>), 1.92 (s, 9H, C(CH<sub>3</sub>)<sub>3</sub>), 1.88 (s, 18H, C(CH<sub>3</sub>)<sub>3</sub>), 1.80 (s, 18H, C(CH<sub>3</sub>)<sub>3</sub>). **MS** (*m/z*-MALDI-TOF, CH<sub>2</sub>Cl<sub>2</sub>): Found: 928.3522 [M]<sup>+</sup>, calculated for [C<sub>62</sub>H<sub>57</sub>I]<sup>+</sup>: 928.3505.

**2-trimethylsilylethynyl-5,8,11,14,17-penta-*tert*-butylhexa-*peri*-hexabenzocoronene (21)<sup>74</sup>**



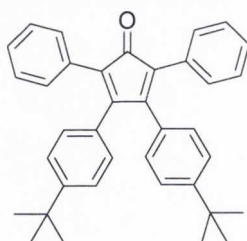
2-iodo-5,8,11,14,17-penta-*tert*-butylhexa-*peri*-hexabenzocoronene (350.0 mg; 0.377 mmol) was dissolved in still-dried THF (~80 mL) and diisopropylamine (~25 mL) and degassed *via* freeze-pump-thaw (x2). PdCl<sub>2</sub>(PPh<sub>3</sub>)<sub>2</sub> (13.2 mg; 0.019 mmol) and CuI (3.6 mg; 0.019 mmol) were added to the Schlenk flask and the solution was degassed once more. Trimethylsilylacetylene (0.11 mL; 0.754 mmol) was added *via* syringe to the flask which was then left to stir for 16 hours under argon at room temperature. The solvent was removed to dryness and the residue was dissolved in CH<sub>2</sub>Cl<sub>2</sub> (~150 mL). This was washed with water (3x150 mL), dried over MgSO<sub>4</sub> and the solvent removed under vacuum. The product was purified *via* column chromatography on silica eluting with petroleum ether:CH<sub>2</sub>Cl<sub>2</sub> (5:1 v/v). Removal of solvent *in vacuo* produced the desired product as a yellow solid. (233 mg; 0.260 mmol; 69 %). <sup>1</sup>H NMR (CDCl<sub>3</sub>, 400.1 MHz): δ 9.12 (s, 2H, H<sup>6</sup>), 9.02 (s, 2H, H<sup>5</sup>), 8.94 (s, 2H, H<sup>4</sup>), 8.75 (s, 2H, H<sup>3</sup>), 8.56 (s, 2H, H<sup>2</sup>), 8.40 (s, 2H, H<sup>1</sup>), 2.09 (s, 9H, C(CH<sub>3</sub>)<sub>3</sub>), 2.03 (s, 18H, C(CH<sub>3</sub>)<sub>3</sub>), 1.92 (s, 9H, C(CH<sub>3</sub>)<sub>3</sub>), 0.73 (s, 9H, Si(CH<sub>3</sub>)<sub>3</sub>). **MS** (*m/z*-MALDI-TOF, CH<sub>2</sub>Cl<sub>2</sub>): Found: 898.4921 [M]<sup>+</sup>, calculated for [C<sub>67</sub>H<sub>66</sub>Si]<sup>+</sup>: 898.4934.

**2-ethynyl-5,8,11,14,17-penta-*tert*-butylhexa-*peri*-hexabenzocoronene (ethynyl-HBC; 7)<sup>74</sup>**



2-trimethylsilylethynyl-5,8,11,14,17-penta-*tert*-butylhexa-*peri*-hexabenzocoronene (**21**) (233.4 mg; 0.260 mmol) was dissolved in a mixture of THF:MeOH (35 mL:35 mL). KF (104.0 mg; 1.790 mmol) was added to the reaction vessel which was left to stir under argon overnight. The solvent was removed *in vacuo* and the residue redissolved in CH<sub>2</sub>Cl<sub>2</sub> (~100 mL). This was washed with water (3x100 mL) and the CH<sub>2</sub>Cl<sub>2</sub> solution was reduced in volume (~5 mL). Excess methanol (~100 mL) was added to the solution with stirring. The fine yellow precipitate obtained was filtered off, washed with methanol (3x50 mL) and dried under vacuum. (178 mg; 0.215 mmol; 83 %). **m.p.** >280 °C. **<sup>1</sup>H NMR** (CDCl<sub>3</sub>, 400.1 MHz): δ 9.17 (s, 2H, H<sup>6</sup>), 9.10 (s, 2H, H<sup>5</sup>), 9.03 (s, 2H, H<sup>4</sup>), 8.90 (s, 2H, H<sup>3</sup>), 8.72 (s, 2H, H<sup>2</sup>), 8.65 (s, 2H, H<sup>1</sup>), 3.59 (s, 1H, C≡CH), 1.94 (s, 9H, C(CH<sub>3</sub>)<sub>3</sub>), 1.89 (s, 18H, C(CH<sub>3</sub>)<sub>3</sub>), 1.80 (s, 18H, C(CH<sub>3</sub>)<sub>3</sub>). **MS** (*m/z*-MALDI-TOF, CH<sub>2</sub>Cl<sub>2</sub>): Found: 826.4568 [M]<sup>+</sup>, calculated for [C<sub>64</sub>H<sub>58</sub>]<sup>+</sup>: 826.4539. **IR** ν (cm<sup>-1</sup>): 3289 (m, C≡C-H), 3036 (w), 2958 (m), 2904 (m), 2864 (m), 2106 (m, C≡C), 1741 (w), 1607 (m), 1576 (w), 1511 (m), 1476 (m), 1459 (m), 1393 (s), 1361 (s), 1267 (s, br), 1201 (m), 1149 (m), 1118 (m), 1103 (m), 1020 (s,br), 944 (w), 865 (s), 830 (s), 779 (m), 749 (m), 671 (m).

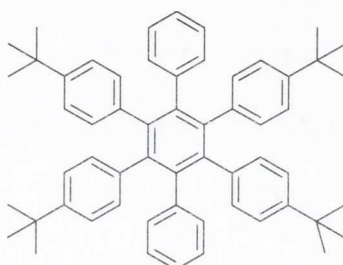
**2,5-bis-phenyl-3,4-bis-(4-*tert*-butylphenyl)cyclopenta-2,4-dienone (**24**)<sup>75</sup>**



1,2-bis-(4-*tert*-butylphenyl)ethane-1,2-dione (**15**) (400.1 mg; 1.242 mmol) and 1,3-diphenyl acetone (262.2 mg; 1.247 mmol) were dissolved in ethanol (5 mL) and were heated under argon to 70°C for 15 minutes. KOH (104.5 mg; 1.5 eq.) in ethanol (3 mL)

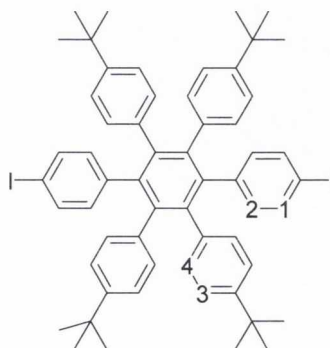
was added in two portions to the flask. The solution was heated to reflux under argon for 5 hours. After this time, the reaction mixture was left to cool at  $-18\text{ }^{\circ}\text{C}$  overnight. The purple precipitate was filtered off, washed with cold ethanol ( $2 \times 10\text{ mL}$ ) and dried under vacuum. (520 mg; 1.05 mmol; 84 %).  $^1\text{H NMR}$  ( $\text{CDCl}_3$ , 400.1 MHz):  $\delta$  7.24 (m, 10H,  $\text{H}_{\text{phenyl}}$ ), 7.15 (d, 4H,  $^3J_{\text{HH}} = 8.5\text{ Hz}$ ,  $\text{H}_{\text{phenyl}}$ ), 6.81 (d, 4H,  $^3J_{\text{HH}} = 8.0\text{ Hz}$ ,  $\text{H}_{\text{phenyl}}$ ), 1.55 (s, 9H,  $\text{C}(\text{CH}_3)_3$ ), 1.27 (s, 9H,  $\text{C}(\text{CH}_3)_3$ ). **MS** ( $m/z$ -ES-MS, THF): Found: 497.2832  $[\text{M}+\text{H}]^+$ , calculated for  $[\text{C}_{37}\text{H}_{37}\text{O}]^+$ : 497.2844.

### 1,4-bis-phenyl-2,3,5,6-tetra-(4-*tert*-butylphenyl)benzene (**25**)<sup>75</sup>



Cyclopentadienone **24** (401.2 mg; 0.808 mmol) and bis(4-*tert*-butylphenyl)acetylene (246.6 mg; 0.849 mmol) in benzophenone ( $\sim 3\text{ g}$ ) were heated in a sandbath under argon for 2 hours at  $150\text{--}200\text{ }^{\circ}\text{C}$ . After this time, the temperature was increased to  $300\text{ }^{\circ}\text{C}$  for a further 4 hours. The reaction mixture was cooled to room temperature and was dissolved in minimum  $\text{CH}_2\text{Cl}_2$  ( $\sim 5\text{ mL}$ ). This was added to a stirring excess of methanol ( $\sim 50\text{ mL}$ ). The resulting fine white precipitate was filtered, washed with cold methanol ( $3 \times 50\text{ mL}$ ) and dried under vacuum. (386 mg; 0.508 mmol; 63 %).  $^1\text{H NMR}$  ( $\text{CDCl}_3$ , 400.1 MHz):  $\delta$  6.79–6.83 (m, 18H,  $\text{H}_{\text{phenyl}}$ ), 6.65 (d, 4H,  $^3J_{\text{HH}} = 8.5\text{ Hz}$ ,  $\text{H}_{\text{phenyl}}$ ), 1.09 (s, 36H,  $\text{C}(\text{CH}_3)_3$ ). **MS** ( $m/z$ -ES-MS, THF): Found: 797.4500  $[\text{M}+\text{K}]^+$ , calculated for  $[\text{C}_{58}\text{H}_{62}\text{K}]^+$ : 797.4489.

### 1,4-bis-(4-iodophenyl)-2,3,5,6-tetra-(4-*tert*-butylphenyl)benzene (**28**)<sup>75</sup>

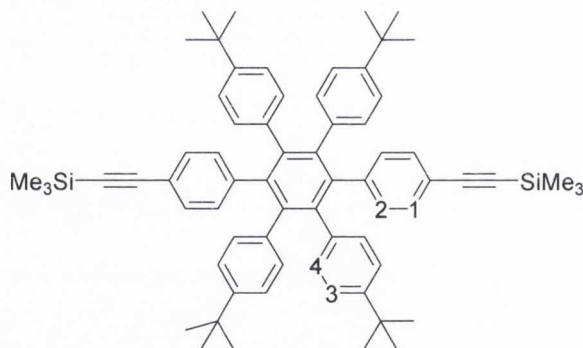


A solution of 1,4-bis-phenyl-2,3,5,6-tetra-(4-*tert*-butylphenyl)benzene (199.7 mg; 0.263 mmol) and (bis(trifluoroacetoxy)iodo)benzene (PIFA) (252.0 mg; 0.993 mmol) in still-

dried  $\text{CH}_2\text{Cl}_2:\text{CHCl}_3$  (28 mL:28 mL) was degassed *via* freeze-pump-thaw (x3). Iodine (91.6 mg; 0.213 mmol) was added to flask. The reaction mixture was stirred in the dark under argon at room temperature overnight. After 18 hours, additional PIFA (67.9 mg; 0.268 mmol) and iodine (25.0 mg; 0.058 mmol) were added to the flask and the reaction allowed to proceed in the dark for a further 6 hours. After this time, a further addition of PIFA (25.7 mg; 0.101 mmol) and iodine (12.0 mg; 0.028 mmol) was made to flask and the reaction left to proceed for a further 18 hours until the reaction was observed by TLC to have gone to completion.

The reaction was diluted with additional  $\text{CH}_2\text{Cl}_2$  (~100 mL) and was washed with  $\text{Na}_2\text{S}_2\text{O}_4$  solution (x1) and water (x2). The solvent was removed from the organic layer to dryness and the residue taken up in diethyl ether (~5 mL). The desired product was obtained by precipitation from a stirring excess of methanol (~50 mL), filtration and washing with methanol. (244 mg; 0.242 mmol; 92 %).  $^1\text{H NMR}$  ( $\text{CDCl}_3$ , 400.1 MHz):  $\delta$  7.15 (d, 4H,  $^3J_{\text{HH}} = 8.0$  Hz,  $\text{H}^1$ ), 6.83 (d, 8H,  $^3J_{\text{HH}} = 8.5$  Hz,  $\text{H}^3$ ), 6.62 (d, 8H,  $^3J_{\text{HH}} = 8.0$  Hz,  $\text{H}^4$ ), 6.56 (d, 4H,  $^3J_{\text{HH}} = 8.0$  Hz,  $\text{H}^2$ ), 1.12 (s, 36H,  $\text{C}(\text{CH}_3)_3$ ). **MS** ( $m/z$ -MALDI-TOF, THF): Found: 1010.2775  $[\text{M}]^+$ , calculated for  $[\text{C}_{58}\text{H}_{60}\text{I}_2]^+$ : 1010.2785.

### 1,4-bis-(4-trimethylsilylethynylphenyl)-2,3,5,6-(4-*tert*-butylphenyl)benzene (**29**)

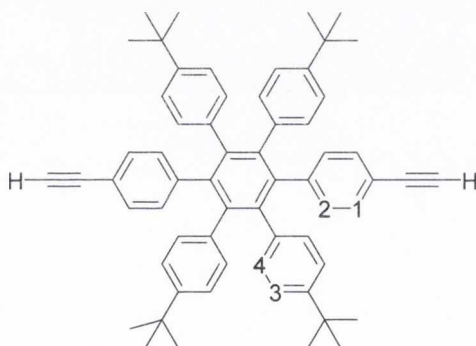


A solution of **28** (41.0 mg; 0.041 mmol) in still-dried THF (30 mL) and diisopropylamine (15 mL) was degassed twice *via* freeze-pump-thaw.  $\text{PdCl}_2(\text{PPh}_3)_2$  (3.3 mg; 0.005 mmol) and CuI (0.9 mg; 0.005 mmol) were added to the vessel and the reaction mixture was degassed once more. Trimethylsilylacetylene (28  $\mu\text{L}$ ; 0.198 mmol) was added *via* syringe to the reaction mixture and this was left to stir at room temperature under argon for 2 days, until the reaction was observed by TLC to have reached completion.

The solvent was removed from the reaction mixture under vacuum and the residue was taken up in  $\text{CH}_2\text{Cl}_2$  (~100 mL). This was washed with water (x3), dried over  $\text{MgSO}_4$  and activated charcoal was added to remove palladium impurities. This was filtered off and the

solvent reduced in volume. This was passed through a short silica plug eluting with  $\text{CH}_2\text{Cl}_2$ . Concentration of the product fractions *in vacuo*, followed by precipitation from a stirring excess of methanol yielded the desired product as an off-white powder. (36 mg; 0.038 mmol; 95 %).  $^1\text{H NMR}$  ( $\text{CDCl}_3$ , 400.1 MHz):  $\delta$  6.97 (d, 4H,  $^3J_{\text{HH}} = 8.3$  Hz,  $\text{H}^1$ ), 6.79 (m, 12H,  $\text{H}^2$ ,  $\text{H}^3$ ), 6.60 (d, 8H,  $^3J_{\text{HH}} = 8.3$  Hz,  $\text{H}^4$ ), 1.11 (s, 36H,  $\text{C}(\text{CH}_3)_3$ ), 0.18 (s, 18H,  $\text{Si}(\text{CH}_3)_3$ ).  $^{13}\text{C} \{^1\text{H}\}$  NMR ( $\text{CDCl}_3$ , 100.6 MHz):  $\delta$  147.92 (4C,  $\text{C}_{\text{quat}}$ ), 141.83 (2C,  $\text{C}_{\text{quat}}$ ), 140.64 (4C,  $\text{C}_{\text{quat}}$ ), 139.48 (2C,  $\text{C}_{\text{quat}}$ ), 137.43 (4C,  $\text{C}_{\text{quat}}$ ), 131.57 (4C, CH,  $\text{C}^2$ ), 131.04 (8C, CH,  $\text{C}^4$ ), 130.48 (4C, CH,  $\text{C}^1$ ), 123.48 (8C, CH,  $\text{C}^3$ ), 119.38 (4C,  $\text{C}_{\text{quat}}$ ), 105.96 (2C,  $\text{C}_{\text{quat}}$ ,  $\text{C}\equiv\text{C}$ ), 93.14 (2C,  $\text{C}_{\text{quat}}$ ,  $\text{C}\equiv\text{C}$ ), 34.24 (4C,  $\text{C}_{\text{quat}}$ ,  $\text{C}(\text{CH}_3)_3$ ), 31.32 (12C,  $\text{C}(\text{CH}_3)_3$ ), 0.17 (6C,  $\text{Si}(\text{CH}_3)_3$ ). MS (*m/z*-ES-MS, THF): Found: 951.5709  $[\text{M}+\text{H}]^+$ , calculated for  $[\text{C}_{68}\text{H}_{79}\text{Si}_2]^+$ : 951.5720.

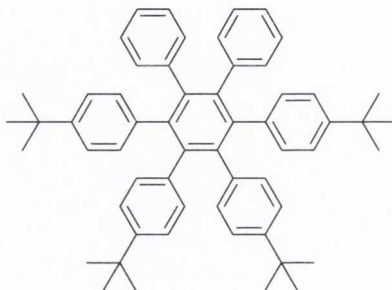
#### 1,4-bis-(4-ethynylphenyl)-2,3,5,6-tetra-(4-*tert*-butylphenyl)benzene (8)



To a solution of **29** (41.4 mg; 0.043 mmol) in THF:MeOH (10 mL:10 mL) was added KF (12.5 mg; 0.216 mmol). The mixture was left to stir overnight under argon at room temperature. After this time, the solvent was removed to dryness and the residue redissolved in  $\text{CH}_2\text{Cl}_2$  (~50 mL). This was washed with water (x3) and the organic layer reduced in volume (~2 mL). The product was precipitated from excess methanol (~50 mL), filtered, washed with cold methanol (3x10 mL) and dried under vacuum. (28 mg; 0.035 mmol; 81 %). **m.p.** >180 °C (decomp.)  $^1\text{H NMR}$  ( $\text{CDCl}_3$ , 600.1 MHz):  $\delta$  6.98 (d, 4H,  $^3J_{\text{HH}} = 8.0$  Hz,  $\text{H}^1$ ), 6.81 (m, 12H,  $\text{H}^2$ ,  $\text{H}^3$ ), 6.63 (d, 8H,  $^3J_{\text{HH}} = 8.1$  Hz,  $\text{H}^4$ ), 2.92 (s, 2H,  $\text{C}\equiv\text{CH}$ ), 1.11 (s, 36H,  $\text{C}(\text{CH}_3)_3$ ).  $^{13}\text{C} \{^1\text{H}\}$  NMR ( $\text{CDCl}_3$ , 150.9 MHz):  $\delta$  148.07 (4C,  $\text{C}_{\text{quat}}$ ),  $\text{C}-\text{C}(\text{CH}_3)_3$ , 142.08 (2C,  $\text{C}_{\text{quat}}$ ), 140.61 (4C,  $\text{C}_{\text{quat}}$ ), 139.61 (2C,  $\text{C}_{\text{quat}}$ ), 137.41 (4C,  $\text{C}_{\text{quat}}$ ), 131.66 (4C, CH,  $\text{C}^2$ ), 131.10 (8C, CH,  $\text{C}^4$ ), 130.52 (4C, CH,  $\text{C}^1$ ), 123.51 (8C, CH,  $\text{C}^3$ ), 118.47 (4C,  $\text{C}_{\text{quat}}$ ), 84.42 (2C,  $\text{C}_{\text{quat}}$ ,  $\text{C}\equiv\text{CH}$ ), 76.31 (2C,  $\text{C}_{\text{quat}}$ ,  $\text{C}\equiv\text{CH}$ ), 34.25 (4C,  $\text{C}_{\text{quat}}$ ,  $\text{C}(\text{CH}_3)_3$ ), 31.33 (12C,  $\text{C}(\text{CH}_3)_3$ ). MS (*m/z*-ES-MS, THF): Found: 829.4737  $[\text{M}+\text{Na}]^+$ , calculated for  $[\text{C}_{62}\text{H}_{62}\text{Na}]^+$ : 829.4749. **Anal. Calcd.** For  $\text{C}_{62}\text{H}_{62}$ : C, 92.26; H, 7.74.

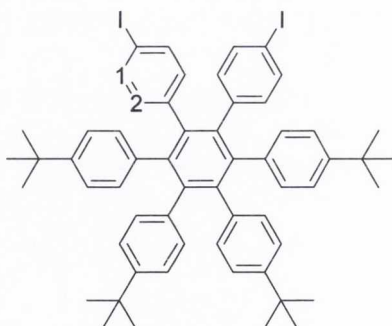
Found: C, 92.11; H, 8.01. **IR**  $\nu$  ( $\text{cm}^{-1}$ ): 3283 (m,  $\text{C}\equiv\text{C}-\text{H}$ ), 2961 (m), 2905 (w), 2866 (w), 2108 (m,  $\text{C}\equiv\text{C}$ ), 1606 (w), 1511 (m), 1476 (m), 1460 (m), 1397 (m), 1365 (s), 1270 (s), 1203 (w), 1148 (w), 1106 (m), 1024 (s), 865 (s), 831 (s), 776 (s), 672 (s).

### 1,2-bis-phenyl-3,4,5,6-tetra-(4-*tert*-butylphenyl)benzene (27)<sup>75</sup>



2,3,4,5-tetra-(4-*tert*-butylphenyl)cyclopenta-2,4-dienone (**16**) (1.002 g; 1.642 mmol) and diphenylacetylene (0.2927 g; 1.643 mmol) were heated at 250 °C in a sandbath under argon for 2 hours. The temperature was then increased to 350 °C for 3.5 hours. The reaction mixture was allowed to cool to room temperature and was dissolved in  $\text{CH}_2\text{Cl}_2$  (~10 mL). Addition of this solution to excess methanol (~100 mL) resulted in the precipitation of the desired product as an off-white powder. This was filtered, washed with cold methanol (3x50 mL) was dried under vacuum. (858 mg; 1.13 mmol; 69 %). **<sup>1</sup>H NMR** ( $\text{CDCl}_3$ , 400.1 MHz):  $\delta$  6.79-6.83 (m, 18H,  $\text{H}_{\text{phenyl}}$ ), 6.64-6.69 (m, 8H,  $\text{H}_{\text{phenyl}}$ ), 1.10 (s, 18H,  $\text{C}(\text{CH}_3)_3$ ), 1.09 (s, 18H,  $\text{C}(\text{CH}_3)_3$ ). **MS** ( $m/z$ -ES-MS, THF): Found: 797.4493  $[\text{M}+\text{K}]^+$ , calculated for  $[\text{C}_{58}\text{H}_{62}\text{K}]^+$ : 797.4489.

### 1,2-bis-(4-iodophenyl)-3,4,5,6-tetra-(4-*tert*-butylphenyl)benzene (30)<sup>75</sup>



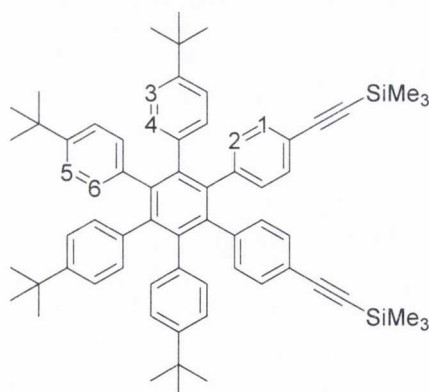
A solution of 1,2-bis-phenyl-3,4,5,6-tetra-(4-*tert*-butylphenyl)benzene (199.9 mg; 0.263 mmol) and (bis(trifluoroacetoxy)iodo)benzene (PIFA) (249.6 mg; 0.983 mmol) in still-dried  $\text{CH}_2\text{Cl}_2:\text{CHCl}_3$  (28 mL:28 mL) was degassed *via* freeze-pump-thaw three times. Iodine (92.0 mg; 0.214 mmol) was added to flask. The reaction mixture was stirred in the



dark under argon at room temperature overnight. After 18 hours, additional PIFA (66.2 mg; 0.261 mmol) and iodine (21.8 mg; 0.051 mmol) were added to the flask and the reaction allowed to proceed in the dark for a further 6 hours. After this time, a further addition of PIFA (23.4 mg; 0.092 mmol) and iodine (7.2 mg; 0.017 mmol) was made to flask and the reaction left to proceed for a further 18 hours until the reaction was observed by TLC to have gone to completion.

The reaction was diluted with additional  $\text{CH}_2\text{Cl}_2$  (~100 mL) and was washed with  $\text{Na}_2\text{S}_2\text{O}_4$  solution (x1) and water (x2). The solvent was removed from the organic layer to dryness and the residue taken up in diethyl ether (~5 mL). The desired product was obtained by precipitation from a stirring excess of methanol (~50 mL), filtration and washing with methanol. (194 mg; 0.192 mmol; 73 %).  $^1\text{H NMR}$  ( $\text{CDCl}_3$ , 400.1 MHz):  $\delta$  7.22 (d, 4H,  $^3J_{\text{HH}} = \text{Hz}$ ,  $\text{H}^1$ ), 6.86 (d, 4H,  $^3J_{\text{HH}} = \text{Hz}$ ,  $\text{H}_{\text{phenyl}}$ ), 6.81 (d, 4H,  $^3J_{\text{HH}} = \text{Hz}$ ,  $\text{H}_{\text{phenyl}}$ ), 6.63-6.67 (m, 8H,  $\text{H}_{\text{phenyl}}$ ), 6.58 (d, 4H,  $^3J_{\text{HH}} = \text{Hz}$ ,  $\text{H}^2$ ), 1.15 (s, 18H,  $\text{C}(\text{CH}_3)_3$ ), 1.11 (s, 18H,  $\text{C}(\text{CH}_3)_3$ ). **MS** ( $m/z$ -MALDI-TOF, THF): Found: 1010.2793  $[\text{M}]^+$ , calculated for  $[\text{C}_{58}\text{H}_{60}\text{I}_2]^+$ : 1010.2785.

### 1,2-bis-(4-trimethylsilylethynylphenyl)-3,4,5,6-(4-*tert*-butylphenyl)benzene (31)

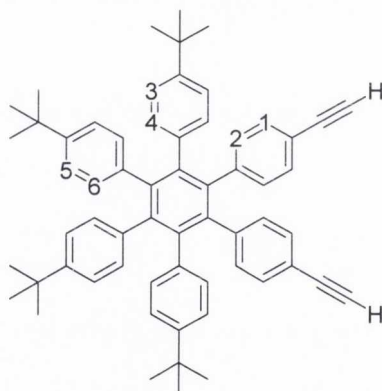


1,2-bis-(4-iodophenyl)-3,4,5,6-tetra-(4-*tert*-butylphenyl)benzene (300.1 mg; 0.297 mmol) in still-dried THF (60 mL) and diisopropylamine (30 mL) was degassed twice *via* freeze-pump-thaw.  $\text{PdCl}_2(\text{PPh}_3)_2$  (25.0 mg; 0.035 mmol) and  $\text{CuI}$  (6.8 mg; 0.036 mmol) were added to the vessel and the reaction mixture was degassed once more. Trimethylsilylacetylene (0.21 mL; 1.486 mmol) was added *via* syringe to the reaction mixture and this was left to stir at room temperature under argon for 2 days, until the reaction was observed by TLC to have reached completion.

The solvent was removed from the reaction mixture under vacuum and the residue was taken up in  $\text{CH}_2\text{Cl}_2$  (~150 mL). This was washed with water (x2), dried over  $\text{MgSO}_4$  and

activated charcoal was added to remove palladium impurities. This was filtered and the solvent reduced in volume. This was passed through a short silica plug eluting with  $\text{CH}_2\text{Cl}_2$ . Concentration of the product fractions *in vacuo*, followed by precipitation from a stirring excess of methanol yielded the desired product as a pale yellow powder. (243 mg; 0.255 mmol; 86 %).  $^1\text{H NMR}$  ( $\text{CDCl}_3$ , 400.1 MHz):  $\delta$  6.98 (d, 4H,  $^3J_{\text{HH}} = 8.5$  Hz,  $\text{H}^1$ ), 6.81 (d, 4H,  $^3J_{\text{HH}} = 8.3$  Hz,  $\text{H}^3/\text{H}^5$ ), 6.79 (m, 8H,  $\text{H}^2$ ,  $\text{H}^3/\text{H}^5$ ), 6.63 (d, 4H,  $^3J_{\text{HH}} = 8.5$  Hz,  $\text{H}^4/\text{H}^6$ ), 6.60 (d, 4H,  $^3J_{\text{HH}} = 8.5$  Hz,  $\text{H}^4/\text{H}^6$ ), 1.11 (s, 18H,  $\text{C}(\text{CH}_3)_3$ ), 1.08 (s, 18H,  $\text{C}(\text{CH}_3)_3$ ), 0.20 (s, 18H,  $\text{Si}(\text{CH}_3)_3$ ).  $^{13}\text{C} \{^1\text{H}\}$  NMR ( $\text{CDCl}_3$ , 100.6 MHz):  $\delta$  148.00 (2C,  $\text{C}_{\text{quat}}$ ), 147.64 (2C,  $\text{C}_{\text{quat}}$ ), 141.60 (2C,  $\text{C}_{\text{quat}}$ ), 141.39 (2C,  $\text{C}_{\text{quat}}$ ), 140.40 (2C,  $\text{C}_{\text{quat}}$ ), 138.96 (2C,  $\text{C}_{\text{quat}}$ ), 137.70 (2C,  $\text{C}_{\text{quat}}$ ), 137.37 (2C,  $\text{C}_{\text{quat}}$ ), 131.52 (4C, CH,  $\text{C}^2$ ), 131.07 (4C, CH,  $\text{C}^4/\text{C}^6$ ), 131.00 (4C, CH,  $\text{C}^4/\text{C}^6$ ), 130.65 (4C, CH,  $\text{C}^1$ ), 123.53 (4C, CH,  $\text{C}^3/\text{C}^5$ ), 123.18 (4C, CH,  $\text{C}^3/\text{C}^5$ ), 119.66 (2C,  $\text{C}_{\text{quat}}$ ), 105.85 (2C,  $\text{C}_{\text{quat}}$ ,  $\text{C}\equiv\text{C}$ ), 93.48 (2C,  $\text{C}_{\text{quat}}$ ,  $\text{C}\equiv\text{C}$ ), 34.26 (2C,  $\text{C}_{\text{quat}}$ ,  $\text{C}(\text{CH}_3)_3$ ), 34.17 3 (2C,  $\text{C}_{\text{quat}}$ ,  $\text{C}(\text{CH}_3)_3$ ), 31.30 (12C,  $\text{C}(\text{CH}_3)_3$ ), 0.11 (6C,  $\text{Si}(\text{CH}_3)_3$ ). MS ( $m/z$ -ES-MS, THF): Found: 989.5290  $[\text{M}+\text{K}]^+$ , calculated for  $[\text{C}_{68}\text{H}_{78}\text{Si}_2\text{K}]^+$ : 989.5279.

### 1,2-bis-(4-ethynylphenyl)-3,4,5,6-tetra-(4-*tert*-butylphenyl)benzene (9)



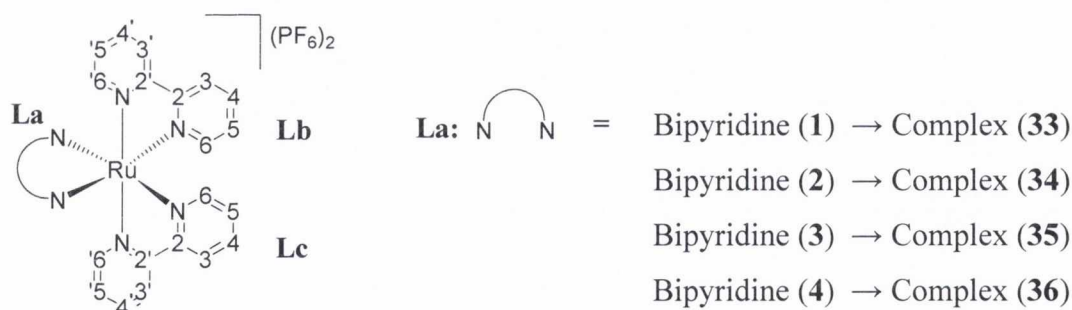
To a solution of **31** (244.1 mg; 0.257 mmol) in THF:MeOH (30 mL:30 mL) was added KF (74.6 mg; 1.284 mmol). The mixture was left to stir overnight under argon at room temperature. After this time, the solvent was removed to dryness and the residue redissolved in  $\text{CH}_2\text{Cl}_2$  (~150 mL). This was washed with water (x3) and the organic layer reduced in volume (~10 mL). The product was precipitated from excess methanol (~100 mL), filtered, washed with cold methanol (3x10 mL) and dried under vacuum. (84 mg; 0.099 mmol; 39 %). **m.p.** > 160 °C.  $^1\text{H NMR}$  ( $\text{CDCl}_3$ , 400.1 MHz):  $\delta$  7.00 (d, 4H,  $^3J_{\text{HH}} = 8.0$  Hz,  $\text{H}^1$ ), 6.78-6.86 (m, 12H,  $\text{H}^3$ ,  $\text{H}^5$ ,  $\text{H}^2$ ), 6.62-6.68 (m, 8H,  $\text{H}^4$ ,  $\text{H}^6$ ), 2.94 (s, 2H,  $\text{C}\equiv\text{CH}$ ), 1.11 (s, 18H,  $\text{C}(\text{CH}_3)_3$ ), 1.09 (s, 18H,  $\text{C}(\text{CH}_3)_3$ ).  $^{13}\text{C} \{^1\text{H}\}$  NMR ( $\text{CDCl}_3$ , 100.6

MHz):  $\delta$  148.11 (2C, C<sub>quat</sub>), 147.74 (2C, C<sub>quat</sub>), 141.83 (2C, C<sub>quat</sub>), 141.42 (2C, C<sub>quat</sub>), 140.43 (2C, C<sub>quat</sub>), 138.96 (2C, C<sub>quat</sub>), 137.67 (2C, C<sub>quat</sub>), 137.35 (2C, C<sub>quat</sub>), 131.62 (4C, CH, C<sup>2</sup>), 131.09 (4C, CH, C<sup>4</sup>/C<sup>6</sup>), 131.04 (4C, CH, C<sup>4</sup>/C<sup>6</sup>), 130.71 (4C, CH, C<sup>1</sup>), 128.41 (2C, C<sub>quat</sub>), 123.54 (4C, CH, C<sup>3</sup>/C<sup>5</sup>), 123.24 (4C, CH, C<sup>3</sup>/C<sup>5</sup>), 118.74 (C<sub>quat</sub>), 84.24 (C<sub>quat</sub>, C $\equiv$ CH), 76.64 (CH, C $\equiv$ CH), 34.27 (2C, C<sub>quat</sub>, C(CH<sub>3</sub>)<sub>3</sub>), 34.19 (2C, C<sub>quat</sub>, C(CH<sub>3</sub>)<sub>3</sub>), 31.31 (12C, C(CH<sub>3</sub>)<sub>3</sub>). **MS** (*m/z*-ES-MS, THF): Found: 845.4481 [M+K]<sup>+</sup>, calculated for [C<sub>62</sub>H<sub>62</sub>K]<sup>+</sup>: 845.4489. **Anal. Calcd.** For C<sub>62</sub>H<sub>62</sub>· $\frac{1}{3}$ (CH<sub>3</sub>OH): C, 91.54; H, 7.81. Found: C, 91.71; H, 7.65. **IR**  $\nu$  (cm<sup>-1</sup>): 3282 (m, C $\equiv$ C-H), 2958 (s), 2903 (m), 2864 (m), 2152 (m, C $\equiv$ C), 2069 (w), 1603 (w), 1512 (m, br), 1463 (w), 1390 (m), 1362 (m), 1255 (s), 1144 (w), 1104 (m), 1016 (s), 865 (s), 836 (s, br), 757 (s), 696 (m).

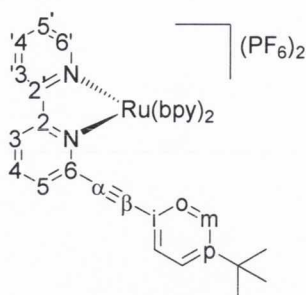
### 5.3 Ruthenium(II) Heteroleptic complexes

In [Ru(bpy)<sub>2</sub>(L)](PF<sub>6</sub>)<sub>2</sub> complexes, the 2,2'-bipyridine ligands cannot be distinguished from each other and accordingly are arbitrarily assigned ligand **b** and ligand **c**. The monosubstituted bipyridine ligand, **L**, is assigned as ligand **a**.

NMR numbering scheme for 2,2'-bipyridine ligands:



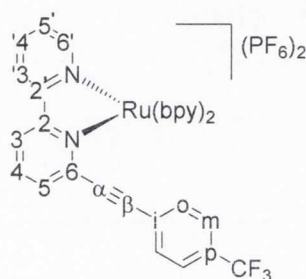
**[Ru(bpy)<sub>2</sub>(6-(4-*tert*-butyl-phenylethynyl)-2,2'-bpy)](PF<sub>6</sub>)<sub>2</sub> (33)**



6-(4-*tert*-butyl-phenylethynyl)-2,2'-bipyridine (**1**) (100.1 mg; 0.320 mmol) was sonicated in ethylene glycol (9 mL) for 10 minutes. The suspension was degassed *via* argon bubbling for 20 minutes. *cis*-Ru(bpy)<sub>2</sub>Cl<sub>2</sub> (147.7 mg; 0.3048 mmol) was added to the flask and the suspension was heated at 110-130 °C for 24 hours under argon. After several hours, the solution gradually turned from purple to orange/red. The solution was cooled and excess saturated KPF<sub>6</sub> solution (~20 mL) was added with stirring to the flask. The bright orange precipitate obtained was filtered off, washed with water (3x25 mL) and diethyl ether (~10 mL) and dried under vacuum. (273 mg; 0.269 mmol; 88 %). **m.p.** > 175 °C (decomp.) <sup>1</sup>H NMR (CDCl<sub>3</sub>, 600.1 MHz): δ 8.46-8.53 (m, 4H, H<sub>a3'</sub>, H<sub>b3</sub>, H<sub>a3</sub>, H<sub>c3'</sub>), 8.44 (d, <sup>3</sup>J<sub>H3H4</sub> = 8.0 Hz, H<sub>c3</sub>), 8.03-8.13 (m, 6H, H<sub>b4</sub>, H<sub>b3'</sub>, H<sub>c4'</sub>, H<sub>a4</sub>, H<sub>c6'</sub>, H<sub>a4'</sub>), 8.00 (ddd, 1H, <sup>3</sup>J<sub>H4H3/5</sub>, <sup>4</sup>J<sub>H4H6</sub> = 7.8, 1.5 Hz, H<sub>c4</sub>), 7.70 (dd, 1H, <sup>3</sup>J<sub>H5H4</sub>, <sup>4</sup>J<sub>H5H3</sub> = 8.0, 1.3 Hz, H<sub>a5</sub>), 7.64 (d, 1H, <sup>3</sup>J<sub>H6H5</sub> = 5.3 Hz, H<sub>b6</sub>), 7.62 (d, 1H, <sup>3</sup>J<sub>H6'H5'</sub> = 5.6 Hz, H<sub>b6'</sub>), 7.57 (d, 1H, <sup>3</sup>J<sub>H6'H5'</sub> = 5.5 Hz, H<sub>a6'</sub>), 7.49-7.54 (m, 2H, H<sub>c6</sub>, H<sub>c5'</sub>), 7.41 (ddd, 1H, <sup>3</sup>J<sub>H5H4</sub>, <sup>3</sup>J<sub>H5H6</sub>, <sup>4</sup>J<sub>H5H3</sub> = 6.8, 6.5, 1.3 Hz, H<sub>b5</sub>), 7.32-7.37 (m, 3H, H<sub>m</sub>, H<sub>a5'</sub>), 7.29 (ddd, 1H, <sup>3</sup>J<sub>H5H4</sub>, <sup>3</sup>J<sub>H5H6</sub>, <sup>4</sup>J<sub>H5H3</sub> = 6.9, 6.4, 1.3 Hz, H<sub>c5</sub>), 7.23 (ddd, 1H, <sup>3</sup>J<sub>H4'H5'/3'</sub>, <sup>4</sup>J<sub>H4'H6'</sub> = 8.0, 1.5 Hz, H<sub>b4'</sub>), 6.93 (d, 2H, <sup>3</sup>J<sub>HoHm</sub> = 8.8 Hz, H<sub>o</sub>), 6.70 (ddd, 1H, <sup>3</sup>J<sub>H5'H4'</sub>, <sup>3</sup>J<sub>H5'H6'</sub>, <sup>4</sup>J<sub>H5'H3'</sub> = 6.7, 6.6, 1.3 Hz, H<sub>b5'</sub>), 1.31 (s, 9H, C(CH<sub>3</sub>)<sub>3</sub>). <sup>13</sup>C {<sup>1</sup>H} NMR (CDCl<sub>3</sub>, 150.9 MHz): δ 158.94 (C<sub>quat</sub>, C<sub>a2</sub>), 158.86 (C<sub>quat</sub>, C<sub>b2</sub>), 158.32 (C<sub>quat</sub>, C<sub>a2'</sub>), 158.03 (C<sub>quat</sub>, C<sub>c2</sub>), 157.99 (C<sub>quat</sub>, C<sub>c2'</sub>), 157.53 (C<sub>quat</sub>, C<sub>b2'</sub>), 154.98 (C<sub>quat</sub>, C<sub>p</sub>), 153.91 (CH, C<sub>c6'</sub>), 152.67 (CH, C<sub>a6'</sub>), 152.45 (2C, CH, C<sub>b6'</sub>, C<sub>b6</sub>), 152.33 (CH, C<sub>c6</sub>), 149.63 (C<sub>quat</sub>, C<sub>a6</sub>), 139.13 (CH, C<sub>c4</sub>), 138.98 (CH, C<sub>b4</sub>), 138.95 (CH, C<sub>c4'</sub>), 138.91 (CH, C<sub>a4'</sub>), 138.84 (CH, C<sub>a4</sub>), 137.13 (CH, C<sub>b4'</sub>), 134.48 (CH, C<sub>a5</sub>), 132.45 (CH, C<sub>o</sub>), 128.82 (CH, C<sub>c5</sub>), 128.68 (CH, C<sub>c5'</sub>), 128.39 (CH, C<sub>a5'</sub>), 128.21 (CH, C<sub>b5</sub>), 127.99 (CH, C<sub>b5'</sub>), 126.35 (CH, C<sub>m</sub>), 125.91 (CH, C<sub>a3'</sub>), 125.50 (CH, C<sub>c3'</sub>), 125.38 (CH, C<sub>c3</sub>), 124.95 (CH, C<sub>b3</sub>), 124.59 (CH, C<sub>b3'</sub>), 124.34 (CH, C<sub>a3</sub>), 118.4 (C<sub>quat</sub>, C<sub>i</sub>), 99.86 (C<sub>quat</sub>, C≡C, C<sub>β</sub>), 86.05 (C<sub>quat</sub>, C≡C, C<sub>α</sub>), 35.64 (C<sub>quat</sub>, C(CH<sub>3</sub>)<sub>3</sub>), 31.28 (3C, C(CH<sub>3</sub>)<sub>3</sub>). **MS** (*m/z*-ES-MS, CH<sub>3</sub>CN): Found 363.1022 (100 %): [M-2(PF<sub>6</sub>)]<sup>2+</sup>, calculated for [C<sub>42</sub>H<sub>36</sub>N<sub>6</sub>Ru]<sup>2+</sup>: 363.1023; Found 871.1414 (25 %): [M-(PF<sub>6</sub>)]<sup>+</sup>, calculated for [C<sub>42</sub>H<sub>36</sub>N<sub>6</sub>F<sub>6</sub>RuP]<sup>+</sup>:

871.1426. **Anal. Calcd.** For  $C_{42}H_{36}N_6F_{12}RuP_2 \cdot \frac{1}{2}(C_2H_6O_2)$ : C, 49.34; H, 3.76; N, 8.03. Found: C, 49.30; H, 3.44; N, 7.82. **IR**  $\nu$  ( $cm^{-1}$ ): 3088 (w), 2966 (m), 2878 (w), 2210 (m,  $C\equiv C$ ), 2188 (w, sh), 1604 (m), 1553 (m), 1509 (w), 1460 (m), 1449 (s), 1428 (m), 1389 (m), 1268 (w), 1229 (m), 1107 (m), 829 (s, br), 760 (s), 728 (m).

**[Ru(bpy)<sub>2</sub>(6-(4-trifluoromethyl-phenylethynyl)-2,2'-bpy)](PF<sub>6</sub>)<sub>2</sub> (34)**

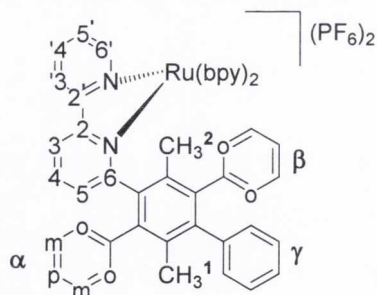


6-(4-trifluoromethyl-phenylethynyl)-2,2'-bipyridine (**2**) (100.3 mg; 0.308 mmol) was sonicated in ethylene glycol (8 mL) for 10 minutes. The suspension was degassed *via* argon bubbling for 20 minutes. *cis*-Ru(bpy)<sub>2</sub>Cl<sub>2</sub> (142.3 mg; 0.294 mmol) was added to the flask and the reaction mixture was heated at 110-130 °C under argon for 25 hours. A colour change from purple to red/orange was observed after 1 hour heating. Excess saturated KPF<sub>6</sub> solution (~15 mL) was added to the reaction mixture with stirring. The bright orange solid obtained was filtered off and washed with water (2x25 mL) and diethyl ether (~5 mL).

The product was purified *via* column chromatography on silica using acetonitrile:saturated KNO<sub>3</sub> solution:water (10:0.5:1.5 v/v) as the solvent system. The solvent was removed *in vacuo* and the residue was redissolved in CH<sub>2</sub>Cl<sub>2</sub> (~100 mL) and was washed with water (3x100 mL) in order to removed excess nitrate salt. The solvent was removed from the organic layer *in vacuo* and ethylene glycol (~0.5 mL) was added to the flask. Excess saturated KPF<sub>6</sub> solution (~20 mL) was added to the flask with stirring. The orange powdery product was filtered off, washed with water (2x25 mL) and diethyl ether (~10 mL). (267 mg; 0.260 mmol; 89 %). **m.p.** >260 °C (decomp.) **<sup>1</sup>H NMR** (CDCl<sub>3</sub>, 600.1 MHz):  $\delta$  8.50-8.55 (m, 3H, H<sub>a3'</sub>, H<sub>a3</sub>, H<sub>c3'</sub>), 8.48 (d, 1H, <sup>3</sup>J<sub>H3H4</sub> = 8.3 Hz, H<sub>b3</sub>), 8.45 (d, 1H, <sup>3</sup>J<sub>H3H4</sub> = 7.9 Hz, H<sub>c3</sub>), 8.05-8.15 (m, 6H, H<sub>c4'</sub>, H<sub>c6'</sub>, H<sub>b3'</sub>, H<sub>b4</sub>, H<sub>a4</sub>, H<sub>a4'</sub>), 8.01 (ddd, 1H, <sup>3</sup>J<sub>H4H3/H5</sub>, <sup>4</sup>J<sub>H4H6</sub> = 7.7, 1.5 Hz, H<sub>c4</sub>), 7.73 (dd, 1H, <sup>3</sup>J<sub>H5H4</sub>, <sup>4</sup>J<sub>H5H3</sub> = 7.9, 1.1 Hz, H<sub>a5</sub>), 7.64-7.66 (m, 2H, H<sub>b6'</sub>, H<sub>b6</sub>), 7.61 (d, 2H, <sup>3</sup>J<sub>HmH0</sub> = 8.3 Hz, H<sub>m</sub>), 7.58 (d, 1H, <sup>3</sup>J<sub>H6'H5'</sub> = 5.7 Hz, H<sub>a6'</sub>), 7.51-7.54 (m, 2H, H<sub>c6</sub>, H<sub>c5'</sub>), 7.42 (ddd, 1H, <sup>3</sup>J<sub>H5H4</sub>, <sup>3</sup>J<sub>H5H6</sub>, <sup>4</sup>J<sub>H5H3</sub> = 7.5, 5.6, 1.1 Hz, H<sub>b5</sub>), 7.37 (ddd, 1H, <sup>3</sup>J<sub>H5'H4'</sub>, <sup>3</sup>J<sub>H5'H6'</sub>, <sup>4</sup>J<sub>H5'H3'</sub> = 6.8, 6.6, 1.1 Hz, H<sub>a5'</sub>), 7.30 (ddd, 1H,

$^3J_{H_5H_4}$ ,  $^3J_{H_5H_6}$ ,  $^4J_{H_5H_3} = 6.8, 6.4, 1.1$  Hz,  $H_{c5}$ ), 7.27 (ddd, 1H,  $^3J_{H_4'H_3'/H_5'}$ ,  $^4J_{H_4'H_6'} = 7.9, 1.1$  Hz,  $H_{b4'}$ ), 7.20 (d, 2H,  $^3J_{H_0H_m} = 7.9$  Hz,  $H_0$ ), 6.75 (ddd, 1H,  $^3J_{H_5'H_4'}$ ,  $^3J_{H_5'H_6'}$ ,  $^4J_{H_5'H_3'}$  = 7.0, 6.2, 1.1 Hz,  $H_{b5'}$ ).  $^{13}C$  { $^1H$ } NMR ( $CDCl_3$ , 150.9 MHz):  $\delta$  159.12 ( $C_{quat}$ ,  $C_{a2}$ ), 158.69 ( $C_{quat}$ ,  $C_{b2}$ ), 158.10 ( $C_{quat}$ ,  $C_{a2'}$ ), 157.95 ( $C_{quat}$ ,  $C_{c2}$ ), 157.92 ( $C_{quat}$ ,  $C_{c2'}$ ), 157.76 ( $C_{quat}$ ,  $C_{b2'}$ ), 153.86 (CH,  $C_{c6}$ ), 152.63 (CH,  $C_{a6}$ ), 152.58 (CH,  $C_{b6}$ ), 152.45 (CH,  $C_{b6}$ ), 152.30 (CH,  $C_{c6}$ ), 148.90 ( $C_{quat}$ ,  $C_{a6}$ ), 139.18 (CH,  $C_{c4}$ ), 139.01 (CH, 3C,  $C_{a4}$ ,  $C_{c4'}$ ,  $C_{b4}$ ), 138.87 (CH,  $C_{a4'}$ ), 137.51 (CH,  $C_{b4'}$ ), 134.76 (CH,  $C_{a5}$ ), 133.23 (CH,  $C_0$ ), 131.80 (q,  $^2J_{CF} = 32$  Hz,  $C_{quat}$ ,  $C_p$ ), 128.82 (CH,  $C_{c5}$ ), 128.69 (CH,  $C_{c5'}$ ), 128.47 (CH,  $C_{a5'}$ ), 128.29 (CH,  $C_{b5}$ ), 128.06 (CH,  $C_{b5'}$ ), 126.25 (q,  $^3J_{CF} = 3$  Hz, CH,  $C_m$ ), 125.97 (CH,  $C_{a3'}$ ), 125.50 (CH,  $C_{c3'}$ ), 125.37 (CH,  $C_{c3}$ ), 125.03 (CH,  $C_{b3}$ ), 125.00 ( $C_{quat}$ ,  $C_i$ ), 124.77 (CH,  $C_{a3}$ ), 124.65 (CH,  $C_{b3'}$ ), 124.90 (q,  $^1J_{CF} = 286$  Hz,  $CF_3$ ), 97.31 ( $C_{quat}$ ,  $C\equiv C$ ,  $C_\beta$ ), 88.05 ( $C_{quat}$ ,  $C\equiv C$ ,  $C_\alpha$ ).  $^{19}F$  NMR ( $CDCl_3$ , 376.6 MHz):  $\delta$  -63.5 ( $CF_3$ ), -72.9 ( $^1J_{PF} = 704$  Hz,  $PF_6$ ). **MS** ( $m/z$ -ES-MS,  $CH_3CN$ ): Found 369.0065 (100 %)  $[M-2(PF_6)]^{2+}$ , calculated for  $[C_{39}H_{27}N_6F_3Ru]^{2+}$ : 369.0089. Found: 883.0941 (32 %)  $[M-(PF_6)]^+$ , calculated for  $[C_{39}H_{27}N_6F_9RuP]^+$ : 883.0935. **Anal. Calcd.** For  $C_{39}H_{27}N_6RuF_{15}P_2 \cdot (H_2O)$ : C, 44.80; H, 2.80; N, 8.04. Found: C, 44.82; H, 2.46; N, 7.88. **IR**  $\nu$  ( $cm^{-1}$ ): 3667 (m), 3599 (w), 3089 (m), 2964 (m), 2916 (m), 2194 (w,  $C\equiv C$ ), 1605 (m), 1561 (m), 1469 (m), 1447 (m), 1322 (s), 1242 (w), 1167 (m), 1112 (m), 1068 (m), 1015 (m), 834(s, br), 764 (s), 730 (m).

**[Ru(bpy)<sub>2</sub>(6-(3,6-dimethyl-2,4,5-triphenyl benz-1-ene)-2,2'-bpy)](PF<sub>6</sub>)<sub>2</sub> (35)**

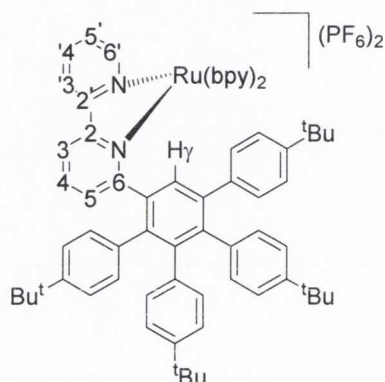


6-(3,6-dimethyl-2,4,5-triphenylbenzene)-2,2'-bipyridine (**3**) (98.6 mg; 0.202 mmol) was sonicated in ethylene glycol (~8 mL) for 10 minutes and was degassed *via* argon bubbling for 10 minutes. *cis*-Ru(bpy)<sub>2</sub>Cl<sub>2</sub> (93.1 mg; 0.192 mmol) was added to the flask and the reaction mixture was heated to 110-130 °C under argon for 24 hours. The orange/red solution was cooled and a bright orange precipitate was obtained following precipitation from saturated KPF<sub>6</sub> solution (~20 mL). The precipitate was washed with water (4x75 mL) and diethyl ether (~20 mL).

The product was purified using column chromatography on silica eluting with CH<sub>3</sub>CN:saturated KNO<sub>3</sub> solution:H<sub>2</sub>O (10:0.5:1.5 v/v). The solvent was removed from the product fractions *in vacuo* and the residue redissolved in CH<sub>2</sub>Cl<sub>2</sub> (~100 mL). This was washed with water (2x100 mL) in order to remove excess nitrate salt. The solvent was removed from the organic layer *in vacuo* and the residue was taken up in ethylene glycol (~1 mL) with sonication. Addition of excess saturated KPF<sub>6</sub> solution (~15 mL) with stirring resulted in the precipitation of the desired product as a bright orange powder. This was filtered off and washed with water (3x 25 mL) and diethyl ether (~20 mL). (164 mg; 0.138 mmol; 72 %). **m.p.** >225 °C (decomp.) **<sup>1</sup>H NMR** (CDCl<sub>3</sub>, 600.1 MHz): δ 8.55 (dd, 1H, <sup>3</sup>J<sub>H<sub>3</sub>H<sub>4</sub></sub> = 8.0 Hz, <sup>4</sup>J<sub>H<sub>3</sub>H<sub>5</sub></sub> = 1.5 Hz, H<sub>a3</sub>), 8.48 (d, 1H, <sup>3</sup>J<sub>H<sub>3</sub>'H<sub>4</sub>'</sub> = 8.3 Hz, H<sub>a3'</sub>), 8.42 (d, 1H, <sup>3</sup>J<sub>H<sub>3</sub>H<sub>4</sub></sub> = 8.1 Hz, H<sub>b3</sub>), 8.37 (d, 1H, <sup>3</sup>J<sub>H<sub>3</sub>'H<sub>4</sub>'</sub> = 8.2 Hz, H<sub>b3'</sub>), 8.34 (d, 1H, <sup>3</sup>J<sub>H<sub>3</sub>H<sub>4</sub></sub> = 8.0 Hz, H<sub>c3</sub>), 8.29 (d, 1H, <sup>3</sup>J<sub>H<sub>3</sub>H<sub>4</sub></sub> = 8.0 Hz, H<sub>c3'</sub>), 8.12 (dd, 1H, <sup>3</sup>J<sub>H<sub>4</sub>H<sub>3/5</sub></sub> = 7.9 Hz, H<sub>a4</sub>), 8.08 (d, 1H, <sup>3</sup>J<sub>H<sub>6</sub>H<sub>5</sub></sub> = 5.5 Hz, H<sub>b6</sub>), 8.05 (dd, 1H, <sup>3</sup>J<sub>H<sub>4</sub>H<sub>3/5</sub></sub> = 7.7 Hz, H<sub>b4</sub>), 7.93-7.98 (m, 2H, H<sub>a4'</sub>, H<sub>c4</sub>), 7.91 (dd, 1H, <sup>3</sup>J<sub>H<sub>4</sub>H<sub>3/5</sub></sub> = 8.2 Hz, H<sub>c4'</sub>), 7.87 (d, 1H, <sup>3</sup>J<sub>H<sub>6</sub>'H<sub>5</sub>'</sub> = 5.4 Hz, H<sub>b6'</sub>), 7.84 (dd, 1H, <sup>3</sup>J<sub>H<sub>4</sub>H<sub>3/5</sub></sub> = 7.9 Hz, H<sub>b4'</sub>), 7.59 (m, 2H, H<sub>a5</sub>, CHCl<sub>3</sub>), 7.46 (d, 1H, <sup>3</sup>J<sub>H<sub>6</sub>H<sub>5</sub></sub> = 5.3 Hz, H<sub>a6'</sub>), 7.26-7.34 (m, 5H, H<sub>b5</sub>, H<sub>b5'</sub>, H<sup>α</sup><sub>P</sub>, H<sup>β</sup>), 7.20 (m, 3H, H<sub>a5'</sub>, H<sub>c5'</sub>, H<sup>γ</sup>), 7.07-7.16 (m, 6H, H<sup>β</sup>, H<sup>γ</sup>, H<sup>α</sup><sub>o</sub>), 6.96-7.02 (m, 4H, H<sub>c6'</sub>, H<sub>c5</sub>, H<sup>γ</sup>, H<sup>α</sup><sub>m</sub>), 6.89 (d, 1H, <sup>3</sup>J<sub>H<sub>o</sub>H<sub>m</sub></sub> = 7.5 Hz, H<sup>β</sup><sub>o</sub>), 6.86 (d, 1H, <sup>3</sup>J<sub>H<sub>o</sub>H<sub>m</sub></sub> = 7.2 Hz, H<sup>β</sup><sub>o</sub>), 6.66 (d, 1H, <sup>3</sup>J<sub>H<sub>6</sub>H<sub>5</sub></sub> = 5.2 Hz, H<sub>c6</sub>), 6.53 (d, 1H, <sup>3</sup>J<sub>H<sub>o</sub>H<sub>m</sub></sub> = 7.6 Hz, H<sup>α</sup><sub>o</sub>), 1.42 (s, 3H, Me<sup>1</sup>), 0.39 (s, 3H, Me<sup>2</sup>). **<sup>13</sup>C {<sup>1</sup>H} NMR** (CDCl<sub>3</sub>, 150.9 MHz): δ 168.08 (C<sub>quat</sub>, C<sub>a6</sub>), 158.76 (C<sub>quat</sub>, C<sub>a2'</sub>, C<sub>b2'</sub>), 158.71 (C<sub>quat</sub>, C<sub>a2</sub>), 158.40 (C<sub>quat</sub>, C<sub>c2'</sub>), 157.58 (C<sub>quat</sub>, C<sub>c2</sub>), 157.44 (C<sub>quat</sub>, C<sub>b2</sub>), 153.89 (CH, C<sub>b6'</sub>), 153.78 (CH, C<sub>b6</sub>), 153.16 (CH, C<sub>c6</sub>), 152.19 (CH, C<sub>a6'</sub>), 151.07 (CH, C<sub>c6'</sub>), 143.46 (C<sub>quat</sub>, C<sub>phenyl</sub>), 141.55 (C<sub>quat</sub>, C<sub>phenyl</sub>), 140.79 (C<sub>quat</sub>, C<sub>phenyl</sub>), 140.74 (C<sub>quat</sub>, C<sub>phenyl</sub>), 139.64 (C<sub>quat</sub>, C<sub>phenyl</sub>), 139.29 (C<sub>quat</sub>, C<sub>phenyl</sub>), 139.05 (CH, C<sub>c4'</sub>), 138.72 (CH, C<sub>a4'</sub>), 138.61 (CH, C<sub>b4'</sub>), 138.15 (2C, CH, C<sub>b4</sub>, C<sub>quat</sub>), 138.13 (CH, C<sub>c4</sub>), 137.97 (CH, C<sub>a4</sub>), 134.78 (CH, C<sub>a5</sub>), 133.85 (C<sub>quat</sub>, C<sub>phenyl</sub>), 132.96 (CH, C<sub>phenyl</sub>), 132.90 (C<sub>quat</sub>, C<sub>phenyl</sub>), 131.46 (CH, C<sub>phenyl</sub>), 131.43 (CH, C<sup>β</sup><sub>o</sub>), 130.84 (CH, C<sup>α</sup><sub>o</sub>), 130.34 (CH, C<sup>α</sup>), 129.97 (CH, C<sup>α</sup><sub>o</sub>), 129.43 (CH, C<sup>β</sup><sub>o</sub>, C<sub>phenyl</sub>), 128.98 (CH, C<sub>c5</sub>), 128.81 (CH, C<sub>c5'</sub>), 128.79 (CH, C<sub>phenyl</sub>), 128.73 (CH, C<sub>phenyl</sub>), 128.55 (CH, C<sub>phenyl</sub>), 128.46 (CH, C<sub>phenyl</sub>), 128.34 (CH, C<sub>b5'</sub>), 128.17 (CH, C<sub>a5'</sub>), 127.42 (CH, C<sup>α</sup>), 127.28 (CH, C<sup>α</sup>), 126.63 (CH, C<sub>b5</sub>), 125.86 (CH, C<sub>a3'</sub>), 125.74 (CH, C<sub>b3'</sub>), 125.23 (CH, C<sub>c3</sub>), 124.94 (CH, C<sub>c3'</sub>), 124.86 (CH, C<sub>a3</sub>), 124.61 (CH, C<sub>b3</sub>), 20.42 (CH<sub>3</sub>, Me<sup>1</sup>), 18.37 (CH<sub>3</sub>, Me<sup>2</sup>). **MS** (*m/z*-ES-MS, CH<sub>3</sub>CN): Found: 451.1345 (100 %) [M-2(PF<sub>6</sub>)]<sup>2+</sup>, calculated for [C<sub>56</sub>H<sub>44</sub>N<sub>6</sub>Ru]<sup>2+</sup>: 451.1336. Found: 1047.2273 (25 %) [M-(PF<sub>6</sub>)]<sup>+</sup>, calculated for [C<sub>56</sub>H<sub>44</sub>N<sub>6</sub>F<sub>6</sub>PRu]<sup>+</sup>: 1047.2313. **Anal. Calcd.**

For  $C_{56}H_{44}N_6F_{12}P_2Ru \cdot 2(H_2O)$ : C, 54.77; H, 3.94; N, 6.84. Found: C, 54.90; H, 3.61; N, 6.57. **IR**  $\nu$  ( $cm^{-1}$ ): 3668 (w), 3074 (br, s), 2975 (m), 2927 (s), 1746 (m), 1600 (m), 1557 (m), 1493 (m), 1466 (s), 1446 (s), 1425 (m), 1382 (m), 1264 (m), 1217 (m), 1160 (w), 1072 (m), 1027 (m), 985 (w), 835 (s, br), 763 (s), 742 (m), 702 (m).

**[Ru(bpy)<sub>2</sub>(6-(2,3,4,5-tetra(4-*tert*-butylphenyl)benz-1-ene)-2,2'-bpy)](PF<sub>6</sub>)<sub>2</sub>(36)**



6-(2,3,4,5-tetra(4-*tert*-butylphenyl)benzene)-2,2'-bipyridine (**4**) (84.8 mg; 0.175 mmol) was sonicated in diethylene glycol monoethyl ether (8 mL) for 10 minutes and was then degassed by argon bubbling for 20 minutes. *cis*-Ru(bpy)<sub>2</sub>Cl<sub>2</sub> (140.1 mg; 0.1839 mmol) was added to the flask and the reaction mixture was heated at 170-180 °C for 3 days. By TLC, a trace of Ru(II) starting material was observed to be still present and so ethylene glycol (~1.5 mL) was added to the flask in order to push the reaction to completion. The reaction mixture was heated for a further 24 hours.

Precipitation from saturated KPF<sub>6</sub> solution was unsuccessful. The reaction residue was taken up in CH<sub>2</sub>Cl<sub>2</sub> (100 mL) and washed with water (3x100 mL). The solvent was removed *in vacuo* from the organic layer and was purified *via* column chromatography on silica eluting with CH<sub>3</sub>CN:saturated KNO<sub>3</sub> solution:H<sub>2</sub>O (10:0.5:1.5 v/v). After removal of solvent, the residue was redissolved in CH<sub>2</sub>Cl<sub>2</sub> and washed with water (~100 mL) in order to remove excess nitrate salt. Ethylene glycol (~1 mL) was added to the flask and the mixture was sonicated and heated until the product was in solution. The addition of excess saturated KPF<sub>6</sub> solution (~20 mL) to the flask produced the desired product as a fine orange precipitate. This was filtered off and washed with water (2x25 mL) and diethyl ether (~20 mL). (80 mg; 0.055 mmol; 31 %). **m.p.** >280 °C (decomp.) **<sup>1</sup>H NMR** (CDCl<sub>3</sub>, 600.1 MHz):  $\delta$  8.66 (d, 1H, <sup>3</sup>*J*<sub>HH</sub> = 7.9 Hz, H<sub>phenyl</sub>), 8.60 (d, 1H, <sup>3</sup>*J*<sub>HH</sub> = 8.3 Hz, H<sub>phenyl</sub>), 8.54 (d, 1H, <sup>3</sup>*J*<sub>HH</sub> = 5.4 Hz, H<sub>phenyl</sub>), 8.51 (d, 1H, <sup>3</sup>*J*<sub>H3'H4'</sub> = 8.3 Hz, H<sub>a3'</sub>), 8.47 (dd, 1H, <sup>3</sup>*J*<sub>H3H4</sub>, <sup>4</sup>*J*<sub>H3H5</sub> = 7.9, 1.1 Hz, H<sub>a3</sub>), 8.42 (d, 1H, <sup>3</sup>*J*<sub>H3'H4'</sub> = 7.9 Hz, H<sub>b3'</sub>), 8.30 (d, 1H, <sup>3</sup>*J*<sub>H3H4</sub> =



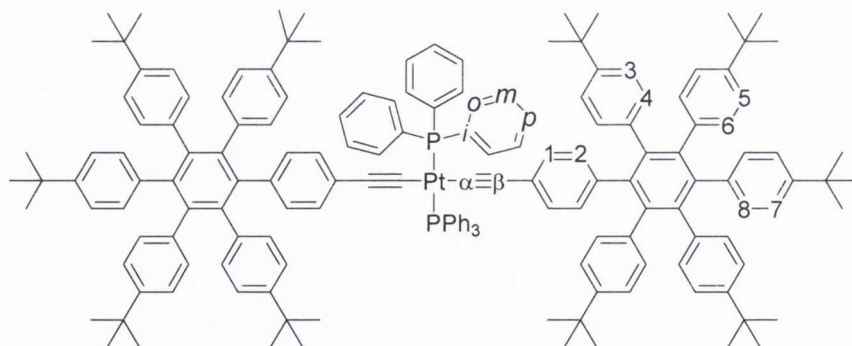
7.9 Hz, H<sub>b3</sub>), 8.24-8.28 (m, 1H, H<sub>phenyl</sub>), 8.12 (ddd, 1H,  $^3J_{H4'H3'/5'}$ ,  $^4J_{H4'H6'}$  = 7.9, 1.1 Hz, H<sub>b4'</sub>), 8.08 (m, 1H, H<sub>phenyl</sub>), 8.03 (m, 2H, H<sub>a4'</sub>, H<sub>c6</sub>), 7.98 (d, 1H,  $^3J_{H3H4}$  = 7.9 Hz, H<sub>c3</sub>), 7.86-7.93 (m, 3H, H<sub>b4</sub>, H<sub>c4</sub>, H<sub>c6'</sub>), 7.84 (dd, 1H,  $^3J_{H4H5/3}$  = 7.9 Hz, H<sub>a4</sub>), 7.76-7.81 (m, 1H, H<sub>phenyl</sub>), 7.66 (d, 1H,  $^3J_{H6'H5'}$  = 4.9 Hz, H<sub>a6'</sub>), 7.54-7.58 (m, 1H, H<sub>phenyl</sub>), 7.41 (dd, 1H,  $^3J_{H5'H4'/6'}$  = 6.6 Hz, H<sub>b5'</sub>), 7.29-7.33 (m, 2H, H<sub>c5</sub>, H<sub>a5'</sub>), 7.20-7.25 (m, 6H, H<sub>b6'</sub>, H<sub>c5'</sub>, H<sub>c4'</sub>, H<sub>b5</sub>, H<sub>phenyl</sub>), 7.16 (d, 1H,  $^3J_{HH}$  = 8.3 Hz, H<sub>phenyl</sub>), 7.12 (m, 3H, H<sub>b6</sub>, H<sub>a5</sub>, H<sub>c3'</sub>), 6.94-7.01 (m, 4H, H<sub>phenyl</sub>), 6.72-6.88 (m, 6H, H<sub>phenyl</sub>), 6.63 (d, 2H,  $^3J_{HH}$  = 8.7 Hz, H<sub>phenyl</sub>), 6.50 (br, 1H, H<sub>phenyl</sub>), 6.49 (d, 1H,  $^3J_{HH}$  = 7.9 Hz, H<sub>phenyl</sub>), 6.44 (d, 1H,  $^3J_{HH}$  = 7.9 Hz, H<sub>phenyl</sub>), 6.34 (dd, 1H,  $^3J_{HH}$ ,  $^4J_{HH}$  = 7.9, 1.9 Hz, H<sub>phenyl</sub>), 5.65 (s, 1H, H<sub>γ</sub>), 1.37 (s, 9H, C(CH<sub>3</sub>)<sub>3</sub>), 1.20 (s, 9H, C(CH<sub>3</sub>)<sub>3</sub>), 1.16 (s, 9H, C(CH<sub>3</sub>)<sub>3</sub>), 1.06 (s, 9H, C(CH<sub>3</sub>)<sub>3</sub>). **<sup>13</sup>C {<sup>1</sup>H} NMR** (CDCl<sub>3</sub>, 150.9 MHz): δ 167.92 (C<sub>quat</sub>, C<sub>a6</sub>), 158.82 (C<sub>quat</sub>, C<sub>a2'</sub>), 158.65 (C<sub>quat</sub>, C<sub>a2</sub>), 158.35 (C<sub>quat</sub>, C<sub>b2</sub>), 158.23 (C<sub>quat</sub>, C<sub>b2'</sub>), 157.76 (C<sub>quat</sub>, C<sub>c2'</sub>), 157.72 (C<sub>quat</sub>, C<sub>c2</sub>), 153.46 (CH, C<sub>b6'</sub>), 153.25 (CH, C<sub>c6'</sub>), 152.90 (CH, C<sub>c6</sub>), 152.46 (CH, C<sub>a6'</sub>), 151.27 (CH, C<sub>b6</sub>), 151.11 (C<sub>quat</sub>, C<sub>phenyl</sub>), 150.76 (C<sub>quat</sub>, C<sub>phenyl</sub>), 150.17 (C<sub>quat</sub>, C<sub>phenyl</sub>), 149.30 (C<sub>quat</sub>, C<sub>phenyl</sub>), 143.68 (C<sub>quat</sub>, C<sub>phenyl</sub>), 141.41 (C<sub>quat</sub>, C<sub>phenyl</sub>), 139.61 (C<sub>quat</sub>, C<sub>phenyl</sub>), 139.21 (CH, C<sub>b4'</sub>), 139.06 (C<sub>quat</sub>, C<sub>phenyl</sub>), 139.00 (CH, C<sub>b4</sub>), 138.91 (CH, C<sub>a4'</sub>), 138.60 (C<sub>quat</sub>, C<sub>phenyl</sub>), 137.90 (C<sub>quat</sub>, C<sub>phenyl</sub>), 137.65 (C<sub>quat</sub>, C<sub>phenyl</sub>), 137.50 (CH, C<sub>a4</sub>), 137.44 (CH, C<sub>c4</sub>), 137.40 (CH, C<sub>c4'</sub>), 136.82 (C<sub>quat</sub>, C<sub>phenyl</sub>), 133.42 (CH, C<sub>a5</sub>), 133.12 (C<sub>quat</sub>), 131.92 (CH, C<sub>phenyl</sub>), 131.76 (CH, C<sub>phenyl</sub>), 131.32 (CH, C<sub>phenyl</sub>), 131.22 (CH, C<sub>phenyl</sub>), 131.02 (CH, C<sub>γ</sub>), 130.30 (CH, C<sub>phenyl</sub>), 129.92 (CH, C<sub>phenyl</sub>), 128.95 (CH, C<sub>b5</sub>), 128.33 (CH, C<sub>b5'</sub>), 128.11 (CH, C<sub>a5'</sub>), 127.25 (CH, C<sub>c5'</sub>), 127.13 (CH, C<sub>c5</sub>), 125.86 (CH, C<sub>phenyl</sub>), 125.80 (CH, C<sub>phenyl</sub>), 125.68 (CH, C<sub>a3'</sub>), 125.36 (CH, C<sub>b3'</sub>), 124.88 (CH, C<sub>phenyl</sub>), 124.79 (CH, C<sub>b3</sub>), 124.48 (CH, C<sub>phenyl</sub>), 124.34 (CH, C<sub>phenyl</sub>), 124.24 (CH, C<sub>c3'</sub>), 124.04 (CH, C<sub>c3</sub>, C<sub>a3</sub>, C<sub>phenyl</sub>), 35.13 (C<sub>quat</sub>, C(CH<sub>3</sub>)<sub>3</sub>), 34.97 (C<sub>quat</sub>, C(CH<sub>3</sub>)<sub>3</sub>), 34.87 (C<sub>quat</sub>, C(CH<sub>3</sub>)<sub>3</sub>), 34.67 (C<sub>quat</sub>, C(CH<sub>3</sub>)<sub>3</sub>), 31.63 (3C, C(CH<sub>3</sub>)<sub>3</sub>), 31.46 (3C, C(CH<sub>3</sub>)<sub>3</sub>), 31.43 (3C, C(CH<sub>3</sub>)<sub>3</sub>), 31.36 (3C, C(CH<sub>3</sub>)<sub>3</sub>). **MS** (*m/z*-ES-MS, CH<sub>3</sub>CN): Found: 587.2565 (100 %) [M-2(PF<sub>6</sub>)]<sup>2+</sup>, calculated for [C<sub>76</sub>H<sub>76</sub>N<sub>6</sub>Ru]<sup>2+</sup>: 587.2588. Found: 1319.4418 (10 %) [M-(PF<sub>6</sub>)]<sup>+</sup>, calculated for [C<sub>76</sub>H<sub>76</sub>N<sub>6</sub>F<sub>6</sub>PRu]<sup>+</sup>: 1319.4775. **Anal. Calcd.** For C<sub>76</sub>H<sub>76</sub>N<sub>6</sub>F<sub>12</sub>P<sub>2</sub>Ru.(H<sub>2</sub>O): C, 61.57; H, 5.30; N, 5.67. Found: C, 61.24; H, 5.12; N, 5.39. **IR** ν (cm<sup>-1</sup>): 2958 (m), 2898 (w), 2859 (w), 1602 (m), 1562 (w), 1513 (m), 1468 (s), 1445 (s), 1397 (m), 1364 (m), 1271 (s), 1226 (w), 1123 (m, br), 1018 (m), 831 (s, br), 762 (s), 734 (m).

## 5.4 *Cis* & *Trans* Pt(II) Complexes

**General Synthetic Procedure:** synthesis of *trans*-[Pt(C≡C-HPB)<sub>2</sub>(PPh<sub>3</sub>)<sub>2</sub>] (**38**), *cis*-[Pt(C≡C-HPB)<sub>2</sub>(dppe)] (**39**), *trans*-[Pt(C≡C-HBC)<sub>2</sub>(PPh<sub>3</sub>)<sub>2</sub>] (**40**) and *cis*-[Pt(C≡C-HBC)<sub>2</sub>(dppe)] (**41**)

A solution of still-dried CH<sub>2</sub>Cl<sub>2</sub>:<sup>1</sup>Pr<sub>2</sub>NH was degassed *via* freeze-pump-thaw and transferred *via* cannula to a dry Schlenk flask containing the appropriate platinum(II) chloride precursor, polyaromatic acetylene and CuI as catalyst. The solution was stirred in the dark at room temperature under argon over several days. When the reaction was complete, the solvent was removed *in vacuo* and the residue was redissolved in CH<sub>2</sub>Cl<sub>2</sub>/CHCl<sub>3</sub> and washed with water (x3). The organic layer was dried over MgSO<sub>4</sub> and the solvent removed to dryness. The complexes *trans*-[Pt(C≡C-HPB)<sub>2</sub>(PPh<sub>3</sub>)<sub>2</sub>] (**38**), *cis*-[Pt(C≡C-HPB)<sub>2</sub>(dppe)] (**39**) and *trans*-[Pt(C≡C-HBC)<sub>2</sub>(PPh<sub>3</sub>)<sub>2</sub>] (**40**) were purified by column chromatography on silica and were subsequently filtered off following precipitation from methanol. *cis*-[Pt(C≡C-HBC)<sub>2</sub>(dppe)] (**41**) was obtained as a pure solid by precipitation from methanol.

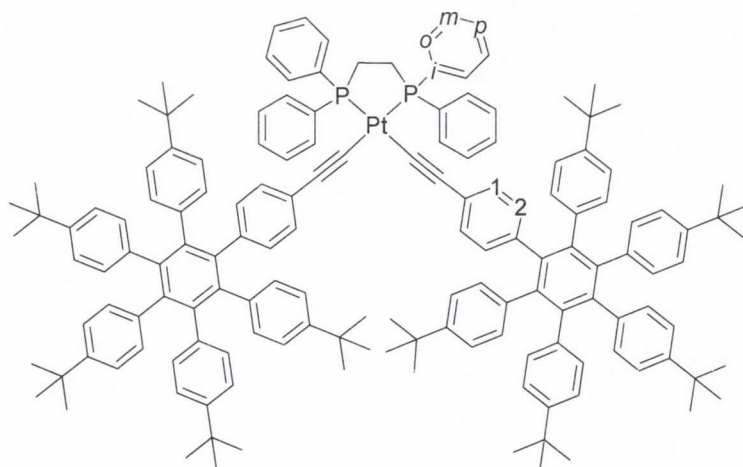
### *trans*-[Pt(C≡C-HPB)<sub>2</sub>(PPh<sub>3</sub>)<sub>2</sub>] (**38**)



*trans*-[Pt(C≡C-HPB)<sub>2</sub>(PPh<sub>3</sub>)<sub>2</sub>] (**38**) was prepared using the general synthetic procedure from ethynyl-hexaphenylbenzene (**6**) (100.3 mg, 0.120 mmol), *cis*-PtCl<sub>2</sub>(PPh<sub>3</sub>)<sub>2</sub> (46.6 mg, 0.059 mmol) and CuI (0.8 mg, 7 mol%) in still-dried CH<sub>2</sub>Cl<sub>2</sub>:<sup>1</sup>Pr<sub>2</sub>NH (~5:1 v/v, 20 mL:4 mL) under argon for 36 hours. Following washing, column chromatography on silica was performed eluting with hexane:CH<sub>2</sub>Cl<sub>2</sub> (2:1 v/v). After removal of solvent, the residue was taken up in minimum CH<sub>2</sub>Cl<sub>2</sub> (~0.5 mL) and was precipitated from a stirring excess of methanol (~30 mL). Filtration yielded the desired product as an off-white powder. (80 mg, 0.033 mmol, 57 %). **m.p.** >280 °C (decomp.) <sup>1</sup>H NMR (CDCl<sub>3</sub>, 600.1 MHz): δ 7.65

(m, 12H, H<sub>0</sub>), 7.21 (t, 6H,  $^3J_{\text{HH}} = 7.3$  Hz, H<sub>p</sub>), 7.14 (t, 12H,  $^3J_{\text{HH}} = 7.3$  Hz, H<sub>m</sub>), 6.79 (m, 12H, H<sup>3</sup>, H<sup>7</sup>), 6.75 (d, 8H,  $^3J_{\text{HH}} = 8.2$  Hz, H<sup>5</sup>), 6.64 (d, 4H,  $^3J_{\text{HH}} = 8.2$  Hz, H<sup>8</sup>), 6.62 (d, 8H,  $^3J_{\text{HH}} = 8.2$  Hz, H<sup>4</sup>), 6.58 (d, 8H,  $^3J_{\text{HH}} = 8.2$  Hz, H<sup>6</sup>), 6.42 (d, 4H,  $^3J_{\text{HH}} = 8.1$  Hz, H<sup>2</sup>), 5.76 (d, 4H,  $^3J_{\text{HH}} = 8.1$  Hz, H<sup>1</sup>), 1.10 (s, 36H, C(CH<sub>3</sub>)<sub>3</sub>), 1.08 (s, 54H, C(CH<sub>3</sub>)<sub>3</sub>).  $^{13}\text{C}$  { $^1\text{H}$ } NMR (CDCl<sub>3</sub>, 150.9 MHz):  $\delta$  147.31 (C<sub>quat</sub>), 147.25 (C<sub>quat</sub>), 147.16 (C<sub>quat</sub>), 140.61 (C<sub>quat</sub>), 140.09 (C<sub>quat</sub>), 140.06 (C<sub>quat</sub>), 139.66 (C<sub>quat</sub>), 138.04 (C<sub>quat</sub>), 137.98 (C<sub>quat</sub>), 137.23 (C<sub>quat</sub>), 134.96 (pt, 12C,  $J_{\text{PC}} = 7$  Hz, CH, C<sub>0</sub>), 131.37 (m, 6C, C<sub>quat</sub>, C<sub>i</sub>), 131.18 (s, 8C, CH, C<sup>4</sup>), 131.06 (s, 4C, CH, C<sup>8</sup>), 131.01 (s, 8C, CH, C<sup>6</sup>), 130.29 (s, 4C, CH, C<sup>2</sup>), 129.97 (s, 12C, CH, C<sub>p</sub>), 129.94 (s, 4C, CH, C<sup>1</sup>), 127.61 (pt, 12C,  $J_{\text{PC}} = 6$  Hz, CH, C<sub>m</sub>), 124.80 (C<sub>quat</sub>), 123.00 (s, 8C, CH, C<sup>3</sup>), 122.97 (s, 4C, CH, C<sup>7</sup>), 122.87 (s, 8C, CH, C<sup>5</sup>), 120.71 (C<sub>quat</sub>), 114.08 (2C, C<sub>quat</sub>, C <sub>$\beta$</sub> ), 113.42 (2C, C<sub>quat</sub>, C <sub>$\alpha$</sub> ), 34.06 (4C, C<sub>quat</sub>), 34.02 (2C, C<sub>quat</sub>), 33.99 (4C, C<sub>quat</sub>), 31.27 (s, 12C, C(CH<sub>3</sub>)<sub>3</sub>), 31.19 (s, 18C, C(CH<sub>3</sub>)<sub>3</sub>).  $^{31}\text{P}$  { $^1\text{H}$ } NMR (CDCl<sub>3</sub>, 162 MHz):  $\delta$  19.3 ( $^1J_{\text{PPT}} = 2657$  Hz, PPh<sub>3</sub>). MS (*m/z*-MALDI-TOF, CHCl<sub>3</sub>): Found: 2394.2241 [M]<sup>+</sup>, calculated for [C<sub>164</sub>H<sub>168</sub>P<sub>2</sub>Pt]<sup>+</sup>: 2394.2269. Anal. Calcd. For C<sub>164</sub>H<sub>168</sub>P<sub>2</sub>Pt·CH<sub>3</sub>OH: C, 81.62; H, 7.14. Found: C, 81.33; H, 7.31. IR  $\nu$  (cm<sup>-1</sup>): 2960 (s), 2897 (m), 2863 (m), 2110 (m, C≡C), 1508 (m), 1475 (m), 1460 (m), 1439 (m), 1393 (m), 1363 (s), 1270 (s), 1200 (w), 1147 (w), 1120 (w), 1100 (s), 1019 (s), 858 (m), 831 (s), 778 (m), 746 (m), 706 (m), 691 (s), 674 (s).

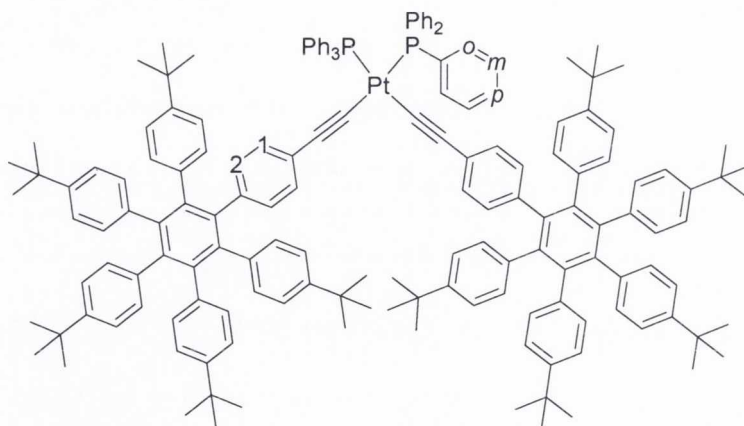
*cis*-[Pt(C≡C-HPB)<sub>2</sub>(dppe)] (39)



*cis*-[Pt(C≡C-HPB)<sub>2</sub>(dppe)] (39) was prepared using the general synthetic procedure from ethynyl-hexaphenylbenzene (6) (100.1 mg, 0.119 mmol), *cis*-PtCl<sub>2</sub>(dppe) (39.1 mg, 0.059 mmol) and CuI (1.0 mg, 8.9 mol%) in still-dried CH<sub>2</sub>Cl<sub>2</sub>:<sup>i</sup>Pr<sub>2</sub>NH (~3:1 v/v, 24 mL:8 mL) under argon for 36 hours. Following washing, column chromatography on silica was

performed eluting using  $\text{CH}_2\text{Cl}_2$ :hexane (1:1 v/v) as solvent system. Removal of solvent yielded the product as a pale yellow solid. (70 mg, 0.031 mmol, 53 %). **m.p.** > 235 °C (decomp.)  **$^1\text{H}$  NMR** ( $\text{CDCl}_3$ , 600.1 MHz):  $\delta$  7.86 (m, 8H,  $\text{H}_o$ ), 7.34 (t, 4H,  $^3J_{\text{HH}} = 7.6$  Hz,  $\text{H}_p$ ), 7.28 (m, 8H,  $\text{H}_m$ ), 6.77 (m, 20H,  $\text{H}_{\text{phenyl}}$ ), 6.67 (d, 4H,  $^3J_{\text{HH}} = 7.9$  Hz,  $\text{H}_{\text{phenyl}}$ ), 6.60-6.64 (m, 20H,  $\text{H}_{\text{phenyl}}$ ,  $\text{H}^2$ ), 6.55 (d, 4H,  $^3J_{\text{HH}} = 8.3$  Hz,  $\text{H}^1$ ), 2.34 (m, 4H,  $\text{CH}_2$ ), 1.09 (m, 90H,  $\text{C}(\text{CH}_3)_3$ ).  **$^{13}\text{C}$   $\{^1\text{H}\}$  NMR** ( $\text{CDCl}_3$ , 150.9 MHz):  $\delta$  147.32 ( $\text{C}_{\text{quat}}$ ), 147.26 ( $\text{C}_{\text{quat}}$ ), 147.16 ( $\text{C}_{\text{quat}}$ ), 140.46 ( $\text{C}_{\text{quat}}$ ), 140.19 ( $\text{C}_{\text{quat}}$ ), 140.14 ( $\text{C}_{\text{quat}}$ ), 139.96 ( $\text{C}_{\text{quat}}$ ), 138.11 ( $\text{C}_{\text{quat}}$ ), 138.08 ( $\text{C}_{\text{quat}}$ ), 137.82 ( $\text{C}_{\text{quat}}$ ), 137.80 ( $\text{C}_{\text{quat}}$ ), 133.49 (pt, 8C,  $J_{\text{PC}} = 6$  Hz, CH,  $\text{C}_o$ ), 131.14 (8C, CH), 131.09 (12C, CH), 130.87 (s, 4C, CH,  $\text{C}_p$ ), 130.64 (s, 4C, CH,  $\text{C}^1$ ), 129.92 (pd, 4C,  $^1J_{\text{PC}} = 54$  Hz,  $\text{C}_{\text{quat}}$ ,  $\text{C}_i$ ), 129.81 (s, 4C, CH,  $\text{C}^2$ ), 128.54 (pt, 8C,  $J_{\text{PC}} = 5$  Hz, CH,  $\text{C}_m$ ), 124.73 ( $\text{C}_{\text{quat}}$ ), 123.10 (8C, CH), 122.96 (4C, CH), 122.90 (8C, CH), 112.98 (2C,  $\text{C}_{\text{quat}}$ ,  $\text{C}\equiv\text{C}$ ), 112.75 (2C,  $\text{C}_{\text{quat}}$ ,  $\text{C}\equiv\text{C}$ ), 34.06 ( $\text{C}_{\text{quat}}$ ), 34.02 ( $\text{C}_{\text{quat}}$ ), 34.01 ( $\text{C}_{\text{quat}}$ ), 31.26 (s, 12C,  $\text{C}(\text{CH}_3)_3$ ), 31.19 (s, 18C,  $\text{C}(\text{CH}_3)_3$ ) 27.76 (m, 2C,  $\text{CH}_2$ ).  **$^{31}\text{P}$   $\{^1\text{H}\}$  NMR** ( $\text{CDCl}_3$ , 162 MHz):  $\delta$  41.3 ( $^1J_{\text{PPt}} = 2279$  Hz,  $\text{PPh}_2$ ). **MS** ( $m/z$ -MALDI-TOF,  $\text{CHCl}_3$ ): Found: 2268.1777  $[\text{M}]^+$ , calculated for  $[\text{C}_{154}\text{H}_{162}\text{P}_2\text{Pt}]^+$ : 2268.1800. **Anal. Calcd.** For  $\text{C}_{154}\text{H}_{162}\text{P}_2\text{Pt}\cdot 2(\text{H}_2\text{O})$ : C, 80.21; H, 7.26. Found: C, 80.30; H, 7.17. **IR**  $\nu$  ( $\text{cm}^{-1}$ ): 2964 (s), 2908 (m), 2870 (m), 2118 (w,  $\text{C}\equiv\text{C}$ ), 2106 (m,  $\text{C}\equiv\text{C}$ ), 1605 (w), 1513 (s), 1476 (m), 1462 (s), 1437 (m), 1393 (s), 1362 (s), 1269 (s), 1202 (m), 1151 (m), 1106 (s), 1017 (s), 861 (m), 832 (s), 780 (m), 744 (m), 706 (m), 689 (s).

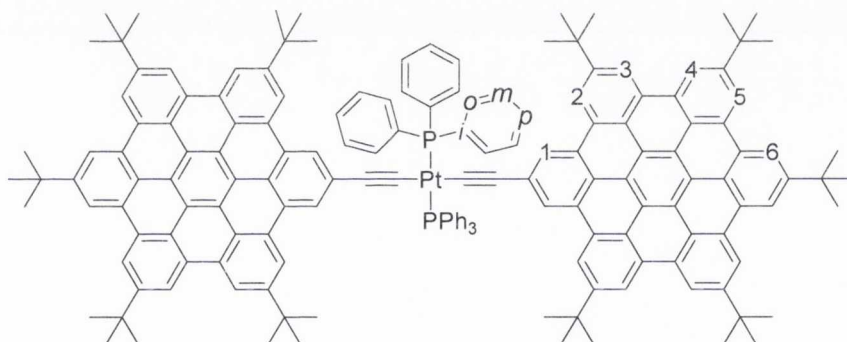
***cis*-[Pt( $\text{C}\equiv\text{C}$ -HPB) $_2$ (PPh $_3$ ) $_2$ ] (42)**



A solution of still-dried  $\text{CH}_2\text{Cl}_2$  (20 mL) was degassed *via* freeze-pump-thaw three times and was transferred *via* cannula to a dry Schlenk flask containing *cis*- $\text{PtCl}_2(\text{PPh}_3)_2$  (41.6 mg; 0.052 mmol), 1-(4-trimethylsilylethynylphenyl)-2,3,4,5,6-penta-(4-*tert*-butylphenyl)benzene (**19**) (100.4 mg; 0.110 mmol) and  $\text{CuI}$  (1.6 mg; 9.6 mol%). A

degassed solution of KF (13.7 mg; 0.236 mmol) in methanol (~5 mL) was added *via* syringe to the reaction mixture and the solution was stirred in the dark at room temperature for 18 hours. When the reaction was complete, the reaction mixture was washed with water (3x40 mL). The organic layer was dried over MgSO<sub>4</sub> and the solvent removed to dryness. The product was purified by column chromatography on silica eluting with petroleum ether:CH<sub>2</sub>Cl<sub>2</sub> (3:2 v/v) and was subsequently filtered off following precipitation from methanol. (10 mg; 0.007 mmol; 15 %). <sup>1</sup>H NMR (CDCl<sub>3</sub>, 400.1 MHz): δ 7.36 (m, 12H, H<sub>o</sub>), 7.11 (t, 6H, <sup>3</sup>J<sub>HH</sub> = 7.5 Hz, H<sub>p</sub>), 6.99 (t, 12H, <sup>3</sup>J<sub>HH</sub> = 7.5 Hz, H<sub>m</sub>), 6.75-6.80 (m, 20H, H<sub>phenyl</sub>), 6.59-6.67 (m, 20H, H<sub>phenyl</sub>), 6.43 (d, 4H, <sup>3</sup>J<sub>HH</sub> = 8.5 Hz, H<sup>2</sup>), 6.14 (d, 4H, <sup>3</sup>J<sub>HH</sub> = 8.5 Hz, H<sup>1</sup>), 1.12 (s, 36H, C(CH<sub>3</sub>)<sub>3</sub>), 1.09 (s, 54H, C(CH<sub>3</sub>)<sub>3</sub>). <sup>31</sup>P {<sup>1</sup>H} NMR (CDCl<sub>3</sub>, 162 MHz): δ 18.0 (<sup>1</sup>J<sub>Pt</sub> = 2318 Hz, PPh<sub>3</sub>). MS (*m/z*-MALDI-TOF, CHCl<sub>3</sub>): Found: 2394.2245 [M]<sup>+</sup>, calculated for [C<sub>164</sub>H<sub>168</sub>P<sub>2</sub>Pt]<sup>+</sup>: 2394.2269.

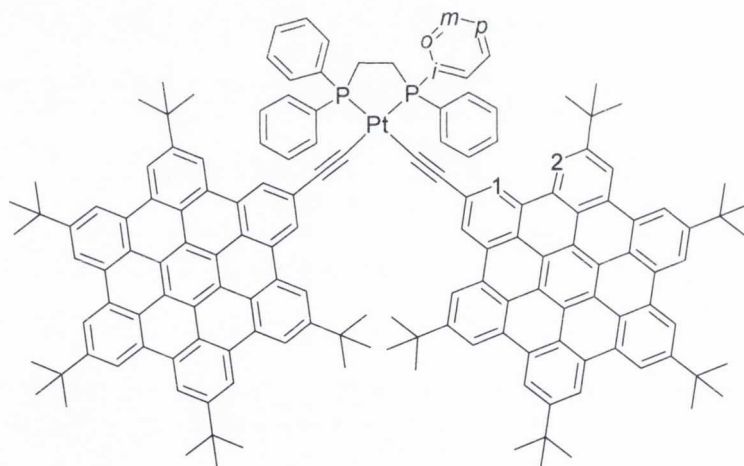
***trans*-[Pt(C≡C-HBC)<sub>2</sub>(PPh<sub>3</sub>)<sub>2</sub>] (40)**



*trans*-[Pt(C≡C-HBC)<sub>2</sub>(PPh<sub>3</sub>)<sub>2</sub>] (40) was prepared using the general synthetic procedure from ethynyl-HBC (7) (100.3 mg, 0.121 mmol), *cis*-PtCl<sub>2</sub>(PPh<sub>3</sub>)<sub>2</sub> (39.9 mg, 0.060 mmol) and CuI (1.1 mg, 10 mol%) in still-dried CH<sub>2</sub>Cl<sub>2</sub>:<sup>1</sup>Pr<sub>2</sub>NH (~2.5:1 v/v, 20 mL:8 mL) under argon over 2 days. Column chromatography on silica was performed eluting first with petroleum ether:chloroform (3:2 v/v) to remove traces of the ethynyl-HBC starting material and gradually changing the solvent system ratio to petroleum ether:chloroform (1:2 v/v) to elute the product. After removal of solvent *in vacuo*, the oily product was taken up in minimum CH<sub>2</sub>Cl<sub>2</sub> (~0.5 mL) and precipitated using excess methanol (~50 mL). Filtration yielded the product as a deep yellow powder. (101 mg, 0.043 mmol, 71 %). **m.p.** > 360 °C. <sup>1</sup>H NMR (CDCl<sub>3</sub>, 600.1 MHz): δ 9.28-9.31 (m, 16H, H<sup>3</sup>, H<sup>4</sup>, H<sup>5</sup>, H<sup>6</sup>), 8.93 (s, 4H, H<sup>2</sup>), 8.40 (s, 4H, H<sup>1</sup>), 8.18 (m, 12H, H<sub>o</sub>), 7.52 (t, 12H, <sup>3</sup>J<sub>HH</sub> = 7.5 Hz, H<sub>m</sub>), 7.44 (t, 6H, <sup>3</sup>J<sub>HH</sub> = 7.5 Hz, H<sub>p</sub>), 1.83 (s, 54H, C(CH<sub>3</sub>)<sub>3</sub>), 1.79 (s, 36H, C(CH<sub>3</sub>)<sub>3</sub>). <sup>13</sup>C {<sup>1</sup>H} NMR (CDCl<sub>3</sub>, 100.6 MHz): δ 148.99 (C<sub>quat</sub>), 148.94 (C<sub>quat</sub>), 135.45 (pt, 12C, J<sub>PC</sub> = 6 Hz, CH,

$C_o$ ), 131.27 (pt, 6C, AXX',  $^1J_{PC}$  and  $^3J_{PC} = 29$  Hz,  $C_{quat}$ ,  $C_i$ ), 130.68 (s, 6C, CH,  $C_p$ ), 130.53 (m,  $C_{quat}$ ), 130.30 ( $C_{quat}$ ), 130.27 ( $C_{quat}$ ), 130.01 ( $C_{quat}$ ), 128.07 (pt, 12C,  $J_{PC} = 5$  Hz, CH,  $C_m$ ), 126.76 ( $C_{quat}$ ), 124.62 (s, 4C, CH,  $C^2$ ), 124.05 ( $C_{quat}$ ), 123.99 ( $C_{quat}$ ), 123.87 ( $C_{quat}$ ), 123.62 ( $C_{quat}$ ), 120.75 ( $C_{quat}$ ), 120.52 ( $C_{quat}$ ), 120.43 ( $C_{quat}$ ), 120.41 ( $C_{quat}$ ), 119.29 (s, 4C, CH,  $C^1$ ), 118.90 (s, 12C, CH,  $C_{HBC}$ ), 118.63 (s, 4C, CH,  $C_{HBC}$ ), 115.41 (2C,  $C_{quat}$ ,  $C\equiv C$ ), 113.74 (2C,  $C_{quat}$ ,  $C\equiv C$ ), 35.79 (4C,  $C_{quat}$ ,  $C(CH_3)_3$ ), 35.75 (6C,  $C_{quat}$ ,  $C(CH_3)_3$ ), 32.13 (s, 12C,  $C(CH_3)_3$ ), 32.04 (s, 18C,  $C(CH_3)_3$ ).  $^{31}P \{^1H\}$  NMR ( $CDCl_3$ , 162 MHz):  $\delta$  19.0 ( $^1J_{PPt} = 2625$  Hz,  $PPh_3$ ). **MS** ( $m/z$ -MALDI-TOF, THF): Found: 2371.0386  $[M+H]^+$ , calculated for  $[C_{164}H_{145}P_2Pt]^+$ : 2371.0469. **Anal. Calcd.** For  $C_{164}H_{144}P_2Pt \cdot 2(CH_3OH)$ : C, 81.85; H, 6.29. Found: C, 82.00; H, 6.28. **IR**  $\nu$  ( $cm^{-1}$ ): 2965 (s), 2905 (m), 2871 (m), 2093 (m,  $C\equiv C$ ), 1606 (m), 1572 (m), 1470 (m), 1437 (m), 1370 (m, br), 1307 (w), 1260 (w), 1157 (s), 1129 (s), 1100 (s), 950 (s), 868 (s), 819 (s), 749 (s), 708 (s), 689 (s).

***cis*-[Pt( $C\equiv C$ -HBC) $_2$ (dppe)] (41)**

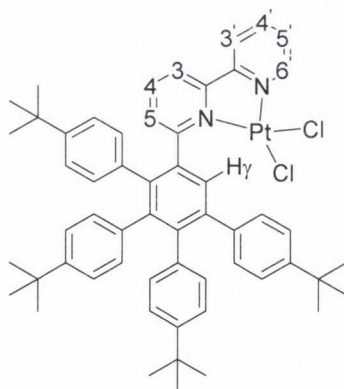


*cis*-[Pt( $C\equiv C$ -HBC) $_2$ (dppe)] (**41**) was prepared using the general synthetic procedure from ethynyl-HBC (**7**) (100.1 mg, 0.121 mmol), *cis*-PtCl $_2$ (dppe) (40.0 mg, 0.060 mmol) and CuI (0.8 mg, 7 mol%) in still-dried CH $_2$ Cl $_2$ : $^i$ Pr $_2$ NH (~3:1 v/v; 24 mL:8 mL) under argon over 2 days. After washing of the residue from the reaction with water (3x150 mL), the organic layer was concentrated *in vacuo* and the compound was precipitated from excess methanol. The bright yellow powder was filtered off and washed with cold methanol (3x100 mL). (121 mg, 0.054 mmol, 89 %). **m.p.** >360 °C.  $^1H$  NMR ( $CDCl_3$ , 400.1 MHz):  $\delta$  9.28 (m, 12H,  $H_{phenyl}$ ), 9.24 (m, 8H,  $H_{phenyl}$ ), 9.19 (s, 4H,  $H^1$ ), 8.17 (m, 8H,  $H_o$ ), 7.50 (m, 12H,  $H_m$ ,  $H_p$ ), 2.56 (m, 4H,  $CH_2$ ), 1.80 (s, 18H,  $C(CH_3)_3$ ), 1.79 (s, 36H,  $C(CH_3)_3$ ), 1.75 (s, 36H,  $C(CH_3)_3$ ).  $^{13}C \{^1H\}$  NMR ( $CDCl_3$ , 150.9 MHz):  $\delta$  148.94 ( $C_{quat}$ ), 148.73 ( $C_{quat}$ ), 133.62

(pt, 8C,  $J_{PC} = 6$  Hz, CH, C<sub>o</sub>), 131.27 (s, 4C, C<sub>p</sub>), 130.42 (C<sub>quat</sub>), 130.36 (C<sub>quat</sub>), 130.31 (C<sub>quat</sub>), 130.19 (C<sub>quat</sub>), 130.17 (C<sub>quat</sub>), 130.09 (C<sub>quat</sub>), 130.01 (pd, 4C,  $^1J_{PC} = 55$  Hz, C<sub>quat</sub>, C<sub>i</sub>), 129.57 (C<sub>quat</sub>), 128.76 (pt, 8C,  $J_{PC} = 5$  Hz, CH, C<sub>m</sub>), 126.43 (C<sub>quat</sub>), 124.84 (s, CH, C<sub>HBC</sub>), 123.90 (C<sub>quat</sub>), 123.86 (C<sub>quat</sub>), 123.73 (C<sub>quat</sub>), 123.71 (C<sub>quat</sub>), 120.60 (C<sub>quat</sub>), 120.39 (C<sub>quat</sub>), 120.31 (C<sub>quat</sub>), 120.23 (C<sub>quat</sub>), 119.45 (s, 4C, CH, C<sup>1</sup>), 118.70 (s, CH, C<sub>HBC</sub>), 118.67 (s, CH, C<sub>HBC</sub>), 118.60 (s, CH, C<sub>HBC</sub>), 118.44 (s, CH, C<sub>HBC</sub>), 113.55 (2C, C<sub>quat</sub>, C≡C), 112.79 (2C, C<sub>quat</sub>, C≡C), 35.61 (C<sub>quat</sub>), 35.54 (C<sub>quat</sub>), 31.92 (s, 12C, C(CH<sub>3</sub>)<sub>3</sub>), 31.85 (s, 18C, C(CH<sub>3</sub>)<sub>3</sub>), 29.54 (s, 2C, CH<sub>2</sub>). **<sup>31</sup>P {<sup>1</sup>H} NMR** (CDCl<sub>3</sub>, 162 MHz): δ 41.2 ( $^1J_{PPt} = 2279$  Hz, PPh<sub>2</sub>). **MS** (*m/z*-MALDI-TOF, THF/Toluene): Found: 2244.9922 [M+H]<sup>+</sup>, calculated for [C<sub>154</sub>H<sub>139</sub>P<sub>2</sub>Pt]<sup>+</sup>: 2245.0000. **Anal. Calcd.** For C<sub>154</sub>H<sub>138</sub>P<sub>2</sub>Pt·CH<sub>3</sub>OH: C, 81.73; H, 6.28. Found: C, 81.59; H, 6.32. **IR** ν (cm<sup>-1</sup>): 2956 (s), 2902 (m), 2872 (m), 2109 (m, C≡C), 2104 (m, C≡C), 1607 (m), 1580 (m), 1480 (m), 1465 (m), 1439 (m), 1395 (w), 1370 (s), 1263 (s), 1110 (s), 1020 (m, br), 944 (m), 867 (s), 809 (m, br), 749 (s), 706 (s), 688 (s).

## 5.5 [Pt(N<sup>^</sup>N)(C≡C-R)<sub>2</sub>]: Precursors and Complexes

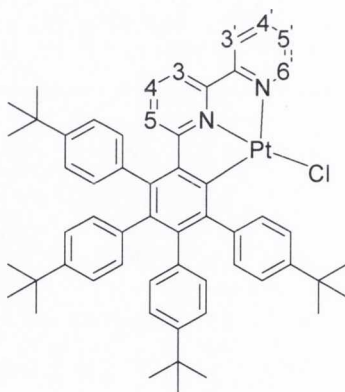
### [Pt(4:N<sup>^</sup>N)Cl<sub>2</sub>] (Pt(N<sup>^</sup>N)Cl<sub>2</sub>; 44)



Still-dried chloroform (15 mL) was degassed three times by freeze-pump-thaw and was transferred *via* cannula to a pre-dried Schlenk flask containing [PtCl<sub>2</sub>(DMSO)<sub>2</sub>] (60.4 mg; 0.143 mmol) and 1-(2,2'-bipyrid-6-yl)-2,3,4,5-tetra-(4-*tert*-butylphenyl) benzene (**4**) (109.1 mg; 0.143 mmol). The orange/yellow reaction mixture was heated to 55 °C for 2 days until no trace of free ligand was detectable by TLC. The volume of solvent was reduced *in vacuo* (~1 mL) and excess methanol (~30 mL) was added. The fine yellow

precipitate obtained was filtered off and washed with cold methanol. (112 mg; 0.109 mmol; 77 %). **m.p.** > 280 °C (decomp.)  $^1\text{H NMR}$  ( $\text{CDCl}_3$ , 600.1 MHz):  $\delta$  9.53 (d, 1H,  $^3J_{\text{HH}} = 5.1$  Hz,  $\text{H}^6$ ), 8.03 (ddd, 1H,  $^3J_{\text{HH}}$ ,  $^4J_{\text{HH}} = 8.1$ , 1.5 Hz,  $\text{H}^4$ ), 7.89 (d, 1H,  $^3J_{\text{HH}} = 8.1$  Hz,  $\text{H}^3$ ), 7.77-7.84 (m, 2H,  $\text{H}^3$ ,  $\text{H}^4$ ), 7.75 (m, 2H,  $\text{H}_{\text{phenyl}}$ ,  $\text{H}_\gamma$ ), 7.38 (dd, 1H,  $^3J_{\text{HH}}$ ,  $^4J_{\text{HH}} = 7.3$ , 2.2 Hz,  $\text{H}^5$ ), 7.32 (ddd, 1H,  $^3J_{\text{HH}}$ ,  $^4J_{\text{HH}} = 6.6$ , 1.5 Hz,  $\text{H}^5$ ), 7.14-7.17 (m, 4H,  $\text{H}_{\text{phenyl}}$ ), 6.96 (br d, 1H,  $^3J_{\text{HH}} = 7.3$  Hz,  $\text{H}_{\text{phenyl}}$ ), 6.88 (d, 2H,  $^3J_{\text{HH}} = 7.3$  Hz,  $\text{H}_{\text{phenyl}}$ ), 6.81 (d, 2H,  $^3J_{\text{HH}} = 8.1$  Hz,  $\text{H}_{\text{phenyl}}$ ), 6.71-6.76 (m, 4H,  $\text{H}_{\text{phenyl}}$ ), 6.67 (br d, 1H,  $^3J_{\text{HH}} = 7.3$  Hz,  $\text{H}_{\text{phenyl}}$ ), 6.51 (br d, 1H,  $^3J_{\text{HH}} = 7.3$  Hz,  $\text{H}_{\text{phenyl}}$ ), 1.24 (s, 9H,  $\text{C}(\text{CH}_3)_3$ ), 1.14 (s, 9H,  $\text{C}(\text{CH}_3)_3$ ), 1.09 (s, 9H,  $\text{C}(\text{CH}_3)_3$ ), 0.96 (s, 9H,  $\text{C}(\text{CH}_3)_3$ ).  $^{13}\text{C} \{^1\text{H}\}$  NMR ( $\text{CDCl}_3$ , 150.9 MHz):  $\delta$  165.39 ( $\text{C}_{\text{quat}}$ ), 157.53 ( $\text{C}_{\text{quat}}$ ), 156.99 ( $\text{C}_{\text{quat}}$ ), 149.45 ( $\text{CH}$ ,  $\text{C}^6$ ), 148.67 ( $\text{C}_{\text{quat}}$ ), 148.34 ( $\text{C}_{\text{quat}}$ ), 147.98 ( $\text{C}_{\text{quat}}$ ), 147.63 ( $\text{C}_{\text{quat}}$ ), 142.55 ( $\text{C}_{\text{quat}}$ ), 142.03 ( $\text{C}_{\text{quat}}$ ), 140.10 ( $\text{C}_{\text{quat}}$ ), 138.54 ( $\text{C}_{\text{quat}}$ ), 138.53 ( $\text{C}_{\text{quat}}$ ), 138.32 ( $\text{CH}$ ,  $\text{C}^4$ ), 137.98 ( $\text{C}_{\text{quat}}$ ), 136.87 ( $\text{CH}$ ,  $\text{C}^4$ ), 136.83 ( $\text{C}_{\text{quat}}$ ), 136.76 ( $\text{C}_{\text{quat}}$ ), 136.40 ( $\text{C}_{\text{quat}}$ ), 133.34 ( $\text{CH}$ ,  $\text{C}_{\text{phenyl}}$ ), 131.59 ( $\text{CH}$ ,  $\text{C}_{\text{phenyl}}$ ), 131.42 ( $\text{CH}$ ,  $\text{C}^5$ ), 130.98 ( $\text{CH}$ ,  $\text{C}_\gamma$ ), 130.49 ( $\text{CH}$ ,  $\text{C}_{\text{phenyl}}$ ), 129.74 ( $\text{CH}$ ,  $\text{C}_{\text{phenyl}}$ ), 129.64 ( $\text{CH}$ ,  $\text{C}_{\text{phenyl}}$ ), 125.63 ( $\text{CH}$ ,  $\text{C}^5$ ), 124.05 ( $\text{CH}$ ,  $\text{C}_{\text{phenyl}}$ ), 123.92 ( $\text{CH}$ ,  $\text{C}_{\text{phenyl}}$ ), 123.34 ( $\text{CH}$ ,  $\text{C}_{\text{phenyl}}$ ), 122.78 ( $\text{CH}$ ,  $\text{C}_{\text{phenyl}}$ ), 122.49 ( $\text{CH}$ ,  $\text{C}_{\text{phenyl}}$ ), 122.37 ( $\text{CH}$ ,  $\text{C}^3$ ), 119.66 ( $\text{CH}$ ,  $\text{C}^3$ ), 34.18 ( $\text{C}_{\text{quat}}$ ), 34.00 ( $\text{C}_{\text{quat}}$ ), 33.91 ( $\text{C}_{\text{quat}}$ ), 33.88 ( $\text{C}_{\text{quat}}$ ), 31.17 (3C,  $\text{C}(\text{CH}_3)_3$ ), 31.07 (3C,  $\text{C}(\text{CH}_3)_3$ ), 31.04 (3C,  $\text{C}(\text{CH}_3)_3$ ), 30.96 (3C,  $\text{C}(\text{CH}_3)_3$ ). **MS** ( $m/z$ -ES-MS, THF): Found: 1048.3693  $[\text{M}+\text{Na}]^+$ , calculated for  $[\text{C}_{56}\text{H}_{60}\text{N}_2\text{NaCl}_2\text{Pt}]^+$ : 1048.3679. **Anal. Calcd.** For  $\text{C}_{56}\text{H}_{60}\text{N}_2\text{Cl}_2\text{Pt}\cdot\text{H}_2\text{O}$ : C, 64.36; H, 5.98; N, 2.68. Found: C, 64.23; H, 5.85; N, 2.47. **IR**  $\nu$  ( $\text{cm}^{-1}$ ): 2962 (s), 2899 (m), 2867 (m), 1608 (m), 1560 (m), 1514 (m), 1461 (s), 1440 (s), 1393 (m), 1362 (s), 1264 (s), 1231 (m), 1200 (w), 1104 (m, br), 1021 (s), 837 (s), 808 (m), 768 (s), 672 (m).

**[Pt(4:N^N^C)Cl] (Pt(N^N^C)Cl; 43)**



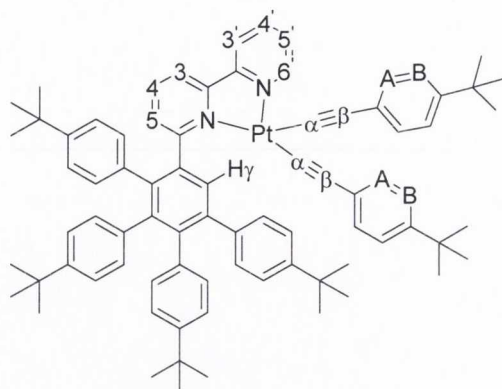
**[Pt(N^N)Cl<sub>2</sub>] (44)** (~15 mg; 0.015 mmol) was dissolved in  $\text{CHCl}_3$  (~0.5 mL). Ethanol (~0.5 mL) was layered on top of the chloroform solution. After a few days, orange crystals



(needles) appeared on standing. (~10 mg; 0.010 mmol; 67 %).  $^1\text{H NMR}$  ( $\text{CDCl}_3$ , 400.1 MHz):  $\delta$  9.31 (d, 1H,  $^3J_{\text{HH}} = 6.0$  Hz,  $\text{H}^{6'}$ ), 7.99 (ddd, 1H,  $^3J_{\text{HH}}$ ,  $^4J_{\text{HH}} = 7.9$ , 1.5 Hz,  $\text{H}^{4'}$ ), 7.80 (d, 1H,  $^3J_{\text{HH}} = 8.3$  Hz,  $\text{H}^{3'}$ ), 7.58 (dd, 1H,  $^3J_{\text{HH}} = 7.5$  Hz,  $\text{H}^{5'}$ ), 7.36 (d, 1H,  $^3J_{\text{HH}} = 7.9$  Hz,  $\text{H}^3$ ), 7.32 (dd, 1H,  $^3J_{\text{HH}} = 7.9$  Hz,  $\text{H}^4$ ), 7.15 (d, 2H,  $^3J_{\text{HH}} = 7.9$  Hz,  $\text{H}_{\text{phenyl}}$ ), 6.99 (m, 6H,  $\text{H}_{\text{phenyl}}$ ), 6.73 (m, 4H,  $\text{H}_{\text{phenyl}}$ ), 6.54 (m, 4H,  $\text{H}_{\text{phenyl}}$ ), 6.19 (d,  $^3J_{\text{HH}} = 8.3$  Hz,  $\text{H}^5$ ), 1.23-1.26 (m, 18H,  $\text{C}(\text{CH}_3)_3$ ), 1.07 (s, 18H,  $\text{C}(\text{CH}_3)_3$ ).  $^{13}\text{C} \{^1\text{H}\}$  NMR ( $\text{CDCl}_3$ , 150.9 MHz): 168.18 ( $\text{C}_{\text{quat}}$ ), 157.28 ( $\text{C}_{\text{quat}}$ ), 154.03 ( $\text{C}_{\text{quat}}$ ), 149.54 ( $\text{C}_{\text{quat}}$ ), 149.04 ( $\text{C}_{\text{quat}}$ ), 148.51 (CH,  $\text{C}^{6'}$ ), 147.24 ( $\text{C}_{\text{quat}}$ ), 147.00 ( $\text{C}_{\text{quat}}$ ), 146.80 ( $\text{C}_{\text{quat}}$ ), 144.28 ( $\text{C}_{\text{quat}}$ ), 144.06 ( $\text{C}_{\text{quat}}$ ), 142.50 ( $\text{C}_{\text{quat}}$ ), 141.37 ( $\text{C}_{\text{quat}}$ ), 139.62 ( $\text{C}_{\text{quat}}$ ), 138.91 ( $\text{C}_{\text{quat}}$ ), 138.68 (CH,  $\text{C}^{4'}$ ), 138.15 ( $\text{C}_{\text{quat}}$ ), 137.52 ( $\text{C}_{\text{quat}}$ ), 137.20 ( $\text{C}_{\text{quat}}$ ), 136.24 (CH,  $\text{C}^4$ ), 131.30 (CH,  $\text{C}_{\text{phenyl}}$ ), 130.81 (CH,  $\text{C}_{\text{phenyl}}$ ), 130.26 (CH,  $\text{C}_{\text{phenyl}}$ ), 129.84 (CH,  $\text{C}_{\text{phenyl}}$ ), 126.46 (CH,  $\text{C}^{5'}$ ), 124.75 (CH,  $\text{C}_{\text{phenyl}}$ ), 124.51 (CH,  $\text{C}^5$ ), 122.66 (CH,  $\text{C}_{\text{phenyl}}$ ), 122.60 (CH,  $\text{C}_{\text{phenyl}}$ ), 122.43 (CH,  $\text{C}_{\text{phenyl}}$ ), 121.04 (CH,  $\text{C}^{3'}$ ), 116.56 (CH,  $\text{C}^3$ ), 34.29 ( $\text{C}_{\text{quat}}$ ), 34.03 ( $\text{C}_{\text{quat}}$ ), 33.82 ( $\text{C}_{\text{quat}}$ ), 33.81 ( $\text{C}_{\text{quat}}$ ), 31.31 (3C,  $\text{C}(\text{CH}_3)_3$ ), 31.18 (3C,  $\text{C}(\text{CH}_3)_3$ ), 31.01 (6C,  $\text{C}(\text{CH}_3)_3$ ). MS ( $m/z$ -ES-MS, THF): Found: 954.4332 [ $\text{M}-\text{Cl}$ ] $^+$ , calculated for  $[\text{C}_{56}\text{H}_{59}\text{N}_2\text{Pt}]^+$ : 954.4326.

### General Synthetic Procedure for $[\text{Pt}(\text{N}^{\wedge}\text{N})(\text{C}\equiv\text{C}-\text{R})_2]$

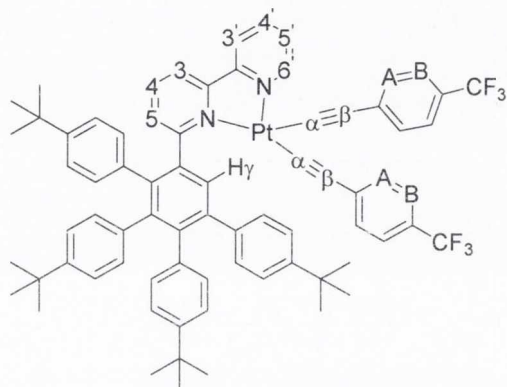
A mixture of still-dried  $\text{CH}_2\text{Cl}_2$ : $^i\text{Pr}_2\text{NH}$  was degassed *via* freeze-pump-thaw and transferred *via* cannula to a dry Schlenk flask containing  $[\text{Pt}(\text{4:N}^{\wedge}\text{N})\text{Cl}_2]$  (**44**) as Pt(II) metal precursor, the appropriate polyaromatic acetylene and CuI as catalyst. The solution was stirred in the dark at room temperature over several days. When the reaction was complete, the solvent was evaporated to dryness and the residue was redissolved in  $\text{CH}_2\text{Cl}_2/\text{CHCl}_3$  and washed with water (x3). The organic layer was dried over  $\text{MgSO}_4$  and the solvent volume was reduced *in vacuo*. **46**, **47** and **48** were purified by column chromatography. **45** and **49** were obtained as pure solids by precipitation from methanol followed by washing with cold methanol. Note: acetylide co-ligands arbitrarily assigned as 1 and 2 in order to link NMR signals on the same ligand.

**[Pt(N<sup>N</sup>)(4-*tert*-butylphenyl acetylene)<sub>2</sub>] (45)**

**45** was prepared using the general synthetic procedure from **44** (100.1 mg; 0.097 mmol) and CuI (1.3 mg; 7 mol%) degassed in still-dried CH<sub>2</sub>Cl<sub>2</sub>:<sup>i</sup>Pr<sub>2</sub>NH (~4:1 v/v, 10 mL:2 mL) with subsequent addition of 4-*tert*-butylphenyl acetylene (0.044 ml; 0.243 mmol) *via* syringe which was stirred under argon for 3 days. Following washing and concentration *in vacuo*, excess methanol (~50 mL) was added to precipitate the product. Filtration and washing with cold methanol yielded the desired product as a bright yellow powder. (77 mg; 0.060 mmol; 62 %). **m.p.** >250 °C (decomp.) <sup>1</sup>H NMR (CDCl<sub>3</sub>, 600.1 MHz): δ 9.88 (d, 1H, <sup>3</sup>J<sub>HH</sub> = 4.9 Hz, H<sup>6'</sup>), 8.08 (br, 1H, H<sub>phenyl</sub>), 8.03 (dd, 1H, <sup>3</sup>J<sub>HH</sub> = 6.8 Hz, H<sup>4'</sup>), 7.96 (d, 1H, <sup>3</sup>J<sub>HH</sub> = 7.9 Hz, H<sup>3'</sup>), 7.83 (s, 1H, H<sub>γ</sub>), 7.80 (d, 1H, <sup>3</sup>J<sub>HH</sub> = 7.5 Hz, H<sup>3</sup>), 7.55 (dd, 1H, <sup>3</sup>J<sub>HH</sub> = 7.9 Hz, H<sup>4</sup>), 7.39 (dd, 1H, <sup>3</sup>J<sub>HH</sub> = 6.4 Hz, H<sup>5'</sup>), 7.34 (d, 2H, <sup>3</sup>J<sub>HH</sub> = 8.3 Hz, H<sub>A1</sub>), 7.15-7.21 (m, 6H, H<sub>A2</sub>, H<sub>B1</sub>, H<sub>B2</sub>), 7.06-7.13 (m, 6H, H<sup>5</sup>, H<sub>phenyl</sub>), 6.58-6.83 (m, 7H, H<sub>phenyl</sub>), 6.44 (d, 1H, <sup>3</sup>J<sub>HH</sub> = 7.2 Hz, H<sub>phenyl</sub>), 6.00 (br, 1H, H<sub>phenyl</sub>), 5.91 (d, 1H, <sup>3</sup>J<sub>HH</sub> = 6.8 Hz, H<sub>phenyl</sub>), 1.26 (m, 27H, C(CH<sub>3</sub>)<sub>3</sub>), 1.14 (s, 9H, C(CH<sub>3</sub>)<sub>3</sub>), 1.13 (s, 9H, C(CH<sub>3</sub>)<sub>3</sub>), 1.08 (s, 9H, C(CH<sub>3</sub>)<sub>3</sub>). <sup>13</sup>C {<sup>1</sup>H} NMR (CDCl<sub>3</sub>, 100.6 MHz): δ 165.51 (C<sub>quat</sub>), 157.24 (C<sub>quat</sub>), 156.32 (C<sub>quat</sub>), 151.20 (CH, C<sup>6'</sup>), 148.68 (C<sub>quat</sub>), 148.53 (C<sub>quat</sub>), 147.95 (C<sub>quat</sub>), 147.68 (C<sub>quat</sub>), 147.30 (C<sub>quat</sub>), 146.55 (C<sub>quat</sub>), 141.63 (C<sub>quat</sub>), 141.44 (C<sub>quat</sub>), 139.92 (C<sub>quat</sub>), 139.72 (C<sub>quat</sub>), 138.81 (C<sub>quat</sub>), 137.91 (C<sub>quat</sub>), 137.87 (CH, C<sup>4'</sup>), 137.38 (C<sub>quat</sub>), 136.96 (C<sub>quat</sub>), 136.77 (C<sub>quat</sub>), 135.91 (CH, C<sup>4</sup>), 132.71 (CH, C<sub>γ</sub>), 132.59 (CH, C<sup>5</sup>), 131.65 (CH, C<sub>phenyl</sub>), 131.53 (CH, C<sub>A1</sub>), 131.32 (CH, C<sub>A2</sub>), 130.86 (CH, C<sub>phenyl</sub>), 129.93 (CH, C<sub>phenyl</sub>), 126.43 (C<sub>quat</sub>), 126.25 (CH, C<sup>5'</sup>), 125.49 (C<sub>quat</sub>), 124.45 (CH, C<sub>B1</sub>), 124.32 (CH, C<sub>B2</sub>), 124.23 (CH, C<sub>phenyl</sub>), 123.05 (CH, C<sub>phenyl</sub>), 122.84 (CH, C<sub>phenyl</sub>), 122.32 (CH, C<sub>phenyl</sub>), 122.26 (CH, C<sup>3'</sup>), 119.49 (CH, C<sup>3</sup>), 104.01 (C<sub>quat</sub>, C<sub>β2</sub>), 99.63 (C<sub>quat</sub>, C<sub>β1</sub>), 80.19 (C<sub>quat</sub>, C<sub>α</sub>), 79.82 (C<sub>quat</sub>, C<sub>α</sub>), 34.40 (C<sub>quat</sub>), 34.29 (2C, C<sub>quat</sub>), 34.19 (C<sub>quat</sub>), 34.02 (C<sub>quat</sub>), 33.95 (C<sub>quat</sub>), 31.39 (9C, C(CH<sub>3</sub>)<sub>3</sub>), 31.32 (9C, C(CH<sub>3</sub>)<sub>3</sub>), 31.29 (9C, C(CH<sub>3</sub>)<sub>3</sub>), 31.24 (9C, C(CH<sub>3</sub>)<sub>3</sub>), 31.20 (9C, C(CH<sub>3</sub>)<sub>3</sub>), 31.17 (9C, C(CH<sub>3</sub>)<sub>3</sub>). **MS** (*m/z*-MALDI-TOF, CHCl<sub>3</sub>): Found: 1269.6469 [M]<sup>+</sup>,

calculated for  $[\text{C}_{80}\text{H}_{86}\text{N}_2\text{Pt}]^+$ : 1269.6439. **Anal. Calcd.** For  $\text{C}_{80}\text{H}_{86}\text{N}_2\text{Pt}\cdot\text{CH}_2\text{Cl}_2$ : C, 71.77; H, 6.54; N, 2.07. Found: C, 72.05; H, 6.68; N, 2.04. **IR**  $\nu$  ( $\text{cm}^{-1}$ ): 2961 (s), 2902 (m), 2869 (m), 2128 (m,  $\text{C}\equiv\text{C}$ ), 2112 (m,  $\text{C}\equiv\text{C}$ ), 1602 (m), 1563 (w), 1509 (m), 1461 (m, br), 1393 (m), 1362 (s), 1260 (s), 1229 (m), 1168 (w), 1104 (m, br), 1019 (m, br), 829 (s), 794 (s), 775 (s), 757 (m), 735 (w).

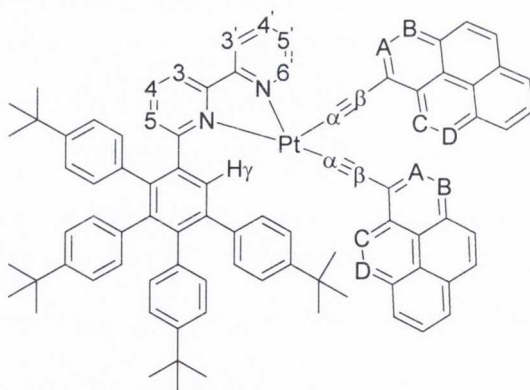
**[Pt(N<sup>^</sup>N)(4-ethynyl-  $\alpha,\alpha,\alpha$ -trifluorotoluene)<sub>2</sub>] (46)**



**46** was prepared using the general synthetic procedure from **44** (100.4 mg; 0.098 mmol) and CuI (1.3 mg; 7 mol%) degassed in still-dried  $\text{CH}_2\text{Cl}_2$ : $^i\text{Pr}_2\text{NH}$  (~4:1 v/v, 20 mL:10 mL) with subsequent addition of 4-ethynyl- $\alpha,\alpha,\alpha$ -trifluorotoluene (0.040 ml; 0.245 mmol) *via* syringe. The reaction mixture was stirred under argon for 3 days. Following washing and solvent removal *in vacuo*, the product was purified by column chromatography on silica using chloroform as eluent. Subsequent solvent removal produced the desired product as a bright yellow powder. (69 mg; 0.054 mmol; 55 %). **m.p.** >180 °C (decomp.) **<sup>1</sup>H NMR** ( $\text{CDCl}_3$ , 600.1 MHz):  $\delta$  9.81 (d, 1H,  $^3J_{\text{HH}} = 5.3$  Hz,  $\text{H}^{6'}$ ), 8.10 (dd, 1H,  $^3J_{\text{HH}} = 7.9$  Hz,  $\text{H}^{4'}$ ), 7.98 (d, 1H,  $^3J_{\text{HH}} = 8.3$  Hz,  $\text{H}^{3'}$ ), 7.93 (br, 1H,  $\text{H}_{\text{phenyl}}$ ), 7.83 (m, 2H,  $\text{H}_\gamma$ ,  $\text{H}^3$ ), 7.70 (m, 1H,  $\text{H}_{\text{phenyl}}$ ), 7.65 (dd, 1H,  $^3J_{\text{HH}} = 7.9$  Hz,  $\text{H}^{4'}$ ), 7.52 (m, 2H,  $\text{H}_{\text{phenyl}}$ ,  $\text{H}^{5'}$ ), 7.48 (d, 2H,  $^3J_{\text{HH}} = 7.9$  Hz,  $\text{H}_{\text{A}2}$ ), 7.38-7.42 (m, 4H,  $\text{H}_{\text{B}2}$ ,  $\text{H}_{\text{B}1}$ ), 7.35 (d, 2H,  $^3J_{\text{HH}} = 7.9$  Hz,  $\text{H}_{\text{A}1}$ ), 7.17 (d, 1H,  $^3J_{\text{HH}} = 7.5$  Hz,  $\text{H}^{5'}$ ), 7.12 (d, 2H,  $^3J_{\text{HH}} = 7.9$  Hz,  $\text{H}_{\text{phenyl}}$ ), 7.06 (br, 1H,  $\text{H}_{\text{phenyl}}$ ), 7.01 (d, 2H,  $^3J_{\text{HH}} = 7.9$  Hz,  $\text{H}_{\text{phenyl}}$ ), 6.55-6.95 (br,  $\text{H}_{\text{phenyl}}$ ), 6.72 (br d, 1H,  $\text{H}_{\text{phenyl}}$ ), 6.63 (br d, 1H,  $\text{H}_{\text{phenyl}}$ ), 6.48 (br d, 1H,  $\text{H}_{\text{phenyl}}$ ), 5.88 (br d, 1H,  $\text{H}_{\text{phenyl}}$ ), 5.67-5.83 (br,  $\text{H}_{\text{phenyl}}$ ), 1.26 (s, 9H,  $\text{C}(\text{CH}_3)_3$ ), 1.14 (s, 18H,  $\text{C}(\text{CH}_3)_3$ ), 1.10 (s, 9H,  $\text{C}(\text{CH}_3)_3$ ). **<sup>13</sup>C {<sup>1</sup>H} NMR** ( $\text{CDCl}_3$ , 150.9 MHz):  $\delta$  167.59 ( $\text{C}_{\text{quat}}$ ), 165.64 ( $\text{C}_{\text{quat}}$ ), 157.18 ( $\text{C}_{\text{quat}}$ ), 155.99 ( $\text{C}_{\text{quat}}$ ), 150.98 ( $\text{CH}$ ,  $\text{C}^{6'}$ ), 148.82 ( $\text{C}_{\text{quat}}$ ), 148.66 ( $\text{C}_{\text{quat}}$ ), 147.96 ( $\text{C}_{\text{quat}}$ ), 147.74 ( $\text{C}_{\text{quat}}$ ), 141.63 ( $\text{C}_{\text{quat}}$ ), 141.51 ( $\text{C}_{\text{quat}}$ ), 139.94 ( $\text{C}_{\text{quat}}$ ), 139.47 ( $\text{C}_{\text{quat}}$ ), 138.41 ( $\text{C}_{\text{quat}}$ ), 138.15 ( $\text{CH}$ ,  $\text{C}^{4'}$ ), 137.93 ( $\text{C}_{\text{quat}}$ ), 136.92 ( $\text{C}_{\text{quat}}$ ), 136.23 ( $\text{C}_{\text{quat}}$ ), 136.23 ( $\text{CH}$ ,  $\text{C}^{4'}$ ), 136.21 ( $\text{C}_{\text{quat}}$ ), 132.66 ( $\text{C}_{\text{quat}}$ ), 132.52 ( $\text{CH}$ ,  $\text{C}_\gamma$ ,  $\text{C}^{5'}$ ),

131.88 (CH, C<sub>A1</sub>), 131.81 (C<sub>quat</sub>), 131.63 (CH, C<sub>A2</sub>), 130.71-130.92 (m, CH, C<sub>phenyl</sub>), 129.70 (CH, C<sub>phenyl</sub>), 128.65 (CH, C<sub>phenyl</sub>), 126.75 (q, C<sub>quat</sub>, <sup>2</sup>J<sub>CF</sub> = 33 Hz, C-CF<sub>3</sub>), 126.44 (CH, C<sup>5</sup>), 125.69 (q, C<sub>quat</sub>, <sup>2</sup>J<sub>CF</sub> = 32 Hz, C-CF<sub>3</sub>), 124.59 (q, C<sub>quat</sub>, <sup>1</sup>J<sub>CF</sub> = 271 Hz, CF<sub>3</sub>), 124.33-124.42 (m, CH, C<sub>B1</sub>, C<sub>B2</sub>), 124.34 (q, C<sub>quat</sub>, <sup>1</sup>J<sub>CF</sub> = 272 Hz, CF<sub>3</sub>), 124.11 (CH, C<sub>phenyl</sub>), 122.96 (m, CH, C<sub>phenyl</sub>), 122.48 (m, CH, C<sub>phenyl</sub>), 122.13 (CH, C<sup>3</sup>), 119.43 (CH, C<sup>3</sup>), 103.27 (C<sub>quat</sub>, C<sub>β1</sub>), 98.78 (C<sub>quat</sub>, C<sub>β2</sub>), 86.04 (C<sub>quat</sub>, C<sub>α</sub>), 85.32 (C<sub>quat</sub>, C<sub>α</sub>), 34.17 (C<sub>quat</sub>), 34.07 (2C, C<sub>quat</sub>), 33.93 (C<sub>quat</sub>), 33.86 (C<sub>quat</sub>), 31.15 (9C, C(CH<sub>3</sub>)<sub>3</sub>), 31.06 (9C, C(CH<sub>3</sub>)<sub>3</sub>), 31.03 (9C, C(CH<sub>3</sub>)<sub>3</sub>), 30.98 (9C, C(CH<sub>3</sub>)<sub>3</sub>). <sup>19</sup>F NMR (CDCl<sub>3</sub>, 376 MHz): δ -62.6 (s, CF<sub>3</sub>), -62.8 (s, CF<sub>3</sub>). **MS** (*m/z*-ESI<sup>+</sup>, acetone): Found: 1315.4767 [M+Na]<sup>+</sup>, calculated for [C<sub>74</sub>H<sub>67</sub>N<sub>2</sub>F<sub>6</sub>NaPt]: 1315.4754. (100 %). Found: 955.4246 [M-2(-C≡C-Ph-CF<sub>3</sub>)+H]<sup>+</sup>, calculated for [C<sub>56</sub>H<sub>59</sub>N<sub>2</sub>Pt]<sup>+</sup>: 955.4248. (10%). **Anal. Calcd.** For C<sub>74</sub>H<sub>67</sub>N<sub>2</sub>Pt.H<sub>2</sub>O: C, 67.77; H, 5.30; N, 2.14. Found: C, 67.77; H, 5.46; N, 1.85. **IR** ν (cm<sup>-1</sup>): 2963 (s), 2906 (m), 2866 (m), 2130 (m, C≡C), 2114 (m, C≡C), 1725 (m), 1608 (m), 1562 (w), 1505 (w), 1461 (m, br), 1363 (m), 1320 (s), 1266 (m), 1230 (w), 1159 (s), 1119 (s), 1101 (s), 1063 (s), 1015 (m), 838 (s), 772 (s), 732 (m).

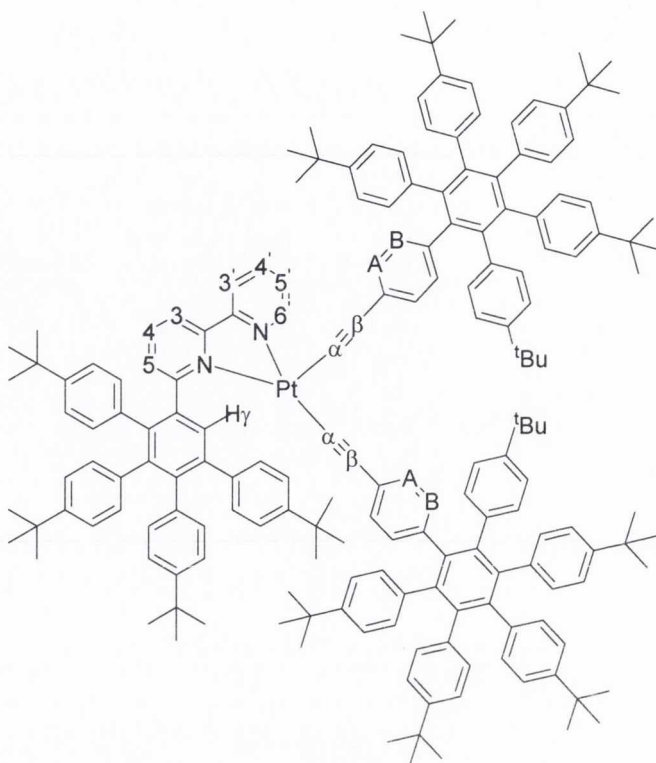
**[Pt(N<sup>^</sup>N)(1-pyrenyl acetylene)]<sub>2</sub> (47)**



**47** was prepared using the general synthetic procedure from **44** (119.8 mg; 0.117 mmol), 1-ethynyl pyrene (54.3 mg; 0.239 mmol) and CuI (1.5 mg; 7 mol %) in still-dried CH<sub>2</sub>Cl<sub>2</sub>:<sup>i</sup>Pr<sub>2</sub>NH (~6:1 v/v, 30 mL:5 mL) under argon for 48 hours. After this time, monitoring of the reaction by TLC (silica, CH<sub>2</sub>Cl<sub>2</sub>:hexane 10:1 v/v) indicated the formation of two new spots. Additional 1-ethynyl pyrene (~10 mg; 0.044 mmol) was added to the reaction mixture. The reaction was stirred for two days until only spot was visible by TLC.

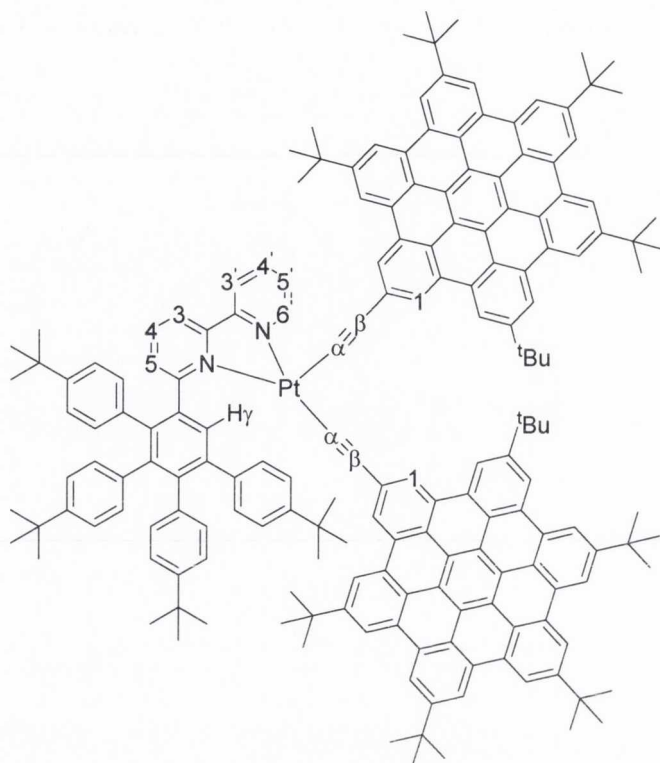
After washing, purification of the product was undertaken by column chromatography on silica eluting firstly with hexane:CH<sub>2</sub>Cl<sub>2</sub> (2:1 v/v) and then changing the solvent ratio to

hexane:CH<sub>2</sub>Cl<sub>2</sub> (1:1 v/v) in order to elute excess pyrene and other impurities. CH<sub>2</sub>Cl<sub>2</sub>:hexane (10:1 v/v) was then used to elute the product. The volume of solvent was concentrated under vacuum (~0.5 mL) and the product precipitated out of diethyl ether (~20 mL). The bright yellow precipitate was filtered and washed with cold diethyl ether (3x10 mL). (51 mg; 0.036 mmol; 31 %). **m.p.** > 360 °C. **<sup>1</sup>H NMR** (CDCl<sub>3</sub>, 600.1 MHz): δ 10.12 (d, 1H, <sup>3</sup>J<sub>HH</sub> = 4.4 Hz, H<sup>6'</sup>), 9.05 (d, 1H, <sup>3</sup>J<sub>HH</sub> = 8.8 Hz, H<sub>C1</sub>), 8.97 (d, 1H, <sup>3</sup>J<sub>HH</sub> = 8.8 Hz, H<sub>C2</sub>), 8.22 (br s, 1H, H<sub>phenyl</sub>), 8.05-8.09 (m, 3H, H<sub>A1</sub>, H<sub>A2</sub>, H<sub>pyr</sub>), 7.99-8.02 (m, 3H, H<sub>B1</sub>, H<sub>pyr</sub>), 7.85-7.97 (m, 7H, H<sup>4'</sup>, H<sup>3</sup>, H<sub>pyr</sub>, H<sub>D1</sub>, H<sub>B2</sub>), 7.73 (dd, 1H, <sup>3</sup>J<sub>HH</sub> = 8.1 Hz, H<sup>4</sup>), 7.70 (d, 1H, <sup>3</sup>J<sub>HH</sub> = 8.1 Hz, H<sup>3'</sup>), 7.60 (d, 1H, <sup>3</sup>J<sub>HH</sub> = 8.1 Hz, H<sup>5</sup>), 7.55 (m, 2H, H<sub>γ</sub>, H<sub>phenyl</sub>), 7.48 (dd, 1H, <sup>3</sup>J<sub>HH</sub> = 6.6 Hz, H<sup>5'</sup>), 7.17 (m, 2H, H<sub>D2</sub>, H<sub>phenyl</sub>), 7.03 (d, 2H, <sup>3</sup>J<sub>HH</sub> = 8.8 Hz, H<sub>phenyl</sub>), 6.94 (d, 2H, <sup>3</sup>J<sub>HH</sub> = 8.8 Hz, H<sub>phenyl</sub>), 6.81 (br, 2H, H<sub>phenyl</sub>), 6.55-6.60 (m, 3H, H<sub>phenyl</sub>), 6.37-6.44 (m, 3H, H<sub>phenyl</sub>), 6.07 (d, 1H, <sup>3</sup>J<sub>HH</sub> = 7.3 Hz, H<sub>phenyl</sub>), 5.52 (d, 1H, <sup>3</sup>J<sub>HH</sub> = 7.3 Hz, H<sub>phenyl</sub>), 5.44 (br s, 1H, H<sub>phenyl</sub>), 4.55 (br, 1H, H<sub>phenyl</sub>), 1.23 (s, 9H, C(CH<sub>3</sub>)<sub>3</sub>), 1.16 (s, 9H, C(CH<sub>3</sub>)<sub>3</sub>), 0.96 (s, 9H, C(CH<sub>3</sub>)<sub>3</sub>), 0.88 (s, 9H, C(CH<sub>3</sub>)<sub>3</sub>). **<sup>13</sup>C {<sup>1</sup>H} NMR** (CDCl<sub>3</sub>, 150.9 MHz): δ 165.55 (C<sub>quat</sub>), 157.03 (C<sub>quat</sub>), 156.23 (C<sub>quat</sub>), 151.45 (CH, C<sup>6'</sup>), 148.83 (C<sub>quat</sub>), 148.59 (C<sub>quat</sub>), 147.41 (C<sub>quat</sub>), 147.29 (C<sub>quat</sub>), 141.73 (C<sub>quat</sub>), 141.55 (C<sub>quat</sub>), 139.97 (C<sub>quat</sub>), 139.84 (C<sub>quat</sub>), 138.48 (C<sub>quat</sub>), 138.02 (CH, C<sup>4'</sup>), 137.15 (C<sub>quat</sub>), 136.35 (C<sub>quat</sub>), 136.27 (C<sub>quat</sub>), 136.21 (CH, C<sub>γ</sub>), 132.79 (CH), 132.51 (C<sub>quat</sub>), 132.14 (CH), 131.89 (C<sub>quat</sub>), 131.84 (C<sub>quat</sub>), 131.68 (C<sub>quat</sub>), 131.28 (CH), 130.78 (CH), 129.99 (CH, C<sub>A1</sub>, C<sub>aryl</sub>), 129.76 (CH, C<sub>A2</sub>), 129.03 (C<sub>quat</sub>), 128.60 (C<sub>quat</sub>), 128.52 (CH, C<sub>C1</sub>, C<sub>phenyl</sub>), 127.59 (CH, C<sub>D1</sub>), 127.49 (CH), 127.30 (CH), 126.98 (CH, C<sub>D2</sub>), 126.84 (CH), 126.68 (CH, C<sup>5'</sup>), 126.33 (CH, C<sub>B2</sub>), 125.79 (CH, C<sub>B1</sub>), 125.41 (2C, CH, C<sup>4</sup>, C<sub>phenyl</sub>), 125.14 (C<sub>quat</sub>), 124.95 (C<sub>quat</sub>), 124.90 (C<sub>quat</sub>), 124.52 (C<sub>quat</sub>), 124.43 (CH, C<sup>5</sup>, C<sub>phenyl</sub>), 124.23 (C<sub>quat</sub>), 124.15 (CH), 124.03 (CH, C<sup>3</sup>), 123.87 (CH), 123.60 (C<sub>quat</sub>), 122.72 (CH), 122.25 (CH), 122.14 (CH, C<sup>3'</sup>), 119.41 (CH), 103.40 (C<sub>quat</sub>, C<sub>β1</sub>), 98.88 (C<sub>quat</sub>, C<sub>β2</sub>), 90.53 (C<sub>quat</sub>, C<sub>α</sub>), 88.98 (C<sub>quat</sub>, C<sub>α</sub>), 34.38 (2C, C<sub>quat</sub>), 33.85 (C<sub>quat</sub>), 33.78 (C<sub>quat</sub>), 31.33 (9C, C(CH<sub>3</sub>)<sub>3</sub>), 31.30 (9C, C(CH<sub>3</sub>)<sub>3</sub>), 31.07 (9C, C(CH<sub>3</sub>)<sub>3</sub>), 30.98 (9C, C(CH<sub>3</sub>)<sub>3</sub>). **MS** (*m/z*-MALDI-TOF, THF): Found: 1405.5841 [M]<sup>+</sup>, calculated for [C<sub>92</sub>H<sub>78</sub>N<sub>2</sub>Pt]<sup>+</sup>: 1405.5813. **Anal. Calcd.** For C<sub>92</sub>H<sub>78</sub>N<sub>2</sub>Pt.2(CH<sub>2</sub>Cl<sub>2</sub>): C, 71.61; H, 5.24; N, 1.78. Found: C, 71.37; H, 5.00; N, 1.69. **IR** ν (cm<sup>-1</sup>): 3051 (m), 2967 (s), 2899 (m), 2864 (m), 2131 (sh m, C≡C), 2104 (s, C≡C), 1596 (m), 1553 (w), 1502 (w), 1483 (m), 1457 (m), 1390 (m), 1359 (m), 1271 (m), 1237 (m), 1180 (w), 1119 (w), 1095 (w), 1018 (m), 841 (s), 814 (s), 769 (s), 759 (s), 717 (s), 676 (m).

[Pt(N<sup>^</sup>N)(1-(4-ethynylphenyl)-2,3,4,5,6-penta-(4-*tert*-butylphenyl)benzene)<sub>2</sub>] (48)

**48** was prepared using the general synthetic procedure from **44** (100.1 mg; 0.097 mmol), ethynyl-HPB (**6**) (167.8 mg; 0.200 mmol) and CuI (1.1 mg; 6 mol %) in still-dried CH<sub>2</sub>Cl<sub>2</sub>:<sup>i</sup>Pr<sub>2</sub>NH (4:1 v/v, 40 mL:10 mL) under argon for 48 hours. Monitoring the reaction by TLC (silica, 2:1 hexane:CH<sub>2</sub>Cl<sub>2</sub> v/v) indicated the formation of two products. Therefore, additional acetylene (5.0 mg; 0.006 mmol) was added to the reaction mixture in order to push the reaction to completion. The reaction was allowed to stir for a further 2 days. The solvent was then removed and the residue redissolved in CHCl<sub>3</sub>. After washing, column chromatography was performed on silica, eluting with hexane:CH<sub>2</sub>Cl<sub>2</sub> (2:1 v/v) to elute impurities and unreacted acetylene. The product was eluted by increasing the ratio gradually to CH<sub>2</sub>Cl<sub>2</sub>:hexane (2:1 v/v). Removal of the solvent produced the product as a pale orange/pink powder. (73 mg; 0.028 mmol; 29 %). **m.p.** > 360 °C. <sup>1</sup>H NMR (CDCl<sub>3</sub>, 600.1 MHz): δ 9.63 (d, 1H, <sup>3</sup>J<sub>HH</sub> = 5.3 Hz, H<sup>6'</sup>), 9.37 (br m, 1H, H<sub>phenyl</sub>), 8.70 (br m, 1H, H<sub>phenyl</sub>), 8.21 (br m, 1H, H<sub>phenyl</sub>), 8.08 (m, 1H, H<sub>phenyl</sub>), 8.03 (br m, 1H, H<sub>phenyl</sub>), 7.85 (dd, 1H, <sup>3</sup>J<sub>HH</sub> = 7.5 Hz, H<sup>4'</sup>), 7.76 (d, 1H, <sup>3</sup>J<sub>HH</sub> = 7.9 Hz, H<sup>3'</sup>), 7.72 (s, 1H, H<sub>γ</sub>), 7.62 (d, 1H, <sup>3</sup>J<sub>HH</sub> = 7.5 Hz, H<sup>3</sup>), 7.46 (dd, 1H, <sup>3</sup>J<sub>HH</sub> = 7.9 Hz, H<sup>4</sup>), 7.30 (br m, 1H, H<sub>phenyl</sub>), 7.19 (m, 1H, H<sup>5'</sup>), 7.10 (d, 1H, <sup>3</sup>J<sub>HH</sub> = 7.9 Hz, H<sup>5</sup>), 7.02 (d, 2H, <sup>3</sup>J<sub>HH</sub> = 8.3 Hz, H<sub>phenyl</sub>), 6.89-6.94 (m, 6H, H<sub>A1</sub>, H<sub>phenyl</sub>), 6.55-6.83 (m, 43H, H<sub>A2</sub>, H<sub>B1</sub>, H<sub>B2</sub>, H<sub>phenyl</sub>), 6.42 (br d, 1H, <sup>3</sup>J<sub>HH</sub> = 8.3 Hz, H<sub>phenyl</sub>), 6.34 (br m, 2H, H<sub>phenyl</sub>), 6.17 (br d, 1H, <sup>3</sup>J<sub>HH</sub> = 6.7 Hz, H<sub>phenyl</sub>), 4.68 (m, 2H, H<sub>phenyl</sub>), 4.50

(br m, 1H, H<sub>phenyl</sub>), 1.22 (s, 9H, C(CH<sub>3</sub>)<sub>3</sub>), 1.19 (s, 9H, C(CH<sub>3</sub>)<sub>3</sub>), 1.15 (s, 9H, C(CH<sub>3</sub>)<sub>3</sub>), 1.07-1.10 (m, 90H, C(CH<sub>3</sub>)<sub>3</sub>), 1.00 (s, 9H, C(CH<sub>3</sub>)<sub>3</sub>). <sup>13</sup>C {<sup>1</sup>H} NMR (CDCl<sub>3</sub>, 150.9 MHz): δ 165.41 (C<sub>quat</sub>), 164.91 (C<sub>quat</sub>), 156.84 (C<sub>quat</sub>), 156.08 (C<sub>quat</sub>), 150.74 (CH, C<sup>6</sup>), 148.31 (C<sub>quat</sub>), 148.24 (C<sub>quat</sub>), 147.98 (C<sub>quat</sub>), 147.65 (C<sub>quat</sub>), 147.37 (C<sub>quat</sub>), 147.28 (C<sub>quat</sub>), 147.23 (C<sub>quat</sub>), 147.16 (C<sub>quat</sub>), 147.10 (C<sub>quat</sub>), 141.75 (C<sub>quat</sub>), 141.15 (C<sub>quat</sub>), 140.57 (C<sub>quat</sub>), 140.53 (C<sub>quat</sub>), 140.49 (C<sub>quat</sub>), 140.28 (C<sub>quat</sub>), 140.25 (C<sub>quat</sub>), 140.19 (C<sub>quat</sub>), 140.16 (C<sub>quat</sub>), 139.79 (C<sub>quat</sub>), 139.75 (C<sub>quat</sub>), 139.03 (C<sub>quat</sub>), 138.70 (C<sub>quat</sub>), 138.16 (C<sub>quat</sub>), 138.10 (C<sub>quat</sub>), 137.95 (C<sub>quat</sub>), 137.84 (C<sub>quat</sub>), 137.77 (C<sub>quat</sub>), 137.56 (CH, C<sup>4</sup>), 137.13 (C<sub>quat</sub>), 137.03 (C<sub>quat</sub>), 136.90 (C<sub>quat</sub>), 136.72 (C<sub>quat</sub>), 136.00 (CH, C<sup>4</sup>), 132.39 (CH, C<sub>γ</sub>), 132.25 (CH, C<sup>5</sup>), 131.71 (CH), 131.46 (CH, C<sub>A2</sub>), 131.22 (CH), 131.12 (CH), 131.07 (CH), 131.01 (CH), 130.88 (CH, C<sub>B1</sub>), 130.50 (CH, C<sub>B2</sub>), 130.46 (CH, C<sub>A1</sub>), 129.77 (CH), 129.71 (CH), 125.98 (CH, C<sup>5</sup>), 125.60 (C<sub>quat</sub>), 125.19 (C<sub>quat</sub>), 124.10 (CH), 123.33 (CH), 123.24 (CH), 122.98 (CH), 122.96 (CH), 122.88 (CH), 122.69 (CH), 122.29 (CH, C<sup>3</sup>), 119.62 (CH, C<sup>3</sup>), 104.84 (C<sub>quat</sub>, C<sub>β2</sub>), 99.81 (C<sub>quat</sub>, C<sub>β1</sub>), 80.57 (C<sub>quat</sub>, C<sub>α</sub>), 79.15 (C<sub>quat</sub>, C<sub>α</sub>), 34.23 (C<sub>quat</sub>), 34.18 (C<sub>quat</sub>), 34.07 (C<sub>quat</sub>), 34.01 (C<sub>quat</sub>), 31.35 (C(CH<sub>3</sub>)<sub>3</sub>), 31.31 (C(CH<sub>3</sub>)<sub>3</sub>), 31.27 (C(CH<sub>3</sub>)<sub>3</sub>), 31.19 (C(CH<sub>3</sub>)<sub>3</sub>), 30.88 (C(CH<sub>3</sub>)<sub>3</sub>). **MS** (*m/z*-MALDI-TOF, THF): Found: 2630.5161 [M]<sup>+</sup>, calculated for [C<sub>184</sub>H<sub>198</sub>N<sub>2</sub>Pt]: 2630.5203. **Anal. Calcd.** For C<sub>184</sub>H<sub>198</sub>N<sub>2</sub>Pt·CH<sub>2</sub>Cl<sub>2</sub>: C, 81.76; H, 7.42; N, 1.03. Found: C, 81.61; H, 7.22; N, 1.13. **IR** ν (cm<sup>-1</sup>): 2960 (s), 2903 (m), 2869 (m), 2130 (sh m, C≡C), 2114 (m, C≡C), 1601 (w), 1509 (m), 1458 (m), 1392 (m), 1361 (m), 1274 (s, br), 1147 (w), 1120 (m), 1101 (m), 1016 (s), 859 (m), 831 (s), 775 (s), 677 (m).

[Pt(N<sup>^</sup>N)(2-ethynyl-5,8,11,14,17-penta-*tert*-butylhexa-*peri*-hexabenzocoronene)<sub>2</sub>] (49)

**49** was prepared using the general synthetic procedure from **44** (80.4 mg; 0.078 mmol), ethynyl-HBC (**7**) (140.2 mg; 0.170 mmol) and CuI (0.8 mg; 5 mol%) in still-dried CH<sub>2</sub>Cl<sub>2</sub>:<sup>i</sup>Pr<sub>2</sub>NH (4:1 v/v, 40 mL:10 mL) under argon for 24 hours. After this time, a very fine orange powdery precipitate was observed in an orange/yellow solution. Additional acetylene (2.0 mg; 0.002 mmol; 3 mol%) was added to the flask in order to push the reaction to completion. After a further 2 days stirring under argon, just one product spot was observed by TLC (CH<sub>2</sub>Cl<sub>2</sub>:hexane 1:1 v/v). After washing and removal of solvent *in vacuo*, the product was precipitated from excess methanol (~50 mL) and the orange/brown precipitate was filtered off and washed with cold methanol. (156 mg; 0.060 mmol; 77 %). **m.p.** > 360 °C. <sup>1</sup>H NMR (C<sub>2</sub>D<sub>2</sub>Cl<sub>4</sub>, 400.1 MHz, 40 °C): δ 10.26 (d, 1H, <sup>3</sup>J<sub>HH</sub> = 5.0 Hz, H<sup>6</sup>), 9.45 (s, 2H, H<sub>HBC</sub>), 9.30-9.38 (m, 14H, H<sub>HBC</sub>), 9.26 (s, 2H, H<sub>HBC</sub>), 9.21 (s, 2H, H<sub>HBC</sub>), 9.13 (s, 2H, H<sub>HBC</sub>), 9.04 (br s, 2H, H<sup>1</sup><sub>HBC</sub>), 8.18 (dd, 1H, <sup>3</sup>J<sub>HH</sub> = 7.0 Hz, H<sup>4</sup>), 8.00 (d, 1H, <sup>3</sup>J<sub>HH</sub> = 9.0 Hz, H<sup>3</sup>), 7.92 (d, 1H, <sup>3</sup>J<sub>HH</sub> = 8.0 Hz, H<sup>3</sup>), 7.77-7.83 (m, 3H, H<sup>4</sup>, H<sub>phenyl</sub>, H<sub>γ</sub>), 7.56 (dd, 1H, <sup>3</sup>J<sub>HH</sub> = 6.5 Hz, H<sup>5</sup>), 7.31 (d, 1H, <sup>3</sup>J<sub>HH</sub> = 7.5 Hz, H<sup>5</sup>), 7.16-7.25 (m, 4H, H<sub>phenyl</sub>), 7.15 (br, 1H, H<sub>phenyl</sub>), 6.89-6.95 (m, 4H, H<sub>phenyl</sub>), 6.79 (m, 4H, H<sub>phenyl</sub>), 1.93 (s, 9H, C(CH<sub>3</sub>)<sub>3</sub>), 1.84-1.90 (m, 81H, C(CH<sub>3</sub>)<sub>3</sub>), 1.33 (s, 9H, C(CH<sub>3</sub>)<sub>3</sub>), 1.17-1.20 (m, 27H, C(CH<sub>3</sub>)<sub>3</sub>). **MS** (*m/z*-MALDI-TOF, Toluene): Found: 2606.3408 [M]<sup>+</sup> 100 %, calculated for [C<sub>184</sub>H<sub>174</sub>N<sub>2</sub>Pt]: 2606.3325; Found: 2669.2783 [M+Cu]<sup>+</sup> 60 %, calculated for



---

$[\text{C}_{184}\text{H}_{174}\text{N}_2\text{CuPt}]^+$ : 2669.2621. **IR**  $\nu$  ( $\text{cm}^{-1}$ ): 3036 (w), 2957 (s), 2904 (m), 2865 (m), 2114 (sh m,  $\text{C}\equiv\text{C}$ ), 2108 (m,  $\text{C}\equiv\text{C}$ ), 1609 (w), 1514 (s), 1478 (m), 1462 (s), 1391 (s), 1359 (s), 1270 (s), 1200 (m), 1150 (m), 1121 (m), 1103 (m), 1018 (s), 862 (s), 831 (s), 781 (s), 676 (m).



## References

- (1) Wu, J.; Müllen, K. In *Carbon-Rich Compounds: From Molecules to Materials*; Haley, M. M., Tykwinski, R. R., Eds.; Wiley-VCH: 2006.
- (2) Allen, M. J.; Tung, V. C.; Kaner, R. B. *Chem. Rev.* **2009**, *110*, 132.
- (3) Watson, M. D.; Fechtenkotter, A.; Müllen, K. *Chem. Rev.* **2001**, *101*, 1267.
- (4) Iyer, V. S.; Wehmeier, M.; Brand, J. D.; Keegstra, M. A.; Müllen, K. *Angew. Chem., Int. Ed. Engl.* **1997**, *36*, 1604.
- (5) Kastler, M.; Pisula, W.; Wasserfallen, D.; Pakula, T.; Müllen, K. *J. Am. Chem. Soc.* **2005**, *127*, 4286.
- (6) Ito, S.; Wehmeier, M.; Brand, J. D.; Kübel, C.; Epsch, R.; Rabe, J. P.; Müllen, K. *Chem. Eur. J.* **2000**, *6*, 4327.
- (7) Fechtenkotter, A.; Tchegotareva, N.; Watson, M.; Müllen, K. *Tetrahedron* **2001**, *57*, 3769.
- (8) Fischbach, I.; Pakula, T.; Minkin, P.; Fechtenkötter, A.; Müllen, K.; Spiess, H. W.; Saalwächter, K. *J. Phys. Chem. B* **2002**, *106*, 6408.
- (9) Van De Craats, A. M.; Warman, J. M.; Fechtenkotter, A.; Brand, J. D.; Harbison, M. A.; Müllen, K. *Adv. Mater.* **1999**, *11*, 1469.
- (10) Herwig, P. T.; Enkelmann, V.; Schmelz, O.; Müllen, K. *Chem. Eur. J.* **2000**, *6*, 1834.
- (11) Wang, Z.; Dötz, F.; Enkelmann, V.; Müllen, K. *Angew. Chem. Int. Ed.* **2005**, *44*, 1247.
- (12) Wu, J.; Pisula, W.; Müllen, K. *Chem. Rev.* **2007**, *107*, 718.
- (13) Van de Craats, A. M.; Stutzmann, N.; Bunk, O.; Nielsen, M. M.; Watson, M.; Müllen, K.; Chanzy, H. D.; Sirringhaus, H.; Friend, R. H. *Adv. Mater.* **2003**, *15*, 495.
- (14) Li, C.; Liu, M.; Pschirer, N. G.; Baumgarten, M.; Müllen, K. *Chem. Rev.* **2010**.
- (15) Wong, W. W. H.; Ma, C.-Q.; Pisula, W.; Yan, C.; Feng, X.; Jones, D. J.; Müllen, K.; Janssen, R. A. J.; Bauerle, P.; Holmes, A. B. *Chem. Mater.* **2010**, *22*, 457.
- (16) Kalyanasundaram, K.; Grätzel, M. *Coord. Chem. Rev.* **1998**, *177*, 347.
- (17) Clar, E.; Ironside, C. T.; Zander, M. *J. Chem. Soc.* **1959**, 142.
- (18) Stabel, A.; Herwig, P.; Müllen, K.; Rabe, J. P. *Angew. Chem. Int. Ed.* **1995**, *34*, 1768.
- (19) Muller, M.; Kubel, C.; Müllen, K. *Chem. Eur. J.* **1998**, *4*, 2099.
- (20) Hyatt, J. A. *Org. Prep. Proced. Int.* **1991**, *23*, 460.
- (21) Kovacic, P.; Koch, F. W. *J. Org. Chem.* **1965**, *30*, 3176.
- (22) Di Stefano, M.; Negri, F.; Carbone, P.; Müllen, K. *Chem. Phys.* **2005**, *314*, 85.
- (23) Rempala, P.; Kroulik, J.; King, B. T. *J. Am. Chem. Soc.* **2004**, *126*, 15002.
- (24) Rempala, P.; Kroulik, J.; King, B. T. *J. Org. Chem.* **2006**, *71*, 5067.
- (25) King, B. T.; Kroulik, J.; Robertson, C. R.; Rempala, P.; Hilton, C. L.; Korinek, J. D.; Gortari, L. M. *J. Org. Chem.* **2007**, *72*, 2279.
- (26) Zhai, L.; Shukla, R.; Wadumethrige, S. H.; Rathore, R. *J. Org. Chem.* **2010**, *75*, 4748.
- (27) Draper, S. M.; Gregg, D. J.; Madathil, R. *J. Am. Chem. Soc.* **2002**, *124*, 3486.
- (28) Draper, S. M.; Gregg, D. J.; Schofield, E. R.; Browne, W. R.; Duati, M.; Vos, J. G.; Passaniti, P. *J. Am. Chem. Soc.* **2004**, *126*, 8694.
- (29) Gregg, D. J.; Bothe, E.; Hofer, P.; Passaniti, P.; Draper, S. M. *Inorg. Chem.* **2005**, *44*, 5654.
- (30) Lankage, B.; Transfer Report, University of Dublin, Trinity College: 2008.
- (31) Gregg, D. J.; Ollagnier, C. M. A.; Fitchett, C. M.; Draper, S. M. *Chem. Eur. J.* **2006**, *12*, 3043.
- (32) Bart, J. C. J. *Acta Crystallogr., Sect. B* **1968**, *24*, 1277.
- (33) Larson, E. M.; Von Dreele, R. B.; Hanson, P.; Gust, J. D. *Acta Crystallogr., Sect. C* **1990**, *C46*, 784.
- (34) Constable, E. C.; Eich, O.; Fenske, D.; Housecroft, C. E.; Johnston, L. A. *Chem. Eur. J.* **2000**, *6*, 4364.
- (35) Wiesler, U. M.; Berresheim, A. J.; Morgenroth, F.; Lieser, G.; Müllen, K. *Macromolecules* **2001**, *34*, 187.
- (36) Morgenroth, F.; Reuther, E.; Müllen, K. *Angew. Chem., Int. Ed. Engl.* **1997**, *36*, 631.
- (37) Weil, T.; Reuther, E.; Müllen, K. *Angew. Chem., Int. Ed.* **2002**, *41*, 1900.
- (38) Schlichting, P.; Duchscherer, B.; Seisenberger, G.; Basche, T.; Brauchle, C.; Müllen, K. *Chem. Eur. J.* **1999**, *5*, 2388.
- (39) Kodis, G.; Terazono, Y.; Liddell, P. A.; Andreasson, J.; Garg, V.; Hambourger, M.; Moore, T. A.; Moore, A. L.; Gust, D. *J. Am. Chem. Soc.* **2006**, *128*, 1818.
- (40) Keirstead, A. E.; Bridgewater, J. W.; Terazono, Y.; Kodis, G.; Straight, S.; Liddell, P. A.; Moore, A. L.; Moore, T. A.; Gust, D. *J. Am. Chem. Soc.* **2010**, *132*, 6588.
- (41) Shen, X.; Ho, D. M.; Pascal, R. A., Jr. *J. Am. Chem. Soc.* **2004**, *126*, 5798.

## References

- (42) Kobayashi, K.; Kobayashi, N.; Ikuta, M.; Therrien, B.; Sakamoto, S.; Yamaguchi, K. *J. Org. Chem.* **2005**, *70*, 749.
- (43) Schlupp, M.; Weil, T.; Berresheim, A. J.; Wiesler, U. M.; Bargon, J.; Müllen, K. *Angew. Chem., Int. Ed.* **2001**, *40*, 4011.
- (44) Haberecht, M. C.; Schnorr, J. M.; Andreitchenko, E. V.; Clark, C. G., Jr.; Wagner, M.; Müllen, K. *Angew. Chem., Int. Ed.* **2008**, *47*, 1662.
- (45) Qin, T.; Ding, J.; Wang, L.; Baumgarten, M.; Zhou, G.; Müllen, K. *J. Am. Chem. Soc.* **2009**, *131*, 14329.
- (46) Brydges, S.; Harrington, L. E.; McGlinchey, M. J. *Coord. Chem. Rev.* **2002**, *233-234*, 75.
- (47) Crocker, M.; Green, M.; Orpen, A. G.; Thomas, D. M. *J. Chem. Soc., Chem. Commun.* **1984**, 1141.
- (48) Quarmby, I. C.; Hemond, R. C.; Feher, F. J.; Green, M.; Geiger, W. E. *J. Organomet. Chem.* **1999**, *577*, 189.
- (49) Gupta, H. K.; Brydges, S.; McGlinchey, M. J. *Organometallics* **1999**, *18*, 115.
- (50) Siegel, A.; Rausch, M. D. *Synth. React. Inorg. Met.-Org. Chem.* **1978**, *8*, 209.
- (51) Mailvaganam, B.; Sayer, B. G.; McGlinchey, M. J. *J. Organomet. Chem.* **1990**, *395*, 177.
- (52) Dijkstra, H. P.; Kruithof, C. A.; Ronde, N.; Van de Coevering, R.; Ramon, D. J.; Vogt, D.; Van Klink, G. P. M.; Van Koten, G. *J. Org. Chem.* **2003**, *68*, 675.
- (53) Dijkstra, H. P.; Meijer, M. D.; Patel, J.; Kreiter, R.; Van Klink, G. P. M.; Lutz, M.; Spek, A. L.; Canty, A. J.; Van Koten, G. *Organometallics* **2001**, *20*, 3159.
- (54) Dijkstra, H. P.; Steenwinkel, P.; Grove, D. M.; Lutz, M.; Spek, A. L.; Van Koten, G. *Angew. Chem., Int. Ed.* **1999**, *38*, 2186.
- (55) Kivala, M.; Boudon, C.; Gisselbrecht, J. P.; Seiler, P.; Gross, M.; Diederich, F. *Angew. Chem., Int. Ed.* **2007**, *46*, 6357.
- (56) Harriman, A.; Ziessel, R. *Coord. Chem. Rev.* **1998**, *171*, 331.
- (57) Ziessel, R.; Hissler, M.; El-ghayoury, A.; Harriman, A. *Coord. Chem. Rev.* **1998**, *178-180*, 1251.
- (58) Benniston, A. C.; Grosshenny, V.; Harriman, A.; Ziessel, R. *Angew. Chem. Int. Ed.* **1994**, *33*, 1884.
- (59) El-ghayoury, A.; Harriman, A.; Khatyr, A.; Ziessel, R. *Angew. Chem. Int. Ed.* **2000**, *39*, 185.
- (60) Harriman, A.; Hissler, M.; Ziessel, R.; De Cian, A.; Fisher, J. *J. Chem. Soc., Dalton Trans.* **1995**, 4067.
- (61) Grosshenny, V.; Harriman, A.; Hissler, M.; Ziessel, R. *J. Chem. Soc., Faraday Trans.* **1996**, *92*, 2223.
- (62) Welter, S.; Salluce, N.; Belser, P.; Groeneveld, M.; De Cola, L. *Coord. Chem. Rev.* **2005**, *249*, 1360.
- (63) Welter, S.; Salluce, N.; Benetti, A.; Rot, N.; Belser, P.; Sonar, P.; Grimsdale, A. C.; Müllen, K.; Lutz, M.; Spek, A. L.; De Cola, L. *Inorg. Chem.* **2005**, *44*, 4706.
- (64) Schlicke, B.; Belser, P.; De Cola, L.; Sabbioni, E.; Balzani, V. *J. Am. Chem. Soc.* **1999**, *121*, 4207.
- (65) Shin, D.; Switzer, C. *Chem. Commun.* **2007**, 4401.
- (66) Shen, W. Z.; Trotscher-Kaus, G.; Lippert, B. *Dalton Trans.* **2009**, 8203.
- (67) Pavia, D. L.; Lampman, G. M.; Kriz, G. S. *Introduction to Spectroscopy*; 2<sup>nd</sup> ed.; Saunders College Publishing, 1996.
- (68) Roberts, J. D.; Weigert, F. J. *J. Am. Chem. Soc.* **1971**, *93*, 2361.
- (69) Matsubara, K.; Oba, A.; Usui, Y. *Magn. Reson. Chem.* **1998**, *36*, 761.
- (70) Vrabel, M.; Hocek, M.; Havran, L.; Fojta, M.; Votruba, I.; Klepetarova, B.; Pohl, R.; Rulisek, L.; Zendlova, L.; Hobza, P.; Shih, I. H.; Mabery, E.; Mackman, R. *Eur. J. Inorg. Chem.* **2007**, 1752.
- (71) Des Abbayes, H.; Clement, J. C.; Laurent, P.; Tanguy, G.; Thilmont, N. *Organometallics* **1988**, *7*, 2293.
- (72) Mueller-Westerhoff, U. T.; Zhou, M. *J. Org. Chem.* **1994**, *59*, 4988.
- (73) Graczyk, A., Ph.D. Thesis, University of Dublin, Trinity College, 2007.
- (74) Murphy, F. A.; Draper, S. M. *J. Org. Chem.* **2010**, *75*, 1862.
- (75) Murphy, F. A., Ph.D. Thesis, University of Dublin, Trinity College, 2008.
- (76) Merkushev, E. B.; Simakhina, N. D.; Koveshnikova, G. M. *Synthesis* **1980**, 486.
- (77) Vos, J. G.; Kelly, J. M. *Dalton Trans.* **2006**, 4869.
- (78) Campagna, S.; Puntoriero, F.; Nastasi, F.; Bergamini, G.; Balzani, V. *Top. Curr. Chem.* **2007**, *280*, 117.
- (79) Kaes, C.; Katz, A.; Hosseini, M. W. *Chem. Rev.* **2000**, *100*, 3553.
- (80) Kalyandundaram, K. *Photochemistry of Polypyridine and Porphyrin Complexes*; 1<sup>st</sup> ed.; Academic Press Limited, 1992.
- (81) Fletcher, N. C. *J. Chem. Soc., Perkin Trans. 1* **2002**, 1831.
- (82) Fletcher, N. C.; Nieuwenhuyzen, M.; Rainey, S. *J. Chem. Soc., Dalton Trans.* **2001**, 2641.
- (83) Friedman, A. E.; Kumar, C. V.; Turro, N. J.; Barton, J. K. *Nucleic Acids Res.* **1991**, *19*, 2595.
- (84) Rutherford, T. J.; Reitsma, D. A.; Keene, F. R. *J. Chem. Soc., Dalton Trans.* **1994**, 3659.

- (85) Crosby, G. A. *Acc. Chem. Res.* **1975**, *8*, 231.
- (86) Balzani, V.; Bergamini, G.; Marchioni, F.; Ceroni, P. *Coord. Chem. Rev.* **2006**, *250*, 1254.
- (87) Medlycott, E. A.; Hanan, G. S. *Coord. Chem. Rev.* **2006**, *250*, 1763.
- (88) Winkler, J. R.; Netzel, T. L.; Creutz, C.; Sutin, N. *J. Am. Chem. Soc.* **1987**, *109*, 2381.
- (89) Juris, A.; Balzani, V.; Barigelletti, F.; Campagna, S.; Belser, P.; Von Zelewsky, A. *Coord. Chem. Rev.* **1988**, *84*, 85.
- (90) Ohsawa, Y.; Hanck, K. W.; DeArmond, M. K. *J. Electroanal. Chem. Interfacial Electrochem.* **1984**, *175*, 229.
- (91) Juris, A.; Barigelletti, F.; Balzani, V.; Belser, P.; Von Zelewsky, A. *Isr. J. Chem.* **1982**, *22*, 89.
- (92) Anderson, P. A.; Keene, F. R.; Meyer, T. J.; Moss, J. A.; Strouse, G. F.; Treadway, J. A. *J. Chem. Soc., Dalton Trans.* **2002**, 3820.
- (93) Glazer, E. C.; Magde, D.; Tor, Y. *J. Am. Chem. Soc.* **2007**, *129*, 8544.
- (94) Kozlov, D. V.; Tyson, D. S.; Goze, C.; Ziessel, R.; Castellano, F. N. *Inorg. Chem.* **2004**, *43*, 6083.
- (95) Del Guerzo, A.; Leroy, S.; Fages, F.; Schmehl, R. H. *Inorg. Chem.* **2002**, *41*, 359.
- (96) Ji, S.; Wu, W.; Wu, W.; Song, P.; Han, K.; Wang, Z.; Liu, S.; Guo, H.; Zhao, J. *J. Mater. Chem.* **2010**, *20*, 1953.
- (97) Carraway, E. R.; Demas, J. N.; DeGraff, B. A.; Bacon, J. R. *Anal. Chem.* **1991**, *63*, 337.
- (98) Orellana, G.; Moreno-Bondi, M. C.; Segovia, E.; Marazuela, M. D. *Anal. Chem.* **1992**, *64*, 2210.
- (99) Price, J. M.; Xu, W.; Demas, J. N.; DeGraff, B. A. *Anal. Chem.* **1998**, *70*, 265.
- (100) Beer, P. D.; Cadman, J. *Coord. Chem. Rev.* **2000**, *205*, 131.
- (101) Buda, M.; Kalyuzhny, G.; Bard, A. J. *J. Am. Chem. Soc.* **2002**, *124*, 6090.
- (102) O'Regan, B.; Grätzel, M. *Nature* **1991**, *353*, 737.
- (103) Nazeeruddin, M. K.; Kay, A.; Rodicio, I.; Humphry-Baker, R.; Müller, E.; Liska, P.; Vlachopoulos, N.; Grätzel, M. *J. Am. Chem. Soc.* **1993**, *115*, 6382.
- (104) Erkkila, K. E.; Odom, D. T.; Barton, J. K. *Chem. Rev.* **1999**, *99*, 2777.
- (105) Olson, E. J. C.; Hu, D.; Hoermann, A.; Jonkman, A. M.; Arkin, M. R.; Stemp, E. D. A.; Barton, J. K.; Barbara, P. F. *J. Am. Chem. Soc.* **1997**, *119*, 11458.
- (106) Kelly, J. M.; Tossi, A. B.; McConnell, D. J.; OhUigin, C. *Nucleic Acids Res.* **1985**, *13*, 6017.
- (107) Collin, J. P.; Jouvenot, D.; Koizumi, M.; Sauvage, J. P. *Inorg. Chem.* **2005**, *44*, 4693.
- (108) Sullivan, B. P.; Salmon, D. J.; Meyer, T. J. *Inorg. Chem.* **1978**, *17*, 3334.
- (109) Rillema, D. P.; Jones, D. S.; Levy, H. A. *J. Chem. Soc., Chem. Commun.* **1979**, 849.
- (110) Koizumi, T.; Tanaka, K. *Angew. Chem., Int. Ed.* **2005**, *44*, 5891.
- (111) Farah, A. A.; Pietro, W. J. *Inorg. Chem. Commun.* **2003**, *6*, 662.
- (112) Onggo, D.; Scudder, M. L.; Craig, D. C.; Goodwin, H. A. *J. Mol. Struct.* **2005**, *738*, 129.
- (113) Bondi, A. *J. Phys. Chem.* **1964**, *68*, 441.
- (114) Orellana, G.; Alvarez, I. C.; Santoro, J. *Inorg. Chem.* **1988**, *27*, 1025.
- (115) Benito, J.; Berenguer, J. R.; Fornies, J.; Gil, B.; Gomez, J.; Lalinde, E. *Dalton Trans.* **2003**, 4331.
- (116) Chen, Y.; Li, K.; Lu, W.; Chui, S. S. Y.; Ma, C. W.; Che, C. M. *Angew. Chem. Int. Ed.* **2009**, *48*, 9909.
- (117) Wang, K. W.; Chen, J. L.; Cheng, Y. M.; Chung, M. W.; Hsieh, C. C.; Lee, G. H.; Chou, P. T.; Chen, K.; Chi, Y. *Inorg. Chem.* **2010**, *49*, 1372.
- (118) Lytle, F. E.; Hercules, D. M. *J. Am. Chem. Soc.* **1969**, *91*, 253.
- (119) James, P. V.; Yoosaf, K.; Kumar, J.; Thomas, K. G.; Listorti, A.; Accorsi, G.; Armaroli, N. *Photochem. Photobiol. Sci.* **2009**, *8*, 1432.
- (120) Wayne, R. P. *Principles and Applications of Photochemistry*; Oxford University Press, 1988.
- (121) Diring, S.; Retailleau, P.; Ziessel, R. *Tet. Lett.* **2007**, *48*, 8069.
- (122) Birckner, E.; Grummt, U. W.; Goeller, A. H.; Pautzsch, T.; Egbe, D. A. M.; Al-Higari, M.; Klemm, E. *J. Phys. Chem. A* **2001**, *105*, 10307.
- (123) Pautzsch, T.; Rode, C.; Klemm, E. *J. Prakt. Chem.* **1999**, *341*, 548.
- (124) Berlman, I. B.; Wirth, H. O.; Steingraber, O. J. *J. Phys. Chem.* **1971**, *75*, 318.
- (125) Nijegorodov, N. I.; Downey, W. S. *J. Phys. Chem.* **1994**, *98*, 5639.
- (126) Chen, P.; Meyer, T. J. *Chem. Rev.* **1998**, *98*, 1439.
- (127) Kober, E. M.; Sullivan, B. P.; Meyer, T. J. *Inorg. Chem.* **1984**, *23*, 2098.
- (128) Bard, A. J.; Faulkner, L. R. *Electrochemical Methods, Fundamentals and Applications*; 2 ed.; John Wiley & Sons: New York 2001.
- (129) Steen, R. O.; Nurkkala, L. J.; Angus-Dunne, S. J.; Schmitt, C. X.; Constable, E. C.; Riley, M. J.; Bernhardt, P. V.; Dunne, S. J. *Eur. J. Inorg. Chem.* **2008**, 1784.
- (130) Barigelletti, F.; Juris, A.; Balzani, V.; Belser, P.; Von Zelewsky, A. *Inorg. Chem.* **1987**, *26*, 4115.
- (131) Ait-Haddou, H.; Bejan, E.; Daran, J. C.; Balavoine, G. G. A.; Berruyer-Penaud, F.; Bonazzola, L.; Smaoui-Chaabouni, H.; Amouyal, E. *J. Chem. Soc., Dalton Trans.* **1999**, 3095.

## References

- (132) Nurkkala, L. J.; Steen, R. O.; Friberg, H. K. J.; Haeggstroem, J. A.; Bernhardt, P. V.; Riley, M. J.; Dunne, S. J. *Eur. J. Inorg. Chem.* **2008**, 4101.
- (133) Pant, D.; Tripathi, U. C.; Joshi, G. C.; Tripathi, H. B.; Pant, D. D. *J. Photochem. Photobiol. A* **1990**, *51*, 313.
- (134) Fernandez, S.; Fornies, J.; Gil, B.; Gomez, J.; Lalinde, E. *Dalton Trans.* **2003**, 822.
- (135) Crosby, G. A.; Demas, J. N. *J. Phys. Chem.* **1971**, *75*, 991.
- (136) Eaton, D. F. *Pure Appl. Chem.* **1988**, *60*, 1107.
- (137) Fery-Forgues, S.; Lavabre, D. *J. Chem. Educ.* **1999**, *76*, 1260.
- (138) Loren, J. C.; Siegel, J. S. *Angew. Chem., Int. Ed.* **2001**, *40*, 754.
- (139) Van Houten, J.; Watts, R. J. *J. Am. Chem. Soc.* **1976**, *98*, 4853.
- (140) Kelly, J. M.; Long, C.; O'Connell, C. M.; Vos, J. G.; Tinnemans, A. H. A. *Inorg. Chem.* **1983**, *22*, 2818.
- (141) Fabian, R. H.; Klassen, D. M.; Sonntag, R. W. *Inorg. Chem.* **1980**, *19*, 1977.
- (142) Amouyal, E.; Penaud-Berruyer, F.; Azhari, D.; Ait-Haddou, H.; Fontenas, C.; Bejan, E.; Daran, J. C.; Balavoine, G. G. A. *New J. Chem.* **1998**, *22*, 373.
- (143) Sabatini, C.; Barbieri, A.; Barigelletti, F.; Arm, K. J.; Williams, J. A. G. *Photochem. Photobiol. Sci.* **2007**, *6*, 397.
- (144) Kozhevnikov, V. N.; Shabunina, O. V.; Kopchuk, D. S.; Ustinova, M. M.; König, B.; Kozhevnikov, D. N. *Tetrahedron* **2008**, *64*, 8963.
- (145) Long, N. J.; Williams, C. K. *Angew. Chem. Int. Ed.* **2003**, *42*, 2586.
- (146) Yam, V. W. W. *Acc. Chem. Res.* **2002**, *35*, 555.
- (147) Schwab, P. F. H.; Levin, M. D.; Michl, J. *Chem. Rev.* **1999**, *99*, 1863.
- (148) Elschenbroich, C. *Organometallics*; 3<sup>rd</sup> ed.; Wiley-VCH: Weinheim, 2006.
- (149) Williams, J. A. G.; Develay, S.; Rochester, D. L.; Murphy, L. *Coord. Chem. Rev.* **2008**, *252*, 2596.
- (150) Klein, A.; Van Slageren, J.; Zalis, S. *Eur. J. Inorg. Chem.* **2003**, 1917.
- (151) Burroughes, J. H.; Bradley, D. D. C.; Brown, A. R.; Marks, R. N.; Mackay, K.; Friend, R. H.; Burns, P. L.; Holmes, A. B. *Nature* **1990**, *347*, 539.
- (152) Bunz, U. H. F. *Chem. Rev.* **2000**, *100*, 1605.
- (153) Davey, A. P.; Elliott, S.; O'Connor, O.; Blau, W. J. *Chem. Soc., Chem. Commun.* **1995**, 1433.
- (154) Ley, K. D.; Schanze, K. S. *Coord. Chem. Rev.* **1998**, *171*, 287.
- (155) Liu, Y.; Li, Y.; Schanze, K. S. *J. Photochem. Photobiol., C: Photochem. Rev.* **2002**, *3*, 1.
- (156) Evans, R. C.; Douglas, P.; Winscom, C. J. *Coord. Chem. Rev.* **2006**, *250*, 2093.
- (157) Baldo, M. A.; O'Brien, D. F.; You, Y.; Shoustikov, A.; Sibley, S.; Thompson, M. E.; Forrest, S. R. *Nature* **1998**, *395*, 151.
- (158) Baralt, E.; Boudreaux, E. A.; Demas, J. N.; Lenhert, P. G.; Lukehart, C. M.; McPhail, A. T.; McPhail, D. R.; Myers, J. B., Jr.; Sacksteder, L.; True, W. R. *Organometallics* **1989**, *8*, 2417.
- (159) Sacksteder, L.; Baralt, E.; DeGraff, B. A.; Lukehart, C. M.; Demas, J. N. *Inorg. Chem.* **1991**, *30*, 2468.
- (160) Silverman, E. E.; Cardolaccia, T.; Zhao, X.; Kim, K. Y.; Haskins-Glusac, K.; Schanze, K. S. *Coord. Chem. Rev.* **2005**, *249*, 1491.
- (161) Liu, Y.; Jiang, S.; Glusac, K.; Powell, D. H.; Anderson, D. F.; Schanze, K. S. *J. Am. Chem. Soc.* **2002**, *124*, 12412.
- (162) Beljonne, D.; Wittmann, H. F.; Koehler, A.; Graham, S.; Younus, M.; Lewis, J.; Raithby, P. R.; Khan, M. S.; Friend, R. H.; Bredas, J. L. *J. Chem. Phys.* **1996**, *105*, 3868.
- (163) Khan, M. S.; Al-Suti, M. K.; Al-Mandhary, M. R. A.; Ahrens, B.; Bjernemose, J. K.; Mahon, M. F.; Male, L.; Raithby, P. R.; Friend, R. H.; Koehler, A.; Wilson, J. S. *Dalton Trans.* **2003**, 65.
- (164) Abe, A.; Kimura, N.; Tabata, S. *Macromolecules* **1991**, *24*, 6238.
- (165) Chan, C. K. M.; Tao, C. H.; Tam, H. L.; Zhu, N.; Yam, V. W. W.; Cheah, K. W. *Inorg. Chem.* **2009**, *48*, 2855.
- (166) Mei, J.; Ogawa, K.; Kim, Y. G.; Heston, N. C.; Arenas, D. J.; Nasrollahi, Z.; McCarley, T. D.; Tanner, D. B.; Reynolds, J. R.; Schanze, K. S. *ACS Appl. Mater. Interfaces* **2009**, *1*, 150.
- (167) Onitsuka, K.; Shimizu, A.; Takahashi, S. *Chem. Commun.* **2003**, 280.
- (168) Onitsuka, K.; Fujimoto, M.; Kitajima, H.; Ohshiro, N.; Takei, F.; Takahashi, S. *Chem. Eur. J.* **2004**, *10*, 6433.
- (169) Tao, C. H.; Zhu, N.; Yam, V. W. W. *Chem. Eur. J.* **2005**, *11*, 1647.
- (170) Tao, C. H.; Yam, V. W. W. *J. Photochem. Photobiol., C: Photochem. Rev.* **2009**, *10*, 130.
- (171) Wu, J.; Fechtenkotter, A.; Gauss, J.; Watson, M. D.; Kastler, M.; Fechtenkotter, C.; Wagner, M.; Müllen, K. *J. Am. Chem. Soc.* **2004**, *126*, 11311.
- (172) El Hamaoui, B.; Laquai, F.; Balushev, S.; Wu, J.; Müllen, K. *Synthetic Met.* **2006**, *156*, 1182.
- (173) Kim, K. Y.; Liu, S.; Kose, M. E.; Schanze, K. S. *Inorg. Chem.* **2006**, *45*, 2509.

- (174) El Hamaoui, B.; Zhi, L.; Wu, J.; Li, J.; Lucas, N. T.; Tomovic, Z.; Kolb, U.; Müllen, K. *Adv. Funct. Mater.* **2007**, *17*, 1179.
- (175) Fogel, Y.; Kastler, M.; Wang, Z.; Andrienko, D.; Bodwell, G. J.; Müllen, K. *J. Am. Chem. Soc.* **2007**, *129*, 11743.
- (176) Lucas, N. T.; Zareie, H. M.; McDonagh, A. M. *ACS Nano* **2007**, *1*, 348.
- (177) Haskins-Glusac, K.; Ghiviriga, I.; Abboud, K. A.; Schanze, K. S. *J. Phys. Chem. B* **2004**, *108*, 4969.
- (178) Sonogashira, K.; Yatake, T.; Tohda, Y.; Takahashi, S.; Hagihara, N. *J. Chem. Soc., Chem. Commun.* **1977**, 291.
- (179) Sonogashira, K.; Fujikura, Y.; Yatake, T.; Toyoshima, N.; Takahashi, S.; Hagihara, N. *J. Organomet. Chem.* **1978**, *145*, 101.
- (180) Fornies, J.; Gomez-Saso, M. A.; Lalinde, E.; Martinez, F.; Moreno, M. T. *Organometallics* **1992**, *11*, 2873.
- (181) Saha, R.; Qaium, M. A.; Debnath, D.; Younus, M.; Chawdhury, N.; Sultana, N.; Kociok-Koehn, G.; Ooi, L. L.; Raithby, P. R.; Kijima, M. *Dalton Trans.* **2005**, 2760.
- (182) Bailar, J. C. J.; Itatani, H. *Inorg. Chem.* **1965**, *4*, 1618.
- (183) Booth, G.; Chatt, J. *J. Chem. Soc., A* **1966**, 634.
- (184) Russo, M. V.; Lo, S. C.; Franceschini, P.; Biagini, G.; Furlani, A. *J. Organomet. Chem.* **2001**, *619*, 49.
- (185) Pidcock, A.; Richards, R. E.; Venanzi, L. M. *J. Chem. Soc., A* **1966**, 1707.
- (186) Rosenberg, B.; Van Camp, L.; Krigas, T. *Nature* **1965**, *205*, 698.
- (187) Rosenberg, B.; Van Camp, L.; Trosko, J. E.; Mansour, V. H. *Nature* **1969**, *222*, 385.
- (188) Petsko, G. A. *Nature* **1995**, *377*, 580.
- (189) Mitoraj, M. P.; Zhu, H.; Michalak, A.; Ziegler, T. *Int. J. Quantum Chem.* **2009**, *109*, 3379.
- (190) Shetty, A. S.; Zhang, J.; Moore, J. S. *J. Am. Chem. Soc.* **1996**, *118*, 1019.
- (191) Khan, M. S.; Al-Mandhary, M. R. A.; Al-Suti, M. K.; Ahrens, B.; Mahon, M. F.; Male, L.; Raithby, P. R.; Boothby, C. E.; Koehler, A. *Dalton Trans.* **2003**, 74.
- (192) Campbell, K.; McDonald, R.; Ferguson, M. J.; Tykwinski, R. R. *J. Organomet. Chem.* **2003**, *683*, 379.
- (193) Bruce, M. I.; Costuas, K.; Halet, J. F.; Hall, B. C.; Low, P. J.; Nicholson, B. K.; Skelton, B. W.; White, A. H. *J. Chem. Soc., Dalton Trans.* **2002**, 383.
- (194) Long, N. J.; Wong, C. K.; White, A. J. P. *Organometallics* **2006**, *25*, 2525.
- (195) Diez, A.; Lalinde, E.; Teresa Moreno, M.; Sanchez, S. *Dalton Trans.* **2009**, 3434.
- (196) Rigamonti, L.; Forni, A.; Manassero, M.; Manassero, C.; Pasini, A. *Inorg. Chem.* **2010**, *49*, 123.
- (197) Mather, G. G.; Pidcock, A.; Rapsey, G. J. N. *J. Chem. Soc., Dalton Trans.* **1973**, 2095.
- (198) Haar, C. M.; Nolan, S. P.; Marshall, W. J.; Moloy, K. G.; Prock, A.; Giering, W. P. *Organometallics* **1999**, *18*, 474.
- (199) Xu, H. B.; Zhang, L. Y.; Chen, X. M.; Li, X. L.; Chen, Z. N. *Cryst. Growth Des.* **2009**, *9*, 569.
- (200) Diez, A.; Fernandez, J.; Lalinde, E.; Moreno, M. T.; Sanchez, S. *Dalton Trans.* **2008**, 4926.
- (201) Younus, M.; Long, N. J.; Raithby, P. R.; Lewis, J. J. *J. Organomet. Chem.* **1998**, *570*, 55.
- (202) Schull, T. L.; Kushmerick, J. G.; Patterson, C. H.; George, C.; Moore, M. H.; Pollack, S. K.; Shashidhar, R. *J. Am. Chem. Soc.* **2003**, *125*, 3202.
- (203) Wang, Z.; Tomovic, Z.; Kastler, M.; Pretsch, R.; Negri, F.; Enkelmann, V.; Müllen, K. *J. Am. Chem. Soc.* **2004**, *126*, 7794.
- (204) Wu, J.; Watson, M. D.; Tchegotareva, N.; Wang, Z.; Müllen, K. *J. Org. Chem.* **2004**, *69*, 8194.
- (205) Blanton, C. B.; Murtaza, Z.; Shaver, R. J.; Rillema, D. P. *Inorg. Chem.* **1992**, *31*, 3230.
- (206) Liu, D.; De Feyter, S.; Cotlet, M.; Stefan, A.; Wiesler, U. M.; Herrmann, A.; Grebel-Koehler, D.; Qu, J.; Müllen, K.; De Schryver, F. C. *Macromolecules* **2003**, *36*, 5918.
- (207) Hard, T.; Fan, P.; Kearns, D. R. *Photochem. Photobiol.* **1990**, *51*, 77.
- (208) Barigelletti, F.; Ventura, B.; Collin, J. P.; Kayhanian, R.; Gaviña, P.; Sauvage, J. P. *Eur. J. Inorg. Chem.* **2000**, *2000*, 113.
- (209) Miskowski, V. M.; Houlding, V. H.; Che, C. M.; Wang, Y. *Inorg. Chem.* **1993**, *32*, 2518.
- (210) Cheung, T. C.; Cheung, K. K.; Peng, S. M.; Che, C. M. *J. Chem. Soc., Dalton Trans.* **1996**, 1645.
- (211) Lai, S. W.; Chan, M. C. W.; Cheung, T. C.; Peng, S. M.; Che, C. M. *Inorg. Chem.* **1999**, *38*, 4046.
- (212) Yan, B. P.; Cheung, C.; Kui, S.; Xiang, H. F.; Roy, V.; Xu, S. J.; Che, C. M. *Adv. Mater.* **2007**, *19*, 3599.
- (213) Lu, W.; Mi, B. X.; Chan, M. C. W.; Hui, Z.; Che, C. M.; Zhu, N.; Lee, S. T. *J. Am. Chem. Soc.* **2004**, *126*, 4958.
- (214) Kui, S. C. F.; Sham, I. H. T.; Cheung, C. C. C.; Ma, C. W.; Yan, B.; Zhu, N.; Che, C. M.; Fu, W. F. *Chem. Eur. J.* **2007**, *13*, 417.
- (215) Qiu, D.; Wu, J.; Xie, Z.; Cheng, Y.; Wang, L. *J. Organomet. Chem.* **2009**, *694*, 737.

## References

- (216) Du, P.; Schneider, J.; Luo, G.; Brennessel, W. W.; Eisenberg, R. *Inorg. Chem.* **2009**, *48*, 4952.
- (217) Wu, P.; Wong, E. M.; Ma, D. L.; Tong, G. M.; Ng, K. M.; Che, C. M. *Chem. Eur. J.* **2009**, *15*, 3652.
- (218) Ma, D. L.; Che, C. M. *Chem. Eur. J.* **2003**, *9*, 6133.
- (219) Chan, C. W.; Cheng, L. K.; Che, C. M. *Coord. Chem. Rev.* **1994**, *132*, 87.
- (220) Hissler, M.; Connick, W. B.; Geiger, D. K.; McGarrah, J. E.; Lipa, D.; Lachicotte, R. J.; Eisenberg, R. *Inorg. Chem.* **2000**, *39*, 447.
- (221) Chan, S. C.; Chan, M. C. W.; Wang, Y.; Che, C. M.; Cheung, K. K.; Zhu, N. *Chem. Eur. J.* **2001**, *7*, 4180.
- (222) Whittle, C. E.; Weinstein, J. A.; George, M. W.; Schanze, K. S. *Inorg. Chem.* **2001**, *40*, 4053.
- (223) Hua, F.; Kinayyigit, S.; Cable, J. R.; Castellano, F. N. *Inorg. Chem.* **2005**, *44*, 471.
- (224) Tam, A. Y. Y.; Lam, W. H.; Wong, K. M. C.; Zhu, N.; Yam, V. W. W. *Chem. Eur. J.* **2008**, *14*, 4562.
- (225) Ji, Z.; Li, Y.; Sun, W. *Inorg. Chem.* **2008**, *47*, 7599.
- (226) Wong, K. M. C.; Yam, V. W. W. *Coord. Chem. Rev.* **2007**, *251*, 2477.
- (227) Kwok, E. C. H.; Chan, M. Y.; Wong, K. M. C.; Lam, W. H.; Yam, V. W. W. *Chem. Eur. J.* **2010**, *16*, 12244.
- (228) Lu, W.; Chan, M. C. W.; Zhu, N.; Che, C. M.; He, Z.; Wong, K. Y. *Chem. Eur. J.* **2003**, *9*, 6155.
- (229) Ni, J.; Wu, Y. H.; Zhang, X.; Li, B.; Zhang, L. Y.; Chen, Z. N. *Inorg. Chem.* **2009**, *48*, 10202.
- (230) Chakraborty, S.; Wadas, T. J.; Hester, H.; Schmehl, R.; Eisenberg, R. *Inorg. Chem.* **2005**, *44*, 6865.
- (231) Lee, J. K. W.; Ko, C. C.; Wong, K. M. C.; Zhu, N.; Yam, V. W. W. *Organometallics* **2007**, *26*, 12.
- (232) Diring, S.; Retailliau, P.; Ziessel, R. *J. Org. Chem.* **2007**, *72*, 10181.
- (233) Ding, J.; Pan, D.; Tung, C. H.; Wu, L. Z. *Inorg. Chem.* **2008**, *47*, 5099.
- (234) Cardenas, D. J.; Echavarren, A. M.; Ramirez de Arellano, M. C. *Organometallics* **1999**, *18*, 3337.
- (235) Cave, G. W. V.; Alcock, N. W.; Rourke, J. P. *Organometallics* **1999**, *18*, 1801.
- (236) Cave, G. W. V.; Fanizzi, F. P.; Deeth, R. J.; Errington, W.; Rourke, J. P. *Organometallics* **2000**, *19*, 1355.
- (237) Cao, Q. Y.; Fu, W. F.; Zhao, X. L. *Acta Crystallogr., Sect. E: Struct. Rep. Online* **2005**, *61*, 427.
- (238) Hofmann, A.; Dahlenburg, L.; Van Eldik, R. *Inorg. Chem.* **2003**, *42*, 6528.
- (239) James, S. L.; Younus, M.; Raithby, P. R.; Lewis, J. J. *Organomet. Chem.* **1997**, *543*, 233.
- (240) Siu, P. K. M.; Lai, S. W.; Lu, W.; Zhu, N.; Che, C. M. *Eur. J. Inorg. Chem.* **2003**, 2749.
- (241) Adams, C. J.; James, S. L.; Liu, X.; Raithby, P. R.; Yellowlees, L. J. *J. Chem. Soc., Dalton Trans.* **2000**, 63.
- (242) Romeo, R.; D'Amico, G.; Guido, E.; Albinati, A.; Rizzato, S. *Inorg. Chem.* **2007**, *46*, 10681.
- (243) Wang, Y.; Stretton, A. D.; McConnell, M. C.; Wood, P. A.; Parsons, S.; Henry, J. B.; Mount, A. R.; Galow, T. H. *J. Am. Chem. Soc.* **2007**, *129*, 13193.
- (244) Komber, H.; Stumpe, K.; Voit, B. *Tet. Lett.* **2007**, *48*, 2655.
- (245) Pomestchenko, I. E.; Luman, C. R.; Hissler, M.; Ziessel, R.; Castellano, F. N. *Inorg. Chem.* **2003**, *42*, 1394.
- (246) Hissler, M.; Harriman, A.; Khatyr, A.; Ziessel, R. *Chem. Eur. J.* **1999**, *5*, 3366.
- (247) Leznoff, C. C.; Suchozak, B. *Can. J. Chem.* **2001**, *79*, 878.
- (248) Kodaira, K.; Okuhara, K. *Bull. Chem. Soc. Jpn.* **1988**, *61*, 1625.
- (249) Wadas, T. J.; Chakraborty, S.; Lachicotte, R. J.; Wang, Q. M.; Eisenberg, R. *Inorg. Chem.* **2005**, *44*, 2628.
- (250) Rachford, A. A.; Goeb, S. b.; Ziessel, R.; Castellano, F. N. *Inorg. Chem.* **2008**, *47*, 4348.
- (251) Miskowski, V. M.; Houlding, V. H. *Inorg. Chem.* **1989**, *28*, 1529.
- (252) Connick, W. B.; Miskowski, V. M.; Houlding, V. H.; Gray, H. B. *Inorg. Chem.* **2000**, *39*, 2585.
- (253) Ji, Z.; Azenkeng, A.; Hoffmann, M.; Sun, W. *Dalton Trans.* **2009**, 7725.
- (254) Cummings, S. D.; Eisenberg, R. *J. Am. Chem. Soc.* **1996**, *118*, 1949.
- (255) Paw, W.; Cummings, S. D.; Adnan Mansour, M.; Connick, W. B.; Geiger, D. K.; Eisenberg, R. *Coord. Chem. Rev.* **1998**, *171*, 125.
- (256) Farley, S. J.; Rochester, D. L.; Thompson, A. L.; Howard, J. A. K.; Williams, J. A. G. *Inorg. Chem.* **2005**, *44*, 9690.
- (257) Cocchi, M.; Virgili, D.; Fattori, V.; Rochester, D. L.; Williams, J. A. G. *Adv. Funct. Mater.* **2007**, *17*, 285.
- (258) Wen, H. M.; Wu, Y. H.; Fan, Y.; Zhang, L. Y.; Chen, C. N.; Chen, Z. N. *Inorg. Chem.* **2010**, *49*, 2210.
- (259) Caspar, J. V.; Meyer, T. J. *J. Phys. Chem.* **1983**, *87*, 952.
- (260) Wilson, J. S.; Chawdhury, N.; Al-Mandhary, M. R.; Younus, M.; Khan, M. S.; Raithby, P. R.; Kohler, A.; Friend, R. H. *J. Am. Chem. Soc.* **2001**, *123*, 9412.



- 
- (261) Siemeling, U.; Bausch, K.; Fink, H.; Bruhn, C.; Baldus, M.; Angerstein, B.; Plessow, R.; Brockhinke, A. *Dalton Trans.* **2005**, 2365.
- (262) Castellano, F. N.; Pomestchenko, I. E.; Shikhova, E.; Hua, F.; Muro, M. L.; Rajapakse, N. *Coord. Chem. Rev.* **2006**, *250*, 1819.
- (263) Four, P.; Guibe, F. *J. Org. Chem.* **1981**, *46*, 4439.
- (264) Price, J. H.; Williamson, A. N.; Schramm, R. F.; Wayland, B. B. *Inorg. Chem.* **1972**, *11*, 1280.
- (265) Iyer, V. S.; Wehmeier, M.; Brand, J. D.; Keegstra, M. A.; Müllen, K. *Angew. Chem. Int. Ed.* **1997**, *36*, 1604.



## Annex

Table 1. Crystal data and X-ray details for **33** and **35**.

Compound	<b>33</b>	<b>35</b>
Empirical formula	C <sub>45</sub> H <sub>40</sub> Cl <sub>8</sub> F <sub>12</sub> N <sub>6</sub> P <sub>2</sub> Ru	C <sub>59</sub> H <sub>48</sub> Cl <sub>8</sub> F <sub>12</sub> N <sub>6</sub> P <sub>2</sub> Ru
Formula weight	1339.44	1483.27
Temperature (K)	150(2)	150(2)
Wavelength (Å)	0.71073	0.71073
Crystal System	Monoclinic	Triclinic
Space Group	<i>C2/c</i>	<i>P1</i>
a (Å)	43.997(9)	10.750(2)
b (Å)	10.867(2)	12.363(3)
c (Å)	24.137(5)	13.715(3)
α (°)	90	104.29(3)
β (°)	113.73(3)	109.57(3)
γ (°)	90	103.46(3)
Volume (Å <sup>3</sup> )	10565(4)	1561.9(5)
Z	8	1
Density calc. (Mg/m <sup>3</sup> )	1.684	1.577
Absorption coefficient (mm <sup>-1</sup> )	0.845	0.684
F(000)	5360	747
Crystal size (mm <sup>3</sup> )	0.20 x 0.10 x 0.10	0.30 x 0.26 x 0.23
Theta range for data collection	1.71 to 25.00°	1.69 to 25.00°
Reflections collected	55127	16404
Independent reflections	9309 [R(int) = 0.0614]	10874 [R(int) = 0.0246]
Completeness to theta	99.9 %	99.9 %
Max. and Min. transmission	0.9202 and 0.8491	0.8584 and 0.8210
Data / restraints / parameters	9309 / 0 / 667	10874 / 29 / 795
Goodness-of-fit on F <sup>2</sup>	1.056	1.048
Final R indices [I>2σ(I)]	R1 = 0.0658, wR2 = 0.1702	R1 = 0.0579, wR2 = 0.1541
R indices (all data)	R1 = 0.0820, wR2 = 0.1798	R1 = 0.0590, wR2 = 0.1555
Largest diff. peak and hole	1.295 and -1.753 e.Å <sup>-3</sup>	1.411 and -0.854 e.Å <sup>-3</sup>

**Table 2.** Crystal data and X-ray experimental details for **43** and **45**.

Compound	<b>43</b>	<b>45</b>
<b>Empirical formula</b>	C <sub>56</sub> H <sub>59</sub> ClN <sub>2</sub> O Pt	C <sub>81</sub> H <sub>96</sub> N <sub>2</sub> O <sub>4</sub> Pt
<b>Formula weight</b>	1006.59	1356.69
<b>Temperature (K)</b>	108(2)	160(2)
<b>Wavelength (Å)</b>	0.71075	0.71075
<b>Crystal System</b>	Monoclinic	Tetragonal
<b>Space Group</b>	<i>C2/c</i>	<i>I4<sub>1</sub>/a</i>
<b>a (Å)</b>	48.298(9)	36.032(7)
<b>b (Å)</b>	6.6097(10)	36.032(7)
<b>c (Å)</b>	37.169(7)	25.334(5)
<b>α (°)</b>	90	90
<b>β (°)</b>	116.925(2)	90
<b>γ (°)</b>	90	90
<b>Volume (Å<sup>3</sup>)</b>	10579(3)	32891(11)
<b>Z</b>	8	16
<b>Density calc. (Mg/m<sup>3</sup>)</b>	1.264	1.096
<b>Absorption coefficient (mm<sup>-1</sup>)</b>	2.740	1.749
<b>F(000)</b>	4096	11296
<b>Crystal size (mm<sup>3</sup>)</b>	0.30 x 0.25 x 0.10	0.30 x 0.05 x 0.04
<b>Theta range for data collection</b>	2.53 to 24.00°	2.27 to 25.00°
<b>Reflections collected</b>	37471	68960
<b>Independent reflections</b>	8215 [R(int) = 0.0554]	14411 [R(int) = 0.1537]
<b>Completeness to theta</b>	98.8 %	99.4 %
<b>Max. and Min. transmission</b>	0.7713, 0.6337	0.9333, 0.6219
<b>Data / restraints / parameters</b>	8215 / 395 / 618	14411 / 550 / 793
<b>Goodness-of-fit on F<sup>2</sup></b>	1.099	1.010
<b>Final R indices [I&gt;2σ(I)]</b>	R1 = 0.0684, wR2 = 0.2024	R1 = 0.1075, wR2 = 0.2730
<b>R indices (all data)</b>	R1 = 0.0806, wR2 = 0.2225	R1 = 0.1810, wR2 = 0.3299
<b>Largest diff. peak and hole</b>	6.821 and -1.471 e.Å <sup>-3</sup>	2.231 and -1.422 e.Å <sup>-3</sup>